AD A129356

RADC-TR-82-339
In-House Report
January 1983

PROCEEDINGS OF THE 1982 ANTENNA APPLICATIONS SYMPOSIUM

Sponsored by
ELECTROMAGNETIC SCIENCES DIVISION
ROME AIR DEVELOPMENT CENTER
HANSCOM AFB, BEDFORD MASS. 01731
AIR FORCE SYSTEMS COMMAND

DTIC
ELECTE
APR 20 1983
H

APPROVED FOR PUBLIC RELEASE; DISTRIBUTION UNLIMITED

DTIC FILE COPY

ROME AIR DEVELOPMENT CENTER
Air Force Systems Command
Griffiss Air Force Base, NY 13441

83 04 20 105

This report has been reviewed by the RADC Public Affairs Office (PA) and is releasable to the National Technical Information Service (NTIS). At NTIS it will be releasable to the general public, including foreign nations.

RADC-TR-82-339 has been reviewed and is approved for publication.

APPROVED: John K. Schindler

JOHN K. SCHINDLER
Chief, Antennas & RF Components Branch
Electromagnetic Sciences Division

APPROVED: Fausto E. Molinet

FAUSTO E. MOLINET, Lt Colonel, USAF
Asst Chief, Electromagnetic Sciences Division

FOR THE COMMANDER: John P. Huss

JOHN P. HUSS
Acting Chief, Plans Office

If your address has changed or if you wish to be removed from the RADC mailing list, or if the addressee is no longer employed by your organization, please notify RADC (EEAA) Hanscom AFB MA 01731. This will assist us in maintaining a current mailing list.

Do not return copies of this report unless contractual obligations or notices on a specific document requires that it be returned.

COMPONENT PART NOTICE

THIS PAPER IS A COMPONENT PART OF THE FOLLOWING COMPILATION REPORT:

(TITLE): Proceedings of the Antenna Applications Symposium (1982) Held at Illinois University at Urbana on 22-24 September 1982.

DTIC ELECTE JUN 17 1983 A

(SOURCE): Rome Air Development Center

Hanscom AFB, Massachusetts 01731

TO ORDER THE COMPLETE COMPILATION REPORT USE AD-A129 356.

THE COMPONENT PART IS PROVIDED HERE TO ALLOW USERS ACCESS TO INDIVIDUALLY AUTHORED SECTIONS OF PROCEEDINGS, ANNALS, SYMPOSIA, ETC. HOWEVER, THE COMPONENT SHOULD BE CONSIDERED WITHIN THE CONTEXT OF THE OVERALL COMPILATION REPORT AND NOT AS A STAND-ALONE TECHNICAL REPORT.

THE FOLLOWING COMPONENT PART NUMBERS COMPRISE THE COMPILATION REPORT:

AN#:		TITLE:
P001	095	An Airborne Rotman Lens Phased Array.
P001	096	Large X-Band Ferrite Scanning Multimode.
P001	097	Low-Cost 1-D Electronically Scanned Dipole Array.
P001	098	Simultaneous Nulling in the Sum and Difference Patterns of a Monopulse.
P001	099	Focused Linear Array for Hyperthermia Research.
P001	100	Structural Stopband Elimination With the Monopole-Slot Antenna.
P001	101	Computer Aided Analysis of a Blass Feed Network for Wide Instantaneous Band Phased Array Application.
P001	102	Optimal Synthesis of E-Scan Space-Fed Antennas.
P001	103	Aperture Efficiency Considerations in the Convolution Synthesis of Symmetrical Hexagonal Arrays.
P001	104	Constraints on Nulling Bandwidth.
P001	105	An Approach to Radar Target Identification.
P001	106	Evaluation of the Monopole-Slot as a Land-Mobile Communications Antenna.
P001	107	Millimeter-Wave Antenna Development.
P001	108	Design of Periodically Corrugated Dielectric Antennas for Millimeter-Wave Applications.
P001	109	Electronically Steerable Spherical Array Provides Multiple Beam Coverage of Hemisphere.
P001	110	Space-Fed, Offset, Plane Wave Cassegrain System for EHF Applications.
P001	111	A Mechanically Scanned, Shaped Beam, 95 GHz Antenna.
P001	112	The Design of a Low Loss and Lightweight Conformal Array Aperture.
P001	113	An S-Band Conformal Array Antenna.
P001	114	A Wire Grid Design of a UHF Antenna.
P001	115	A C-Band Transponder Antenna System.
P001	116	Microstrip Patch Antennas on Thick Curved Substrates.
P001	117	Power Testing of Duroid Stripline Antennas and Associated Circuits.
P001	118	SHF SATCOM Microstrip Phased Array Antenna.

COMPONENT PART NOTICE (CON'T)

AD#:		TITLE:
P001 119		A Circular Parabolic Reflector Antenna With Offset Monopulse Feed.
P001 120		Low Sidelobe Scanning Beams for Parabolic Reflectors.
P001 121		Advanced 30/20 GHz Multiple Beam Antennas for Communications Satellites.
P001 122		Instantaneous Polarization Measurement System.
P001 123		Practical Aspects of Spherical Near-Field Testing.
P001 124		Sidelobe Identification and Discrimination.

Accession For	
NTIS GRA&I	☑
DTIC TAB	☐
Unannounced	☐
Justification	
By	
Distribution/	
Availability Codes	
Dist	Avail and/or Special
A-1	

This document has been approved for public release and sale; its distribution is unlimited.

UNCLASSIFIED

SECURITY CLASSIFICATION OF THIS PAGE (When Data Entered)

REPORT DOCUMENTATION PAGE		READ INSTRUCTIONS BEFORE COMPLETING FORM
1. REPORT NUMBER RADC-TR-82-339	2. GOVT ACCESSION NO. AD-A129356	3. RECIPIENT'S CATALOG NUMBER
4. TITLE (and Subtitle) Proceedings of the 1982 Antenna Applications Symposium		5. TYPE OF REPORT & PERIOD COVERED In-House 6. PERFORMING ORG. REPORT NUMBER
7. AUTHOR(s) N/A		8. CONTRACT OR GRANT NUMBER(s)
9. PERFORMING ORGANIZATION NAME AND ADDRESS Rome Air Development Center (EEA) Hanscom AFB Massachusetts 01731		10. PROGRAM ELEMENT, PROJECT, TASK AREA & WORK UNIT NUMBERS 62702F 46001401
11. CONTROLLING OFFICE NAME AND ADDRESS Rome Air Development Center (EEA) Hanscom AFB Massachusetts 01731		12. REPORT DATE January 1983 13. NUMBER OF PAGES 702
14. MONITORING AGENCY NAME & ADDRESS(if different from Controlling Office)		15. SECURITY CLASS. (of this report) Unclassified 15a. DECLASSIFICATION/DOWNGRADING SCHEDULE

16. DISTRIBUTION STATEMENT (of this Report)

Approved for public release; distribution unlimited.

17. DISTRIBUTION STATEMENT (of the abstract entered in Block 20, if different from Report)

18. SUPPLEMENTARY NOTES

Nicholas P. Kernweis, Contract Monitor

19. KEY WORDS (Continue on reverse side if necessary and identify by block number)

Phased Array Antennas
Millimeter Wave Antennas
Microstrip and Conformal Antennas
Reflector Antennas; Measurement

20. ABSTRACT (Continue on reverse side if necessary and identify by block number)

The Proceedings of the 1982 Antenna Applications Symposium is a collection of the State-of-the-Art papers relating to Phased Array Antennas, Millimeter Wave Antennas, Microstrip and Conformal Antennas and Reflector Antennas.

DD FORM 1 JAN 73 1473

UNCLASSIFIED

SECURITY CLASSIFICATION OF THIS PAGE (When Data Entered)

RADC-TR-82-339

(14)

PUBLICATION RELEASE

TITLE: 94 GHz Antenna Techniques

AUTHOR(S): Oren B. Kesler

ORGANIZATION: Texas Instruments Incorporated

The paper described above will be presented and published at the 1982 Antenna Applications Symposium at the University of Illinois, Urbana, Illinois, September 22-24, 1982.

The material is:

technically accurate

suitable for publication and/or presentation

does not violate proprietary rights

unclassified and cleared for unlimited distribution

Signatures:

Author Oren B. Kesler

Organization/Sponsoring Agency Texas Instruments Incorporated

Date: August 20, 1982

Preface

The Antenna Symposium held at the University of Illinois was co-sponsored by RADC (EEA) Electromagnetic Sciences Division, Hanscom AFB, Bedford, MA and the University of Illinois, Urbana, IL under contract number F19628-82-M-0003.

Accession For
NTIS GRA&I
DTIC TAB
Unannounced
Justification
By
Distribution/
Availability Codes
Dist | Avail and/or Special
A

Contents

* WELCOME by D. C. Drucker, Dean of Engineering, University of Illinois, at Urbana-Champaign

KEYNOTE SPEAKER: Radar Antenna Technology by R. Hill, Naval Sea Systems Command, Washington, D.C. 9

* WELCOME/OVERVIEW OF AIR FORCE ANTENNA NEEDS by Allan Schell, RADC/EE, Hanscom AFB, MA

SESSION I Wednesday, 22 September - Phased Arrays

1. An Airborne Rotman Lens Phased Array by K. Ewen and G. D. Brunner 15
2. Large X-Band Ferrite Scanning Multimode Array by H. Shnitkin and P, Smith 45
3. Low-Cost 1-D Electronically Scanned Dipole Array by D. E. Bostrom, R. E. Hodges, and C. Quan 53
* 4. Magnetostatic Wave (MSW) Delay Lines for Phased Array Antennas by J. C. Sethares
5. Simultaneous Nulling in the Sum and Difference Patterns of a Monopulse Radar by R. L. Haupt 75
6. Focused Linear Array for Hyperthermia Research by W. Gee, R. Chandra, S. W. Lee, R. Mittra, C. Cain, and R. Magin 95

* NOT INCLUDED IN THIS REPORT

PAGE BLANK-NOT FILMED

Contents

7. Structural Stopband Elimination With the Monopole-Slot Antenna by D. Paschen and P. E. Mayes 125

8. Computer Aided Analysis of a Blass Feed Network for Wide Instantaneous Band Phased Array Application by J. Wojtowicz, P. Hacker, and K. Ramsey 143

9. Optimal Synthesis of E-Scan Space-Fed Antennas by J. L. Bauck and S. M. Daniel 167

10. Aperture Efficiency Considerations in the Convolution Synthesis of Symmetrical Hexagonal Arrays by J. P. Shelton and S. R. Laxpati 197

11. Constraints on Nulling Bandwidth by P. R. Franchi 231

12. An Approach to Radar Target Identification by M. Hurst, R. Mittra, and S. W. Lee 245

13. Evaluation of the Monopole-Slot as a Land-Mobile Communications Antenna by B. Halpern and P. E. Mayes 259

SESSION II - Thursday, 23 September - Millimeter Wave Antennas

14. Millimeter-Wave Antenna Development by R. B. Dybdal 291

15. 94 GHz Antenna Techniques by O. B. Kesler - AD-P 000 584 301

16. Design of Periodically Corrugated Dielectric Antennas for Millimeter-Wave Applications by F. Schwering and S. T. Peng 333

17. Electronically Steerable Spherical Array Provides Multiple Beam Coverage of Hemisphere by T. H. Taylor, Jr. 355

18. Space-Fed, Offset, Plane Wave Cassegrain System for EHF Applications by L. M. Schwab, A. R. Dion, and D. L. Washington 367

19. A Mechanically Scanned, Shaped Beam, 95 GHz Antenna by J. Green and H. Shnitkin 393

* 20. EHF Satcom Aircraft Antenna Study by G. Skahill

* 21. Millimeter Wave Microstrip Antennas by F. Lalezari and R. E. Munson

Microstrip and Conformal Antennas

22. The Design of a Low Loss and Lightweight Conformal Array Aperture by D. J. Martin, C. A. Chuang, and N. Moldovan 413

* NOT INCLUDED IN THIS REPORT

Contents

23. An S-Band Conformal Array Antenna by C. A. Chuang 429

24. A Wire Grid Design of a UHF Antenna by M. S. Sohel and T. G. Pickard 443

25. A C-Band Transponder Antenna System by P. J. Conroy 467

26. Microstrip Patch Antennas on Thick Curved Substrates by N. G. Alexopoulos, P. L. E. Uslenghi, and N. K. Uzunoglu 473

27. Power Testing of Duroid Stripline Antennas and Associated Circuits by George J. Monser 485

28. SHF SATCOM Microstrip Phased Array Antenna by Brian C. Considine and David L. Wandrei 505

SESSION III - Friday, 24 September - Reflectors, Measurements and Accessories

29. A Circular Parabolic Reflector Antenna With Offset Monopulse Feed by M. J. Dick, D. Killion, E. Mehner, R. Justice 535

30. Low Sidelobe Scanning Beams for Parabolic Reflectors by C. C. Hung 565

* 31. Application of MMIC Modules in Future Multiple Beam Satellite Antenna Systems by J. Smetana

32. Advanced 30/20 GHz Multiple Beam Antennas for Communications Satellites by R. W. Myhre 581

33. Instantaneous Polarization Measurement System by W. F. McNaul 613

34. Practical Aspects of Spherical Near-Field Testing by J. J. Tavormina 633

(35) Ultra Low Sidelobe Planar Near Field Measurement Study by K. Grimm 663 - A117744

36. Sidelobe Identification and Discrimination by P. R. Eberhardt 683

* NOT INCLUDED IN THIS REPORT

KEYNOTE - "RADAR ANTENNA TECHNOLOGY"

1982 Antenna Application Symposium
University of Illinois
22 Sept 1982

To tell you the truth I don't recall exactly how I got to be your keynoter this morning. In my government career in Radar, I've been to many conferences such as this, and generally the keynoter is some very senior official from DOD who can talk of money to be devoted to certain research - very impressive - whereas I am buried so far down in the trenches of NAVSEA that it was hard just to climb out to get to Illinois, let alone say anything profound. I'm just an ordinary "user", I guess, who can share with you some thoughts on antenna technology. Actually, this conference reminds me a bit of the power tube conference held every two years out at Monterey where that community deliberately tries to compare notes with its "user-community" - and they ask enthusiastically for system people to attend and participate - and I think it's quite to everyone's advantage.

My own background is indeed radar systems for the Navy, a considerable phased array emphasis over the last twenty years - I'll try not to favor that point too much as we proceed.

It might be well to reflect upon the nature of antennas - their "character" so to speak - from an applications point of view - then we'll talk about problems and challenges in both antenna design and use, field use, for both "conventional" antennas (we've got to find another adjective for non phased arrays) and phased arrays.

The antenna - I do considerable teaching in radar and I point out to students how the antenna, more vividly than any other of the subsystems, displays its purpose and a good deal of that of the radar. The very term has a biologic ring to it so apt - it is our probe of our surroundings, very visible - exposed (something more about that later), has a wavelength dependence usually quite visible, beam shape, beam and scan dimensions usually estimable by inspection, feed details reveal even a second level of design detail about monopulse or pattern sophistication - the antenna, then, speaks loudly of its own purpose.

Not, again, unlike in the power tube and transmitter design areas, has the antenna in the last twenty years come to be recognized for the signal processing element it is. Now, certainly, it samples space and we'd like that "spatial response function" (or "sampling window" or pattern to us) to be an impulse - but we do know that our limited aperture, true to sampling theory, results in certain aliasing of spatial data - because of multiple target and clutter and jamming or interference concerns, one wants low sidelobes or as "unfolded" an estimate of the nature of our surroundings as possible - this prevails in even rather static system operations, fixed installations. But then we move the earth as a parallel sheet under, say, a high preformance APY-1 (AWACS) radar, expecting to look down on it (the earth) and discern by doppler discrimination targets moving even at a tank's pace over its surface! Doesn't take much geometric imagination to see the relationships among sidelobes, ground clutter, and doppler processing in the design of this important antenna.

PAGE BLANK-NOT FILMED

So we see the antenna as an element of the signal processing - the "spatial transfer function" which is of much more interest to us than is its pattern alone or even the simple containment of its input impedance near the center of a Smith chart.

The character of an antenna - it speaks vividly of the functions of the radar; it is our space probe and a true element of the signal and target detection processes.

I mentioned problems and challenges in antenna design, fundamental design toward an impulse-like spatial sensitivity - I believe we've gone through a period of fascination (that's perhaps too harsh a term - I mean it very kindly) with adaptive processes in the form of the coherent sidelobe canceller loops - a step toward completely adaptive apertures growing naturally out of the Syracuse (GE and University of) work of Sid Applebaum and others - and are settling into a proper emphasis upon low sidelobe design in the "main" antenna itself with cancellers as needed - again the earlier mentioned APY-1 work at Westinghouse involved some of the real dedication to low sidelobe design - the use of cancellers as a supplement only was exemplified in the British work on their shipboard "STIR" (Surveillance and Target Indication Radar) wherein the horizontal line feed and horizontally disposed precision cylindrical reflector attested to the low sidelobe design and a rather directive auxiliary was used with a canceller loop to treat just the nearest-in first sidelobe, not quite as low as the rest in their design. The Westinghouse motivation - doppler processing in a look-down airborne radar; the British motivation - to effect automated detection in a truly reliable way.

CSLC itself reminds us of the signal processing nature of such antennas - this feature is not so much "side-lobe cancellation", you know, as it is signal cancellation (jamming signal, a composite of several sources perhaps) - extensions go to other forms of adaptation - the multi path-effect reduction work of Warren White, the partial adaptive array work of Ross Turner at CRC-Ottawa and the Aperture Signal Processing of ITT's STL Harlowe division in England.

Incidentally, the precision feed and reflector design of the British STIR made it quite heavy in its early version, particularly with its shipboard stabilizing apparatus included - one needs to keep up with what the newer materials, the composites and matrix materials can offer in lighter weight designs, structurally as rigid and precise.

A further discomfort with these extraordinary low sidelobe designs is the sensitivity to siting, to nearby objects - several have found that objects nearby can cause a pattern degradation that is more severe over, also, a wider angle than the degradation similarly induced to an antenna of less ambitious excitation control. This concern of the user in siting makes one wonder if a localized parameter store wouldn't be desirable, a sort of burned-in weighting or auxiliary control specifically tailored to the site. The term "parameter store" conjures the memory of the measured pattern store used in the SPG-59 experimental phased array (spherical) radar of the later aborted Typhon weapon system of the early 1960's in the Navy - occupied two semi-trailers or some such on the deck of the demonstration ship - scaring us all away from radar processes that would require "parameter storage" - but we should be alert to the fact that today, such storage would require nothing of the sort and might be quite attractive indeed - technology has, perhaps, made it so.

I said I'd return to the matter of antennas being (obviously) exposed - we've been concerned over their inherent survivability. As this subject is treated, from time to time one encounters a "there's obviously nothing we can do about the antennas" comment - a first blush - that's just not so. Some imagination in survivable antennas, new materials again, but also new forms - the feed kept in a well armored mount (pedestal) with the reflector extended (easily replaceable?) makes more sense perhaps than the common extension of a waveguide run and feed horn in front of a centered reflector which I assume was an earlier eg-over-the-axis desire perhaps not so necessary today.

While still on the reflectors or "conventional" antennas, I want to give some credit to those pursuing the "mirror scan" techniques - some qualification, however. When couched in terms of a regular, continuous, say 360°, scanning antenna for air or surface search I fail to see much appeal - BUT - when the low inertia mirror above is caused to flit rapidly about (without, you see, moving the feed at all - and withits reflective 2:1 angle advantage, beam position per unit mirror position) then I believe we're on the right track for something contributive, something more toward dwell matching to our heterogeneous surroundings. All the difference in the world to me between those two kinds of applications.

Our mentioning adaptive processing of one type or another brings to mind one other variable that remains basically under antenna control and which one wonders if we're exploiting to full advantage - I'm refering to polarization - we do very little with it as a controllable characteristic in Navy radars, yet there must be strategies to employ gainfully. The paper by Gary Evans and Hoover of Westinghouse in 1980 (this conference) attests to method, that in admittedly a phased array context, and to method being a bit complex. Polarization control, adaptivity - not well exploited, I think, in fielded systems of either simple or array antenn

As long as I've mentioned phased arrays, perhaps we'd better move right in to that subject.

Little has changed the field of antenna design so profoundly as has the advent of the phased array - think of it: determined illumination function, adaptation possibilities in elemental control, inercialess beam positioning, data dependent immediate operations - and indeed it has been so, witness the SPY-1 of AEGIS among others. Match with this antenna to the heterogeneous surroundings. Finally, how like the antenna operation in nature, in insects responsive to that being sensed and rarely if ever scanning in some orderly left-to-right for-want-of-better-strategy manner. And, by its nature, we antenna engineers have been brought back into the factory, piecepart design and construction much more complex than that involved in other antenna ("conventional") production. Now therein lies a problem - cost. Those of us users happiest with the system behavior phased arrays have brought us, should be as unhappy at the price that must be paid to purchase them - millions of dollars per face in practice - not a proud scene. Obviously the community must "R&D the cost down" to stretch for a verb (pardon) - not indict phased array use to the degree some do, but to help reduce cost. This "factory process" was in the development at RCA of the SPY-1 arrays quite an awakening for me - went from exhaustive trade offs on paper comparing the cost of ferrite and of garnet material weighing same against certain thermal characteristics, to a realization within a year that if the materials had been free the array would still have cost millions - soon we were legitimately into vendor defaults, factory work-around plans, incoming inspection and chancey sampling, test with statistical foundation and so on. In addition to this RCA experience, we've

tried to sustain an interest and some investment in alternatives - the microwave group at Hughes Fullerton has always been helpful, a good mix of pure microwave theory and manufacture. The thick film on alumina circuitry for phased arrays, possible after they solved the conductor adhesion problem in one compound a few years ago, is an example. Also, I was there recently, being shown some diodes suitable for the phase shift function in a module - but which "diodes" were of considerable dimension, little rectangular prisms, not at all the fly spec more commonly seen. "Oh," it was explained to me, "that's the way we've ordered them from the supplier, in an encapsulation such that the robot can grab them in the manufacture of the modules." A small matter, but impressed me well.

I might state that here is a role of engineering not very well represented in the symposium or in others like it, I suppose - easily could a session here have been justified, a session in "antenna manufacture" - it's so important, so much a part of "complete" engineering that I would encourage such consideration next time. Probably difficult to get too far into what industry may regard as proprietary, but nonetheless I think you should try to treat the subject. We should all try to dramatize, lend some excitement to this important part of engineering!

A few things that have a cost reduction potential (but precious few) have caught my eye in the last decade. While we may legitimately include amplifiers in arrays for certain whole-system advantages, that isn't going to do much to reduce array cost. If anything, cost will remain somewhere around the sum of the costs of an array and a transmitter; this is expected since an amplifying array will still be element emphatic. There's another branch of pursuit, however, in which fixed aperture operation is achieved with more "amorphous" structures, perhaps not arrays in the piece part design and construction at all. The RADANT approach of AMP in Paris was of some interest to me several years ago largely because it was different, a break away from building and stacking phase shifers. This control of the permitivity of large dielectric sheets in which varactor diodes are strung on thin control wires (tape-like) in a grid is not without design problems and limitations - and perhaps fine granularity and excitation control will be forever difficult - but it was imaginative and for some radar applications perhaps suitable now. While hardly "amorphous", there surely is simplicity to some of the micro-strip approaches such as the Ball Aerospace conformal array matters presented here in 1980. For just plain being different, I've got to cite the "array" described as the "crow's nest" by Wilder of FFM in Germany (1980 IEEE International Radar Conference).

Still with regard to cost, one needs to cite the 1970's successful developments in the testing of phased arrays - whether you're thinking of proof of development and design verification, or of acceptance testing for arrays in production, or of diagnostics at a nearly per-element level, the comparison between what we did on a multi-axis step rotation mount big enough to take patterns in the conventional way on the 16,000-lbs original SPY-1 antenna (including the torment we went through to determine what sampling of patterns to do in the first place) and what can be done at the near-field test facility now at RCA brings credit indeed to what in my experience were the efforts of Georgia Tech, the National Bureau of Standards (Boulder), Jan Snieder in the Netherlands, Bill Patton at RCA and others (Hughes in Firefinder testing, for example) contributing to this technique. I note that several papers concerning this subject are to be given here on Friday.

Finally, another word on phased arrays, on fielding them (a word good for any antenna, actually, - any piece of military equipment) - we must expect the unexpected. I'm reminded of our early 1960's experiences at NRL with the Blass reflect-array (diode controlled short circuit for reflective position in the necks of waveguide horns constituting each element) when Keith Meads called me at BuShips to indicate we had a problem, a noise source "jamming" in effect radar reception - the source appeared to be in the array itself and, curiously, active in the receive period to be sure, but only after transmissions - couldn't be duplicated or caused in receive-only operation of the array. Seems one phase shifter - one diode - had developed a bit of an ionized or carbonized path around the junction such that the several hundred volts of back bias (if that were the state involved) was not enough to cause conduction to initiate, but <u>was</u> enough to <u>sustain</u> the breakdown if the added r.f. field during transmit were enough to trigger conduction - and it was. Here, then an example of <u>one</u> phase shifter, among over 2000, causing complete array failure - yet how often have we all used the old refrain "of course, the array's performance is not appreciably degraded with even 10% of the elements failed". Of course, we mean passive benign failures in that claim - yet that isn't necessarily how they fail, or can fail, evidenced the Blass experience; one more "active" failure or, similarly, less than 10% in some orderly way (a region, a periodic structure, a row) can be a more serious matter, perhaps induced by a control or feed failure with localized, not random, consequences.

Oh - but in general we've come a long way, haven't we, from the time just twelve or so years ago when the assertion of phased array suitability was met with the user comment "but how will I know it's forming a beam?" - no reflector to look at!

Now to wrap up - I've keynoted, so I guess I should rattle off the <u>key notes</u> I've sounded, key words from this address:

Antenna's nature - element of signal processing whose spatial transfer function is of interest

low sidelobe design, precision, heavy, new materials, site sensitivity, can be adapted out? aided by use of "parameter store"?

mirror scan use: <u>irregular</u> scan

polarization control well exploited?

arrays - cost, the factory process, R&D the cost down, the factory process as crucial and exciting <u>engineering</u>, dare to be different in research - like RADANT, Crow's Nest, huzzah for near field testing; careful of the 10% rule, that's not what's going to happen

My thanks to those who invited me to speak to you and to you kind enough to listen. Good luck in what promises to be a splendid conference.

AD P001095

AN AIRBORNE ROTMAN LENS PHASED ARRAY

Kenneth Ewen and Gary D. Brunner

Goodyear Aerospace Corporation

Arizona Division

Litchfield Park, Arizona 85340

ABSTRACT

An airborne single axis phased array has been designed using a folded Rotman Lens as a cost and performance effective alternative to a phase shifter steered array.

Significant aircraft space and weight restrictions were met by use of a folded parallel plate lens for power division and beam steering in the azimuth plane and air stripline for power division in the elevation plane. Mechanical design of the antenna emphasized producibility of the components using numerically-controlled milling machines and repetitive assembly techniques.

1. INTRODUCTION

Airborne radars in reconnaissance, guidance, and weapon delivery modes are placing increasingly severe requirements on antennas, including wide instantaneous and total bandwidths, wide angle beam scan, selectable beamwidths, and sidelobe control. These requirements must be met in the face of aircraft volume, weight, and environmental restrictions that call for unique solutions.

PAGE BLANK-NOT FILMED

In particular, synthetic aperture radar (SAR), which has been used in Goodyear Aerospace Corporation-produced operational reconnaissance radars such as the AN/UPD-8 since the mid 1960s, will be used in fire control, weapon delivery, and higher performance reconnaissance radars. Instantaneous bandwidths in excess of 100 megahertz (MHz) will be required for range resolution; wide angle scan will provide aircraft motion compensation, target acquisition, tracking and identification; and sidelobe control will be necessary for aircraft survivability.

The next generation reconnaissance aircraft will have interchangeable pods holding a variety of sensors. Antennas must be compatible with pod diameters, compete with other electronics for area and location, and operate in a nonpressurized environment over temperature extremes.

Phased arrays have promised to satisfy many of the requirements, but have been plagued by cost, weight, environmental, power, and performance problems.

This paper will describe a Goodyear Aerospace-sponsored Rotman lens phased array suitable as a prototype for an antenna for a pod-mounted reconnaissance radar. This single axis scanned array offers a cost-effective alternative to a phased array, and for wideband systems can provide superior performance.

2. PERFORMANCE REQUIREMENTS

On the basis of assumptions made regarding the performance requirements of future reconnaissance radars a set of minimum antenna

performance requirements was generated which are representative of the requirements for an advanced pod-mounted system operating in X-band. The results are presented in Table 1. Also considered were the physical and environmental constraints imposed by a pod installation which are presented in Table 2.

3. CONCEPTUAL DESIGN

3.1 General - In anticipation of the operational needs of next generation reconnaissance radars Goodyear Aerospace sponsored a study to define an

TABLE 1 – MINIMUM ANTENNA REQUIREMENTS

Gain	≥ 33 dB
Azimuth beamwidth	≤ 1.8 deg
Azimuth sidelobes	≤ -18 dB
Azimuth beam pointing	±20 deg both sides of aircraft
Elevation beamwidth	Shaped or selectable
Elevation sidelobes	≤ -13 dB
Elevation beam pointing	±25 deg both sides of aircraft
Instantaneous bandwidth	= 120 MHz

TABLE 2 – PHYSICAL ANTENNA CONSTRAINTS

Volume	27-in.-dia x 72-in.-long cylinder
Weight	≤ 250 pounds (lb)
Altitude	≤ 40,000 feet (ft)
Temperature	-65 deg Centigrade (C) minimum, +125 deg C maximum

optimum antenna approach for these applications. Tradeoffs were performed among various antenna types including mechanically steered reflectors and arrays and electronically scanned arrays (ESAs). The outcome of this effort was a concept for a lens-fed planar array which achieved azimuth scanning through the motion of a small feed horn within the antenna envelope. By realizing beam scanning without physically steering the antenna, the swept volume demands of the antenna were minimized and the available aperture was maximized. By relying on a mechanical approach the cost/complexity penalties of electronic scanning were avoided. The true time delay nature of the scanning produced in this manner and reliance on TEM propagation paths throughout the lens results in an inherently wide bandwidth.

Elevation beam steering would be accomplished by conventional roll axis control and elevation beam selection is employed in preference to beam shaping because of the left/right look direction requirement. The advantages offered by this concept were sufficiently compelling to warrant development of a prototype model with the antenna performance requirements set forth earlier serving as performance objectives. A drawing of the prototype concept illustrating the key development areas is shown in Figure 1.

3.2 Lens Concept - The backbone of the candidate approach is the wide angle constrained microwave lens used to feed the planar array. Constrained microwave lenses are characterized by the fact that they do not obey Snell's Law, the feature which results in their wide angle scanning

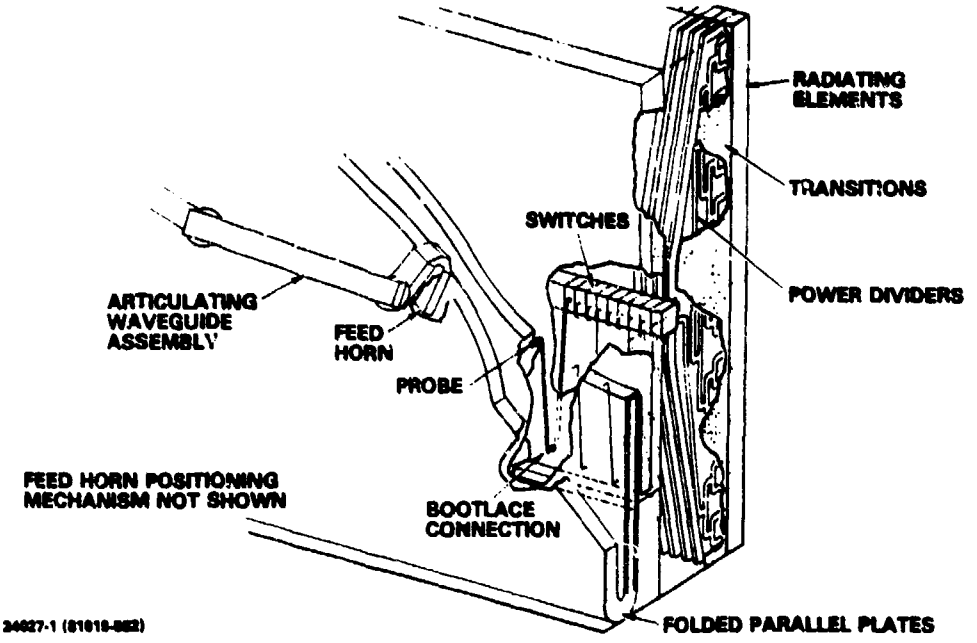

Figure 1 – Rotman Lens Phased Array

properties. Snell's Law is circumented by establishing fixed path lengths (transmission line connections) between corresponding points on the two surfaces (or contours) of the lens. Under these conditions lens performance becomes dependent on specification of the inner and outer lens contours, the path length variation and position within the lens, and the focal path. Ruze[1] studied constrained lenses having collinear constant electrical length paths between inner and outer lens faces which produced a lens design having two points of perfect focus located symmetrically with respect to the axis. A lens configuration offering performance advantages over the Ruze type was investigated by Rotman and Turner[2]. Figure 2 depicts the Rotman lens configuration schematically using his notation. The optimum focal path for the Rotman lens is a circular arc, R, passing through the three perfect focal points, F_1, G, and F_2.

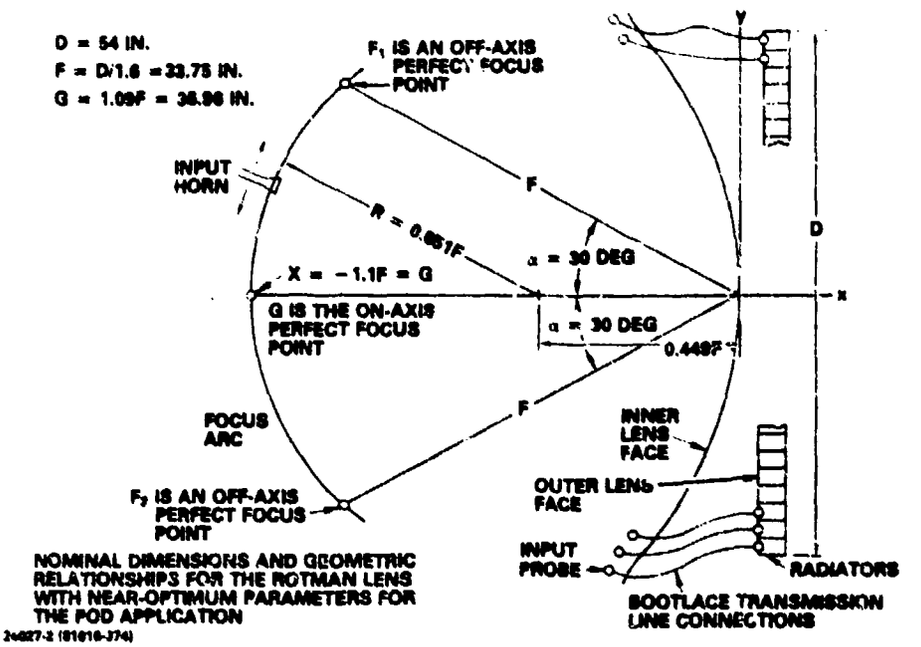

Figure 2 — Rotman Lens Concept

4. IMPLEMENTATION

4.1 Block Diagram - A functional description of the main developmental areas associated with implementation of the Rotman lens phased array is presented here, with a more detailed discussion of design considerations following.

The radiating aperture is a 54-in. long by 18-in. high assembly of 80 vertical radiators. Each vertical radiator consists of 20 contiguous open-ended waveguide elements joined on their narrow walls and is connected to a power divider assembly containing one 16-way and one four-way corporate power divider network, and a three-way switch. The 20 outputs of the power divider network transition to the 20 waveguide

elements of the vertical radiator. The three-way switch permits selection of either 4-, 16-, or 20-element vertical apertures.

The input of each vertical power divider assembly connects to the output of a "bootlace" lens element, a length of semirigid coaxial cable cut to a dimension determined from the lens design equations based on its position within the aperture. The input end of the bootlace lens is in turn connected to the output of the parallel plate region through an array of E-field probes extending into the parallel plate region along a contour, and at intervals, specified by the lens design. The parallel plate region is terminated by a reflecting surface behind the probe array which corresponds to the inner lens contour.

To accommodate the 37-in. focal length of the lens within the 27-in. dia allocated to the antenna, the parallel plates are folded. The input end of the parallel plate region is open to permit traversal by the feed horn which illuminates the lens. The H-plane feed horn extends into the parallel plate region and travels on a track mounted to an outer surface of the parallel plates with a contour corresponding to the focal arc of the lens system. The feed horn is driven by a direct current (DC) torque motor through a steel band drive. Position is controlled by a feedback loop and position sensing is accomplished by means of a linear sensor mounted directly to the drive track. Connection of the microwave signal to the moving feed horn is through an articulating waveguide assembly comprised of three rotary joints and interconnecting waveguide. A stationary waveguide run connects the articulating waveguide assembly with the antenna

input through a roll axis rotary joint in the rear mounting plate. A DC torque motor provides the roll axis drive. Mounting of the antenna is by means of forward and aft mounting plates. The antenna is enclosed in a thin-walled composite cylinder for pressurized operation in a nonpressurized pod.

Overall antenna length including the fore and aft mounting plates is 68 in. The maximum diameter is 25 in. at the rear plate. The microwave section is 13.5-in. deep including feed waveguide and will roll within a 10.7-in. radius.

Front and rear views of the antenna are shown in Figure 3. The front view shows the radiating array and the vertical power dividers, while the rear view is of the complete antenna less the pressure cylinder and forward mounting plate. Figure 4 is a section through the vertical midplane of the antenna showing the folded lens, bootlace cables, and vertical assembly relationships.

4.2 Lens System Design -

4.2.1 Lens Parameters - The choice of lens parameters will depend upon the design scan angles, maximum desired scan angle, lens depth, and number of radiators and can be established by analysis[2]. In addition, the aperture illumination as a function of the feed horn, lens output curve, and scan angle must also be considered.

The antenna azimuth dimension had been fixed at 54 in. by available mechanical space, with a total of 80 radiators from radiator voltage standing wave ratio (VSWR) calculations. Additional tradeoffs established that

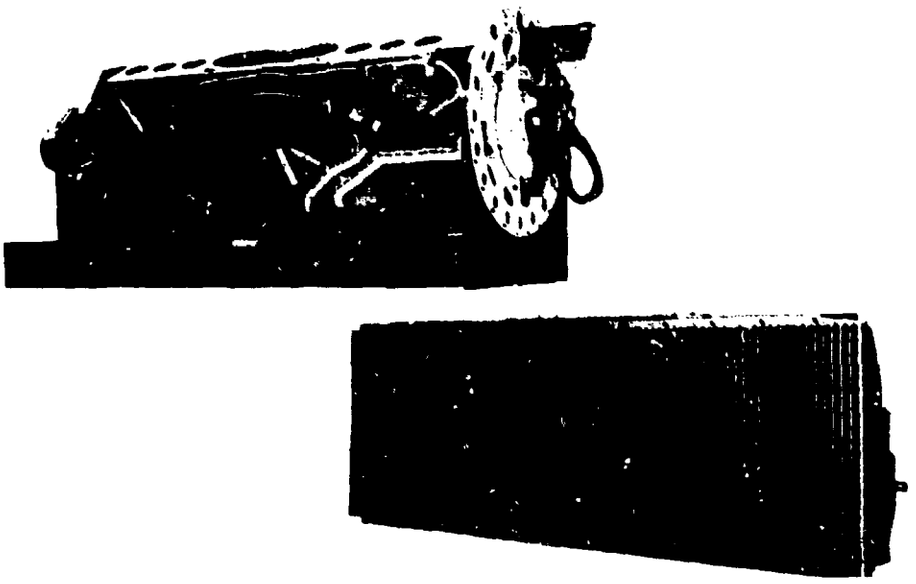

Figure 3 – Rotman Lens Phased Array Antenna

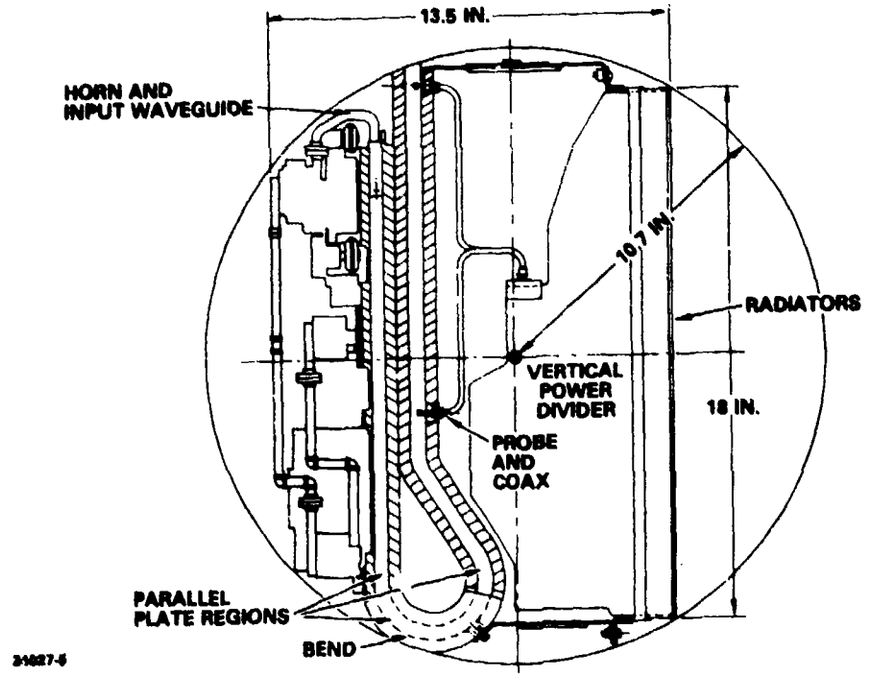

Figure 4 – Antenna Cross Section

G = 36.956 in., F = 33.75 in., and α = 30 degrees would provide acceptable aperture phase errors for all scan angles over a 0 to ±38-deg region and a mechanical geometry suitable for folding.

Additional calculations were made of sidelobes, beamwidth, and gain loss expected for various scan angles and feed horn aperture. Typical data is shown in Figure 5 and the expected antenna performance for the selected horn dimensions is given in Figure 6. Performance obtained with the 2-in. aperture horn was considered a best compromise between beamwidth, sidelobe, and relative gain loss, based upon expected overall radar performance.

Calculations were also performed to establish feasibility of a low sidelobe (≈40 dB) antenna, and while the data indicated that this level was achievable, a low sidelobe design was not pursued on this effort.

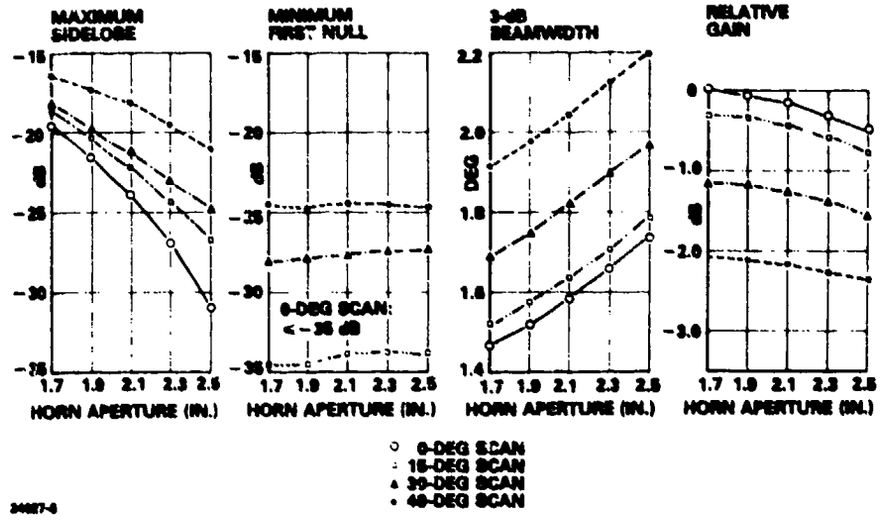

Figure 5 – Computed Lens Performance for Horn Feed

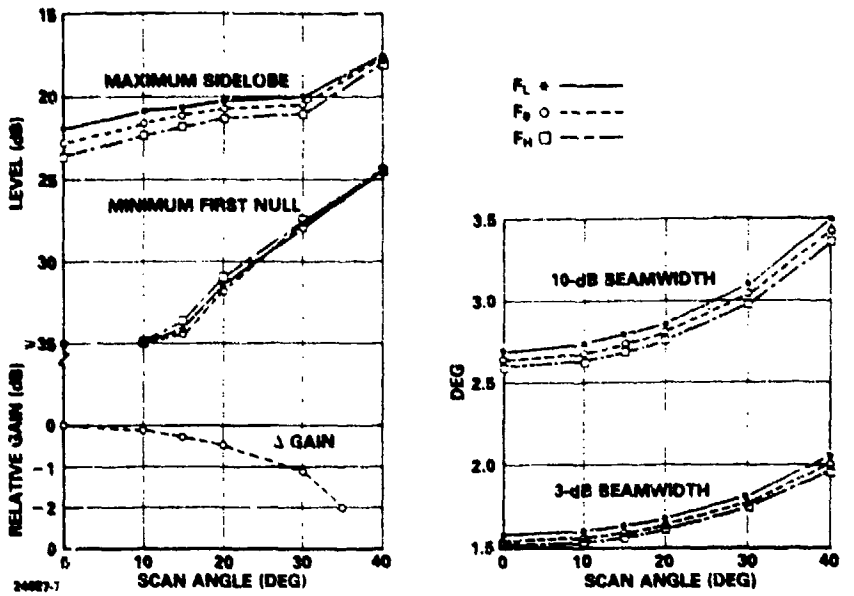

Figure 6 — Expected Performance for Selected Feed

4.2.2 Lens Output Probes and Cables - The output probes in a Rotman lens are not uniformly spaced, but rather are a function of radiator location from the centerline. The spacings for this design are shown in Figure 7.

Large spacings on the edge probes can lead to a grating lobe being generated internally in the parallel plate region which would degrade the radiated pattern and gain data. The incidence angle at which the grating lobe will enter visibile space is

$$\theta_i = \sin^{-1}\left[\frac{\lambda}{S} - 1\right] \quad , \tag{1}$$

where S is the average spacing to the adjacent probes.

Incidence angles between each probe and the horn are shown in Figure 8 for four scan angles. The use of this data and Equation (1) established that no more than four probes up to a scan angle of 30 deg and six

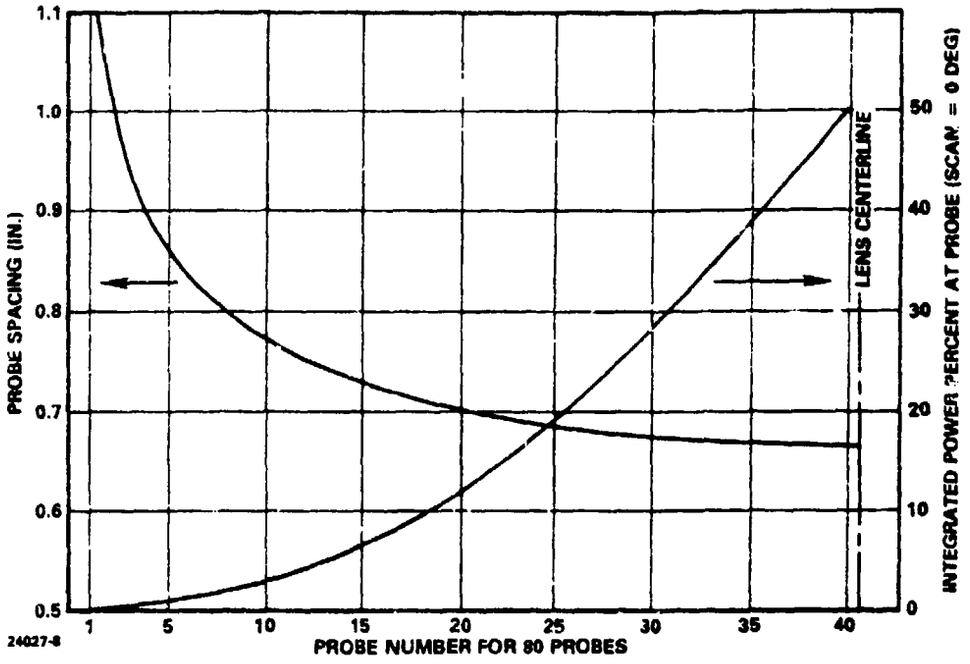

Figure 7 – Probe Spacings

probes at 40 deg could establish a grating lobe and that only 1 to 2 percent of the total energy would be incident on those probes. Moreover, Figure 8 shows that the spacing of the edge probes is rapidly varying, and the periodicity of the spacing is nonexistent. This led to the conclusion that any grating lobe effects would be negligible.

A waveguide simulator was used to match the probes in an array environment. Inspection of Figure 8 will show that a probe matched over a range of incidence angles of 0 to 35 deg would cover virtually all probes of a ±30-deg scan region. The waveguide simulator in Gustincic[3] simulates the operation of a probe in an infinite array by consideration of the TE10 mode in waveguide as composed of two plane waves with incidence angle θ given by

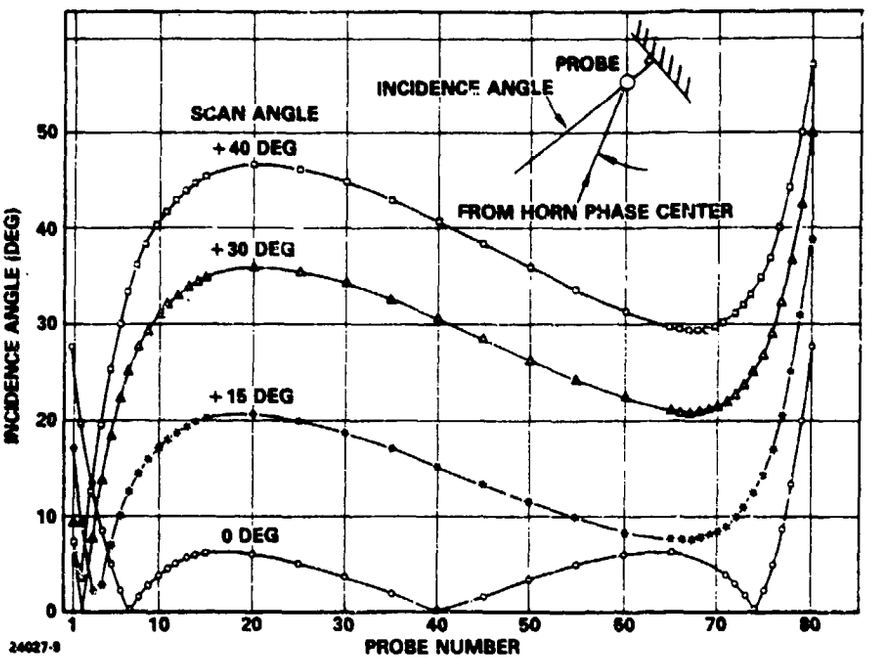

Figure 8 – Probe Incidence Angle from Horn

$$\sin \theta = \frac{\lambda}{2a} \quad , \tag{2}$$

where a is the guide width. In theory any angle of incidence can be simulated, provided higher order modes are suppressed and the probe spacing being simulated is maintained by use of multiple probes when required.

The probe was matched to a VSWR of under 1.10 at an incidence angle of 31 deg by adjustment of the distance between the probe and the end short plate, and by addition of a capacitive button to the probe tip. Incidence angles less than 31 deg were expected to also have an acceptable VSWR.

The bootlace cables are standard UT-141 semirigid with solid dielectric. A number of alternates were considered, but all were either too expensive to offset any performance improvements, were supplied only in

precut lengths with connectors attached, or did not exhibit good phase stability during environmental testing.

Good phase stability in the selected cable was achieved by an initial heating of the cables to an elevated temperaure, trimming off the extruded teflon, and attachment of the SMA connectors. Additional tests over a wide range of temperatures demonstrated that the cable phase could be controlled to better than 3 deg using this technique.

4.2.3 Lens Folding - A major obstacle to be overcome in the implementation of the lens fed array was accommodation of the parallel plate propagation region within the antenna envelope. For acceptable phase deviation and scan angle results, a lens F/D $\cong$ 0.7 was required, which posed a space factor problem. The most acceptable solution to this problem was to fold the parallel plates. However, the bend introduced by folding creates a phase shift which will be dependent on the angle of incidence, θ_i, at the bend. Because θ_i will be both probe number and scan angle dependent, compensation will be difficult. Calculations showed that, for a ±30-deg scan, θ_i will vary from 0 to 30 deg for probes near the lens center, and from 30 to 70 deg for edge probes. The largest differential change is on the order of 40 deg.

Computation of the phase shift was made by two methods. The first used equations in Marcuvitz[4] for an E-plane waveguide bend, with changes in θ_i made by adjustment of the waveguide width. The second method (Bahar[5]) required solving the wave equation in cylindrical coordinates.

Because the bend angle can assume any angle, the solution requires Hankel functions of real, non-integer order.

The two solutions are compared in Figure 9 for a 180-deg E-bend with a 1-in. centerline bend radius and 0.5-in. plate separation. The agreement is well within acceptable tolerances, and Marcuvitz[4] equations were subsequently incorporated into the lens design computer program.

Several approaches to fabricating the folded parallel plates were investigated. The approach which best met the requirements of low weight, low propagation loss, structural integrity and intraplate alignment without intraplate support, was a precision assembly of 10 aluminum numerically-controlled machinings. Alignment is controlled through the inner

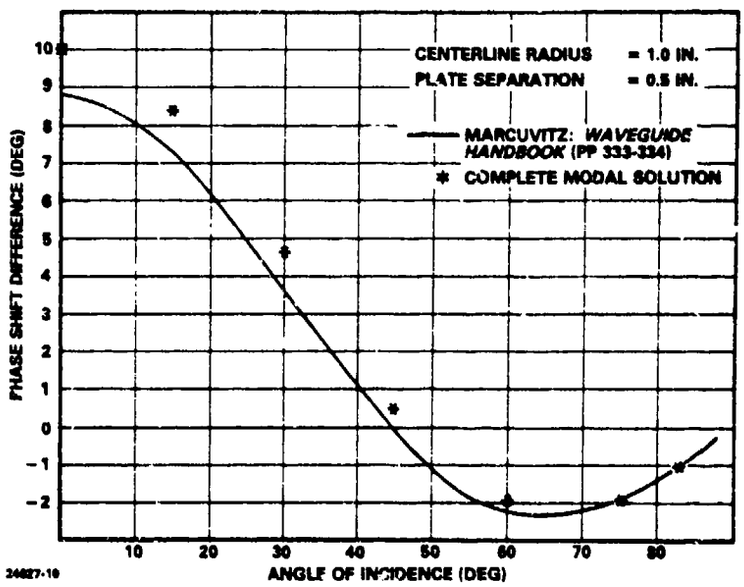

Figure 9 – Phase Shift Difference Between Unfolded and Folded Parallel Plate at 180-Deg E-Plane Bend

and outer bend sections and the end caps which tie them together. The flat plate sections bolt to the bends with close tolerance tongue and groove joints ensuring alignment. An optimum balance between weight and structural integrity was achieved by machining a quilted pattern on the outer surfaces, thereby incorporating integral structural stiffeners. Plate thickness between the structural stiffeners was reduced to 0.020 to 0.030 in.

4.2.4 Feed Horn - A conventional H-plane flared horn with a 2- by 0.4-in. aperture was used as the lens feed. Quarter-wave chokes were used to reduce radio frequency (RF) breakdown potential between the horn and the parallel plates. Teflon buttons on both top and bottom of the horn worked as a low-friction contact and centering mechanism between the plates.

Initial lens calculations used a theoretical H-plane horn pattern. After selection of the 2-in. aperture was made, a number of horn patterns were measured in a parallel plate and used to further refine the calculated performance.

Feed horn positioning required special attention. A search for a suitable means of position sensing led to a device known as the Inductosyn, manufactured by Farrand Controls. The Inductosyn provides highly precise linear position sensing and permits the position sensing to be accomplished directly at the feed horn. The Inductosyn consists of a stationary printed circuit approximately 0.5-in. wide extending the length of the feed horn track, a sensing element which mounts to the feed horn, and remote electronics. The overall closed loop horn positioning accuracy is on the order of ±0.004 in., which is equivalent to a worst-case angular uncertainty

of ±1 arc minute (0.017 deg). The Inductosyn was chosen over comparable optical sensors because of its tolerance to accumulated surface contaminants as well as its tolerance to wide temperature excursions.

Another aspect of the feed horn positioning problem is the design of a transmission line connection between the roll axis rotary joint (the antenna system input) and the feed horn which is capable of accommodating the wide range of feed horn motion. High power handling capability, low loss, and reliability were the governing design considerations. The approach followed which produced excellent results was an articulating waveguide assembly made up of two movable waveguide sections connected to each other and to the horn and stationary input waveguide by three rotary joints.

The feed horn mounts to a hardened V-groove track via rollers. The feed horn track is concentric with the focal arc and is positioned so that the feed horn phase center falls on the focal arc. The feed horn is positioned by a servoloop consisting of a steel tape drive band connected to a DC torque motor with the Inductosyn providing the loop error signal. The loop electronics are contained in a separate antenna control unit located remote from the antenna.

4.3 Array Design -

4.3.1 Waveguide Radiator - The radiator is an open-ended waveguide. The dimensions are shown in Figure 10 and were analyzed using Diamond's[6] infinite array analysis. The computed E-plane scan admittance normalized to the waveguide is also shown in Figure 10.

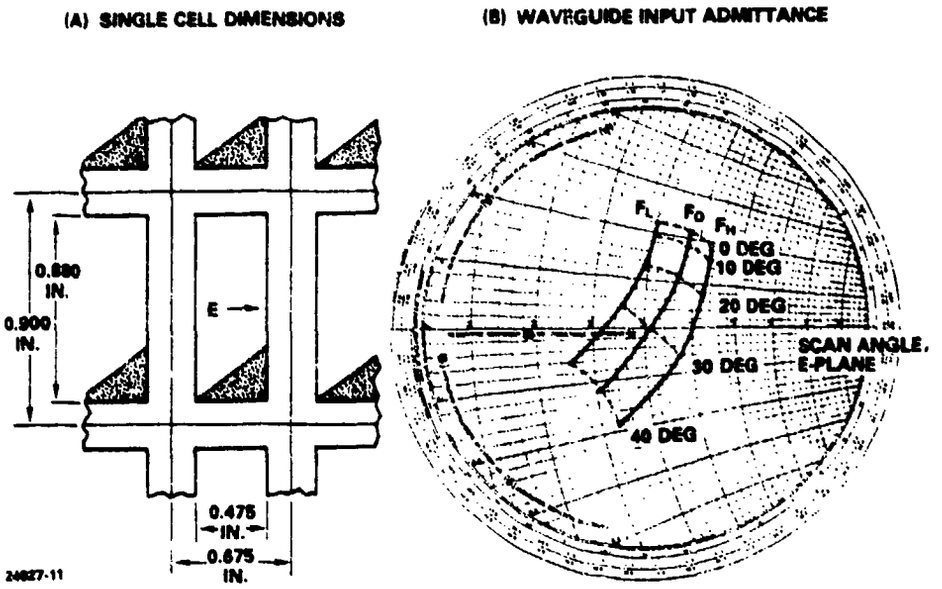

Figure 10 – Waveguide Infinite Array Admittance

4.3.2 Vertical Radiating Assembly - Selection and design of the vertical radiating assembly involved a significant part of the total antenna design effort. Because the antenna contained 80 of the assemblies, weight and total cost of the design would be critical to overall antenna success. In addition, total insertion loss must also be minimized.

Each vertical assembly contained 20 open-ended waveguide radiators, an airstrip power divider with an integral stripline to waveguide transition, a three-way stripline mechanical switch, and the coax to stripline input connector. The assembly is shown in exploded form, minus the airstrip-to-switch card finger contacts, in Figure 11.

Mechanical design of the array addressed several objectives. It was desired that the array have inherent structural integrity and that it contribute to the basic structural stiffness of the entire antenna assembly with

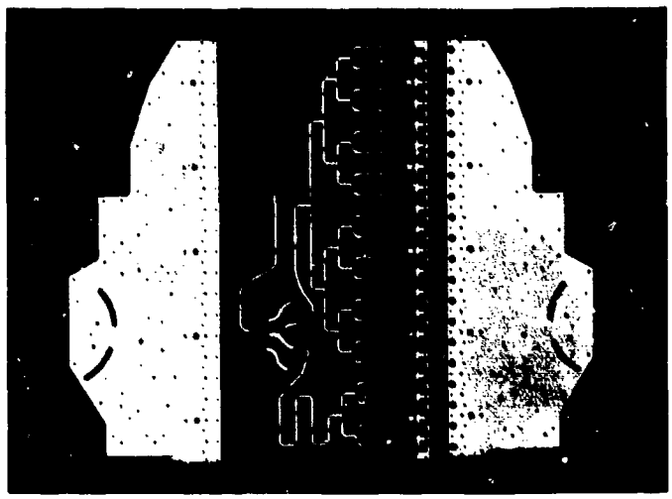

24027-12

Figure 11 — Vertical Power Divider Assembly

a minimum of additional structure. Assembly of the array should be straightforward with a minimum of fixturing or specialized alignment and fitting techniques. Weight and cost were to be minimized.

The answer to these objectives was found to lie in the design of a three-sided, thin-walled aluminum extrusion with an interlocking edge design. The open-ended waveguide elements are formed by dip brazing aluminum partitions into the extrusion at appropriate intervals to provide a single vertical element of the array. The interlocking edge feature satisfies the ease of assembly criterion and contributes to the goal of inherent structural integrity. Low cost and weight are inherent in the use of an extrusion.

A waveguide assembly, including partitions and holes drilled for alignment, assembly, and the waveguide-to-stripline transition is shown in Figure 12. Mechanical relationship of adjoining extrusions, waveguide-to-stripline transition, and spacer is shown in Figure 13.

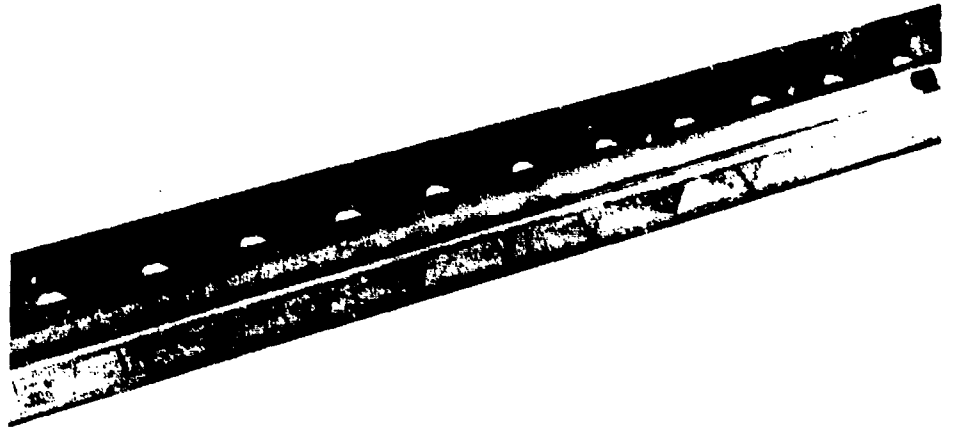

24027-13

Figure 12 – Radiator Assembly

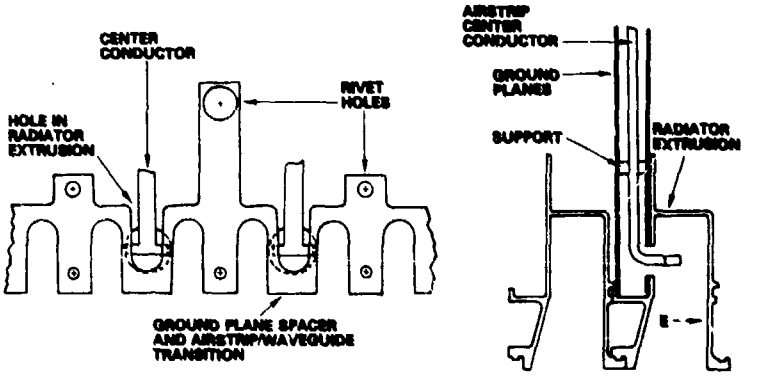

24027-14

Figure 13 – Waveguide to Power Divider Assembly

4.3.3 Elevation Power Divider - The elevation power divider is balanced stripline with air dielectric. Ground plane spacing is 0.200 in. and the rectangular center conductor is 0.050-in. thick.

Design of the T-junctions was largely empirical, as published data is not accurate for cases where the center conductor width and thickness becomes an appreciable fraction of a wavelength. The use of high quality test fixtures and an automated network analyzer for removal of test set

errors was found to be essential. In addition, all dimensions established in the laboratory had to be checked using end mills and cutters representative of those to be used in production, to optimize performance on a unit-to-unit basis.

The center conductor is supported by nylon spacers with a small pin through the center conductor. The capacitive effect of the pin was compensated for by a reduction in the conductor width over a total length of approximately $\lambda/4$. The number and location of the standoffs was based upon a vibration analysis and an allowable deviation of the center conductor from a centered location between the ground planes.

The stripline to waveguide transition is an integral part of the stripline. After machining, the T-shaped adapter is bent at a right angle and inserted through a hole in the waveguide wall. A spacer bar both spaces the ground planes and provides a square coax section in the vicinity of the transition to suppress higher order modes.

Measured VSWR of a 16-port power divider, including the stripline to waveguide transition, is shown in Figure 14. Similar data was obtained on the four-port divider.

4.3.4 Elevation Beam Switch - A mechanically movable stripline card is used to select one of three elevation beams. Contact between the card and the power divider center conductor is through beryllium copper fingers.

A torque motor and shaft is used to actuate the switches. A lever arm connects each card to the shaft, and the card is constrained in lateral movement by nylon rollers located between the ground planes.

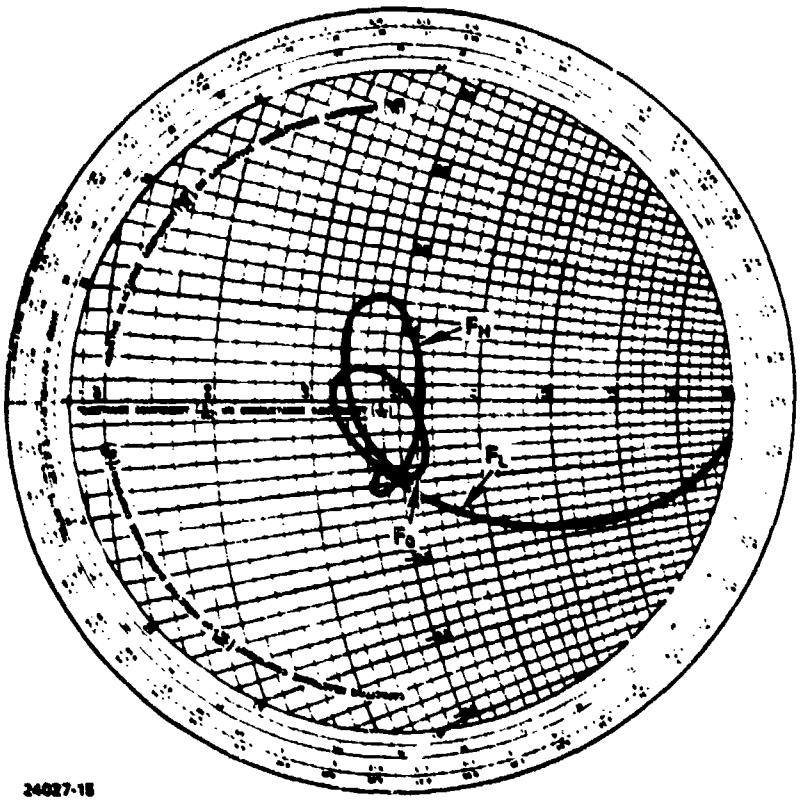

Figure 14 – Sixteen-Port Power Divider Admittance

The beryllium copper fingers represented a significant experimental design effort to realize a design capable of maintaining contact over board variations in thickness, warpage, and deflections, while at the same time providing acceptable VSWR and insertion loss at an acceptable manufacturing price.

Measured VSWR of the switch card, including fingers and airstrip support posts located next to the card, was under 1.15 in all positions.

An additional factor was the angular positional accuracy of the card relative to the fingers. Tests showed that misalignment of ±0.020 in. was acceptable.

To date the switches have been actuated several hundred times with no evidence of degradation. This has included operation during an environmental test simulating a typical aircraft pod.

4.3.5 Pressure Cylinder - A requirement for pressurization is imposed by transmitter peak power levels and operation in an unpressurized pod at high altitudes. The impracticality of pressurizing the basic antenna is evident when the problem of sealing the feed horn access to the parallel plate region is addressed. Pressure containment was achieved by enclosing the antenna in a thin-wall composite cylinder having good microwave transmission as well as excellent structural and temperature properties.

5. ANTENNA PERFORMANCE

This antenna was tested on a 2250-ft range. Both transmit and test antennas are about 35 ft above flat terrain. The range has been used for production X-band antenna testing for about eight years, and has measured amplitude ripples over a 4-ft-high by 8-ft-wide aperture of 0.5 dB maximum.

Peak azimuth sidelobes for three frequencies and a scan angle of +38 to -30 deg are shown in Figure 15 for the 20-port switch position. Very similar data was measured for the 16-port and four-port positions.

Antenna gain loss, measured at the feed horn for zero-deg scan, ranged from -2.4 to -3.0 dB, relative to the theoretical aperture gain. An additional 0.9 dB of loss occurred in three azimuth and one roll axis rotary joints, and over 5 ft of connecting waveguide. Typically, scanning to 30 deg introduced an additional 0.5 dB of loss, with 0.7 dB at 38 deg.

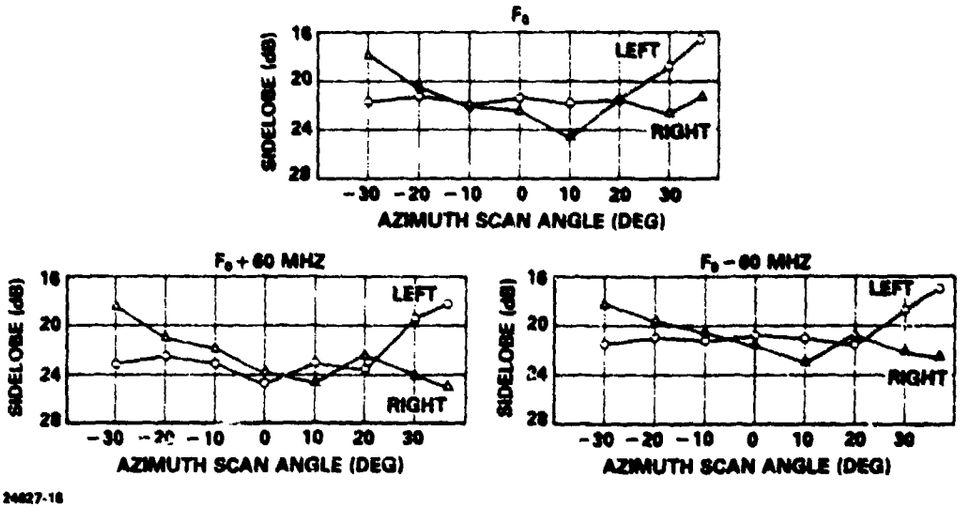

Figure 15 – Peak Azimuth Sidelobes

Typical azimuth and elevation patterns are shown in Figures 16 through 22. A full ±90-deg azimuth cut is shown in Figure 22. Overall falloff of the lobes is excellent out to about 45 deg, but relatively high lobes are present in the 45- to 70-deg region. These lobes vary in amplitude, but in general are present for all scan angles measured. Their cause was not established, but could be due to an illumination error over the lens probes or to reflections caused by extraneous structure around the antenna mount.

Because a Rotman lens is a wideband device, data was measured at a frequency 10 percent above the center design frequency. Despite known mismatches in the elevation power divider, the beam switch, and the lens, no azimuth or elevation pattern degradations were measured. More importantly, little or no change in beam position was measured, further confirming the suitability of a lens as a wideband, widescan antenna.

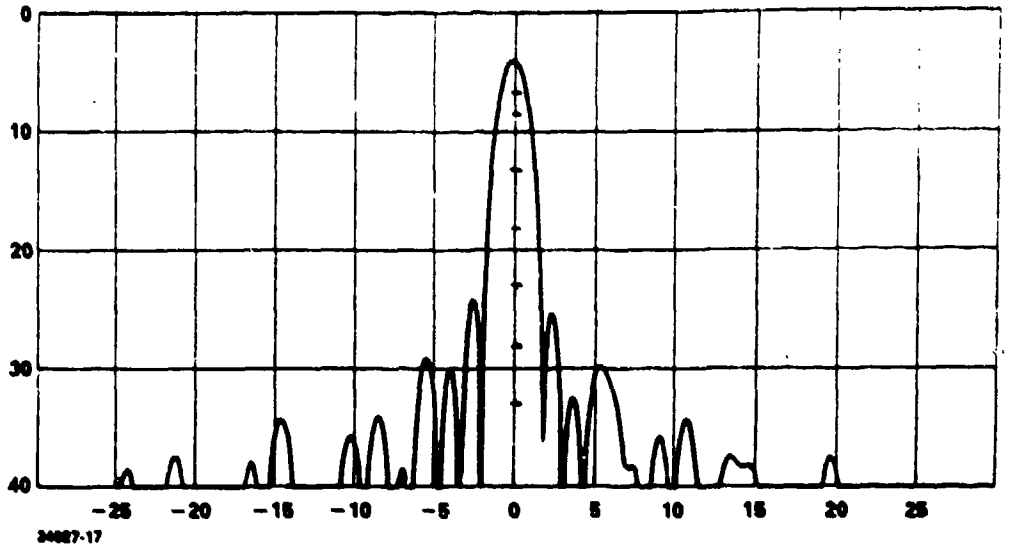

Figure 16 -- Zero-Deg Scan, Frequency = F_o, Azimuth Cut

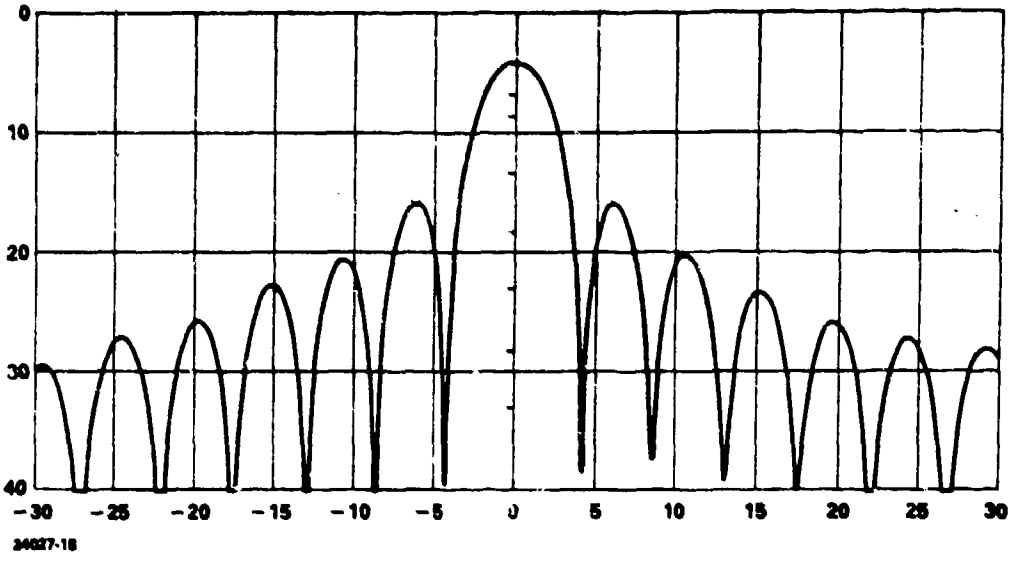

Figure 17 -- Zero-Deg Scan, Frequency = F_o, Elevation Cut

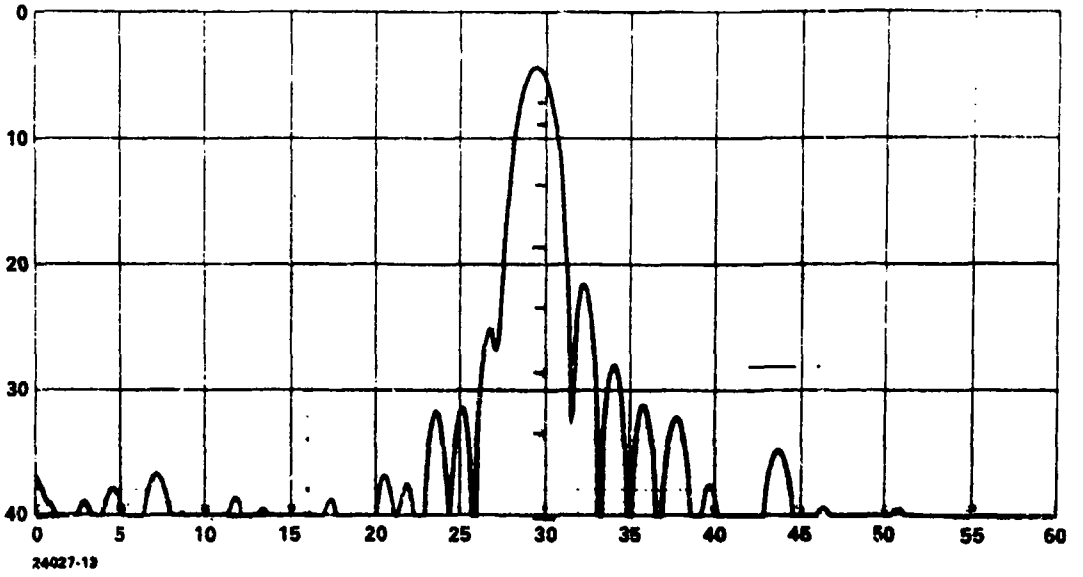

Figure 18 – Thirty-Deg Scan, Frequency = F_o, Azimuth Cut

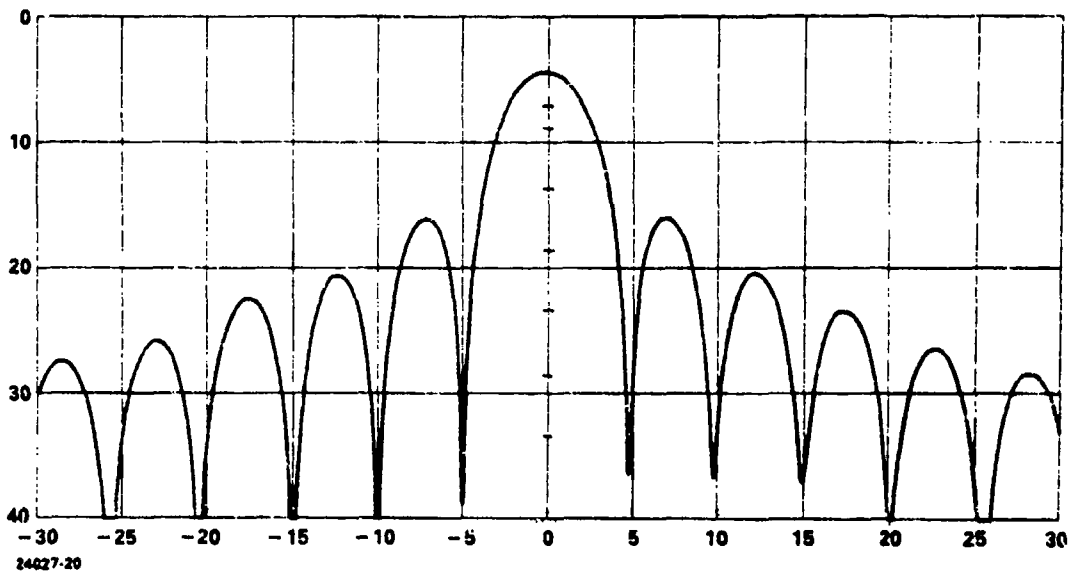

Figure 19 – Thirty-Deg Scan, Frequency = F_o, Elevation Cut

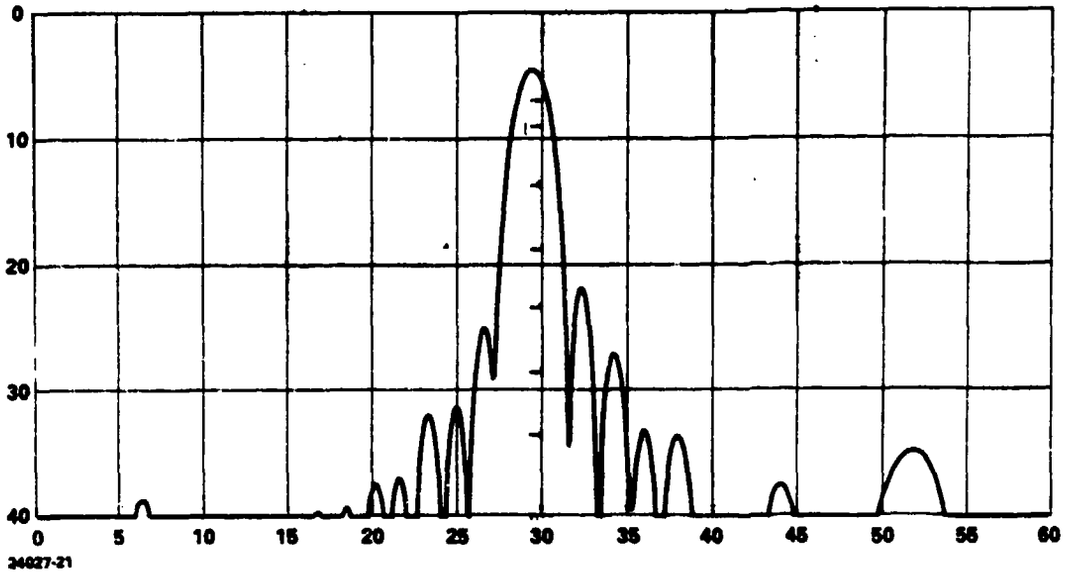

Figure 20 — Thirty-Deg Scan, Frequency = F_o - 60 MHz, Azimuth Cut

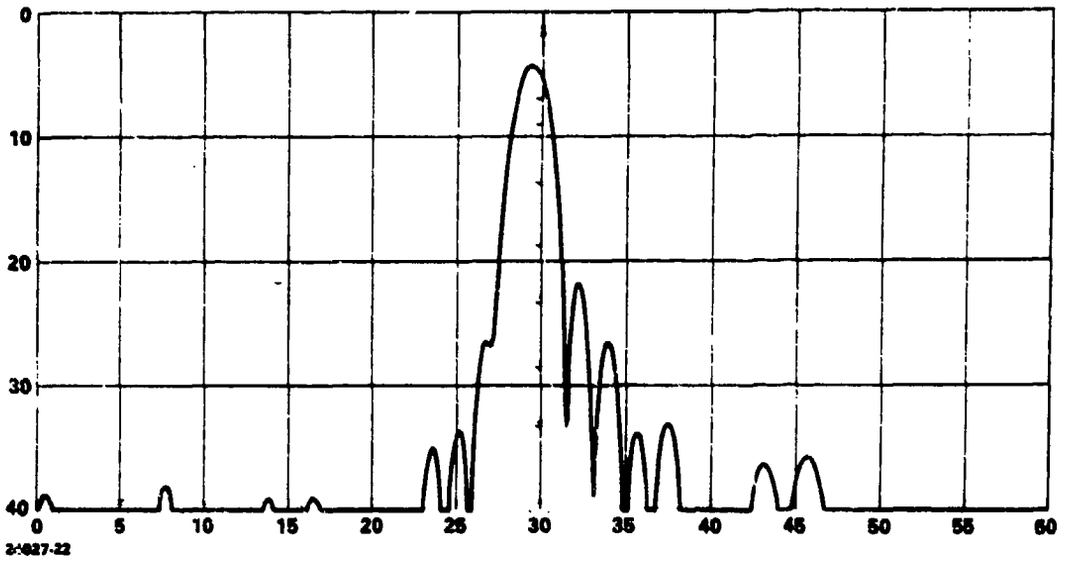

Figure 21 — Thirty-Deg Scan, Frequency = F_o + 60 MHz, Azimuth Cut

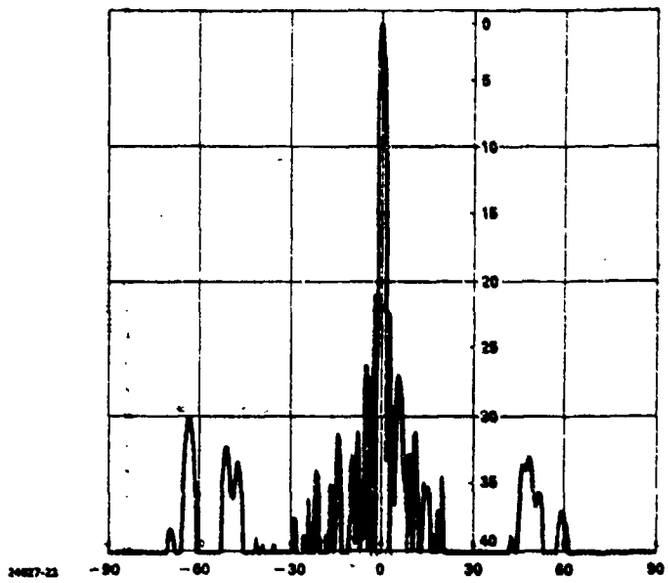

Figure 22 — Zero-Deg Scan, Frequency = F_o, Full ± 90-Deg Azimuth Cut

6. PRODUCIBILITY

A major concern throughout the development effort was producibility of the antenna on a moderate to rge scale as well as the immediate single unit fabrication. This concern is reflected in several aspects of the mechanical design. In particular, components of the vertical radiators and power dividers were designed with production quantities in mind. Both the ground planes and the circuits of the power divider networks are capable of being fabricated by precision stamping although quantities involved in the prototype did not warrant the expenditure for tooling. The extrusion approach to the vertical radiators is another example of a manufacturing technique suitable for volume production.

Assembly was addressed again in the area of the multi-element array. The interlocking edge feature of the vertical radiators and the repeating

planar nature of the power dividers both contributed to a simple stacking assembly procedure which did not rely on complex fixturing or highly skilled personnel.

7. SUMMARY

This paper has described a wideband, wide scan antenna with application to pod-mounted reconnaissance radars. A folded lens as a performance effective alternate to a phase shifter scanned array has been demonstrated. A key to the overall success of the antenna was a philosophy which emphasized minimal weight, producibility, and suitability for production during all stages of development. The design is expected to be readily adaptable to specific program requirements.

8. ACKNOWLEDGEMENTS

A number of people contributed to the success of this antenna by contributing ideas, moral support, and hard work. In particular, W.C. Woody provided invaluable ideas and concepts for the overall antenna design; W.O. Klever served as project lead engineer; H.A. Burger developed the vertical power divider and switch; A.C. Brown, Jr. provided the parallel plate bend and probe analysis; B.W. McIntyre provided a consistently high level of laboratory data; and R.E. Meyer led the mechanical design team and shepherded the antenna through the fabrication, assembly, and test phases. Their contributions are gratefully acknowledged.

REFERENCES

1. Ruze, J. (1950) Wide-angle metal-plate optics, Proc. IRE Vol 38:53.

2. Rotman, W. and Turner, R.F. (1963) Wide-angle microwave lens for line source applications, IEEE Trans. Vol AP-11:623.

3. Gustincic, J.J. (1972) The determination of active array impedance with multielement waveguide simulators, IEEE Trans. Vol AP-20:589.

4. Marcuvitz, N. (1950) Waveguide Handbook, McGraw-Hill, New York, p. 333.

5. Bahar, E. (1969) Fields in waveguide bands expressed in terms of coupled local annular waveguide modes, IEEE Trans.- MTT, Vol 17:210.

6. Diamond, B.L. (1968) A generalized approach to the analysis of infinite planar array antennas, Proc. IEEE Vol 56:1837.

AD P001096

LARGE X-BAND FERRITE SCANNING MULTIMODE ARRAY

Presented by
Harold Shnitkin and Peter Smith
Norden Systems, Inc.
Norwalk, CT 06856

Prepared for
Electromagnetic Sciences Division
Rome Air Development Center
USAF Systems Command
and
Electromagnetics Laboratory
Department of Electrical Engineering
University of Illinois
Urbana, Illinois 61801

LARGE X-BAND FERRITE SCANNING MULTIMODE ARRAY

Harold Shnitkin and Peter Smith
Norden Systems, Inc.
Norwalk, CT. 06856

ABSTRACT

A large, electronically scanned array antenna has been developed to meet the requirements of the airborne radar sensor for the PAVE MOVER system. This antenna is capable of performing in three modes; full aperture transmit and receive, two section elevation interferometer on receive, and three section space diverse azimuth interferometer on receive. Dual feeds provide illuminations for low azimuth sidelobes in all modes, and ferrite phase shifters are used to scan the beams and effectively select the mode of operation.

Design, construction and performance details are presented.

1. Introduction

The TAWDS Airborne Radar Antenna scans electronically over 120° in azimuth and mechanically over 190° in roll. It consists of a 134" wide by 11" high slotted waveguide aperture at X-band, 432 ferrite phase shifters, a beam-steering computer and a dual

mode feed. It performs in three modes: full aperture transmit, two-section elevation interferometer receive, and three section space diverse azimuth interferometer receive.

2. Mode Switching

For the transmit and elevation interferometer modes a monotonically tapered amplitude distribution across the entire azimuth aperture is excited by the front set of series feeds and the 3-way corporate feed shown in Figures 1 and 2. Monotonically tapered amplitude distributions are also excited across each partial aperture, for the azimuth interferometer mode, by the rear sets of series feeds and elevation combiners. Ferrite phase shifts are then used to select either of the two orthogonal phase functions in each of the six array sections to form the appropriate beams, thus achieving low azimuth sidelobes in all modes.

3. Slotted Array

To achieve $\lambda/2$ spacing in azimuth for grating lobe free scanning to $\pm 60°$, 432 single ridge waveguide arrays with offset shunt slots in the broad wall, were used. Each ridge guide array is center-fed by a double ridge waveguide, interfacing with its ferrite phase shifter.

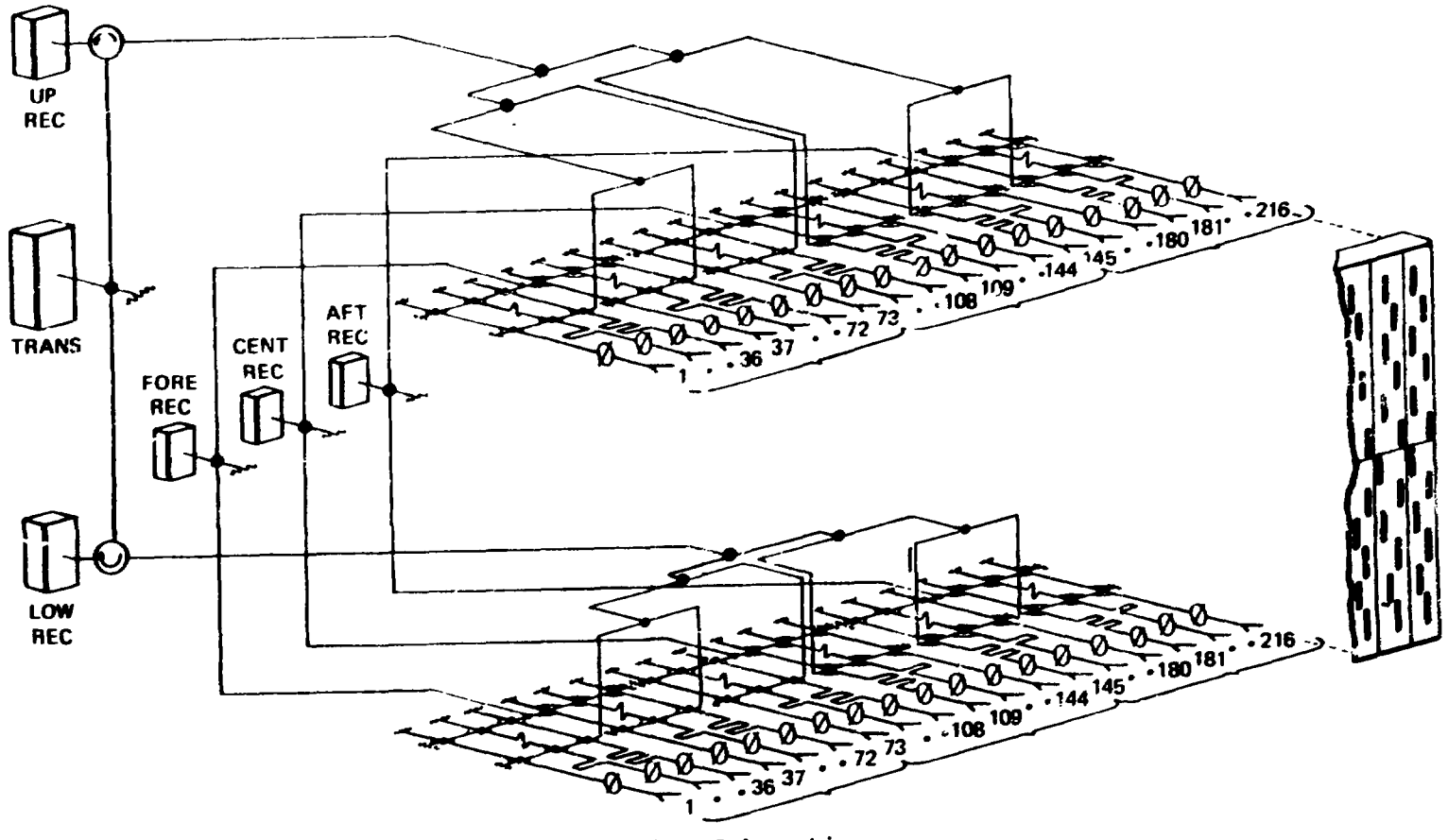

Figure 1. Schematic

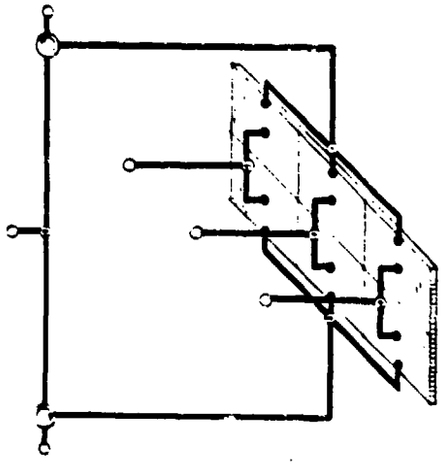

Figure 2. Multiaperture (Schematic)

4. Ferrite Phase Shifters

Non-reciprocal latching ferrite phase shifters (MFR-E.M.S.) are used to achieve the advantages of low insertion loss (0.8 dB), small size, low power dissipation and rapid phase switching (10 μsec). They are reset each PRI for transmit and the selected receive mode. Two phase shifters and drivers are packaged into a unit with provision for 6-BIT phase data linearization to ±2° over two temperature ranges. TTL inputs select transmit/receive ferrite current polarity and the high/low temperature calibration.

5. Beam Steering Computer

The digital beam steering computer converts AZ and EL scan angle, frequency, beam broadening, full or 1/3 aperture, broadside calibration for two modes and four

frequencies, and temperature input data into a binary digital data stream for loading the storage registers in each ferrite driver. The computer further contains PROMS, burned with antenna broadside phase calibration values.

6. Dual Mode Feed

The cascaded 36 element directional coupler feeds, employing the principle of a Blass-Type dual beam feed form the dual mode feeds in each of the six aperture sections.

The feed schematic, as shown in Figure 1, shows the couplers, terminations, and compensating delay lines. Not shown are additional 180° delay sections between the two cascaded sets of 36 couplers required to make the full aperture feed orthogonal to the 1/3 aperture feed.

The feed assembly consists of two rows of cross-guide couplers interconnected by semi-rigid coaxial cables, as shown in Figure 3.

7. Performance

The assembled antenna, as shown in Figure 4, has the performance shown in Table 1.

Table 1. TAWDS Antenna Performance

Frequency:	3.5% in X-band
RF Power: Peak, Avg.	8 Kw, 1.6 Kw
Net Broadside Gain: Full, 1/3	35 dB, 31 dB
Gain Loss at 60° Scan:	4 dB
Electronic Scan Range: AZ, EL	120°, 8°
Beamwidth: AZ Full, AZ 1/3, EL	0.7°, 2°, 8°
Polarization	Horizontal
Beam Positioning Time:	10 μsec.

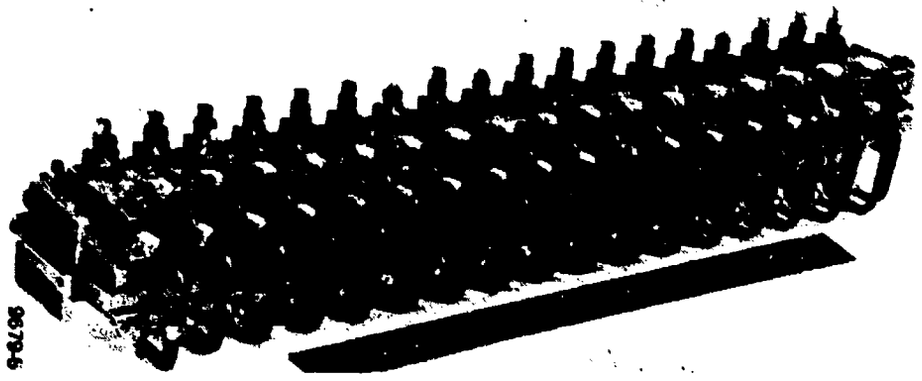

Figure 3. Coupler Feed

Figure 4. Array Assembly

AD P001097

LOW-COST 1-D ELECTRONICALLY SCANNED DIPOLE ARRAY

D. E. BOSTROM, R. E. HODGES, C. QUAN
ANTENNA DEPARTMENT
RADAR SYSTEMS GROUP
HUGHES AIRCRAFT COMPANY
EL SEGUNDO, CA 90009

ABSTRACT

This paper describes a 2 x 12 element linear array that is electronically scanned with 4-bit diode phase shifters. The antenna is cantilever mounted at one end to a trunnion assembly with the array axis oblique to the horizontal roll axis. In operation the fan-shaped beam generated by the linear array provides 280 degree azimuthal scan envelope as station mounted in an aircraft.

This antenna design is based on a modular design concept for optimum array performance and reliability at minimum cost. The radiating elements consist of printed circuit dipoles with an integrated microstrip balun and feed assembly. The dipole feeds are excited from miniature coaxial lines which, in turn, are routed from the ground plane to the PIN diode phase shifters. The phase shifters are fed by means of a stripline/coax corporate feed assembly. This corporate feed structure is a matched feed which employs hybrid couplers to minimize the formation of reflection lobes. The amplitude distribution obtained from this feed is

PAGE BLANK-NOT FILMED

a 20 dB Taylor, selected to produce the requisite sidelobe level. The phase of the output ports is equalized by adjusting the coax cable lengths which feed the phase shifters.

The data and results presented include gain, radiation patterns, details of the components utilized, and cost.

1. INTRODUCTION

The antenna system described in this paper is designed to operate as an airborne tracking antenna in an L-band data link system used for accurate weapon delivery. A typical mission scenario is shown in Figure 1. The antenna is pod mounted in the aft station to provide data communication following the weapon delivery and target lock-on phase. It is an obliquely oriented array of dipole radiating elements which forms a fanned beam that may be pointed anywhere in its 280 degree azimuthal scan envelope. PIN diode phase shifters associated with each azimuth array element pair provide interelement phase shifts which electronically scan the beam relative to the direction of flight. The array assembly is rotated about the direction of flight on a trunnion to select the orientation of the electronic scan plane, port or starboard.

The rotating electronic scanned array has the advantage of providing the needed gain, sidelobe performance, and scan rate at a relatively modest cost per unit. It is one of the first electronic scanned arrays to complete the pilot production phase.

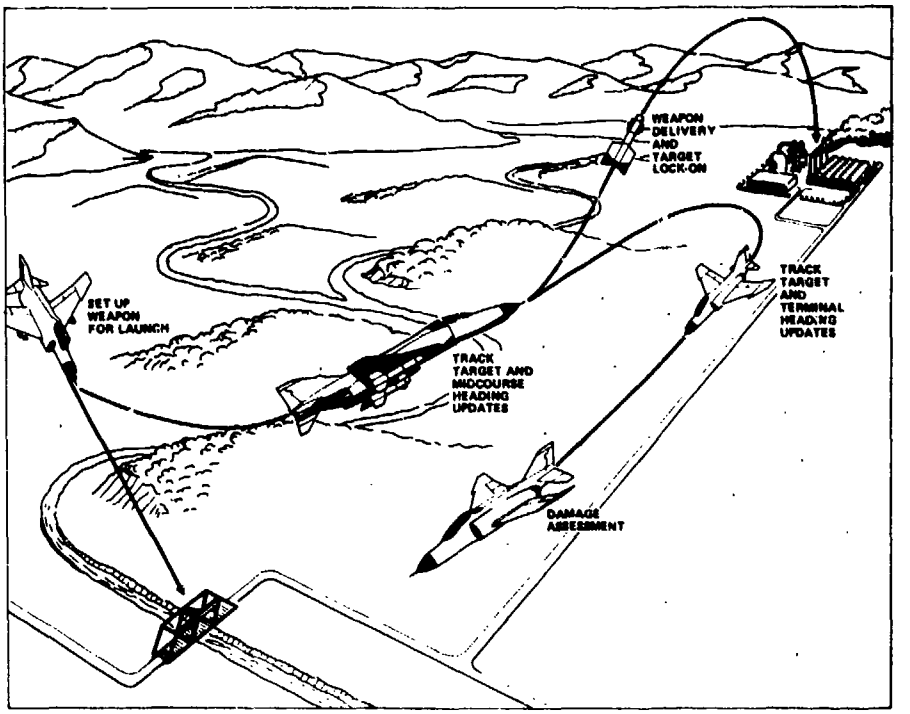

Figure 1. Typical Mission Scenario

The system has proven to be a durable and reliable design over several years of testing and field use on a variety of aircraft. In addition, the modular design concept allows the units to be quickly mass-produced and easily repaired in the event of damage or component failure.

2. GENERAL DESIGN DESCRIPTION

A photograph of the array aperture appears in Figure 2 and a photograph showing the rear of the antenna with radome and mounting sleeve appears in Figure 3. Figure 4 presents a partially exploded view of the array assembly to assist in identifying the subassemblies and to illustrate the packaging concept. As can be

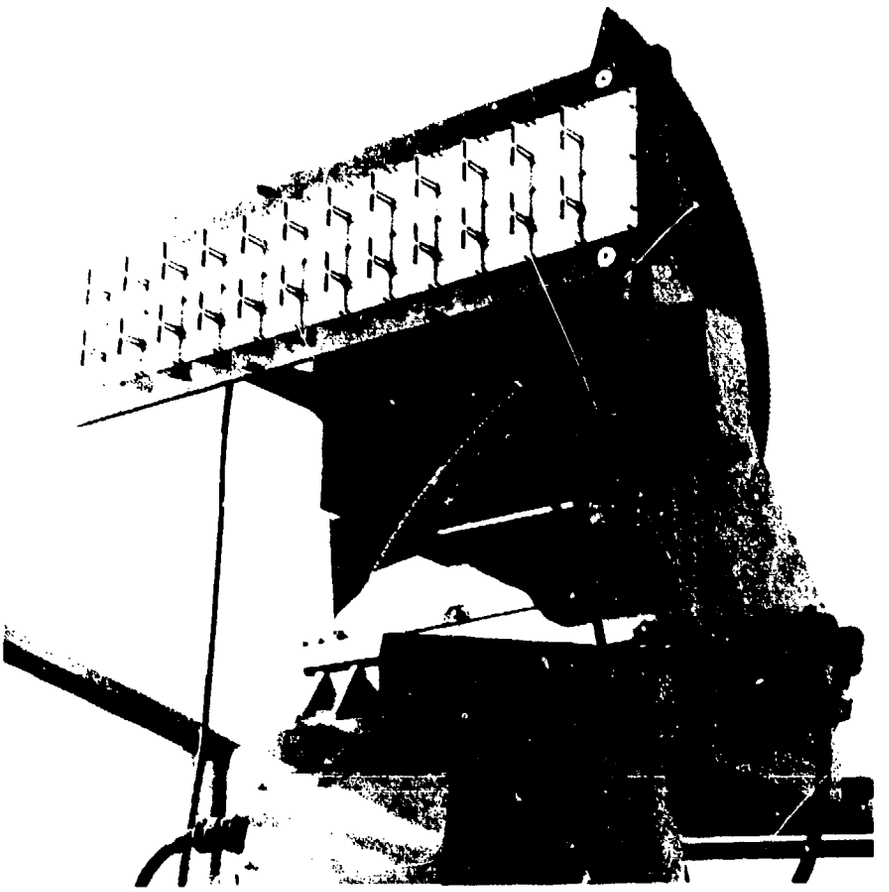

Figure 2. Array During Range Testing

seen, the antenna comprises three major subassemblies: (1) the array, (2) the microwave feed circuit and phase shifters, and (3) the scan electronics. These subassemblies are mounted to a central frame and chassis as separate modules. This procedure allows more flexibility in the design of individual components, simplifies procurement, and has obvious advantages in the maintenance and repair cycle of units in the field.

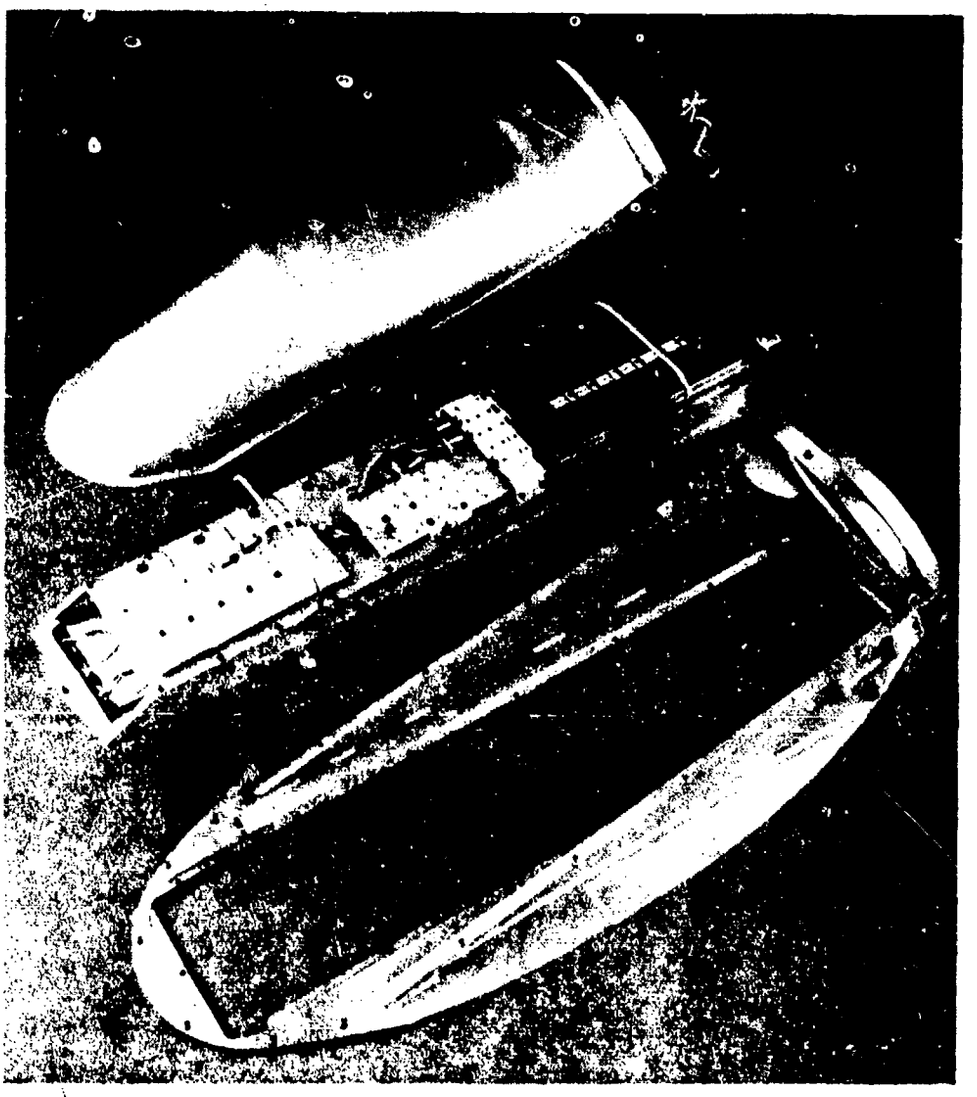

Figure 3. Rear View of Antenna with Mounting Sleeve

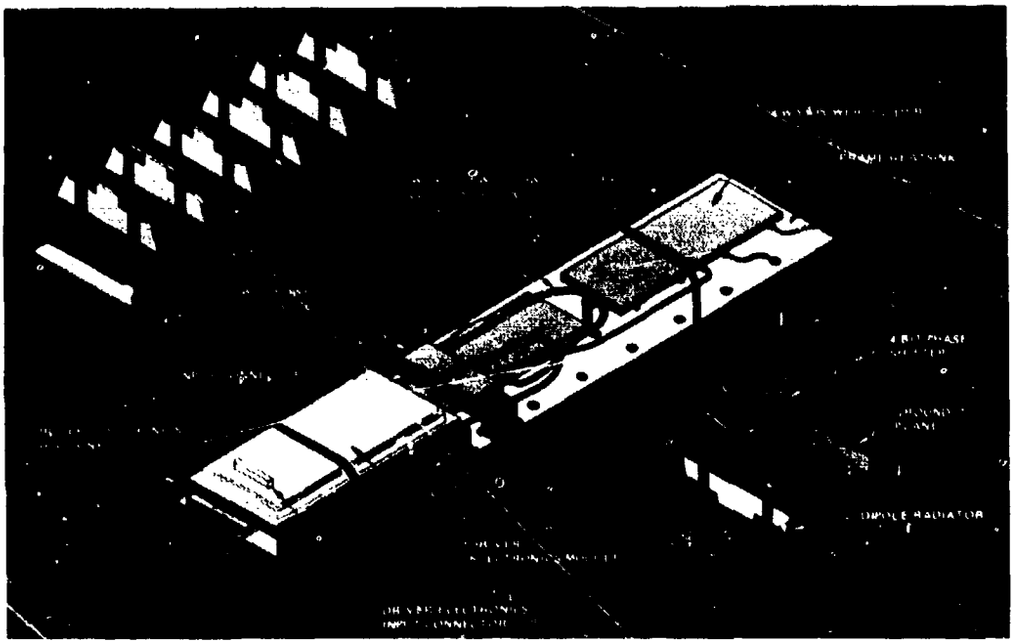

Figure 4. Partially Exploded View of Antenna

Figure 5 shows a functional isometric diagram of the array. The radiating portion of the system consists of a linear array of 12 dipole pairs. Each dipole pair is spaced at approximately one-half wavelength to obviate grating lobes. Beam scanning is accomplished by means of 12 4-bit diode phase shifters, which are interposed between the output of the array feed network and the array elements. The feed network is designed to produce a 20 dB Taylor amplitude distribution to achieve the required sidelobe level.

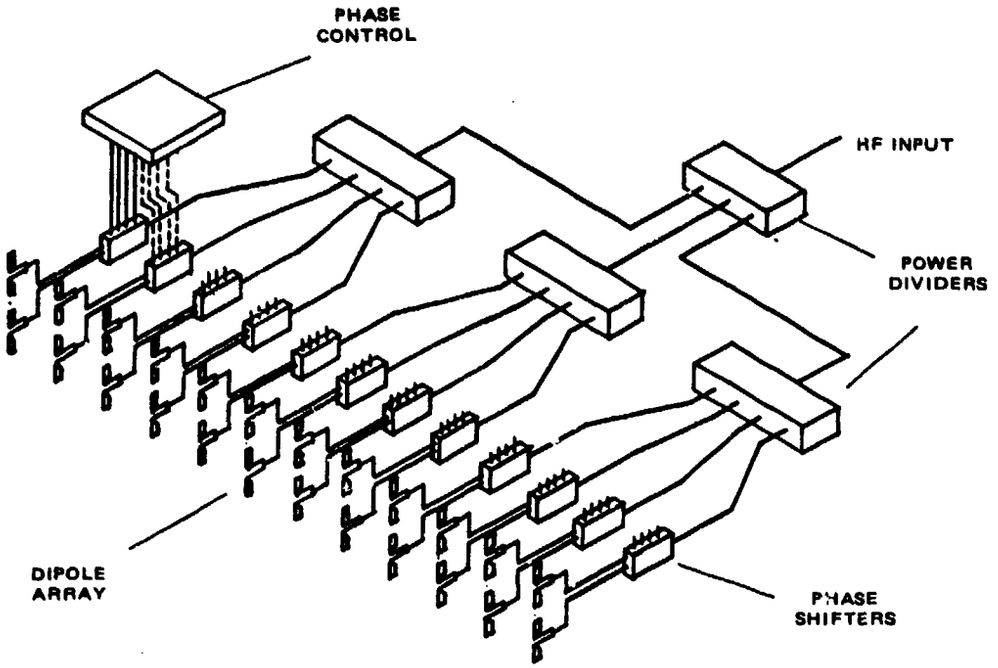

Figure 5. Functional Isometric Diagram

3. DETAILED DESIGN DESCRIPTION

3.1 Array Elements

The dipole assemblies shown in Figure 6 consist of a pair of half-wavelength resonant dipoles matched to a microstrip feed line

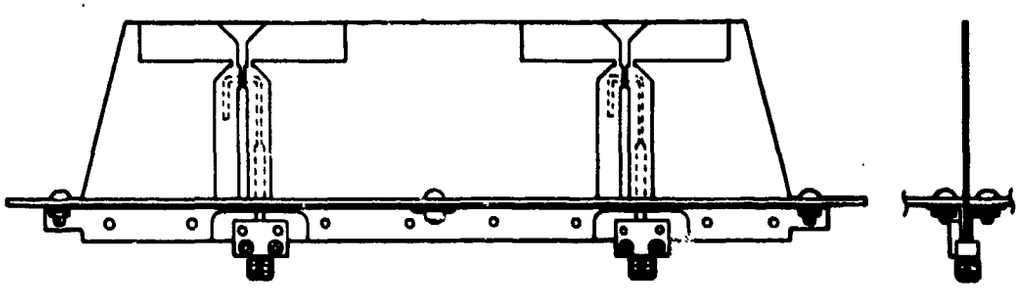

Figure 6. Dipole Assemblies

using a Bauer and Wolfe balun and fed by an SMA coaxial launcher. These units are designed to achieve a maximum input VSWR of 2:1 in the array over the scan angle and bandwidth. The elements are located one-quarter wavelength above the ground plane to maximize the element factor gain in the array. Spacing between elements was selected to achieve the correct beamwidth in the elevation plane.

The units are produced by printed circuit board photo-etching techniques on copper clad G-10 fiberglass boards. The mounting rail is an aluminum extrusion, and the launcher fitting is a SMA connector mounted to the rail and board. Thus, the units are lightweight, inexpensive, and readily mass-produced.

3.2 Phase Shifters

Beam steering is achieved by using 4-bit PIN diode phase shifters as shown in Figure 7. The circuit that contains the 180° and 90° bits employs two reflection-type phase shifters, each with a 180° hybrid coupler, while the 45° and 22.5° bits utilize two loaded line phase shifters. Capacitors are included to isolate the DC bias current of each bit. The circuit also incorporates a reactive 3 dB power divider to feed the signal into the pair of dipoles. Two development models are shown in Figure 8.

Thick film technology is well known as a low-cost manufacturing process of hybrid circuits; thus it is utilized to fabricate

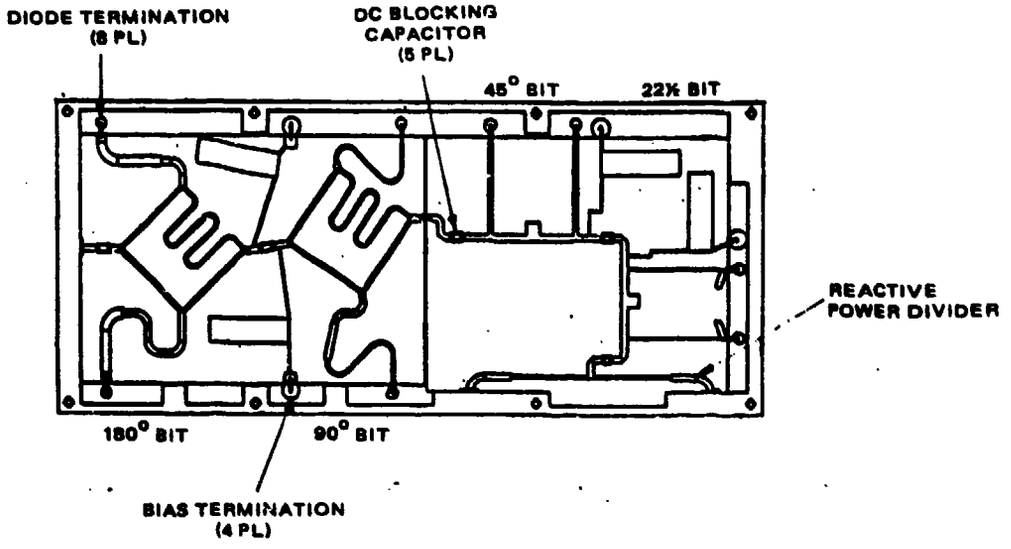

Figure 7. Phase Shifter Circuits

the microstrip circuitry onto two alumina boards. In this process, the conductor initially comes in the form of a paste or "ink." With this ink, the circuit pattern is screen printed onto bare alumina substrates. The printed materials are then fired in an oven to temperatures over 900°C. This firing causes the metal to fuse to the substrate and removes impurities from the metal. The process can then be repeated to print the ground plane onto the opposite side of the substrate. Similarly, additional components such as the capacitors and protective glass cover coat may be fabricated onto the substrate using multilayer printing, as shown

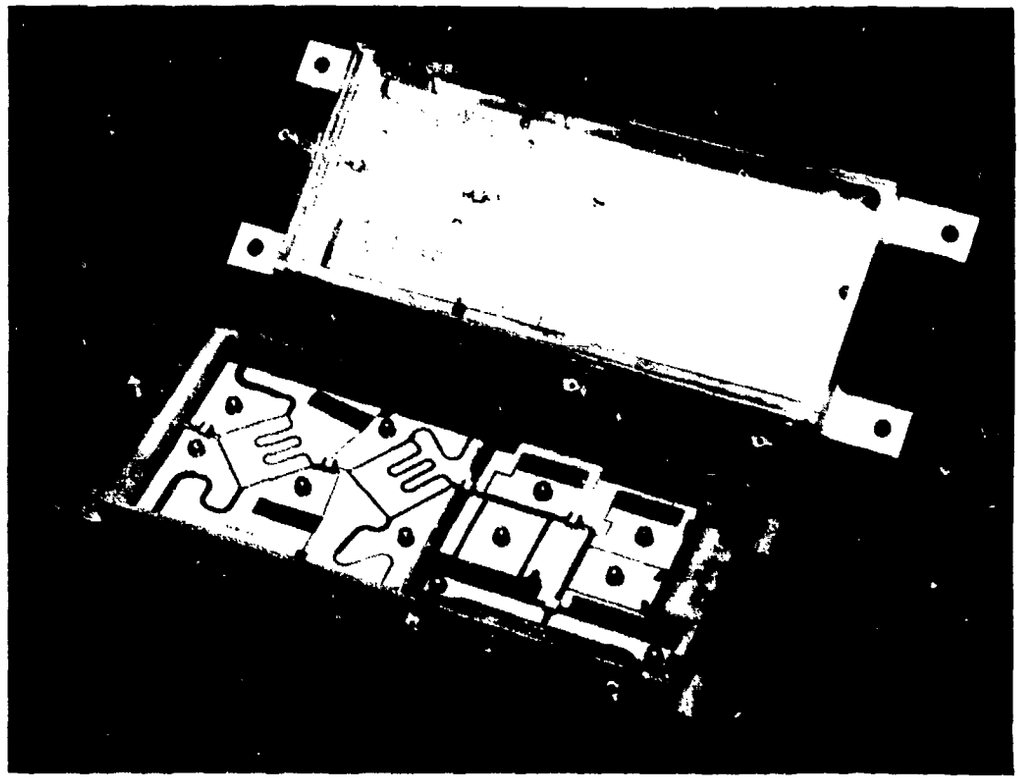

Figure 8. Two Phase Shifter Development Models

in Figure 9. Hermetically sealed diodes and glass coated substrates obviate the need to seal the entire phase shifter. Extensive screening is performed on each phase shifter to assure its performance and reliability. This thick film technology provides for the ready manufacture of low-cost, reliable microstrip circuits.

Typical production units exhibit a maximum input VSWR of 1.6:1 over the band for all bit states. The phase command

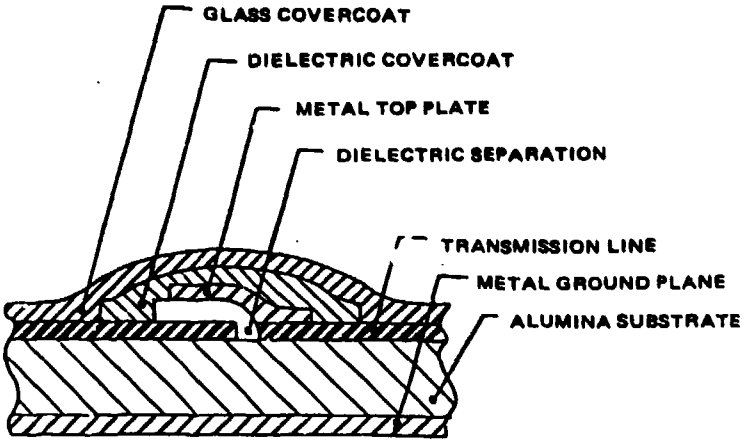

Figure 9. Thick Film Capacitor Cross Section

accuracy is less than ±6°. Insertion loss for the units is typically 2.0 dB.

3.3 Microwave Feed Circuit

The microwave feed circuit, which can be seen in Figures 3 through 5, consists of one three-way and three four-way power dividers. These units are all stripline designs constructed on fiberglass reinforced teflon substrate. The power splits are selected to form the required 20 dB Taylor distribution. To do this, the three-way power divider is constructed from a pair of 3 dB proximity couplers. The center four-way divider uses a standard "rat race" hybrid feeding two Parad and Moynihan hybrids, while the outboard four-ways are designed with three of the latter two hybrids each. Each unit has a maximum VSWR of about 1.20:1 over the required band. The total power divider insertion

loss of 0.60 dB combines with a total coax cable loss of 0.76 dB to yield 1.36 dB in feed losses for the array. The assembly is phase trimmed by adjusting the coax cable length at the feed output to produce the required phase at all 12 output ports.

3.4 Scan Electronics

The scan electronics provide the bias signals to the PIN diodes in the phase shifters, which select the desired beam position. A total of 31 beam positions are commanded by a TTL parallel input to the array.

The elevation scan step size is determined by the gain degradation allowable at the crossover point of any two adjacent beams, and by the requirement that no "peak" quantization lobes occur with quantized beam steering. The beam positions were selected so that the crossover levels between adjacent beam positions are no more than 1 dB below the beam peak. Because the beamwidth varies as a function of scan angle, a curve for beamwidth versus scan angle was generated and used to calculate the scan step sizes for each of the 30 beam positions off broadside. The resulting scan step sizes change with scan angle in a nonlinear fashion, while the crossover gain remains nearly constant.

The phase data for each beam position are stored in programmable read-only memories. The desired beam position is designated

by means of a 5-bit parallel word. The total phase loading delay and beam switching time is less than 15 μs. The circuits of the scan electronics are in TTL, constructed with dual in-line packages on standard PC board. After assembly, the board is conformal coated.

3.5 Physical Design Features

Mounting the array in a pod allows the system to be used on a variety of aircraft. Thus, the system must be capable of operating in temperatures ranging from -65°F at 60,000 feet to +160°F at sea level and a multivehicle mechanical environment. Analysis and testing to meet these requirements is first performed on the individual components. These components are then mounted to the frame assembly. Following assembly, the array is phase trimmed, temperature cycled, and electrical tested. Again, Figure 4 portrays the modularity. Note the handles on the rear which allow the unit to be set on its back. Normal handling is done with a secondary frame which replaces the pod mount and allows the unit to set face down with the dipoles clear. All assembly is done with hex head stainless steel screws into inserts. The frame contains 125 inserts for mounting.

With the frame containing the majority of the mounting inserts, the other pieces simply use clearance holes for mounting, simplifying their tolerances.

Weight of the array was not a prime requirement, however, the environment analysis study sized the unit's construction, resulting in a weight of 29 pounds.

3.6 Reliability Testing

3.6.1 Temperature Cycling

Following final assembly and prior to range testing, the complete array is subjected to a thermal cycling acceptance test. This test involves two cycles. In each cycle the array is raised from ambient temperature to 160°F at a rate of 7°F/minute where it endures a 60 minute soak, then cooled at the same rate to -70°F for another 60 minute soak, and finally returned to ambient temperature. Since field testing has shown that the connections between the phase shifter substrate and its SMA connector tabs were subject to thermal cycling failures, and to substantiate the reliability of bonding alumina substrates to their cast housings, these units were subjected to a more extensive thermal test prior to assembly. It was found that the bonding procedure and a redesigned connector tab survived 300 cycles.

3.6.2 High Power Testing

The only candidate for high power failure is the stripline corporate feed, and the loads associated with its hybrids. These units were high power tested by applying an appropriate amount of power to the input ports and alternately terminating the outputs

in effective open and short circuits to focus this power on the loads. No failures have occurred in these tests.

3.6.3 Field Tests of Array

Over the past 7 years, seven original engineering units have been in continuous field testing, serving to prove the system performance. In these tests, the principal source of failure has been the connector tabs on the phase shifters, mentioned above. It is worth noting that, generally, several of these tabs fail before unacceptable system performance results. In one case, a connector tab on a dipole failed, but it is possible that this was damaged in handling the unit. Nevertheless, these results indicate that the units tend to "fail gracefully" rather than catastrophically.

4. SYSTEM PERFORMANCE

4.1 Performance Summary

The electrical performance of the array is summarized in Table 1. Note that the polarization of the array is linear vertical. Figure 10 shows the measured gain envelope for a typical array. The result of the beam position selection (discussed in the driver electronics section) is to "pair" the beam positions about the ideal locations available in a 4-bit phase shifter design. This is the source of quantization error mentioned below,

TABLE 1. ARRAY DESIGN AND PERFORMANCE SUMMARY

Number of elements	Two rows by 12 columns = 24
Polarization	Linear vertical
Electronic beam steering	±70° in azimuth
Number of beam positions	31
Frequency	L-band
Bandwidth	8 percent
Broadside beam gain	15.3 dB at broadside
Sidelobe level	17.5 dB maximum at broadside
Input VSWR	2.0:1
Power handling	50 W

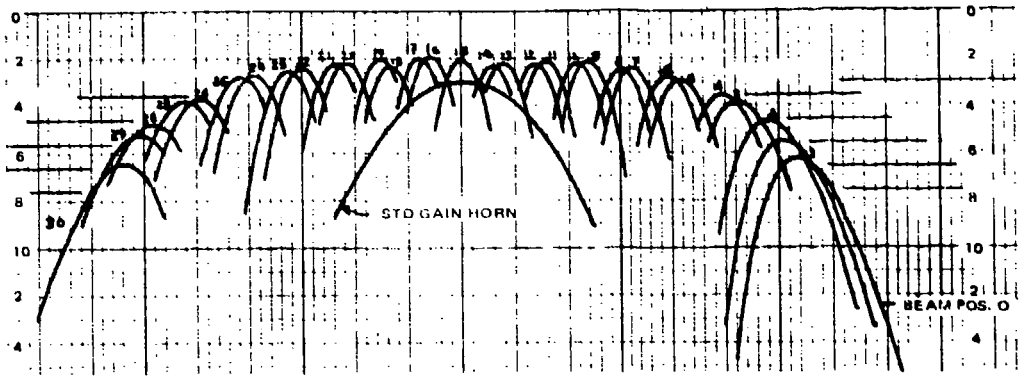

Figure 10. Typical Measured Array Gain Envelope

and results in sidelobe degradation. Figure 11 shows a typical Smith Chart plot of the array input impedance for all beam positions superimposed.

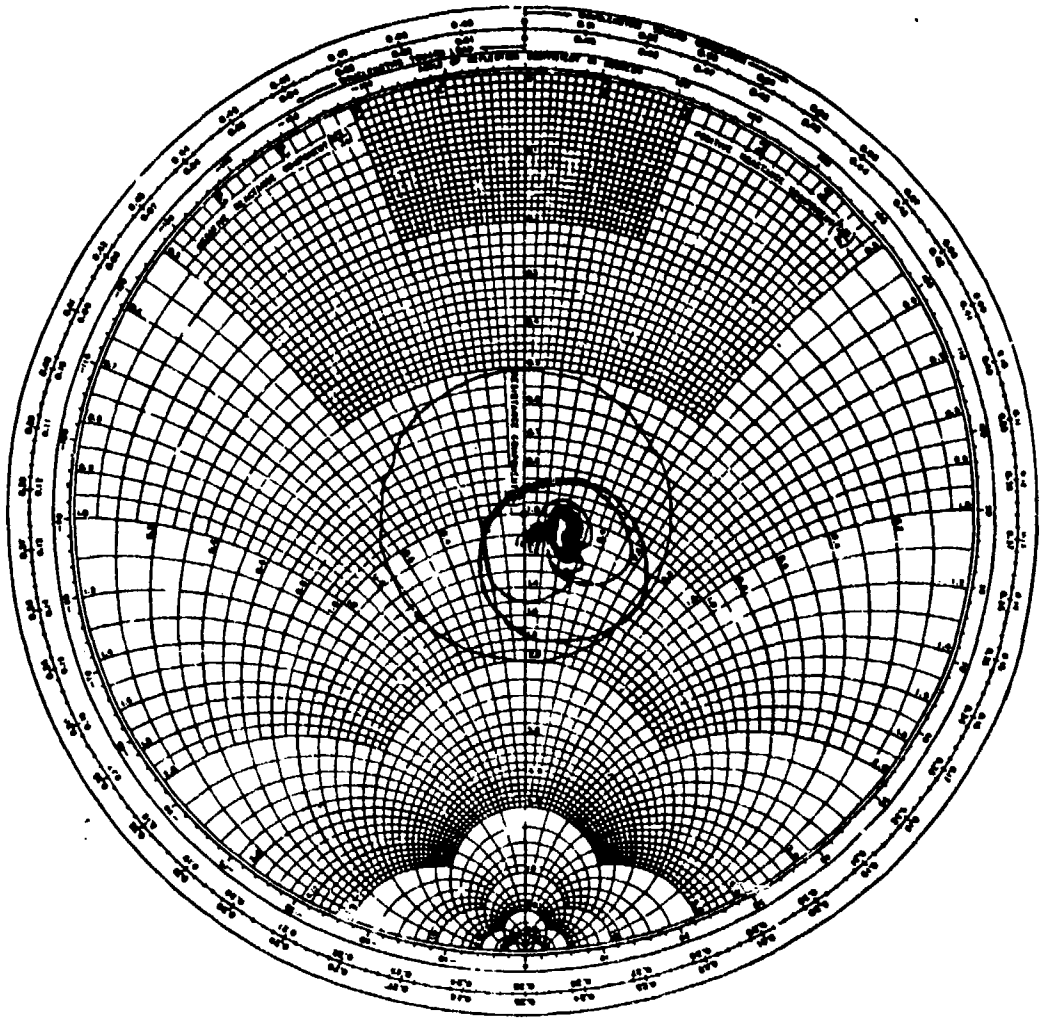

Figure 11. Input VSWR for All Beam Positions

4.2 Antenna Patterns

The antenna patterns shown in Figures 12a, 12b, and 12c present the measured performance in the azimuth plane at broadside, 32.0° and 63.0° respectively. These typical patterns show that the 3 dB beamwidth varies inversely as the cosine of scan angle.

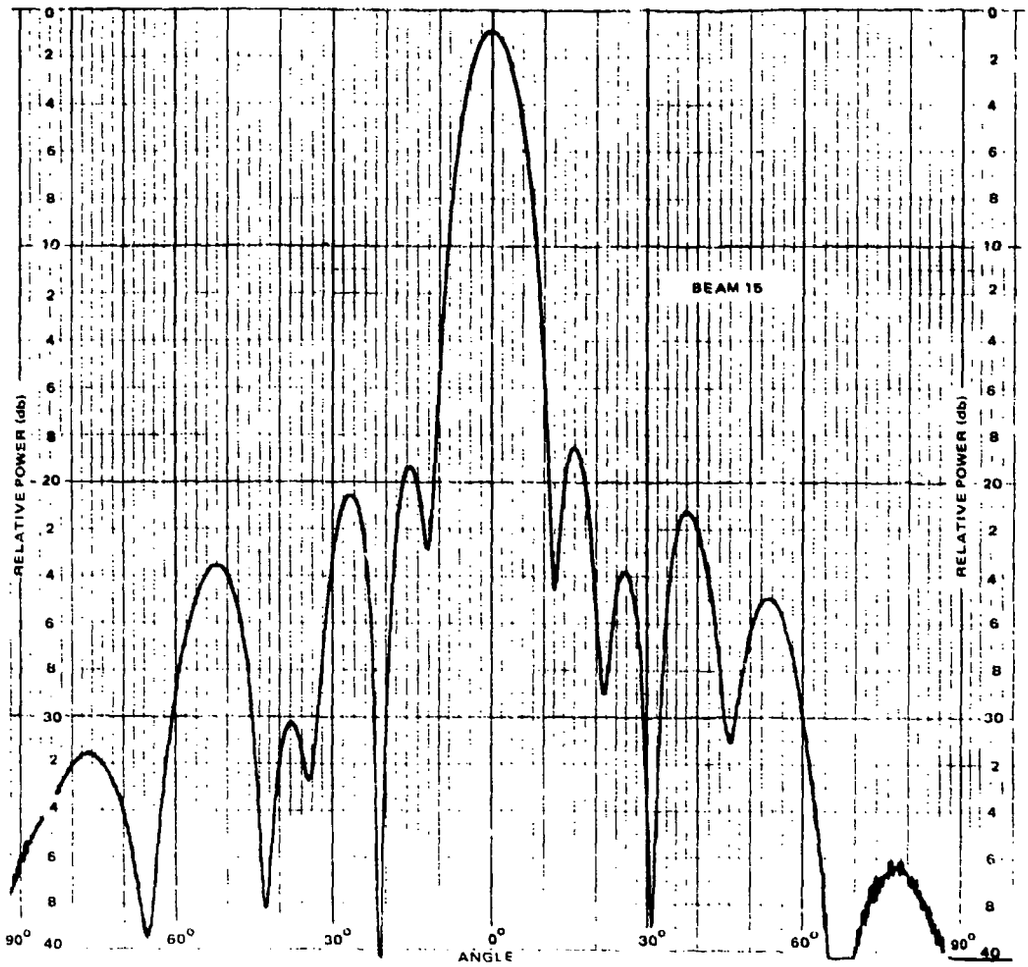

Figure 12a. Azimuth Radiation Pattern at Broadside

The array sidelobe performance degrades with increasing scan angle due to phase quantization and mutual coupling. Furthermore, inevitable errors in the amplitude and phase distribution which occur in the manufacturing process result in an occasional discrete sidelobe exceeding a peak sidelobe specification for some particular beam position and frequency combinations. This raises the problem

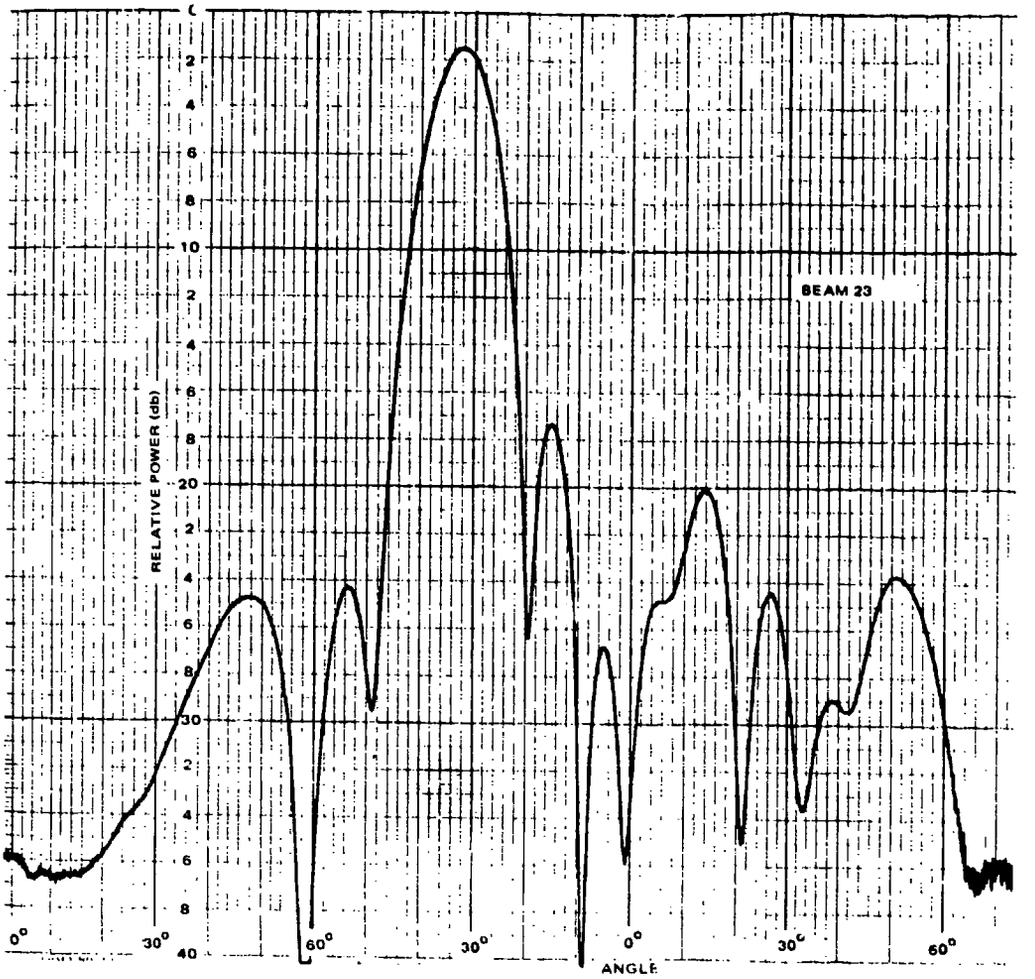

Figure 12b. Azimuth Radiation Pattern with Beam Steered to 32°

of how best to define the sidelobe specification. Ideally, one would specify a maximum RMS sidelobe level over all beam positions and frequencies. However, the cost of implementing such a measurement procedure in a manufacturing environment is clearly prohibitive. Therefore, a method of defining the sidelobe performance was adopted to serve as a relative indicator of the

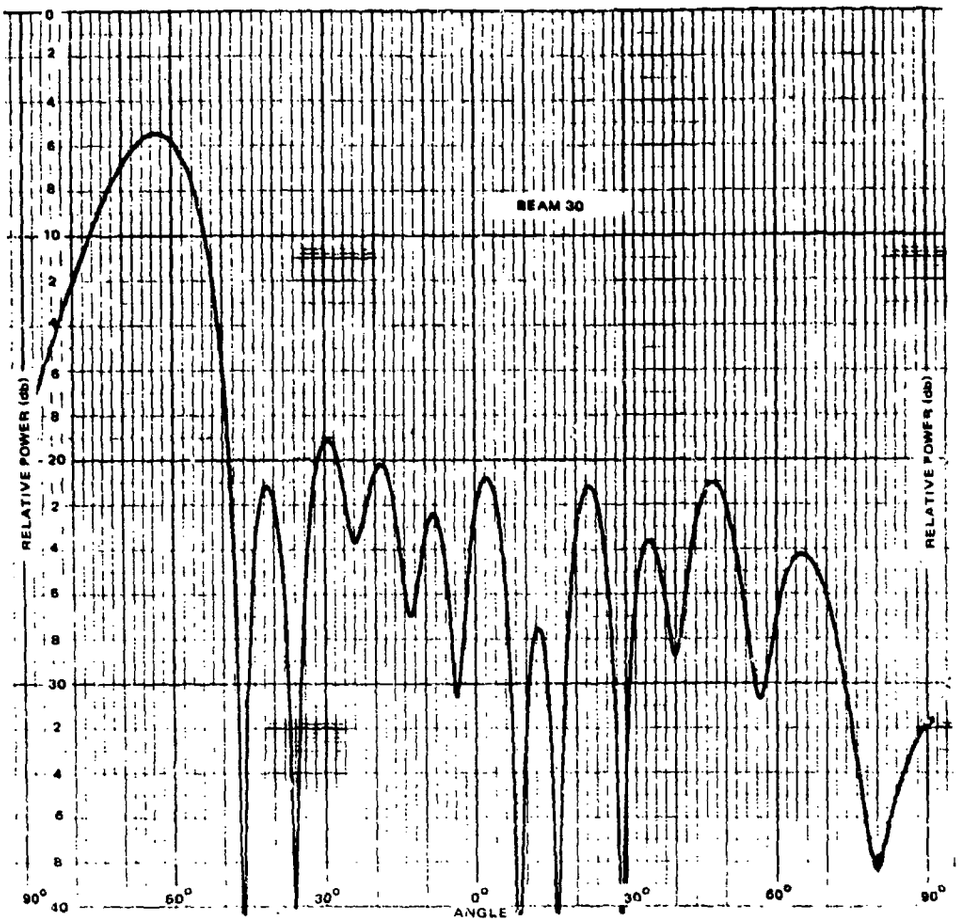

Figure 12c. Azimuth Radiation Pattern with Beam Steered to 63.0°

acceptability of a given production unit. In this definition, the maximum peak RMS sidelobe level (the RMS value of the peak sidelobe level over all beam positions at a single frequency) is specified. The value of the specification was generated from measurements of the first seven antennas fabricated.

5. COSTS

This antenna represents a portion of an 8 year development program with the goal of providing a competitive, cost effective system. The antenna has progressed from a custom engineering item to a production item in which components are procured in a competitive bidding process. Currently, assembly and test are being moved out of engineering to make this antenna a true production line item. Table 2 shows some of the approximate costs now being realized for a manufactured quantity of 40. This total

TABLE 2. MANUFACTURING COSTS (40)

Item	Cost
Frame	$ 1,210
Handles (2)	42
Heat sinks (2 different)	485
Dipole assemblies (12)	1,800
Phase shifters (12)	4,800
Power dividers (4)	1,258
Scan electronics	2,500
Coax cables (39)	423
Wire harness	818
Miscellaneous hardware	120
	$13,456

has been reduced by a factor of five over the last 8 years despite the industry inflation.

6. CONCLUSIONS

The feasibility and producibility of the rotating electronically scanned array has been demonstrated and substantiated through a preproduction contract for 10 antennas. The antenna has been shown to provide coverage at intermediate gain levels over a 78 percent spherical scan envelope. In addition, it has been shown that this design allows for low cost mass production.

7. ACKNOWLEDGEMENTS

The authors would like to express their appreciation to the following companies and individuals for the help and efforts in making this array a successful design: Struthers Electronics Corporation, Arthur Fisher; Microwave Development and Manufacturing, Charles Watson; Hughes Aircraft Company-Newport Beach, Richard Himmel; and the Armament Division AFSC at Eglin Air Force Base, Florida.

AD P001098

SIMULTANEOUS NULLING IN THE SUM AND DIFFERENCE PATTERNS OF A MONOPULSE RADAR

RANDY L. HAUPT
Electromagnetic Sciences Division
Rome Air Development Center
Hanscom AFB, MA 01731

Abstract

Adaptive nulling in a monopulse antenna requires consideration of both the sum and difference channels. This paper describes a phase only nulling technique which simultaneously places nulls in the far field sum and difference patterns using one set of phase shifters.

1. Introduction

In the past few years, considerable research and development has been done in the field of adaptive antennas. Communication and sonar systems have reaped some of the benefits of adaptive antenna technology, while radars lag behind. Some of the reasons for this dichotomy are adaptive techniques are not well suited for microwave frequencies; radars have large antennas, hence more adaptive loops; and a radar has tight time constraints due to target searching. As a result, only a handfull of radars incorporating sidelobe cancelling techniques exist today. Fully adaptive radar antennas with many degrees of freedom are not practical to implement at this time.

Monopulse radars present an even more difficult adaptive antenna problem. A monopulse antenna uses two antenna patterns simultaneously: 1) a sum pattern to detect and range a target and 2) a difference pattern to determine the angular location of the target. Most adaptive antenna research has ignored the difference pattern, even though both patterns must have a null in the direction of the interference to enhance the radar's performance. Placing a

null in the sum pattern will not automatically place a null in the difference pattern. Consequently, most system requirements have assumed that the sum channel requires separate adaptive weights and control from the difference channel.

This paper has a dual purpose. First, it shows that a null can theoretically be placed in the sum and difference channels of a monopulse antenna using one set of adaptive weights. An adaptive technique incorporating this theory would greatly reduce the hardware and software requirements for a monopulse antenna. A second reason for writing this paper is to emphasize the need for adapting in the difference channel. I know of monopulse antennas being designed for adaptive circuitry in the sum channel only. In order to maintain tracking performance, the difference pattern must be adapted as well.

2. Nulling in Antenna Patterns

This section of the paper shows that a null synthesized in the sum pattern will not necessarily result in a null in the difference pattern and visa versa. An equally spaced linear array of isotropic elements is used in the analysis (Fig. 1). The output of each element passes through a phase shifter which steers the mainbeam as well as provides the adaptive cancellation. Next the signal is split into a sum channel signal and a difference channel signal. Each channel has an amplitude weighting, designed to give a certain

sidelobe level. All the sum channel signals are added together in phase and the resultant signal goes to a receiver. One half of the array's difference channel signals receive a 180° phase shift before being added together with the other half of the difference channel signals. Phase only nulling in the sum channel can be accomplished using a phase only beam space algorithm[1,2]. The algorithm generates a cancellation beam in the direction of interference, then subtracts the beam from the quiescent pattern to get a resultant pattern with a null in the direction of interference.

The phase and amplitude weights for the sum channel are

$$W_n = a_n e^{j\theta n} \qquad (1)$$

where θ_n is the adapted phase setting and a_n the amplitude weight. For low sidelobe antennas W_n may be approximated by

$$W_n = a_n (1+j\theta_n) \qquad (2)$$

The far field pattern of this weight is

$$S(u) = \sum_{n=1}^{N} a_n(1+j\theta_n)e^{jkd_n u} \qquad (3)$$

k = propagation constant = $2\pi / \lambda$

λ = wavelength

$d_n = d_o$

$u = \sin \theta$

θ = angle from boresight

$$= \sum_{n=1}^{N} a_n e^{jkd_n u} + j \sum_{n=1}^{N} \theta_n a_n e^{jkd_n u} \qquad (4)$$

The jammers are known to be at the angles θ_m and m ranges from 1 to M, the number of jammers.

The first summation in equation 4 is the far field antenna pattern of the quiescent weights. The second summation is the cancellation beams generated by the adaptive weights. At each jammer angle θ_m, the quiescent pattern and cancellation beam match in amplitude, but are 180° out of phase.

$$j \sum_{n=1}^{N} a_n \theta_n e^{jks_n u_m} = -\sum_{n=1}^{N} a_n e^{jkd_n u_m} \quad m=1,2,\ldots,M \qquad (5)$$

Use Euler's formula to put the exponent into real and imaginary form

$$j \sum_{n=1}^{N} a_n \theta_n (\cos(kd_n um) + j\sin(Kd_n um)) \qquad (6)$$

$$= -\sum_{n=1}^{N} a_n(\cos(kd_n u_m) + j\sin(kd_n u_m))$$

Next, equate the real and imaginary parts

$$\sum_{n=1}^{N} a_n \theta_n \cos(kd_n u_m) = \sum_{n=1}^{N} a_n \sin(kd_n u_m) \quad (7)$$

$$\sum_{n=1}^{N} a_n \theta_n \sin(kd_n u_m) = \sum_{n=1}^{N} a_n \cos(kd_n u_m) \quad (8)$$

Because $a_n \sin kd_n u_m$ is an odd function, it equals zero when summed from 1 to N. Thus, equation 7 equals zero. The second equation does not equal zero as long as θ_n is an odd function. Equation 8 can be put into the matrix form

$$Ax = B$$

where

$$A = \begin{bmatrix} a_1 \sin(kd_1 u_1) & a_2 \sin(kd_2 u_1) \ldots & a_N \sin(kd_N u_1) \\ a_1 \sin(kd_1 u_2) & a_2 \sin(kd_2 u_2) \ldots & a_N \sin(kd_N u_2) \\ \vdots & \vdots & \vdots \\ a_1 \sin(kd_1 u_M) & a_2 \sin(kd_2 u_M) \ldots & a_N \sin(kd_N u_M) \end{bmatrix}$$

$$X = \begin{bmatrix} \theta_1 \\ \theta_2 \\ \cdot \\ \cdot \\ \cdot \\ \theta_N \end{bmatrix}$$

$$B = \begin{bmatrix} \sum_{n=1}^{N} a_n \cos(kd_n u_1) \\ \cdot \\ \cdot \\ \cdot \\ \sum_{n=1}^{N} a_n \cos(kd_n u_m) \end{bmatrix}$$

This equation has more unknowns than equations. It can be solved using the method of least squares.

$$x = A^T(AA^T)^{-1}B \qquad (9)$$

The vector x contains the adapted weights θ_n that give M nulls in the direction of the jammers.

Figure 2 shows the far field pattern of a 20 element array with a 35 dB Taylor distribution $\bar{n} = 6$. The next figure shows the cancellation beams used to place a null in the pattern at 22° and 59°. In phase only nulling, a cancelling beam in the θ_m direction has a corresponding beam at $-\theta_m$. When these two patterns are added together the pattern in Figure 4 is obtained. This

pattern has nulls in the desired directions. At $-\theta_m$ the cancellation patterns and quiescent pattern add in phase to raise the sidelobes of the resultant pattern in those directions.

Applying these phase shifts to the array in Figure 1 puts nulls in the sum pattern. These phase shifters are shared by both the sum and difference channels. A 35 dB, $\bar{n} = 6$ Bayliss amplitude distribution on a 20 element array has a far field pattern shown in Figure 5. The phase shifters, θ_n, change this pattern into the one in Figure 6. Nulls are not formed at the angles θ_m. In fact, the difference pattern has worse characteristics after the adapting. A similar analysis can be done for the difference pattern.

$$W_n = b_n e^{j\theta_n} \; ; \; b_n = \text{difference amplitude weights} \qquad (10)$$

$$\approx b_n (1+j\theta_n) \qquad (11)$$

The difference far field pattern is given by

$$D(U) = \sum_{n=1}^{N} b_n(1+j\theta_n) e^{jkd_n u} \qquad (12)$$

At the angles θ_n, $D(u_m)$ is zero

$$j \sum_{n=1}^{N} b_n\theta_n \left(\cos(kd_nu_m) + j\sin(kd_nu_m)\right)$$

$$= \sum_{n=1}^{N} b_n\left(\cos(kd_nu_m) + j\sin(kd_{11}u_m)\right) \qquad (13)$$

Equating the real and imaginary parts gives

$$\sum_{n=1}^{N} b_n\theta_n \cos(kd_nu_m)$$

$$= \sum_{n=1}^{N} b_n\sin(kd_nu_m) \qquad (14)$$

$$\sum_{n=1}^{N} b_n\theta_n\sin(kd_nu_m) = \sum_{n=1}^{N} b_n\cos(kd_nu_m) \qquad (15)$$

Unlike the sum amplitude distribution, the difference amplitude weights are an odd function. Instead of equation 14 going to zero, equation 15 equals zero. Likewise, this equation may be put into matrix form and solved for the adaptive weights, θ_n. Some results are shown in Figures 7 and 8. Figure 9 shows the difference adapted weights applied to the sum pattern. Again, the desired nulls do not appear.

In order to simultaneously place nulls in the sum and difference patterns, one set of adaptive weights could be placed in the sum channel, while another is placed in the difference channel. This

method calls for an extensive duplication of hardware. In addition, phased arrays are normally built with one set of phase shifters that are shared by both channels. This technique could not be readily implemented on existing antennas. These problems can be overcome by using a special technique that simultaneously places nulls in the sum and difference patterns using the one set of phase shifters shared by both channels. Such a technique is described in the following section.

3. Simultaneous Nulling in Sum and Difference Patterns

Equations 8 and 14 hold true for placing nulls in the sum and difference patterns. Rather than solving these two systems of equations separately, they are combined into one system of equations. The resulting matrix equation $Ax = B$ has the components

$$A = \begin{bmatrix} a_1\sin(kd_1u_1) \cdots & a_N\sin(kd_Nu_1) \\ \vdots & \vdots \\ a_1\sin(kd_nu_m) \cdots & a_N\sin(kd_Nu_m) \\ b_1\cos(kd_1u_m) \cdots & b_N\cos(kd_Nu_1) \\ \vdots & \vdots \\ b_1\cos(kd_1u_m) \cdots & b_N\cos(kd_Nu_m) \end{bmatrix}$$

$$x = \begin{bmatrix} \theta_1 \\ \theta_2 \\ \vdots \\ \theta_n \end{bmatrix}$$

$$B = \begin{bmatrix} \sum_{n=1}^{N} a_n \cos(kd_n u_1) \\ \vdots \\ \sum_{n=1}^{N} a_n \cos(kd_n u_m) \\ -\sum_{n=1}^{N} b_n \sin(kd_n u_1) \\ \vdots \\ \sum_{n=1}^{N} b_n \sin(kd_n u_m) \end{bmatrix}$$

The least mean square solution to this equation yields a θ_n which has nulls in both the sum and difference patterns.

The previous cases run for the sum and difference patterns were tried again for the new technique. The results appear in Figures 10 and 11. These patterns were obtained by placing a phase shift of θ_n on the phase shifters of the array in Figure 1.

4 Conclusion

The technique described in this paper is only theoretical and not meant for direct implementation. However, it does draw attention to the need for simultaneous nulling in the sum and difference channels of a monopulse antenna. Nulling only in the sum channel is not adequate. Also, the techique developed shows that it is theoretically possible to simultaneously null in both the sum and difference patterns using one set of adaptive weights. Even though

this method of nulling is theoretical, it has potential for practical implementation. For instance, an adaptive loop could be used to adjust the height of the cancellation beams for a non ideal pattern. In this way the nulls are adaptively formed rather than synthesized.

References

1. Baird, Charles A. and Rassweiller, George G. "Adaptive Sidelobe Nulling Using Digitally Controlled Phase Shifters". IEEE Trans. Ant. and Prop. Vol. AP-24, No. 5, Sep 1976, pp 638-649.

2. Shore, Robert A. "Nulling in Linear Array Patterns with Minimization of Weight Perturbations." RADC report to be published.

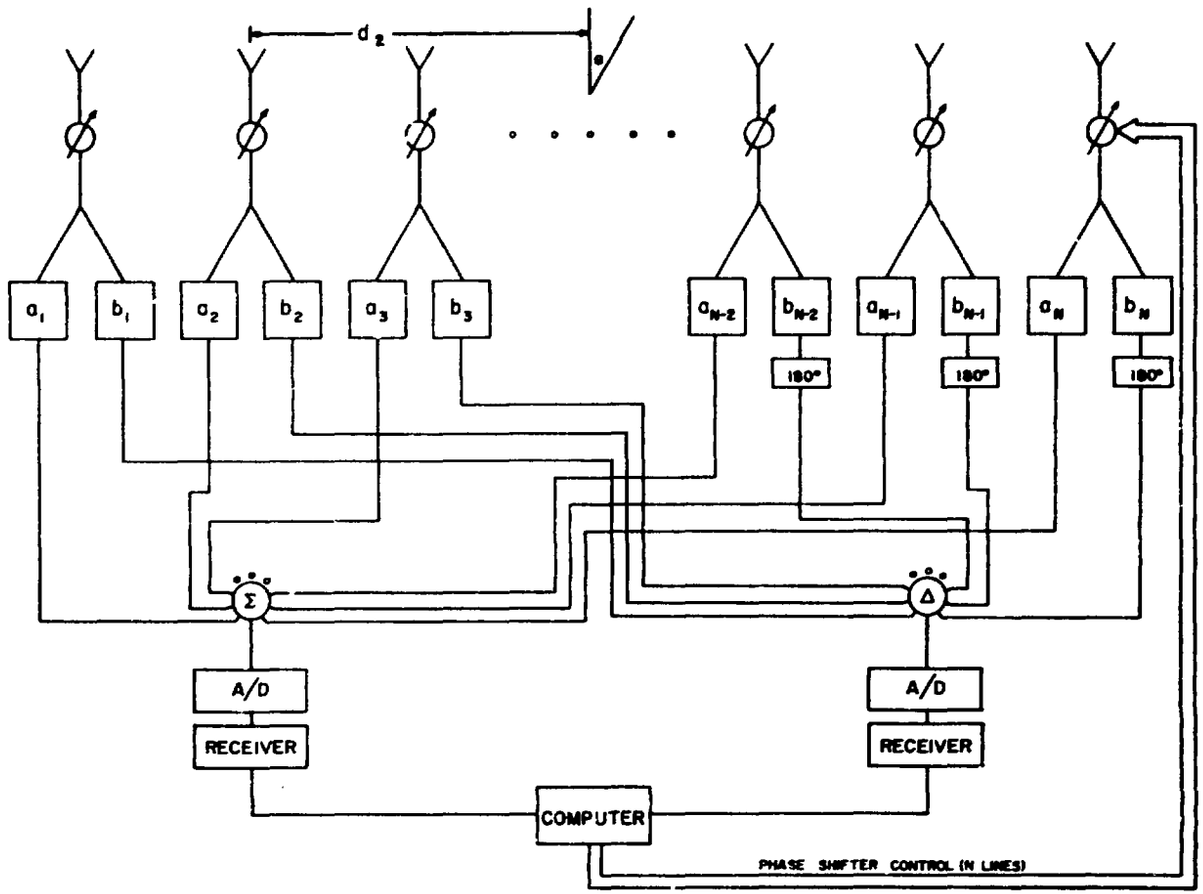

Fig. 1 Monopulse Phased Array

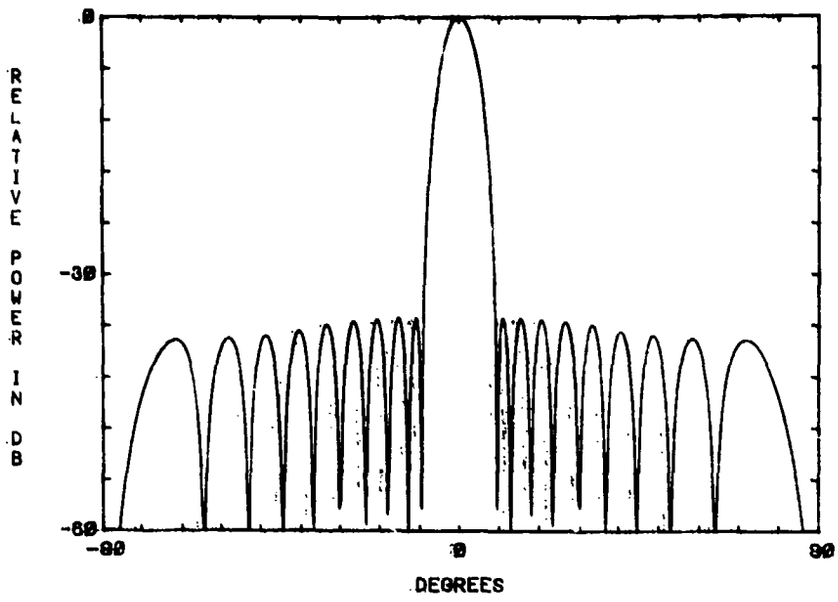

Fig. 2 Quiescent Far Field Sum Pattern

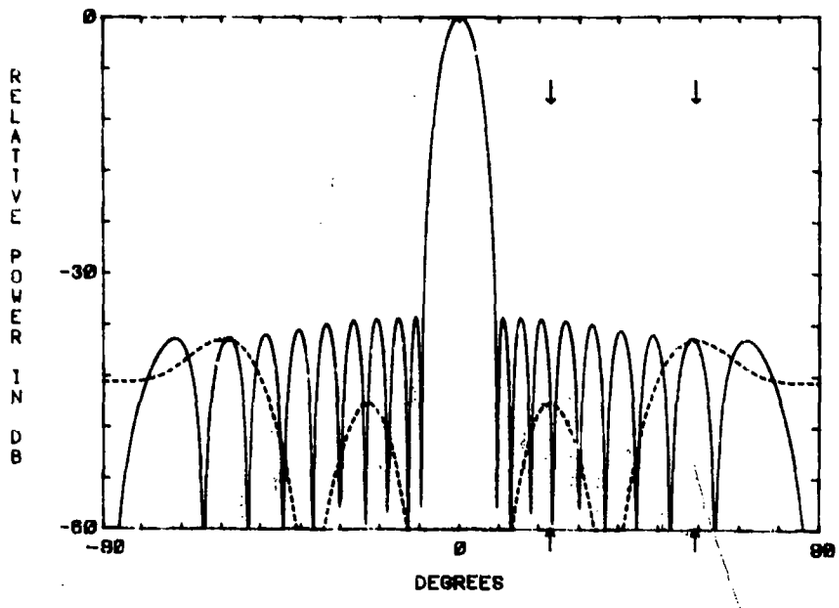

Fig. 3 Sum Pattern and Its Cancellation Beams

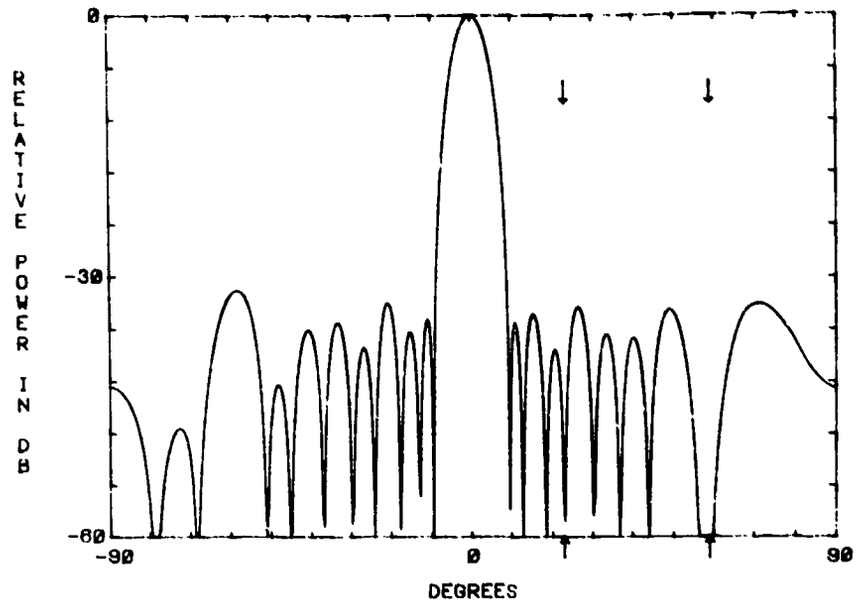

Fig. 4 Result of Adding Quiescent Pattern and Cancellation Beams

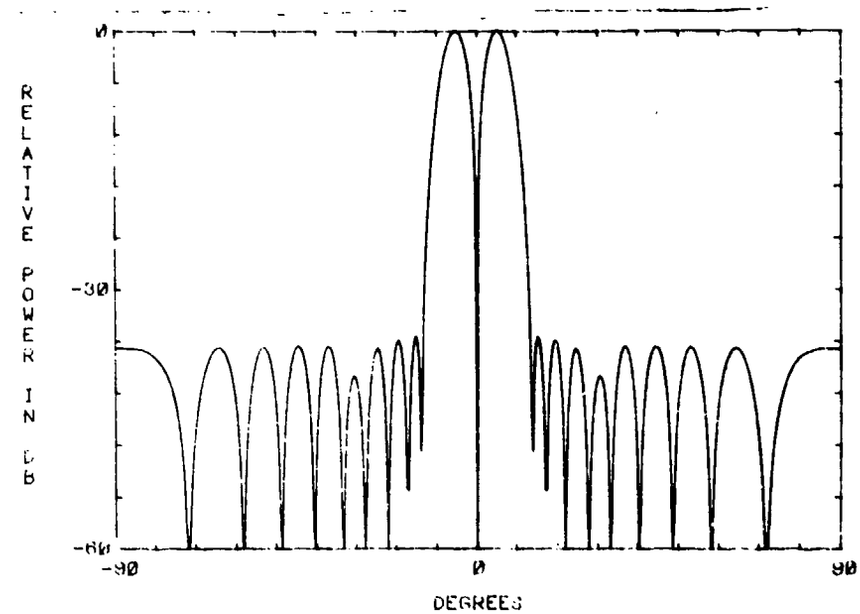

Fig. 5 Quiescent Far Field Difference Pattern

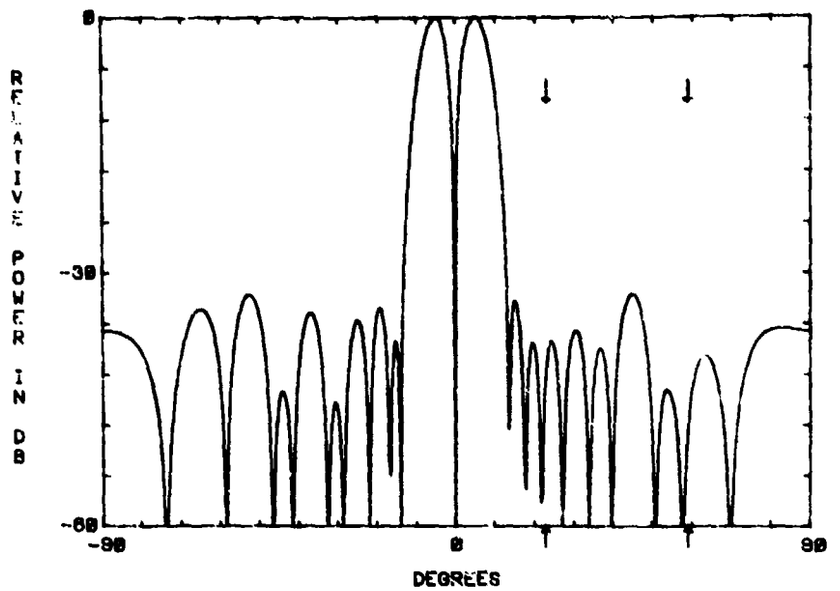

Fig. 6 Far Field Difference Pattern When Phase Shifters are Adjusted for Nulls in the Sum Channel

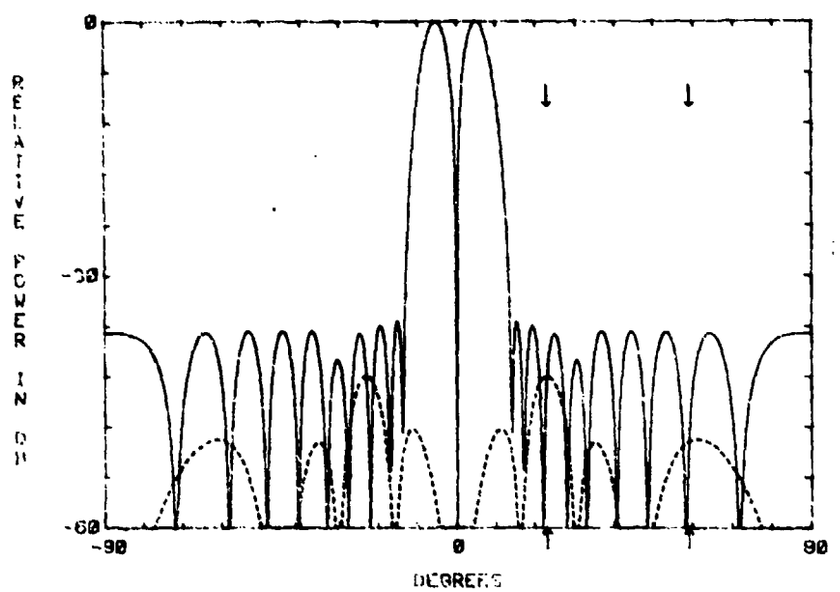

Fig. 7 Difference Pattern and Its Cancellation Beams

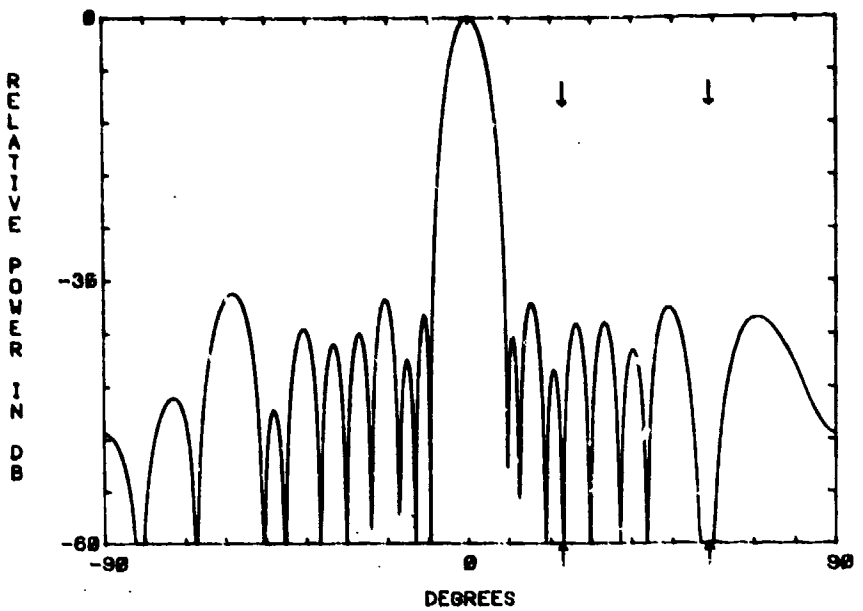

Fig. 8 Result of Adding Quiescent Difference Pattern and Difference Cancellation Beams

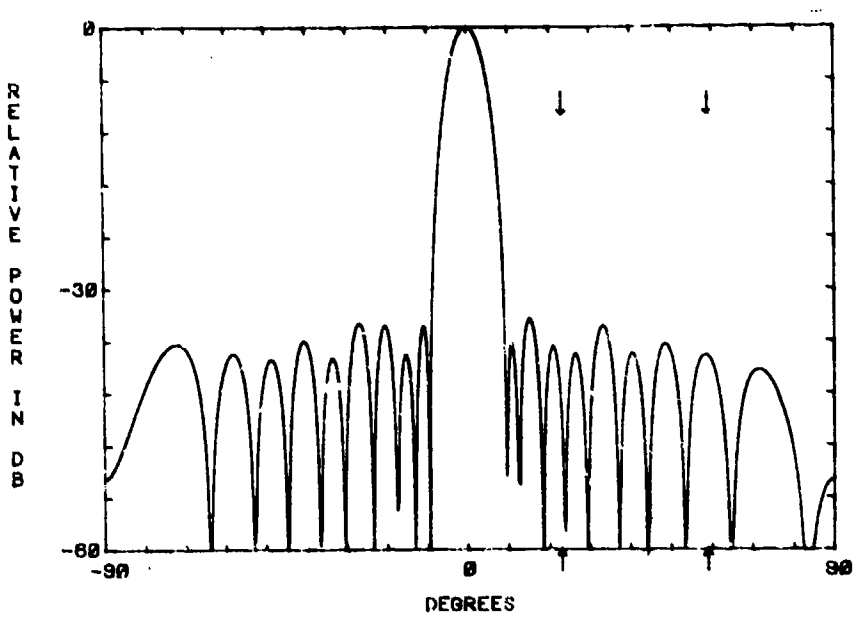

Fig. 9 Far Field Sum Pattern When Phase Shifters Are Adjusted for Nulls in the Difference Channel

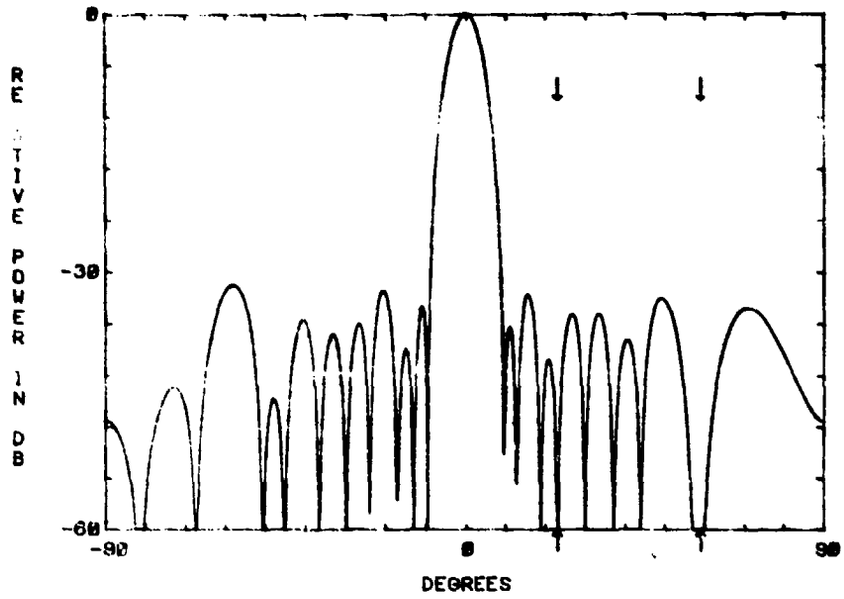

Fig. 10 Far Field Sum Pattern Resulting from Simultaneous Nulling

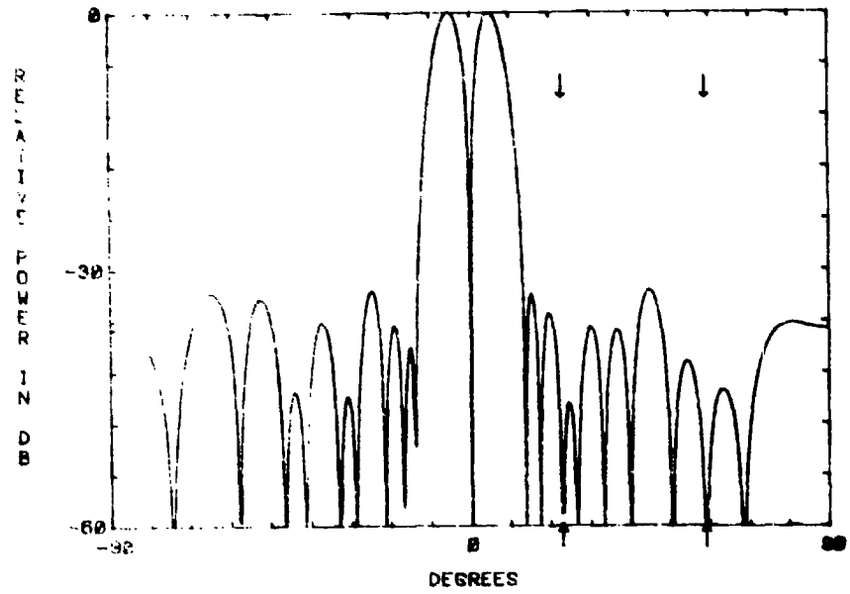

Fig. 11 Far Field Difference Pattern Resulting from Simultaneous Nulling

AD P001099

FOCUSED LINEAR ARRAY FOR HYPERTHERMIA RESEARCH

W. Gee, S.W. Lee and R.Mittra
Electromagnetics Laboratory

and

C. Cain and R. Magin
Bioacoustics Laboratory

University of Illinois
Urbana, Illinois 61801

ABSTRACT

Recent research has shown that treatment of tumors with localized heat (42 - 45 degrees Celsius) can cause partial or even complete tumor regression. Heating with microwave energy may prove to be a viable clinical procedure. A promising approach to microwave hyperthermia applicator design is to use phased array antennas to rapidly scan an arbitrary tumor volume with a minimal diameter beam or heating spot.

The design and analysis of a focused linear array at 2450 MHz for microwave hyperthermia research will be described. Four titanium dioxide loaded horn antennas with apertures of 0.79 x 0.53 inch and a feed network with weighted phase shifts were used to implement the focusing array for focal distances of 3.0 to 4.0 inches. The array was submerged in deionized water in order to reduce the array size, and to provide a better impedance match to a high dielectric media representative of the human tissues. Power radiation pattern

PAGE BLANK-NOT FILMED

measurements were taken at different focal planes in 0.5 inch increments to determine the focusing characteristics and beam spot size. Due to the high attenuation of the medium, focal planes beyond 4.0 inches were not taken. The measured half power beamwidth (HPBW) was approximately 0.5 inch at the focal point. A computer program was developed to predict the array performance. The theoretical predictions for the array patterns are in close agreement with the laboratory measurements.

1. INTRODUCTION

A single dielectric-loaded open-ended waveguide, horn, or coaxial antenna are generally used by bioengineering researchers as the principal microwave hyperthermia applicators[1]-[4]. The problem with a single-element applicator is that it does not have focusing ability. Thus, the RF energy cannot be efficiently directed to the intended tumor, and in fact spills over the adjacent healthy tissue.

One way to solve the focusing problem is to use a phased array, which is the subject of the present paper. Phased array technology of course is well established in radar/communication systems. However, the phased array used in the present application is different from a conventional one in the following two aspects:

(i) The focal point of the present array beam is only several inches away from the radiating aperture, in contrast to the infinite distance for the conventional array.

(ii) The present array is immersed in a lossy medium (water) instead of the unbounded lossless free space.

Because of the differences mentioned above, the design of a phased array applicator for hyperthermia is not at all trivial. In the present paper, we first develop a theory for analyzing an arbitrary array designed for a near-field focusing, and then verify our theory by experiment with a four-element linear array.

2. THEORETICAL MODEL

A nineteen element hexagonal planar array was chosen as the candidate for this hyperthermia study. Figure 1a and 1b depicts the geometry of the phased array used in the mathematical formulation. Two dielectric mediums are considered, that is, ϵ_1 represents the layer of deionized water serving as the impedance matching section between the antenna array and the human interface, and ϵ_2 represents the human tissue layer. d_1 is the distance between the plane of the antenna array and the surface of the human tissue. d_2 is the distance from the surface of the human tissue to the desired focal point or depth of the tumor.

Let us consider the field at an observation point A with rectangular coordinates (x, y, z) due to the radiation from a typical m-th array element located at (x_m, y_m, z_m). By geometrical optics, we trace a ray from the m-th element to A. The incident angle θ_{m1} and the refracted angle θ_{m2} due to the m-th element can be readily found from the simultaneous equations below.

$$\begin{cases} \tan\theta_{m1} = \dfrac{\sqrt{(x-x_m)^2+(y-y_m)^2}}{} - (z-d_1)\tan\theta_{m2} & (1a) \\ \tan\theta_{m2} = \dfrac{Re(k_1 \sin\theta_{m1})}{Re\sqrt{k_2^2 - (k_1 \sin\theta_{m1})^2}} & (1b) \end{cases}$$

where

$$k_n = \frac{2\pi}{\lambda}\sqrt{\epsilon_n' - j\epsilon_n''}\,, \quad n = 1, 2 \qquad (2)$$

The time convention used in the present paper is $\exp(+j\omega t)$. Thus, the negative imaginary part of ϵ_n in (2) represents loss in the medium. In the present application, medium 1 (water) is usually denser than medium 2 (tissue) i.e., $Re(k_1) > Re(k_2)$. Total reflection occurs if

$$(Re\, k_1)\sin\theta_{m1} > Re\, k_2 \qquad (3)$$

The present ray analysis is not capable to describe the total

reflection phenomenon. Thus, for each θ_{m1} found from (1), we must check that it satisfies

$$(Re\, k_1) \sin\theta_{m1} < Re\, k_2 \quad (\text{no total reflection}) \tag{4}$$

For all the computations reported in this paper, (4) is indeed satisfied. The transmission coefficients at the water-tissue interface are denoted by $(T_{m\parallel}, T_{m\perp})$ for (parallel, perpendicular) components, respectively. These coefficients are given by the well-known expression [5]

$$\begin{cases} T_{m\parallel} = \dfrac{2}{n+C} & (5) \\[2ex] T_{m\perp} = \dfrac{2}{1+nC} & (6) \end{cases}$$

where

$$n = \sqrt{\frac{\epsilon_2}{\epsilon_1}} \tag{7}$$

$$C = \frac{\sqrt{1 - \frac{\epsilon_1}{\epsilon_2}\sin^2\theta_{m1}}}{\cos\theta_{m1}} \tag{8}$$

The incident E-field due to the m-th element at observation point A can be written as:

$$\vec{E}_m^i = \frac{e^{-jkr}}{4\pi r}\left[\hat{\theta}_m U_{\theta m} + \hat{\phi}_m U_{\phi m}\right] \tag{9}$$

where

$$U_{\theta m} = \left\{ V_{xm} (\cos\theta)^{g_1} \cos\phi_m + V_{ym} (\cos\theta)^{g_2} \sin\phi_m \right\} \tag{10}$$

$$U_{\phi m} = \left\{ -V_{xm} (\cos\theta)^{g_2} \sin\phi_m + V_{ym} (\cos\theta)^{g_1} \cos\phi_m \right\} \tag{11}$$

V_{xm} = voltage excitation coefficient for E_x-component

V_{ym} = voltage excitation coefficient for E_y-component

$$\phi_m = \tan^{-1}\left(\frac{y - y_m}{x - x_m}\right) \tag{12}$$

In (10), the element pattern is approximated by $(\cos\theta)^g$ function in the manner described in [5]. Let us assume that the array is linearly polarized in the x-direction. Thus, we set $V_{xm} = 1$, $V_{ym} = 0$ in (10) and (11). Then the transmitted electromagnetic field at the observation point A due to the m-th element is given by:

$$\vec{E}_m^t(A) = \frac{e^{-j k_1 \left(\frac{d_1 - z_m}{\cos\theta_{m1}}\right)} e^{-j k_1 \sin\theta_{m1} (z - d_1) \tan\theta_{m2} - j(z-d_1)\sqrt{k_2^2 - (k_1 \sin\theta_{m1})^2}}}{4\pi \left(\frac{d_1 - z_m}{\cos\theta_{m1}} + \frac{z - d_1}{\cos\theta_{m2}}\right)} \tag{13}$$

$$\times \left\{ \hat{x} \left[U_{\theta m} T_{m\parallel} \cos\theta_{m2} \cos\phi_m - U_{\phi m} T_{m\perp} \sin\phi_m \right] \right. \tag{14}$$

$$+ \hat{y} \left[U_{\theta m} T_{m\parallel} \cos\theta_{m2} \sin\phi_m + U_{\phi m} T_{m\perp} \cos\phi_m \right] \tag{15}$$

$$\left. + \hat{z} \left[-U_{\theta m} T_{m\parallel} \sin\theta_{m2} \right] \right\} \tag{16}$$

The total electric field E at the observation point A due to the entire array is given by:

$$\vec{E}^t(A) = \sum_m W_m \vec{E}_m^t(A) \tag{17}$$

where

$$W_m = |W_m| e^{j\alpha_m} = \text{weighting factor of } m\text{-th element} \tag{18}$$

The phase factor α_m in (19) is to be determined in the manner described next. In order to focus the array field at a focal point F, we must have

$$\alpha_m = (-1)\{\text{phase of } \vec{E}_m^t(F) \cdot \hat{x}\} \tag{19}$$

when (19) is used in (17), all the terms in the summations are added in phase at point F (not at other observation points of course). Finally, the total incident power of the array can be calculated by superposition of power as follows:

$$P_{inc} = \frac{1}{8\pi Z} \frac{(q_1+q_2+1)}{(2q_1+1)(2q_2+1)} \sum_m \{|W_m|^2\} \quad \text{watts} \tag{20}$$

where

$$Z = \sqrt{\mu_o/\epsilon_o}\, Re\, G_1 \tag{21}$$

And the normalized electric field with respect to a 1.0 watt incidence can be approximated by:

$$\vec{E}_m^t \sim \frac{1}{\sqrt{P_{inc}}} \sum_m \vec{E}_m^t W_m \tag{22}$$

3. EXPERIMENTS AND SIMULATIONS

In order to demonstrate the focusing concept and validate the theoretical model, a four element linear array was fabricated and radiation power pattern measurements were conducted with the array submerged in a tank of deionized water as depicted in Figure 2 to determine the focusing characteristics.

Four dielectric (titanium dioxide) loaded horn antennas were used to form the linear array. The feed network consists of a four way in-phase power divider and line stretchers which provide the weighted phases required for focusing the array at the desired focal point. Figure 3 depicts the hyperthermia system block diagram. There are impedance mismatches between the antennas and the deionized water layer. Ferrite isolators were incorporated to prevent RF power from reflecting back into the power generator.

Figure 4a illustrates the relative power pattern of the four element linear array with equal phase excitation (non-focusing) with element positions (x_m, y_m, z_m): (-2",0.,0.), (-.67,0.,0.), (.67,0.,0.) and (2.,0.0.) measured at 3.5 inches cut-plane. Figure 4b depicts the relative power pattern with the same element position as Figure 4a but phased for focal plane at 3.5 inches. Similarly, with the array focused at 3.5 inches as in (4b), relative power patterns were taken at cut-planes 0.5 inch in front and 0.5 inch behind the focal plane as shown in Figure 4c and Figure 4d, respectively.

Next the antenna element spacings (positions) were brought closer together, that is, (-1.35",0.,0.), (-.45,0.,0.), (.45,0.,0.) and (1.35,0.,0.). Again, the array was phased to focus at the focal plane of 3.5 inches and the relative power patterns were taken at the focal plane and cut-planes 0.5 inch

in front and behind the focal plane as shown in Figures 5a, 5b, and 5c, respectively.

At this writing, the actual relative dielectric constant of the deionized water has not been measured. However, for the sake of expediency, the dielectric constant of 76.7-j12.04 [7] was assumed throughout our computer analyses. Attenuation measurements were conducted with two similar antennas in the water bath and the loss agreed fairly close with the calculation made with the assumed loss tangent. Figure 6 shows the attenuation of the deionized water used in this series of experiments. For example, the computed loss using the assumed loss tangent is shown below:

since

$$\epsilon_r = 76.7 - j12.04$$

$$\sqrt{\epsilon_r} = 8.78 - j.69$$

and

$$k = \frac{2\pi}{\lambda}\sqrt{\epsilon_r} = k' - jk'' = 4.505 - j.3540 \ cm^{-1}$$

then

$$p = 10 \log e^{-2k''\delta} = -3.0753 \ dB/cm$$

At the same time, the radiation pattern of a single dielectric loaded horn was taken to determine the exponential Q1 and Q2 for the element pattern factor in equations (10) and (11). Figure 7 depicts the computed element pattern factor for various values of exponent Q and the actual measured Q.

At this point in time, the nineteen element hexagonal array has not been built; however, computer simulation of radiation patterns has been carried out in both 2-dimensional and 3-dimensional graphics for sensitivity studies. For examples, Figure 8a depicts the relative power pattern of the nineteen element hexagonal array in a single medium (water) case focused at 3.5 inches from the plane of the array. Figure 8b depicts the relative power pattern of two mediums (water and muscle tissue) focused at 4.5 inches from the plane of the array. Figure 9a and 9b illustrates a 3-dimensional plot of the nineteen element array for single and two medium cases, respectively.

4. RESULTS AND CONCLUSIONS

The experiments conducted with the four element linear array has successfully demonstrated that the focusing of an array in the near field can be accomplish by properly adjusting the phase of each antenna element. Computer simulation of the actual linear array provided relative power patterns in close agreement with the laboratory measurements. Some slight

deviation or glitches were noted between the theoretical and the actual measurements, but they are traced to the imperfection of the equipment. For instance, each antenna element is not exactly identical and there are certain amount of accumulated errors in phase matching of the feed network. However, it is evident that the nineteen element hexagonal planar array can offer an improvement in the beam spot size and suppressing the intermediate sidelobes and at the same time pushing the grating lobes outside the visible region.

Further studies will be continued, they will include an optimization routine to find the minimal beam spot size and best geometry of the array. Also, the optimal frequency range will be determined whereby losses can be minimized and at the same time maintaining the integrity of the focusing capability. Additional formulation will be made to find the power density of the spot beam at boresight and throughout the scan region and at different depth of pentration. Furthermore, a search will be conducted for a low loss high dielectric material and that has the property of a coolant.

ACKNOWLEDGEMENT

The authors wish to thank Nelson Bong and Roland Gilbert for their invaluable assistance with the computer programming and graphics and to Pam Miller, Hieu Tran and Raju Chandra for painstakingly making all the radiation pattern measurements and data reductions.

REFERENCES

[1] Paglione, R., et al; (1981) 27 MHz Ridged Waveguide Applicators for Localized Hyperthermia Treatment of Deep-Seated Malignant Tumors; Microwave Journal.

[2] Christensen, D. A., and Durney, C. H.; (1981) Hyperthermia Production for Cancer Therapy: A Review of Fundamental Methods; Journal of Microwave Power 16(2).

[3] Dobson, J.; (1980) Equipment for Local and Regional Hyperthermia, NCI Workshop on Hyperthermia equipment.

[4] Burdette, E.C., Cain, F.L., and Seals, J.; (1980) In-Vivo Probe Measurement Technique for Deter mining Dielectric Properties at VHF through Microwave Frequencies, IEEE Trans. Microwave Theory Technique 28 414-427.

[5] Born, M. and Wolf, E.; (1970) Principles of Optics , 4th Ed.,397, New York Pergamon Press.

[6] Lee, S.W.; Chapter 1 in Antenna Handbook , ed. by Y.T. Lo and S.W. Lee , to be publish by International Telephone and Telegraph Corp., Indianapolis,IN

[7] Sam, H.W., (1977) Reference Data For Radio Engineers , International Telephone and Telegraph Corp., Indianapolis, IN. ,p. 4-30

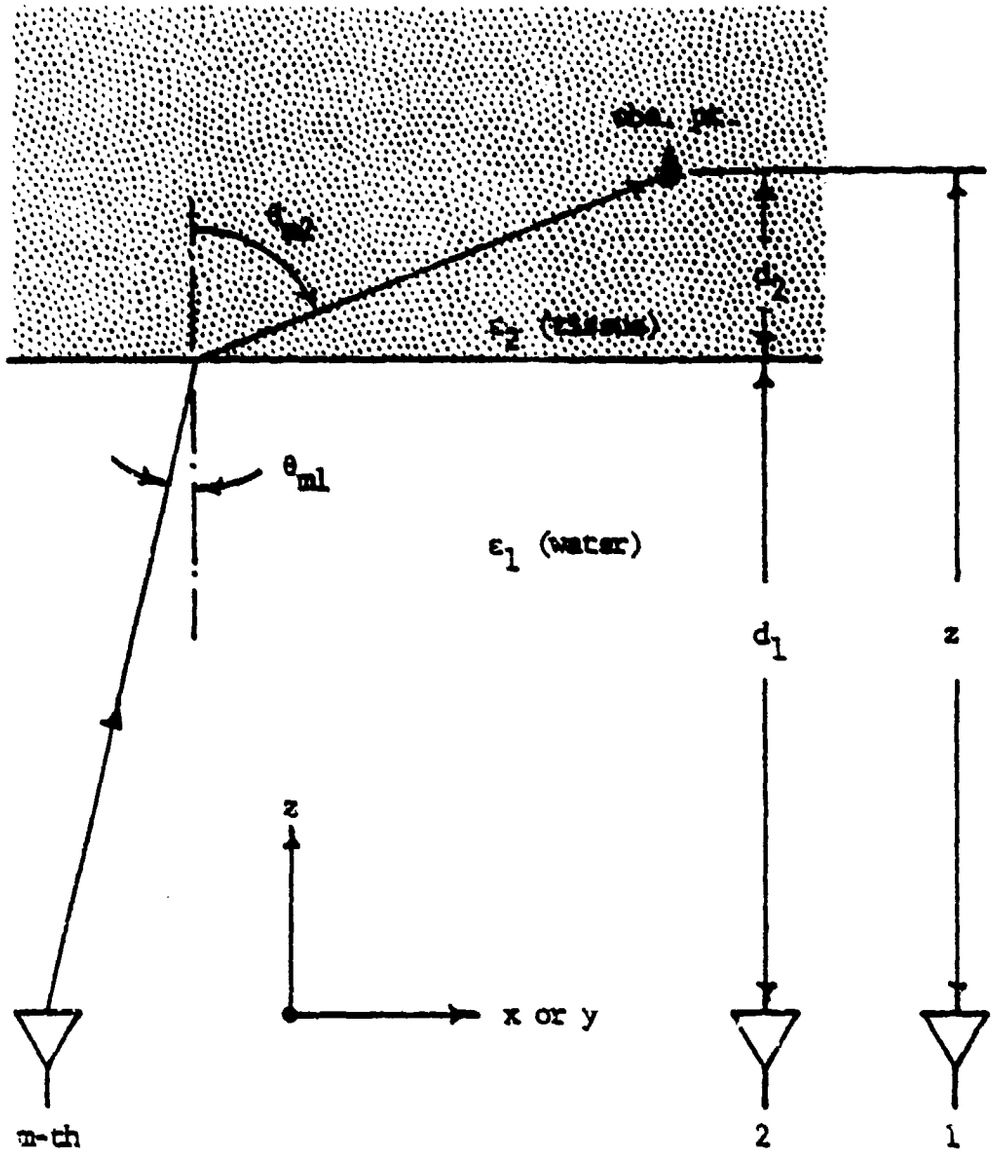

Figure 1a. Geometry of Hyperthermia Study Model

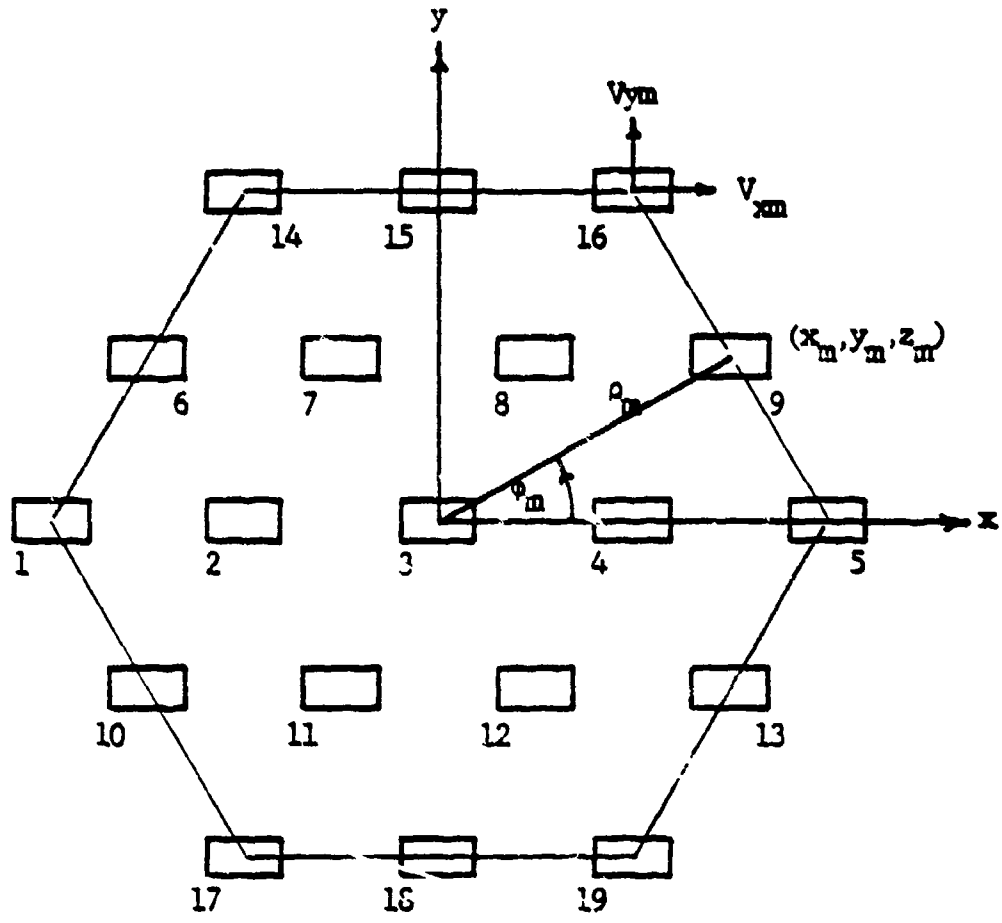

Figure 1b. Geometry of Nineteen Element Hexagonal Planar Array

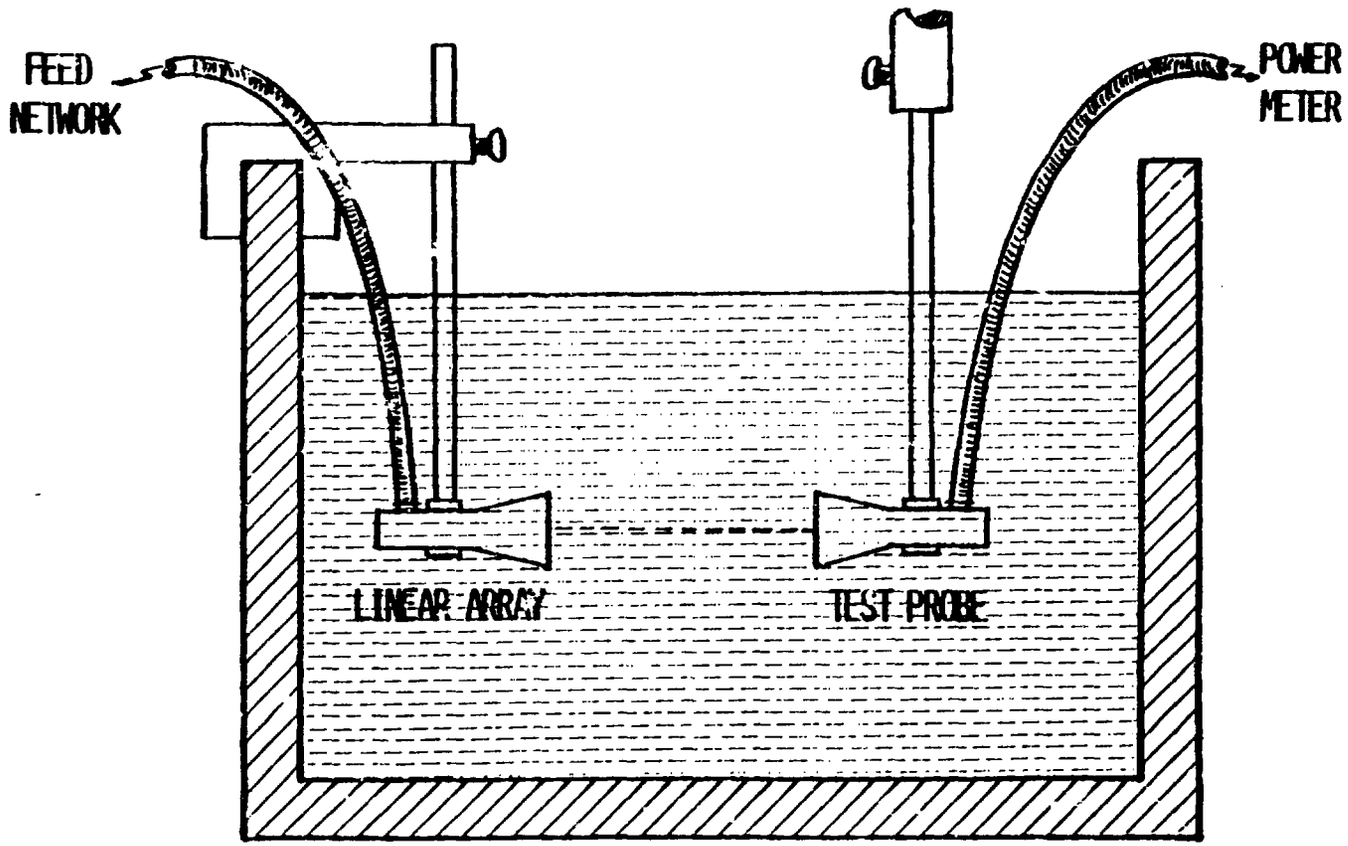

Figure 2. Illustration of Hyperthermia Laboratory Measurement Set-Up.

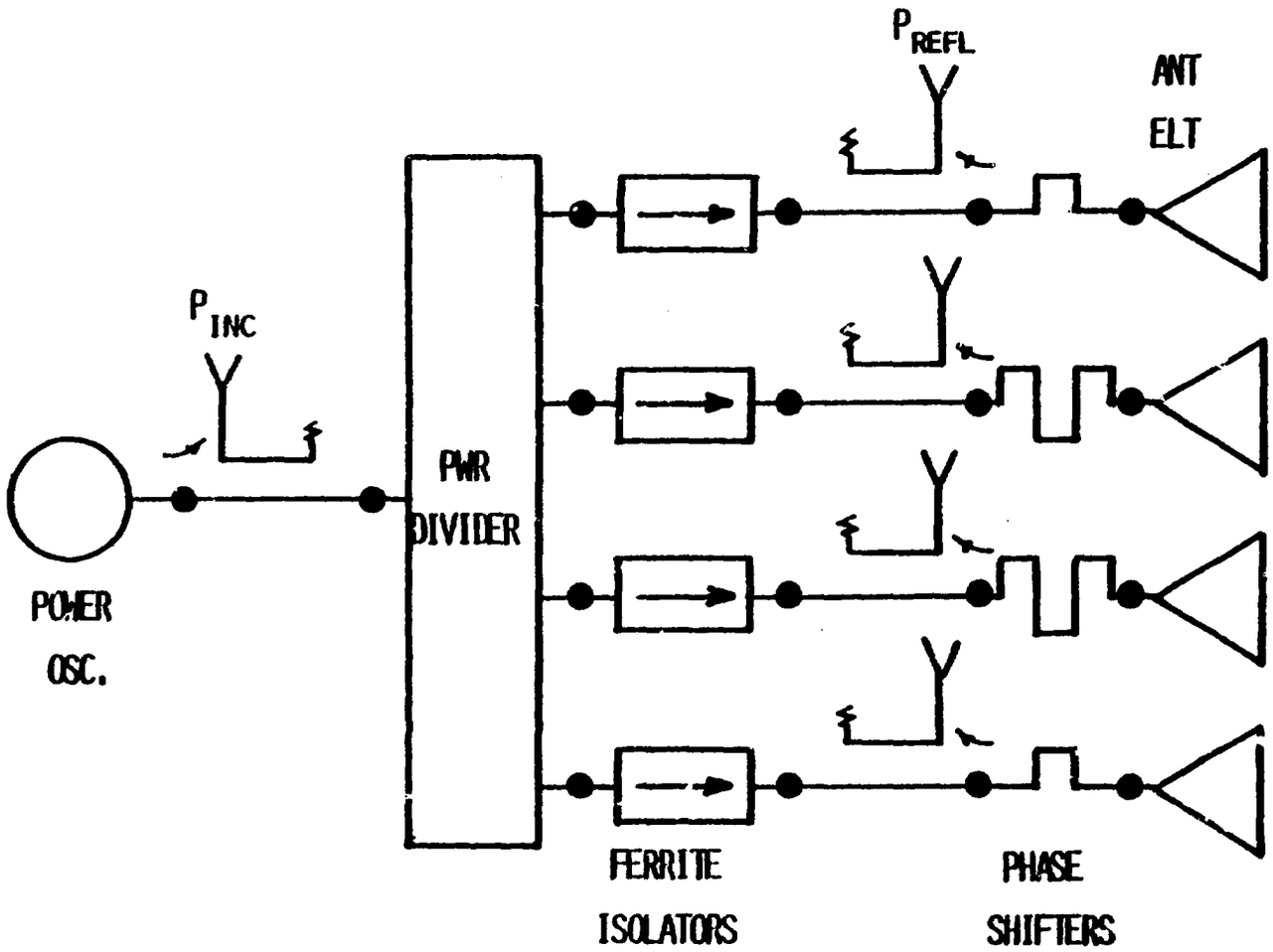

Figure 3. Four Element Linear Array Hyperthermia System Diagram

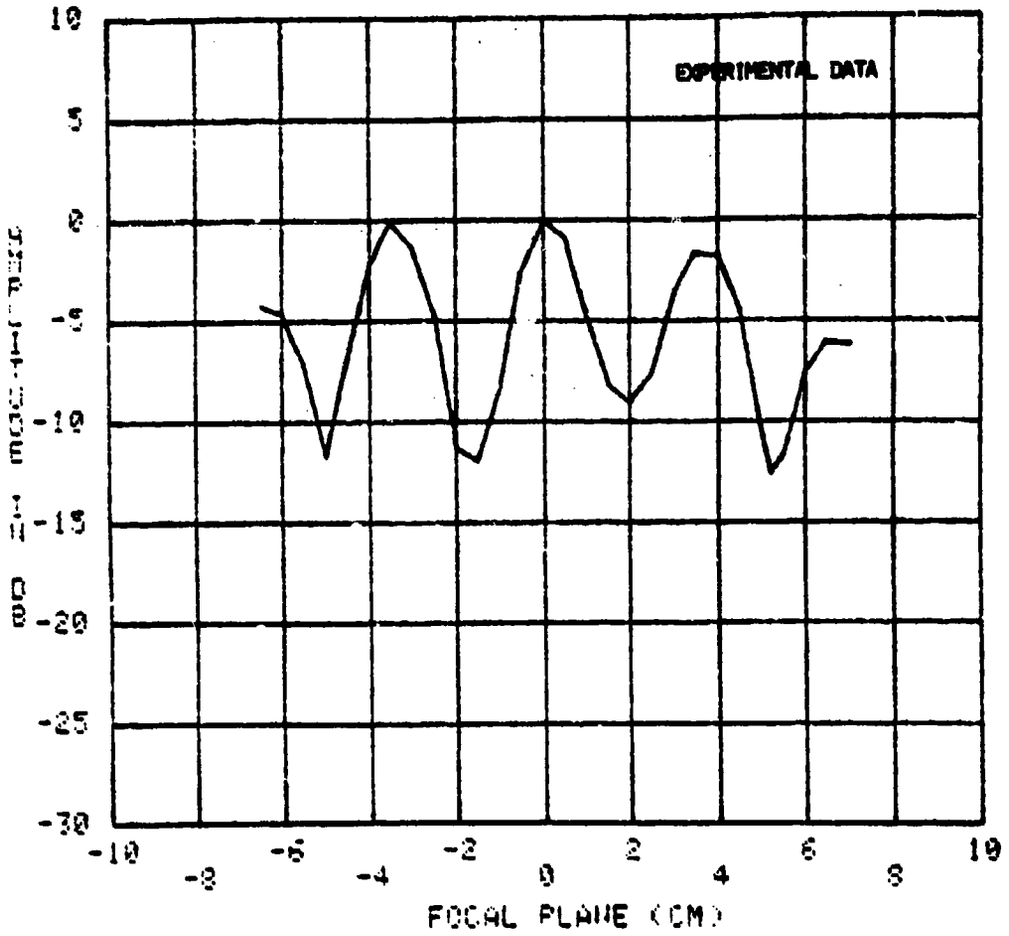

Figure 4a. Relative power pattern of the four element linear array with equal phase excitation (non-focusing) and element coordinates (inches): (-2.,0.,0.), (-.67,0.,0.), (.67,0.,0.) and (2.,0.,0.) measured at cut-plane = 3.5 inches.

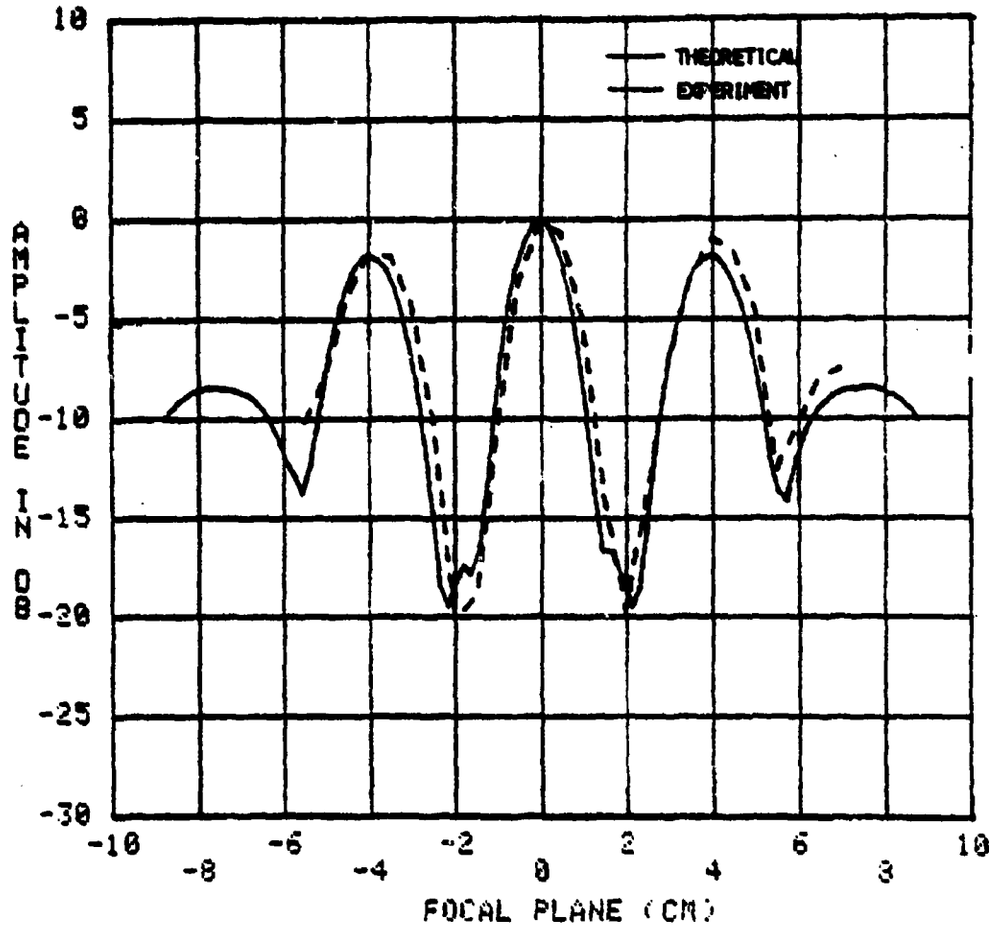

Figure 4b. Relative power pattern of the four element linear array phased for focal plane = 3.5 inches with element coordinates (inches): (-2.,0.,0.), (-.67,0.,0.), (.67,0.,0.) and (2.,0.,0.) measured along the focal plane.

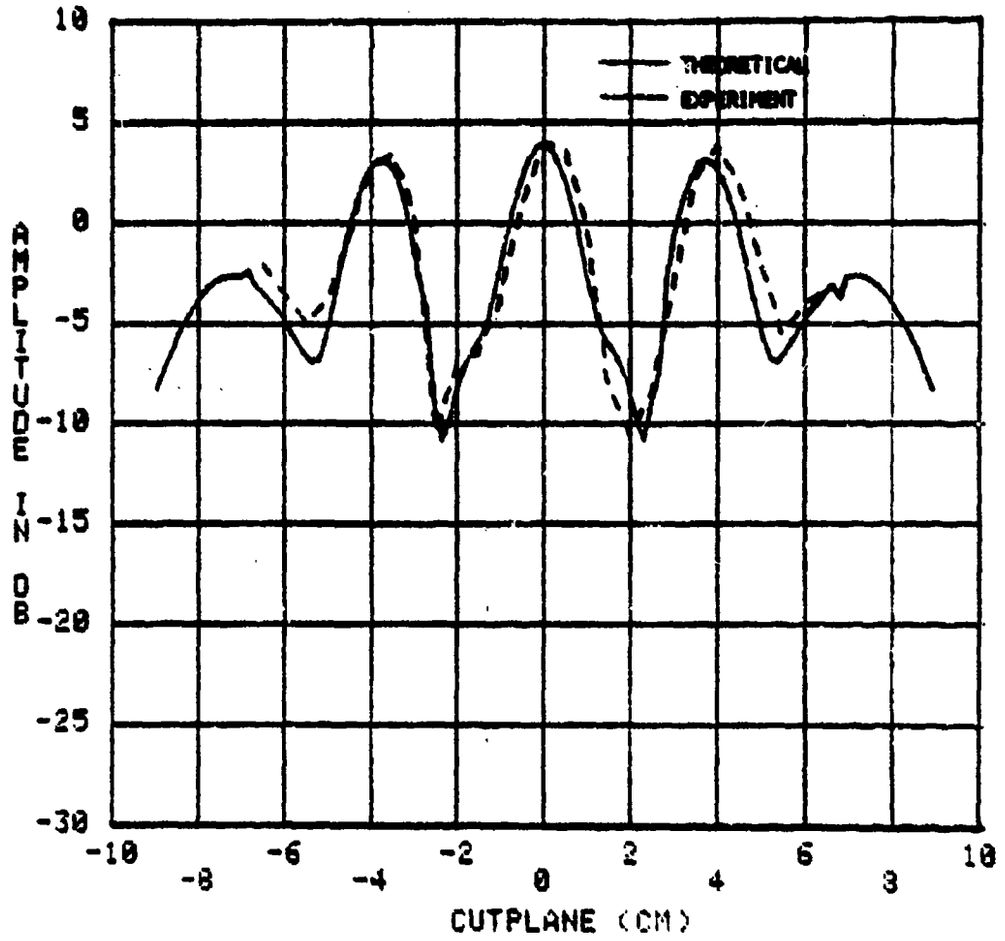

Figure 4c. Relative power pattern of the four element linear array phased for focal plane = 3.5 inches with element coordinates (inches): (-2.,0.,0.), (-.67,0.,0.), (.67,0.,0.) and (2.,0.,0.) measured at cut-plane = 3.0 inches.

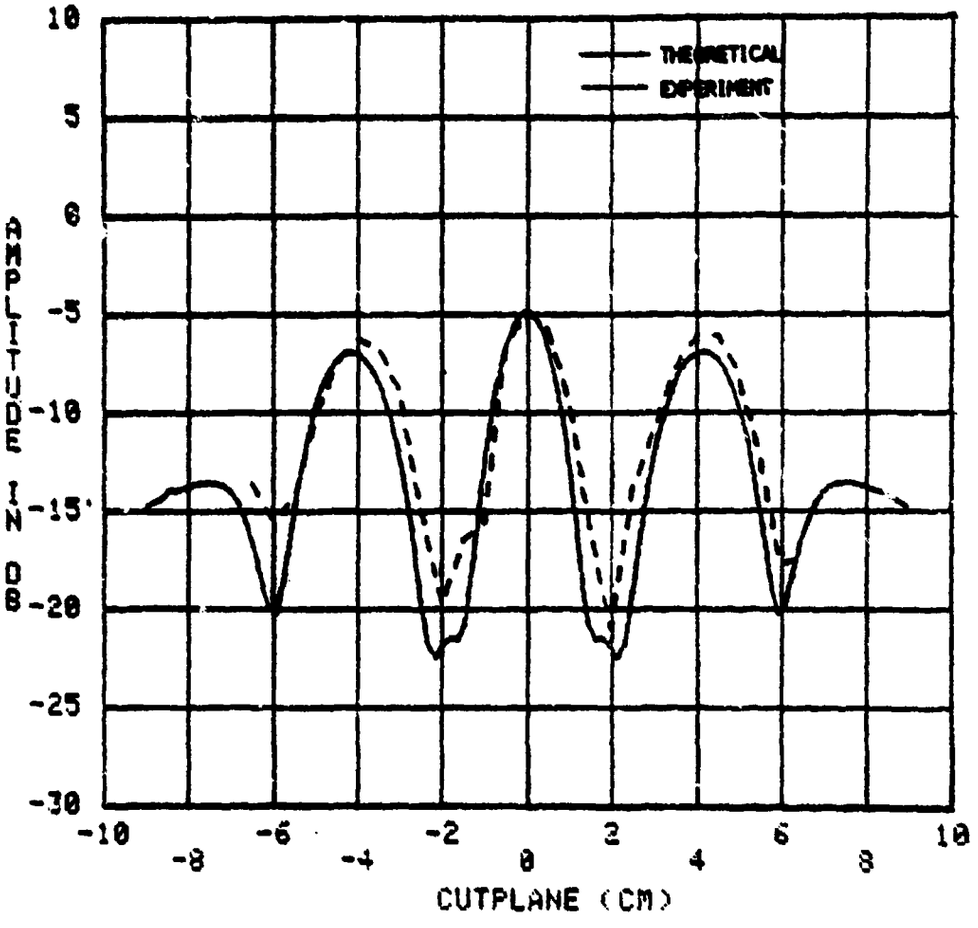

Figure 4d. Relative power pattern of the four element linear array phased for focal plane = 3.5 inches with element coordinates (inches): (-2.,0.,0.), (-.67,0.,0.), (.67,0.,0.) and (2.,0.,0.) measured at cut-plane = 4.0 inches.

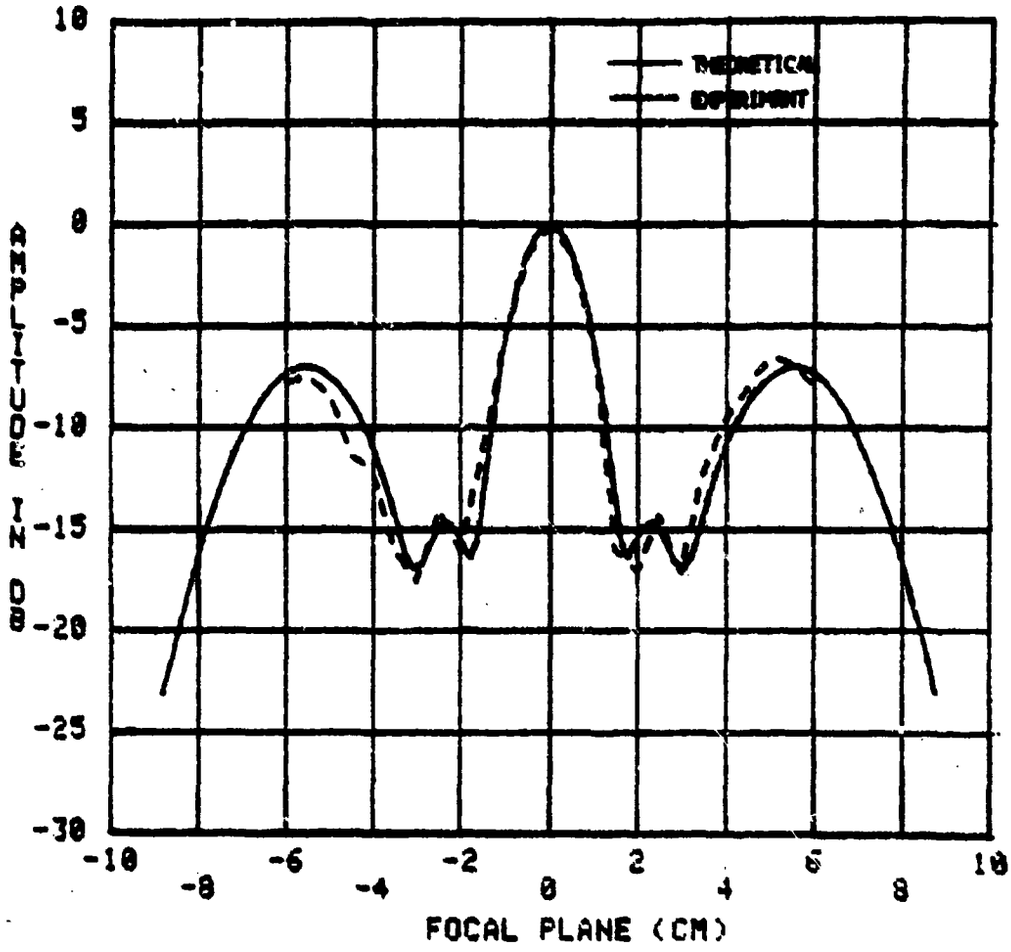

Figure 5a. Relative power pattern of the four element linear array phased for focal plane = 3.5 inches with element coordinates (inches): (1.35,0.,0.), (-.45,0.,0.), (.45,0.,0.) and (1.35,0.,0.) measured along the focal plane.

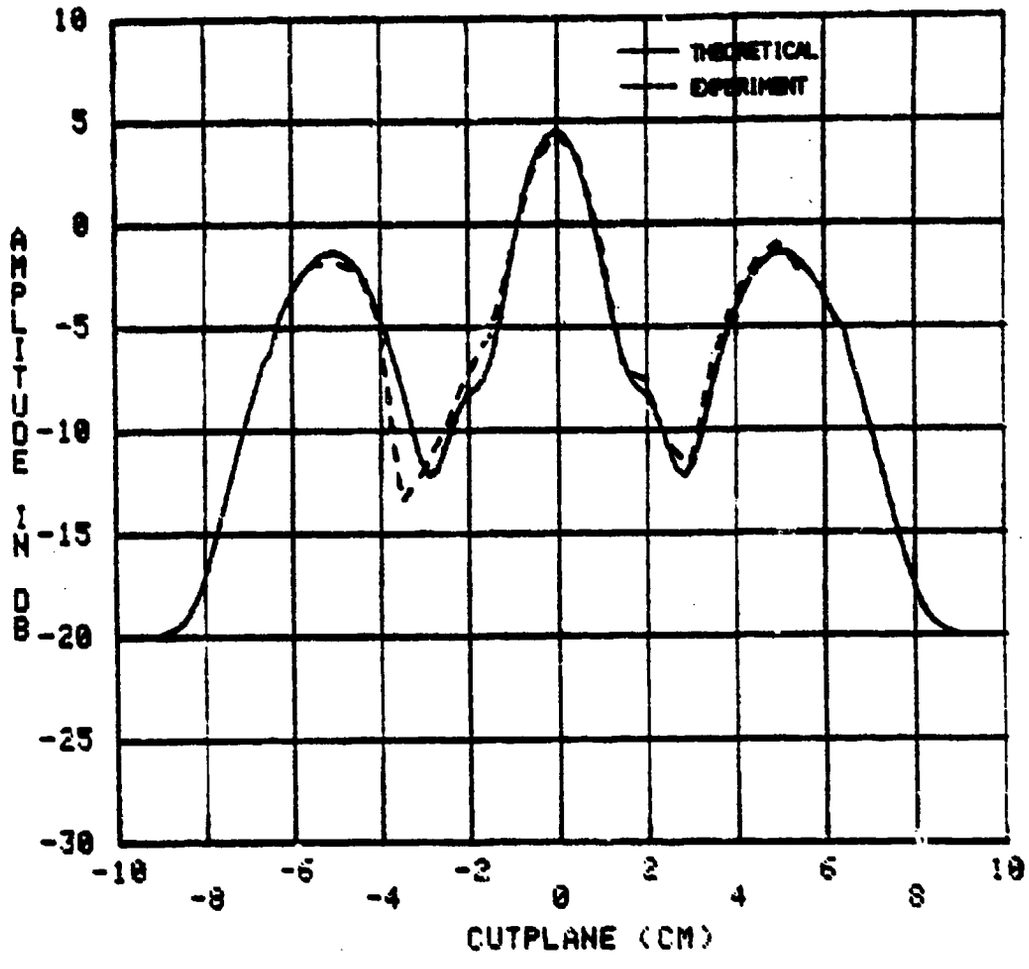

Figure 5b. Relative power pattern of the four element linear array phased for focal plane = 3.5 inches with element coordinates (inches): (-1.35,0.,0.), (-.45,0.,0.), (.45,0.,0.) and (1.35,0.,0.) measured at cut-plane = 3.0 inches.

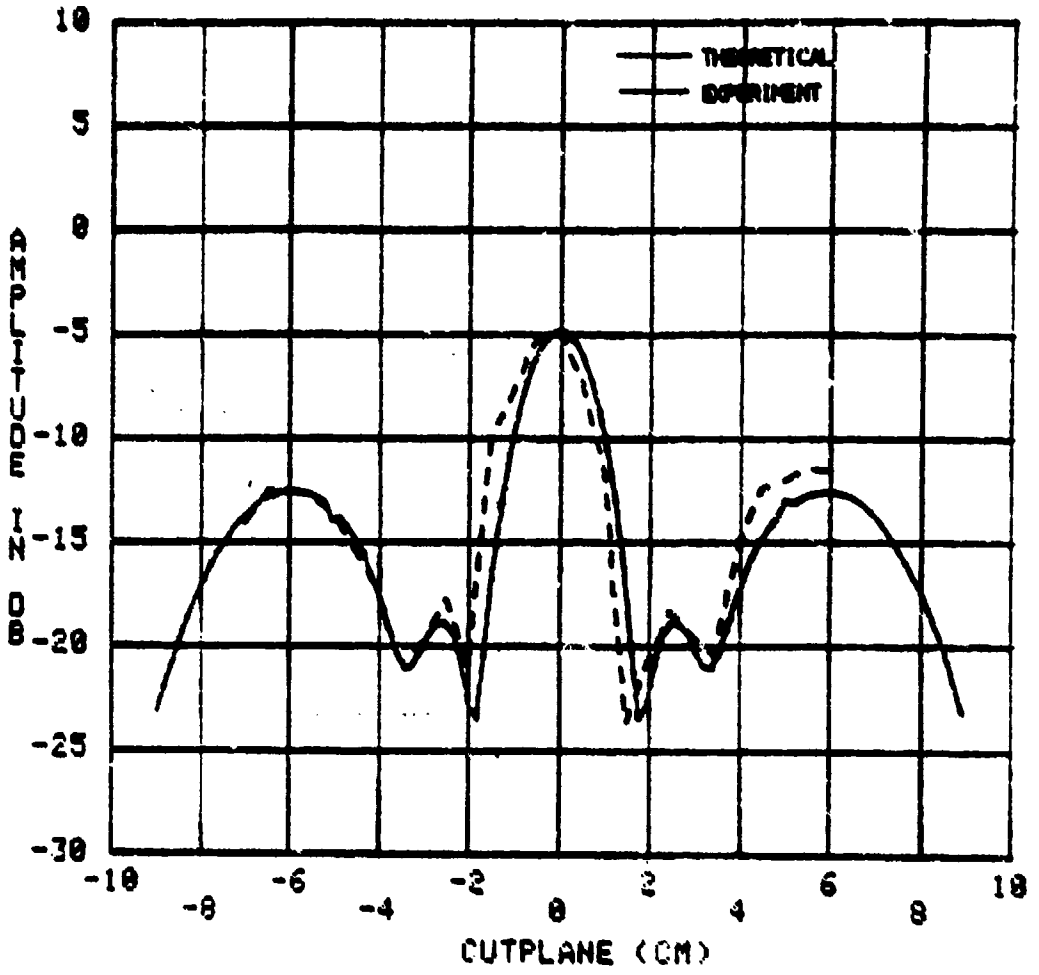

Figure 5c. Relative power pattern of the four element linear array phased for focal plane = 3.5 inches with element coordinates (inches): (-1.35,0.,0.), (-.45,0.,0.), (.45,0.,0.) and (1.35,0.,0.) measured at cut-plane = 4.0 inches.

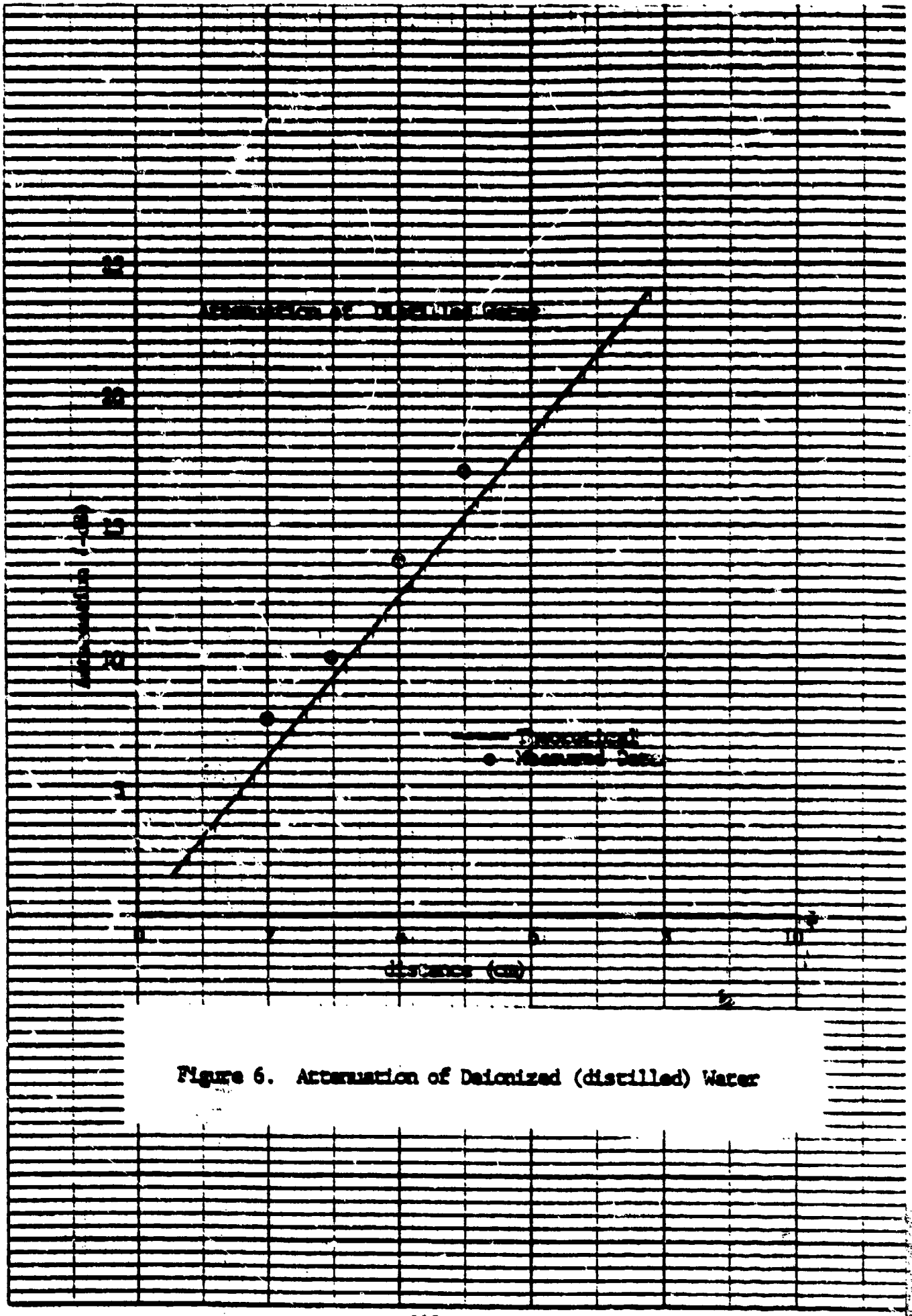

Figure 6. Attenuation of Deionized (distilled) Water

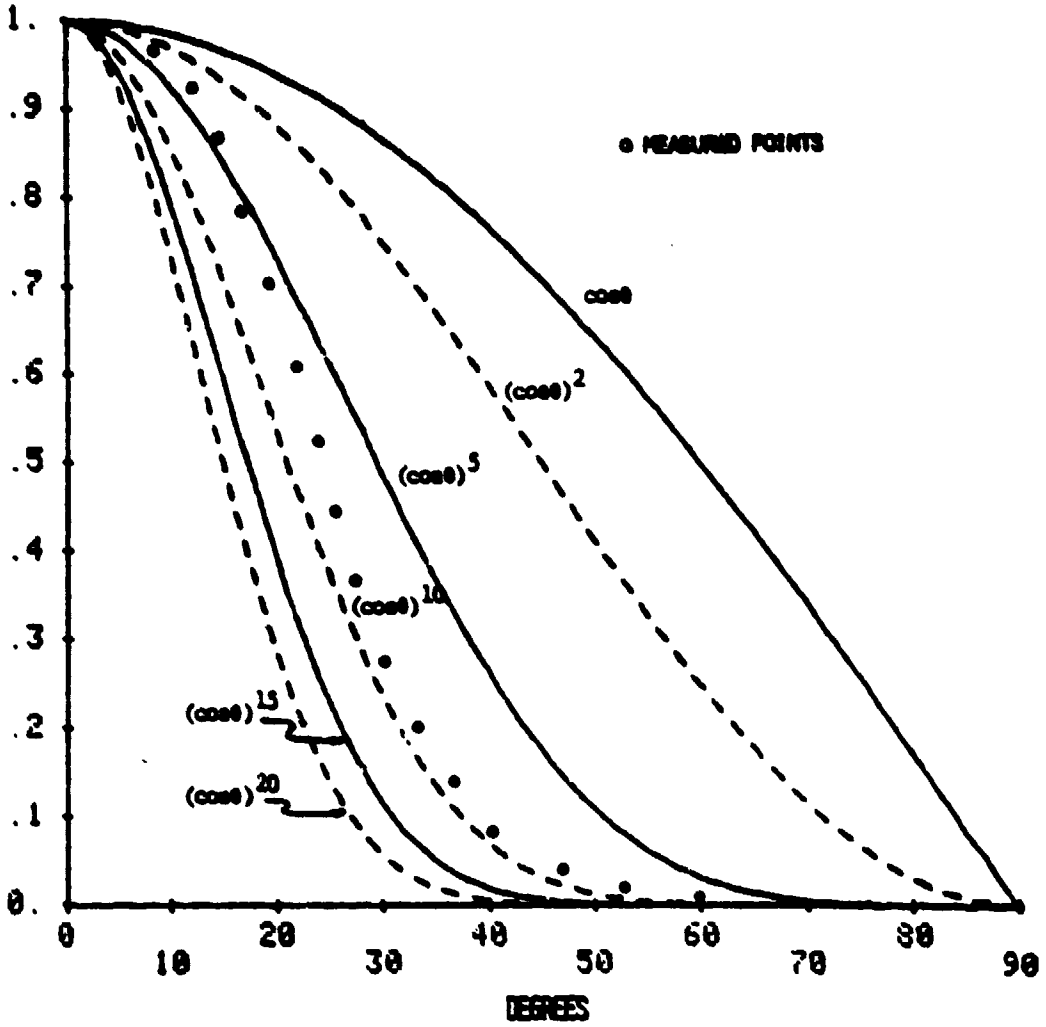

Figure 7. Element Pattern Approximation

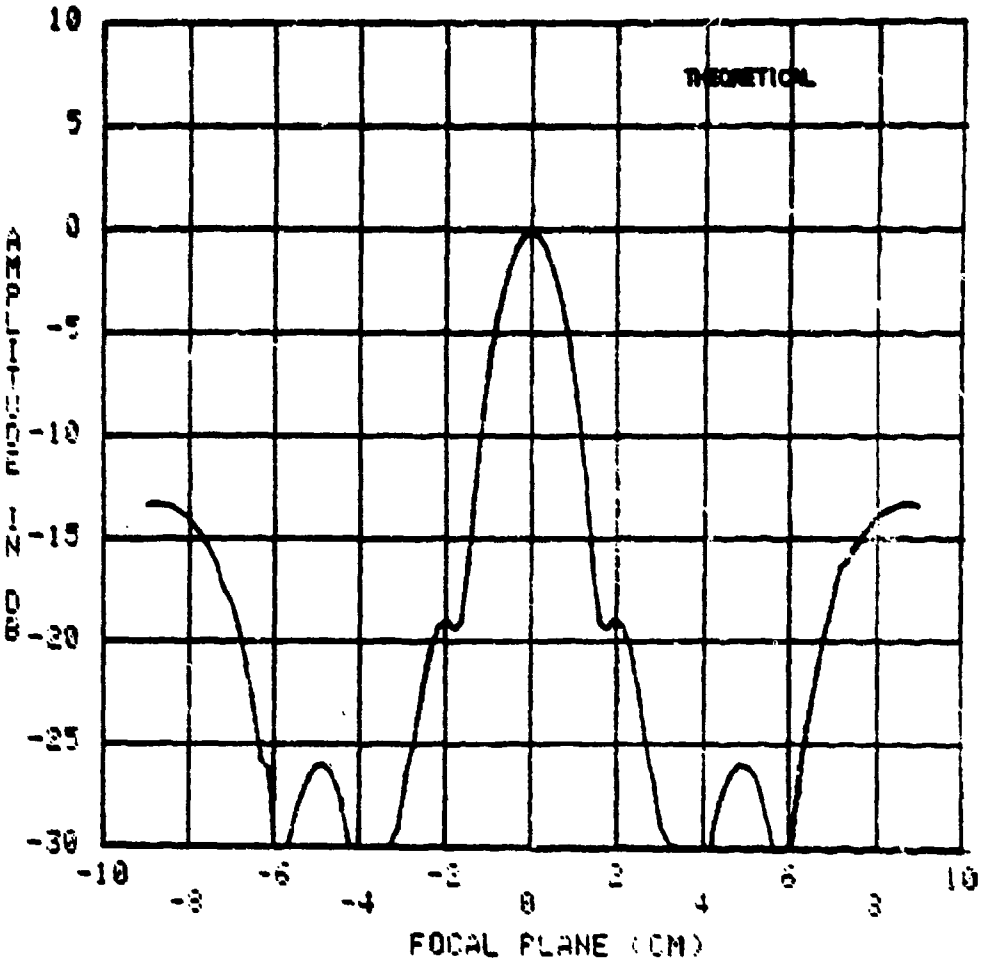

Figure 8a. Relative power pattern of the nineteen element array in a single medium (water) focused at 3.5 inches from the plane of the array.

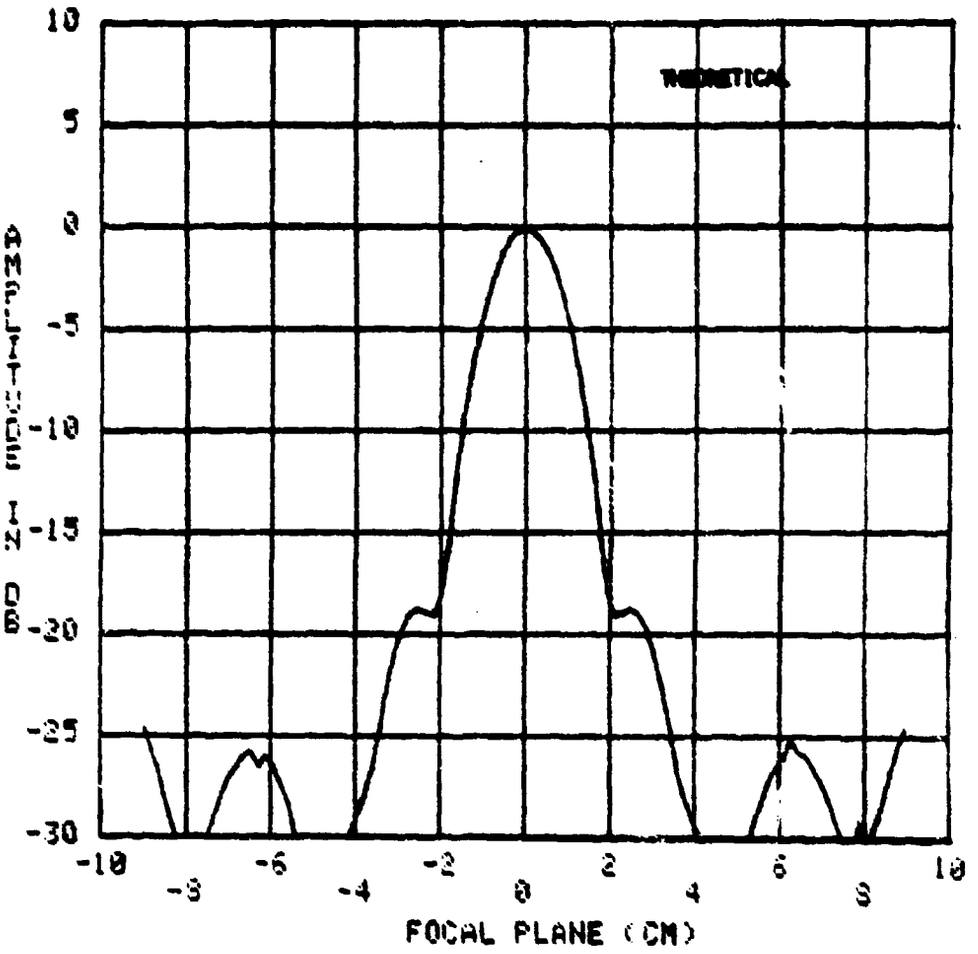

Figure 8b. Relative power pattern of the nineteen element array with two mediums (water and muscle tissue) and focal plane at 4.5 inches from the plane of the array.

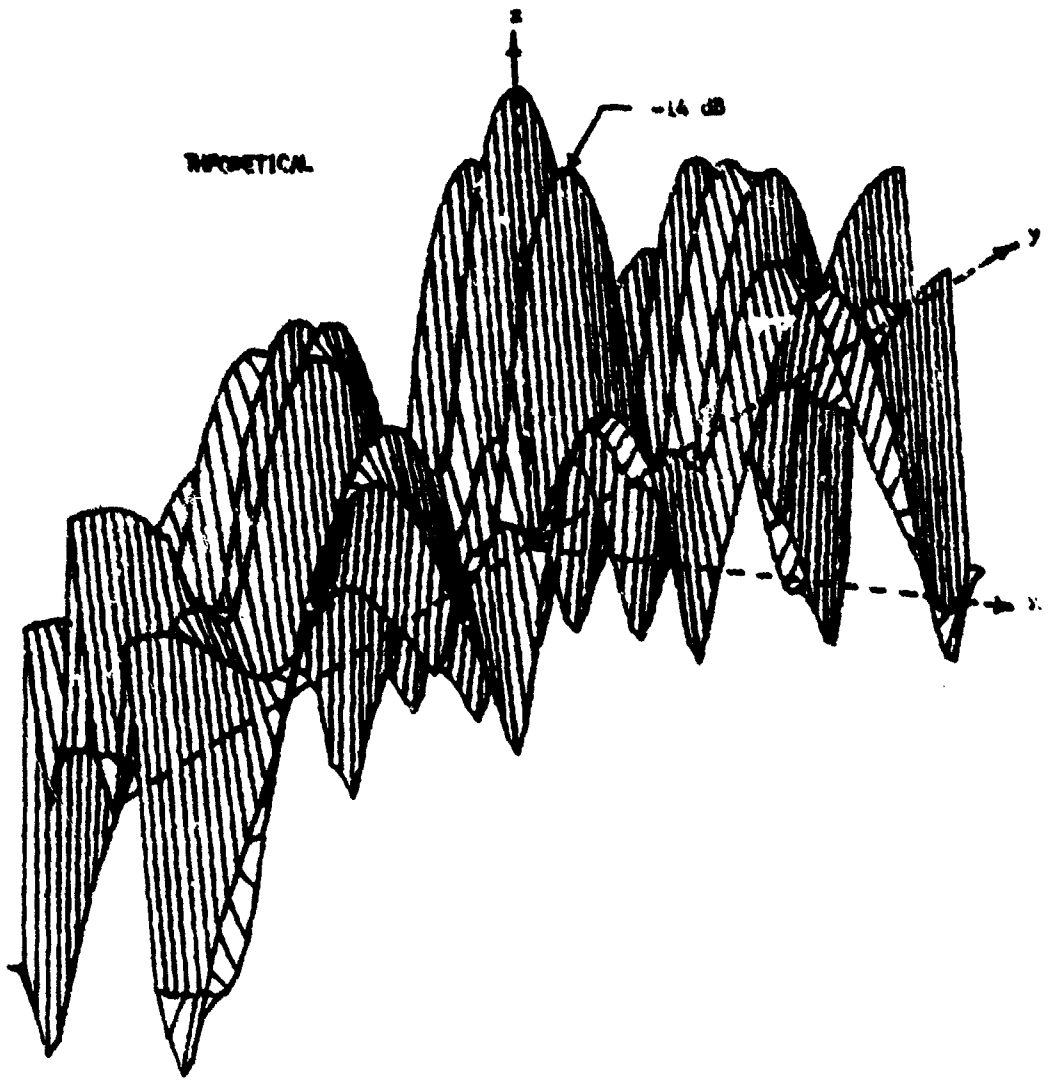

Figure 9a. 3-dimensional illustration of the nineteen element array in a single medium (water) focused at 3.5 inches from the plane of the array.

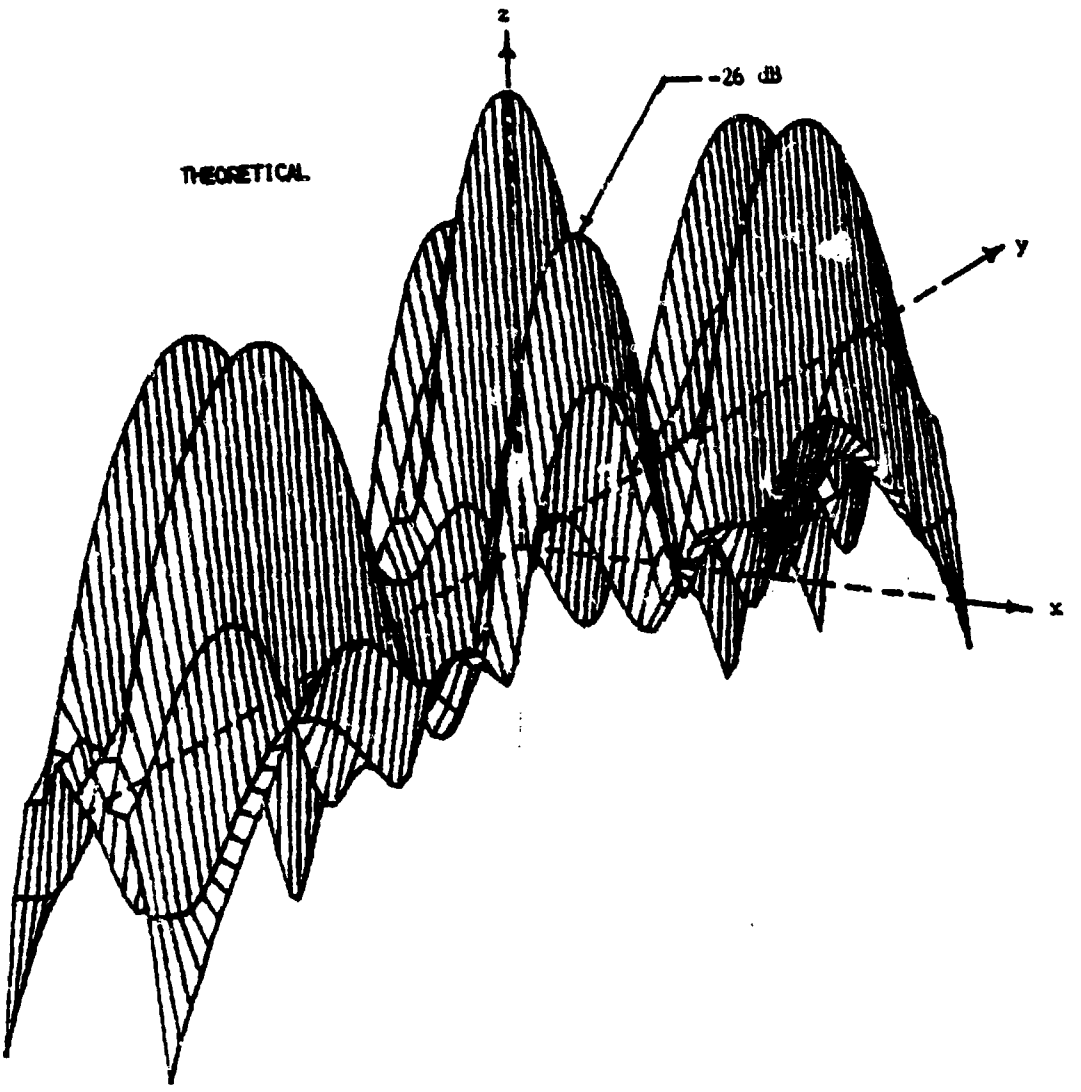

Figure 9b. 3-dimensional illustration of the nineteen element array with two mediums (water and muscle tissue) focused at 4.5 inches from the plane of the array.

AD P001100

STRUCTURAL STOPBAND ELIMINATION WITH THE MONOPOLE-SLOT ANTENNA

D. A. Paschen
Ball Aerospace Systems Division
Boulder, CO 80306

and

P. E. Mayes
Electrical Engineering Department
University of Illinois
Urbana, IL 61801

ABSTRACT

Using unmatched elements in a series-fed, periodic array produces high input VSWR at frequencies where a structural stopband occurs. The monopole-slot antenna is a two-port element which can be designed to provide broadband match to a stripline feeder. Then no additional matching is required to eliminate a structural stopband. A frequency scanning array was designed and tested to illustrate that monopole-slot elements can be used in a series-fed array without causing an impedance anomaly at broad-side scan.

1. INTRODUCTION

When unmatched elements in a series-fed array are located an integral number of half-wavelengths apart, the reflections add in phase to create a high VSWR on the feed line. This phenomenon is called a structural stopband and prohibits the flow of energy down the feed line to the radiating elements. Two examples of a structural stopband are well-known: (1) in frequency-scanning arrays broadside radiation occurs when the elements are an integral number of wavelengths apart on the feed line, and a structural stopband usually results[1], and (2) in log-periodic

antennas where the feed line can not be directly transposed, a structural stopband usually occurs due to the extra length of feedline required for phasing between elements[2]. Other methods have been used to eliminate the structural stopband effects in arrays of unmatched elements[3-5], but the use of a "matched" antenna provides an easy solution to the problem.

2. DEVELOPMENT OF THE MONOPOLE-SLOT

The monopole-slot antenna, which was developed and first presented in 1970[6], is an example of a "matched" antenna. This antenna consisted of a cavity-backed slot with a microstrip feed to which a monopole was attached. A later version of the monopole-slot antenna was constructed out of stripline[7]. This antenna, shown in Figure 1, consists of a stripline fed slot and a quarter-wavelength monopole attached to the center conductor through a hole in the dielectric at the center of the slot. These antennas make use of radiating elements with complementary impedances. The reflections at the antenna feed due to each element tend to cancel, and this results in a "matched" antenna with an impedance which is very nearly frequency independent.

The monopole-slot is a two-port antenna, and when used as a single element, the second port is terminated. Since the input impedance is nearly constant over large frequency intervals, the bandwidth is determined by the coupling (the amount of energy radiated as opposed to being dissipated in the termination).

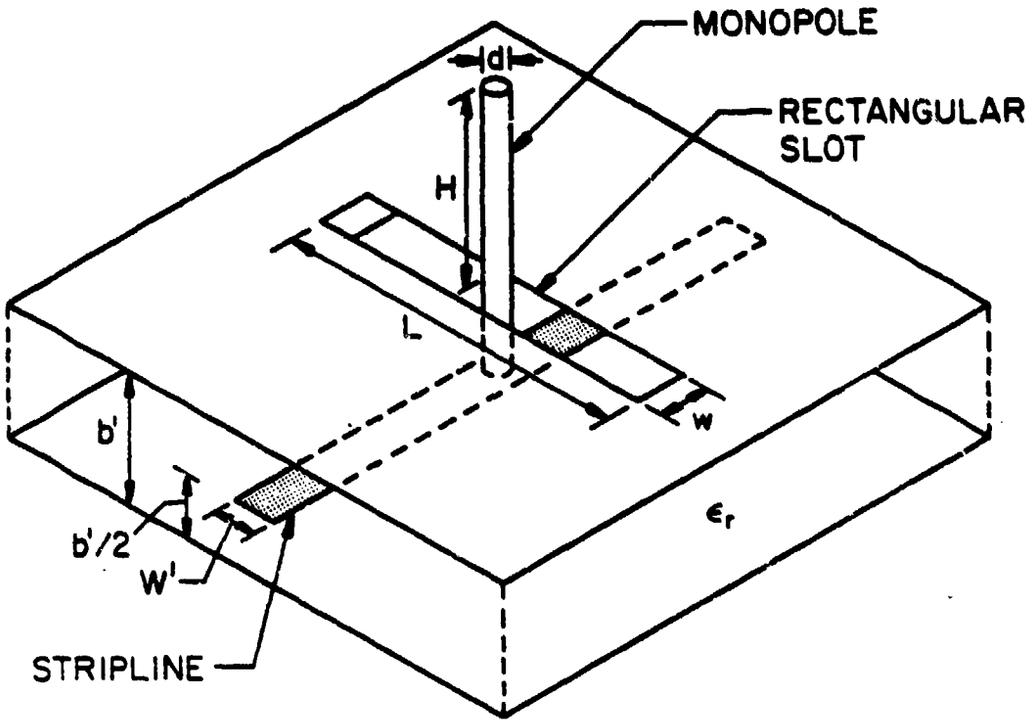

H MONOPOLE HEIGHT
d MONOPOLE DIAMETER
L RECTANGULAR SLOT LENGTH
w RECTANGULAR SLOT WIDTH
b' GROUND PLANE SPACING
W' STRIPLINE WIDTH
ϵ_r RELATIVE DIELECTRIC CONSTANT

Figure 1. Stripline-Fed Monopole-Slot.

Figure 2 shows a plot of the coupling or efficiency of a typical monopole-slot versus normalized frequency. When used in a series array, the antenna should be operated in regions of lower coupling so that energy will be supplied to elements further down the feed line. By adjusting the size of the antenna so that it operates in the desired coupling region, almost any type of amplitude distribution can be obtained across the array.

3. SINGLE ELEMENT DATA

Figure 3 shows the S-parameters for a monopole-slot designed for use in a three-element frequency scanning array. The VSWR is less than 1.3 to 1 over the 22% band from 1.6 to 2.0 GHz. The antenna used an 85-ohm feed line with cascaded quarter-wavelength transformers to 50 ohms at the ports. Most of the variation in the input impedance is believed due to the transformers. The antenna dimensions were:

L = 3.2 inches

W = .4 inches

H = 1.5 inches

d = 3/32 inches

Cavity size = 3 × 6 inches

b' = 3/8 inches

$\varepsilon_r = 2.62$

$Z_o = 85$ ohms

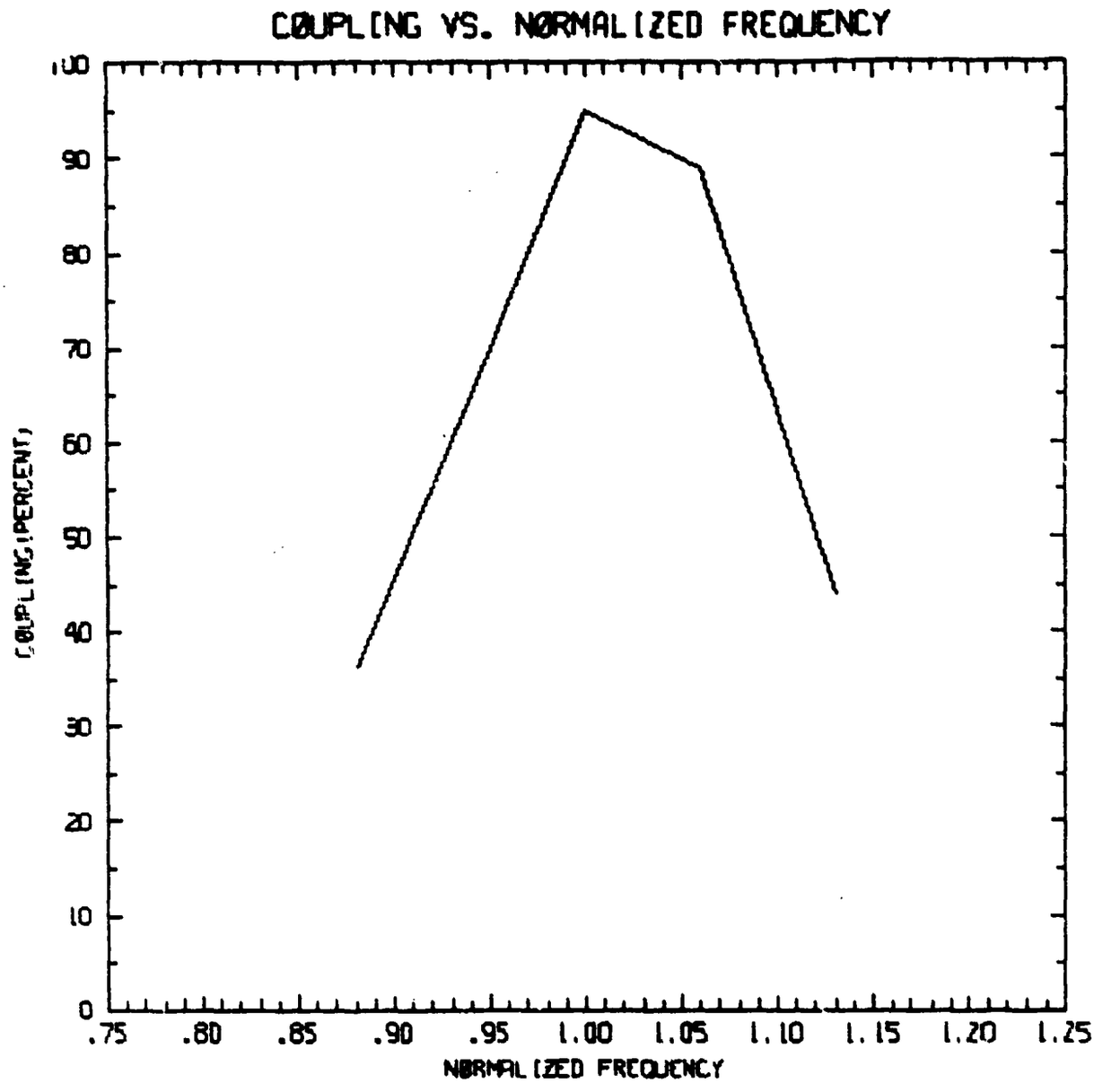

Figure 2. Coupling from Feed Line to the Monopole-Slot Antenna.

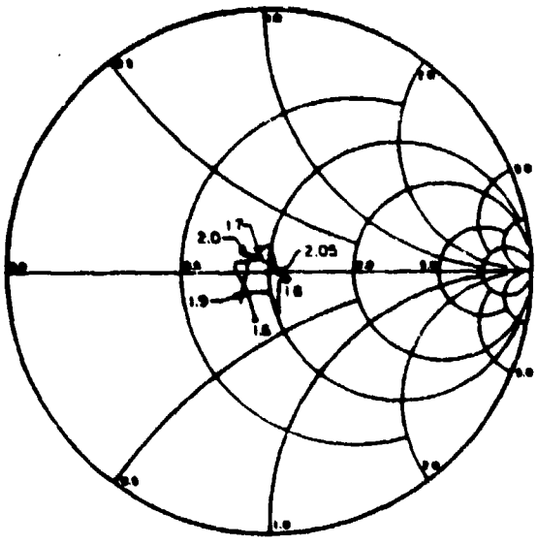

S_{11}

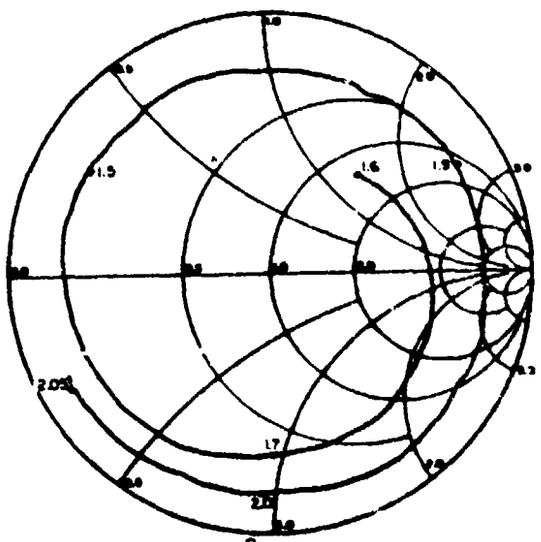

S_{21}

Figure 3. Monopole-Slot S-Parameters (Frequencies in GHz).

Figure 4 shows the radiation patterns in azimuth for this antenna. The asymmetries in the patterns are due to an off-center location in the ground plane.

4. COUPLING

Because of the "matched" nature of the monopole-slot, the internal scattering can be almost completely eliminated. However, the external coupling is also an important factor in causing impedance anomalies in arrays. Measurements were taken of the coupling between ports of two monopole-slots of the dimensions shown previously. Figure 5 shows the coupling paths between two antennas and Figure 6 shows the S-parameters for antennas which were located 5.4 inches apart. The coupling is significant only for S_{23} which is the case where the main beams are facing.

5. ARRAY DESIGN

A three-element frequency-scanning array was constructed to verify that the structural stopband had been eliminated. The following values were used in the construction of the array:

Slot length - 3.2 inches

Slot width - 0.4 inches

Monopole height - 1.5 inches

Monopole diameter - 3/32 inches

Cavity size - 3 × 6 inches

Element spacing - 5.4 inches

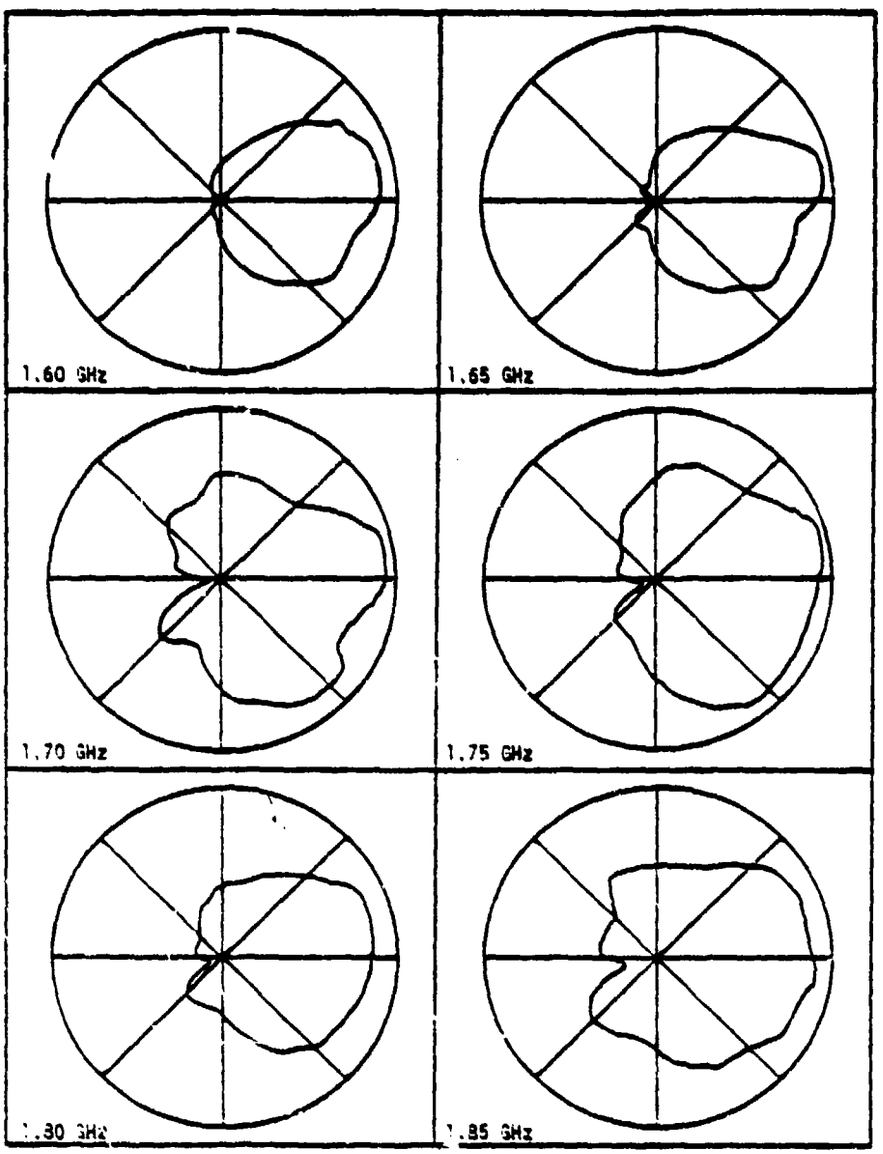

Figure 4. Monopole-Slot Azimuth Patterns.

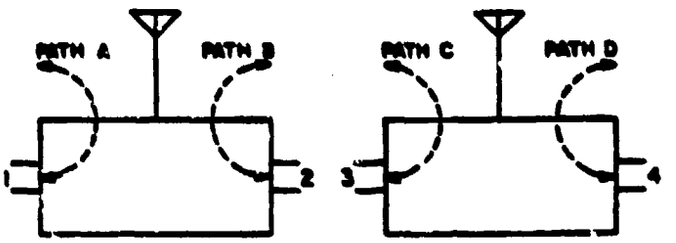

Figure 5. Coupling Paths Between Two Elements.

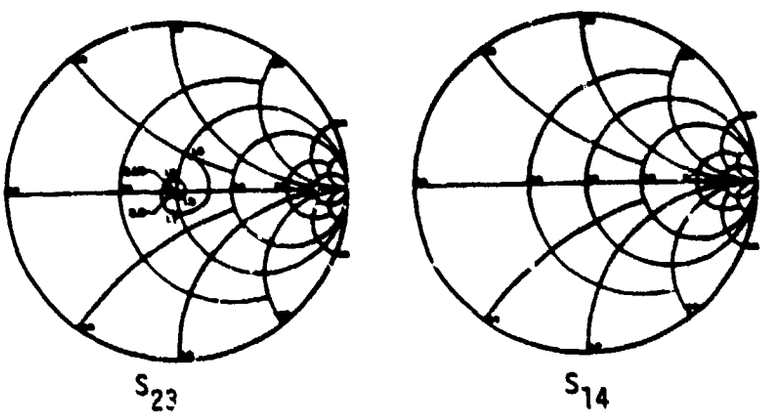

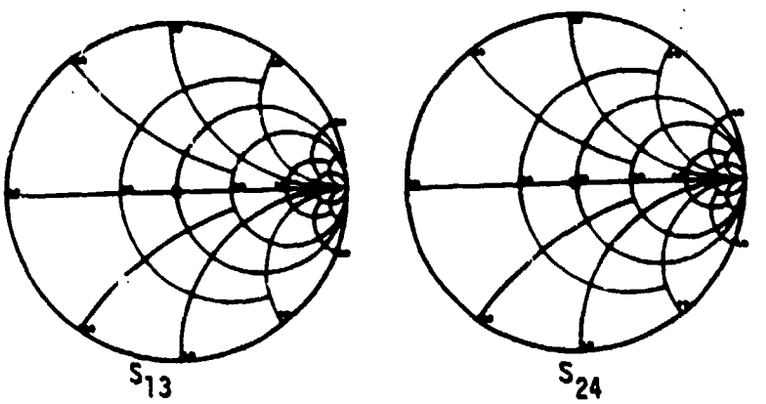

Figure 6. S-Parameters Between Two Elements.

Line length between elements - 23.1 inches

Backfire frequency - 1.60 GHz

Broadside frequency - 1.85 GHz

Dielectric constant - 2.62

Characteristic impedance - 85 ohms

The S-parameters for the three-element frequency scanning array are shown in Figure 7 and the radiation patterns are shown in Figure 8.

The absence of an impedance mismatch in S_{11} at 1.93 GHz, where broadside radiation occurs, verifies that the structural stopband has been eliminated. Due to the spacing chosen so that the excess feed line could be run in the sides of the cavity, grating lobes appear in the patterns shown. In order to eliminate the grating lobes, the array was modified so that the side cavity walls are common between elements and the feed line is fed in through the narrow ends of the cavity as shown in Figure 9. Figures 10 and 11 show the S-parameters for the new array and the radiation patterns for the broadside and near broadside cases to show the elimination of both the structural stopband and grating lobes.

6. CONCLUSION

The monopole-slot antenna which has an input impedance that is stable over a wide bandwidth has many advantages for use in array applications. It can be used in a series array without

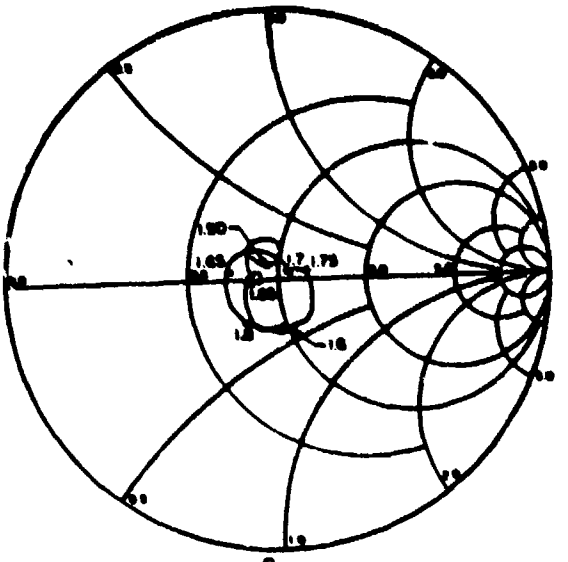

S_{11}

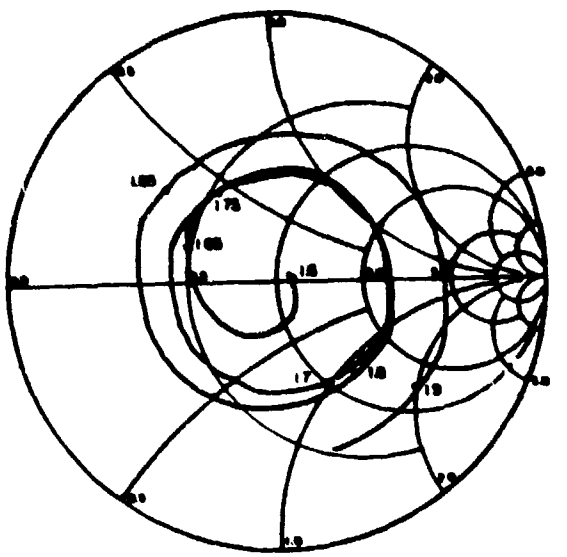

S_{21}

Figure 7. S-Parameters for the Three-Element Frequency Scanning Array (Frequencies in GHz)

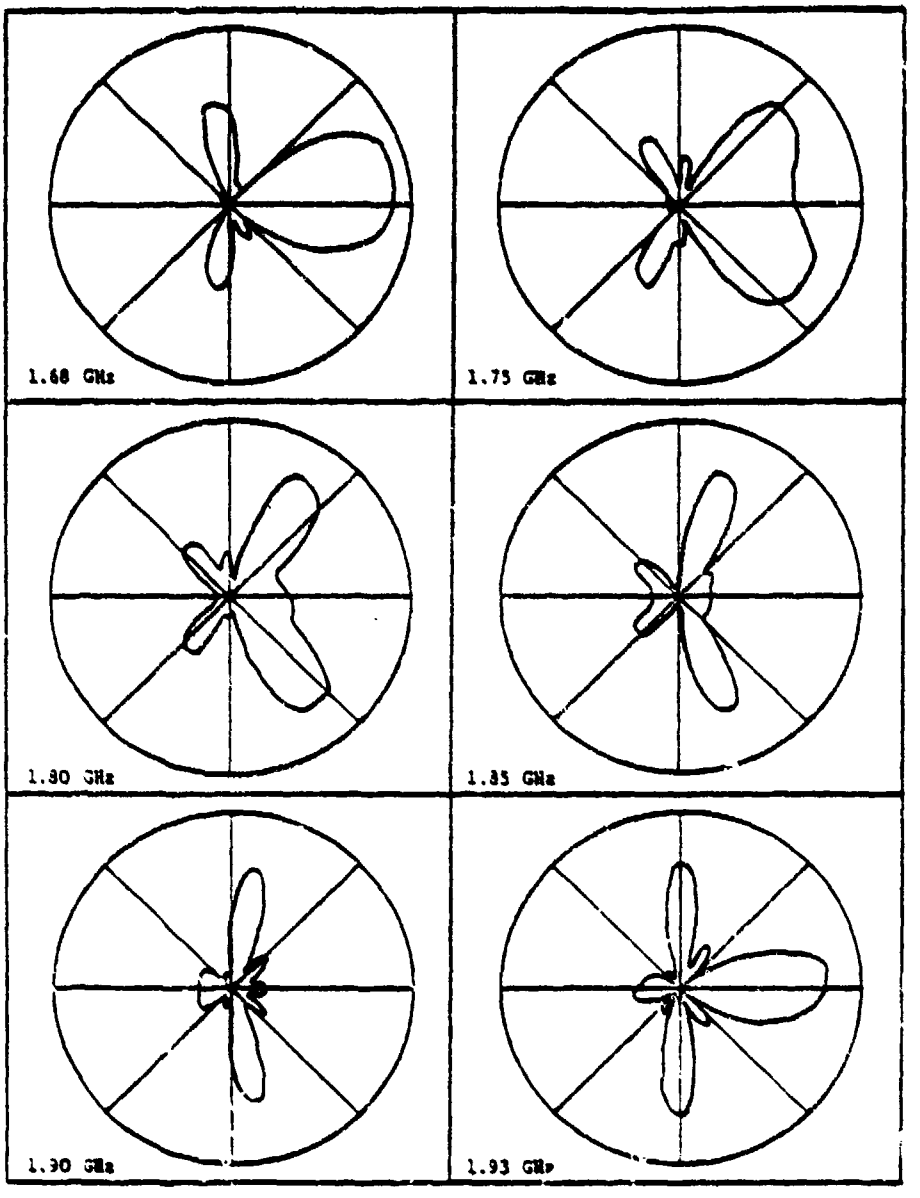

Figure 8. Radiation Patterns for the Three-Element Frequency-Scanning Array.

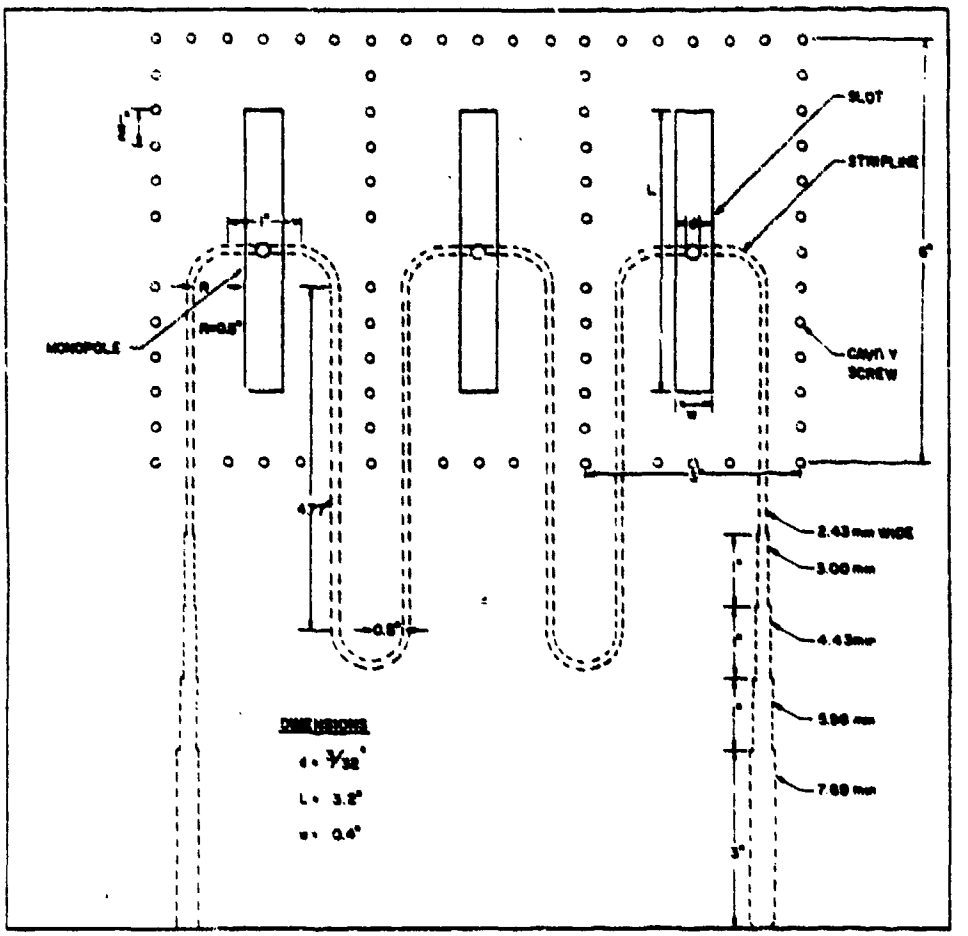

Figure 9. New Three-Element Frequency Scanning Array Showing Feed Line Location.

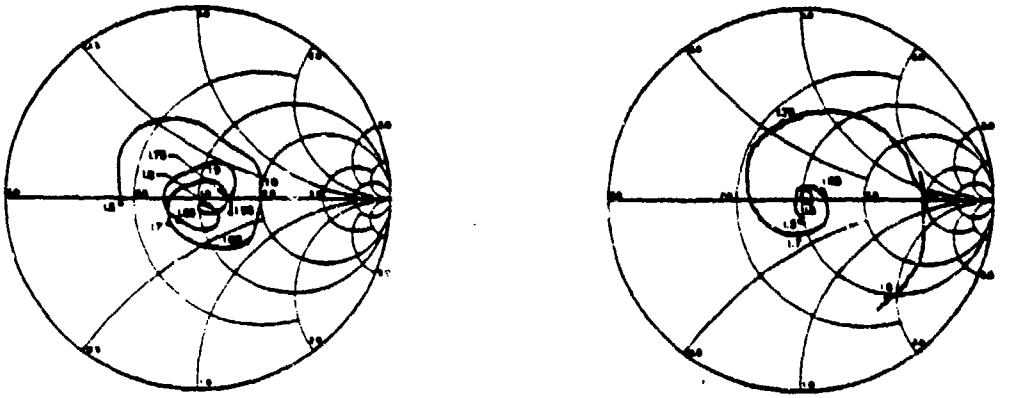

S_{11} S_{12}

Figure 10. S-Parameters for New Three-Element Array.

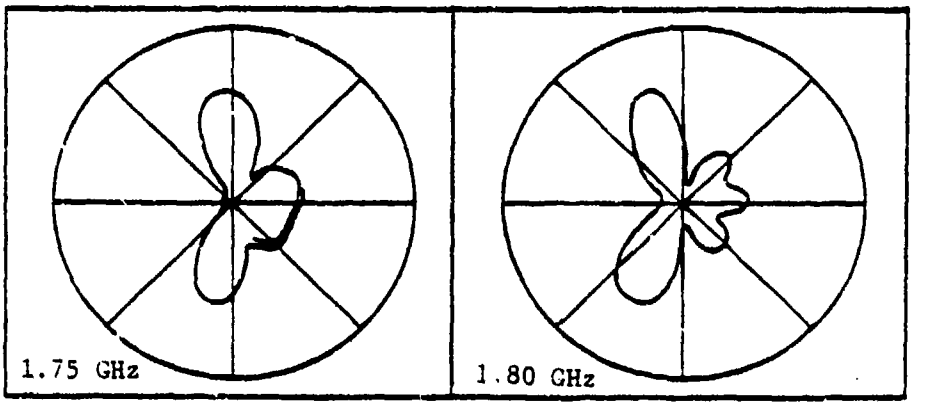

Figure 11. Azimuth Patterns at Broadside for New Array

producing the effects of internal scattering such as structural stopbands. Also the size can be adjusted to produce the desired amount of coupling to the feed line so that the desired amplitude distribution is achieved.

ACKNOWLEDGEMENT

This work was supported in part by a grant from the Aileen S. Andrew Foundation.

REFERENCES

1. Begovich, N. A. (1966) Frequency scanning, Chapter 2, Microwave Scanning Antennas, Vol. III, R. C. Hansen, Ed., Academic Press, New York.

2. Ingerson, P. and Mayes, P. (1968) Log-periodic antennas with modulated impedance feeders, IEEE Trans. Antennas Propagat. AP-16:663-642.

3. Renken, G. W. (1971) Minimizing the impedance anomaly at broadside in a frequency-scanning stripline-fed periodic slot array, Technical Report No. 71-12, Antenna Laboratory, University of Illinois, Urbana, IL.

4. Fritz, W. A. and Mayes, P. E. (1973) A frequency-scanning, stripline-fed periodic slot array, Technical Report

No. 73-17, Electromagnetics Laboratory, Department of Electrical Engineering, Engineering Experiment Station, University of Illinois, Urbana, IL.

5. Green, P. B. and Mayes, P. E., (1974) 50 Ω log-periodic monopole array with modulated-impedance microstrip feeder, IEEE Trans. Antennas Propagat., AP-22:332-334.

6. Mayes, P. E. and Wiesenmeyer, F. M. (1970) The monopole-slot - An electrically small DF and communications antenna, Abstracts of the Twentieth Annual Symposium, USAF Antenna Research and Development Program, AFAL, Wright-Patterson AFB, Ohio and University of Illinois, Urbana, IL.

   See also

   Mayes, P. E., Warren, W. T. and Wiesenmeyer (1972) The monopole-slot: A sma. broad-band unidirectional antenna, IEEE Trans. Antennas Propagat., AP-20:489-493.

7. Cwik, T. A. (1981) The hybrid slot antenna, M.S. Thesis, Department of Electrical Engineering, University of Illinois, Urbana, IL.

   See also

   Mayes, P. E. and Cwik, T. (1980) The hybrid slot, a low-profile energy-density antenna, Abstracts of the International Conference on Transportation Electronics, Detroit, MI.

   and

Mayes, P. E. and Cwik, T. (1980) The hybrid slot, a versatile low-profile radiator with small reflection coefficient, Abstracts of the Antenna applications Symposium, Deputy for Electronic Technology, Rome Air Development Center, Electronic Systems Division, Air Force Systems Command, and Electromagnetics Laboratory, Department of Electrical Engineering, University of Illinois, Urbana, IL.

AD P001101

Computer Aided Analysis of a Blass Feed Network for Wide Instantaneous Band Phased Array Application

J. Wojtowicz, P.S. Hacker, K.G. Ramsey

September 22 - 24, 1982

Prepared for

1982 ANTENNA APPLICATIONS SYMPOSIUM
University of Illinois
Urbana, Illinois

By

WESTINGHOUSE ELECTRIC CORPORATION
Systems Development Division
Baltimore, Maryland

INTRODUCTION

Emerging and next generation radar system studies have identified a need for phased array antennas with wide instantaneous bandwidths. Typical phased array antenna bandwidths which are compatible with these system requirements are in the range of 5 to 10%.

PERFORMANCE ANALYSIS DESCRIPTION

A straightforward method of approaching this problem is shown in block diagram form in figure 1. The antenna feed network of figure 1 effects wide instantaneous bandwidth by employing switchable time delay networks to feed each radiating element so that beam scanning capability is achieved. Variable time delay units rather than variable phase shifters are used to scan the array because of the inherent frequency sensitivity of the antenna beam of a phase scanned array. This principle is illustrated in figure 2. In order to scan the beam of the array in figure 2 to an angle θ, a phase shift:

$$\Delta\phi = \frac{2\pi L}{\lambda} = \frac{2\pi s \sin\theta}{\lambda}$$

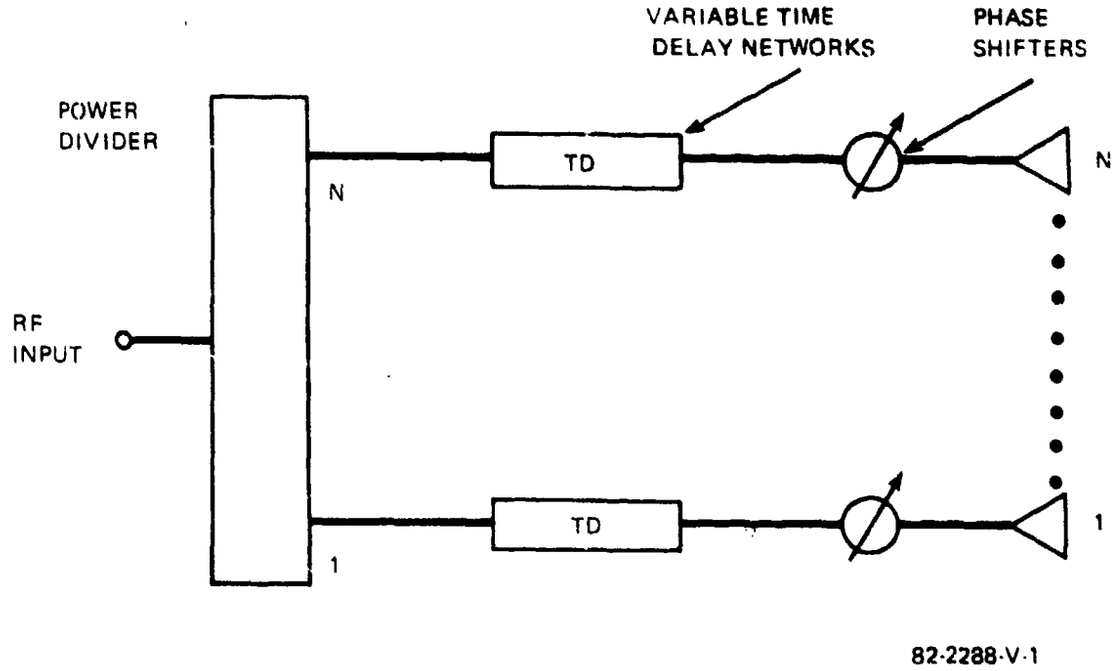

Figure 1. Conventional Wide Instantaneous Bandwidths Feed Network

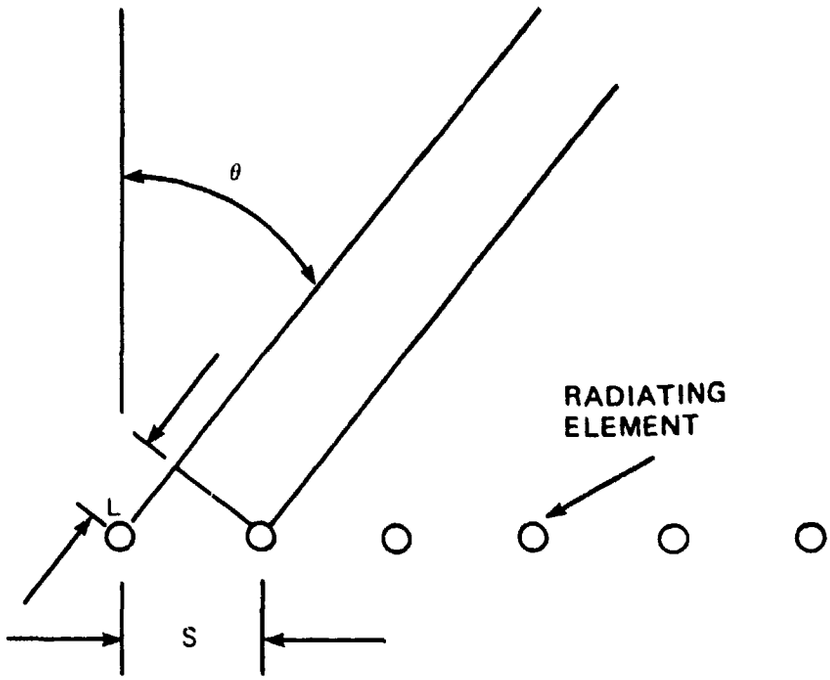

82-2288-V-2

Figure 2. Array Scanning Geometry

must be applied to adjacent radiators. If $\Delta\phi$ is constant with frequency, as is the case with most microwave phase shifters, then θ varies with frequency. Under these circumstances, wide instantaneous bandwidth is not obtained. If, however, interelement phase shift is obtained with TEM air transmission time delay equal to:

$$T = \frac{2\pi s}{\lambda} \sin\theta = \frac{2\pi a}{\lambda}$$

where: a = the required difference in length between the feeding time delay circuits of two adjacent radiating elements.

T is not a function of frequency and the value of θ, the scan angle is:

$$\theta = \sin^{-1}(a/s)$$

which is not a function of frequency.

Continuously variable time delay beam scanning, however desirable, is not practical, though, since time delay networks are inherently fixed geometry

devices. Discrete approximations to the ideal characteristic have significant complexity in terms of the required numbers of components even for small numbers of discrete time delay positions per network. A three position time delay network, used to feed a single phased array radiating element, is shown in figure 3. Four RF switches and three sections of fixed length TEM transmission line are required for each three position time delay network. The block diagram of figure 1, therefore, represents considerable hardware complexity even for a small number of discrete time delay values per network.

An alternate approach to the problem of obtaining wide angle, wide instantaneous band electronic scanning is to use a Blass feed network with N outputs and M inputs, as shown in figure 4. If M can be made significantly less than N, then considerable reduction in feed network complexity can be achieved since the number of switchable time delay networks is equal to M.

The feed network of figure 4 takes a single input, splits it M ways and applies voltage weighting factors, which if used to feed an M element array would produce a low sidelobe pattern. Each of the outputs of the M-way power divider is fed through an L-position switchable time delay network to an

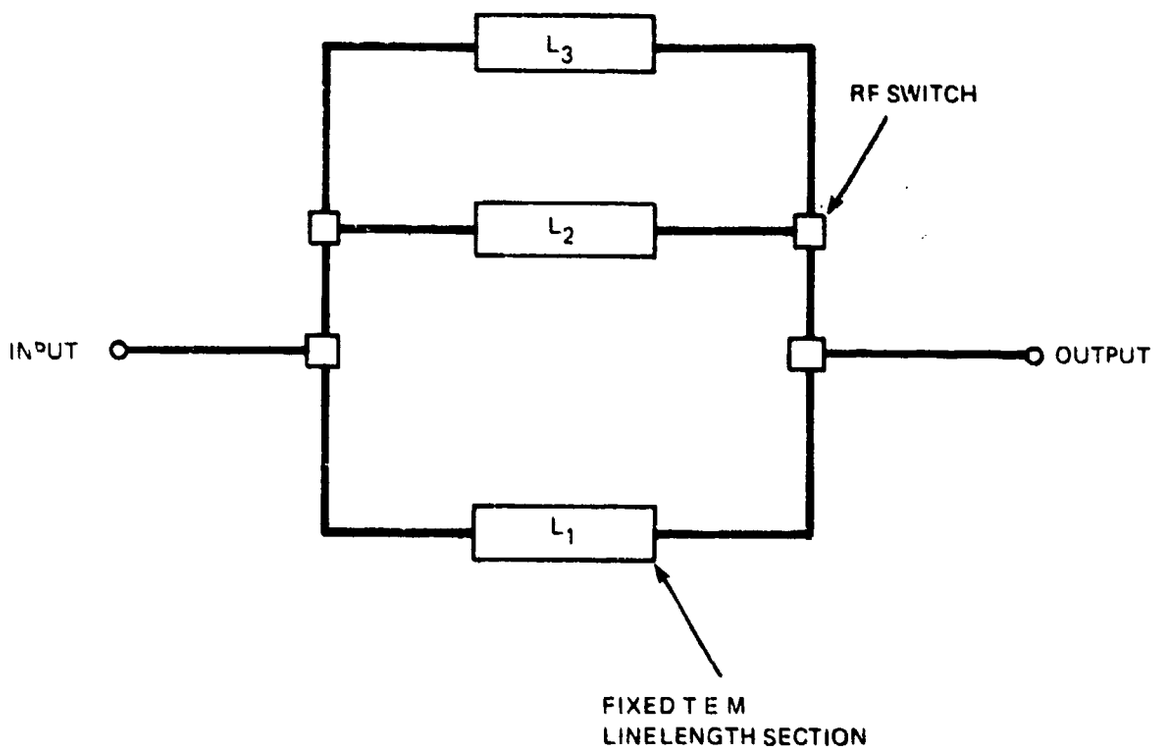

Figure 3. Position Time Delay Network

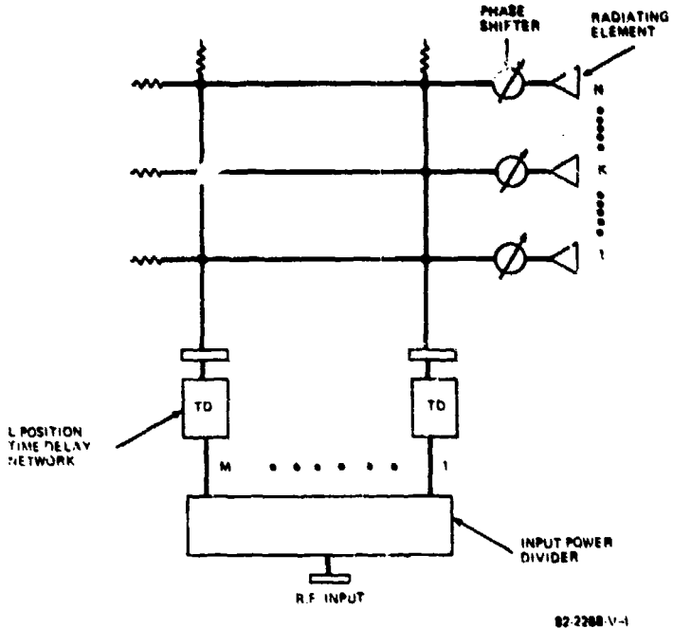

Figure 4. Wide Instantaneous Bandwidth Overlapping Subarray Feed Network

N-port series feed power divider. The M series feed power divider are coupled to the radiating aperture as shown in figure 4. This type of cross coupled feed network is known as a Blass feed network.

Each of the N-port series feed networks provides a sin (Mx)/sin x voltage distribution at the radiating aperture as shown in figure 5. Adjacent sin (Mx)/sin x distributions are offset from each other along the aperture such that the M sin (Mx)/sin x distributions form an orthogonal set. That is, for any pair of distributions in the set:

$$\sum_{K=1}^{N} A_K B_K^* = 0$$

where the A_K's are the aperture voltages from one sin (Mx)/sin x distribution and the B_K's are the aperture voltages from any other sin (Mx)/sin x distribution on the aperture.

A qualitative method of predicting the pattern performance from the feed network of figure 4 is to consider the part of the aperture illuminated by the mainlobe of a sin (Mx)/sin x distribution to be an element of a M element

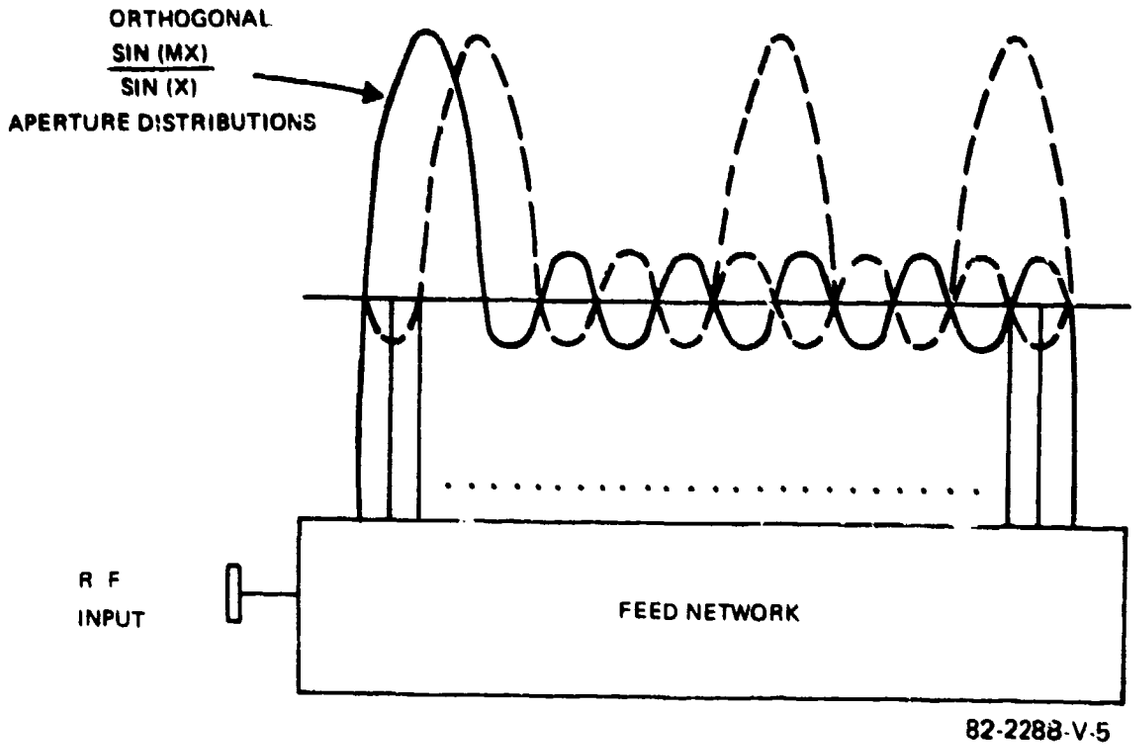

Figure 5. Overlapping Sub-Aperture Voltage Distributions

array. There are M such elements with low sidelobe weights (established by the input power divider of figure 4) spaced at intervals of approximately(N/M) $\lambda/2$ so that an array factor/element factor situation as shown in figure 6 is produced. An array factor with low sidelobes but many grating lobes is produced. However, the element pattern associated with the sin (Mx)/sin x aperture distributions "filters" out all primary responses except one, as shown.

Using the feed network of figure 4 for obtaining wide instantaneous, wide angle scanning, it is found that perfect time delay compensation for the "array factor" can be accomplished only at scan angles corresponding to the L-discrete positions of the switchable time delay circuits which feed the Blass feed matrix. At scan angles other than these, some amount of beam shift versus frequency is encountered.

At the perfect time delay scan angles, which correspond to the discrete time delay network positions, instantaneous bandwidth is limited to some extent by the phase versus frequency characteristics of the series fed

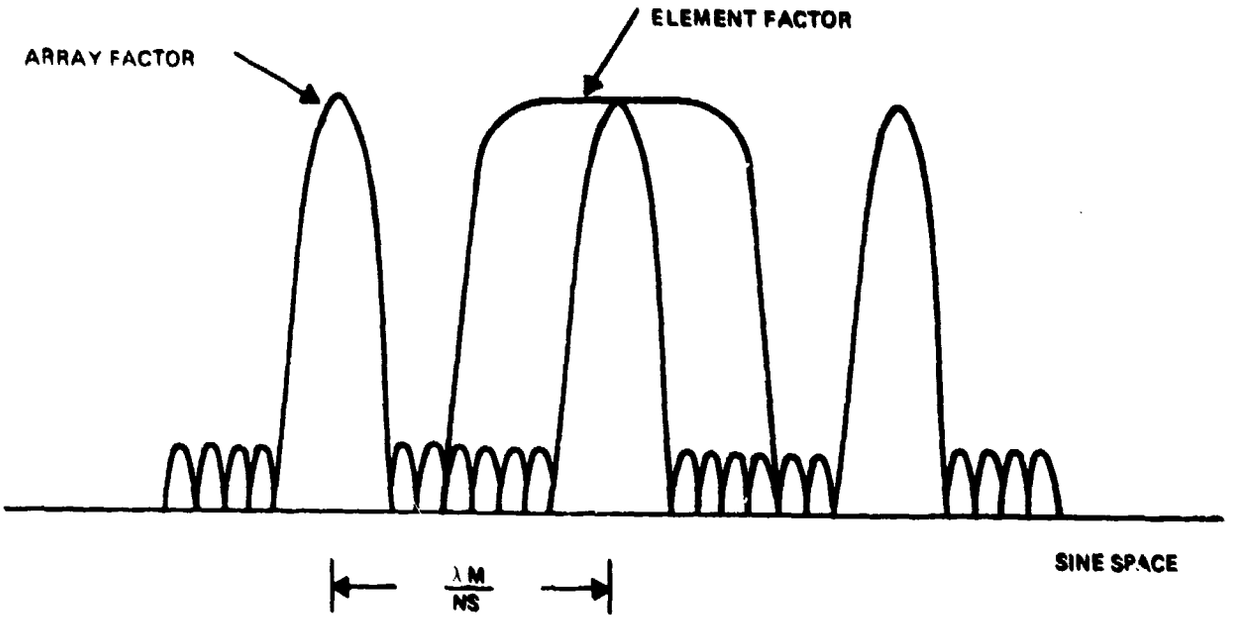

Figure 6. Overlapping Subarray Feed Network Patterns $f = f_o$

manifolds which comprise the Blass feed network. The phase slope variation of the individual series feed manifolds results in the relative motion of the element pattern with respect to the array factor. This effect is shown in figure 7.

Computer aided analysis of the antenna and feed network shown in figure 4 was performed in order to quantify instantaneous bandwidth characteristicts. The series feed power divider assemblies were assumed to be configured with ideal directonal couplers having infinite directivity and constant coupling with frequency. This was done in order to examine first order effects in detail, with tolerance studies being scheduled for a subsequent time frame.

Figure 8 shows a diagram of the Blass feed network and the way in which signals from the rear most power dividers fan out to the radiating aperture. The superposition of signals from the many coupling paths shown in figure 8 was the major item of investigation in the analysis of the antenna system shown in figure 4.

The configuration parameter which were used for the performance analysis of the antenna system of figure 4 are shown in table 1.

Table 1. Antenna Configuration Parameters

Parameter (see figure 4)	Parameter Value
N	108
M	12
L	3
Array Factor Design Sidelobe Level	60 dB Tschebycheff
Array Maximum Scan Angle	$\pm 45^{\circ}$
Desired Instantaneous Bandwidth	6%

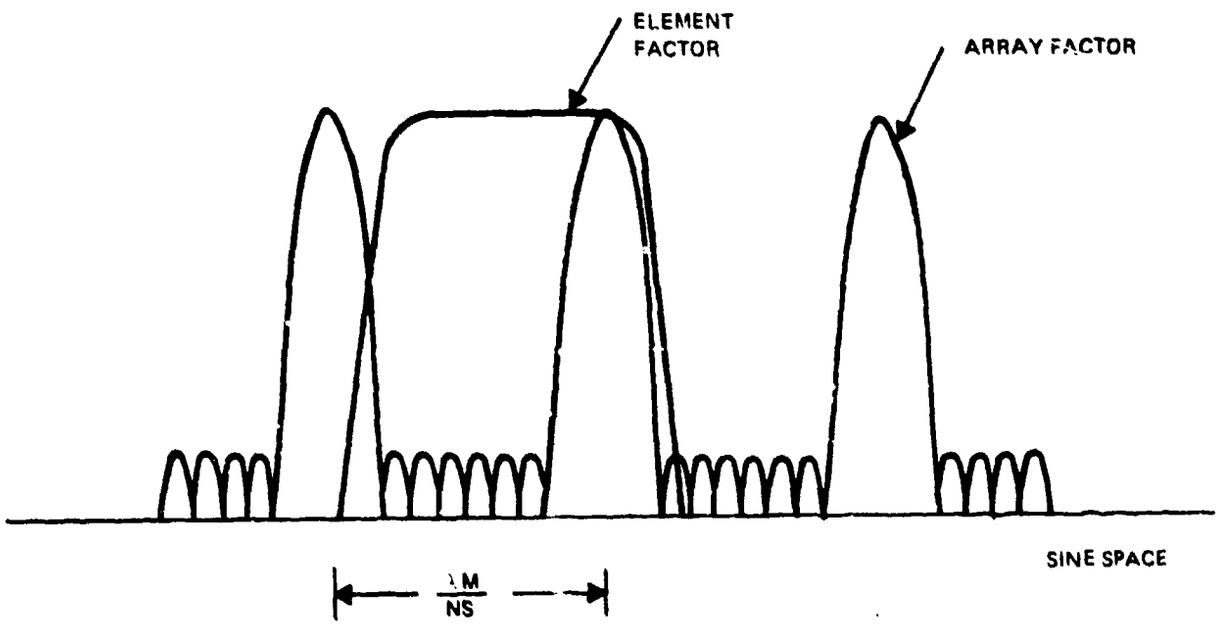

S - INDIVIDUAL RADIATING ELEMENT SPACING

82-2288-V-7

Figure 7. Relative Motion of Element Pattern and Array Factor at $f = f_o + f$

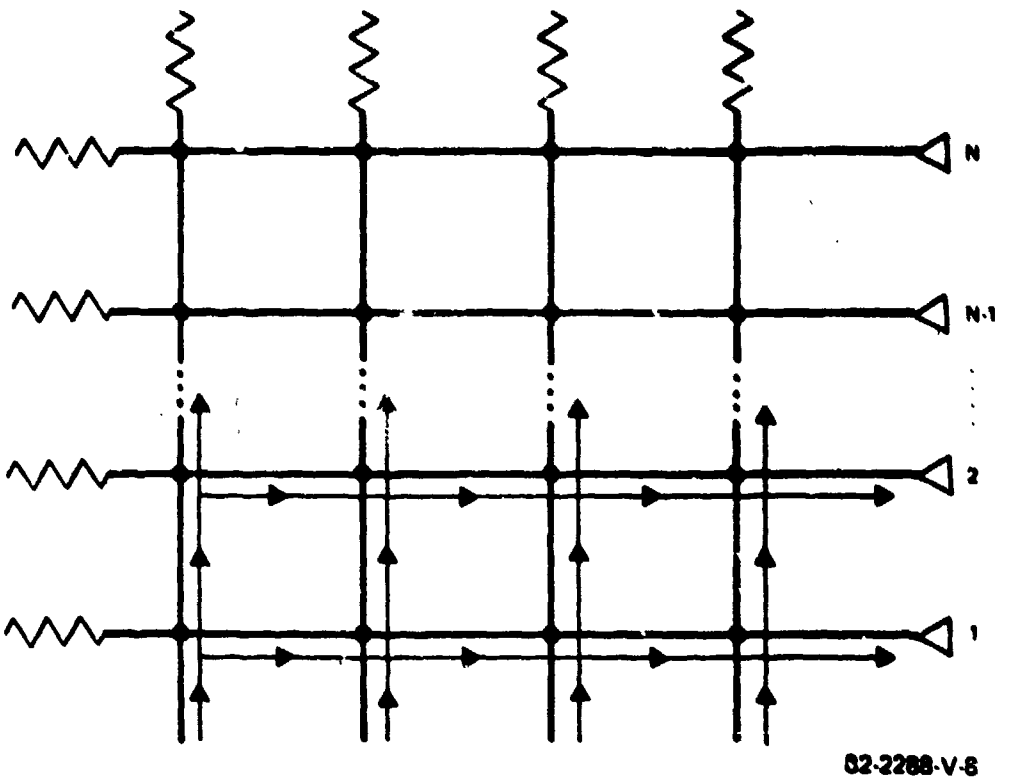

Figure 8. Blass Feed Network Signal Flow

For L=3 discrete time delay network positions, the region of sine space between $\pm \sin^{-1}(45^{o})$ was broken into 3 regions as shown in figure 9 and the three exact time delay compensation angles of 0^{o} and $\pm \sin^{-1}[2/3 \sin 45^{o}]$ chosen to provide optimum wide instantaneous bandwidth pattern performance. An additional factor included in the analytical effort was the use of waveguide time delay sections rather than TEM transmission line time delay sections. This was done in order to retain the flexibility of operating the modelled antenna system at high power levels. The use of waveguide in the 3 position time delay networks tended to restrict instantaneous bandwidth slightly because of waveguide dispersion but this effect was found to be essentially negligible when a performance comparison with time delay networks using TEM transmission line delay was made.

Computed patterns for the wide instantaneous band phased array antenna system shown in figure 4 are shown in figures 10 through 22. Figure 10 shows a center frequency pattern with perfect time delay settings for f_o and 0^{o} scan. All patterns in figures 10 through 22 show the array pattern with solid lines and an individual subaperture patterns with dotted lines for reference.

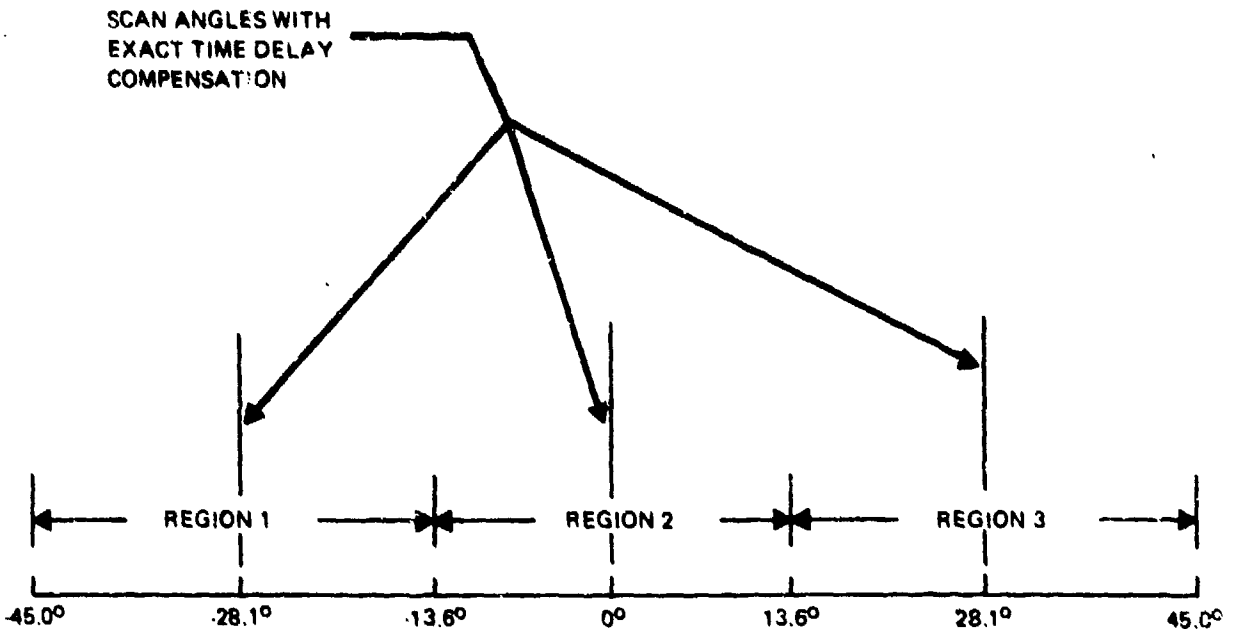

82-2288-V-9

Figure 9. Scan Angle Coverage Diagram

Figures 11 through 13 show patterns over a 6% band centered at $f = 0.941\ f_o$ for a scan angle of -45^o. For the -45^o scan angle, time delay networks were set for perfect compensation at -28.1^o as shown in figure 9.

Comparison of the patterns in figures 12 and 13 show that for scan angles at maximum distance from the time delay compensated scan angle that sidelobes are maintained quite well over the required 6% instantaneous bandwidth and that beam pointing is relatively constant over the instantaneous band of interest. The remaining patterns show sidelobe and pointing angle performance over the required 6% instantaneous bandwidth at the other three scan angle/operating band extremes. The operating band for the antenna configuration of figure 4 was 17.6%.

SUMMARY

In the course of the analytical effort described above, it was found that the parameters of table 1 were close to optimum in terms of pattern performance and minimum antenna system complexity. The number of time delay network positions, L, and the number of Blass feed network elements (and time delay elements), M, were the major controlling factors for array complexity.

Preliminary analysis showed that for M smaller than 12, the near sidelobes of the array exceeded desired levels and that for L less than 3, excessive beam motion is incurred over the required instantaneous bandwidth.

The beam motion versus frequency over the 6% instantaneous bandwidth for the scan angle and operating band extremes addresed by the patterns of figures 11 through 22 was less than a beamwidth in all cases, and can be reduced by increasing the value of L, the number of discrete positions of the switchable time delay networks.

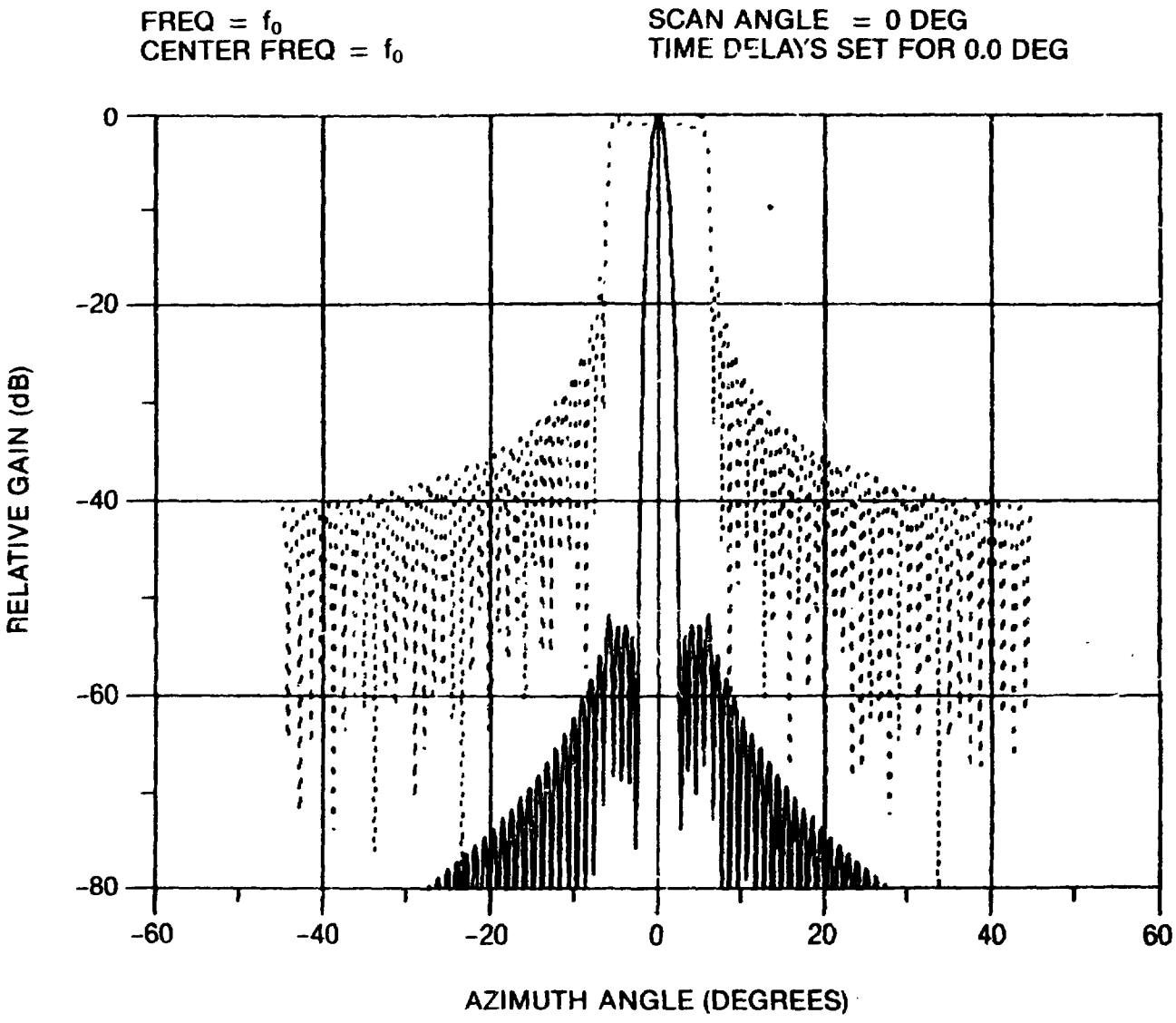
FREQ = f_0
CENTER FREQ = f_0
SCAN ANGLE = 0 DEG
TIME DELAYS SET FOR 0.0 DEG
RELATIVE GAIN (dB)
0
-20
-40
-60
-80
-60
-40
-20
0
20
40
60
AZIMUTH ANGLE (DEGREES)
82-2288-V-10

Figure 10

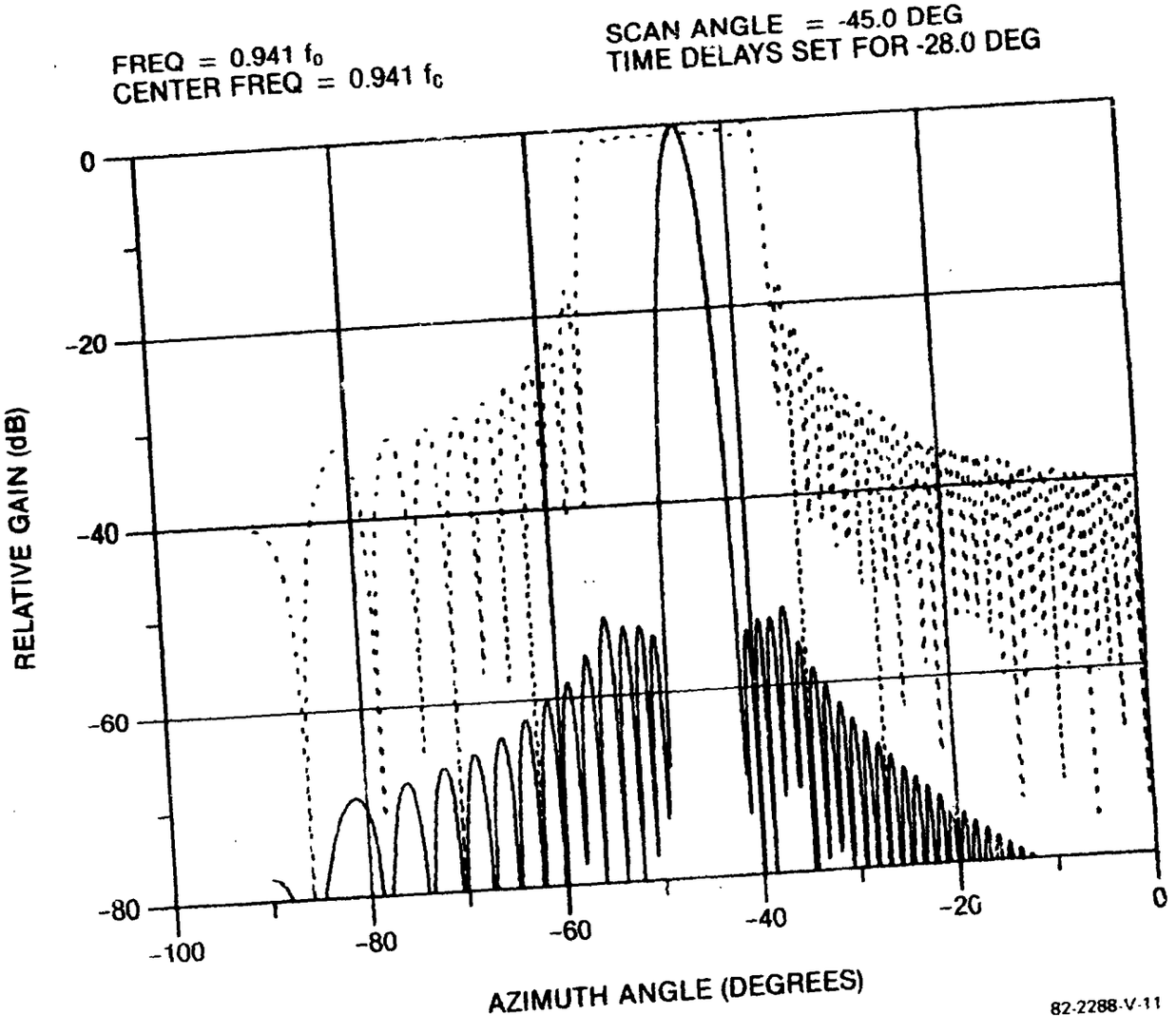
FREQ = 0.941 f_o
CENTER FREQ = 0.941 f_c
SCAN ANGLE = -45.0 DEG
TIME DELAYS SET FOR -28.0 DEG
RELATIVE GAIN (dB)
0
-20
-40
-60
-80
-100
-80
-60
-40
-20
0
AZIMUTH ANGLE (DEGREES)
82-2288-V-11

Figure 11

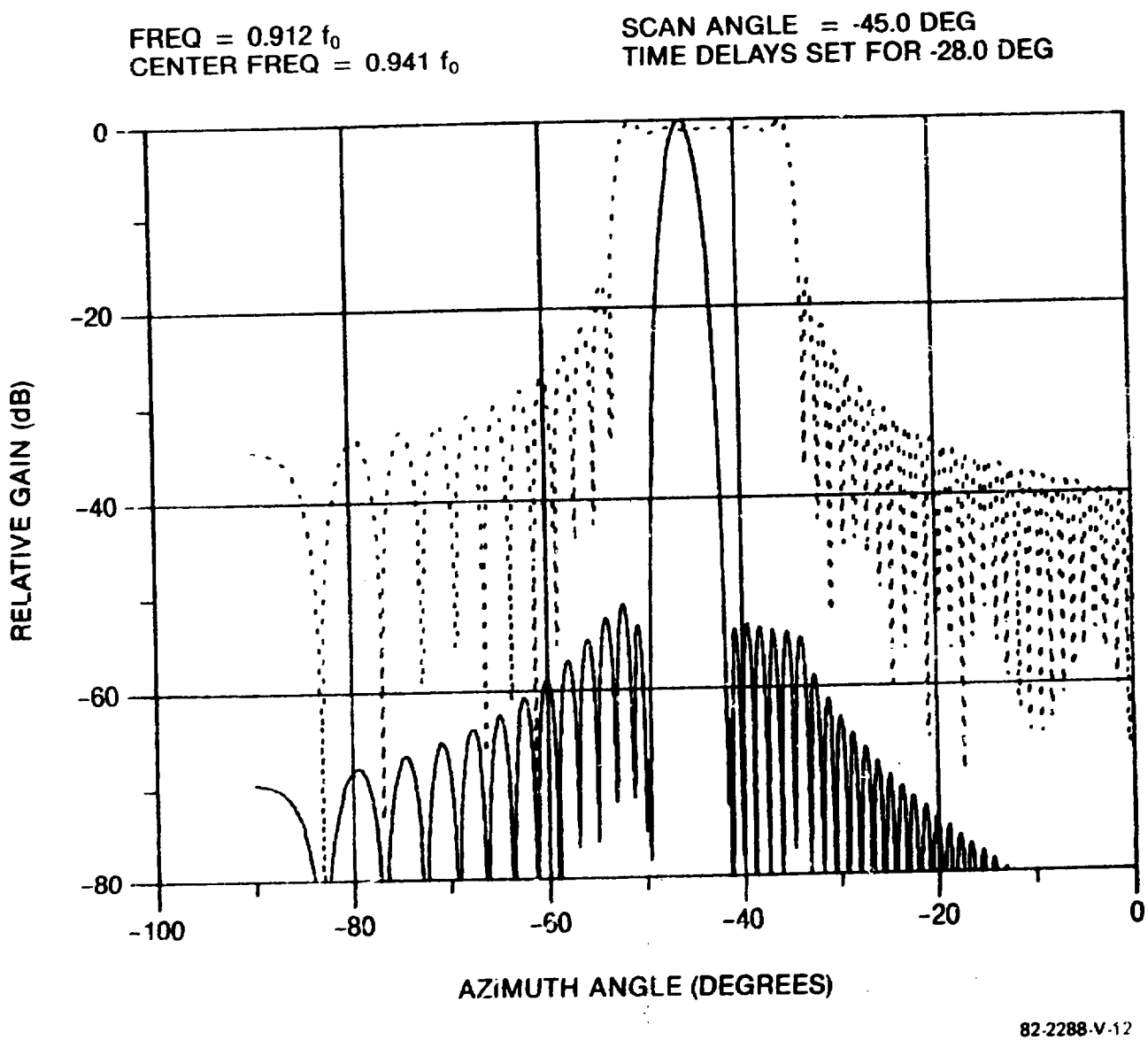
FREQ = 0.912 f_0
CENTER FREQ = 0.941 f_0
SCAN ANGLE = -45.0 DEG
TIME DELAYS SET FOR -28.0 DEG
RELATIVE GAIN (dB)
0
-20
-40
-60
-80
-100
-80
-60
-40
-20
0
AZIMUTH ANGLE (DEGREES)
82-2288-V-12

Figure 12

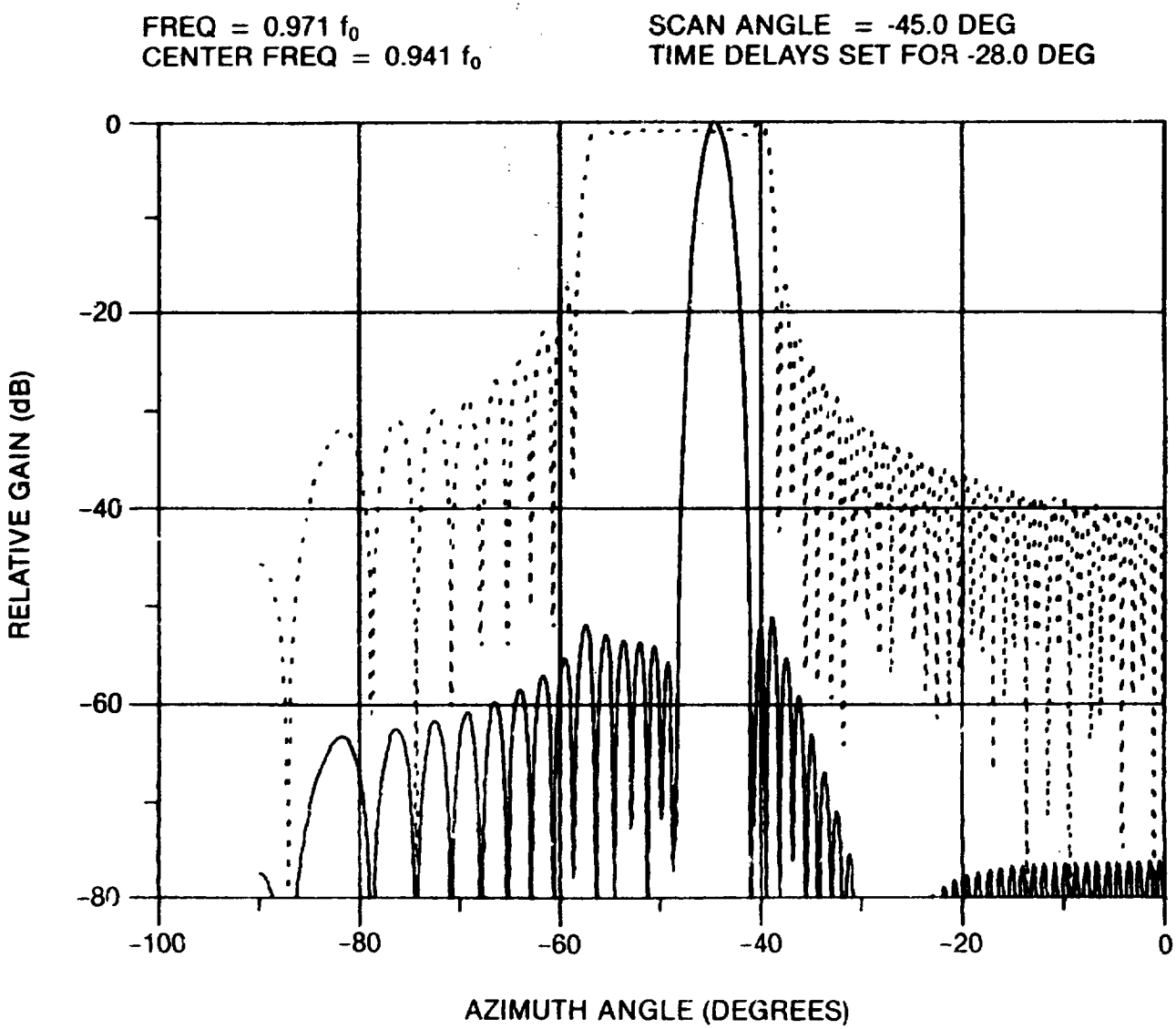
FREQ = 0.971 f_0
CENTER FREQ = 0.941 f_0
SCAN ANGLE = -45.0 DEG
TIME DELAYS SET FOR -28.0 DEG
RELATIVE GAIN (dB)
0
-20
-40
-60
-80
-100
-80
-60
-40
-20
0
AZIMUTH ANGLE (DEGREES)
82-2288-V-13

Figure 13

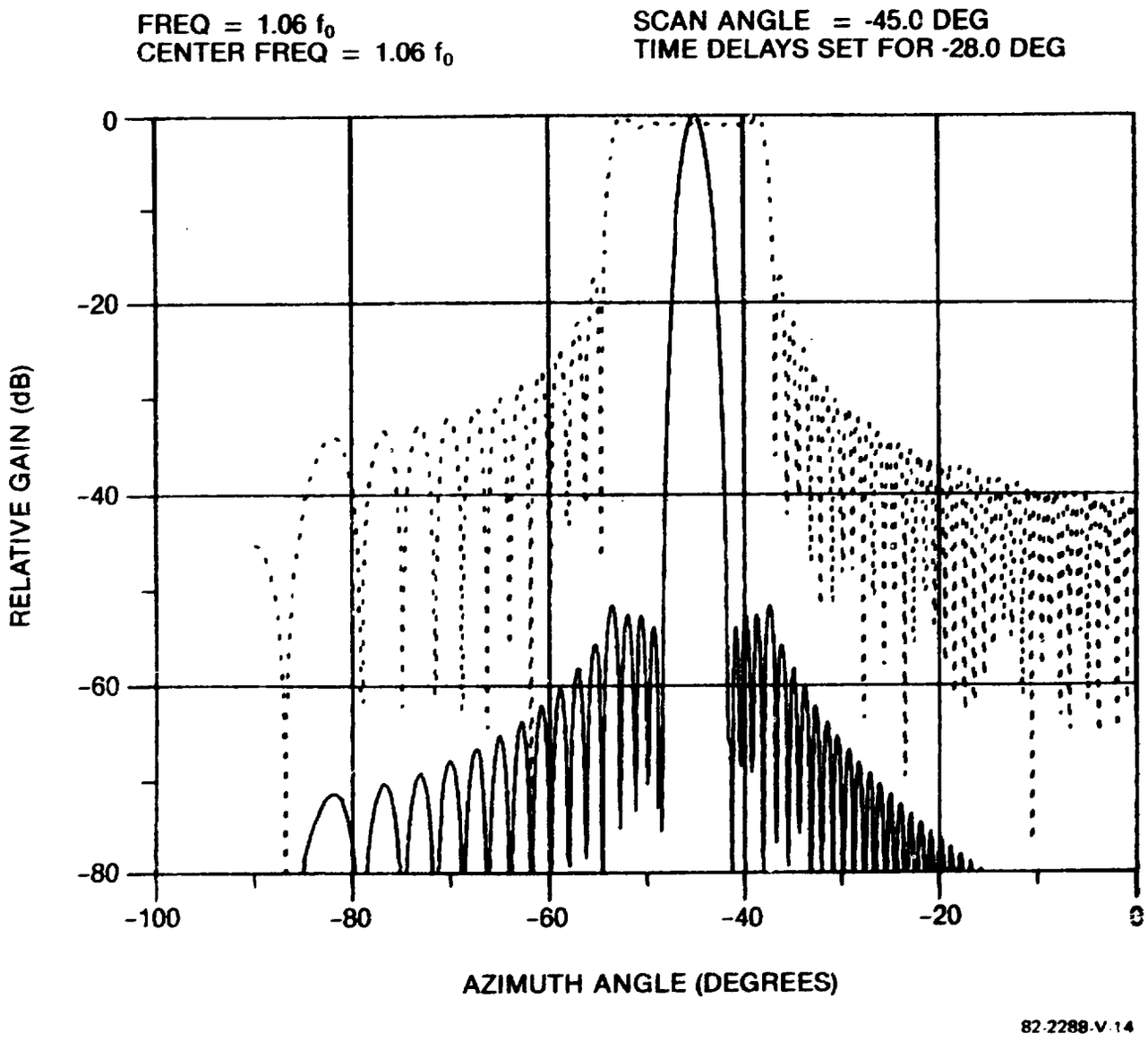
FREQ = 1.06 f_0
CENTER FREQ = 1.06 f_0
SCAN ANGLE = -45.0 DEG
TIME DELAYS SET FOR -28.0 DEG
RELATIVE GAIN (dB)
0
-20
-40
-60
-80
-100
-80
-60
-40
-20
0
AZIMUTH ANGLE (DEGREES)
82-2288-V-14

Figure 14

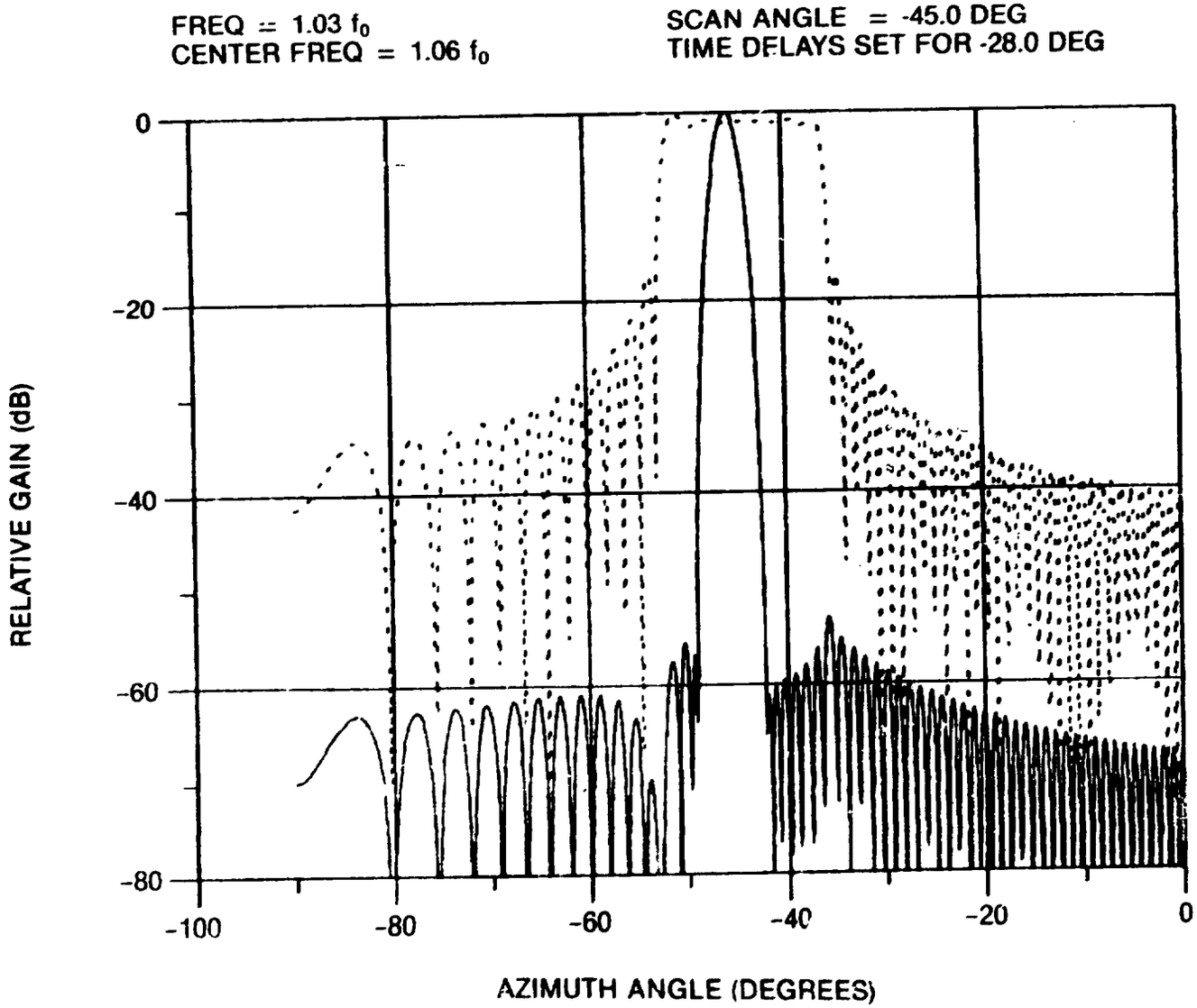
FREQ = 1.03 f_0
CENTER FREQ = 1.06 f_0
SCAN ANGLE = -45.0 DEG
TIME DELAYS SET FOR -28.0 DEG
RELATIVE GAIN (dB)
0
-20
-40
-60
-80
-100
-80
-60
-40
-20
0
AZIMUTH ANGLE (DEGREES)
82-2288-V-15

Figure 15

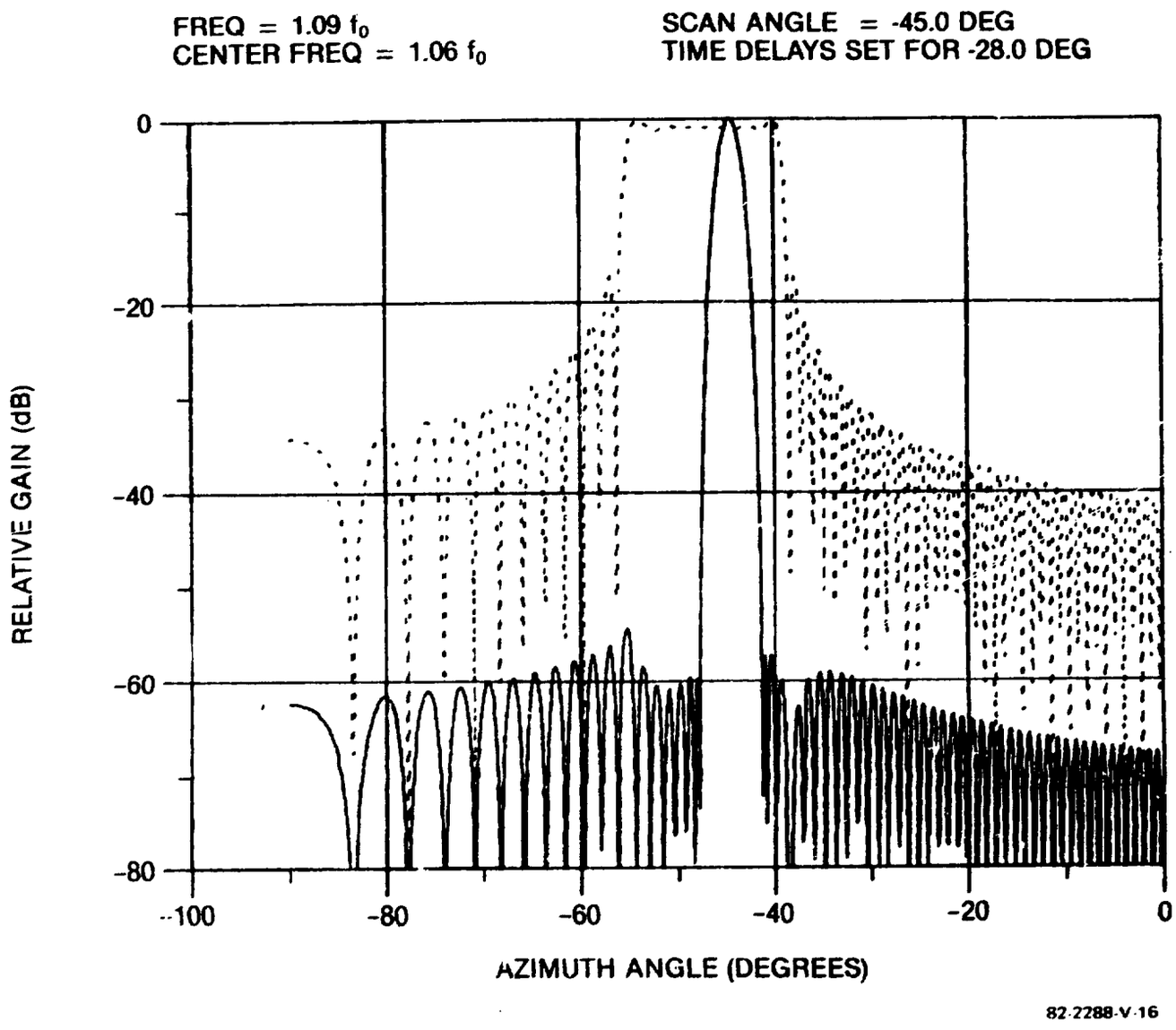
FREQ = 1.09 f_0
CENTER FREQ = 1.06 f_0
SCAN ANGLE = -45.0 DEG
TIME DELAYS SET FOR -28.0 DEG
RELATIVE GAIN (dB)
0
-20
-40
-60
-80
-100
-80
-60
-40
-20
0
AZIMUTH ANGLE (DEGREES)
82-2288-V-16

Figure 16

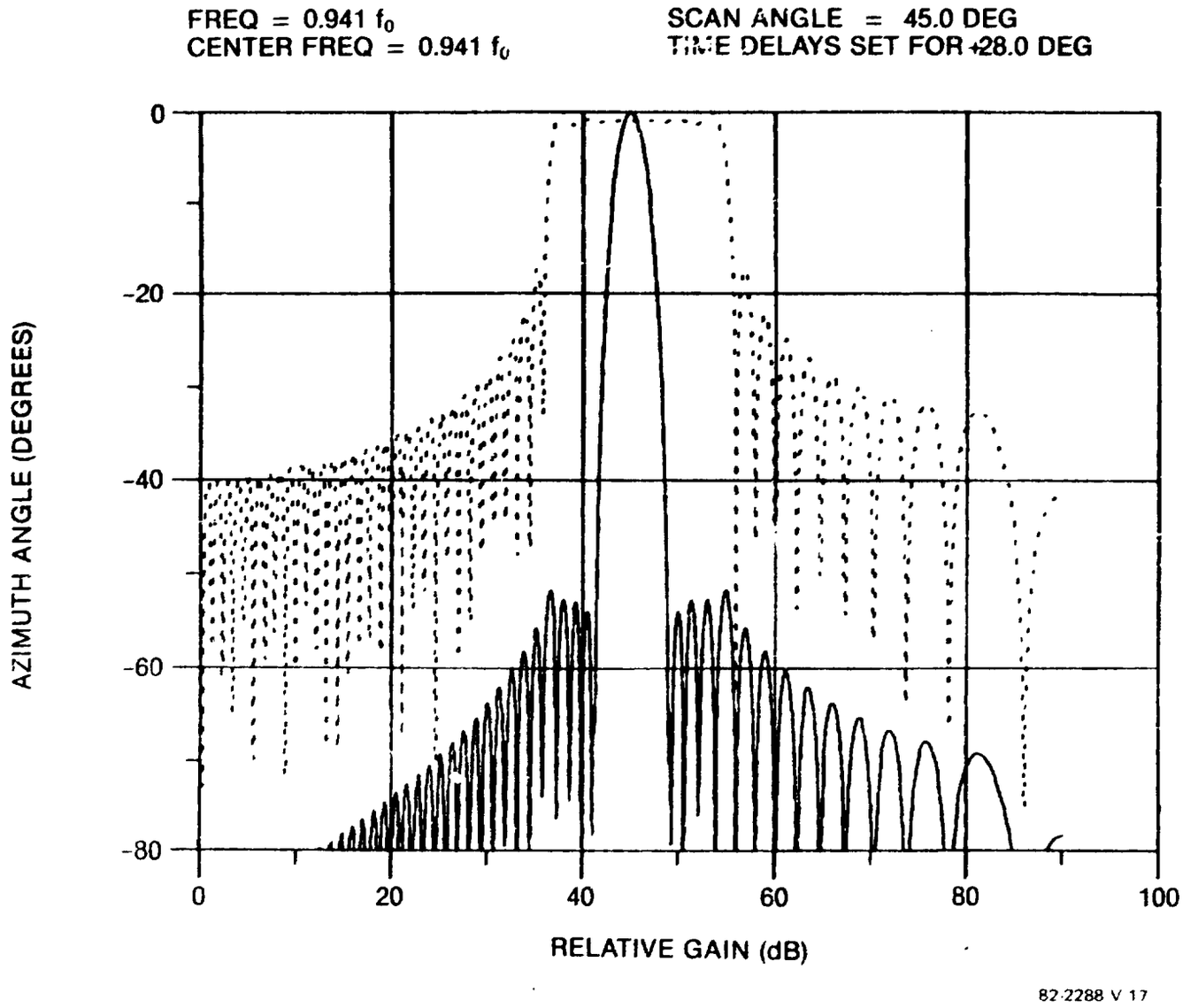
FREQ = 0.941 f_0
CENTER FREQ = 0.941 f_0
SCAN ANGLE = 45.0 DEG
TIME DELAYS SET FOR +28.0 DEG
AZIMUTH ANGLE (DEGREES)
0
-20
-40
-60
-80
0
20
40
60
80
100
RELATIVE GAIN (dB)
82-2288 V 17

Figure 17

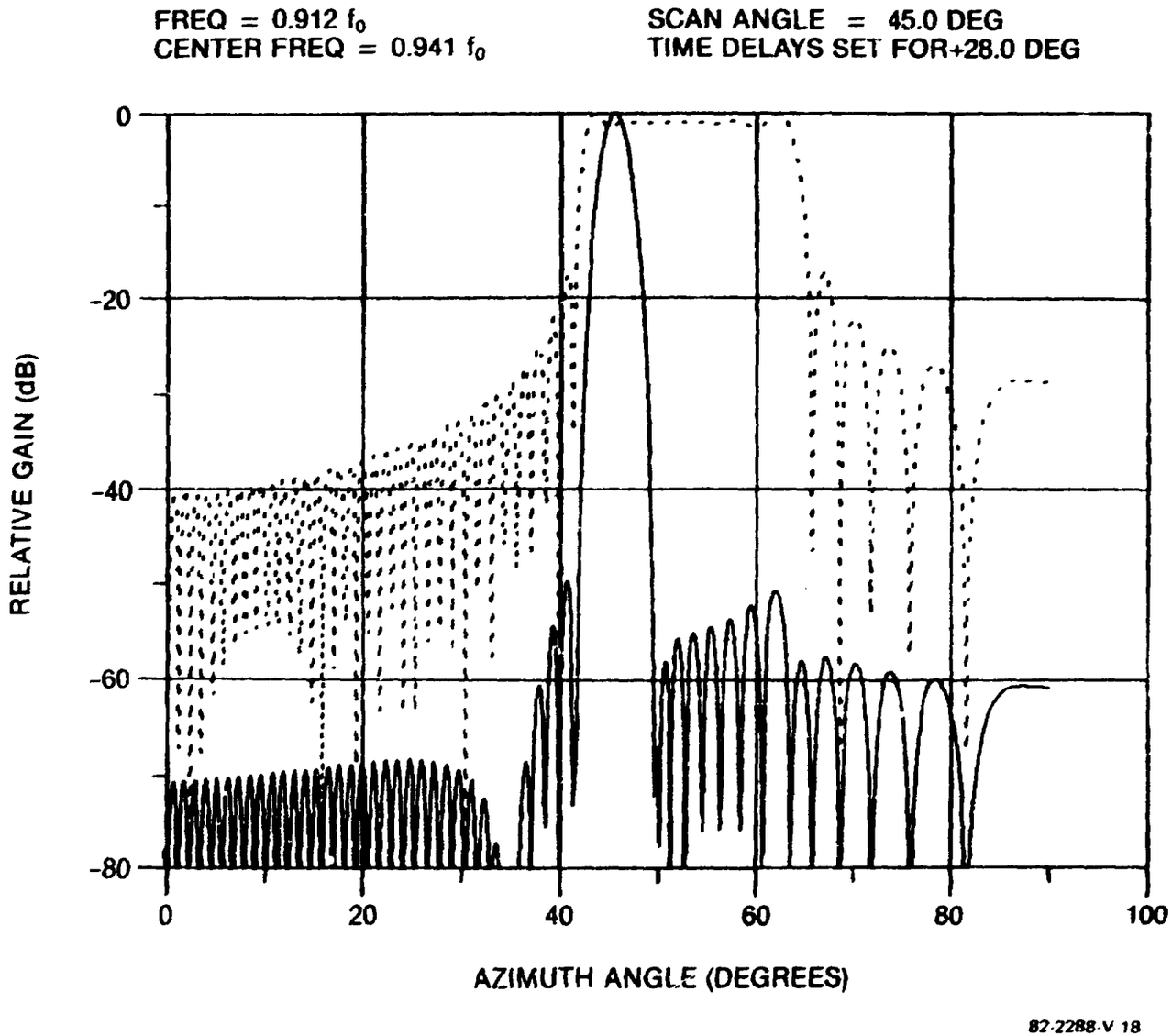
FREQ = 0.912 f_0
CENTER FREQ = 0.941 f_0
SCAN ANGLE = 45.0 DEG
TIME DELAYS SET FOR+28.0 DEG
RELATIVE GAIN (dB)
0
-20
-40
-60
-80
0
20
40
60
80
100
AZIMUTH ANGLE (DEGREES)
82-2288-V 18

Figure 18

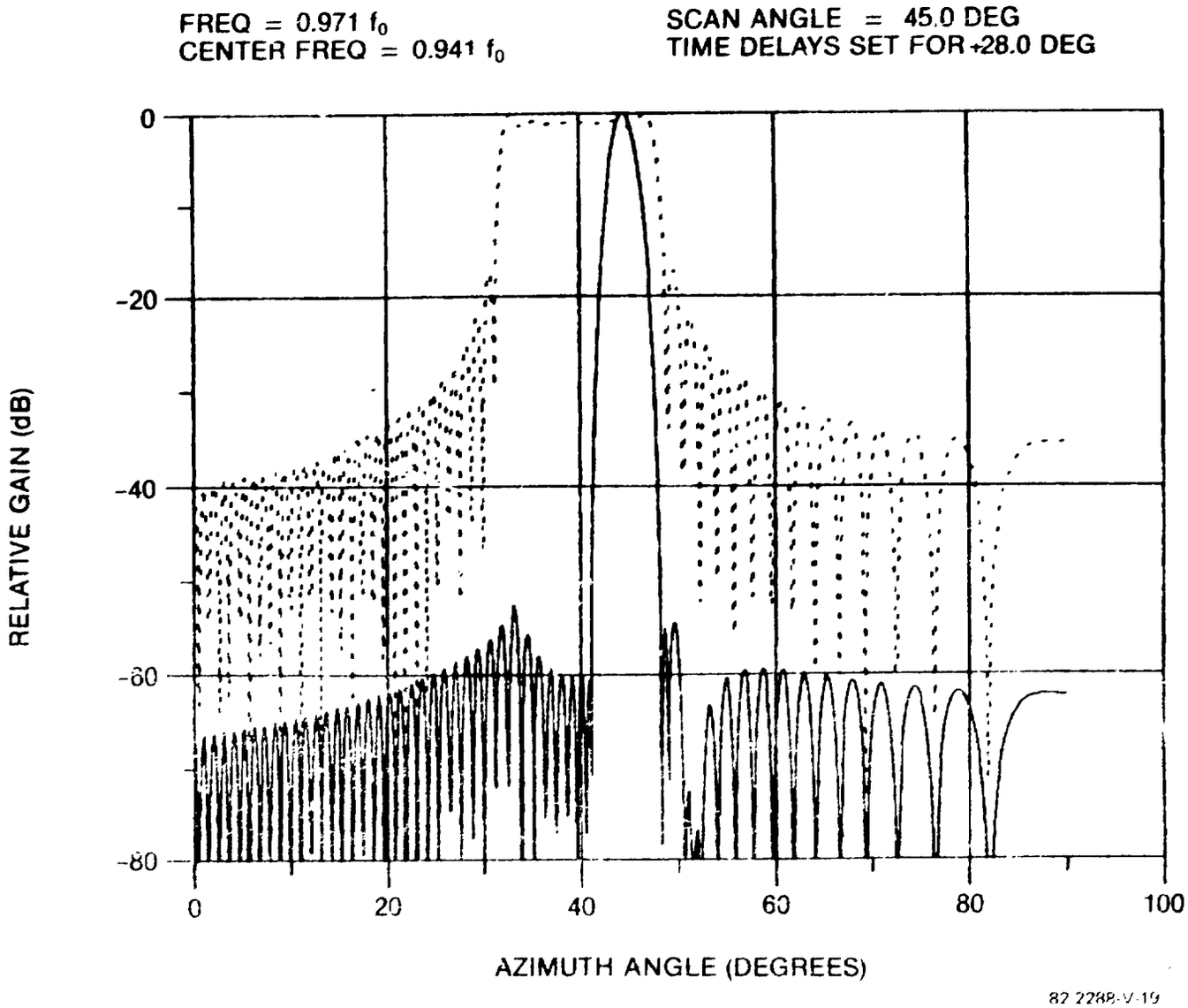
FREQ = 0.971 f_0
CENTER FREQ = 0.941 f_0
SCAN ANGLE = 45.0 DEG
TIME DELAYS SET FOR +28.0 DEG
RELATIVE GAIN (dB)
0
-20
-40
-60
-80
0
20
40
60
80
100
AZIMUTH ANGLE (DEGREES)
82 2288-V-19

Figure 19

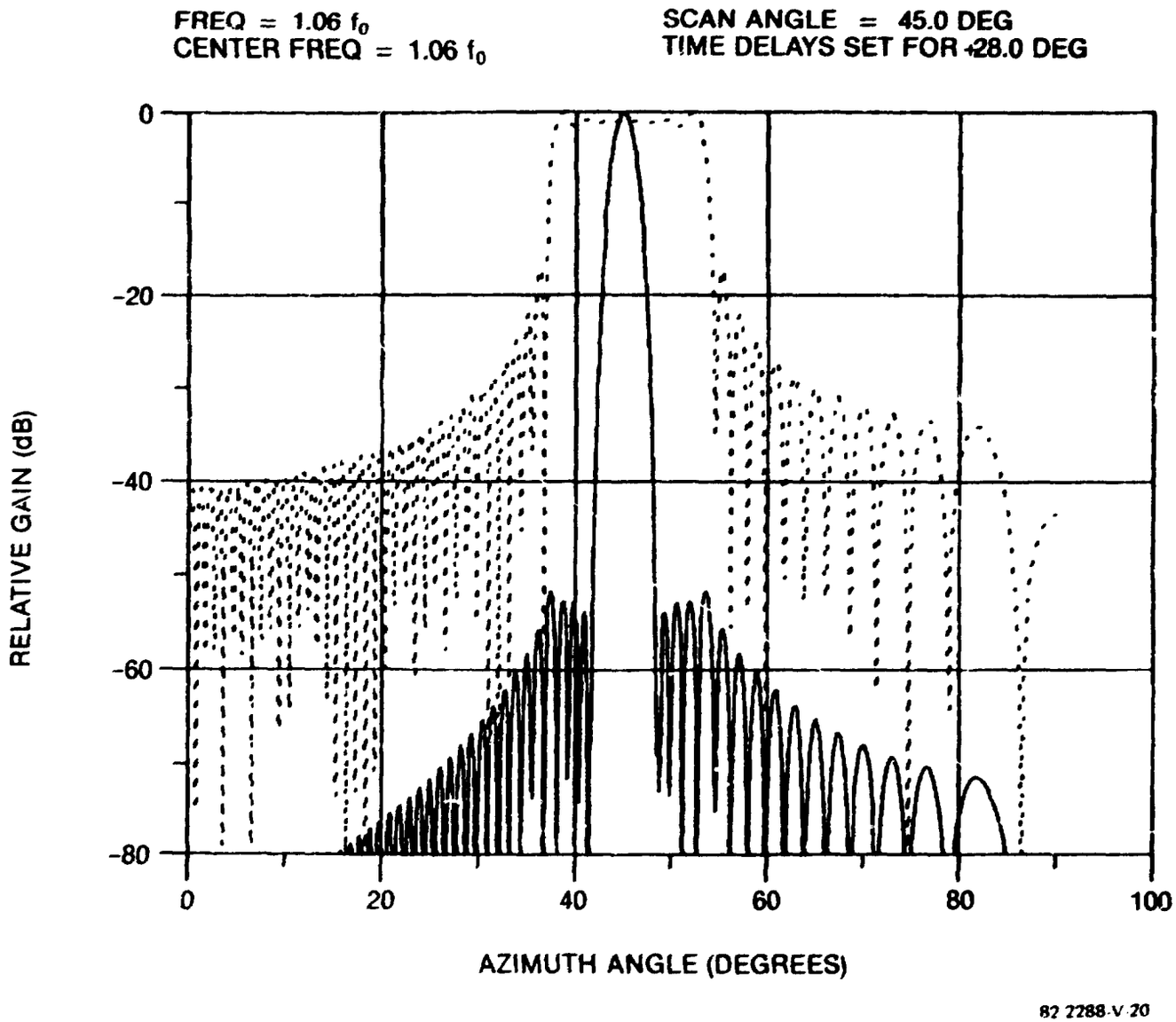
FREQ = 1.06 f_0
CENTER FREQ = 1.06 f_0
SCAN ANGLE = 45.0 DEG
TIME DELAYS SET FOR +28.0 DEG
0
-20
-40
-60
-80
RELATIVE GAIN (dB)
0
20
40
60
80
100
AZIMUTH ANGLE (DEGREES)
82 2288-V 20

Figure 20

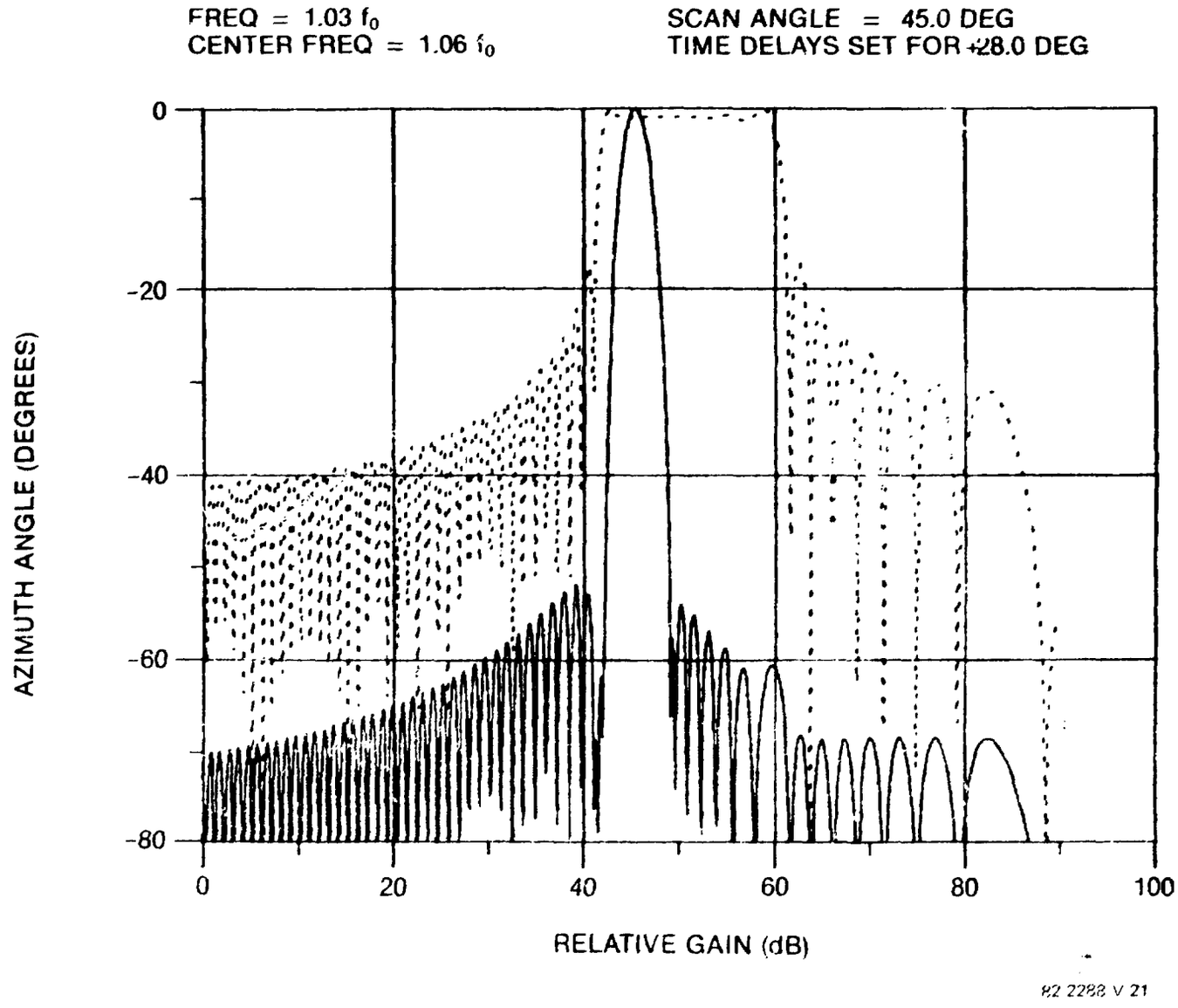
FREQ = 1.03 f_0
CENTER FREQ = 1.06 f_0
SCAN ANGLE = 45.0 DEG
TIME DELAYS SET FOR +28.0 DEG
AZIMUTH ANGLE (DEGREES)
0
-20
-40
-60
-80
0
20
40
60
80
100
RELATIVE GAIN (dB)
82 2288 V 21

Figure 21

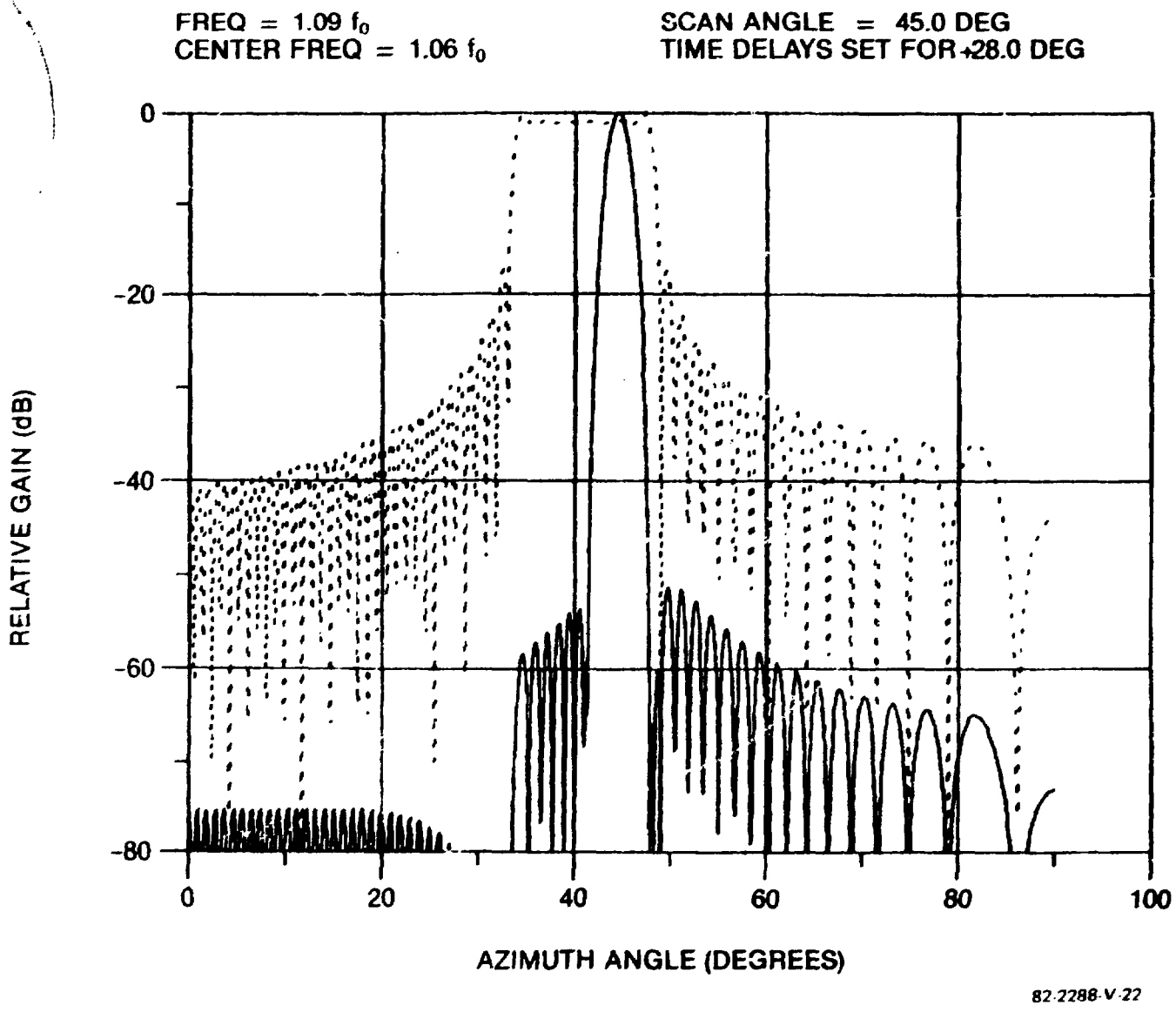
FREQ = 1.09 f_0
CENTER FREQ = 1.06 f_0
SCAN ANGLE = 45.0 DEG
TIME DELAYS SET FOR +28.0 DEG
RELATIVE GAIN (dB)
0
-20
-40
-60
-80
0
20
40
60
80
100
AZIMUTH ANGLE (DEGREES)
82-2288-V-22

Figure 22

AD P001102

OPTIMAL SYNTHESIS OF E-SCAN SPACE-FED ANTENNAS

J. L. Bauck and S. M. Daniel
Motorola Government Electronics Group
Radar Operations Systems Office
Systems and Technology Section
Tempe, Arizona 85282

ABSTRACT

A minimum-mean-square (MMS) formulation is employed in the synthesis of two space-fed E-scan antenna designs. Based on ray-tracing, the underlying mathematical model expresses the illumination of a primary radiation array as a linear function of the complex weights of a secondary radiation array. The MMS formulation leads to a linear system whose solution is the desired excitation weight vector solution. Part I addresses the first design in which the illumination is an amplitude window over the radiation array where E-scanning is accomplished via dedicated phase shifter control. By contrast, the second design, presented in Part II, involves a complex illumination which accommodates E-scanning without the need for phase shifters at the radiation array. Specific numerical examples included demonstrate the validity of the synthesis approach for each design.

1.0 PART I. RADIATION ARRAY PHASE-SHIFTER E-SCAN CONTROL

The design of space-fed antennas has been motivated by the need to alleviate the practical complexity associated with

power distribution over large arrays. As such, a small excitation array is used to illuminate the primary array from a certain distance with the aim of achieving the desired power distribution otherwise possible with a more complex corporate-fed approach. Of course, while circumventing a practical difficulty, the space-fed design introduces the analytical problem of determining the optimal excitation array distribution to achieve the desired illumination. Following a brief description of the space-fed antenna in question, a systematic, numerically-oriented approach is presented which produces a MMS estimate of the desired excitation.

1.1 Statement of the Problem

Consider the dual parallel-plate space-fed antenna shown in Figure 1. Among its essential parts is a waveguide feedport for illuminating an excitation array of M transceiver elements having appropriate complex (amplitude and phase) weighting that gives rise to a desired illumination at the radiation array of L transceiver elements equipped with phase shifters for cylindrical aberration correctior and E-scanning.

The central problem at hand is that of determining the complex excitation weighting $\{a_m,\phi_m\}_{m=1}^{M}$ which will give rise to a desired illumination over the radiation array, while simultaneously compensating for cylindrical attenuation and phase aberrations in each of the two lenses.

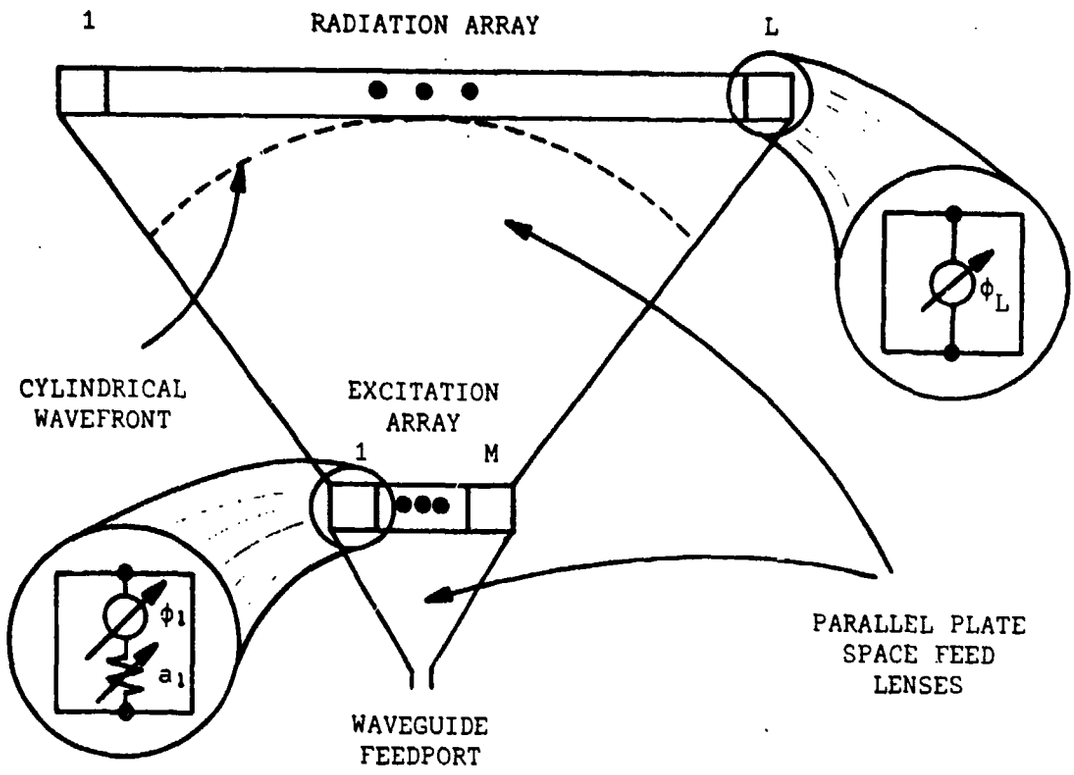

Figure 1. Space-Fed Antenna Configuration

1.2 Mathematical Formulation

Given a desired amplitude illumination over the radiation array, the corresponding complex excitation weight vector

$$\underline{w} \equiv \{w_m\}_{m=1}^{M} = \{a_m e^{j\phi_m}\}_{m=1}^{M} \tag{1}$$

may be derived by solving a complex linear system resulting from a MMS formulation of the problem.

1.2.1 Mathematical Model

Figure 2 shows the essential geometry of the space-fed array in question, where all dimensions are given ir half wavelengths of some reference frequency. The pertinent parameters to be noted in the Figure are

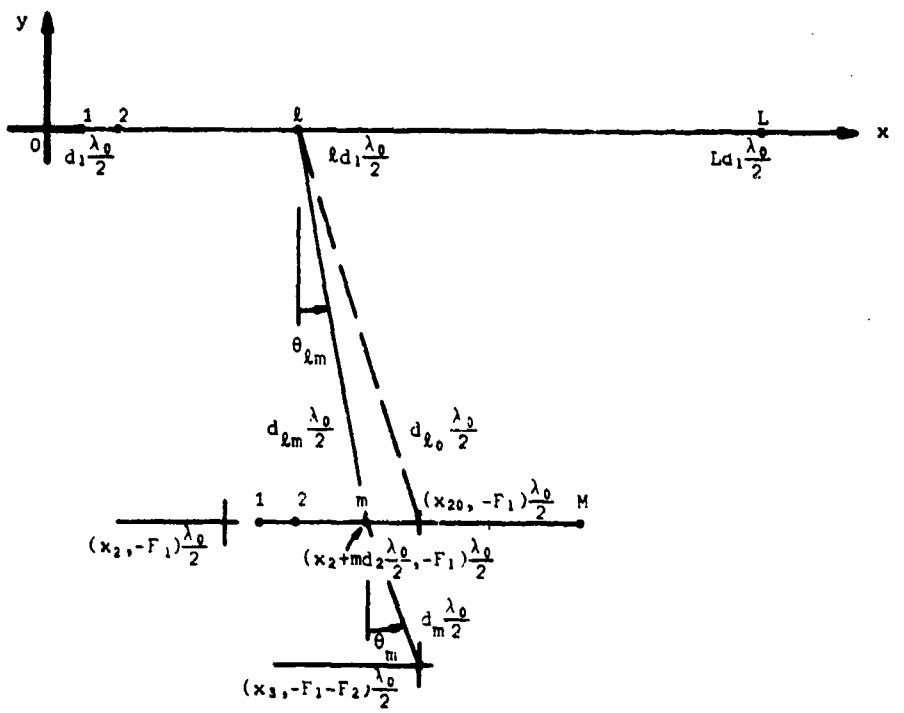

Figure 2. Essential Geometry of Space-Fed Antenna

L = number of equispaced radiation array elements

d_1 = radiation array interelement spacing in units of $\frac{\lambda_0}{2}$

F_1 = minimum distance between arrays in units of $\frac{\lambda_0}{2}$

M = number of equispaced excitation array elements

d_2 = excitation array interelement spacing in units of $\frac{\lambda_0}{2}$

F_2 = minimum distance between feedport and excitation array in units of $\frac{\lambda_0}{2}$

x_2 = x-axis displacement of excitation array in units of $\frac{\lambda_0}{2}$

= $\frac{1}{2}(Ld_1-Md_2)$, if centered with respect to radiation array

x_3 = x-axis position of feedport in units of $\frac{\lambda_0}{2}$

= $\frac{L}{2}d_1$, if centered with respect to radiation array

$d_{\ell 0}$ = distance between ℓ-th radiation array element and reference point, $(x_{20},-F_1)\frac{\lambda_0}{2}$, on excitation array, in units of $\frac{\lambda_0}{2}$

$$= \frac{\lambda_0}{2}\sqrt{(\ell d_1-x_{20})^2+F_1^2} \qquad (2)$$

$d_{\ell m}$ = distance between the ℓ-th radiation array element and m-th excitation array element, in units of $\frac{\lambda_0}{2}$

$$= \frac{\lambda_0}{2}\sqrt{(x_2+md_2-\ell d_1)^2+F_1^2} \qquad (3)$$

d_m = distance between m-th element of excitation array and feedport in units of $\frac{\lambda_0}{2}$

$$= \frac{\lambda_0}{2}\sqrt{(x_3-x_2-md_2)^2+F_2^2} \tag{4}$$

In view of the above definitions, it is possible to express the illumination at the ℓ-th radiation element as the superposition of excitation element contributions

$$g(\ell,f,\underline{w}) = \sum_{m=1}^{M} w_m h(m,\ell,f) \tag{5}$$

clearly a function of frequency, f, and the excitation weight vector, $\underline{w}$. More specifically,

$$h(m,\ell,f) = c_{\ell m} e^{-j2\pi f(\tau_m+\tau_{\ell m})} \tag{6}$$

where

τ_m = time delay between feedport and m-th excitation array element

$$= \frac{\lambda_0}{2c} d_m$$

$$= \frac{1}{2f_0} d_m \tag{7}$$

$\tau_{\ell m}$ = time delay between ℓ-th radiation array element and m-th excitation array element

$$= \frac{1}{2f_0} d_{\ell m} \tag{8}$$

and

$$c_{\ell m} = \alpha_m \alpha_{\ell m} \varepsilon_{\ell m} e^{j(\phi_m + \phi_\ell)} \tag{9}$$

with

α_m = relative $r^{-\frac{1}{2}}$ attenuation between the feedport and the m-th excitation element

$$= \sqrt{\frac{F_2}{d_m}} \tag{10}$$

$\alpha_{\ell m}$ = relative $r^{-\frac{1}{2}}$ attentuation between the m-th and ℓ-th excitation and radiation array elements, respectively

$$= \sqrt{\frac{F_2}{d_{\ell m}}} \tag{11}$$

$\varepsilon_{\ell m}$ = ℓ-th radiation array element radiation pattern

$$= \sin\left(\frac{\pi f d}{f_0} \cos\theta_{\ell m}\right) \cos^{\frac{1}{2}}\theta_{\ell m} \tag{12}*$$

ϕ_m = cylindrical phase error correction at m-th excitation array element

* Here, $d=0.62 \frac{\lambda_0}{2}$ in accordance with reference 1.

$$= \pi(d_m - F_2) \tag{13}$$

ϕ_ℓ = cylindrical phase error correction at ℓ-th radiation array element with respect to excitation array reference point, $(x_{20}, -F_1)\frac{\lambda_0}{2}$

$$= \pi(d_{\ell_0} - F_1) \tag{14}$$

1.2.2 Minimum Mean Square Synthesis

In view of (5), the illumination of the radiation array elements may be represented compactly in matrix notation as

$$\underline{g} = H\underline{w} \tag{15}$$

where

$\underline{g}$ = the L-component illumination vector

$$= \{g(\ell, f, \underline{w})\}_{\ell=1}^{L} \tag{16}$$

H = The M x L transition matrix

$$= \{\{h(m, \ell, f)\}_{\ell=1}^{L}\}_{m=1}^{M} \tag{17}$$

Given a desired illumination

$$\underline{e} = \{e(\ell)\}_{\ell=1}^{L} \tag{18}$$

we wish to derive an excitation vector $\underline{w}$ such that $\underline{g}$ closely approximates $\underline{e}$ in some sense. Using a MMS criterion, the weight vector we seek minimizes a quadratic performance index

$$\begin{aligned} J(\underline{w}) &= \| \underline{g}-\underline{e} \|^2 \\ &= \| H\underline{w}-\underline{e} \|^2 \\ &= (H\underline{w}-\underline{e})^{*T}(H\underline{w}-\underline{e}) \end{aligned} \tag{19}$$

whence, the desired solution satisfies the necessary conditions that

$$\begin{aligned} \underline{0} &= \tfrac{1}{2}\nabla_{\underline{w}} J(\underline{w}) \\ &= H^{*T}(H\underline{w}-\underline{e}) \\ &= C\underline{w}-\underline{b} \end{aligned} \tag{20}$$

where

$$C = H^{*T}H$$

= M x M complex-valued covariance matrix

$$\underline{b} = H^{*T}\underline{e}$$

= M-component complex-valued forcing vector

Most generally, the desired minimum-norm solution is given by

$$\hat{\underline{w}} = C^{+}\underline{b} \tag{21}$$

where C^{+} stands for the pseudoinverse of C and is identical to the actual inverse, C^{-1}, if it exists. In the present paper, solution (21) is obtained by using the complex form of the conjugate gradients method[2,3].

1.3 Performance Analysis

The mathematical model of the previous section was implemented on a computer, and the results are presented here in graphical form. The aperture illuminations which were approximated are those of Taylor[4] and Bayliss[5], the latter of which is used for "difference" field patterns in monopulse applications. In all cases, the sidelobe level of the ideal field pattern was chosen to be -50 dB, relative to the peak of the main lobe, and the number of approximately equal sidelobes adjacent to the main beam was chosen to be 12. For comparison with the main results, these ideal patterns are shown in Figures 3 and 4. These are array factors only, and do not include an element factor. Notice that in Figure 4, the Bayliss pattern has a very deep null at $\theta=0^{\circ}$, which is obscurred by the ordinate of that graph.

Figures 5 and 6 show results obtained using the MMS synthesis technique for Taylor and Bayliss patterns, respectively.

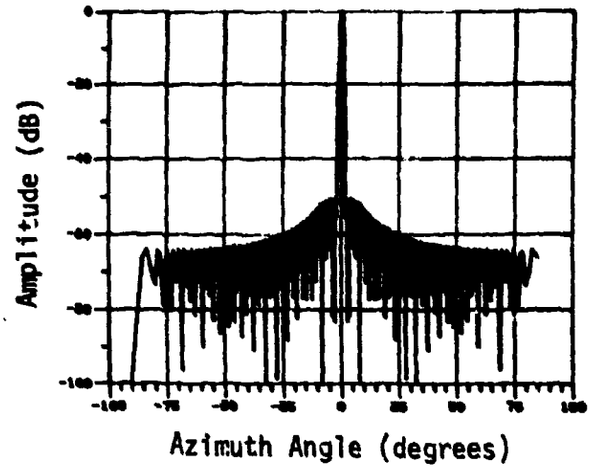

Figure 3. Field Pattern Corresponding to Ideal Taylor Aperture Distribution.

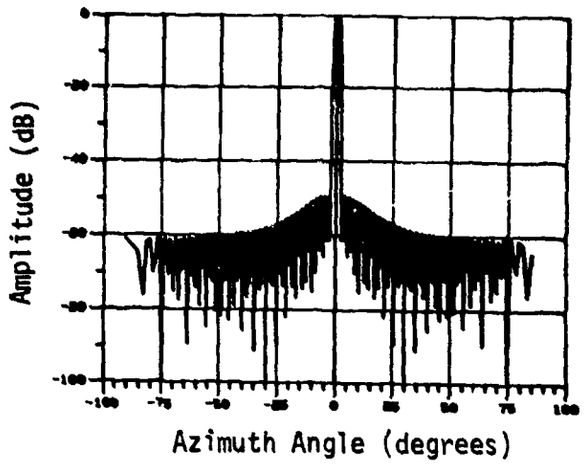

Figure 4. Field Pattern Corresponding to Ideal Bayliss Aperture Distribution.

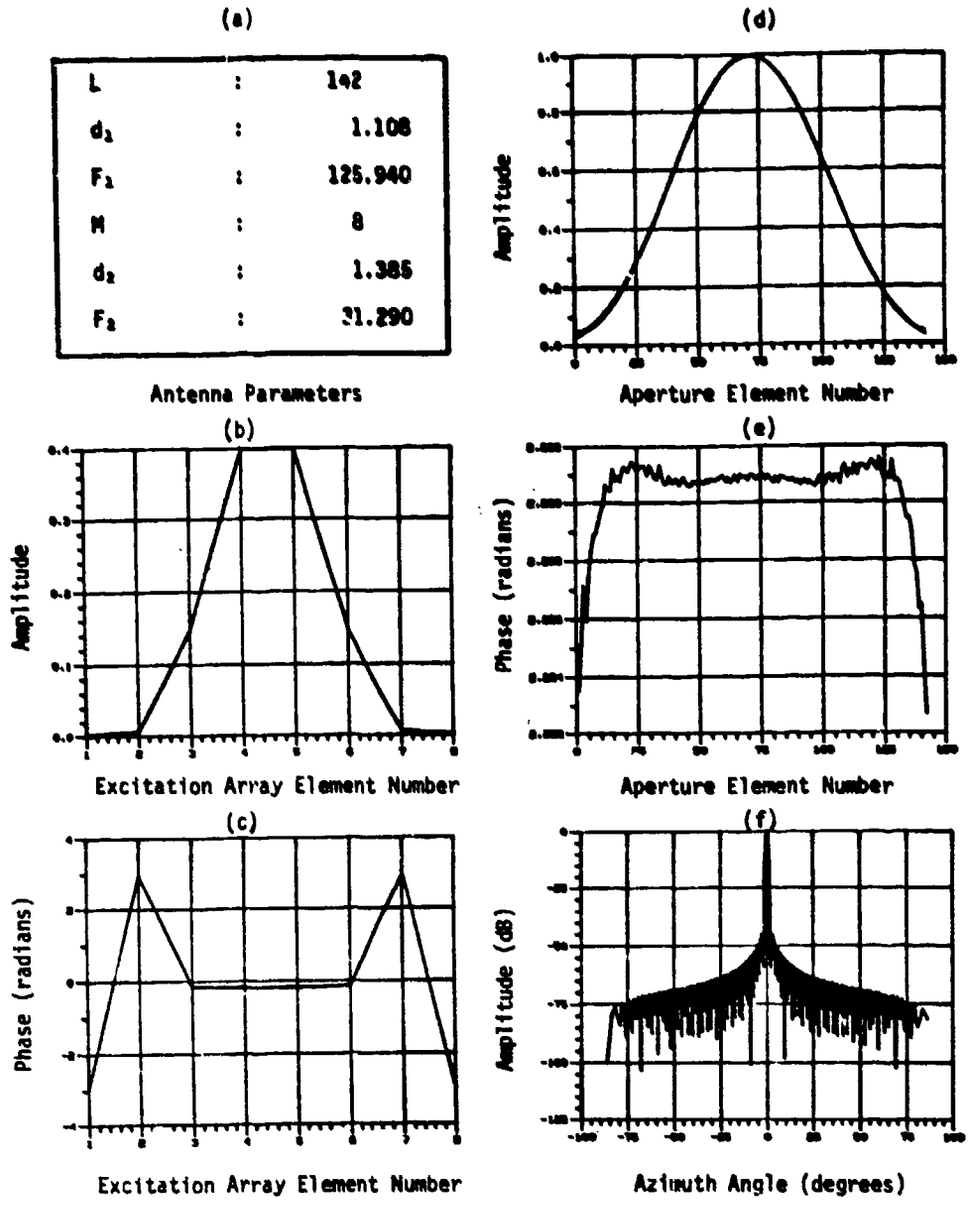

Figure 5. Taylor Approximation Example. (a) Antenna Parameters. (b) Amplitude of Excitation Array Weights. (c) Phase of Excitation Array Weights. (d) Amplitude of Aperture Illumination. (e) Phase of Aperture Illumination. (f) Amplitude of Field Pattern.

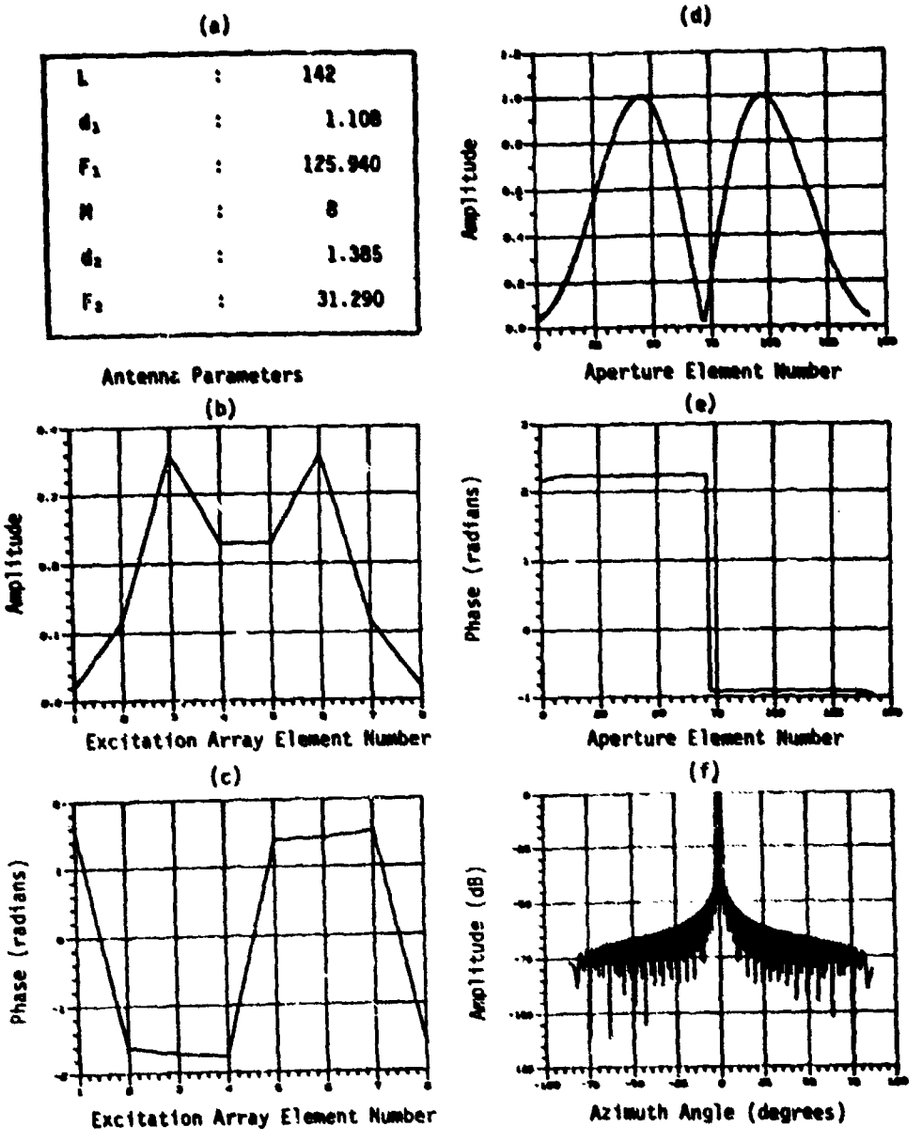

Figure 6. Bayliss Approximation Example. (a) Antenna Parameters. (b) Amplitude of Excitation Array Weights. (c) Phase of Excitation Weights. (d) Amplitude of Aperture Illumination. (e) Phase of Aperture Illumination. (f) Amplitude of Field Pattern.

The following comments apply to these and subsequent Figures which show graphical results:

Part (a) is a list of pertinent antenna and feed structure parameters.

Part (b) is a plot of the amplitude of the optimum excitation array weights, $\{a_m\}_{m=1}^{M}$.

Part (c) is a plot of the phase of the optimum excitation array weights, $\{\phi_m\}_{m=1}^{M}$, not including the correction for a spherical wavefront in the excitation lens.

Part (d) is a plot of the amplitude of the aperture illumination; the dotted line is the ideal (desired) illumination, and the solid line is that illumination which is actually achieved.

Part (e) is a plot of the achieved phase illumination. The desired phase illumination is a constant. (Absolute phase is unimportant.)

Part (f) is a plot of the amplitude of the resulting field pattern.

The results, (d) - (f), are those that would be obtained by operating the antenna at the frequency for which it was optimized. Phase shifter quantization effects are not included. The element pattern, $\cos^{\frac{1}{2}}\theta$, is included, via pattern multiplication, in the field plots.

Inspection of Figures 5 and 6 shows that the desired illumination is approximated quite well, resulting in maximum

sidelobes around -45 dB. Figure 5(a) shows that only four of the eight excitation weights differ significantly from zero. An example (not shown) was done with M=4, with the result that the four weights almost exactly replicated the central four weights of Figure 5(b), in both amplitude and phase. As a final comment, a defocusing technique was discovered, after these plots were made, whereby the aperture errors could be reduced even further, and which gave a final field pattern with sidelobes that were very close to the ideal -50 dB level. This comment will be amplified in Part II.

2.0 PART II. EXCITATION ARRAY COMPLEX WEIGHT E-SCAN CONTROL

By replacing the cylindrical phase error compensation $\{\phi_\ell\}_{\ell=1}^{L}$ with a true time delay compensation $\{T_\ell\}_{\ell=1}^{L}$, it is possible to improve the wideband performance of the spacefed antenna described in Part I. Focusing the radiation array to a point behind the excitation array will also improve the overall performance. However, such improvements are of little consolation when one is faced with the costly prospect of supplying a large number, L, of rather expensive high-resolution phase shifters. It is precisely this economic consideration which has motivated the space-fed design alternative discussed below; namely, one in which the radiation phase shifters are eliminated, transferring the burden of E-scanning to the excitation array.

2.1 Statement of the Problem

Figure 7 shows the functional block diagram of a spacefed antenna subsystem concept involving excitation array E-scan control. Besides a time delay compensation of the cylindrical wavefront over the radiation array, other more prominent features include a large concave excitation array of N elements, a small contiguous number, M, of which is activated with precomputed weighting from a PROM lookup table via a matrix switch.

Given an azimuth scanning requirement of 80°, (-40° to 40°), with a desired resolution of 0.05°, the storage capacity of the PROM table is 3200M words (1600M amplitudes, 1600M phases) for a single instantaneous frequency band. For M=16, this amount to 51.2k words, certainly a modest amount by modern standards. When a certain scan angle is desired, the appropriate set of 2M words is fetched from PROM and applied to the corresponding set of M activated excitation array elements.

Figure 8 shows the conceptual structure of the matrix switch, which routes M amplitude- and phase-weighted feedports to the appropriately selected M-subset of the N excitation array elements. To be noted here is the fact that only N switches are needed to accomplish a continuous activation of M contiguous elements over the N-element excitation array.

The problem at hand is the derivation of excitation array curvature and the solution of M-dimensional complex weight vectors corresponding to desired scan angles.

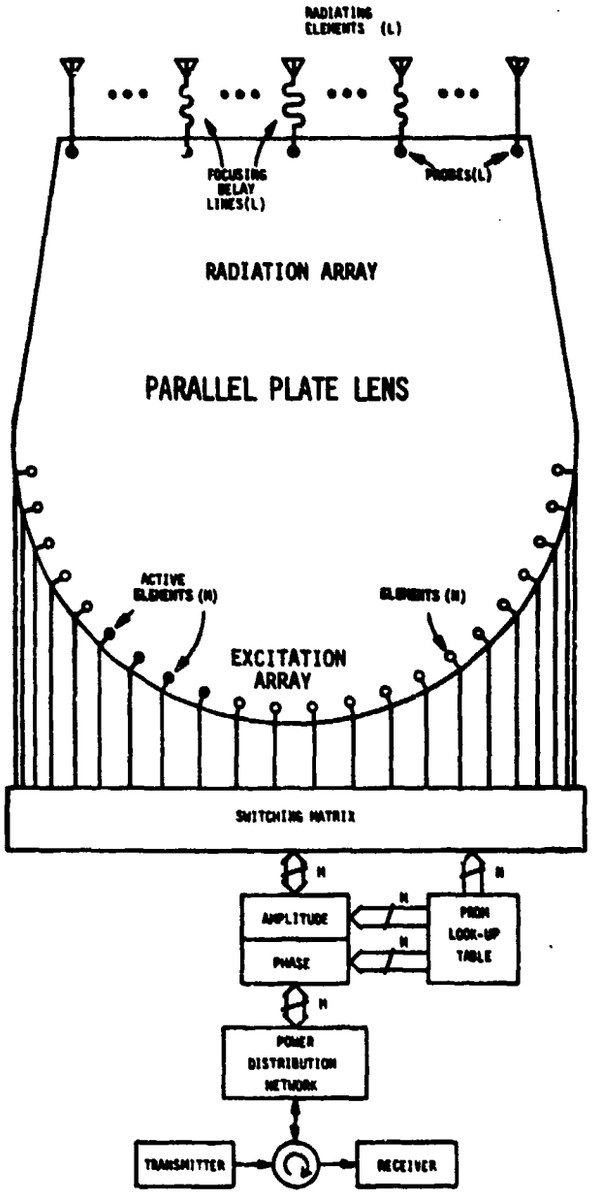

Figure 7. Functional Block Diagram of Space-Fed Antenna with Excitation Array Control

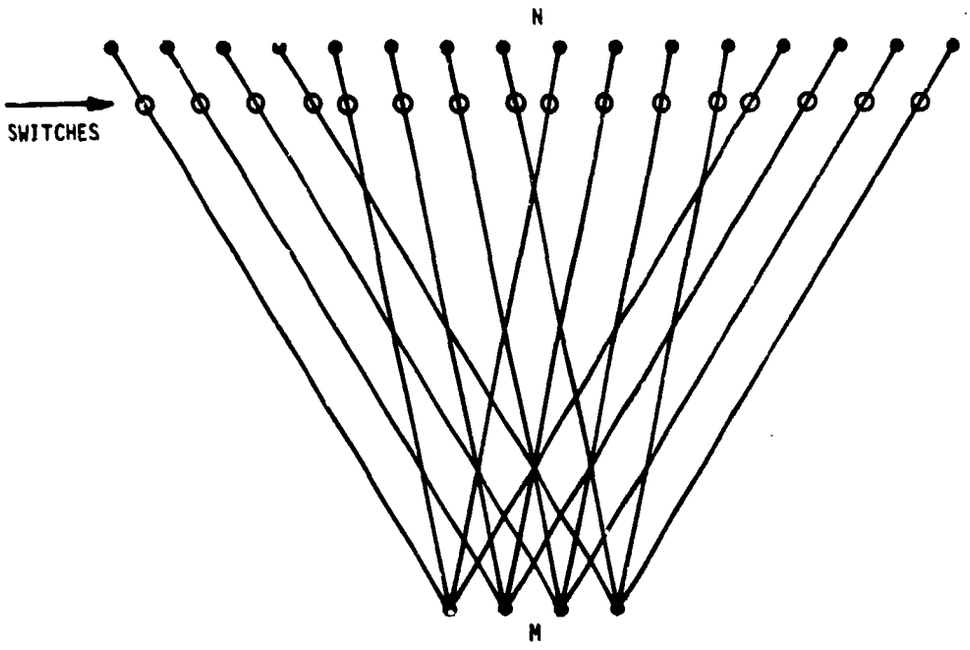

All transmission paths
are equal in length.

Figure 8. Details of M-to-N Switching Matrix. Any M consecutive elements out of N may be selected by using N Switches.

2.2 Mathematical Formulation

Given a desired illumination over the radiation array, specified by both an amplitude weighting and a phase shading associated with a certain scan angle, θ_s, the corresponding weighting vector

$$\underline{w}^s = \{w_m^s\}_{m=1}^M = \{a_m^s e^{j\phi_m^s}\}_{m=1}^M \tag{22}$$

may be derived in a similar way as in Part I.

2.2.1 Mathematical Model

The geometry pertinent to the space fed antenna design of Figure 7 is given in Figure 9. As before, all dimensions are in units of half wavelengths of some reference frequency. To be noted here is the focal point $(d_1\frac{L+1}{2}, -F_1)\frac{\lambda_0}{2}$, with respect to which the delay equalization is set at the radiation array.

Assuming that the k-th M-element excitation subarray is activated, the resulting illumination at the ℓ-th element of the radiation array is given by

$$g(k,\ell,k,\underline{w}^s) = \sum_{m=1}^{M} w_m^s h(k+m,\ell,f) \quad ; \quad k=0,\ldots,N-M \tag{23}$$

where

w_m^s = the m-th complex weight applied to the (k+m)-th excitation element

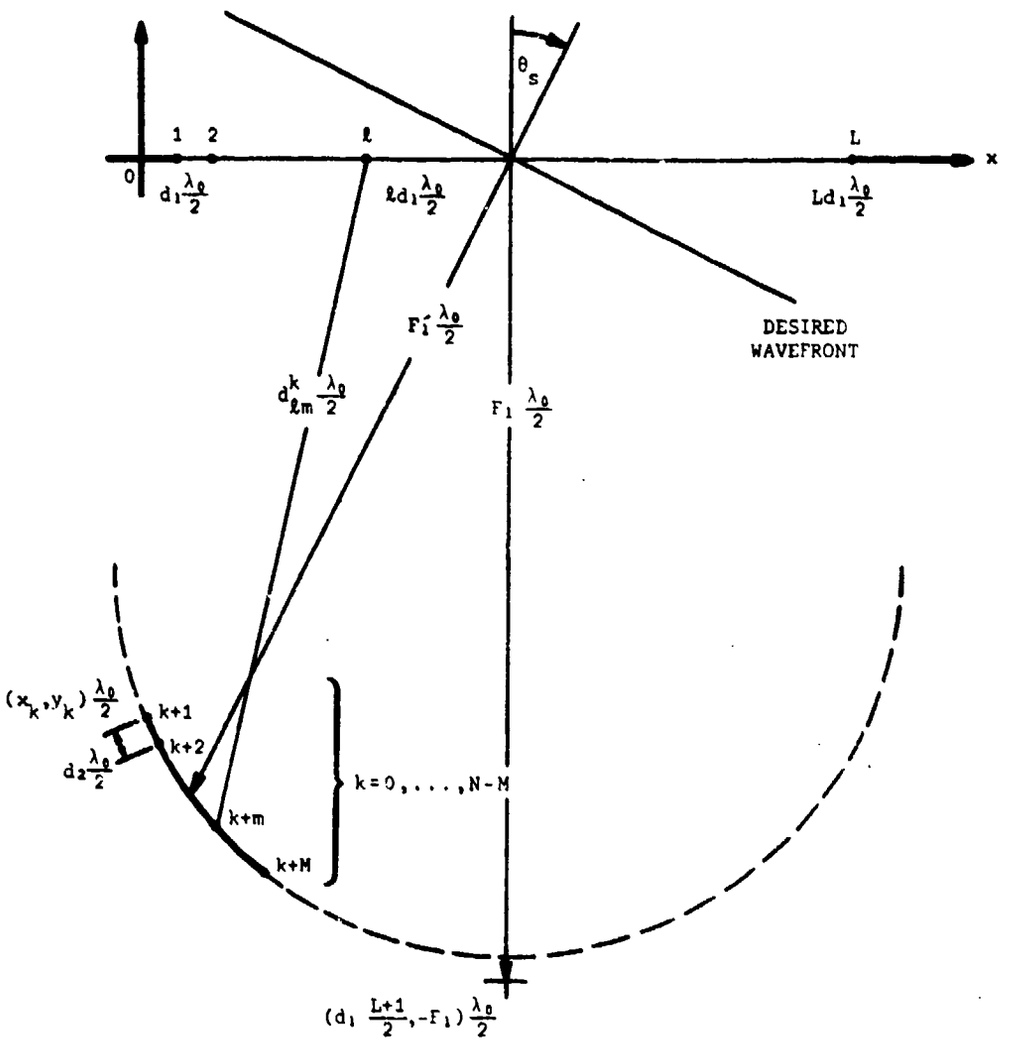

Figure 9. Geometry of Alternate Space-Fed Antenna

and

$$h(k+m,\ell,f) = c^k_{\ell m} e^{-j2\pi f\tau^k_{\ell m}} \qquad (24)$$

Here,

$\tau_{\ell m}^{k}$ = the time delay between the (k+m)-th excitation element and the ℓ-th radiation element

$$= \frac{1}{2f_0} d_{\ell m}^{k} \tag{25}$$

and

$$c_{\ell m}^{k} = \alpha_{\ell m}^{k} \varepsilon_{\ell m} e^{j2\pi f T_{\ell}} \tag{26}$$

where

$\alpha_{\ell m}^{k}$ = the relative r^{-1} attenuation between the ℓ-th and (m+k)-th elements of the radiation and excitation array, respectively

$$= \sqrt{\frac{F_1}{d_{\ell m}^{k}}} \tag{27}$$

T_{ℓ} = the time delay compensation (time advance) at the ℓ-th radiation array element with respect to the focal point and relative to the central point on the array

$$= \frac{1}{2f_0} \left(\sqrt{\left(\frac{L+1}{2} - \ell\right)^2 d_1^2 + F_1^2} - F_1 \right) \tag{28}$$

and $\varepsilon_{\ell m}$ is the ℓ-th element radiation pattern as given by (12).

2.2.2 Minimum Mean Square Synthesis

Given a desired illumination over the radiation array,

$$\underline{e} = \{e_\ell\}_{\ell=1}^{L} = \{a_\ell^s \, e^{-j\frac{\pi d_1 \ell}{f_0}\sin\theta_s}\}_{\ell=1}^{L} \tag{29}$$

the desired MMS weight vector solution is given by

$$\hat{\underline{w}}^s = C_k^+ \underline{b}^k \tag{30}$$

where, as in Part I, C_k^+ is the psendoinverse of the M x M matrix $C_k = H_k^{*T} H_k$, $\underline{b}^k = H_k^{*T} \underline{e}^k$, and $H_k = \{\{h(k+m,\ell,f)\}_{\ell=1}^{L}\}_{m=1}^{M}$. It should be noted that θ_s determines k and that this value of k applies for other values of scan angle in the neighborhood of θ_s, although $\hat{\underline{w}}^s$ will be distinct in each case.

2.3 Performance Analysis

Results for the alternate spacefed antenna design are presented here in the same form as in Part I, and include Figures 10, 11, and 12, in which a Taylor illumination was approximated for scan angles of 0°, 20°, and 40°, respectively. The maximum sidelobe performance for these three cases was excellent: -50 dB, -49.3 dB, and -42.6 dB, respectively. These results were obtained using an

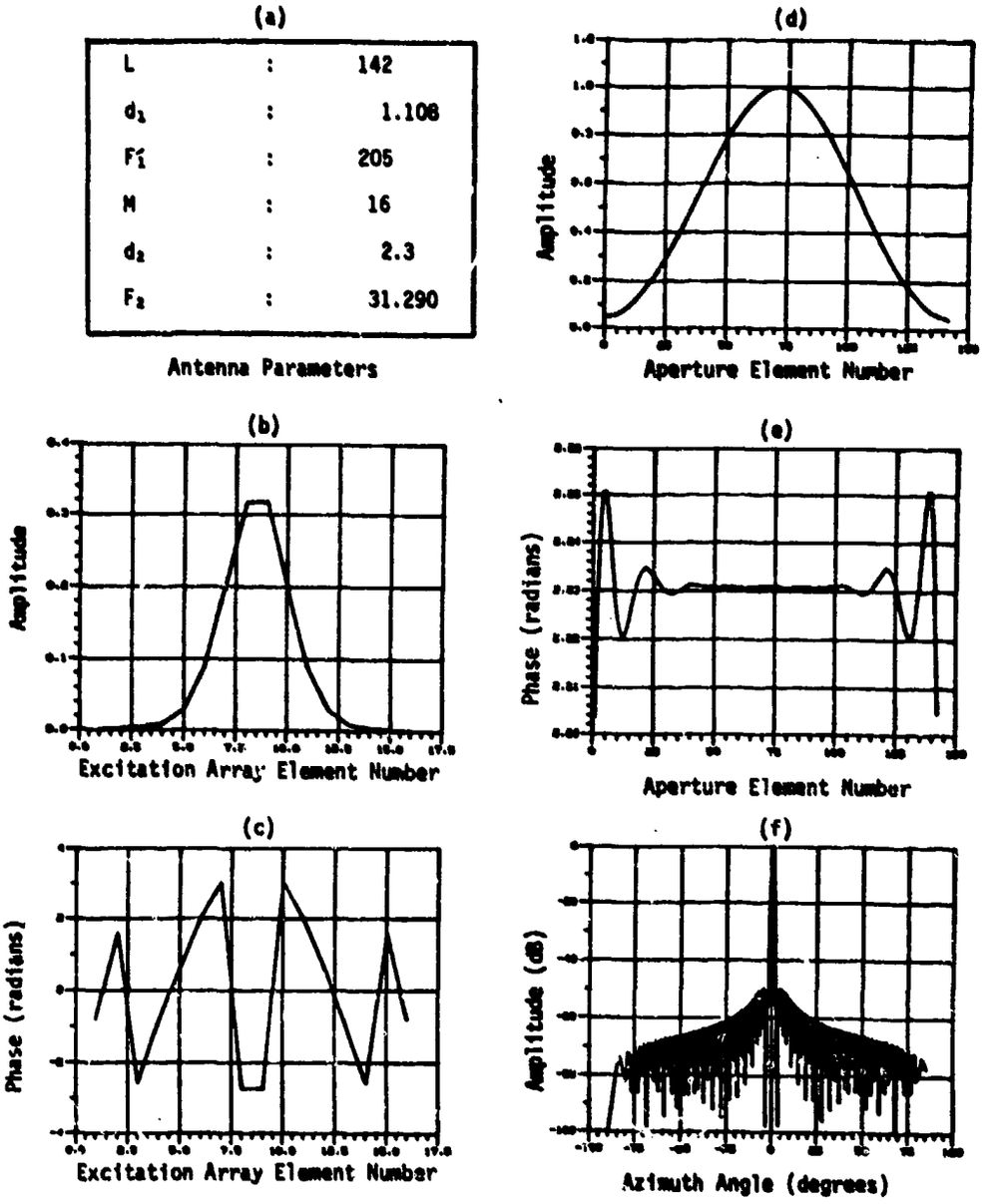

Figure 10. Taylor Approximation Example -- 0° Scan Angle. (a) Antenna Parameters. (b) Amplitude of Excitation Weights. (c) Phase of Excitation Weights. (d) Amplitude of Aperture Illumination. (e) Phase of Aperture Illumination. (f) Amplitude of Field Pattern.

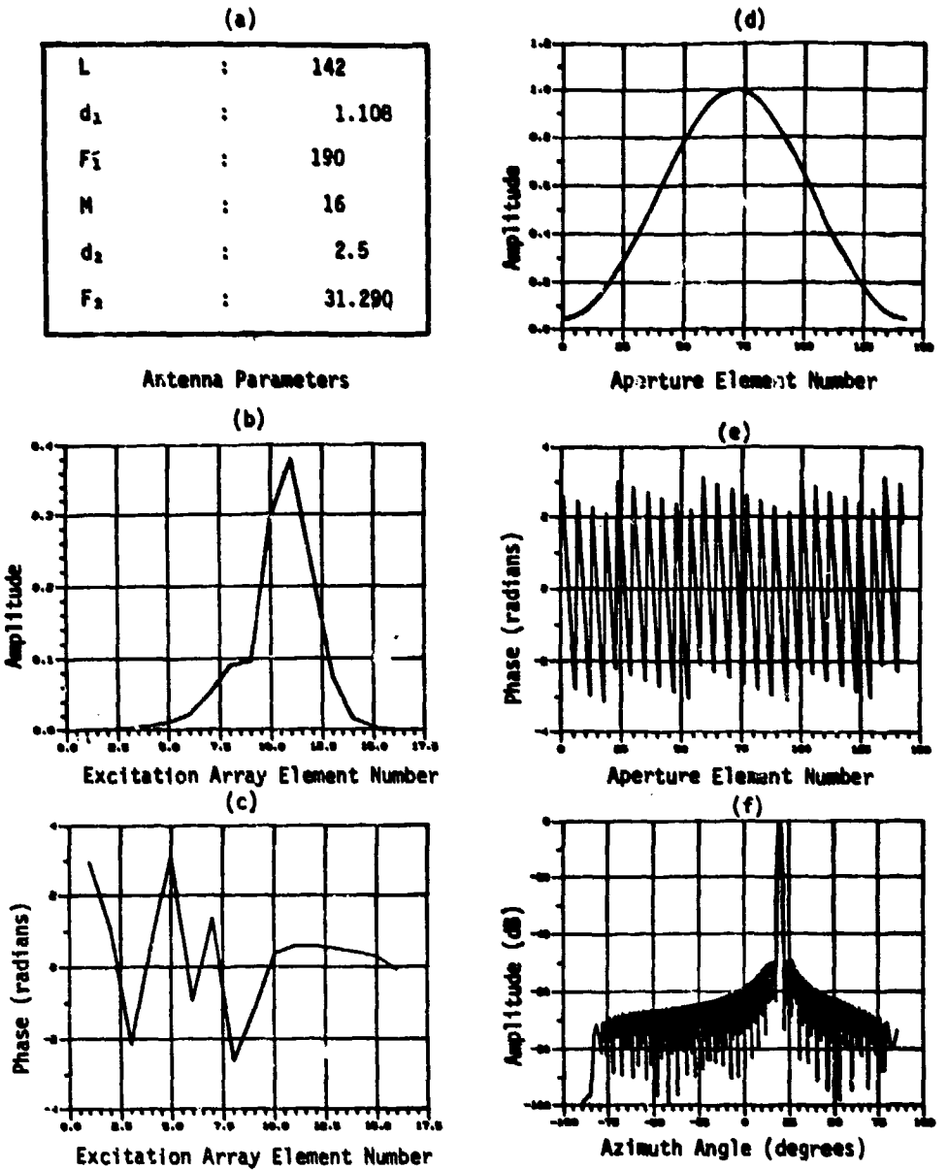

Figure 11. Taylor Approximation Example -- 20° Scan Angle. (a) Antenna Parameters. (b) Amplitude of Excitation Weights. (c) Phase of Excitation Weights. (d) Amplitude of Aperture Illumination. (e) Phase of Aperture Illumination. (f) Amplitude of Field Pattern.

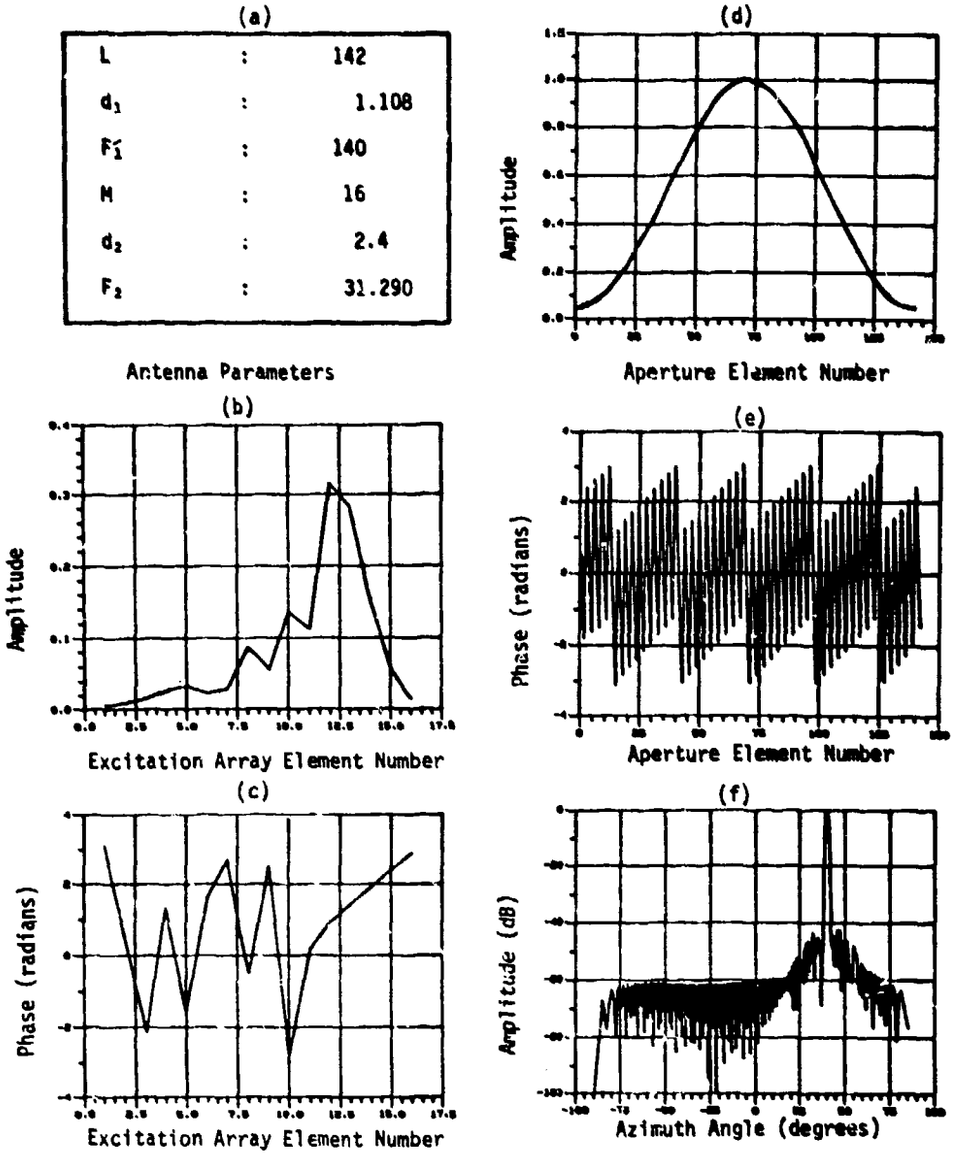

Figure 12. Taylor Approximation Example -- 40° Scan Angle. (a) Antenna Parameters. (b) Amplitude of Excitation Weights. (c) Phase of Excitation Weights. (d) Amplitude of Aperture Illumination. (e) Phase of Aperture Illumination. (f) Amplitude of Field Pattern.

omnidirectional element pattern, rather than that of (12); this change had a negligibly small effect on the final results. In all cases, the number of active excitation elements, M, was 16. The distance F_1 was chosen to be 225 $\frac{\lambda_0}{2}$ in order to get low sidelobes at a 40° scan angle. If a smaller range of scanning was required, or if the sidelobe requirement was relaxed, F_1 could assume a smaller value. For 0° scanning conditions, the front array is focused at a distance of F_1, but for non-zero scan angles it is conjectured that it may not be well-focused at F_1 or possibly even at any distance, due to asymmetrical path lengths and, therefore, asymmetrical $r^{-\frac{1}{2}}$ losses between symmetrically located elements on the front array and the intended focal point.

Once an acceptable value for F_1 of 225 $\frac{\lambda_0}{2}$ was established, an iterative procedure was initiated to simultaneously find the best values for F_1' and d_2, which resulted in having F_1' less than F_1 for all scan angles, without exception. This was interpretted as forcing a slight de-focusing of the radiation array, which would effectively cause more of the centrally located M excitation elements to become more active, instead of having some turned almost completely off, as was the case when F_1' was the same as F_1. With more activity among the M elements, more degrees of freedom are effectively available for synthesizing a useful aperture illumination. Although the field pattern showed large variations in maximum sidelobe level for large changes in these two parameters,

it was relatively insensitive to variations of roughly 10 percent of the final values selected for both F_1' and d_2. For 0°, 20°, and 40° scan angles, the final values for F_1', respectively, were $205\ \frac{\lambda_0}{2}$, $190\ \frac{\lambda_0}{2}$, and $140\ \frac{\lambda_0}{2}$, and the final values for d_2 were $2.3\ \frac{\lambda_0}{2}$, $2.5\ \frac{\lambda_0}{2}$, and $2.4\ \frac{\lambda_0}{2}$, respectively. Notice that for the larger scan angles, the deviation from a globally circular array is significant and favors using a smaller number of excitation elements than would a circular arrangement. An approximate calculation of the number of elements required in the excitation array (N in Figure 7) based on the above numbers gave a number of around 110, less than the number of elements in the front array.

A difference (Bayliss) pattern was approximated for 0°, 20°, and 40° scan angles using exactly the same final values of F_1, F_1', and d_2, and with the directional elements of (12) in place. Sidelobe levels of -47 dB, -48.4 dB, and -33 dB were achieved, respectively. The depth of the center null could not be gauged from these plots, since the 512 point FFT program used to compute the field patterns lacks the resolution necessary to determine this information. The exception is at 0° where the FFT computes a field pattern point at exactly the center of the null. This gave a number below -100 dB (the lower limit of the plotting program) which is of course meaningless in the context of a real antenna with random errors, but which nonetheless illustrates the effectiveness of the MMS solution method.

3.0 CONCLUSIONS AND RECOMMENDATIONS

Employing an underlying mathematical model based on ray-tracing, a MMS formulation has led to the successful synthesis of two distinct space-fed antenna designs, as demonstrated via computer simulation. It is important to note that this synthesis approach was instrumental in showing the effectiveness of the second of the two antenna designs involving a relatively small number of phase shifters.

The design and hence the performance of practical space-fed antennas could be improved by enhancing the underlying mathematical model, such as including coupling between array elements and incorporating more accurate element patterns. Finally, a computer-in-the-loop approach could be mechanized to carry out the MMS adjustment of the excitation weights in a feedback fashion, thus relieving the designer from the burden of searching, substantiating and incorporating improvements of the mathematical model in an attempt to represent more faithfully the practical effects in an open-loop numerical procedure.

REFERENCES

1. Kobus, J.P. (1981) Antenna Subsystem for Wideband Adaptive Ground Antenna System (WAGAS), Motorola Inter-Office Memorandum, March 13, 1981.

2. Hestenes, M.R. and Stiefel, E. (1952) Methods of Conjugate Gradients for Solving Linear Systems, J. of Research of the National Bureau of Standards 49 (No.5) : 409-436.

3. Daniel, S.M. (1971) Optimal Solution to the Two-Dimensional Scattering Problem , Ph.D. Thesis, Electrical Engineering Department, University of Illinois, Urbana-Champaign.

4. Taylor, T.T. (1955) Design of Line-Source Antennas for Narrow Beamwidth and Low Sidelobes, IRE Trans Ant. Prop. 3 : 16-28.

5. Bayliss, E.T. (1968) Design of Monopulse Antenna Difference Patterns with Low Sidelobes, Bell Sys. Tech. J. 47 : 623-650.

AD P001103

APERTURE EFFICIENCY CONSIDERATIONS IN THE CONVOLUTION SYNTHESIS OF SYMMETRICAL HEXAGONAL ARRAYS

J. Paul Shelton and Sharad R. Laxpati*
Naval Research Laboratory
Washington, D.C. 20375

ABSTRACT

The investigation of the application of null synthesis procedures to planar arrays, described in previous papers by these authors, is continued. The null synthesis of symmetrical hexagonal arrays is evaluated in terms of the maximum achievable aperture illumination efficiency (AIE). Computed values of maximum AIE are presented for hexagonal arrays of 7, 19, 37, 61, and 91 elements using seven-element, one-parameter canonical arrays (referred to as $H_{(7)}$). A 19-element, three-parameter canonical array is introduced ($H_{(19)}$), and maximum AIE is given for arrays of 19, 37, 61, and 91 elements. Contour plots of radiation patterns, showing zero loci and sidelobe levels are presented for both uniformly illuminated and synthesized maximum AIE arrays. Zero loci, sidelobe levels, and aperture illumination distributions are compared for these arrays.

1. INTRODUCTION

Synthesis of regular hexagonal arrays has been described by several authors during the past decade. Recently, the authors of this paper have investigated hexagonal array synthesis in which small arrays are convolved to synthesize large arrays. Such a technique is well suited to snythesize a set of prescribed nulls of a large array. This paper is a report on the status of the on-going work by the authors.

---

*Also with the Department of Information Engineering, University of Illinois Chicago at Illinois 60680

Aside from the use of separable illumination for a planar array, which thereby utilizes well known syntehsis procedures for linear arrays, a synthesis technique that has been studied extensively is based on a transformation technique that maps a linear array into a planar array. The technique was presented by Baklanov[1] and by Tseng and Cheng[2] for square arrays and was later adapted for rectangular arrays by Goto[3,4]. Since the transformation maps a two dimensional (θ, ϕ) pattern of a planar array into a one dimensional (θ) pattern of a linear array, the resultant pattern has ring sidelobes (whose heights are independent of ϕ) with non-circular contours. Furthermore, the technique fundamentally synthesizes a linear array; thus, it enables one to use any of the optimal or non-optimal synthesis techniques for linear arrays. Elliott[5] extended the technique to synthesize arbitrary sidelobe topography. Goto,[3,6] has discussed the application of this transformation technique to hexagonal arrays, whereas Goto[7] and Cheng and Chen[8] have treated optimal syntheses of regular hexagonal arrays. In order to synthesize a k-ring hexagonal array, synthesis of a (2k+1) element linear array is needed. Thus, in the synthesis procedure there are at most k degrees of freedom; i.e. up to k different parameters may be specified to control the hexagonal array pattern.

Although the transformation synthesis procedure is straightforward, it is rather cumbersome; the voltage excitations of the planar array are obtained from those of the corresponding linear array after extensive numerical computation which is reminiscent of the computation of coefficients in Chebyshev synthesis. Furthermore, it is difficult to provide any intuitive understanding of the null loci as well as illumination (voltage) tapers. The examples discussed by the researchers would indicate no simple relationship to the voltage tapers of the corresponding linear array. This is contrary to what one would have expected from the

technique. To be specific, if a Taylor type illumination and sidelobe structure is used as a linear array design, then although the sidelobes of the hexagonal array will have similar structure in all azimuth planes, the aperture illumination will not exhibit the behavior of the corresponding linear array illumination. The synthesis procedure yields a twelve-fold symmetry in the aperture plane; a feature that is analogous to the rotational symmetry of one-dimensional circular Taylor illumination. Thus, the synthesis of a hexagonal array may be thought of as an extension of the one-dimensional circular aperture synthesis to two dimensions.

The synthesis procedure for hexagonal arrays described by Kinarsson[9] retains the symmetry feature and potentially increases the degrees of freedom to the maximum possible commensurate with the symmetry requirements. The procedure is numerical and is capable of providing optimal patterns (i.e. optimizes aperture illumination efficiency (AIE) for a fixed sidelobe level). The problem is formulated as a quadratic programming problem and requires a number of iterations and a large computer to obtain the solution.

Shelton[10] studied regular hexagonal arrays in depth and considered a synthesis procedure in which small hexagonal arrays are convolved to snythesize large hexagonal arrays but confined to one degree of freedom which leads to hexagonal arrays with binomial voltage excitations and twelve-fold symmetry. Laxpati[11,12] introduced a null synthesis technique for planar arrays, which is based on the convolution process and is a generalization to the previous synthesis procedure. This procedure, which utilized a canonical four-element diamond array, can be utilized to synthesize prescribed arbitrary nulls and/or sidelobe topography. For a k-ring hexagonal array, the procedure has at most 1.5K degrees of freedom.

An important characteristic of this null synthesis procedure is that it is non-iterative and can be readily implemented on a small computer. It also provides a larger number of degrees of freedom than the transformation synthesis procedure. In an attempt to evaluate the potential of the null synthesis procedure, the present authors presented a study[13,14] which introduces the canonical arrays and discusses their role in the synthesis of various planar arrays including regular hexagonal arrays. The results indicated that AIE is dependent on the canonical arrays employed to synthesize the large array; it is also dependent on the number of degrees of freedom. Since AIE is the ratio of the directivity of the designed antenna excitation to the directivity of uniform excitation, it would be an important criterion in the selection of canonical arrays, if not constrained by the symmetry requirements.

The primary objective of this paper is to consider the null synthesis procedure for hexagonal arrays with twelve-fold symmetry (thus employing smaller hexagonal arrays as canonical arrays) and optimize the AIE. Syntheses of hexagonal arrays with 2, 3, 4 and 5 rings are considered. In the next section, after reviewing the convolution (null) synthesis technique, symmetry and other characteristics of hexagonal array are introduced. More detailed objectives are also put forth. Section 3 analyses the 1- and 2-ring (seven or 19 element) hexagonal arrays which are used as canonical arrays in the synthesized examples presented in Section 4. Also discussed in Section 4 is the simple technique used to achieve the near optimum value of AIE as well as the impact on it of using H_7 (seven element, 1-ring hexagonal array) and H_{19} (19 element, 2-ring hexagonal array) as building blocks. Section 5 shows the plots of patterns of the synthesized arrays and compares them with those of uniform arrays. Finally, in Section 6, some concluding remarks are offered.

2. Objectives of Convolution Synthesis

2.1 Background

This investigation of a convolution synthesis procedure for planar arrays was initiated because there were no zero-locus synthesis procedures analogous to those which are commonly used for linear arrays. In contrast with the polynomial representation of linear arrays which allows the pattern function to be expressed in terms of its roots, there is no mathematical formalism which allows the pattern function of a planar array to be expressed in terms of its zero loci. This situation is not surprising because, whereas a linear array has a finite set of zeros which can be related to the coefficients of the polynomial describing the pattern function, the symmetrical planar arrays being considered here have continuous zero loci with an infinite number of locations, and their pattern functions are not expressible as polynomials. On the other hand, the concept of array convolution and pattern multiplication still holds.

This concept of array convolution and pattern multiplication has been proposed by these authors in previous papers. It is in effect what such procedures as Taylor's do, without relating the zero locations to the pattern function expressions. For example, an alternative approach to the Taylor synthesis would relate the pattern zeros to small two- or three-element arrays and then convolve them to determine the overall array excitation directly without being concerned about the polynomial expression.

The objective of this convolution synthesis is to select appropriate small arrays, which we will refer to as canonical, determine their zero loci from a number of small arrays to give a desired multiplied pattern from a large array, and finally convolve the small arrays to determine the array distribution of the large array.

This procedure is not without drawbacks. Whereas the linear-array zero locus procedures such as Taylor's tend to produce array excitations with good aperture efficiency, this is not necessarily the case with planar arrays. One of the primary objectives of the analysis of this technique is to evaluate the aperture efficiency with which patterns of given sidelobe levels can be synthesized. Furthermore, there is not a readily available procedure for relating the zero loci to a given specified sidelobe level, as is the case for Taylor's and Dolph's techniques.

Therefore, the present status of this investigation is to seek answers to the questions of exactly how well will the convolution procedure work and what is a specific technique for selecting the required zero loci.

2.2 Specific Objectives of this Paper

One specific objective of this paper is to analyze and present the pattern characteristics of uniform symmetrical hexagonal arrays as large as 91 elements. A disadvantage of dealing with planar arrays with nonseparable pattern functions is that the characteristics of those patterns are not generally familiar to workers in the field. Essentially anyone reading this paper will know what a sin Nx/sin x pattern function looks like and that it is the pattern of a uniform N-element linear array. How many of us know how to describe even qualitatively the characteristics of a uniform hexagonal array? Locations and levels of sidelobes will be presented, and zero loci will be plotted.

Characteristics of two canonical arrays will be considered. The seven-element array with one degree of freedom has been analyzed previously. The 19-element array with three degrees of freedom is analyzed, and procedures for determining the array coefficients in terms of specified zero locations or vice versa will be discussed.

Using these canonical arrays, arrays as large as 91 elements will be synthesized for maximum aperture efficiency (AIE), and the radiation patterns, aperture distributions, and zero loci of these arrays will be presented and compared with those of the uniform arrays.

3. Analysis of Canonical Arrays

The zero-locus characteristics of two canonical arrays are analyzed in this section. The first is the one parameter seven-element array (h_7) and the second is the three-parameter 19-element array (H_{19}).

The coordinate system used for representing radiation pattern functions is shown in Figure 1. The pattern function coordinate

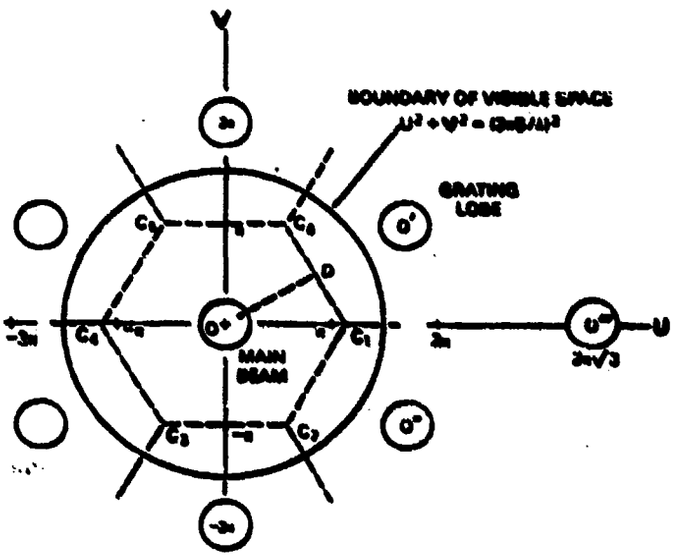

Fig. 1 - Pattern-function representation in the uv plane

corresponding to the x coordinate of the array is u, and the coordinate corresponding to the y coordinate of the array is v. A grating-lobe pattern is also shown, which results from a "stable" triangular array lattice, that is, a lattice for which the triangles have one horizontal side. The coordinate system is defined so that the angular distance from the mainlobe to the nearest grating lobe is 2π.

The grating-lobe pattern of Fig. 1 has the spatial periodicity of the reciprocal lattice of the antenna-array lattice. The coordinates of the grating lobes are

$$u(m) = m\pi\sqrt{3}$$

and

$$v(m,n) = 2\pi(n - \frac{m}{2}).$$

The general pattern function for arbitrary excitation has the periodicity of the grating lobes in the u-v plane, and the cell defined by the hexagon $C_1C_2C_3C_4C_5C_6$ completely describes the function. Furthermore, with the symmetry constraints which we have placed on the array, 1/12 of the cell, defined by the triangle OC_1D, is sufficient to completely describe the pattern functions with which we are concerned. Also shown in Fig. 1 is a circle defined by $u^2 + v^2 = (2\pi s/\lambda)^2$, which represents the boundary of visible space. The radius of this circle is directly proportional to s. The synthesis procedures considered here address the hexagonal cell without regard to any limitations imposed by s. That is, pattern functions are synthesized over the entire cell even though part of the cell could be excluded from visible space by appropriate selection of s.

We first consider the pattern characteristics of seven-element arrays for which the center element has unit excitation and the

outer elements are excited with amplitude a. The pattern function is given by

$$E(u,v,a)=1+a\left(4\cos\frac{u}{\sqrt{3}}\cos v + 2\cos\frac{2u}{\sqrt{3}}\right),$$

and for values of a less than 1 the main lobe broadens and the locus of zeros moves away from the main lobe. The zeros for the x-axis cut are given by

$$\cos\frac{u}{\sqrt{3}} = \frac{1}{2}\left(-1 \pm\sqrt{3 - \frac{1}{a}}\right), \qquad (1)$$

and the zeros for the y-axis cut are given by

$$\cos v = -\frac{1+2a}{4a}. \qquad (2)$$

Equations (1) and (2) can be examined to establish some limits on the ranges of a which we will investigate. Zeros for real values of v are found on the y-axis cuts for $a \geq 1/2$ and $a \leq -1/6$. Zeros are found on the u-axis for $a \geq 1/3$ and $a \leq -1/6$. For $-1/6 < a < 1/3$ the pattern function has no zeros for real u or v. These restrictions on u and v are simply due to the pattern function and are unrelated to restrictions on u and v which result from the boundary of the visible region.

Figure 2 illustrates how the locus of zeros moves with variation in the parameter a. The locus approaches 0 as $a \to -1/6$ from below, and it approaches C_1 as $a \to 1/3$ from above. It can be shown that for a near $-1/6$ ($a = -(1/6) - \varepsilon$)

$$u \approx v \approx 3\sqrt{2\varepsilon} \quad \text{(in radians)} \qquad (3)$$

and that for a near 1/3 ($a = 1/3 + \delta$)

$$\Delta u \approx \pm 3\sqrt{6\delta}, \qquad (4)$$

where $u = 2\pi\sqrt{3} + \Delta u$. Equations (3) and (4) indicate that the locus of zeros becomes circular in the neighborhoods of O and C_1

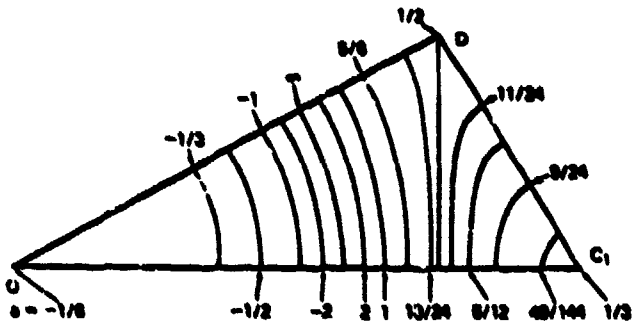

Fig. 2 - Locus of zeros for various values of a

Other characteristics of the pattern function which are of interest and easily determined are the pattern values at C_1 and D. The pattern values at O, C_1, and D are

$$E_O = 1 + 6a,$$

$$E_{C_1} = 1 - 3a,$$

and

$$E_D = 1 - 2a.$$

We next consider the pattern characteristics of nineteen-element arrays for which the center element has unit excitation and the outer elements are excited with amplitudes a, b, and c, as indicated in Figure 3. The pattern function is given by

$$E(u,v,a,b,c) = 1 + 2a\cos\frac{2u}{\sqrt{3}} + 2b\cos\frac{4u}{\sqrt{3}} + 4\cos v\left(a\cos\frac{u}{\sqrt{3}} + c\cos\frac{3u}{\sqrt{3}}\right) + \cos 2v\left(2c + 4b\cos\frac{2u}{\sqrt{3}}\right). \quad (5)$$

Unlike the seven-element array, for which the zero locus is determined by the value of a and the entire family is easily plotted in Figure 2, the nineteen-element array has a much more complex family of loci which cannot be easily plotted. An idea of the possible loci can be obtained by considering the behavior of E(u, v, a, b, c) on the u and v axes.

On the u axis, Equation (5) yields, for v = o,

$$E(u,o,a,b,c) = 1+2c+4a\cos\frac{u}{\sqrt{3}} + (2a+4b)\cos\frac{2u}{\sqrt{3}}$$

$$+ 4a\cos\frac{3u}{\sqrt{3}} + 2b\cos\frac{4u}{\sqrt{3}} \qquad (6)$$

Equation (6) can be expanded into a quartic polynomial in $\cos u/\sqrt{3}$, implying that there can be four zeros in u for appropriate values of a, b, and c.

On the v axis, Equation (5) yields, for u = o,

$$E(o,v,a,b,c) = 1+2a+2b+4(a+c)\cos v+(4b+2c)\cos 2v \qquad (7)$$

Equation (7) can be expanded into a quadratic polynomial in cos v, implying that there can be two zeros in v for appropriate values of a, b, and c.

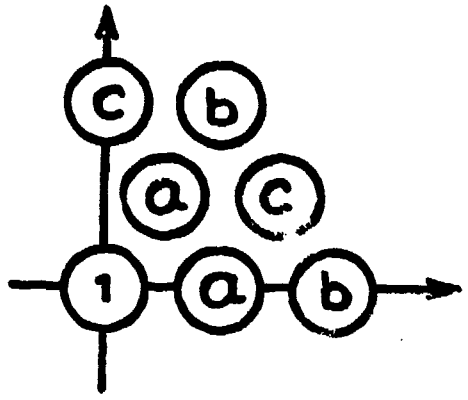

Fig. 3 - Assignment of coefficients for 19-element canonical array

Some useful relationships for symmetrical hexagonal arrays are as follows:

$$N = 3n_r^2 + 3n_r + 1,$$

where N is the number of elements in an array with n_r rings.

$$n_e = \text{Int}\,(n_r^2/4 + n_r), \tag{8}$$

where n_e is the number of independent element voltages in an array with n_r rings.

4. Computation of Maximum AIE for Convolved Arrays

It has been noted that the number of degrees of freedom available from a hexagonal array synthesized by the convolution technique being considered here is less than the number of independent voltages which can be placed on the array, so that in general a precise synthesis cannot be achieved. That is, if we were to require a radiation pattern function to be defined as precisely as possible, then it would require independent control of the maximum possible number of elements in the array. In other words, the convolution synthesis procedure cannot realize all possible array voltage distributions. This situation raises the following important questions, which must be answered before we proceed further in developing the synthesis procedure:

1. How close to any given array voltage distribution can the convolution synthesis approach?
2. Under what conditions is the synthesis procedure useful?
3. How do these answers change as the size of the array increases?

The basis for the concern for the degradation in the performance of the synthesis procedure with increasing array size is indicated by Table 1, in which the number of elements, number

of rings, and number of independent element voltages are listed for various arrays.

Table 1. Some Parameters of Symmetrical Hexagonal Arrays

Number of Rings, n_r	Number of Elements N	Number of Independent Element Voltages, n_e
1	7	1
2	19	3
3	37	5
4	61	8
5	91	11
6	127	15
7	159	19

From Equation (8) we see that the ratio of the number of rings to the number of independent elements is

$$R_r = \frac{n_r}{\text{Int}\left(\frac{n_r^2}{4} + n_r\right)}$$

$$\approx \frac{4}{n_r + 4} \qquad (9)$$

Equation (9) is approximate for odd n_r and precise for even n_r. If we use seven-element arrays (H_7) for the synthesis, the number of degrees of freedom is equal to n_r. If we use one 19-element array (H_{19}), the number of degrees of freedom becomes $n_r + 1$ and increases by one for each additional H_{19} that is used in the synthesis. Thus, if the number of H_{19} arrays used is m, the ratio of degrees of freedom to the number of independent elements is

$$R_f = \frac{4+m/n_r}{4+n_r} \qquad (10)$$

Equation (10) and Table 1 need not cause us to despair of achieving a useful synthesis for larger arrays because, for example, the usefulness of a Taylor synthesis, which has $\bar{n}$ degrees of freedom, is independent of the size of the array. Thus, we can point to a case for which the number of degrees of freedom need not be comparable to the number of independent element voltages.

We have selected the gain function as the basis for a figure of merit for the convolution synthesis procedure. The advantages of this choice are that the maximum possible gain of any array is readily identified as N (assuming unity element gain), and the maximum gain achievable from a given synthesis procedure is straightforwardly determined. A figure of merit which can be applied to arrays of all sizes is then maximum efficiency or AIE, which is the ratio of the achieved gain to N.

We have examined the characteristics of arrays ranging in size from 7 to 91 elements by applying the convolution synthesis procedure so as to maximize the AIE. Seven-(H_7) and 19-element (H_{19}) arrays were used. Initially, arrays synthesized entirely with H_7 arrays were examined. Then a synthesis procedure using one H_{19} array plus a number of H_7 arrays was tried.

Of course, the seven-element array is a trivial case for both H_7 and H_{19}, and the 19-element array is a trivial case for H_{19}.

In order to determine the maximum gain available from the procedure, a straightforward hill-climbing technique was used. This technique involves the measurement of rate of change of gain with respect to all variable parameters and the use of a steepest-ascent path to the maximum gain condition. The procedure can be carried out on a programmable calculator (with some patience) or in minutes using a desk-top computer.

As is the case in many optimization techniques, the hilltop that one may achieve may be local rather than global. To avoid this pitfall, it is desirable to make judicious choices of the initial values of the parameters. This was accomplished by first evaluating the zero loci of uniformly excited hexagonal arrays, then attempting to match the zero loci of the H_7 or H_{19} arrays with those of the uniform array that we wish to approximate. For H_7, we use Equation (1) or (2) to determine the trial value of a for a given zero locus. For H_{19} we must select three points on the zero loci and then select from Equations (5), (6) and (7) in order to form a set of three simultaneous equations in a, b, and c, the solution of which will yield the desired initial values.

The steps in the analysis are as follows: The trial values of the coefficients of the various arrays being used in the convolution process are selected. The arrays are convolved to determine the element voltages for the large array. This convolution can be done either numerically after the coefficient values are selected or algebraically prior to selection of numerical values. From a computational standpoint, the use of algebraic expressions is more efficient. Once the element voltages have been determined, the gain and efficiency are easily calculated from $G = (\Sigma E)^2/\Sigma E^2$. Each coefficient is then incremented and the corresponding increment in gain determined, so that a steepest ascent path to the maximum can be followed.

Table 2 lists the resulting H_7 and H_{19} coefficients for the synthesis procedures that were attempted, together with the element voltages and values of AIE. The values of AIE are plotted vs N in Figure 4. Case B for the 61-element array is not included in Figure 4 because it represents a local rather than a global maximum. The near-circular zero locus close to the main beam was synthesized with one of the H_7 arrays, indicated by $a_2 = -.2142$ in Table 2. It was found that the global maximum

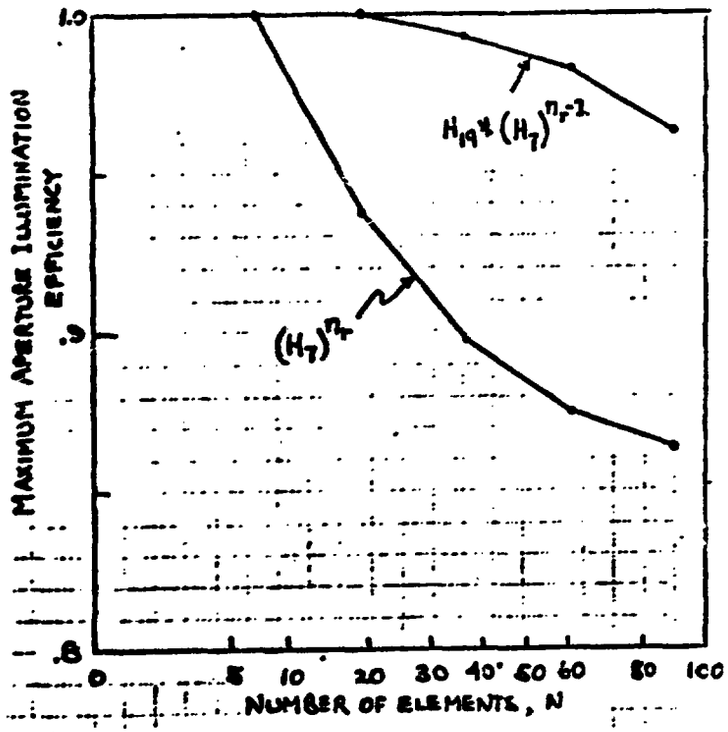

Figure 4. Maximum AIE vs. N

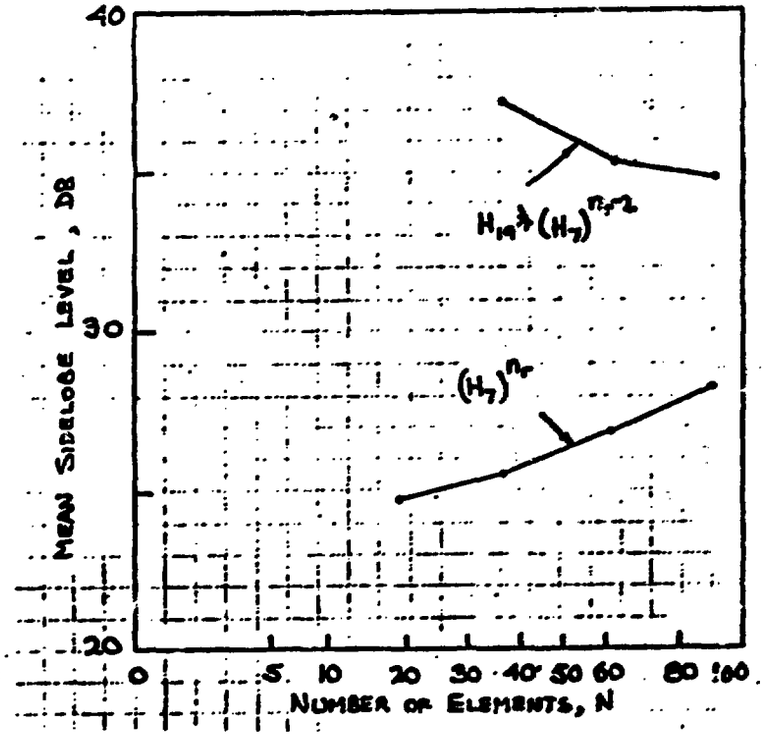

Figure 5. Mean level of random sidelobes vs. N

Table 2. Parameters of Optimized Synthesized Arrays for N=19 through 91

Number of Elements		19	37	37	61	61	61	91	91
Synthesis Procedure		$(H_7)^2$	$(H_7)^3$	$H_{19}*H_7$	$(H_7)^4$	$H_{19}*(H_7)^2$ Case A	$H_{19}*(H_7)^2$ Case B	$(H_7)^5$	$H_{19}*(H_7)^3$
Coefficients	H_{19} a			-.2242		-.2304	.3392		-.2108
	b			.5356		.3457	.1626		.2775
	c			-.0885		-.1945	.2845		-.2013
	H_7 d	-.5750	-.2625	.5747	-.2181	.5701	-.2142	-.1991	-.9159
	e	.4100	.4395		-.5340	3.7858	.5382	-.3322	1.0647
	f		-6.845		1.0546			-1.7203	.4904
	g				.4016			.6541	
	h							.3786	
Array Element Voltages	0	-.4145	2.453	.2269	.3198	.9039	-.2427	-.3702	-.2400
	1	-.4008	2.449	.2989	.3191	.8729	-.1458	-.3499	-.3014
	2	-.2358	3.309	.3050	.2292	.8382	-.1483	-.4314	-.3134
	3	-.4715	2.018	.2694	.3646	.9845	-.1843	-.3993	-.2698
	4		.7867	.3078	.4439	.8442	-.1184	-.2705	-.3070
	5		2.300	.2569	.3434	.8835	-.1075	-.3559	-.2644
	6				.04941	.6804	-.0626	-.4305	-.3682
	7				.1977	.9783	-.1356	-.4856	-.2439
	8				.2963	.9933	-.1861	-.3760	-.3351
	9							-.0282	-.1327
	10							-.1489	-.3019
	11							-.2819	-.2621
AIE		.9367	.8973	.9931	.8748	.9821	.9341	.8639	.9633

occurs when the inner two ring zero loci are synthesized with the H_{19} array. The marked improvement that is obtained by using one H_{19} array in place of two of the H_7 arrays is readily apparent from Figure 4.

We are encouraged to speculate that maximum AIE may be asymptotic with some value, perhaps in the range of .8 to .85, for increasing N for the $(H_7)^{n_r}$ procedure. The maximum AIE available from $H_{19}*(H_7)^{n_r-1}$ will always exceed that obtained with $(H_7)^{n_r}$, but it is impossible to estimate from Figure 4 whether there is a separate asymptote for this case.

A qualitative idea of the relevance of these AIE optimizations can be obtained by considering the effect of reduced aperture efficiency on the radiation pattern. If the gain

reduction is due to random fluctuations in the aperture distribution, then the power contained in those fluctuations will be distributed randomly into sidelobes. Phase fluctuations would have the same effect, but we have no phase errors. These random sidelobes will limit our ability to synthesize low-sidelobe radiation patterns.

Using this argument, the mean level of the random sidelobes can be estimated, and the results are plotted in Figure 5.

On the other hand, it is noted that the convolution synthesis procedure can be used to achieve arbitrarily low sidelobes. For example, Shelton showed that a synthesis process of the form $(H_7)^{n_r}$, with all array coefficients equal to 1/3, compresses all zero loci to the corners of the hexagonal pattern cell and results in an aperture distribution analogous to the linear array with binomial voltages. It will be demonstrated in the next section that, in general, $(H_7)^{n_r}$ produces ring sidelobes of arbitrarily controllable height.

5. Plots of Patterns

The arrays synthesized and presented in the previous section exhibit a twelve-fold symmetry in both aperture and pattern planes. Thus, it suffices to show the patterns in 1/12 of the hexagonal pattern cell (shown in figure 1). The symmetry in the pattern plane is demonstrated here, in figure 6, for the case of a uniform H_{19} array. The normalized field pattern contours are plotted in the first quadrant of the normalized u-v space. Also shown in this figure are the section of the pattern cell and the twelve-fold symmetric triangular cell. The position of the main beam ($u = v = 0$) is indicated on the plot by ◇. It is clear from figure 1 that it is sufficient to plot the patterns in the triangular cell adjoining the coordinate axis; this will be the use in the plots that follow.

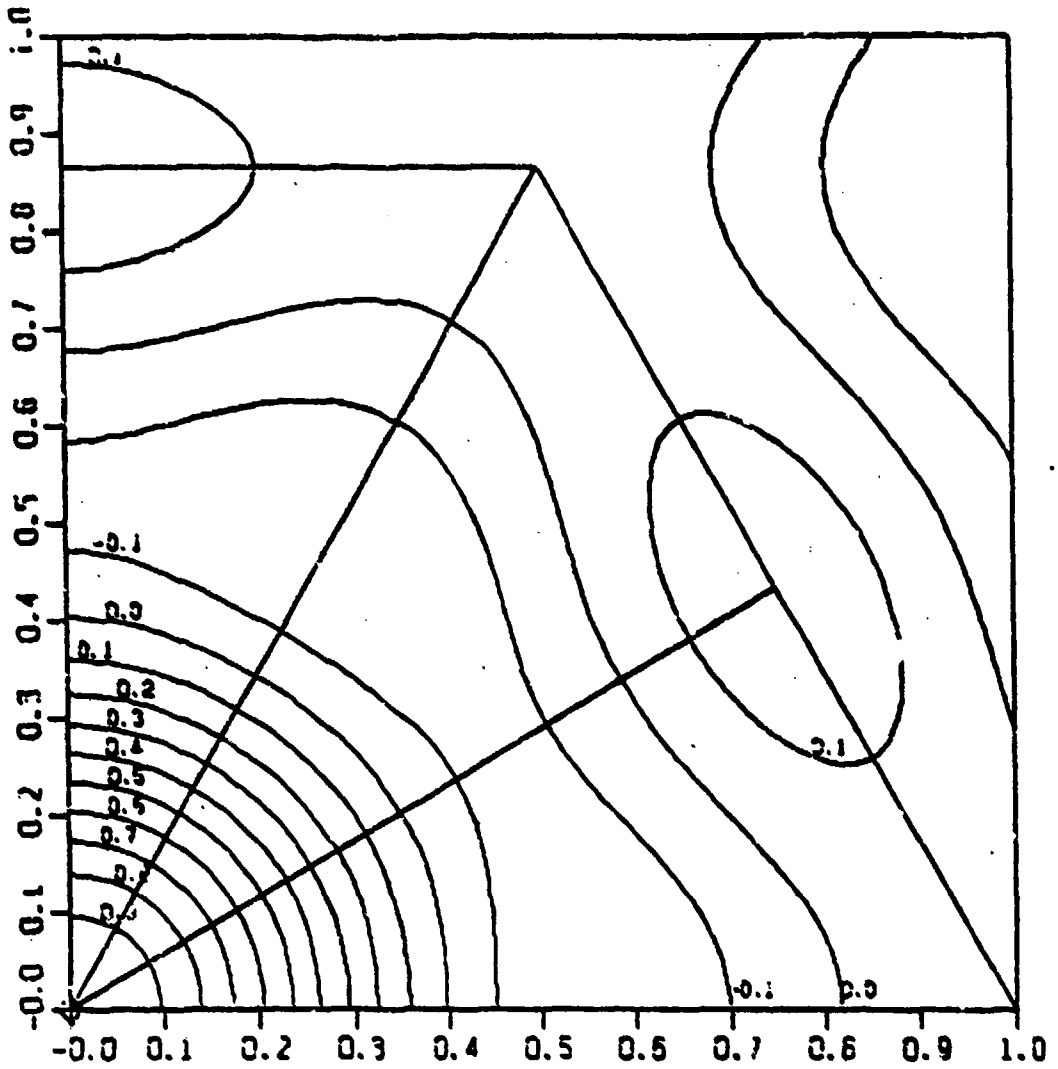

Fig. 6 - Field pattern of a uniform H_{19} array showing the symmetries and the pattern cell

For a synthesized array, there are two basic aspects that must be studied to evaluate the synthesis. One of these is the element voltages and voltage (illumination) taper; the other is the pattern structure/topography. The synthesis technique studied in this paper is based on the location of pattern nulls; hence, it would be instructive to look closely at the null loci,

and compare them with those of the corresponding uniform arrays. These characteristics of the synthesis are discussed in the following.

The element voltages for each of the large array (discussed in the previous section) are obtained by direct convolution of the element voltages of the corresponding H_7 and/or H_{19} subarrays. Due to symmetry, it is sufficient to calculate the element voltages for a small number of elements in the large array; this number is equal to the number of degrees of freedom for the array. From the subarray element voltages presented in Table 2, the voltages for the large arrays were computed; these are shown in Table 3, wherein the voltages are normalized with respect to the center element. One of the characteristics of these voltages is that it is the lowest for the outermost element; this is, of course, a direct consequence of the convolution method of synthesis. With the exception of the outermost element, the voltages vary over a 3 to 1 range.

An interesting question that may be raised in optimization of the AIE is how do the null loci differ from that of the corresponding uniform array which has an AIE = 1. In figure 7, the null loci of a uniform H_{19} are shown along with those of the synthesized H_{19} array. The synthesized array has larger beamwidth between nulls. The null loci of uniform H_{37}, and two synthesized H_{37} arrays are shown in figure 8. The H_{37} array synthesized from only H_7 subarrays has larger beamwidth between nulls; however, the array synthesized using H_{19} and H_7 arrays has null loci that is identical to that of the uniform array; i.e. equal beamwidth between nulls.

The null loci of H_{61} arrays are shown in figure 9: for uniform array in (a); for array convolved from four H_7 arrays in (b); for array convolved from H_{19} and two H_7 arrays, where all zeros of the H_{19} are near the main beam, in (c); and in (d)

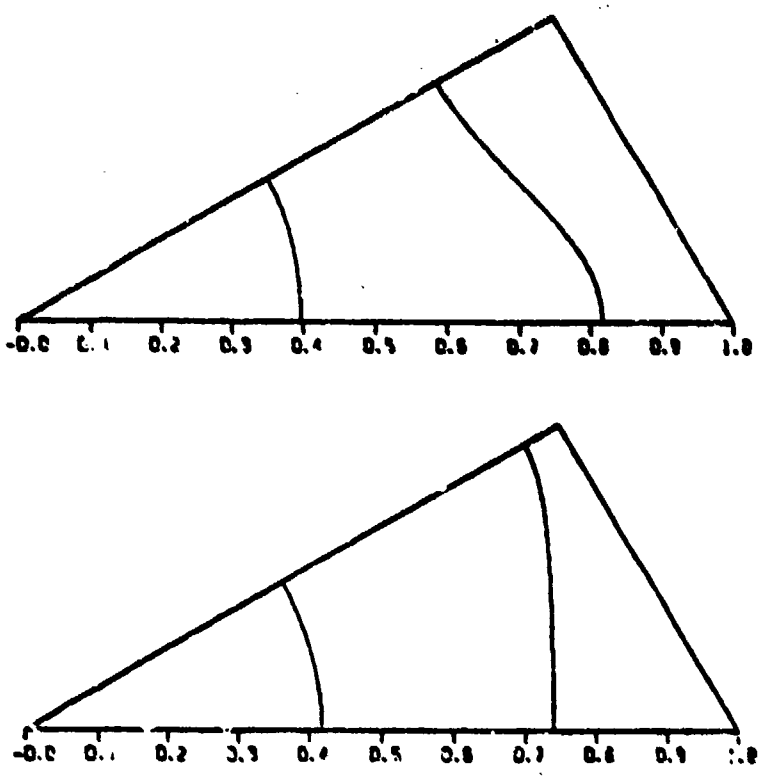

Fig. 7 - Null loci plots of H_{19} arrays: (a) uniform (b) $H_7 * H_7$

for array convolved with one H_7 subarray zero near the main beam. The beamwidth between nulls for (b) and (d) is larger than and for (c) equal to that of the uniform array in (a).

Figure 10 shows the null loci for three different H_{91}. The beamwidth between nulls for (b), the array synthesized from five H_7 elements, is larger than that of the uniform array in (a). The array synthesized with one H_{19} and three H_7 elements has first two null loci (figure 10c) identical to those of the uniform array.

For all of the synthesized arrays, the loci of nulls away from the main beam are considerably different from those of the corresponding uniform arrays.

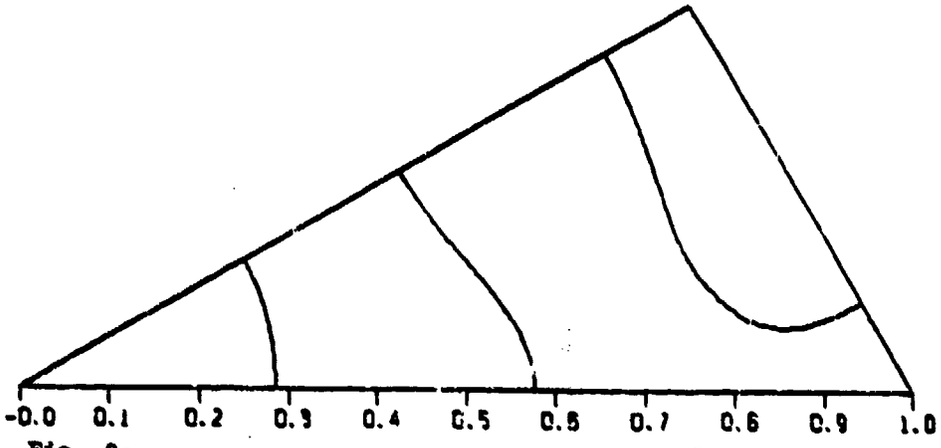

Fig. 8a

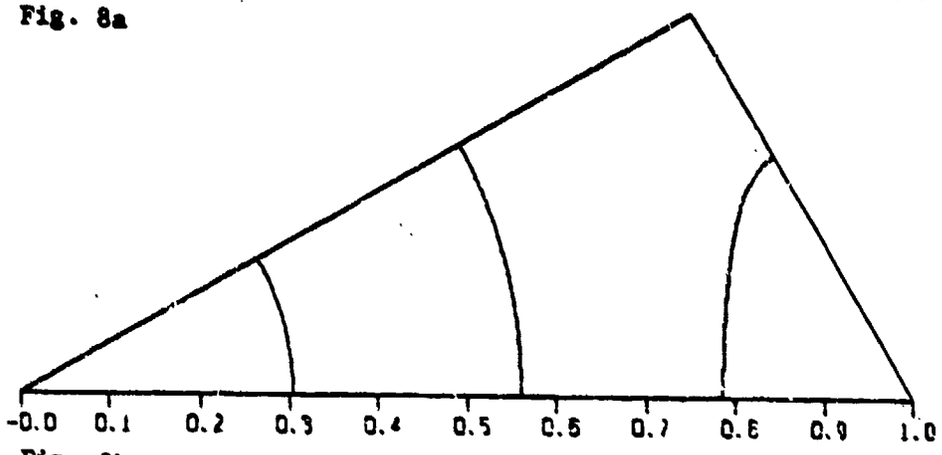

Fig. 8b

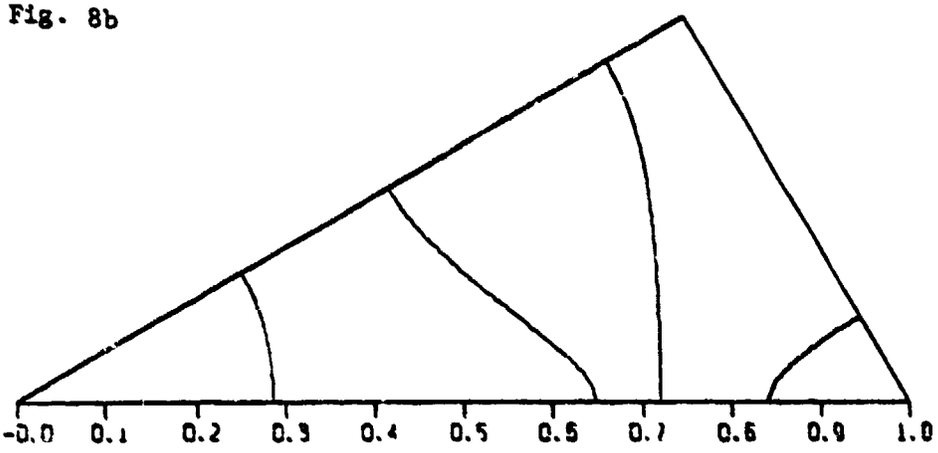

Fig. 8c

Figure 8. Null loci plots of H_{37} arrays:
(a) uniform, (b) $H_7 * H_7 * H_7$,
(c) $H_{19} * H_7$

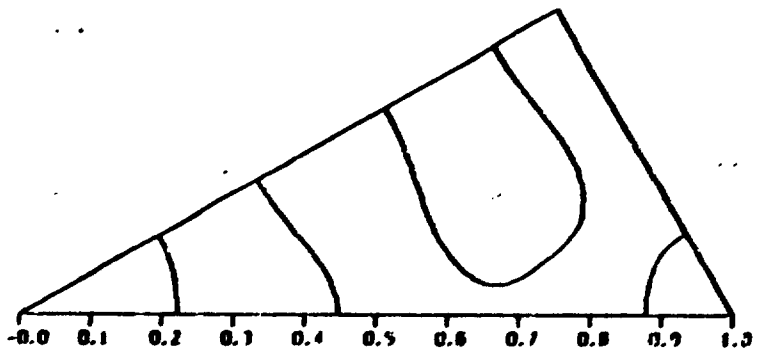

Fig. 9a

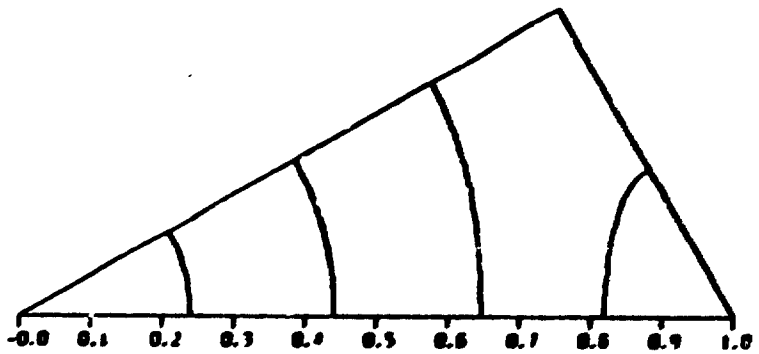

Fig. 9b

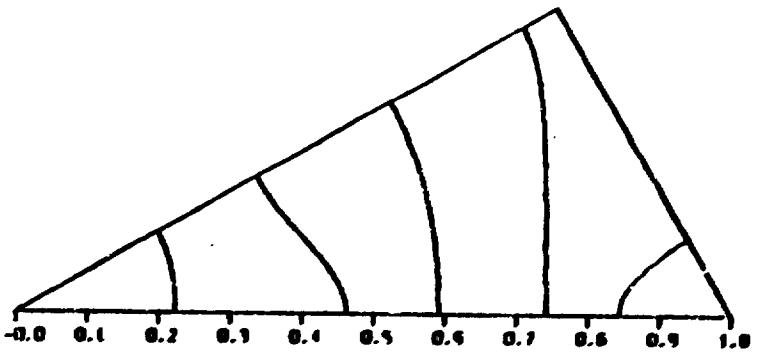

Fig. 9c

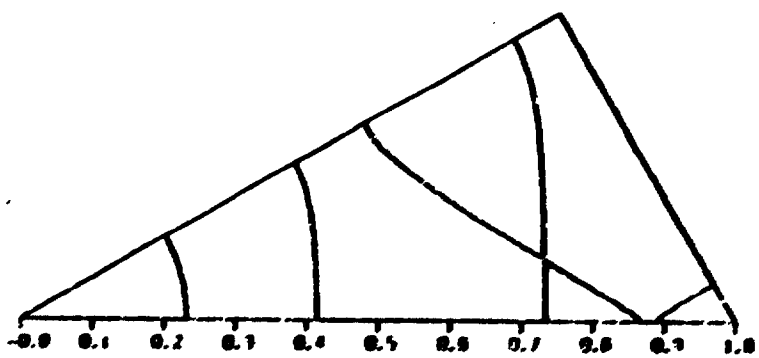

Fig. 9d

Figure 9. Null loci plots of H_{61} arrays: (a) uniform, (b) $(H_7^*)^4$, (c) $H_{19}{}^*H_7{}^*H_7$, case A., (d) $H_{19}{}^*H_7{}^*H_7$, case B.

Table 3. Element Voltages for Various Synthesized Arrays

Element No.	N_7	N_{37}	N_{19}	N_{61}	N_{61} Case A	N_{61} Case B	N_{91}	N_{91}
n	N_{19}	N_{37}	N_{37}	N_{61}	N_{61}*	N_{61}†	N_{91}	N_{91}
0	1.0	1.0	1.0	1.0	1.0	1.0	1.0	1.0
1	.967	.999	1.317	.998	.910	.598	.999	1.236
2	.569	1.349	1.344	.717	.927	.611	1.166	1.306
3	1.138	.823	1.187	1.140	1.003	.759	.917	1.124
4		.913	1.336	1.388	.956	.455	.730	1.279
5		.938	1.132	1.074	.955	.814	.962	1.118
6				.155	.753	.259	1.185	1.334
7				.678	1.082	.641	1.312	1.016
8				.927	.659	.74.	1.016	1.479
9							.076	.553
10							.381	1.258
11							.761	1.009

* All N_{19} zeros close to the main beam
† One N_7 zero close to the main beam

In order to understand the effect of AIE optimization on the overall array performance, it is also necessary to examine the pattern topography. This is best accomplished through contour plots of power patterns in u-v space. In the following, the power contours are in 3 dB steps and are plotted in the triangular cell. Once again, the u-v space is normalized and the scale

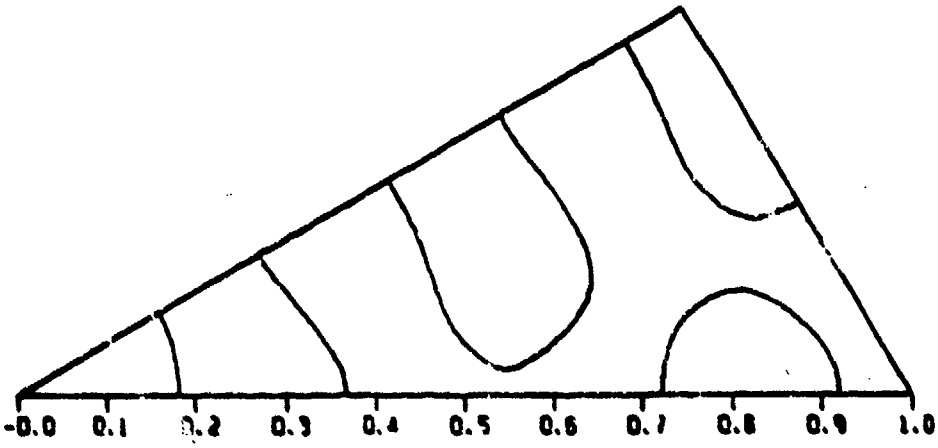

Fig. 10a

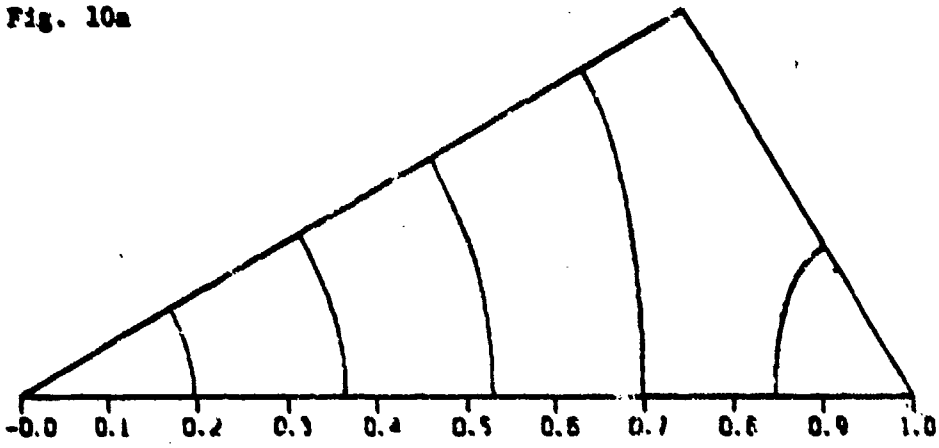

Fig. 10b

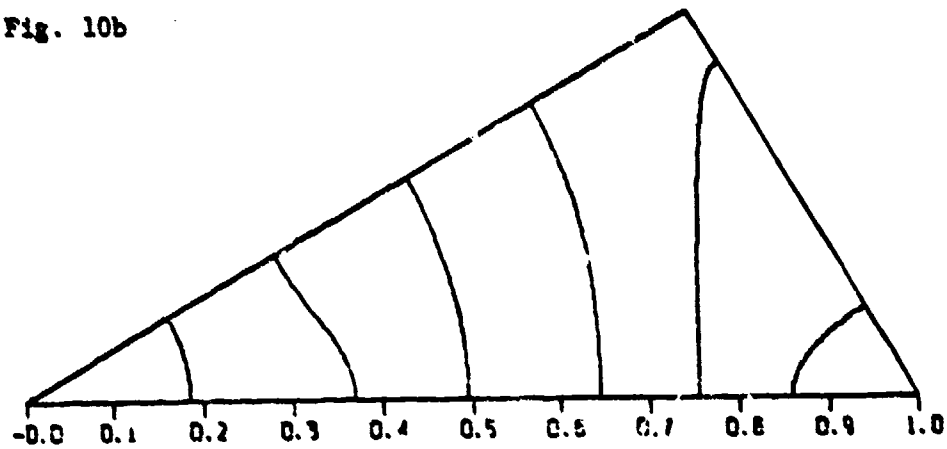

Fig. 10c

Figure 10. Null loci plots of H_{01} arrays: (a) uniform, (b) $(H_7^*)^5$, (c) $H_{19}^*(H_7^*)^4$

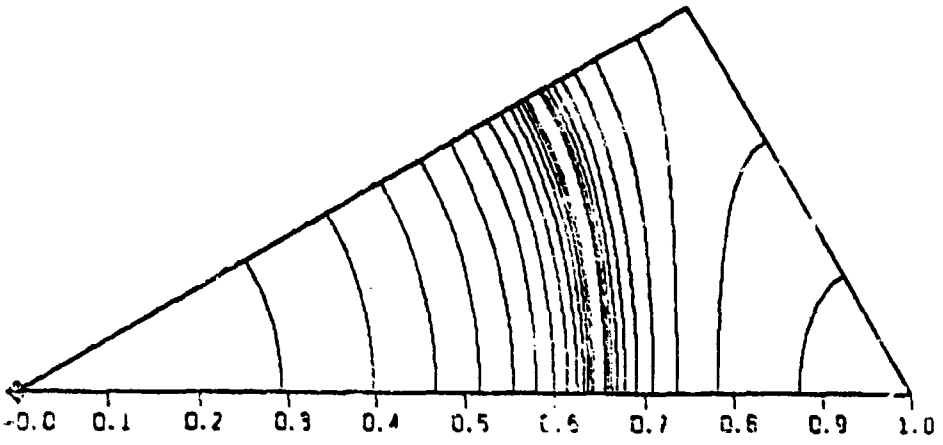

Fig. 11a

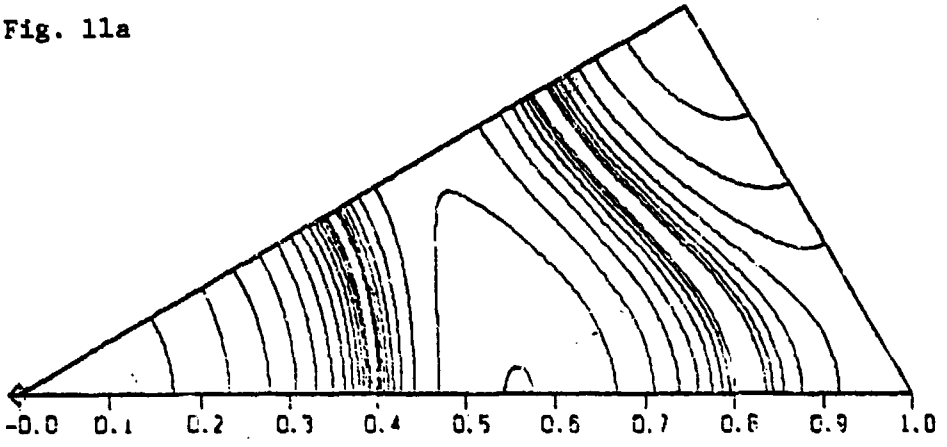

Fig. 11b

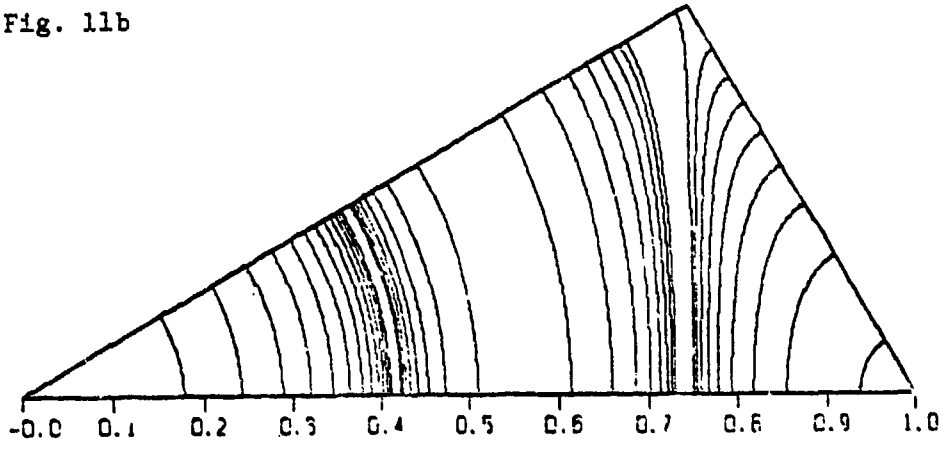

Fig. 11c

Figure 11. Power pattern for (a) uniform H_7, (b) uniform H_{19}, (c) $H_7 * H_7$.

is shown along the coordinate axis only. Furthermore, contour levels are not shown for the sake of clarity; however, the levels may be readily determined from the fact that the lowest contour level shown in all plots is -39dB.

Figure 11(b) and (c) show the patterns of a uniform H_{19} and of the H_{19} array synthesized from the convolution of two H_7 subarrays. The 3dB beamwidth of synthesized array is slightly larger. Notice the similarity of the pattern in (c) with the pattern in (a) which is for a uniform H_7 array. The ring-like structure of the pattern is quite apparent.

Patterns of H_{37} array for the cases of a uniform and the two synthesized arrays are shown in figure 12. The near-in side lobe level of the synthesized arrays is within 0.5dB (greater than) of that of the uniform array. The pattern of figure 12 has a ring-like near-in sidelobe structure and the main beam is relatively flat. This is depicted by multiple ◇ symbols near the main beam. Also, the 3dB beamwidth is larger. However, the pattern of figure 12(c) has 3dB beamwidth slightly less than that of the uniform array.

Patterns for the three designed H_{61} arrays and a uniform H_{61} array are shown in figure 13. Pattern in (b) are for the array synthesized with four H_7 subarrays and has a strong ring-like structure. The near-in sidelobe level is slightly below that of the uniform array shown in (a); however, the 3dB beamwidths are identical for two arrays. The pattern topography of figure 13(c) near the main beam and the first sidelobe peak is nearly identical to that of the uniform array. Recall that this array is synthesized using a H_{19} array with all its zeros near the main beam. Although the first and second nulls are identical (as pointed out previously), the 3dB beamwidth is marginally larger. The H_{61} array for which the pattern is shown in fig. 13(d) is synthesized using a H_7 array with its zero near the main

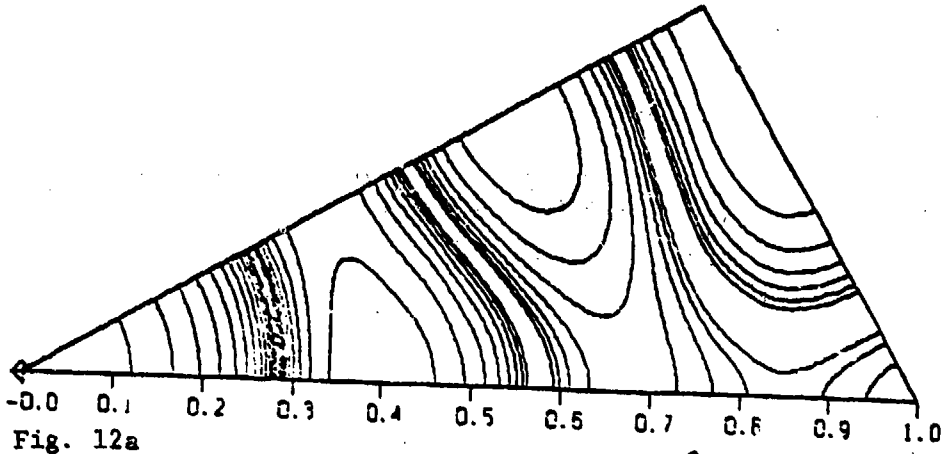

Fig. 12a

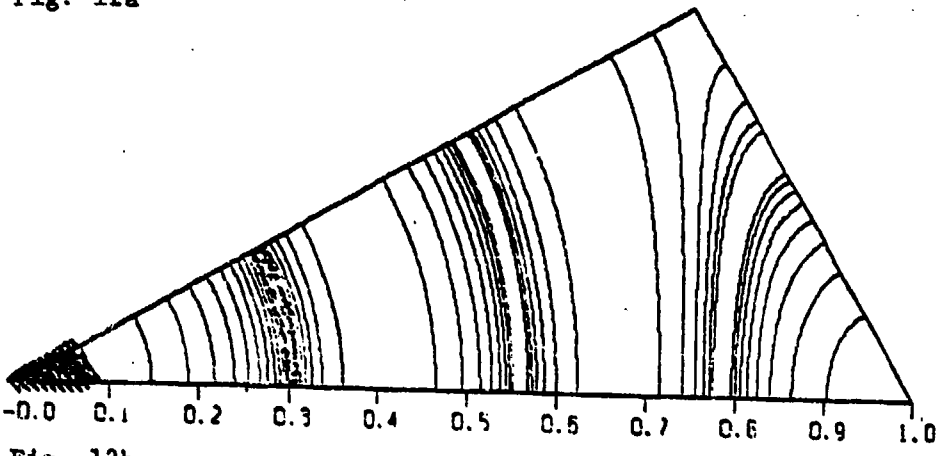

Fig. 12b

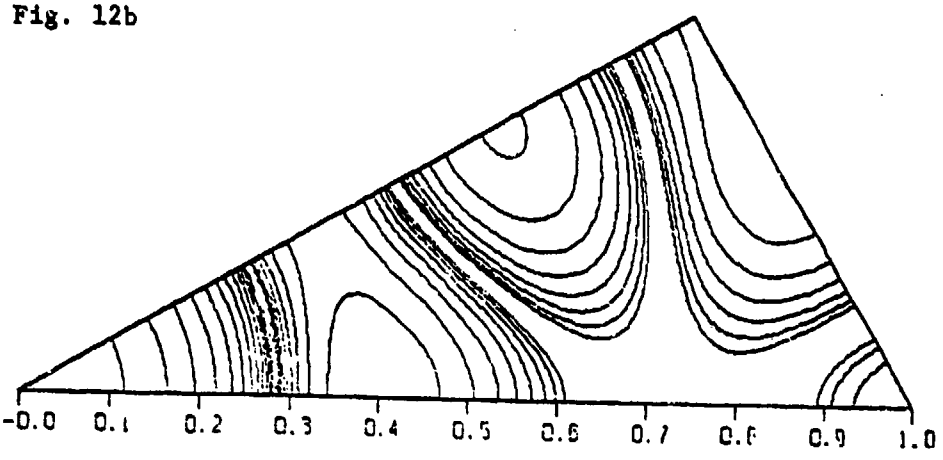

Fig. 12c

Figure 12. Power patterns for 37 element arrays: (a) uniform, (b) $H_7 * H_7 * H_7$, (c) $H_{19} * H_7$.

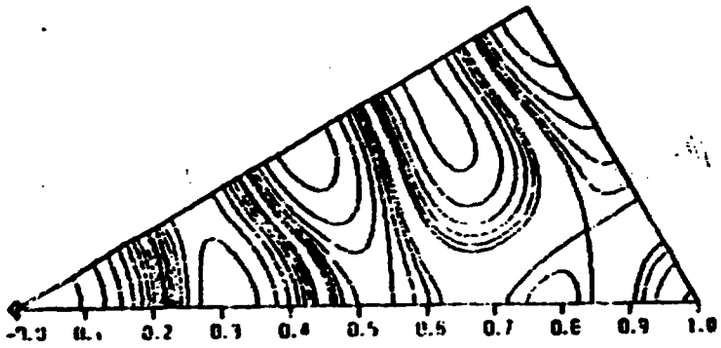

Fig. 13a

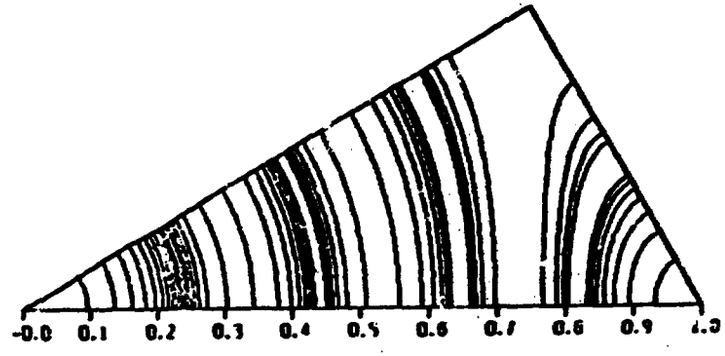

Fig. 13b

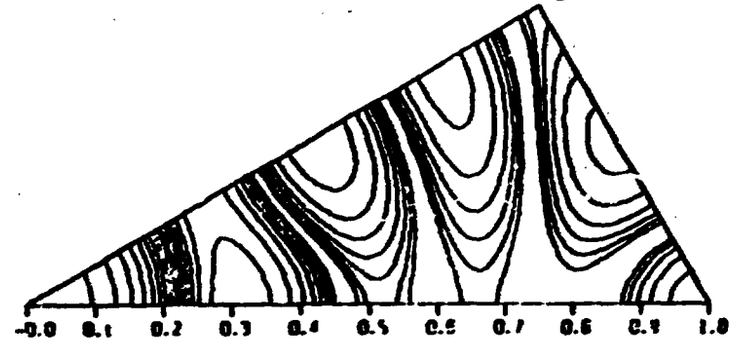

Fig. 13c

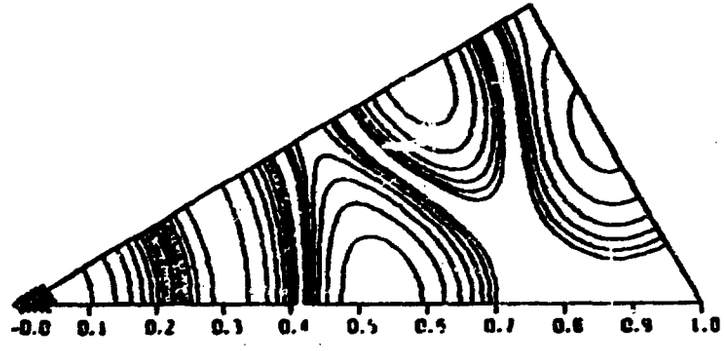

Fig. 13d

Figure 13. Power patterns for 61 element arrays: (a) uniform, (b) $(H_7*)^4$, (c) $H_{19}*H_7*H_7$, case A, (d) $H_{19}*H_7*H_7$, case B.

beam. This results in a ring-like pattern around the near-in sidelobe peak; however, the widening of the ring array from the coordinate axis may, in fact, result in a sidelobe peak near the edge of the cell and it may show up if the pattern plot was generated in smaller dB steps.

Shown in figure 14 are the patterns for H_{91} arrays: uniform, and the two arrays synthesized with H_7 and H_{19} arrays. Figure 14(b) shows patterns of the array generated from five H_7 subarrays which exhibit ring-like structure of a H_7 array. The 3dB beamwidth is greater than that of the uniform array. The pattern in figure 14(c) has a sidelobe level nearly identical to that of the uniform array; and the 3dB beamwidth is slightly larger.

From the patterns presented in this section, the following general characteristics of the synthesized arrays may be readily identified. In all of the syntheses, the ring-like sidelobe structure near the main beam is generated in optimized arrays provided the zeros of the H_7 subarrays are near the main beam; however, this generally leads to lower AIE. Another interesting feature is that the number of sidelobe peaks in the triangular cell are less than or equal to those of corresponding uniform arrays.

6. Conclusions

An analysis of 7 and 19 element symmetric hexagonal arrays which form canonical arrays in the synthesis of larger arrays is carried out. Also shown are the null loci and pattern plots of uniformly excited 7, 19, 37, 61 and 91 element hexagonal arrays.

The null loci of larger uniform arrays are utilized as initial data in the convolution synthesis of them for high aperture illumination efficiency. The synthesis is carried out by convolving one or more of either 7 and/or 19 element canonical arrays. The AIE of the convolved array is optimized by a hill

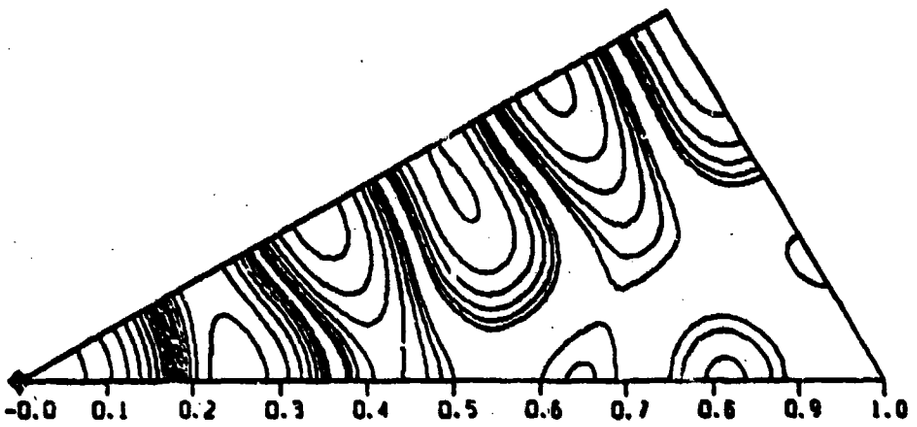

Fig. 14a

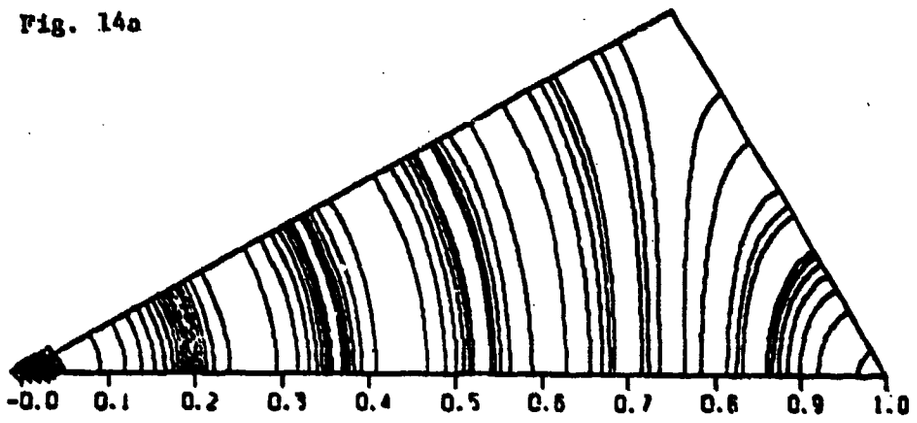

Fig. 14b

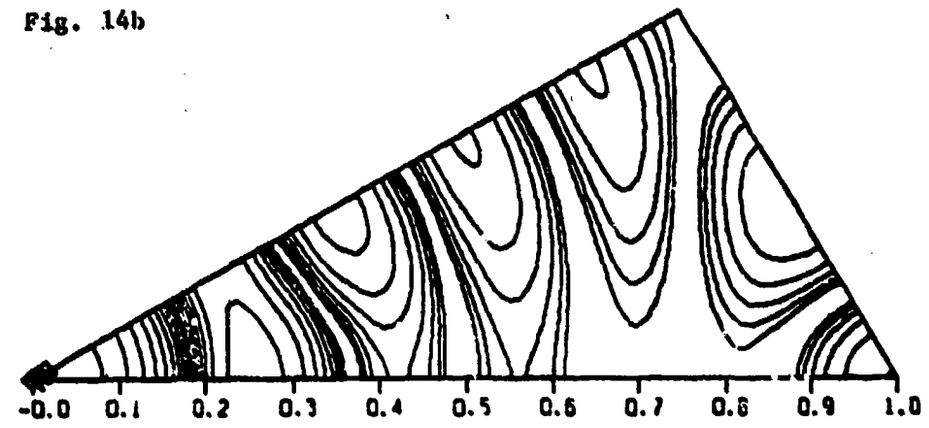

Fig. 14c

Figure 14. Power pattern for H_{91} arrays: (a) uniform, (b) $(H_7^*)^5$, (c) $H_{19}^* (H_7^*)^4$.

climbing process. The aperture illumination, AIE, null loci and patterns are presented for several different arrays of as large as 91 elements. The null loci and the pattern topography of each of these arrays are compared with those of the corresponding uniform arrays. Two useful features are identified. If the synthesis procedure utilizes only H_7 canonical arrays, then the main beam and usually the first sidelobe exhibit nearly circular locus. Synthesis of larger arrays with the H_{19} canonical array leads to patterns that have main beam null locus identical to that of the corresponding uniform array.

Aperture illumination efficiencies for syntheses involving only H_7 subarrays appear to have an asymptotic value in the range of 0.8 to 0.85. Synthesis of still larger arrays must be carried out to establish this bound conclusively. However, as it should be expected, the syntheses utilizing the H_{19} array exhibit higher AIE than the synthesis utilizing only H_7 arrays.

These convolution synthesis results, in addition to determining the maximum AIE of the convolved arrays, may provide the basis for a low-sidelobe synthesis technique. If a procedure analogous to the Taylor synthesis is used, in which the zeros of the maximum-gain configuration are pushed outward from the main beam, the starting maximum-gain configuration for the hexagonal array case may be the maximum-AIE convolved arrays.

7. Acknowledgment

The authors would like to thank Dr. Henry J. Bilow of NRL for the use of his graphics programs.

8. References

1. Baklanov, Ye. V. (1966) Chebyshev distribution of currents for a plane array of radiators, Radio Engrg. and Electronic Phys. 11:640-642.

2. Tseng, F. I. and Cheng, D.K. (1968) Optimum scannable planar arrays with an invariant sidelobe level, Proc. IEEE 56 (No. 11):1771-1778.
3. Goto, N. (1972) Pattern synthesis of planar arrays, Electronics and Commun. in Japan 55 (No. 1):68-73.
4. Goto, N. (1972) Nonseparable pattern of planar arrays, IEEE Trans. Antennas and Propagat. AP-20 (No. 1):104-106.
5. Elliott, R.S. (1977) Synthesis of rectangular planar arrays for sum patterns with ring side lobes of arbitrary topography Radio Science 12 (No. 5):653-657.
6. Goto, N. (1972) Pattern Synthesis of hexagonal planar arrays, IEEE Trans. Antennas and Propagat. AP-20 (No. 4):479-481.
7. Goto, N. (1972) A synthesis of array antennas for high directivity and low sidelobes, IEEE Trans. Antennas and Propagat. AP-20 (No. 4):427-431.
8. Cheng, David K. and Chen, Y.K. (1980) Optimum planar hexagonal arrays, Digest of the International Symposium on Antennas and Propagation, Quebec, Canada, 335-337.
9. Einarsson, Olov. (1979) Optimization of planar arrays, IEEE Trans. Antennas and Propagat. AP-27 (No. 1):86-92.
10. Shelton, J. Paul (1980) A Pattern-Synthesis Procedure for Regular Hexagonal Arrays, NRL Report 8368.
11. Laxpati, Sharad R. (1981) A Null Synthesis Technique for Planar Arrays, NRL Report 8478.
12. Laxpati, S. R. (1980) Synthesis of planar arrays based on convolution technique, Electronics Letters. 16 (No. 24) 918.
13. Laxpati, Sharad. R. and Shelton, J. Paul (1981) Theory of null synthesis of planar arrays, Digest of the International Symposium on Antennas and Propagation, Los Angeles. 40-43.
14. Shelton, J. Paul and Laxpati, Sharad. R. (1981) Applications of null synthesis to hexagonal arrays, Digest of the International Symposium on Antennas and Propagation, Los Angeles. 44-47.

AD P001104

CONSTRAINTS ON NULLING BANDWIDTH

Peter R. Franchi

Electromagnetic Sciences Division
Rome Air Development Center
Hanscom AF Base, MA

ABSTRACT

Recently there has been substantial interest in wideband nulling techniques and accompanying physical limitations imposed by the antenna system. Pattern nulls may be imposed deterministically or adaptively and the antenna patterns are often degraded by excitation errors. This paper is concerned with wide angle nulls in ideal (non-errored) patterns. For such patterns wide angle nulls are equivalent to wideband nulls.

For an M-element array there are at most M-1 nulls possible in angle. A limiting possibility would be to move all M-1 nulls to within some small angular region, Δu, and accept the fact that the resulting pattern would bare no resemblance to the original; this approach would give the lowest possible null depth for any particular wide angle band. In this paper the null depth and width are examined with the constraint that the fewest nulls be moved. This constraint is imposed because of the assumption that the original pattern before being nulled was desirable. A closed form solution is given for both equally spaced nulls and equal amplitude nulls.

CONSTRAINTS ON NULLING BANDWIDTH

Introduction

Since the deterministic pattern over some angular region varies linearly with frequency one obvious method of producing broad band nulls with frequency independent weights is to generate them over the corresponding angular region (see Fig. 1). If the angular region is treated in this manner, the questions then become: how low will the sidelobe region be over what angular extent, and at what price? It is the solution to these questions that is the purpose of this paper.

An array of K elements has K-1 possible nulls in its pattern. One possible approach[1] is to move all K-1 nulls into the angular region desired. This approach should give the lowest possible energy over that nulled angular region but a badly deteriorated pattern outside the null region. A second approach[2] is to reduce the pattern in the nulled region to its lowest possible value while keeping the pattern outside that region as close to the original as possible. A third idea[3] is to move the nulls in a semi linear fashion to create a smooth variation. Many other approaches are certainly possible. The approach followed here is to move just the M nulls of the K-1 possible while leaving the remaining K-1 -M nulls unchanged.

One of the serious problems of adaptive antennas with frequency independent weights is the wide band nulling capability of particular

antennas. It is possible to design types of antennas that have inherent wide band nulling behavior, but as a general rule, however, obtaining deep nulls over a large bandwidth is quite difficult. There are two basic limitations. One is the behavior of the deterministic pattern itself, whose angular response varies inversely with frequency. At any one frequency a null may be moved to or generated at any angle, but that null will change angle with frequency. This would mean a null only in the center of any finite bandwidth. A second limitation is caused by errors. It will not, in general, be true that all errors behave similar to the deterministic pattern in terms of frequency. Some will, some will not. This second limitation is not addressed in this paper.

Two approximations are used to determine the relationship between null width, number of nulls moved and null depth; first, the array is very large, and second the region to be nulled is not near the main beam. The results of using these two approximations is that Schelkunoff polynomial method expressing the array factor as a complex polynomial can be used for a local region of angular space rather than the entire unit circle. In fact, the error caused by using a linear local region rather than the entire circle is a serious concern because using the ratio of the two pattern before and after perterbation effectively cancels the large error terms. From Schelkunoff[4]

$$f(\theta) = \sum_{i=0}^{n-1} a_i e^{jkid\cos\theta} \qquad (1)$$

where $a_i = |a_i| e^{j(\delta_i + i\delta)}$

$i\delta$ denotes the progressive phase shift

$$f(\theta) = \sum_{i=0}^{m-1} |a_i| e^{j\delta_i} b_i \qquad (2)$$

where $b_i = e^{j\delta_i}$

$$\text{So} \quad f \doteq \sum_{i=0}^{m-1} |a_i| b_i \qquad (3)$$

if δ_i is small

then f(θ) can be written

$$f \doteq \prod_{i=1}^{m-1} (b - b_i) \qquad (4)$$

where b_i are the zeros of the far-field pattern. This expression shows that the field at any angle given by t is proportional to the product of the distances from that point to all the nulls in the pattern.

Sidelobe Levels by Distance from Nulls

In Fig. 3 the nulls are represented by points and the observation point by a circle with "a" representing the distance between nulls.

Then the initial sidelobe level, SLL_0, is given by

$$SLL_0 \propto \frac{a}{2}\cdot\frac{a}{2}\cdot\frac{3a}{2}\cdot\frac{3a}{2}\cdot\frac{5a}{2}\cdot\frac{5a}{2}\cdots\frac{(2M_0-1)a}{2} \qquad (5)$$

$$SLL_0 \propto \prod_{m=1}^{M_0/2}\frac{a^2(2m-1)^2}{4} \qquad (6)$$

where M_0 represents a large number far from the observation point. Moving a specific number of nulls, N, from their original location closer together, will reduce the sidelobe energy within that region given by ΔM.

For a centrally located lobe, the new sidelobe level is SLL_1 which is

$$SLL_1 \propto \left(\frac{a'}{2}\right)^2\left(\frac{3a'}{2}\right)^2\left(\frac{5a'}{2}\right)^2\cdots\left(\frac{2N+1}{2}\right)^2 a'^2\cdots\left(\frac{2M_0-1}{2}\right)^2 \qquad (7)$$

For simplicity the null bandwidth is defined from edge lobe peak to edge lobe peak and a' is the spacing between nulls within ΔM for the perturbed pattern.

$$SLL_1 \propto a'^N \prod_{m=1}^{N/2}\left(\frac{2m-1}{2}\right)^2 a^{M_0-N} \prod_{m=N/2+1}^{M_0/2+1}\left(\frac{2m-1}{2}\right)^2 \qquad (8)$$

The sidelobe reduction is ΔSLL

$$\Delta SLL = \frac{SLL_1}{SLL_0} = \frac{a'^N a^{M_0-N}}{a^{M_0}} = \left(\frac{a'}{a}\right)^N \tag{9}$$

but $a' = \frac{\Delta\mu}{N-1}$ and $\Delta\mu = (M-1)a - a + a'$

M_0 = the original number of nulls in $\Delta\mu$

$$\Delta SLL = \left(\frac{M-2}{N-2}\right)^N \quad \text{in field} \tag{10}$$

$$\Delta SLL = \left(\frac{M-2}{N-2}\right)^{2N} \quad \text{in power} \tag{11}$$

Since the null at the center of the reduced region will be lower than any other lobe in the nulled region, an estimate of the reduction in an edge sidelobe is also desired for equally spaced nulls. The edge sidelobe level is SLL_E

$$SLL_E \propto \frac{a'}{2}\cdot\frac{a'}{2}\cdot\frac{3a'}{2}\cdot\frac{5a'}{2}\cdots\left(\frac{2(N-1)-1}{2}\right)a'\cdot\frac{a}{2}\cdot\frac{3a}{2}\cdots\left(\frac{2(N-M)-1}{2}\right)a \tag{12}$$

The equation for the unperturbed pattern can be written

$$SLL_0 \propto \frac{a}{2}\cdot\frac{3a}{2}\cdots\left(\frac{2M-1}{2}\right)a\cdot\frac{a}{2}\cdot\frac{3a}{2}\cdots\left(\frac{2(N-M)-1}{2}\right)a \tag{13}$$

Therefore $$\Delta SLL = \frac{SLL_E}{SLL_0} = \frac{\frac{a'^N}{2^N}\prod_{m=1}^{N-1}(2m-1)}{\frac{a^N}{2^N}\prod_{1}^{M}(2m-1)\prod_{1}^{N-M}(2m-1)} \quad \text{in field} \tag{14}$$

$$\frac{a'}{a} = \frac{M-2}{N-2}$$

$$\Delta SLL = \left(\frac{M-2}{N-2}\right)^{2N}\left[\prod_{N-M+1}^{N-1}(2m-1)\Big/\prod_{1}^{M}(2m-1)\right]^2 \quad \text{in power} \tag{15}$$

Equal Amplitude Ripple in the Nulled Band

The previous equations give reductions in the central lobe and of an edge lobe of a nulled region as a function of the original number of nulls M, which is related to the angular bandwidth or nulled region and N the number of nulls that are moved. Both equations are for equally spaced nulls in the nulled region. Another useful expression is derived for equal amplitude lobes by placing nulls at unequal spacings. For nulls (in the nulled region) that are located at a large distance from the unchanged nulls, Cheybshev spacing provides equal lobes. The location of a set of nulls is given by

$$\cos\frac{\pi}{2N}(2\rho+1) \qquad \text{for N even}$$

and

$$\cos\frac{\pi}{N}\rho \qquad \text{for M odd}$$

As before

$$SLL_0 \propto \left(\frac{a}{2}\right)^2 \cdot \left(\frac{3a}{2}\right)^2 \cdot \left(\frac{5a}{2}\right)^2 \cdots \left(\frac{2N-1}{2}\right)^2 a^2 \cdots \quad \text{nulls beyond aM} \tag{16}$$

$$SLL_{ch} \propto \prod_{p=1}^{N/2} \cos^2\left(\frac{\pi}{2N}(2p-1)\right) \quad \text{for } \Delta\mu = 2 \tag{17}$$

$$\Delta\mu = (M-1)a - a + a' \tag{18}$$

$$\Delta\mu = (M-1)a + \frac{(M-2)}{(N-2)}a \tag{19}$$

$$a = \frac{\Delta\mu\,(N-2)}{(N-1)(M-2)} \cdots \tag{20}$$

$$\text{or} \quad a = \frac{2(N-2)}{(N-1)(M-2)} \tag{21}$$

Therefore the equation for the sidelobe reduction in power is

$$\Delta SLL_{ch} = \left[\frac{(M-2)(N-1)}{(N-2)}\right]^{2N} \left[\prod_{1}^{N/2} \frac{\cos\frac{\pi}{2N}(2m-1)}{2m-1}\right]^4 \tag{22}$$

Conclusions

Some equations have been devised to give sidelobe reduction as a function of angular bandwidth (proportional to frequency bandwidth) and number of nulls moved. Both equally spaced nulls and

equal amplitude lobes in the nulled region are treated. Several limitations are required. These include: 1) consideration of serious internal reflections 2) nulling regions are not very close to the main beam 3) arrays must be large, and 4) for the equal amplitude with large bandwidth, the formulas are most accurate for large sidelobe reduction.

REFERENCES

1. Shore, R. A. and Fante, R. L., "Sector Sidelobe Nulling", RADC-TR-81-32 In House Report, Nov 1981.
2. Steyskal, H., "Wideband Nulling Performance Versus Number of Pattern Constraints for an Array Antenna", IEEE Transaction on Antennas and Propagation, to be published.
3. Tseng, F. I., "Design of Array and Line-Source Antenna for Taylor Patterns with a Null", IEEE Transaction on Antennas and Propagation, 79 July, pp 474-479.
4. Collin, R.E. and Zucker, F. J., "Antennas Theory Part I, Inter-University Electronics Series, pp 158-160.

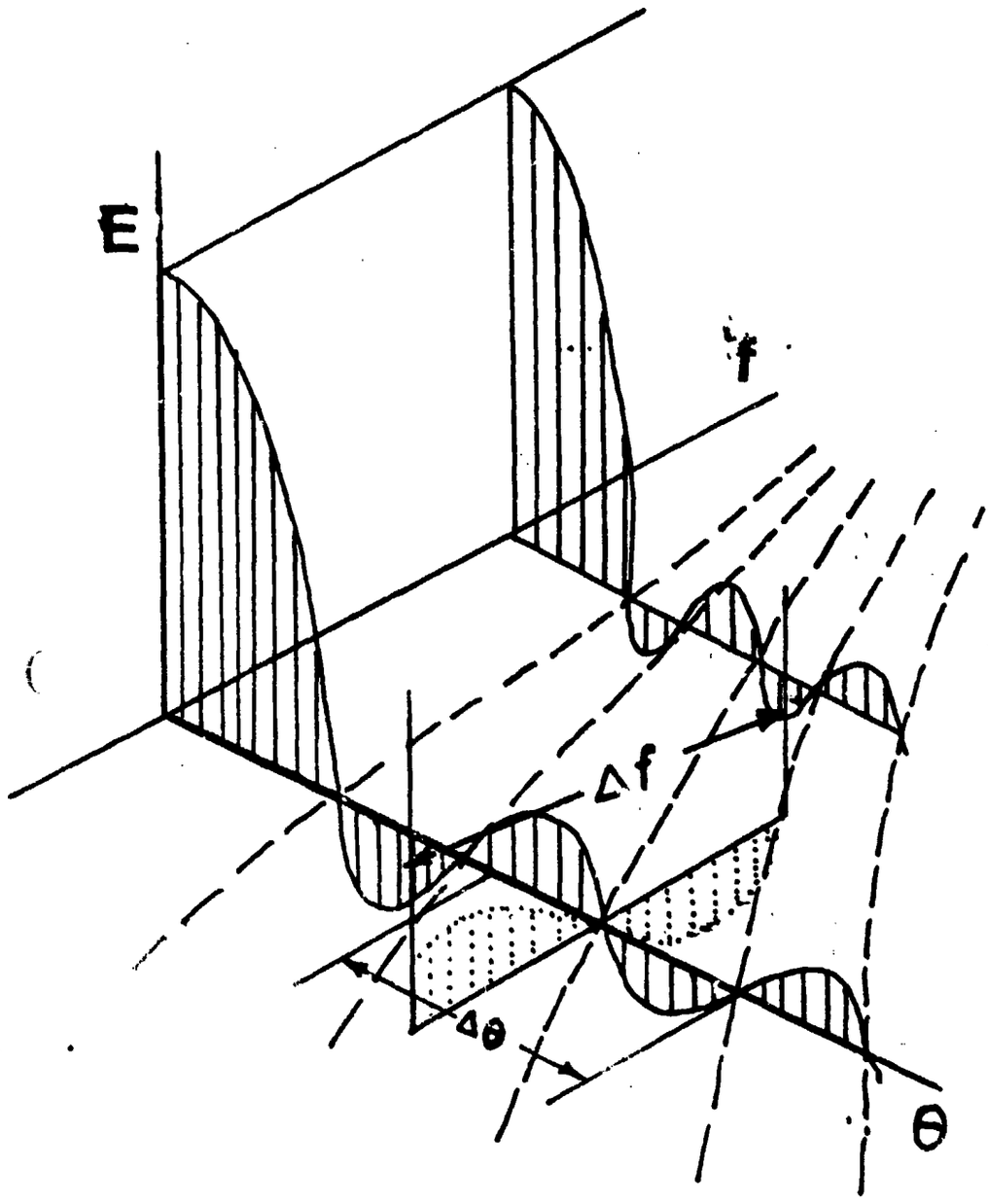

Angle versus Frequency

Fig 1

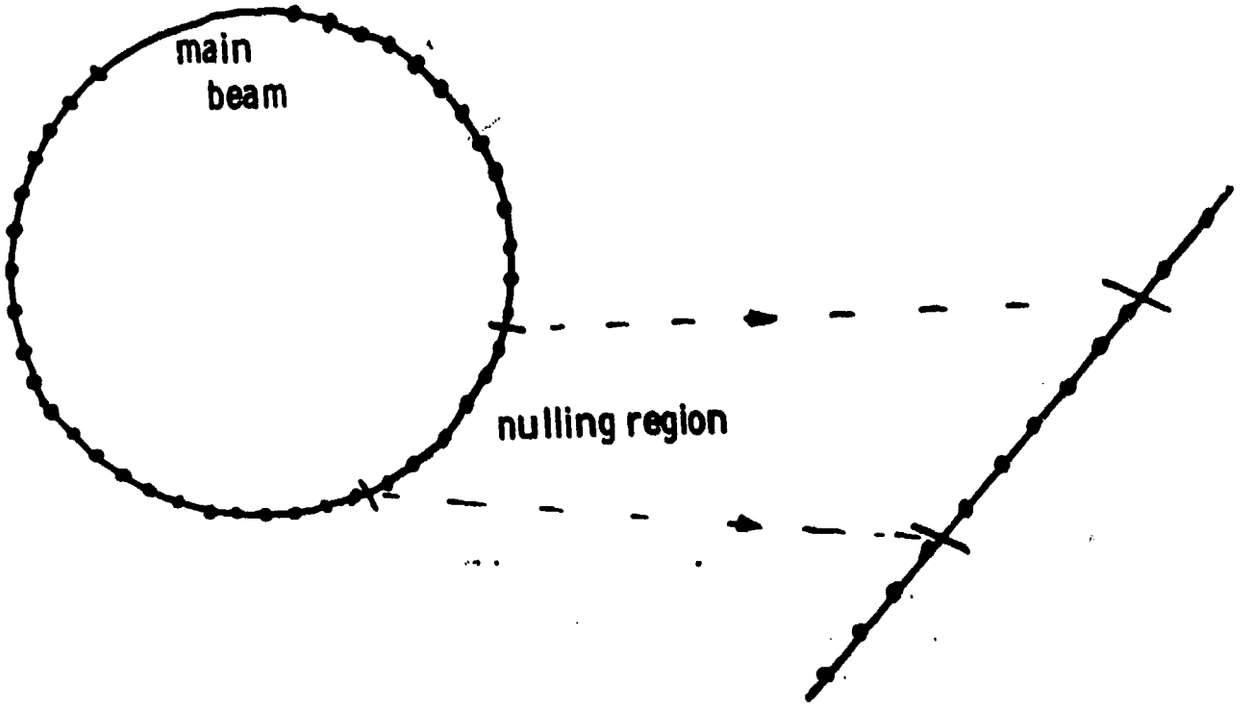
main
beam
nulling region

Fig. 2

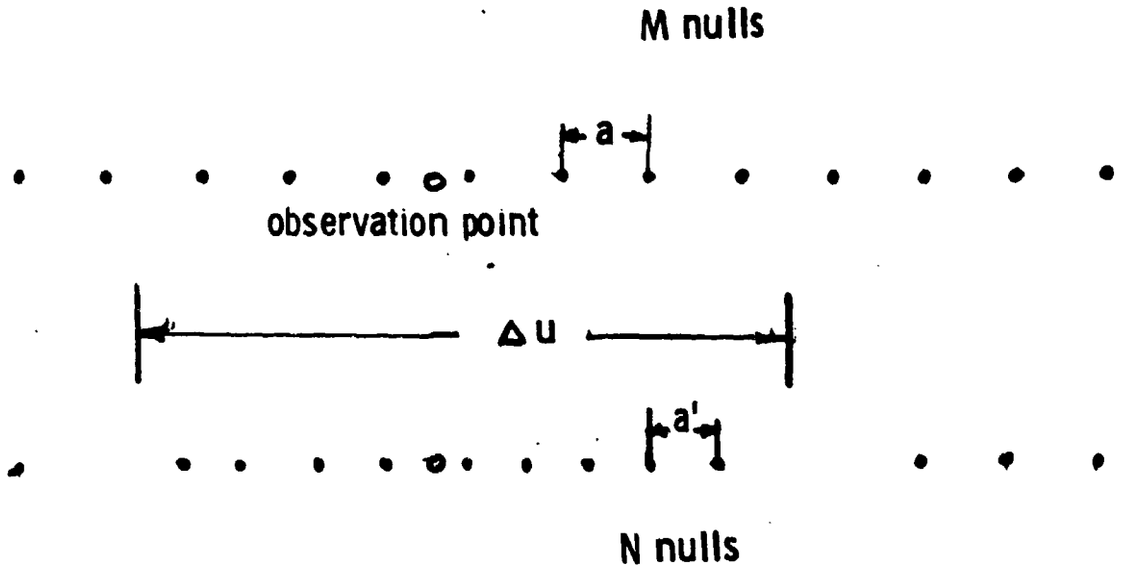
M nulls
a
observation point
Δu
a'
N nulls

Fig 3

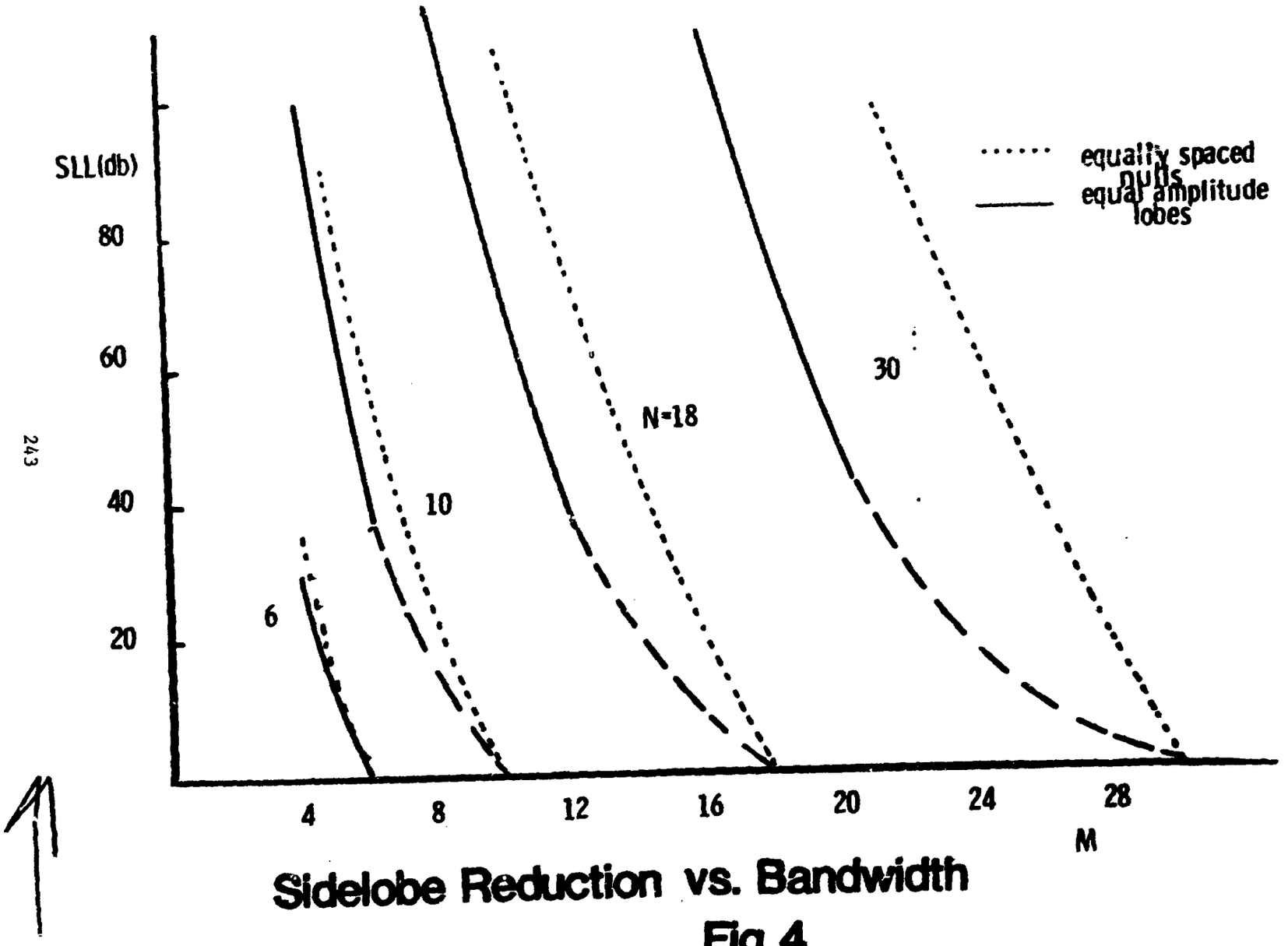

Sidelobe Reduction vs. Bandwidth

Fig 4

AD P001105

AN APPROACH TO RADAR TARGET IDENTIFICATION

M. P. Hurst, R. Mittra and S. W. Lee
Electromagnetics Laboratory
and
The Coordinated Science Laboratory
University of Illinois
Urbana, Illinois

ABSTRACT

At the operating frequencies of most surveillance radars, airborne targets are large compared to a wavelength, and their RCS characteristics can, therefore, be described in terms of returns from scattering centers. If the spatial distribution and relative strengths of these scattering centers can be determined, the target can be identified by comparison with data for known targets. The method proposed here enables one to extract this information from RCS data gathered noncoherently within a modest bandwidth.

The work reported in this paper was supported in part by the Office of Naval Research Grant N00014-81-K-0245 and, in part, by the Joint Services Electronics Program under Grant N00014-79-C-0424.

BEST AVAILABLE COPY

1. INTRODUCTION

A back-scattered cw signal from a target with N scattering centers can be decomposed in' , N signals, each with a different phase and magnitude. The physics of the scattering process (reflection or diffraction) determines the relative magnitude of each contribution, while the phase is dependent on the distance from the scattering center to the observation point. Let the incident field be

$$\bar{H}^i(\bar{r}) = \bar{H}\, e^{-jkz} \quad . \tag{1}$$

The back-scattered field as measured by a linearly polarized receiving antenna can then be expressed as

$$H(k,z) \sim \frac{e^{jkz}}{z} \sum_{n=1}^{N} A_n'(k)\, e^{j2k\hat{z}\cdot\bar{r}_n} \tag{2}$$

where $\bar{r}_n$ is the location of scattering center n and $A_n'(k)$ is a weighting coefficient determined by the scattering process. For a small range of k, $A_n'(k)$ can be approximated by

$$A_n'(k) \simeq A_n\, e^{\gamma_n k} \quad , \quad \gamma_n \text{ real.} \tag{3}$$

For a fixed value of z, we then have

$$H(k) \propto \sum_{n=1}^{N} A_n\, e^{(\gamma_n + jd_n)} \tag{4}$$

where $d_n = 2\hat{z} \cdot \bar{r}_n$. $\gamma_n + jd_n \triangleq \xi_n$ is a spatial frequency and has dimensions of length. The problem at hand is to characterize a radar target by determining the values of the unknowns in (4) from knowledge of H(k) sampled over a finite bandwidth. A method for solving this type of nonlinear problem was introduced by Prony in 1795.[1,2,3]

2. PRONY'S METHOD

Assume that a set of 2N data points satisfies the relation

$$H(k_n) \triangleq H_n = \sum_{i=0}^{N-1} A_i e^{\xi_i k_n}$$

$$= \sum_{i=0}^{N-1} A_i e^{\xi_i (k_0 + n\Delta k)} \qquad n = 0, 1, \ldots, 2N-1 \qquad (5)$$

where Δk is the spacing between successive samples and the A's and ξ's are 2N complex unknowns to be determined. Letting

$$z_i \triangleq e^{\xi_i \Delta k}, \qquad (6)$$

Eq. (5) can be written

$$H_n = \sum_{i=0}^{N-1} A_i z_i^n e^{\xi_i k_0} . \qquad (7)$$

We now construct a polynomial with unknown coefficients α_n whose roots are the z_i's:

$$\prod_{i=0}^{N-1} (z-z_i) = \sum_{n=0}^{N} \alpha_n z^n = 0 \quad \text{for } z = z_i. \tag{8}$$

A system of linear equations involving only the α's and the (known) H's can be obtained as follows. Using (7), we can write

$$\sum_{n=0}^{N} \alpha_n H_n = \sum_{n=0}^{N} \alpha_n \sum_{i=0}^{N-1} A_i z_i^n e^{\xi_i k_0}$$

$$= \sum_{i=0}^{N-1} A_i e^{\xi_i k_0} \left[\sum_{n=0}^{N} \alpha_n z_i^n \right] . \tag{9}$$

The bracketed term vanishes because of (8) and, thus,

$$\sum_{n=0}^{N} \alpha_n H_n = 0 \quad . \tag{10}$$

An additional N-1 equation can be obtained similarly. We then have

$$\sum_{p=0}^{N} \alpha_p H_{p+\ell} = 0 \quad , \qquad \ell = 0, 1, \ldots, N-1. \tag{11}$$

Equation (11) represents N equations which can be solved for the N unknown α's. (Equation (8) implies that α_N has been arbitrarily chosen to equal unity, which is permissible because of the homogeneous nature of the equation.) If the α's are known, an appropriate polynomial root finding technique can be used to find the z_i's in (8) and, therefore, the ξ_i's in (6). The only remaining unknowns, the A's, can be found by solving another system of N linear equations obtained directly from (7). Thus, Prony's method involves the inversion of two N x N matrices and the factoring of

an N^{th} order polynomial.

The values found through Prony's method are exact if the initial data are exact and of the assumed form. In practice, neither condition will be strictly satisfied. It is therefore desirable to introduce some redundancy and find solutions representing the "best fit" to the measured data. This can be done by increasing the number of data points beyond 2N and modifying Eq. (10) to read

$$\sum_{p=0}^{N-1} \alpha_p H_{p+\ell} = -H_{N+\ell} , \qquad \ell = 0, 1, \ldots, M-1 \tag{12}$$

where M is the number of data points. In matrix form, the left-hand side of this equation becomes the product of an N x M matrix and the vector of α's. If both sides of the equation are multiplied on the left by the M x N matrix which is the transpose of the matrix of H values, an N x N matrix is obtained on the left and the solution can proceed as before. Results obtained in this way are optimal in the least squared error sense.

3. REQUIREMENTS OF PRONY'S METHOD

The spacing between successive samples of H(k) must be chosen such that the Nyquist criterion is satisfied, i.e., Δk must be less than half the period of the highest frequency component of H(k). As can be seen from Eq. (4), this (spatial) frequency is equal to

the d_n of greatest absolute value, d_{max}. Choosing the origin midway between the two extreme scattering centers, we have the requirement

$$\Delta k \leq \frac{1}{2} \cdot \frac{2\pi}{|d_{max}|} \leq \frac{\pi}{\ell} \tag{13}$$

where ℓ is the length of the scatterer.

Sampling theory states that the bandwidth ($k_{max} - k_{min}$) must be greater than the number of spatial frequencies present, N, divided by d_{max}. In practice, this is not a significant restriction. The actual bandwidth requirements are dependent upon the amount of noise present, as discussed below.

Ideally, one should know a priori how many spatial frequencies (the number of scattering centers) are present in order to apply Prony's method. However, good results can still be obtained by assuming a number of spatial frequencies greater than the number actually present and discarding spurious frequencies generated by the algorithm. These can usually be identified by their low relative amplitudes and by comparing results for the same data with different assumptions of spatial frequencies present. "True" frequencies always appear while different spurious ones are produced in each case. If none of the frequencies survive this test, it can be concluded that too few frequencies were assumed. Figure 1 shows the results of analyzing back-scattered data from a pie-shaped cylinder (as calculated using GTD formulas) under the

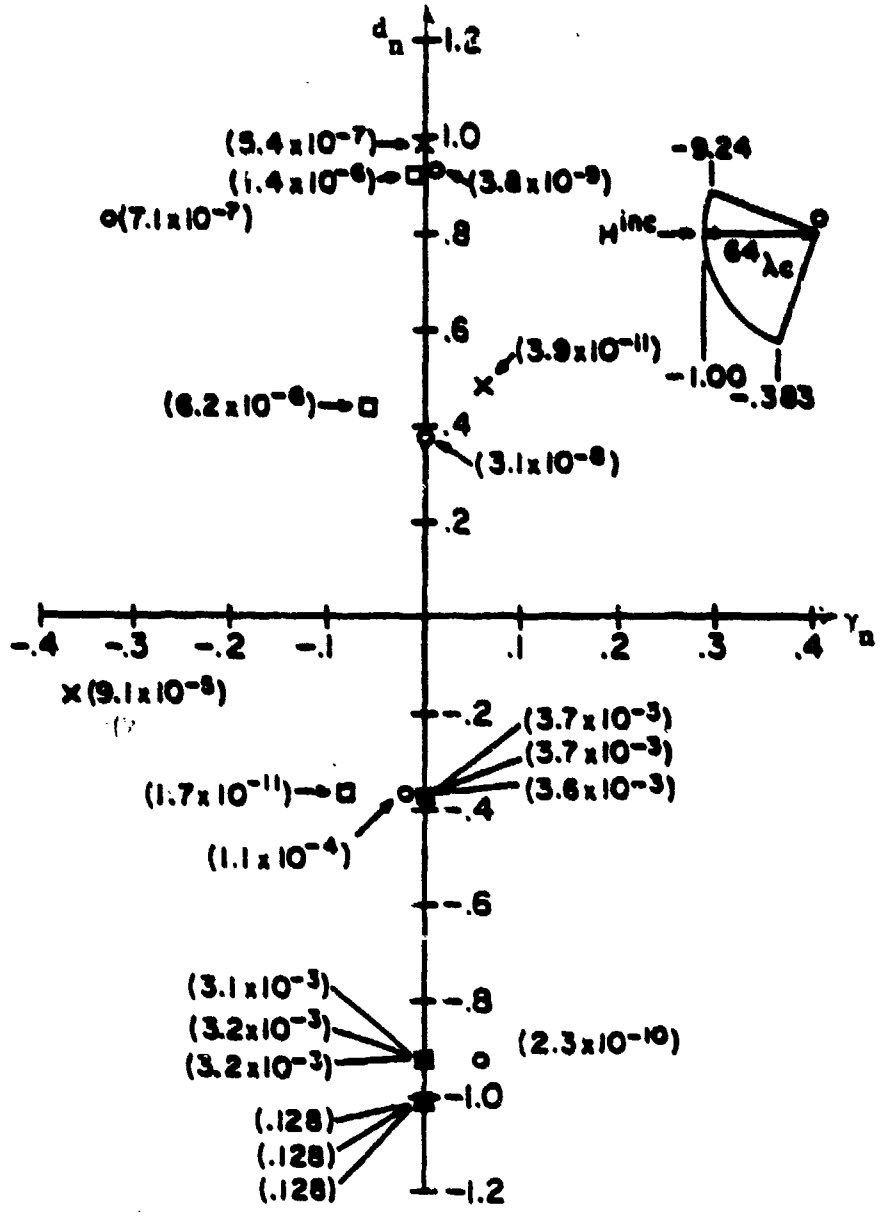

Figure 1. Calculated spatial frequencies of pie-shaped cylinder under three different assumptions as to the number of frequencies present. The numbers in parenthesis represent amplitudes.

assumptions that 5, 6, and 7 frequencies are present. It can be seen that the three scattering center locations are correctly identified in each case while the spurious frequencies of different cases do not coincide.

4. NONCOHERENT DETECTION

Implicit in the above analysis is the assumption that the measured data points (the H_n's) are complex, which implies coherent detection by the radar receiver. Useful results can also be obtained from data gathered noncoherently. Consider the case where the field analyzed is that due to two sources at $z = z_0 \pm \frac{d}{2}$ with amplitudes A and B. We then have

$$|H(k,z)| \propto \left| A\, e^{jk(z - z_0 + \frac{d}{2})} + B\, e^{jk(z - z_0 - \frac{d}{2})} \right| \tag{14}$$

$$= \sqrt{A^2 + B^2 + 2AB \cos kd} \quad .$$

From this equation, it can be seen that the spectral content of $|H(k)|$ is determined by the location of the sources relative to each other and contains no information as to their absolute location in space. As a consequence of this, when more than two scattering centers are present, the results of analysis are ambiguous. For example, a case in which the scattering centers at z_0, $z_0 + d_1$, and $z_0 + d_1 + d_2$ is indistinguishable from those where the locations

are z_0, $z_0 + d_2$, and $z_0 + d_1 + d_2$.

5. NOISE PERFORMANCE

One advantage of using noncoherent detection is greater immunity to noise. There is little noise tolerance in the case of coherent detection, but the imaginary part of the spatial frequencies (the quantity of most interest) can be extracted from noncoherent data even when Gaussian noise is added to give an RMS SNR of 2 or less. Table 1 shows the effect of bandwidth on accuracy in the presence of noise. In the table the average percent error in the 3 spatial frequencies of a square cylinder under various noise and bandwidth conditions are compared. Each entry is the average of ten cases with different noise (of the same statistics).

TABLE 1

AVERAGE PERCENT ERROR IN THE THREE CALCULATED SPATIAL FREQUENCIES OF A SQUARE CYLINDER (NONCOHERENT DETECTION)

SNR	30% BW	25% BW	20% BW	15% BW	10% BW
100	.04	.05	.06	.06	.09
10	4.63	3.53	2.85	4.84	2.10
4	6.97	7.22	6.80	8.38	8.14
2	10.44	10.68	10.45	10.84	11.72

The actual amount of noise that would be present in a practical situation would, of course, depend on the environment. It should be noted, however, that the signal-to-noise ratio can be made arbitrarily large by increasing the time of observation at each (cw) frequency and, thereby, averaging out the error (assuming target motion is negligible). The total observation time can be reduced by interrogating the target at several frequencies simultaneously by transmitting a signal with a "comb" spectrum. Other workers have also reported success with new techniques for reducing the noise sensitivity of Prony's method.[4,5] Both coherent and noncoherent detection schemes can therefore be expected to be successful in a practical environment.

6. SPLIT SPECTRUM ANALYSIS

In some instances, a single radar may not possess sufficient bandwidth for the desired level of accuracy. In such cases, a modified Prony's method can be used to analyze simultaneously data gathered by two or more radars operating in different, noncontiguous bands. For the case of two bands ranging from k_0 to $k_0 + (M_1-1)\Delta k$ and from $k_0 + M_2\, k$ to $k_0 + (M_3-1)\Delta k$, Eq. (8) becomes

$$\sum_{n=0}^{N+M_2-M_1} \alpha_n z^n = \left[\prod_{i=0}^{N-1} (z-z_i)\right] \cdot \left[\prod_{\ell=1}^{M_2-M_1} (z-z_\ell^{ex})\right] \qquad (15)$$

where the z^{ex} are "extraneous" roots chosen such that as many as

(M_2-M_1) of the α's are equal to 0 and the polynomial takes the form

$$\alpha_0 + \alpha_1 z + \ldots + \alpha_{q_1} z^{q_1} + \alpha_{q_2} z^{q_2}$$

$$+ \alpha_{q_{2+1}} z^{q_{2+1}} + \ldots + z^{N+M_2-M_1} = 0 \, . \qquad (16)$$

Equation (12) then becomes

$$\sum_{p=0}^{q_1} \alpha_p H_{p+\ell} + \sum_{p=q_2}^{N+M_2-M_1-1} \alpha_p H_{p+\ell} = - H_{N+M_2-M_1+\ell} \, , \qquad (17)$$

$$\ell = 0, 1, \ldots, L-1.$$

L, q_1, and q_2 are chosen such that

$$L = M_1 - q_1 = (M_3 - M_2) - (N+M_2-M_1-z_2-1) \qquad (18)$$

in order to form a rectangular matrix from Eq. (17). (Several choices for these parameters will generally be possible.) The α's can now be found as before. It must be recalled, however, that the polynomial in (16) has extraneous roots which must somehow be distinguished from the roots of interest. This can be done by first finding the approximate values of the roots by analyzing one of the constituent bands in the standard way. A convenient way of finding the roots of interest in Eq. (16) is to use an algorithm which can utilize approximate values of the roots as initial guesses. The remaining unknowns can be found as before. Table 2 compares results

from the analysis of data from a square cylinder for the wide-bandwidth case, the same frequency band with two gaps (three subbands), and the lowest subband by itself. In arriving at the figures for the split spectrum case, the (same) data were analyzed for eight different values of the parameter L and the results were averaged. It can be seen that the split spectrum results are quite comparable to those for the entire band without gaps, even though more than half of the data was discarded.

TABLE 2

ERROR IN THE THREE LOWEST SPATIAL FREQUENCIES OF A SQUARE CYLINDER AS CALCULATED BY THE STANDARD AND MODIFIED PRONY'S METHOD

Note that the entire band contained 222 data points (BW = 83%) and each subband 35 points (BW = 20%, 14%, 10%).

Spatial frequency	Entire band without gaps	Lowest band alone	Three sub-bands together
d_1	1.74	39.07	1.92
d_2	0.09	1.56	1.06
$d_1 + d_2$	0.68	4.99	0.46
TOTAL	2.51	45.62	3.44

7. CONCLUSIONS

A method of radar target identification has been proposed which distinguishes targets by the locations of their scattering centers in space. The technique is workable with coherent and non-coherent radars possessing bandwidths on the order of 20%. The effect of noise has been considered, and a method for utilizing split spectrum measurements has been presented. The proposed technique would require only minor modifications to existing radars to be implemented.

ACKNOWLEDGEMENT

The authors would like to thank the Lawrence Livermore Laboratory for supplying the computer code for the Prony algorithm.

REFERENCES

1. Prony, R. (1795) Essai experimental et analytique sur les lois del la dilatabilite de fluides elastiques et sur celles del la force expansion de la vapeur de l'alkool, A differentes temperatures, J. L'Ecole Polytech, Paris, 1(No. 2):24-76.
2. Hildebrand, F. B. (1974) Introduction to numerical analysis, 2nd Edition, McGraw-Hill, New York, pp. 457-462.
3. Van Blaricum, M. L. and R. Mittra (1978) Problems and solutions associated with Prony's method for processing transient data, IEEE Transactions, 26:175-182.
4. Price, H. J. (1979) An improved Prony algorithm for exponential analysis. Paper presented at the International IERE Symposium on Electromagnetic Compatibility, San Diego, CA.
5. Van Lint, V.A.J. and M. L. Van Blaricum (1978) Applications of Prony's method to SGEMP data analysis. Paper presented at the Nuclear EMP Meeting, University of New Mexico, Juen.

AD P001106

EVALUATION OF THE MONOPOLE-SLOT AS A LAND-MOBILE COMMUNICATIONS ANTENNA

B. M. Halpern and P. E. Mayes
Department of Electrical Engineering
University of Illinois
Urbana, IL

Abstract

Land-mobile communication systems designed to operate over the upper portion of the UHF band in an urban environment are very susceptible to frequent wide signal variations, also known as fades, which arise due to the presence of many obstructions in the propagation path between the transmitter and receiver. Degradation of system performance resulting from this type of fading must be overcome by means other than an increase in transmitter power.

This paper describes a method of combating multipath fading which makes use of the fact that the resultant vertical electric field and horizontal magnetic fields of the incident waves at the same point in space are uncorrelated, and therefore, statistically independent. The method described incorporates a selection diversity combiner in the mobile unit. The inputs of the combiner stem from the outputs of a single multiport antenna, such as the monopole-slot antenna, which responds to the vertical electric field and either the x or y component of the magnetic field of a vertically polarized transmitted wave.

The VSWR at both ports of a medium-profile monopole-slot antenna is on the order of 2:1 over a 10% band and its efficiency is greater than 80% over a comparable band, as well. In addition, the monopole-slot antenna can be augmented to provide an omnidirectional transmit pattern in azimuth, if so desired.

1. Introduction

In mobile communication systems, the need arises for a broadband antenna which is both electrically small and well-matched to a transponder. The monopole-slot antenna, which was introduced

in 1970 by Mayes and Wiesenmeyer [1], was designed to satisfy these criteria. A monopole-slot antenna is shown in Figure 1.

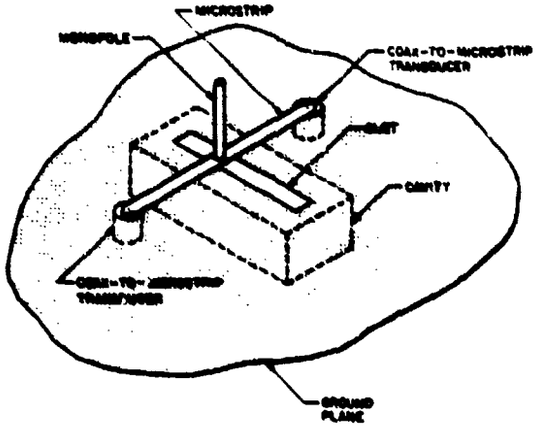

Fig. 1. The monopole-slot antenna with a microstrip feed

The monopole-slot antenna also provides a form of diversity reception that can be used to overcome difficulties associated with multipath propagation. These problems are particularly severe in UHF and microwave land-mobile communication in urban environments. The objective of this paper is to provide data evaluating the monopole-slot antenna for use in the new land-mobile service over the 800-900 MHz band.

The monopole-slot antenna shown in Figure 1 consists of a center-fed, cavity-backed linear slot in a horizontal plane and a vertical monopole. Both elements are excited at the same point by a single microstrip transmission line which is connected to the transponder at one end and to a matched load at the other

end. The complementary impedance characteristics of the monopole and slot result in an antenna which has a stable input impedance over a wide range of frequencies.

The radiation fields of the monopole-slot antenna are the sum of the fields produced by the two radiating elements. When the fields of the two elements are properly weighted, the resulting azimuthal radiation pattern is a cardioid with maximum along the axis perpendicular to the slot in the direction of the port which is fed [2]. The direction of the cardioid is reversed when the termination and signal source are interchanged. The directional properties of a well-designed monopole-slot antenna are maintained over a wide range of frequencies.

In 1980, the monopole-slot was modified by Cwik to incorporate a stripline feed [3], and it was demonstrated by Paschen [2] that the broadband nature of the monopole-slot remains. Since this structure improves both the mechanical strength and RF shielding of the feed, the stripline-fed monopole-slot is better suited for use in land-mobile systems.

The monopole-slot antenna contains elements which respond to both the vertical electric fields and the horizontal magnetic fields of azimuthally incident waves. It has previously been demonstrated that the monopole-slot antenna reduces fading caused by moving through a standing-wave field [3]. This has prompted

an investigation of the use of the monopole-slot antenna in diversity receiving systems.

2. THE MEDIUM PROFILE MONOPOLE-SLOT ANTENNA

2.1 Design Criteria

Two monopole-slot antennas for use over the proposed land-mobile communication band from 825 to 890 MHz were built and tested. In addition to the criteria stated in the introduction, two additional design criteria were used. The antenna was to operate with maximum efficiency over the transmit portion of the band (825-845 MHz), and the height of the monopole was to be reduced as much as possible without seriously degrading the performance of the antenna; hence the name "medium-profile".

2.2 The Antenna

In the previous work by Mayes, Wiesenmeyer, et al. [1], [4], [5], on various monopole-slot antennas which incorporated microstrip feeds, the cavity had little effect on antenna performance since the antenna was operated far below the lowest cavity resonance. Concurrent with this research, Paschen [2] showed that a stripline-fed monopole-slot antenna could also be designed to operate in a band between the TE_{101} and TE_{103} cavity resonances. Figure 2 shows such an antenna. It was designed to operate over the band from 820 to 890 MHz. The antenna was constructed using two sheets of 3/16 in. thick, single-clad Rexolite 2200

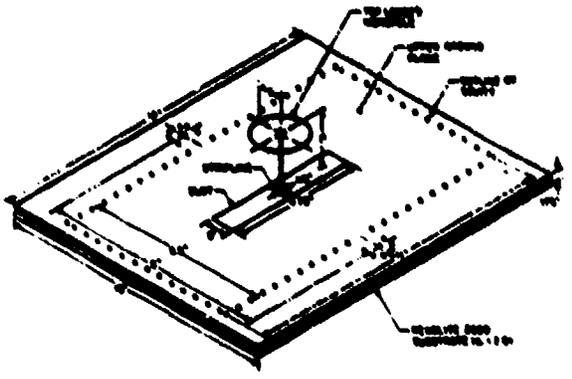

Fig. 2. Capacitively top-loaded monopole-slot antenna designed to operate between the TE_{101} and TE_{103} cavity resonances

board with a 50-ohm stripline feed. The dimensions of the cavity are 6.5 in. by 11.0 in. and its TE_{101} and TE_{103} resonances were calculated to be 654 MHz and 1146 MHz, respectively. The monopole was capacitively top-loaded with a circular patch of copper tape and the width and length of the slot were adjusted to yield s_{11} and s_{21} loci which indicated the best match and highest efficiency over the operating band. The performance criteria stated in Section 2.1 were best met using an antenna with the following dimensions:

Monopole	Slot
Height = 1.0 in.	Width = 0.9 in.
Radius of Top-Loading Patch = 0.9 in.	Length = 4.75 in.

The scattering parameters of this monopole-slot antenna were measured. The s_{11} measurements are phase-referenced to the center of the antenna while the s_{21} measurements are phase-referenced to the antenna ports. The s-parameters of the monopole-slot antenna are shown in Figure 3. The s_{11} locus reveals that the VSWR at the input port of antenna is less than 2:1 over the entire operating band.

The efficiency of the monopole-slot antenna is defined as the ratio of power radiated to power input and can be calculated directly from the scattering parameters using Equation (1).

$$e \triangleq \frac{P_{rad}}{P_{in}} = \left[\frac{1 - |s_{11}|^2 - |s_{21}|^2}{1 - |s_{11}|^2} \right] \times 100\% \qquad (1)$$

The s_{11} and s_{21} loci for this antenna reveal that the antenna is at least 76 percent efficient over the entire operating band. The efficiency of this antenna over the transmit band ranges from 84 percent at 825 MHz to 89 percent at 845 MHz.

The azimuthal radiation patterns for the first monopole-slot antenna are shown in Figure 4. The F/B ratios over the receive band, which extends from 870 to 890 MHz, were calculated to be around 12 dB, while those calculated over the transmit band were found to be around 16 dB. The monopole appears slightly dominant over both bands.

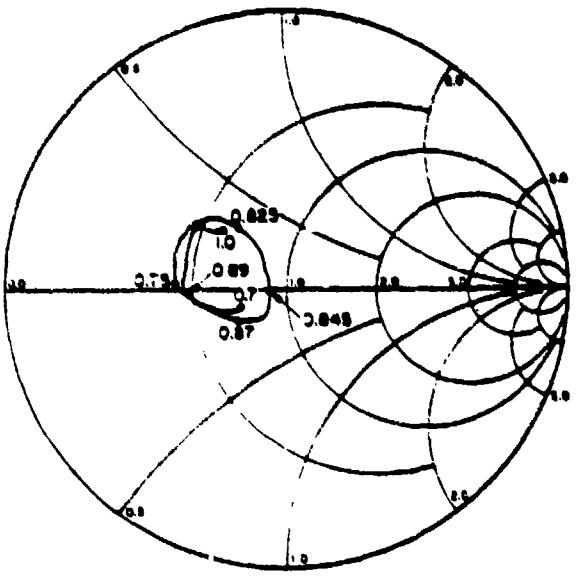

(a) s_{11}

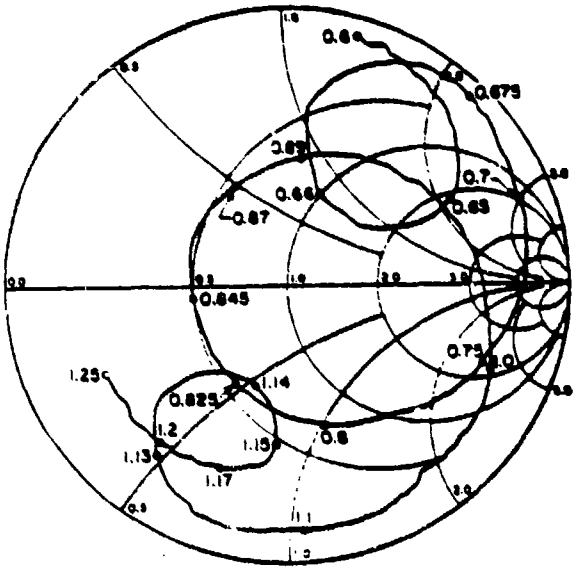

(b) s_{21}

Fig. 3. s_{11} and s_{21} for the monopole-slot antenna shown in Fig. 2

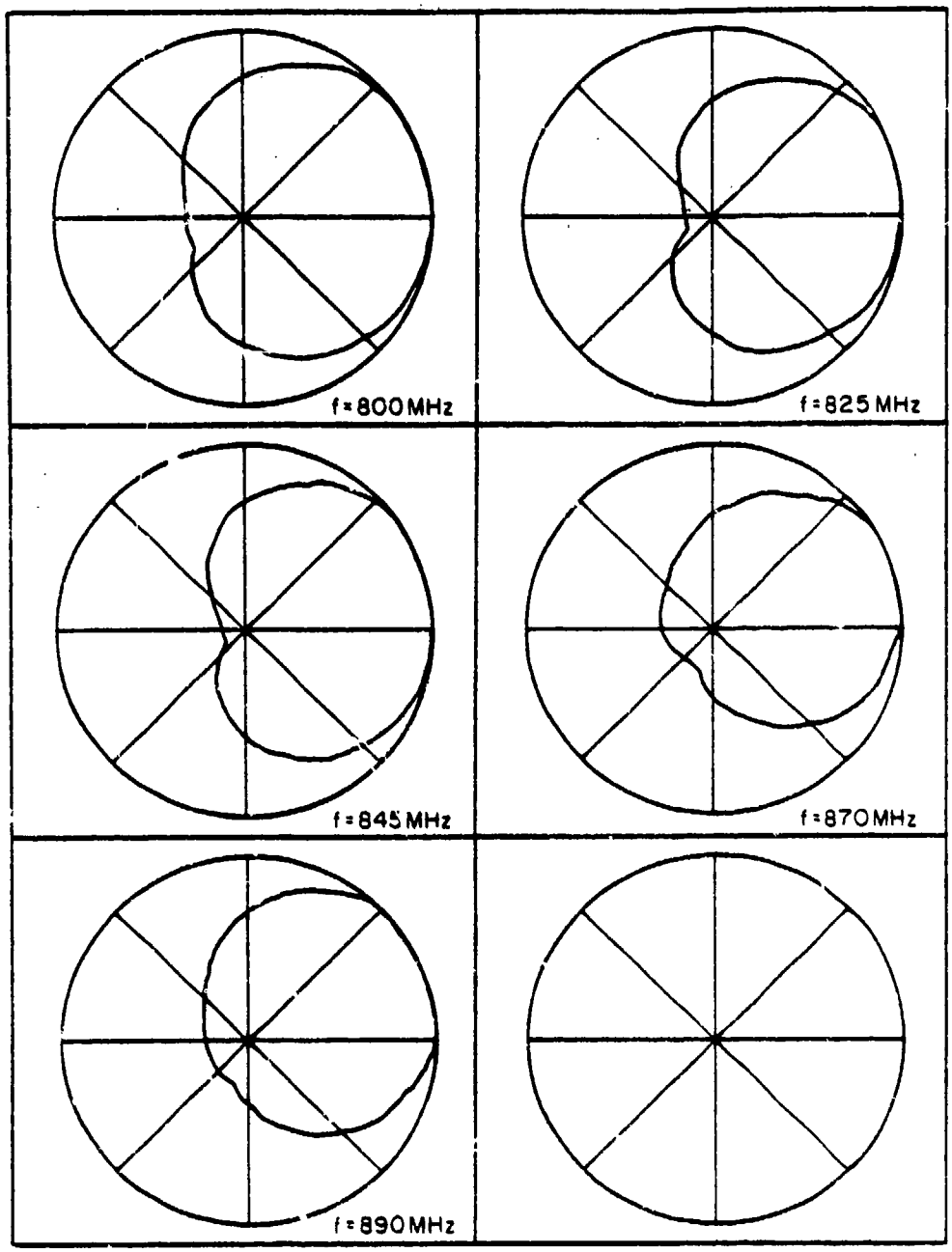

Fig. 4. Azimuthal radiation patterns for the monopole-slot antenna shown in Fig. 2

Since the best overall performance of the low-profile hybrid-slot antenna was observed when operating near a cavity resonance, the second monopole-slot antenna was designed to operate in the vicinity of the TE_{101} cavity resonance [6]. It was constructed using two sheets of 3/16 in. thick, single-clad Rexolite 2200 board and a 50-ohm stripline feed. The dimensions of the cavity were 4.2 in. by 9.0 in. and its TE_{101} resonance was calculated to be 962 MHz. The best performance of this antenna was achieved using a conical monopole and linear slot whose dimensions are given below.

Conical Monopole	Slot
Height = 1.0 in.	Width = 0.3 in.
Radius at Truncation = 1.2 in.	Length = 7.6 in.

The antenna is shown in Figure 5.

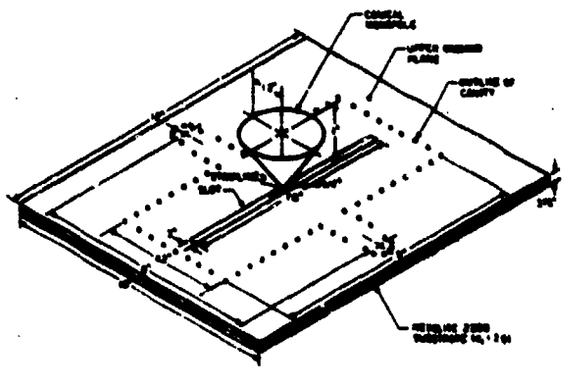

Fig. 5. Conical-monopole-linear-slot antenna designed to operate below the TE_{101} cavity resonance

Inspection of Figure 6 reveals that VSWR is less than 1.75:1 at the input over the entire operating band while the efficiency is in excess of 72 percent over this band. The efficiency of this antenna over the transmit band ranges from 81 percent at 825 MHz to 85 percent at 845 MHz. The effects of the TE_{101} cavity resonance appear suppressed in both the s_{11} and s_{12} loci.

The patterns, which are shown in Figure 7, indicate a slight dominance by the slot over the entire operating band. F/B ratios over the receive band range from 13 dB at 870 MHz to 28 dB at 890 MHz.

Thus far it has been demonstated that a medium-profile monopole-slot antenna can be made to operate satisfactorily over the land-mobile communication band from 825 to 890 MHz. The remainder of this work evaluates the performance of a selection-diversity mobile receiving system which employs a two-port antenna, such as the ones discussed, in a multipath environment.

3. A RECEPTION SCHEME FOR UHF LAND-MOBILE COMMUNICATION WHICH INCORPORATES A MONOPOLE-SLOT ANTENNA AT THE MOBILE

3.1 Background

Systems designed to operate over the 800-900 MHz band in an urban environment are very susceptible to wide signal variations, also known as fades, which arise due to the presence of many obstructions in the propagation path between the transmitter and

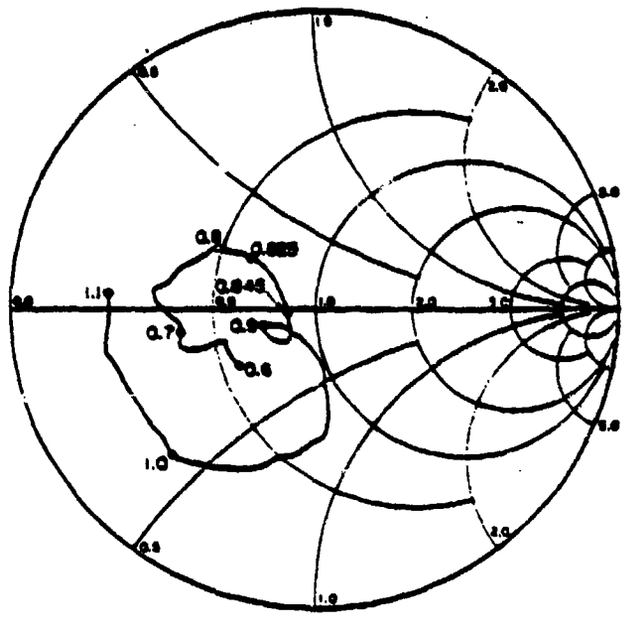

(a) s_{11}

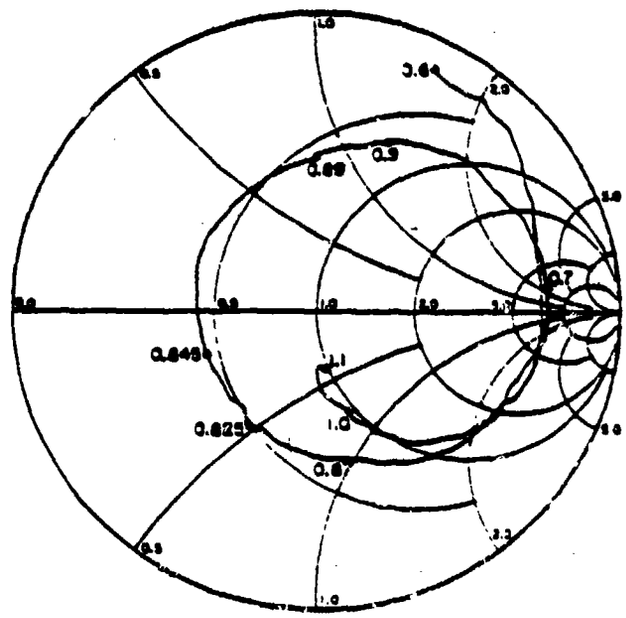

(b) s_{21}

Fig. 6 s_{11} and s_{21} for the conical-monopole-linear-slot antenna shown in Fig. 5

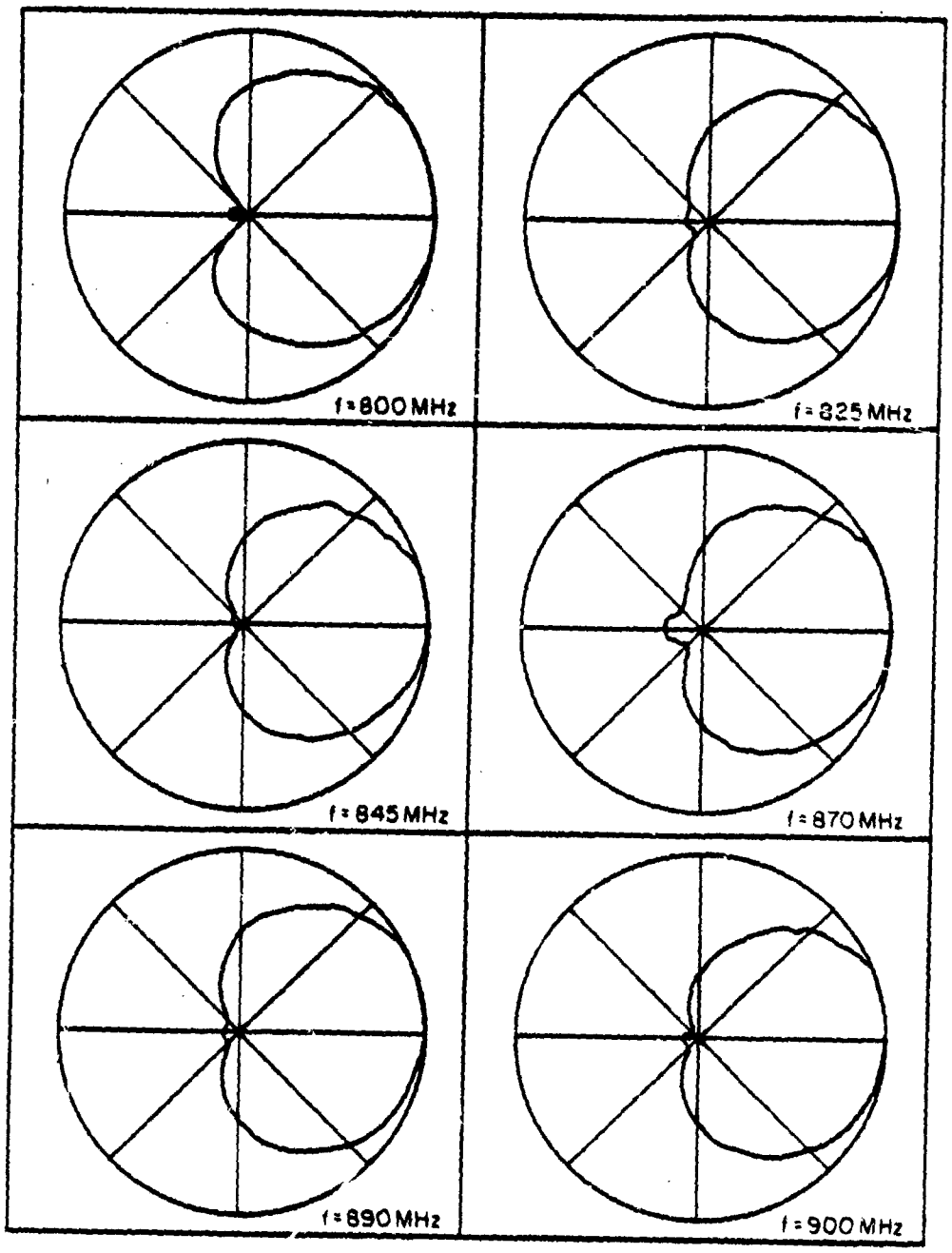

Fig. 7 Azimuthal radiation patterns for the conical-monopole-linear-slot antenna shown in Fig. 5

receiver. Degradation of system performance resulting from this type of fading must be overcome by means other than an increase in transmitted power.

Described herein is a method of combating multipath fading which makes use of the fact that the resultant vertical electric field and horizontal magnetic fields of the incident waves at the same point in space are uncorralated, and therefore, statistically independent [7], [8].

3.2 A SIMPLE, DYNAMIC MODEL OF MULTIPATH FADING IN URBAN LAND-MOBILE COMMUNICATION

The following is a widely used model of a land-mobile communication system in an urban environment that has been validated experimentally. The reader is referred to Jakes [7] for a more detailed description.

Figure 8 depicts a mobile unit, in which the receiver is located, traveling with velocity, v, in the x-direction. A vertically polarized wave ($\overline{E} = \hat{z}\, E_z$) is transmitted from a fixed location, scattered, and received by the mobile. The transmitted signal is an unmodulated carrier of angular frequency, ω_c. The scattered waves are assumed to be vertically polarized and originating from fixed scatterers at random locations. The resultants of the three field components seen by the mobile can be derived

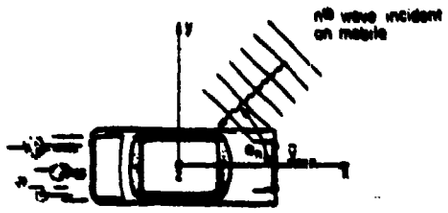

Fig. 8. Plane-wave incident on mobile

from the sum of N vertically polarized plane waves, incident azimuthally at random angles, α_n, with respect to the velocity of the mobile.* It is assumed that no direct propagation path between the transmitter and the mobile exists. This is often the case in an urban environment.

Due to the random orientation and location of the mobile, the phases of the incident waves, ϕ_n, are assumed to be a random set which are uniformly distributed between 0 and 2π. The relative time delays of the incident waves are assumed to be of the same order of magnitude as the reciprocal of the carrier frequency. The distribution of incident power, $p(\alpha)$, is assumed to be uni-

*The assumption that all waves incident on the mobile are confined to azimuthal propagation paths is valid when one considers the fact that in reality the incident waves are confined to a relatively small spread in elevation. Experimental data presented by both Jakes [7] and Clarke [8] affirm the validity of this assumption. The effects of elevation angle have been accounted for in Aulin's model [9].

form over the range in arrival angle between $-\pi$ and π*. One must note, however, that the amplitudes, phases, and arrival angles of the incoming waves are assumed to be statistically independent, and therefore, independent random variables.

The Doppler shift in angular frequency, ω_n, of each of the incident waves is found by projecting the respective wave vector onto the velocity vector of the mobile.

$$\omega_n = -\bar{\beta}_n \cdot \bar{v} = \beta v \cos \alpha_n \tag{2}$$

where $\bar{\beta}_n = \beta[-\hat{x} \cos \alpha_n - \hat{y} \sin \alpha_n]$, $\beta = \frac{2\pi f_c}{c}$, f_c = carrier frequency, and $c = 3 \times 10^8$ m/sec.

The resultant electric and magnetic fields at the origin of the coordinate system on the mobile are expressed in phasor form by Equations (3) through (5)

$$E_z = \mathrm{Re}\left\{\left[E_0 \sum_{n=1}^{N} c_n e^{j\theta_n(t)} \right] e^{j\omega_c t}\right\} \tag{3}$$

*The uniform distribution of incident power over arrival angle does not imply that waves will be incident on the mobile from every direction at all times. Instead, it implies that since the position and orientation of the mobile with respect to the transmitter and scatterers are unknown and randomly changing, the likelihood that a wave is incident from any given angle, α_n, is the same. The distribution, $p(\alpha)$, can, therefore, be interpreted as an average, as opposed to an instantaneous description of a stochastic process.

$$H_x = \mathrm{Re}\left\{\left[-\frac{E_o}{\eta_o}\sum_{n=1}^{N} c_n \sin\alpha_n\, e^{j\theta_n(t)}\right] e^{j\omega_c t}\right\} \qquad (4)$$

$$H_y = \mathrm{Re}\left\{\left[\frac{E_o}{\eta_o}\sum_{n=1}^{N} c_n \cos\alpha_n\, e^{j\theta_n(t)}\right] e^{j\omega_c t}\right\} \qquad (5)$$

where

E_o = amplitude of the transmitted wave

η_o = intrinsic impedance of free space

c_n = the amplitude of the n^{th} incident wave relative to the amplitude of the transmitted wave

$\theta_n(t)$ = phase of the n^{th} incident wave

$$\theta_n(t) = \omega_n t + \phi_n \qquad -\beta v \le \omega_n \le \beta v \qquad (6)$$

Equation (6) reveals that the phase of each of the incident waves is determined by two independent random variables; the Doppler frequency, ω_n, and the phase, ϕ_n. Since both $\omega_n t$ and ϕ_n are uniformly distributed on $[0,2\pi]$, $\theta_n(t)$ is also a random variable which is uniformly distributed on $[0,2\pi]$. The time-varying nature of the random phase, $\theta_n(t)$, results in a random frequency modulation of the received signal, which has adverse effects on the performance of the system [7].

The amplitudes of the incident waves are normalized such that $\sum_{n=1}^{N} \langle c_n^2 \rangle = 1$, where $\langle\ \rangle$ denotes the ensemble average of a random variable.

Since the maximum Doppler shift is small when compared to the carrier frequency, the incident fields are narrow-band random processes. When the number of incident waves, N, is assumed to be large, the resultant fields are described by a normal (Gaussian) probability density function as predicted by the central limit theorem. The Gaussian model assumes a constant mean received signal power since it describes an ergodic process [10]. The validity of this model results from the fact that local signal variations are much more abrupt than variations due to a change in the position of the mobile.

The resultant fields incident on the mobile (Equations (3)-(5)) are usually discussed in terms of random modulation of the carrier, ω_c. Due to the random, time-varying nature of the phases of the incident waves, both the amplitude and frequency of the carrier are randomly modulated. The design of a communication system is influenced to a great extent by the signal-to-noise ratio (SNR) of the received signal; thus the distributions of the random envelopes of the resultant incident field components are of great importance. It has been shown that the random envelopes are Rayleigh distributed; thus their densities are of the form given by Equation (7) [10].

$$p(r) = \frac{2r}{(r_{rms})^2} e^{-(r/r_{rms})^2} \qquad r > 0 \qquad (7)$$

where r is the respective envelope, and r_{rms}, its root-mean-square value. The rms values of the envelopes of the resultant magnetic fields are less than the rms values of the envelopes of the resultant electric field by a factor of $1/\sqrt{2}$ [7].

When the envelope of one of the field components drops below its rms value, a fade is said to have occurred. Inspection of Equation (7) reveals that deep fades ($r \ll r_{rms}$) are much less likely to occur than shallower ones. This is an important characteristic of Rayleigh fading [7].

The rates at which fades occur have been shown to be proportional to both the velocity of the mobile and the carrier frequency. In addition, it has been shown that the rates of fading of the envelope of H_y are greater than the rates of fading of the envelope of E_z by a factor of 1.2 while the rates of fading of the envelope of H_x are less than those experienced by the envelope of E_z by a factor of 0.58 [7].

3.3 AN ILLUSTRATIVE EXAMPLE OF THE RAYLEIGH FADING PHENOMENON

To illustrate the effects of Rayleigh fading that one might encounter, an example is presented below. A mobile is traveling at a speed of 30 MPH through the center of a large city. The receiver in the mobile is tuned to receive a carrier at 880 MHz and no direct propagation path exists between the base station

and the mobile. A vertical whip (monopole) antenna which responds to the vertical electric field is positioned atop the vehicle. The maximum Doppler shift of the carrier frequency is about 79 Hz. The level crossing rate and average fade duration for 30 dB fades of the resultant electric field strength are 6.23 sec^{-1} and 160 μ-sec, respectively. If the speed of the mobile is increased to 60 MPH, the level crossing rate for 30 dB fades of the electric field strength is doubled to about 12.5 sec^{-1} and the average fade duration becomes about 80 μ-sec. This results in an annoying, if not devastating, effect on the performance of the receiver.

If a 10 GHz carrier is used, the effects are even more notable. For a mobile traveling at a speed of 30 MPH, the level crossing rate and average fade duration for 30 dB fades of the electric field strength are about 71 sec^{-1} and 14 μ-sec, respectively.

This example shows that the performance of a land-mobile communication system in an urban environment is severely hampered by the effects of Rayleigh fading due to multipath propagation. In the next section the grounds will be established for a receiving scheme which mitigates the effects of multipath propagation on the performance of such a system.

3.4 CORRELATION OF THE RESULTANT FIELD COMPONENTS AT A COMMON LOCATION ON THE MOBILE

In Section 3.2 differences were noted to exist between the level crossing rates and average durations of fades of the envelopes of the three resultant field components seen at the mobile. In addition to the difference in the Doppler effects on waves incident from different angles, the scatterers which give rise to these waves are randomly positioned in azimuth. Hence, both the amplitudes and phases of waves incident from different directions are statistically independent, and therefore uncorrelated. Since the resultants of the three field-components seen by the mobile are linear combinations of the respective field components of waves incident from different directions, both the envelopes and phases of all three resultant field components are statistically independent at a common location on the mobile [7], [8].

3.5 PERFORMANCE CHARACTERISTICS OF THE MONOPOLE-SLOT ANTENNA IN A RAYLEIGH-FADING (URBAN) ENVIRONMENT

The monopole-slot antenna which was described in Section 2 contains elements which respond to the vertical electric fields and either the x- or y-component of the magnetic fields of incident plane waves. The monopole, which is an electric dipole, responds to E_z; and the slot, which is a magnetic dipole, responds to either H_x or H_y, depending on how the antenna is

oriented. Hence, the signals appearing at the two ports of the monopole-slot antenna are linear combinations of the resultants of E_z and either H_x or H_y [6]. Since the level crossing rates of the envelope of H_x are less than those of the envelope of H_y by a factor of $\frac{1}{\sqrt{3}}$ it appears favorable to orient the monopole-slot antenna atop the mobile so it responds to E_z and H_x. This is accomplished by orienting the slot so its length is along the centerline of the vehicle as shown in Figure 9. The signals appearing at ports 1 and 2 of this antenna are denoted by f and g, respectively, and are expressed in Equations (8) and (9).

$$\text{Port 1: } f = k[E_z + aH_x] \text{ Volts} \tag{8}$$

$$\text{Port 2: } g = k[E_z - aH_x] \text{ Volts} \tag{9}$$

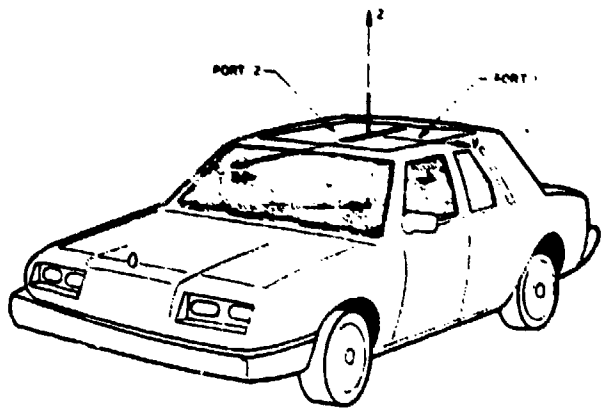

Fig. 9. Orientation of the monopole-slot antenna on a mobile

The constant, a, in (8)-(9), has been shown to be the ratio of the moment of the equivalent magnetic current of the slot to the moment of the equivalent electric current of the monopole and its image. The dimension of "a" is ohms. The constant, k, which also appears in (8)-(9) is the moment of the equivalent electric current of the monopole, normalized by one ampere; its dimension is length. For a monopole-slot antenna designed to operate near the resonances of both radiating elements, the parameter, a, can be calculated from the front-to-back (F/B) ratio of its azimuthal radiation pattern* [6]. Typical values of "a" for a well-designed monopole-slot antenna range from 0.6 η_0 when the monopole is slightly dominant (F/B ≈ 12 dB) to 1.5 η_0 when the slot is slightly dominant (F/B ≈ 14 dB). A cardioid pattern is observed when the parameter, a, is exactly equal to η_0. A plot of the F/B ratio vs. a/η_0 is shown in Figure 10.

It was previously noted that signals due to E_z, H_x, and H_y, individually, would be statistically independent. Signals due to E_z and H_x individually can be obtained from the output ports of the monopole-slot of Figure 9 by introducing f and g into the sum and difference ports of a 180° hybrid. In what follows, it is

*The operating band of the monopole-slot as a land-mobile communications antenna is defined as the band over which it is most efficient. Experimental data suggest that this band is centered about the frequency at which both the monopole and slot are resonant.

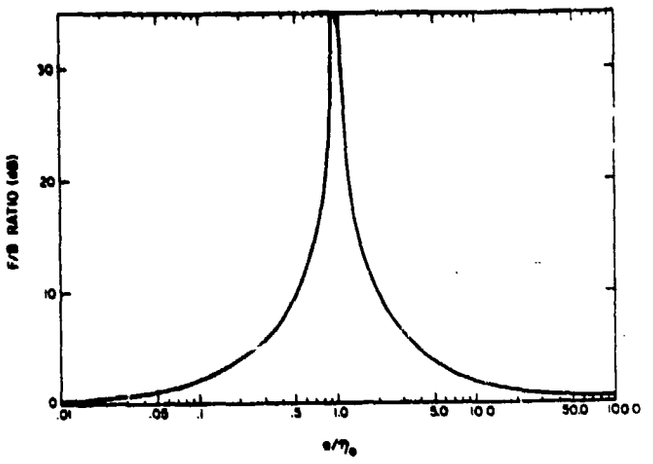

Fig. 10. Front-to-back ratio vs. a/η_0 over the operating band of a well-designed monopole-slot antenna

shown that this additional signal processing is unnecessary.**

Since the resultant components proportional to E_z and H_x of the signals at ports 1 and 2 of the monopole-slot are uncorrelated, the performance of this antenna as a receiving antenna in a Rayleigh-fading environment is most easily assessed by examining the statistical properties of the two signals, f and g. When Equations (8)-(9) are divided by the constant, k, expressions for the normalized signals at ports 1 and 2 are obtained.

$$\text{Port 1:} \quad F = f/k = E_z + aH_x \tag{10}$$

$$\text{Port 2:} \quad G = g/k = E_z - aH_x \tag{11}$$

**Although reception does not require isolation of the signal components proportioned to E_z and H_x, respectively, transmission using only the omnidirectional pattern of the monopole is often desirable. This is accomplished by feeding both ports of the monopole-slot antenna with signals equal in both magnitude and phase, and can be done either by feeding only the sum port of the hybrid or by using an in-line power divider with equal phase shift on the two arms.

The resultants of E_z and aH_x are compler Gaussian random processes with zero-mean; hence, the two signals, F and G, are also Gaussian variates with zero-mean.

The envelopes of F and G, denoted by r_F and r_G, respectively, are Rayleigh distributed with identical densities which are given by Equation (12).

$$p(r) = \frac{r}{\sigma^2} e^{-r^2/2\sigma^2} \tag{12}$$

where r = either r_F or r_G. The rms values of both envelopes are

$$r_{rms} = E_o \sqrt{1 + \frac{a^2}{2\eta_o^2}} \tag{13}$$

which is greater than the rms values of the envelopes of either E_z or H_x. An identical result would have been obtained, had the monopole-slot been oriented to respond to E_z and H_y [6].

The biggest advantage gained by using a monopole-slot antenna in a land-mobile communication system which must operate in an urban environment becomes apparent when the correlation between the envelopes of the two signals, F and G, is analyzed. The correlation between the two envelopes is usually expresses in terms of their correlation coefficient, ρ [10]. It can be shown that the correlation coefficient of the two envelopes, r_F and r_G, is

$$\rho = \left[\frac{2\eta_o^2 - a^2}{2\eta_o^2 + a^2} \right]^2 , \tag{14}$$

which is highly dependent on the parameter, a.* A plot of ρ versus a/η_o is shown in Figure 11. Inspection of Equation (14) reveals that if the monopole-slot is designed in such a way that $a = \sqrt{2}\ \eta_o$, the fading properties of its two outputs, f and g, will be independent.** [6]

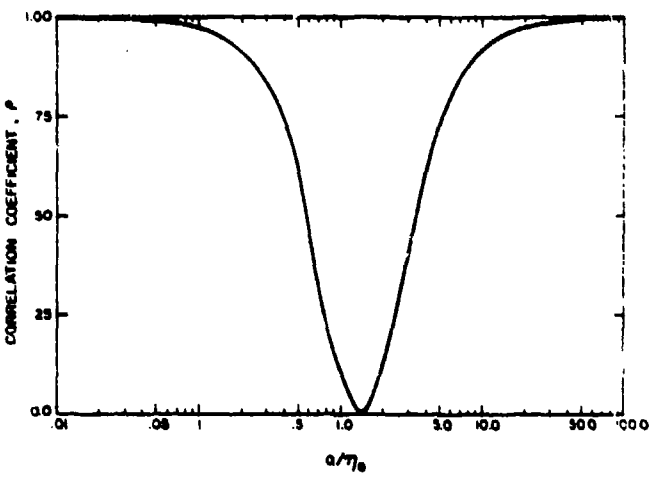

Fig. 11. Correlation coefficient, ρ, of $|F|^2$ and $|G|^2$ vs. a/η_o

For a well-designed monopole-slot antenna, the value of "a" ranges from 0.6 η_o for slight domination by the monopole, to 1.5

*The same correlation coefficient results when the monopole-slot is oriented to respond to E_z and H_y.

**When $a = \sqrt{2}\ \eta_o$, the azimuthal radiation pattern has a F/B ratio of ≈ 15 dB and the slot is slightly dominant. Also, for this value of "a" the rms values of the components of F and G due to the incident electric fields equal the rms values of the components due to the incident magnetic fields. In Section 3.2, it was noted that the rms value of either the x-or y-component of the incident magnetic fields less than the rms value of the incident electric field by a factor of $1/\sqrt{2}$; hence when the slot is slightly dominant, this difference is offset and the two signal components have the same rms value.

η_o for slight domination by the slot. The corresponding limits of the correlation coefficient of r_F and r_G for a well-designed monopole-slot are therefore 0.48 and 0.003, respectively. This implies that the outputs of a monopole-slot antenna whose slot is slightly dominant will have fading characteristics which are almost independent.

In the next section, it is shown how the performance of a land-mobile communication receiver which must operate in an urban environment can be greatly improved by connecting the two outputs of a well-designed monopole-slot antenna to a selection-diversity combiner prior to detection.

3.6 A SELECTION-DIVERSITY RECEPTION SCHEME WHICH INCORPORATES THE MONOPOLE-SLOT ANTENNA

In the selection-diversity combiner, the signals from two or more diversity branches are sampled and the branch containing the strongest signal is connected to the receiver.* Ideally, the fading properties of the signals are statistically independent; however, it has been demonstrated that nearly optimal performance of a dual-branch, selection-diversity combiner is obtained as long as the magnitude of the correlation coefficient of the two enve-

*In practice, the branch containing the strongest signal plus noise is connected to the receiver. However, it is assumed that the average noise power at both ports of a monopole-slot antenna is equal; thus the switching in this case is assumed to be governed by the signal strengths at both inputs to the selection combiner.

lopes is within the range from 0 to 0.5 [11]. Since the correlation coefficient of the envelopes of the two outputs of a well-designed monopole-slot antenna does indeed fall within the range from 0 to 0.5, the analysis is shown only for a dual-diversity system in which the two envelopes are assumed to be uncorrelated.

The envelopes of both signals available from the monopole-slot antenna are Rayleigh distributed. The probability that either envelope is less than or equal to a specified level, R, is

$$P(r \leq R) \int_0^R p(r)\, dr = 1 - e^{-\rho^2}, \tag{15}$$

where

$$\rho = \frac{R}{\sqrt{2}\,\sigma} = \frac{R}{r_{rms}}, \text{ and } r_{rms} \text{ denotes the rms value of either } r_F \text{ or } r_G.$$

When the two signals available from a monopole-slot antenna are used as inputs to an ideal dual-diversity selection combiner, the evelope of the signal at the output of the combiner is expressed as

$$r_o = \max \{r_F, r_G\}. \tag{16}$$

Since r_F and r_G can be assumed to be statistically independent, it can be shown that the probability that the envelope of the signal at the output of the combiner is less than or equal to the same specified value, R, is

$$P(r_o \leq R) = [1-e^{-1.5\rho_o^2}]^2, \tag{17}$$

where $\rho_o = R/r_{orms}$ and $r_{orms} = \sqrt{1.5}\, r_{rms}$ [28].

Inspection of Equation (17) leads to two very important conclusions. The rms value of the envelope of the signal at the output of an ideal dual-diversity selection combiner is greater than the rms value of the envelope of either of its inputs by a factor of $\sqrt{1.5}$. Also, the probability of encountering deep fades in the envelope of the signal at the output of the combiner is much less than the probability of encountering fades of equal depth on either of its inputs. For example, the probability of encountering a 30 dB fade in the envelope of either output of a monopole-slot antenna is about 10^{-3}, while the probability of encountering a fade of equal depth in the envelope of the output of the combiner is about 2×10^{-6}; this represents an improvement over the former case by about 500-fold! The virtual elimination of deep fades at the output of an ideal dual-diversity selection combiner represents the potential for a substantial reduction in the transmitted power required for the satisfactory operation of land-mobile communication system.

Thus far, it has been assumed that the selection combiner is ideal; that is, it performs a noiseless switching function. In reality, of course, this is not true. In addition to the shot noise and thermal noise which are inherent in an electronic switch, the switching action itself produces phase transients in

the combiner output. In FM systems, switching transients are interpreted as large instantaneous frequency shifts and are audible at the detector output as "pops". Although it is impossible to eliminate switching transients from the output of a selection combiner, it is possible to reduce their effects on system performance. By switching branches only when deep fades are in progress, a technique known as "switch-and-stay", and by using less abrupt switching techniques such as "soft-switching", the contamination of the receiver input can be minimized [7]. In many applications, it is also desirable to apply a short blanking pulse to the detector output whenever switching occurs. This eliminates the annoying "clicks" from the audio channel [7].

If selection combining proves to be unacceptable as a means for improving system performance, other methods of diversity combining can be used. One such method is equal-gain diversity combining [7], [11]. This method offers nearly optimal performance and it is not impaired by switching transients. However, equal gain combining is a form of post-detection diversity combining and it therefore requires much more complex circuitry than selection combining. Due to its inherent complexity, equal-gain combining results in a system which is also more costly than one which incorporates selection combining.

Conclusion

It has been demonstrated that a medium-profile monopole-slot antenna can be made to operate satisfactorily over the band from 800-900 MHz. Two design were considered and tested; one in which the monopole was capacitively top-loaded, and the other in which a conical monople was used. The height of the monopole in both cases was one inch. Throughout the operating band (825-890 MHz), both antennas maintained relatively stable impedance characteristics; the maximum VSWR was 2:1 on a 50-ohm feed line. The efficiencies of both antennas were in excess of 80% over the operating band, and F/B ratios in the azimuthal radiation patterns in excess of 12 dB were maintained.

The monopole-slot antenna responds to both the vertical electric fields and either the x or y component of the horizontal magnetic fields of the incident waves in a linear fashion. Hence, it was herein demonstrated that the monopole-slot antenna could be designed to provide two outputs with independent fading properties. With this in mind, it was shown that if the two signals appearing as outputs of a well-designed monopole-slot antenna are processed using an ideal dual-diversity selection combiner, the potential exists for a vast improvement in system performance. Deep fades in the output of such a combiner can be virtually eliminated; thus the potential also exists for substantial savings in the transmitted power required to maintain satis-

factory system operation. The selection combiner does have one major drawback in that it introduces phase transients to its output; thus the switching action must carefully controlled and monitored if the benefits of selection combining are to be realized.

References

[1]. Mayes, P. E., Warren, W. T., and Wiesenmeyer, F. M. (1972) The monopole-slot, an electrically small DF and communications antenna. Abstracts of the Twentieth Annual Symposium, USAF Antenna Research and Development Program, AFAL, Wright-Patterson AFB, Ohio and the University of Illinois at Urbana-Champaign.

[2]. Paschen, D. A. (1982) The stripline fed monopole-slot antenna as an array element. M.S. Thesis, Department of Electrical Engineering, University of Illinois at Urbana-Champaign.

[3]. Cwik, T. A. (1981) The Hybrid Slot Antenna, M.S. Thesis, Department of Electrical Engineering, University of Illinois at Urbana-Champaign.

[4]. Mayes, P. E., Warren, W. T., Homa, M., and Mandeville, W. T. (1971) Techniques for increasing the efficiency bandwidth for the monopole-slot antenna. Abstracts of the Twenty-First Annual Symposium, USAF Antenna Research and Development Program, AFAL, Wright-Patterson AFB, Ohio and the University of Illinois at Urbana-Champaign.

[5]. Mayes, P. E., Warren, W. T., and Wiesenmeyer, F. M. (1972) The monopole-slot: a small broad-band unidirectional antenna. IEEE Trans. Antennas Propagat. 20(No. 4): 489-493.

[6]. Halpern, B. M. (1982) The monopole-slot as a two-port diversity antenna for mobile radio. M.S. Thesis, Department of Electrical Engineering, University of Illinois at Urbana-Champaign.

[7]. Jakes, W. C., Jr. (1974) Microwave Mobile Communications, J. Wiley and Sons, New York.

[8]. Clarke, R. H. (1968) A statistical theory of mobile radio reception. Bell Syst. Tech. J. 47 (No. 6): 957-1000.

[9]. Aulin, T. (1979) A modified model for the fading signal at a mobile radio channel. IEEE Trans. Veh. Technol., 28(No. 3): 182-203.

[10]. Papoulis, A. (1965) Probability, Random Variables, and Stochastic Processes, McGraw-Hill, New York.

[11]. Schwartz, M, Bennett, W. R., and Stein, S. (1966) Communication Systems and Techniques, McGraw-Hill, New York.

AD P001107

MILLIMETER-WAVE ANTENNA DEVELOPMENT*

R. B. Dybdal
Electronics Research Laboratory
The Aerospace Corporation

ABSTRACT

Antenna technology for millimeter-wave system applications has had a long history of development on a component level, and as systems evolve from planning to implementation, a significant amount of development effort remains to realize practical designs. The antenna itself offers a key rationale for millimeter-wave systems, which stems from the ability to achieve high angular resolution from physically small dimensions. A review of technology demonstrations is provided, and identification of future development areas will be made.

I. INTRODUCTION

The impetus for millimeter-wave systems basically stems from the wide available bandwidths which have been allocated (Ref.1), the desire for increased survivability, spectral crowding at lower frequencies, and reduced sensitivity to propagation limitations compared with electro-optical systems. In the radar arena, the millimeter-wave spectrum allocations offer the ability to effectively utilize wide bandwidth, high resolution waveforms and frequency diversity to suppress clutter, reduce detectability, enhance immunity to countermeasure systems, and improve tracking performance. The ability to achieve high resolution from compact antenna designs enhances tracking performance, and combined with diffuse clutter characteristics, is particularly attractive in the low elevation angle regime. The most effective use of millimeter radar designs basically capitalize on the ability to achieve resolution in angle, range, and target discrimination. Passive sidelobe control techniques

8/20/82

* This work was supported under Air Force Contract No. F04701-82-C-0083.

which become more practical with the compact dimensions offer enhanced immunity to intentional and mutual interference and LPI (Low Probability of Intercept) performance to enhance system survivability. The rationale developed from these considerations lead to the attractiveness of millimeter-wave systems.

A wide variety of antenna development has been demonstrated to date which forms a basis for the practical implementation of millimeter-wave systems. The generic design problems of millimeter-wave antennas compared with microwave designs include a greater mechanical and electrical precision in their manufacture, increased sensitivity to ohmic losses, and a limited availability of commercial components. The wide bandwidth spectral allocations represent a small percentage bandwidth at millimeter wavelengths, which generally establishes the difficulty of component development. Future development efforts for radar antenna applications include increased emphasis on tracking systems, the integration of electronics into the antenna structure, designs which offer variable beamwidth performance, and ancillary components such as radomes.

II. TECHNOLOGY STATUS

The purpose of this section is to survey the development of reflector, lens, array, and horn technologies. The compact physical size of millimeter-wave antennas for specified gain levels is illustrated in Fig. 1 for a typical 55% efficiency. The small physical size provides tractability to meet system objectives which would be difficult to achieve at lower frequencies.

A. Reflector Designs

One well-developed millimeter-wave antenna technology is reflector designs, and a wide variety of techniques have been demonstrated in both the electrical design and in manufacturing techniques. The current state of the art for fabrication of reflector surfaces has developed to the point that 80 dB gain levels may be realized, and more modest gain levels can be achieved

with off-the-shelf reflectors. The mechanical tolerance requirements for reflector designs are well understood (Ref. 2), and reflector antennas with values of D/ε of 2×10^4 are available commercially in diameters up to 4 ft. Because of the high sensitivity to ohmic loss (1 dB/ft at 90 GHz for straight waveguide), Cassegrain feed systems are particularly attractive to minimize the length of waveguide runs.

An example of passive sidelobe control techniques for reflectors is shown in Fig. 2. In this design (Ref. 3), an absorber-lined tunnel is used to surround the aperture, and functions to reduce the sidelobe contributions which result from edge diffraction, spillover, feed radiation and blockage. This development is an example of a technique which is practical at millimeter wavelengths because of the small physical size. The addition of a tunnel of this proportion to a large reflector would be limited by practical consideration.

B. Lens Designs

Lens designs are also more attractive at millimeter wavelengths. Dielectric designs, which are unattractive at lower frequencies because of excessive dielectric weight, become more feasible at higher frequencies, particularly because the outer lens surface can be utilized as a radome. An example of this design may be found in Ref. 4, which also illustrates the capability to realize extremely wide bandwidth operation inherent in this design concept.

Inhomogeneous lens designs have also been demonstrated at millimeter wavelengths. A geodesic Luneberg lens which fed a reflector was used in the AN/MPS-29 radar (Ref. 5) in the late 1950s.

C. Array Designs

The development of millimeter array antenna designs has lagged other technologies. This situation results in part from a limited phase shifter technology basis and because compact antennas lead to more feasible mechanical pointing techniques without the necessity for electronic beam steering required at lower frequencies. Waveguide slot arrays have been demonstrated (Ref. 6). Current research efforts are being devoted to the integration of electronics into the antenna structure, a situation which results in part from the limited power output of solid state power amplifiers.

D. Horn Designs

Millimeter wave horn antenna technology is also well developed. Standard gain horns are commercially available over the complete millimeter-wave spectrum. Gain levels up to 30 db are available with lens correction techniques to result in compact designs. High performance horn designs, including diagonal, dual-mode, and corrugated configurations, have also been demonstrated. Electroforming techniques are particularly attractive to achieve precise manufacturing.

III. DEVELOPMENT ISSUES

One area which will require increased development for radar applications is tracking systems. Monopulse horn techniques have been demonstrated at millimeter wave frequencies, but further development in this area is warranted.

The development of techniques for changing the beamwidth of an antenna is attractive for some applications. While very small beamwidths are highly desirable for target resolution performance, smaller beamwidths are needed to enhance system acquisition.

The development of ancillary components is also needed for practical system designs. Radome technology is a particularly challenging effort because configurations with high mechanical strengths are necessarily several wavelengths thick. The development of rotary joints is another area which would benefit from further efforts. RF components, such as duplexers, represent yet another area required for radar designs.

IV. MEASUREMENT CONSIDERATIONS

While millimeter antenna systems are physically compact, the far field range needed for their evaluation is quite large, as illustrated in Fig. 3. This situation coupled with the limited sensitivity of conventional instrumentation, results in a challenging measurement problem to characterize the antenna over the high dynamic range inherent in millimeter-wave antenna designs. The

sensitivity of conventional instrumentation is limited because harmonic mixing techniques are used to extend the frequency range of conventional receivers. A phase-locked system has been developed to utilize a fundamental mixer to recover the sensitivity lost in the harmonic mixing process (Ref. 7); a 30 dB sensitivity increase was demonstrated at Ka-band frequencies.

V. SUMMARY

A brief summary of millimeter-wave antenna technology has been presented. On a component level, reflector and horn techniques have had the most extensive demonstrations followed by lens designs; array antenna technology lags other areas. The demonstrations to date form a good basis to project future system performance and development effort is required to meet the objectives for practical applications. Further development of ancillary components is warranted. Measurement techniques for millimeter-wave antennas will provide challenges for future development.

REFERENCES

1. ....., Joint Special Issue on the 1979 World Administrative Radio Conference, IEEE Trans Communications COM-29, August 1981.

2. J. Ruze, "Antenna Tolerance Theory - A Review," Proc. IEEE 54, pp. 633-640, April 1966.

3. R. B. Dybdal and H. E. King, "Performance of Reflector Antennas with Absorber-Lined Tunnels," 1979 IEEE International Symposium on Antennas and Propagation, Seattle, WA, pp. 714-717, June 18-22, 1979.

4. W. Rotman and J. C. Lee, "Dielectric Lens Antenna for EHF Airborne Satellite Communication Terminals," Lincoln Lab Tech Report 592, February 16, 1982.

5. M. W. Long, W. K. Rivers, and J. C. Buterworth, "Combat Surveillance Radar AN/MPS-29 (XE-1)",6th Tri-Service Radar Symposium Record pp. 230-244.

6. C. A. Strider, "Millimeter-Wave Planar Arrays," 1974 Millimeter-Wave Techniques Conference NELC San Diego, CA pp. B6-1-11, March 26-28, 1974.

7. R. B. Dybdal, T. T. Mori and H. E. King, "High Sensitivity Millimeter-Wave Instrumentation," 1981 IEEE International Symposium on Antennas and Propagation, Los Angeles, CA pp. 119-122, June 16-19, 1981.

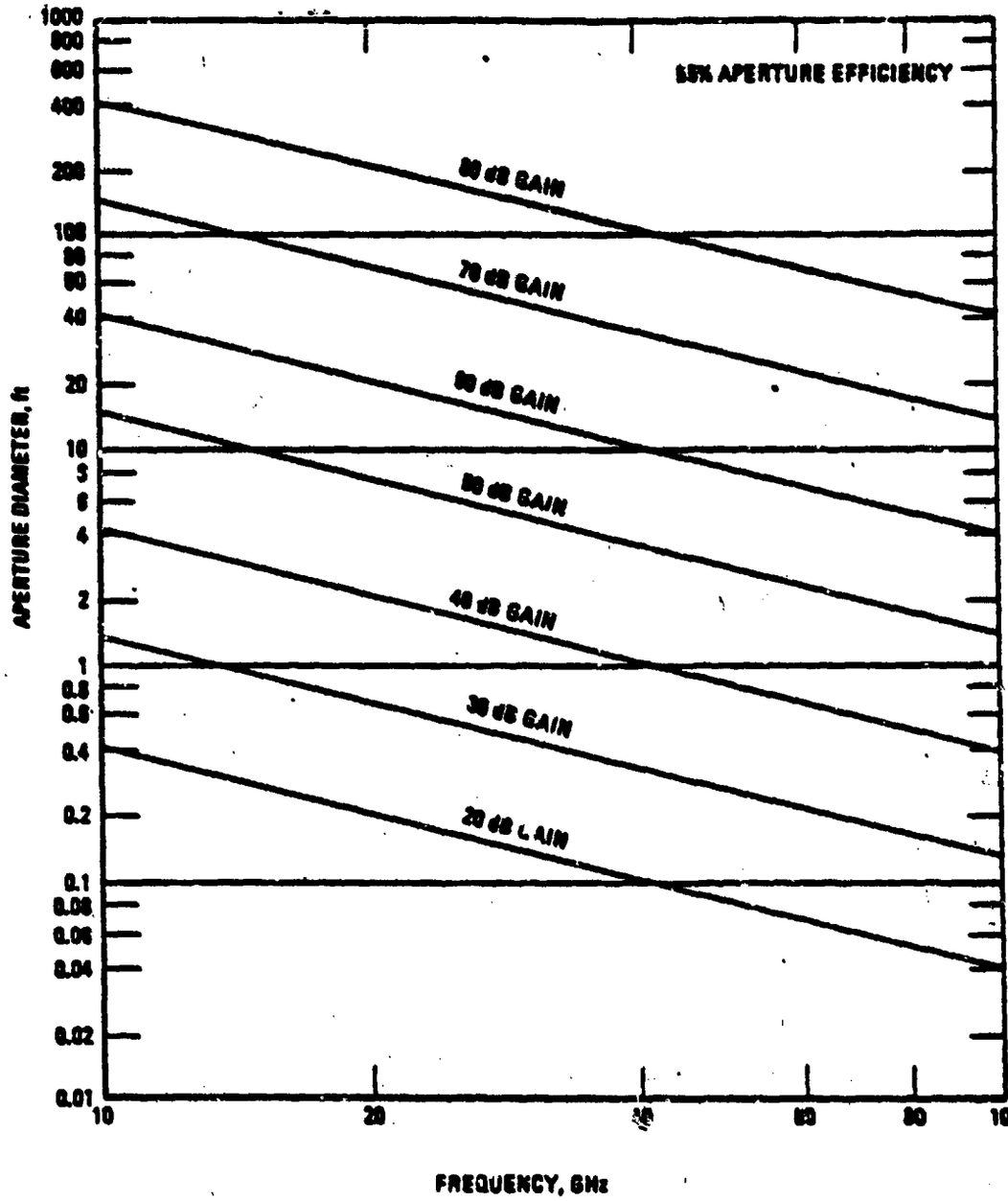

Fig. 1. Representative Antenna Dimensions for a Given Gain Level as a Function of Frequency

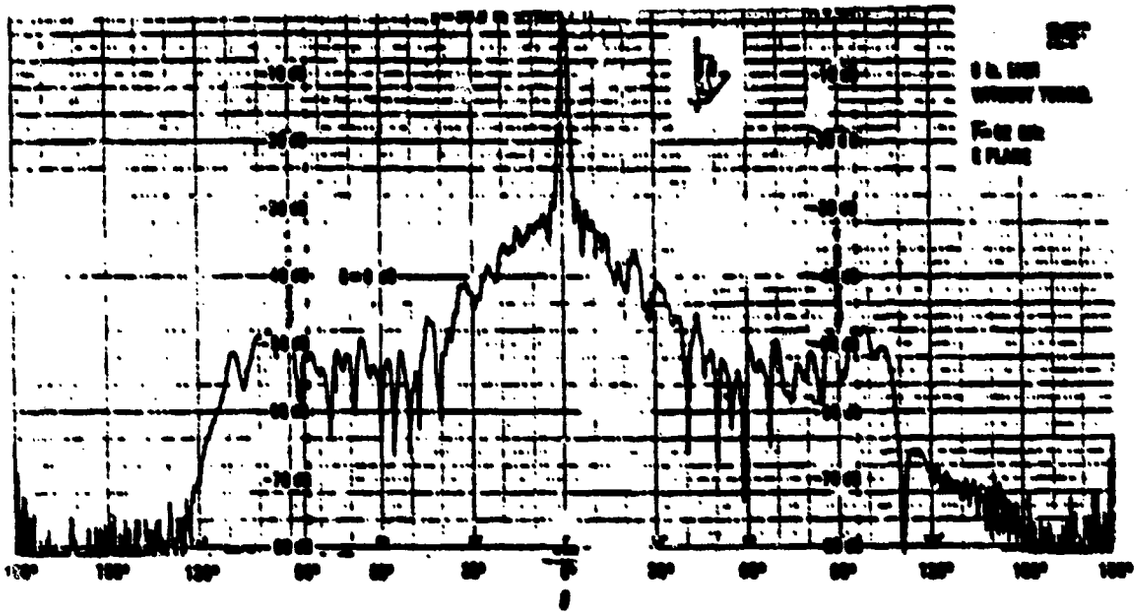

(a) E-Plane Without Tunnel

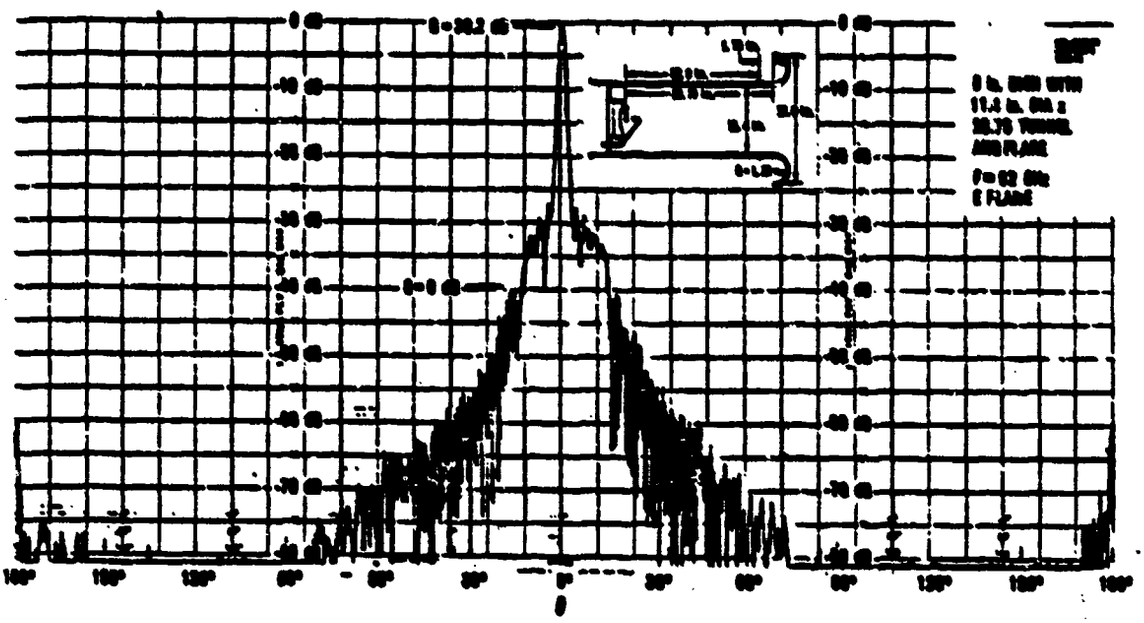

(b) E-Plane With Tunnel

Fig. 2. 92 GHz Measurements of a 6 in Reflector With and Without Absorber-Lined Tunnel

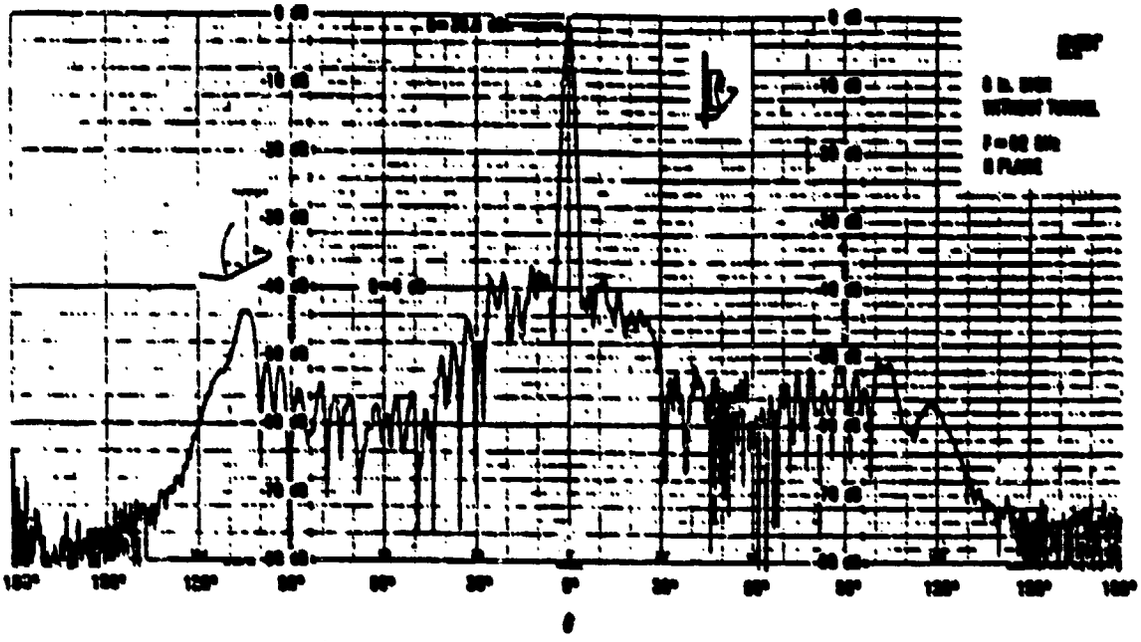

(c) H-Plane Without Tunnel

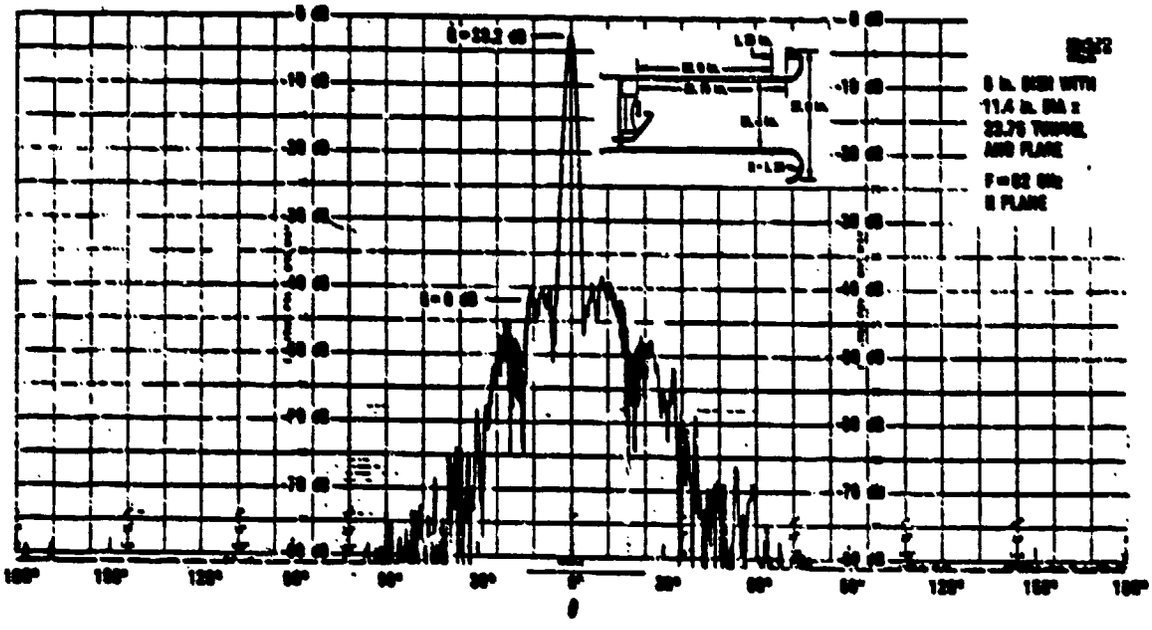

(d) H-Plane With Tunnel

Fig. 2 cont. 92 GHz Measurements of a 6 in Reflector With and Without Absorber-Lined Tunnel

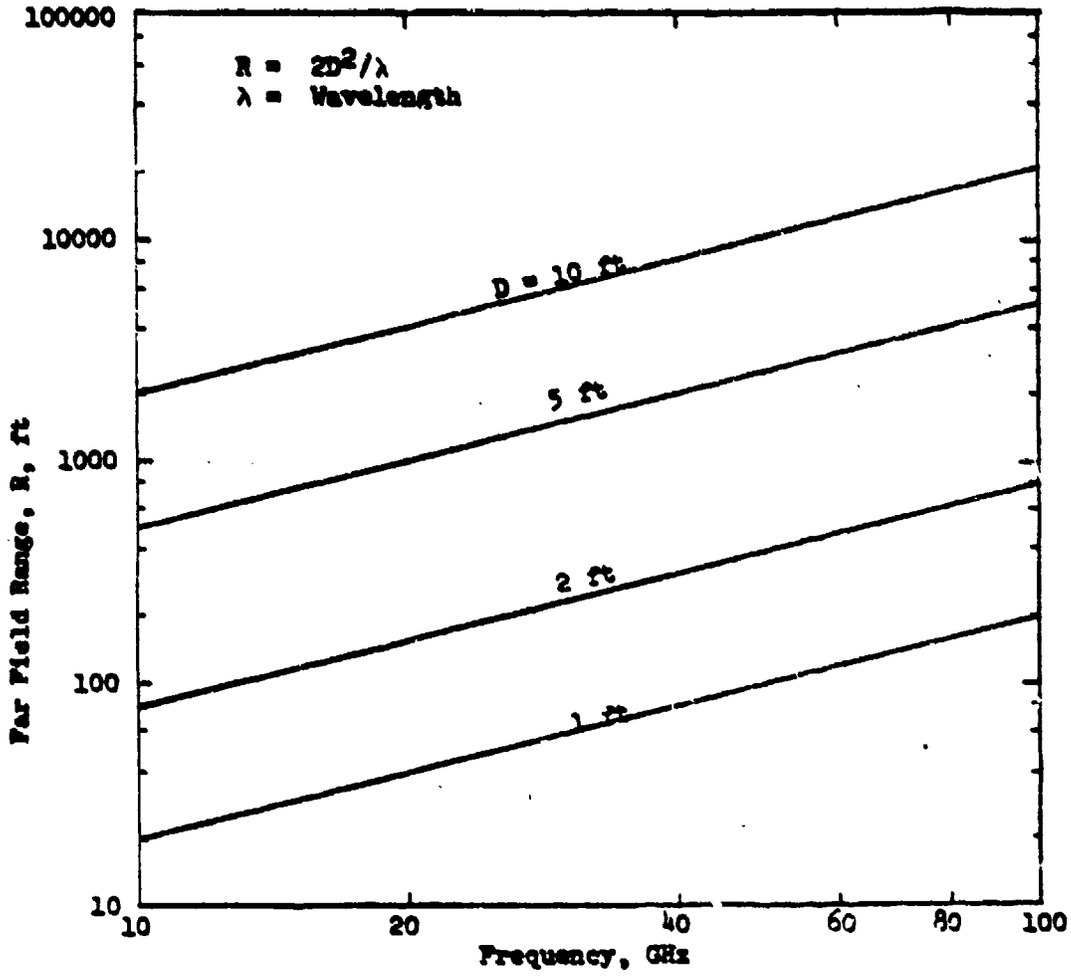

Fig. 3. Far Field Range Requirements

Dupe of AD-B060 584L

94 GHz ANTENNA TECHNIQUES

Oren B. Kesler
Texas Instruments Incorporated
Equipment Group
Dallas, Texas 75266

ABSTRACT

A summary of a study is given to devise, develop, and demonstrate 94 GHz flat plate antenna/array configurations that are mechanically steerable over 45° in both axes through use of low cost gimbal mechanisms. Emphasis is placed on low cost, weight, and volume, while providing antenna configurations that possess a high degree of reproducibility in manufacture. Antennas under consideration incorporate integral dual axes monopulse networks and are in the 5 to 6 inch diameter size range.

94 GHz ANTENNA TECHNIQUES

1.0 Introduction

Researchers have been investigating millimeter wave antennas for a number of years with the hopes of mass producing low cost, high performance antennas. Such antennas are possible in the frequency range of 40 GHz and below. Above 40 GHz examples of low cost mass produced antennas do not exist. Attempts to scale low frequency antenna designs to the atmospheric window at 94 GHz have not been entirely successful for a number of reasons. The primary reasons for the difficulties at 94 GHz are the lack of suitable materials and close tolerances which require large capital equipment investments not readily available to researchers because the payoff has not been proven. Also, low level funding has not been conducive to an encompassing investigation utilizing multiple disciplines. The purpose of this paper is to summarize the results of an investigation of 94 GHz antenna techniques[1]. During the investigation, emphasis was placed on identifying concepts that would lend themselves to quality, low cost, production.

The objective of this investigation is to devise, develop, and demonstrate 94 GHz four lobe monopulse antennas that are mechanically steerable over ± 45° in both axes through use of low cost gimbal mechanisms. Emphasis is placed on cost, weight, and volume. This effort includes a study of currently employed or technically feasible

low cost 94 GHz antenna techniques.

The antenna performance goals given in Table 1 represent the technical definition of the problem. These goals define a challenging problem if all are to be achieved and if the unspecified monopulse parameters are to be optimized. Accordingly, a fresh approach in examining the problem has been taken. Not only have lower frequency methods been examined for extension, but also new approaches have been defined and examined.

Table 1: Antenna Performance Goals

Antenna Size	5-6" Diameter
Antenna Gain	40 dBi (w/uniform illum)
Sidelobes	-18 dB Difference pattern -20 dB Sum Pattern
Bandwidth	2%
Polarization	Linear-horizontal
Cross Polarized Response	-25 dB Max
Antenna Volume	30 Cubic inches
Scan Limits	± 45 Degrees

2.0 94 Ghz Antenna Issues

Two of the overriding issues are (1) the distribution of the energy from the source to the radiating aperture in a spatially coherent fashion, and (2) the high tolerances required. The first issue divides antennas into two categories, arrays and space fed apertures such as reflectors. The second issue is a factor in every conceivable antenna configuration because fabrication problems eli-

minate the possibility of scaling many lower frequency antenna designs. Desired tolerances are typically in the fractional mil range. Thus, fabrication approaches must be formulated before an antenna design may be considered viable. In light of these issues, the following approach to the techniques study has been taken: (1) examine transmission lines for antennas, (2) identify promising lines with respect to cost, producibility loss, etc., (3) conceive antenna approaches, (4) develop fabrication approaches for the antenna concepts, and (5) evaluate identified concepts.

Evaluated approaches include, the multimode microstrip feed twist reflector, the twelve element feed twist reflector, the waveguide feed twist reflector, the photolithographic array (see appendix A for a description), the waveguide array, and the groove guide array[1]. During the course of this work the following novel concepts for antenna application were developed; (1) multimode microstrip four lobe monopulse feed, (2) independent microstrip radiator and feed line for broader bandwidths, (3) parasitically excited microstrip elements, (4) slotline ground plane feed-throughs for multilayer application, and (5) microstrip to waveguide transitions using coax at millimeter frequencies.

3.0 Trade-Off Study

A number of technology trends or conclusions in the areas of transmission lines, arrays, and twist relectors resulted from the trade-off study.

The best dielectrics to be used in 94 GHz transmission lines are air, fused silica, alumina, duroid, and teflon. Air has the lowest loss but is more difficult to use in some transmission line configurations such as stripline. Fused silica and alumina allow high tolerance surface finishes so that accurate metalization and circuit etching can be achieved but they are more difficult to machine and cut. In some applications, the dielectric constants of fused silica and alumina are higher than desired. Duroid and teflon have relatively low loss but their mechanical and thermal characteristics are undesirable for 94 GHz circuits.

Closed metallic waveguides, inverted microstrip and groove guide[2,3] are the most attractive transmission lines for millimeter wave antennas[4]. Theoretical attenuations for WR-10 waveguide, groove guide (fused silica), and inverted microstrip (fused silica) are respectively 0.066 dB/inch, 0.169 dB/inch, and 0.28 dB/inch. Fabrication technique development is needed for waveguide and groove guide transmission lines with maintenance of tolerances as a major problem. Additional inverted microstrip parametric characteristics are needed for antenna design including the characteristic impedance, propagation constant, attenuation constant, and field distribution as a function of geometry and frequency.

The technology for six inch diameter 94 GHz antenna arrays is immature. Tolerance problems and the lack of fabrication techniques limit the development of waveguide and groove guide arrays. How-

ever, the waveguide and groove guide arrays are capable of low losses and photolithographic arrays have a low cost potential. Development of inverted microstrip circuitry, radiating elements, slotline layer coupling, and waveguide transitions are necessary. Losses for large arrays are not negligible. Development of photolithographic arrays, at this point in the state of millimeter wave technology, may be better suited at 35 GHz where losses and tolerance requirements are less, and practical rotary joints are available.

The best low cost antenna approach meeting the performance goals is the polarization twist reflector antenna, which does not require a rotary joint. The best high power millimeter wave antenna is a polarization twist reflector antenna with a waveguide comparator and feed shown in Figures 1 and 2 respectively. The comparator can be custom fabricated using presently available components. Costs for these components are moderate but will decrease when production levels warrant a reduction. The twist reflector with a twelve element microstrip feed shown in Figure 3 is a viable low cost antenna approach. Concept alternatives using inverted microstrip can reduce losses. After development of the feed has been achieved, the recurring costs appear to be low yielding a very attractive antenna approach. The twist reflector with a multimode microstrip monopulse feed is another potential low cost antenna approach. The feed produces optimal patterns, uses photolithograph fabrication techniques, and does not require a comparator

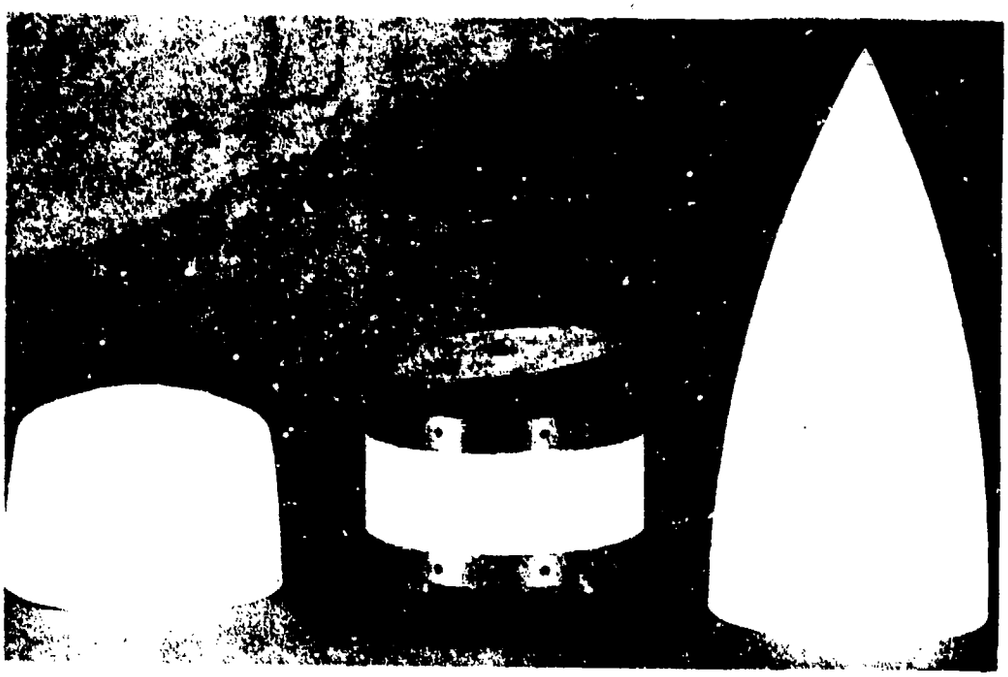

Figure 1. 94 GHz Twist Reflector and Radome

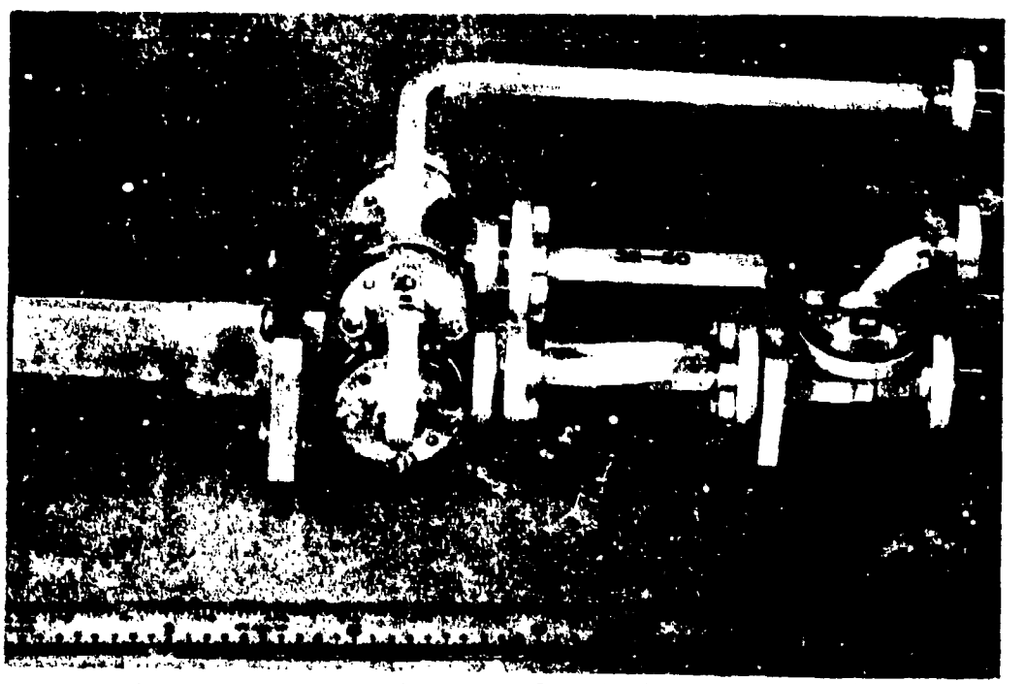

Figure 2. Four Lobe Monopulse Optiumum H-Plane Feed

network. Phase matching of cables, however, is required for this feed approach.

Since the multimode microstrip monopulse feed is a new concept, a description is given as follows. Figure 4 shows an exploded view of the feed in the simplest configuration. The aperture consists of four microstrip patch radiators on two sides of a dielectric layer. The upper rectangular patch, excited in the lowest mode with the lower large patch as a groundplane, produces the sum pattern. The lower three patches are separated from a ground plane by an air space or another dielectric layer. Dimensions of the larger patch are such that the resonant frequency of the second mode is the design frequency. This odd mode naturally produces the elevation difference pattern. The difference azimuth pattern is produced by exciting the remaining two patches out of phase. A choke around the sum feed probe, shown in the figure, minimizes the effects of the probe on the elevation difference patch. Figure 5 shows the top view of a slightly different arrangement where azimuth patches are fed by phase matched microstrip lines. In both of the previous figures standard waveguide to coax transition techniques were used. The feed configurations of the sum and elevation difference patches are asymmetrical causing asymmetrical amplitude and phase pattern tendencies over the band. Figure 6 shows a symmetrically excited configuration that guarantees symmetrical sum and elevation difference patterns as given in Figures 7

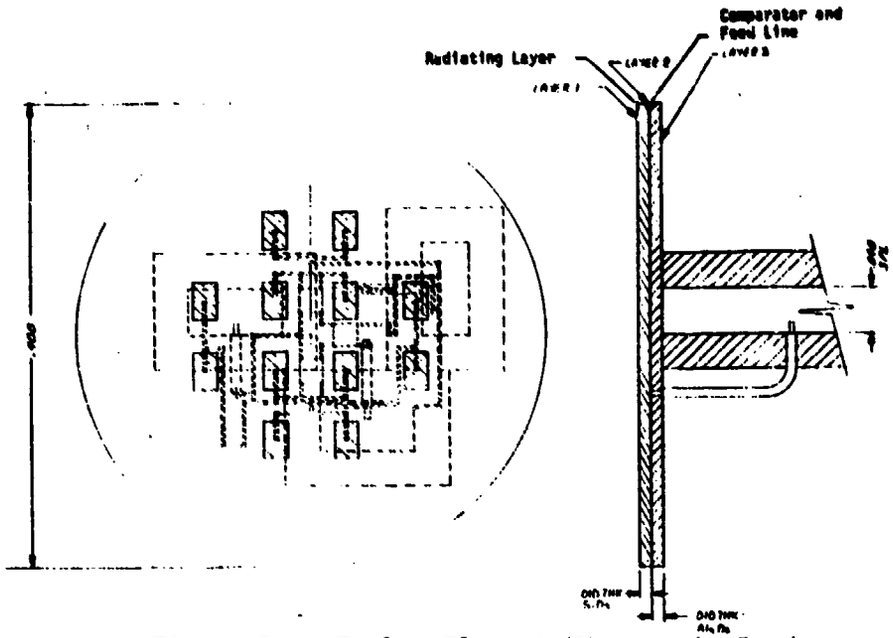

Figure 3. Twelve Element Microstrip Feed

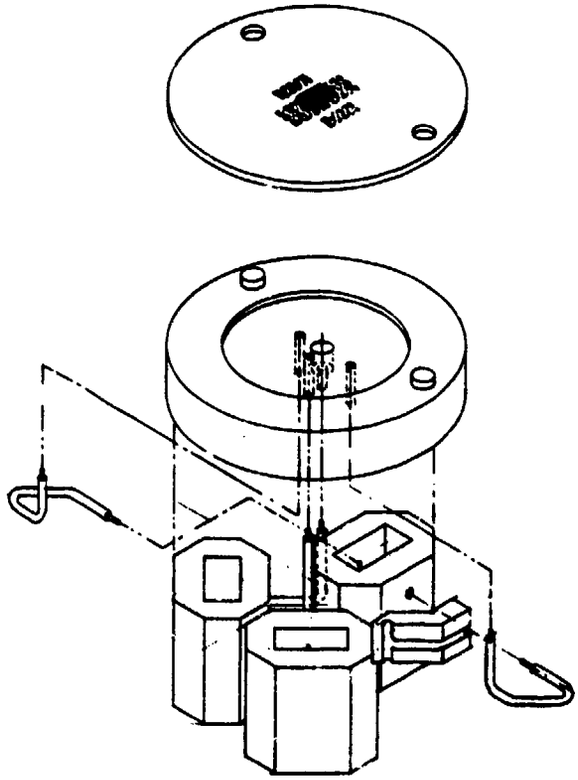

Figure 4. Multimoded Microstrip Monopulse Feed

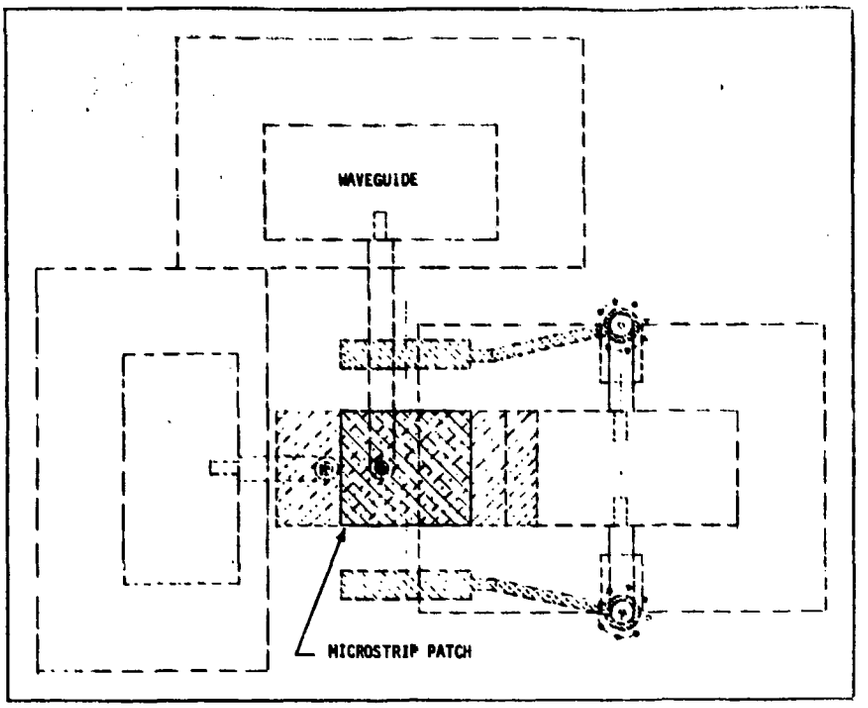

Figure 5. Multimode Microstrip with Improvement Phase Matching

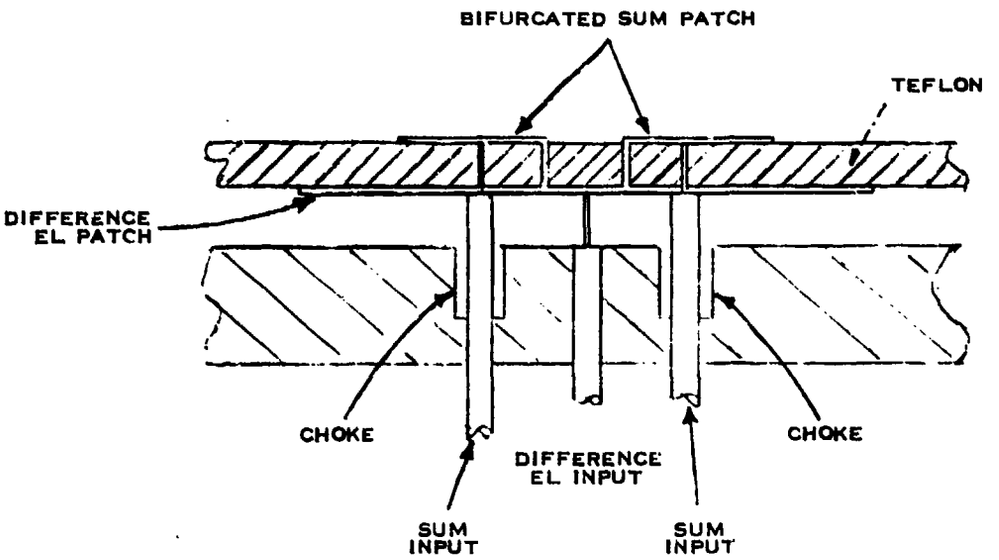

Figure 6. Symmetrical Sum and Difference Elevation Element Configuration

and 8 respectively. The large difference patch is excited at the center while the sum patch has been bifurcated into two half patches excited out of phase.

An overall comparison summary of the evaluated antenna approaches is given in Table 2. The comparison shows that theoretically the twist reflector patterns exhibit a small degradation with scan whereas the arrays have a slow delta pattern rolloff. The monopulse slope of the waveguide feed twist reflector depends upon the degree of feed optimality selected, i.e., multimode in two, one, or no planes[5]. Losses are generally higher and bandwidths generally lower for the arrays than the twist reflector. The arrays can meet the 2% bandwidth requirement while the twist reflector approaches can attain at least twice that value. The metallic lines on the twist reflector act as a natural polarization filter. The degree of cross polarization increase with increasing scan angle depends upon the reflector F/D and the curvature of the metallic lines. Overall a waveguide array with broadwall slots would yield the lowest cross-polarization level.

For this comparison, the arrays, with the exception of the inverted microstrip photolithographic array, are five inches in diameter. The inverted microstrip array is six inches in diameter because of its increased loss. The relectors also are six inches in diameter to accomodate the loss in gain caused by amplitude taper and spill-over.

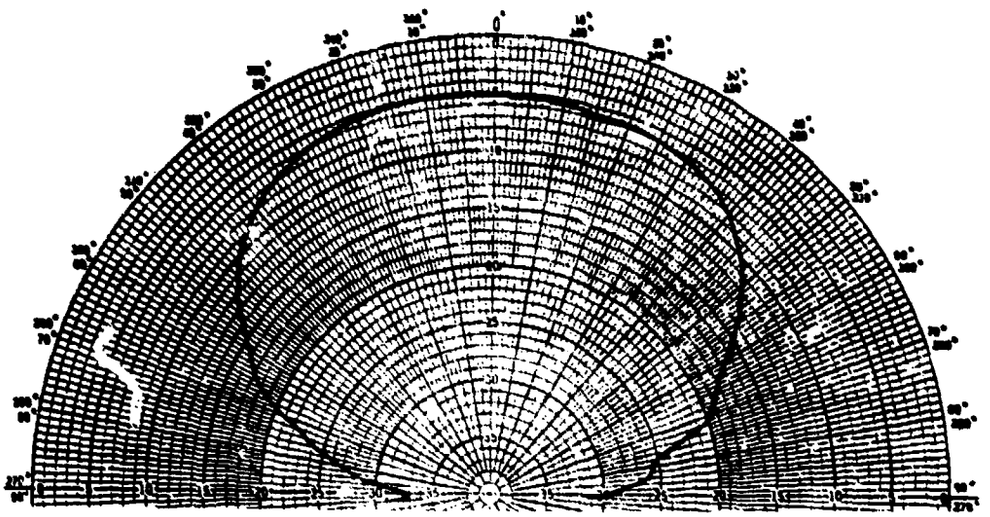

Figure 7. E-Plane Sum Pattern, 1.88 GHz

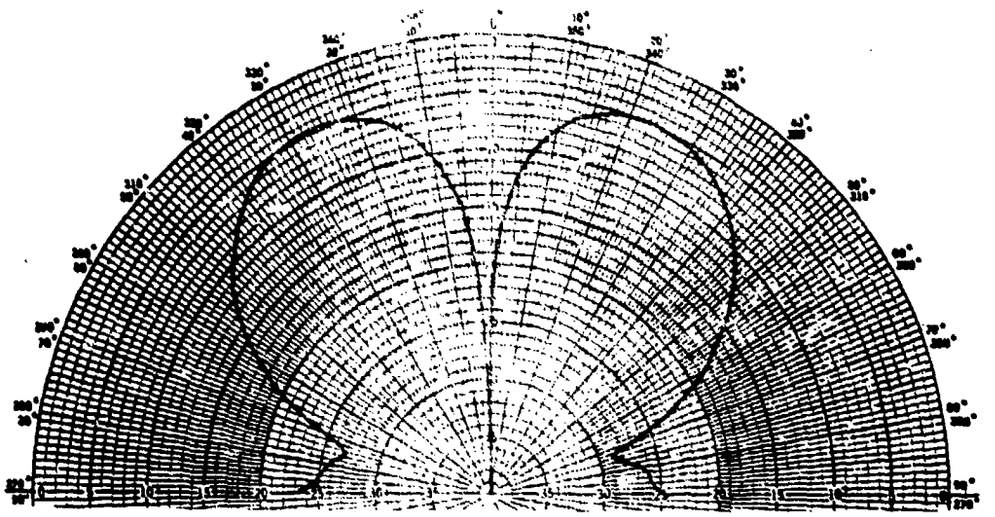

Figure 8. E-Plane Difference Elevation Pattern, 1.88 GHz

Table 2. Comparison of Antenna Approaches

CHARACTERISTIC	MULTIMODE MICROSTRIP POLARIZATION TWIST REFLECT.	T2 ELEMENT POLARIZATION TWIST REFLECTOR	WAVEGUIDE POLARIZATION TWIST REFLECT.	INVERTED MICROSTRIP ARRAY	SLOT WAVE GUIDE ARRAY	GROOVE GUIDE ARRAY
THEORETICAL PATTERN INTEGRITY	SMALL PATTERN DEGRADATION WITH SCAN	SMALL PATTERN DEGRADATION WITH SCAN	SMALL PATTERN DEGRADATION WITH SCAN	SLOW Δ ROLLOFF; DISCONTINUITY RADIATION	SLOW Δ ROLLOFF	SLOW Δ ROLLOFF
THEORETICAL LOSSES (dB) (EXCLUDING AMPLITUDE TAPER)	1.2	1.5	1.4	2.6	2.4	2.2
BANDWIDTH (%)	5	5	4.3	2	2	2
CROSSPOLARIZATION	LOW-SOME INCREASE WITH SCAN	LOW-SOME INCREASE WITH SCAN	LOW-SOME INCREASE WITH SCAN	DISCONTINUITY RADIATION	EXCELLENT DUE TO BROADWALL SLOTS	GOOD
APERTURE DIMENSIONS(IN)						
(DIAMETER)	6.0	6.0	6.0	6.0	5.0	5.0
(DEPTH)	2.6	2.6	2.6	0.6	0.3	0.3
(SWEPT DEPTH)	4.0	4.0	4.0	4.2	3.5	3.5
ANT. SWEPT VOL, W/O GIMBAL (IN^3)	104	104	104	110	85	85
WEIGHT(LBS) (W/O GIMBAL)	0.7	0.7	0.8	0.3	0.3	0.5
(WITH GIMBAL)	3.7	3.7	3.7	3.5	3.5	3.7
COMPLEXITY OF FAR (RELATIVE)	2.0	3.0	5.0	5.0	10.0	10.0
COST (RELATIVE)	2.0	3.0	6.0	5.0	10.0	9.0
COMPLEXITY OF GIMBAL MOTION (TO ACQUIRE ± 45° SCAN)	± 22.5°	± 22.5°	± 22.5°	± 45°	± 45°	± 45°
ROTARY JOINT REQUIRMT.	NO	NO	NO	YES	YES	YES

Finally, projections have been made on the complexity of fabrication and cost. The characteristics are evaluated using a scale from 1 to 10. Ten represents maximum cost and complexity. This is a subjective evaluation as perceived in today's technology. The cost is based upon a projection of recurring production costs and does not necessarily give a reasonable indication of the nonrecurring development costs. The array concepts rate the highest risk, primarily because the technology is immature or that there has been insufficient work in high tolerance antenna fabrication techniques. The waveguide array and the groove guide array are considered the most complex and costly. The inverted microstrip array and the waveguide feed polarization twist reflector rank lower in cost and complexity. And the twelve element feed twist reflector and the multimode feed twist reflector are the simplest and least costly.

4.0 Twist Reflector Results

The polarization twist reflector has several advantages that make it particularly attractive for 94 GHz application[6]. A high quality scanning antenna with relatively small swept volume is possible without the use of rotary joints or a complex feed manifold. Low sidelobe difference patterns with low cross-polarization over a wide frequency band is characteristic of the antenna. The cost is reduced since photolithographic fabrication techniques and common materials can be used.

A spherical bearing gimbal and several two axis four-bar linkage gimbals for the twist reflector are possible. Both hydraulic actuators or direct drive torque motors are useful twist reflector gimbal actuators. The direct drive torque motor, when used with the two axis four-bar linkage gimbal, is very attractive because of its form factor, simplicity, accuracy, and low cost. Encoders or resolvers/synchros should be used for the position pickoffs since potentiometers do not have the necessary accuracy for the small antenna beamwidths.

A five inch diameter polarization twist reflector was designed, fabricated and tested. This work confirmed the trade off study selection of the twist reflector. The scanning performance, including the gain, beamwidths, null depths, and the cross polarization, is very good. The comparator, custom fabricated using presently available waveguide components, has excellent isolation.

Experience has shown that the critical components, and in particular the feed, must be designed for the selected fabrication technique in order to readily maintain the required tolerances. Using the design to tolerance approach, an H-plane multimode waveguide feed was made that significantly improves the gain and matchs the principal plane beamwidths.

The geometry and dimensional parameters of a single H-plane waveguide modes is shown in Figure 9. The aperture guide width, a_2,

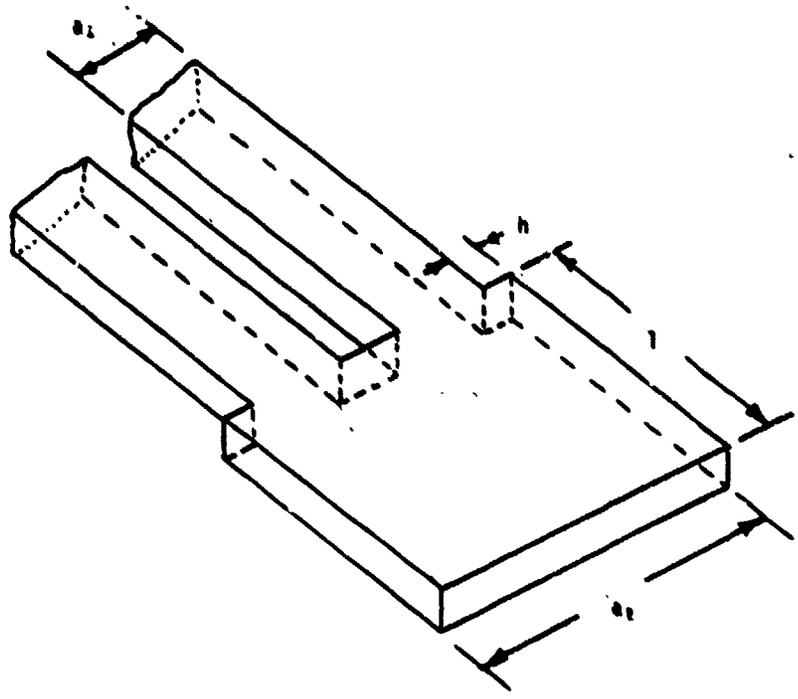

Figure 9. H-Plane Waveguide Moder

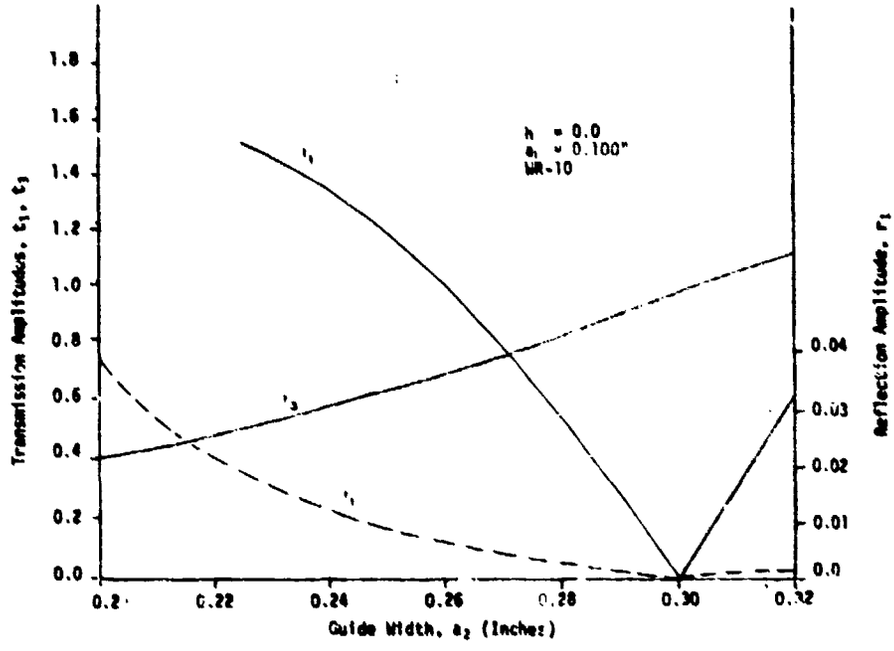

Figure 10. H-Plane Moder Transmission and Reflection at 94 GHz

is selected to propagate three modes and to produce the correct difference feed pattern edge taper. In addition, the parameters a_1, h, and a_2 are chosen to minimize the reflections back into the feed waveguides while yielding the desired transmission amplitude ratio t_3/t_1. The appropriately selected modal ratio t_3/t_1 in Figure 10 and the correct modal phasing determined by length l yields an optimum sum aperture distribution. The principal plane monopulse patterns of the twist reflector are shown in Figure 11. These patterns, scanned to the boresight, display excellent beamwidth, sidelobe, null depth and symmetry characteristics.

In addition to the waveguide feed, the twelve element microstrip feed and the multimode microstrip feed are attractive approaches and warrant further study. The polarization twist reflector, with one of the three feeds, will satisfy all of the antenna goals.

5.0 Recommendations For Further Work

This work has identified a number of promising 94 GHz antenna concepts. However, considerable work remains to define the key components of the concepts and to develop and verify the fabrication techniques. In particular, it is recommended that further investigations be made in photolithographic array techniques. The investigation should apply E-beam and photolithographic technologies, used in the fabrication of surface acoustic wave (SAW) devices where micron tolerances are commonplace, to the problem of fabricating low cost, high tolerance, antenna arrays. Equipment is currently avail-

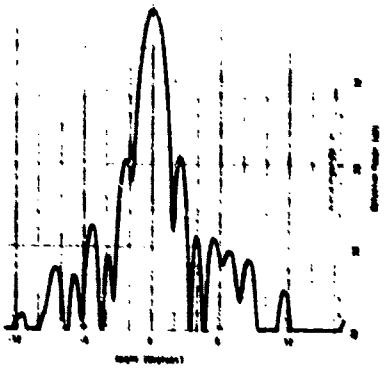

E-PLANE SUM PATTERN
(94 GHZ)

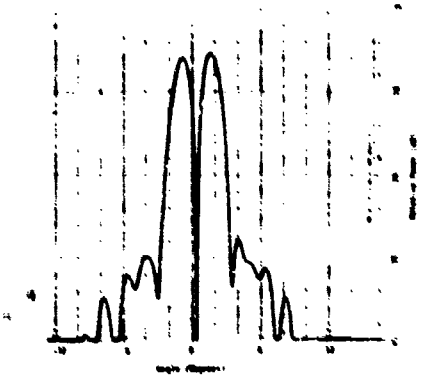

E-PLANE DIFFERENCE PATTERN
(94 GHZ)

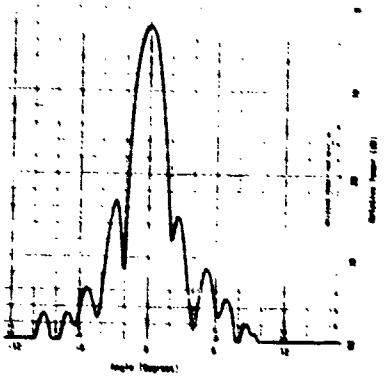

H-PLANE SUM PATTERN
(94 GHZ)

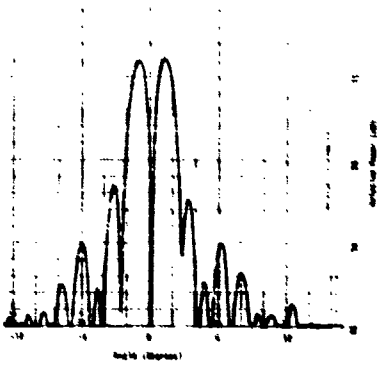

H-PLANE DIFFERENCE PATTERN
(94 GHZ)

Figure 11. Principal Plane Twist Reflector Patterns

able to make high tolerance masks for etching circuits using E-beam lithography and ion milling. Six inch diameter masks can be made with this equipment. Thus the capability exists to make very high tolerance millimeter wave networks of a diameter required for the antenna aperture. The recommended approach to develop a manifold fabrication technique uses,

1. Photolithography as with SAW devices
2. Layered construction
3. Substrates with high uniformity and smooth surfaces
4. Thin metalizations
5. Minimal number of feedthroughs
6. Capacitively coupled microstrip radiators.

This approach would be used to investigate the critical components,

1. Inverted microstrip transmission line and component characterizations
2. Layered coupling
3. Radiators
4. Transmission line to radiator coupling
5. Resonant subarrays.

Results of these investigations would benefit the development of the 12 element feed and the multimode microstrip feed for the polarization twist reflector.

It is recommended that a program be formulated to explore the application of this high tolerance technology to millimeter wave antennas

and networks. Such a program would make a significant contribution toward developing high performance, low cost millimeter wave antennas.

6.0 Acknowledgement

This work was partially supported by the Air Force Avionics Laboratory, Wright Patterson AFB, Ohio.

7.0 References

1. Kesler, O.B., and J. George (1981) 94 GHz Antenna Techniques, AFWAL-TR-80-1222.

2. Tischer, F.J., (1963) The Groove Guide, A Low-Loss Waveguide for Millimeter Waves, IEEE Trans. on MTT 11:291-296.

3. Yee, H.Y. and N.F. Audeh (1965) Wave Propagation in Groove Guides, Proc. of the National Elect. Conference. Vol. XXXI:18-23.

4. Rivera, J. and T Itoh (1979) A Comparative Study of Millimeter-Wave Transmission Lines, Microwave Laboratory Report No. 794, University of Texas

5. Hannan, P.W. 91961) Optimum Feeds for All Three Modes of a Monopulse Antenna II: Practice, IRE Trans. on Ant. and Prop. AP-9, No.5: 454-461.

6. Kesler, O.B., Montgomery, W.F., and C.C. Liu (1979) A Millimeter-Wave Scanning Antenna for Radar Application, Proc. of the 1979 Ant. Appl. Symp., Univ. of Ill./RADC.

7. Knorr, J.B. (1974) Slot-Line Transitions, IEEE Trans. on MTT, 22 No.5: 548-554.

APPENDIX A: Photolithographic Arrays

Photolithographic fabrication techniques have characteristics that are desirable for construction of 94 GHz antennas. Photolithography is potentially a low cost, high tolerance, and reproducible method. However, the use of photolithography is not sufficient to guarantee the success of a low cost 94 GHz antenna. Conventional microstrip and stripline array techniques without some modifications are not likely to succeed when applied to such large antennas. Thus a modified antenna approach, which will be called a photolithographic array, is defined as an antenna characterized by properties given in Table A-1. In addition to the use of photolithographic fabrication techniques, the array consists of a layered construction with a minimal number of interconnections.

Table A-1. Generic Photolithographic Array Features

Photolithographic Fab Techniques
Layered Construction
Homogeneous Substrates
Interconnections Minimal
High Tolerances
Reproducible
Low Cost

Figure A-1 shows an assembly drawing illustrating the array concept. The figure shows a back structure with three waveguide ports. The waveguides transition to transmission lines in the layered media via a small section of coax. The first layer contains the monopulse comparator and part of the power dividing manifold. Additional

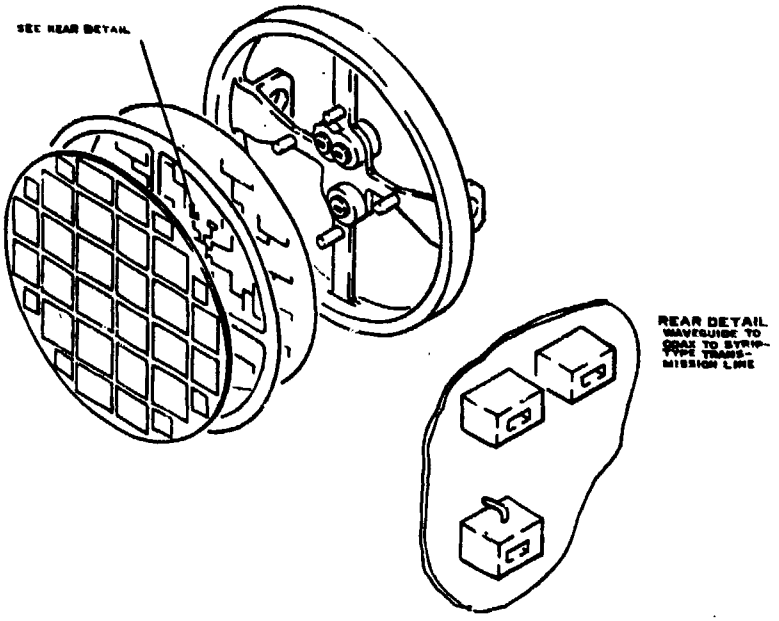

Figure A-1. 94 GHz Array Assembly

layers of power dividing manifolds may be included as required. Finally, there is a radiating aperture layer with perhaps some power division. Figures A-2 through A-6 give additional details of the concept. The array strongback mechanically holds the array in proper alignment and provides attachment points to the gimbal. The layered dielectric transmission media in this particular array are 0.010 inches thick fused silica, 0.010 inches thick air, and 0.015 inches thick fused silica. Air and fused silica are two low loss dielectric media whose uniformity and consistancy can be very accurately maintained. In addition, fused silica allows a highly polished and smooth surface. Then a thin metalization may be applied so that highly accurate components may be photolithographi-

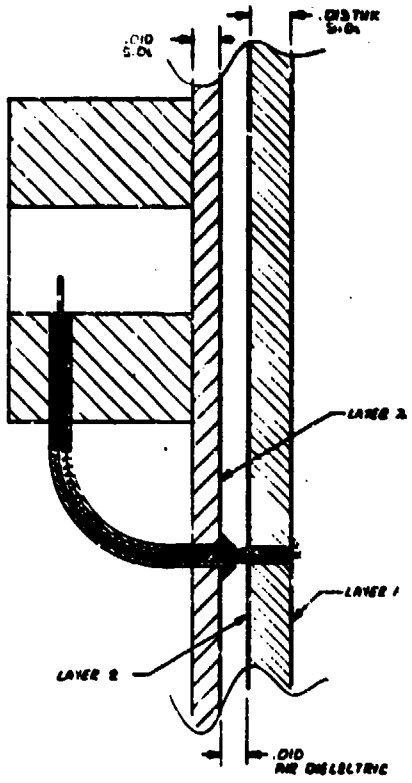

Figure A-2. Array Cross Section, Microstrip Radiators and Inverted Microstrip Feed

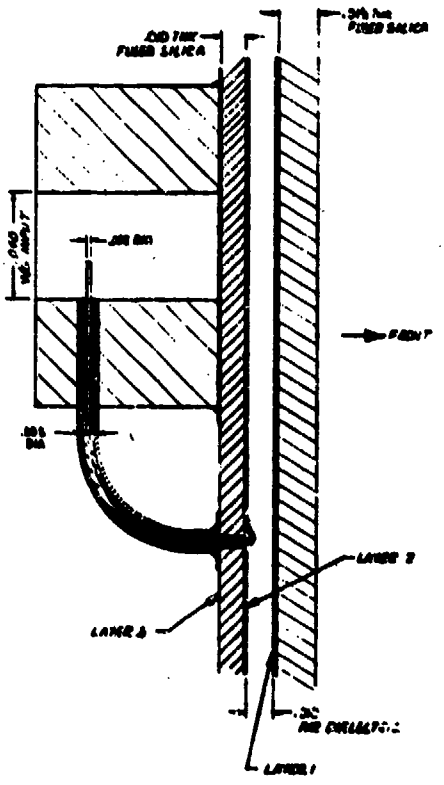

Figure A-3. Array Cross Section, Inverted Microstrip Radiators and Microstrip Feed

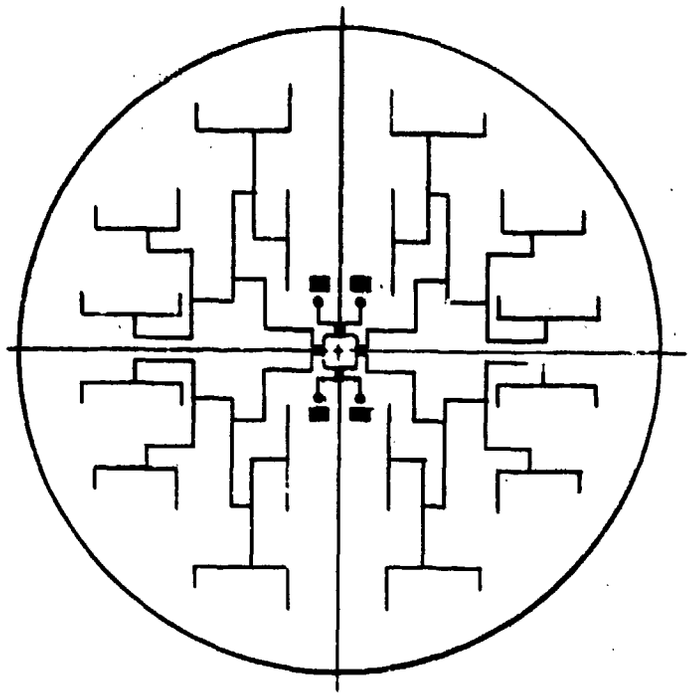

Figure A-4. Manifold/Comparator Layer

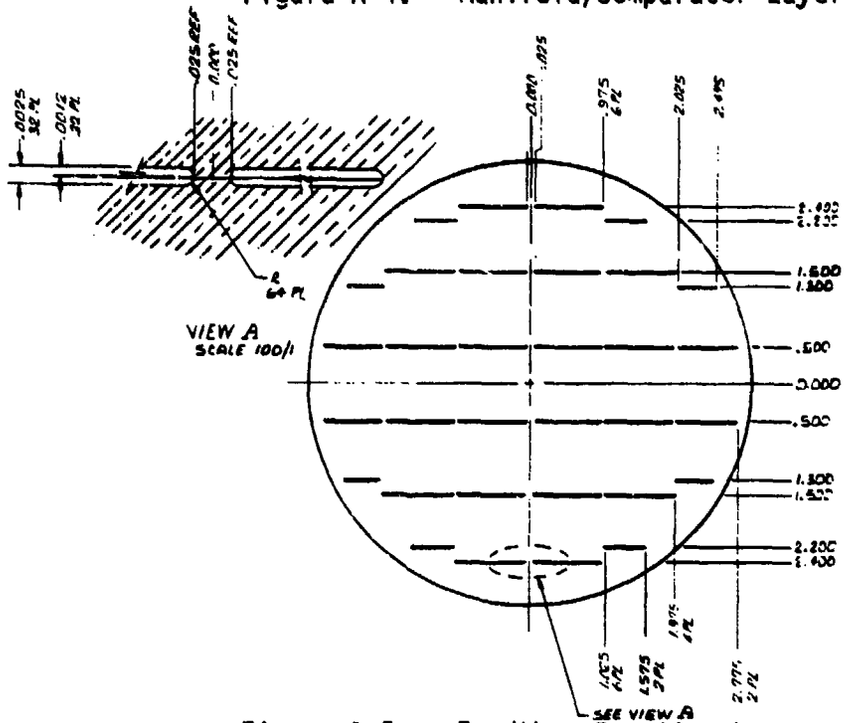

Figure A-5. Feedthru Coupling Layer

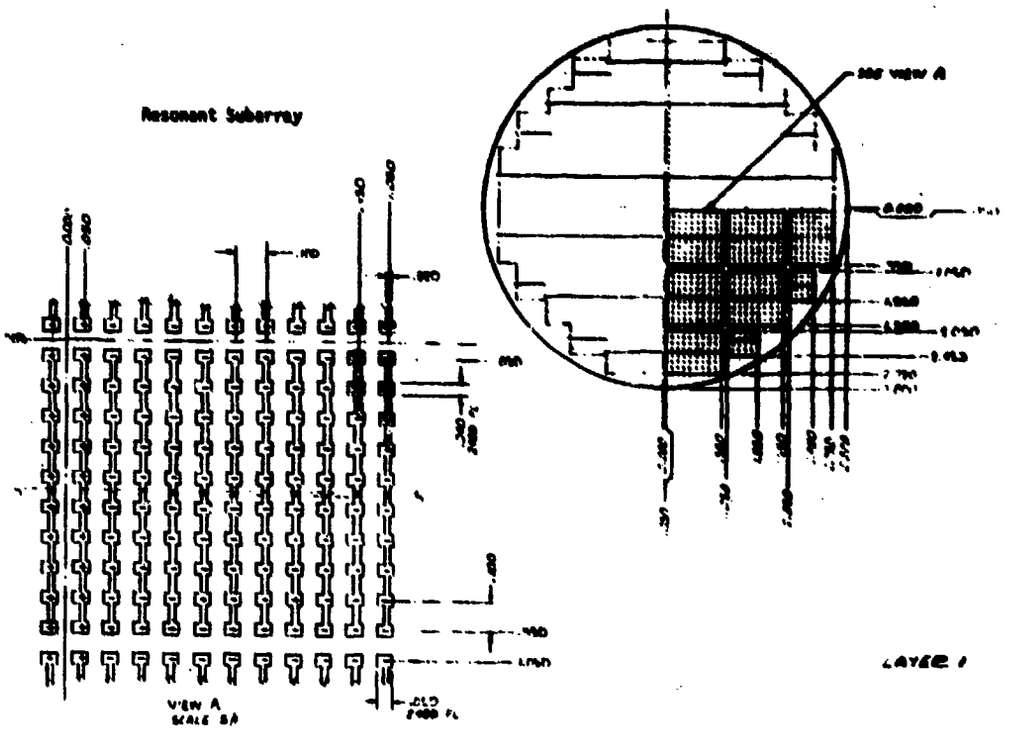

Figure A-6. Radiating Layer

cally etched. Smooth substrate finishes and thin metalizations are necessary to achieve accurate line definition without undercutting by the etch process. These two requirements disallow many copper clad materials normally used in the microwave region.

The layered antenna structure may take a variety of configurations depending upon the type of transmission lines used. Figures A-2 and A-3 show the array cross section for two possibilities, each with three layers. In Figure A-2, layer three is the comparator and array manifold using inverted microstrip transmission lines. Details of the circuitry layout are shown in Figure A-4. Layer

two is the feedthru coupling layer consisting of slotlines shown in Figure A-5. Electromagnetic energy from the feed manifold couples to the slotlines[7] and in turn couples to transmission lines in the radiating layer 1 shown in Figure A-6. Radiating elements in the resonant subarrays are microstrip patches that are fed by offsetting them from the centerline of the transmission line. The amount of offset controls the element amplitude analogous to broadwall slotted waveguide arrays. In Figure A-2 the manifold/comparator layer and the radiating layer are respectively inverted microstrip and microstrip. An alternate scheme shown in Figure A-3 uses an inverted microstrip radiating layer and a microstrip manifold/comparator layer.

A simple approach to the array excitation is to subdivide each quadrant into eight rectangular subarrays of uniform amplitude. With appropriately chosen voltages for each subarray adequate patterns may be obtained.

A more complicated manifold and comparator for independent sum and difference patterns for an array of this size is possible but not propitious at this juncture in the state of the art. Pattern improvement at the expense of increased sophistication may be achieved by smoothly varying the element excitation within a subarray. Such procedure requires a unique microstrip element offset from the transmission line centerline for each radiating element.

The photolithographic array concept has generally been described; however, there are a number of possibilities for specific implementation. At this point the photolithographic array is a concept only and considerable development is required to prove the concept. In the following paragraphs further discussion of details is given to exemplify the concept and to define the critical components.

Table A-2 lists the array critical components with suggested possibilities for each. The photolithographic structure is a layered structure with a minimum number of interlayer connections. Microstrip, inverted microstrip, and slotline are three transmission lines amenable to photolithography.

Table A-2. Array Critical Components

1. Transmission Lines
   - Microstrip
   - Inverted Microstrip
   - Slotline
2. Layer Coupling
   - Slotline to Microstrip
   - Slotline to Inverted Microstrip
3. Radiators
   - Microstrip
   - Inverted Microstrip
   - Suspended Microstrip
4. Transmission Line to Radiator Coupling
   - Inverted Microstrip
   - Inverted Microstrip/Suspended Microstrip
5. Components
   - Power Divider
   - Hybrid
6. Resonant Subarrays

For the layered array concept to be a successful, a minimal number of interconnections between layers must be used. Electromagnetic

coupling between layers is more amenable to fabricating a large array. One technique of layer coupling to form a feed thru between a microstrip layer and an inverted microstrip layer is illustrated in Figure A-7. In the figure, energy propagating along the microstrip line transfers to the slotline and then along the slotline. From the slotline energy is transitioned to the inverted microstrip. Microstrip to slotline transitions have been reported[7] with at least 30% bandwidths which is more than adequate bandwidth.

Inverted microstrip to slotline transitions have not been reported and would need development. An attractive feature of the layered structure as represented in Figure A-7 is the ability to overlay circuitry in the microstrip and inverted microstrip which shares a common ground plane. The ground plane isolates the two circuit layers and allows layer coupling at the slotline holes in the ground plane. A similar layer coupling between inverted microstrip and inverted microstrip is shown in Figure A-8. The dual slotline consists of the dielectric substrates. The dielectric allows energy to be more tightly confined to the neighborhood of the slotline than would be the case with a solid conducting ground plane.

The radiating elements may take several configurations depending upon the transmission lines used to feed the radiators. Figure A-9 shows a variety of microstrip type radiators. Figures A-9 a. and c. show conventional microstrip patch radiators fed by a coaxial

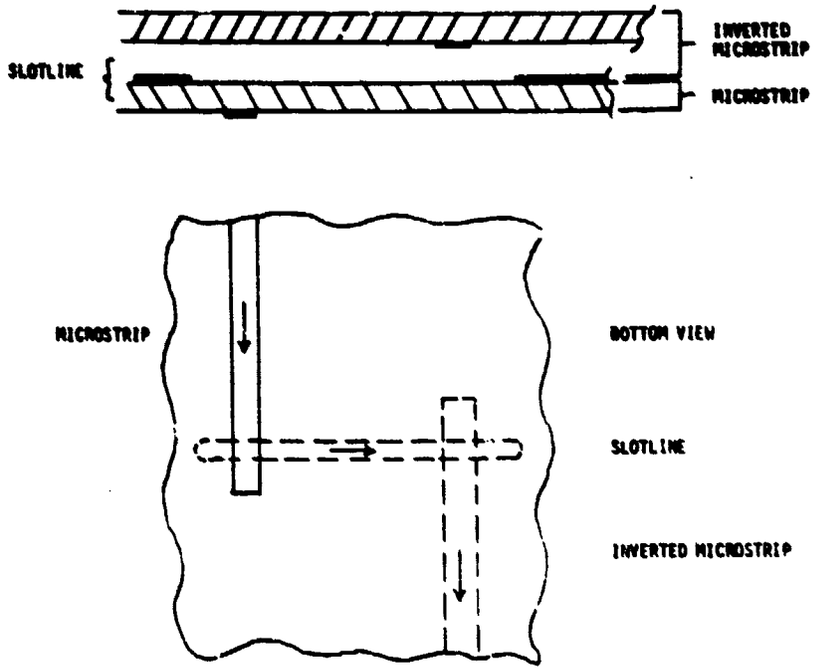

Figure A-7. Layer Coupling (Microstrip/Inverted Microstrip)

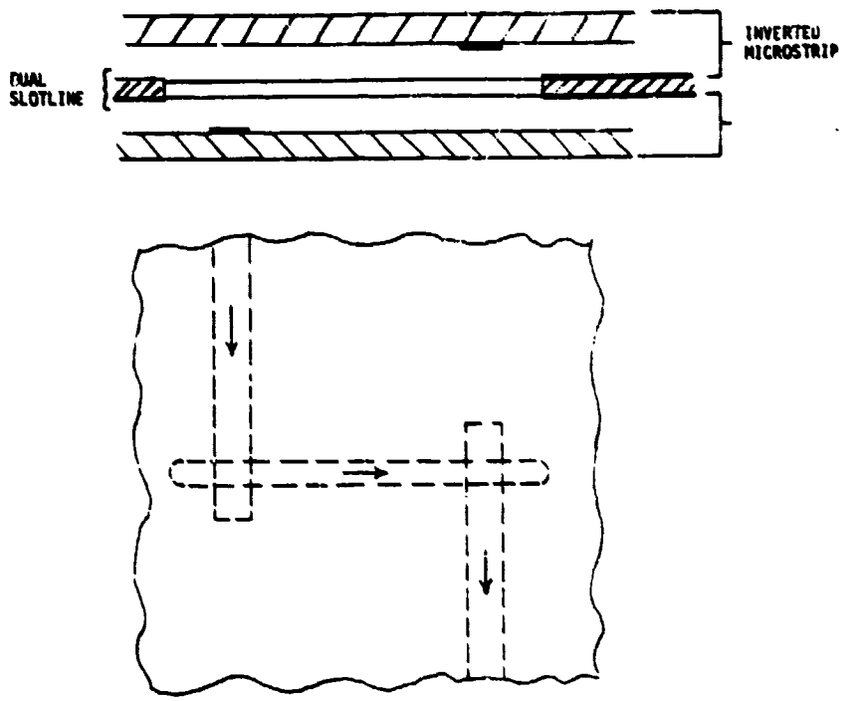

Figure A-8. Layer Coupling (Inverted Microstrip/Inverted Microstrip)

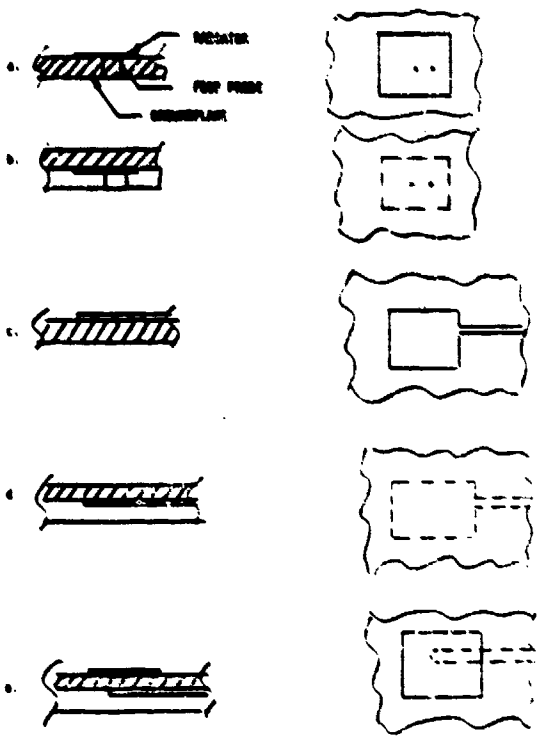

Figure A-9. Microstrip Radiators

probe and a microstrip line respectively. Figures A-9 b. and d. give the corresponding radiators with an inverted microstrip medium. The radiator using a coaxial feed probe is probably not practical for a large array but may be useful for only a few elements. Figure A-9 e. shows a new radiator configuration. The transmission line in inverted microstrip is independent of the suspended microstrip radiating element. The inverted microstrip transmission line feeds the radiator by capacitive coupling. Thus the transmis-

sion line can be designed with an air substrate height sufficiently small so that radiation loss is reasonable yet the distance between the microstrip radiator is sufficiently far from the ground-plane so that larger bandwidths may be obtained. Such independent control of the transmission line and the radiator is not possible in the more conventional approaches in Figures A-9 c. and d. that typically produce smaller bandwidths.

Design analysis capability for transmission line to radiator coupling for inverted microstrip and inverted microstrip/suspended microstrip is necessary as the next step toward the array development. Knowledge of the transmission line parametric analysis will aid in the analysis of power dividers such as the Wilkinson "tee" and the ring hybrid in inverted microstrip, but such designs must be verified. Finally, the resonant subarray concept with the relevant transmission lines and radiators is critical to the array concept and must be studied and developed.

AD P001108

DESIGN OF PERIODICALLY CORRUGATED DIELECTRIC ANTENNAS FOR MILLIMETER-WAVE APPLICATIONS

F. Schwering

US Army Communications-Electronics Command

Ft. Monmouth, N.J. 07703

and

S. T. Peng

Polytechnic Institute of New York

333 Jay Street

Brooklyn, N.Y. 11201

[redacted]

ABSTRACT

Periodic dielectric waveguide structures were extensively analyzed and were understood in the context of integrated-optics theory. Recently, it has been also demonstrated experimentally that this class of structures offer many advantages for use as millimeter-wave antennas. A considerable effort is currently under way to fully develop its potential. Making use of the available analytic method previously devised, we have carried out an extensive and systematic analysis of periodically corrugated dielectric antennas. The results are exhibited in a way that is most pertinent to millimeter-wave applications. On the basis of the obtained numerical data, a set of design guidelines for the corrugated dielectric antennas is established herein.

DTIC

1. Introduction

A dielectric waveguide with a periodic perturbation, or simply a periodic dielectric waveguide, has been shown to hold substantial promise as a leaky-wave antenna for millimeter applications[1-5]. Such an antenna structure may be conveniently fabricated on a uniform dielectric waveguide to form a completely integrated mm-wave system. In addition, the dielectric leaky-wave antennas offer the advantage of electronic beam steering[1,2]. Therefore, in recent years, a considerable effort has been made for a better understanding of this particular class of antennas in order to explore its applications to mm-wave systems.

In this paper, we present a systematic analysis of the periodically corrugated dielectric waveguide for use as a leaky-wave antenna for mm-wave applications. We recognize that this class of structures has been extensively analyzed for integrated-optics applications[7] such as beam-to-surface-wave couplers, distributed feedback reflectors, and filters. In fact, leaky-wave antennas and optical periodic couplers are based on the same physical principle[4,7] and a great deal of information on the basic wave characteristics of the optical devices can simply be carried over for the understanding of the mm-wave antennas. However,because of the substantial difference in the permittivity of the materials commonly used in the two frequency ranges and because of different processes by which these devices are

constructed, the design procedures for mm-wave antennas differ from that for optical couplers in many respects. The main purpose of this paper is to make use of the existing theoretical tools[4,7] for developing design guidelines for the particular class of corrugated dielectric leaky-wave antennas, appropriately taking into account special requirements for mm-wave applications.

For mm-wave applications, a corrugated dielectric antenna has ,at most, a few wavelengths in width, in contrast to thousands of wavelengths for most optical couplers. Therefore, an optical periodic coupler can be formulated as a two dimensional boundary value problem that may support independent TE or TM modes propagating normally to the grooves of the corrugation. It has been shown[8,9] that to investigate the effect of finite antenna width, the most basic problem to be solved is the guiding of waves propagating at an oblique angle in an infinitely wide periodic structure. This is a three dimensional electromagnetic boundary value problem that supports only hybrid modes, e.g., it requires the coupling between TE and TM modes. Such a vector boundary value problem has been formulated[8] and the propagation characteristics for the general case of oblique guidance have been subsequently analyzed. The effect of the finite antenna width on the performance of the corrugated dielectric antenna has been reported[9]. It has been shown[8,9] that for an antenna structure of finite width, the longitudinal phase constant is determined by the

unperturbed uniform waveguide and the decay constant does not differ from that of the two-dimensional case, as long as the width of the antenna is not very small. In this work, we shall assume that the antenna width is large enough so that the leakage constant can be obtained from the simpler normal guidance case.

2. Design of the periodically corrugated dielectric antenna

The configuration of a dielectric antenna structure is shown in Fig.1. Such an electromagnetic structure has been previously analyzed in the context of optical periodic couplers[7] and many radiation characteristics of the structure have been known. The antenna structure is characterized by four parameters : the thickness of the uniform region, t_f, the thickness of the corrugation region, t_g, the period of the corrugation, d, and the aspect ratio $a = d_1/d$. Since the lengths can always be normalized to the free-space wavelength, it is not necessary to consider the frequency of the source as an independent parameter. On the other hand, since a corrugated dielectric antenna is expected to be fabricated from an originally uniform waveguide by machining, it is more appropriate to use the original waveguide height $h = t_g + t_f$ as a parameter. This means that when the waveguide is machined, both t_g and t_f will change. Therefore, it is necessary to investigate the combined effect of change in t_f and t_g on the propagation characteristics of the antenna structure.

Because of the periodicity of the leaky-wave antenna, the electromagnetic fields everywhere must consist of all the space harmonics. For TM modes, we have :

$$H_y(x,z) = \sum_{n=-\infty}^{\infty} I_n(z)\exp(ik_{xn}x) \qquad (1)$$

where I_n is the n-th harmonic amplitude of the magnetic field and k_{xn} is the x-component of the propagation constant of the n-th harmonic and is related to that of the fundamental harmonic by :

$$k_{xn} = k_{xo} + 2n\pi/d = \beta - j\alpha + 2n\pi/d = \beta_n - j\alpha \qquad (2)$$

where β and α are the propagation and attenuation constants of the fundamental harmonic, respectively. It is noted that the propagation constant of the n-th harmonic differs from that of any other harmonic but the attenuation constant, α, is the same for all harmonics. By solving the boundary value problem, it has been shown that k_{xo} and the harmonic amplitudes, $\{I_n | n = 0,+1,+2,..\}$, can be determined in terms of the eigenvalues and eigenvectors of a coupling matrix characterizing the corrugation region. For the given antenna structure on a ground plane of infinite extend, because the energy can only radiate into the air region, it is unnecessary to determine explicitly the harmonic amplitudes, if we are interested only in the case of single beam radiation. In the present study, therefore, we are left with only the determination of the dispersion root k_{xo} of the antenna. For simplicity, k_{xo} will be referred to as the leaky wave constant. Since α may be used as a measure of

the rate of energy leakage, it will also be called the leakage or radiation constant, in constrast to the phase constant β.

In the air region where the medium is uniform, each harmonic propagates independently as a plane wave. The transverse propagation constant of the n-th harmonic is given by :

$$k_{zn} = (k_o^2 - k_{xn}^2)^{1/2} \tag{3}$$

For a very shallow corrugation or t_g very small, it is intuitively expected that $k_{xo} = \beta_{sw} = k_o n_{eff}$, where β_{sw} is the longitudinal propagation constant of the unperturbed structure, as shown in Fig.2. Under such an approximation and invoking (2), we obtain, from (3) :

$$k_{zn} = k_o[1 - (n_{eff} + n\lambda/d)^2]^{1/2} \tag{4}$$

For only the n = -1 harmonic to radiate, we must have $k_{z,-1}$ real and all k_{zn} imaginary for $n \neq -1$. These conditions can alternatively be expressed as :

$$\frac{\lambda}{n_{eff} + 1} < d < \frac{\lambda}{n_{eff} - 1}, \quad \text{for } n_{eff} > 3 \tag{5}$$

$$\frac{\lambda}{n_{eff} + 1} < d < \frac{2\lambda}{n_{eff} + 1}, \quad \text{for } n_{eff} < 3 \tag{6}$$

Under these conditions, the n = -1 harmonic radiates into the air region at an angle (with respect to the z-axis) :

$$\theta_{rad} = \sin^{-1}(\beta_{-1}/k_0) = \sin^{-1}(n_{eff} - \lambda/d) \qquad (7)$$

The sign of θ_{rad} determines the forward or backward radiation. Although the above design formulas are derived under the assumption that t_g is very small, they also hold for t_g large, if the normalized phase constant or the effective index of refraction, n_{eff}, is accurately obtained for a given t_g.

It is noted that n_{eff} of a periodic dielectric waveguide does not depend appreciably on the period d of the structure. Eq.(7) shows that the choice of the period d is simply determined by the radiation angle. Therefore, the effect of the period d on the antenna performance will not be further elaborated.

2.1. Effect of the corrugation thickness t_g on the radiation angle

As a uniform slab of the thickness h is machined, the dielectric material is scooped out. As a result, the effective thickness of the corrugated slab is reduced, and so is the effective dielectric constant. It has been well known[4,7] that the effective dielectric constant of the corrugated slab may be simply determined by a uniform double layer structure with the volume average of the dielectric constant for the periodic corrugation region. As an example, Fig.2 shows the effective dielectric constant as a function of the corrugation thickness for a periodic silicon slab with the aspect ratio $d_1/d = 0.5$. In Fig.2, the solid

curves are for fixed thickness of the origional slab, $h = t_f + t_g$, as a parameter, whereas the dashed curves are for fixed thickness of the uniform portion of the corrugated structure. For example, in the case of an originally uniform slab of thickness $h = 0.2\lambda$, a corrugation of the thickness $t_g / \lambda = 0.05$ and an aspect ratio $a = d_1 / d = 0.5$ will result in an antenna structure with an effective dielectric constant $\epsilon_{eff} = 10$, as marked by the cross labelled by A on the curve for $h/\lambda = 0.2$ in Fig.2. The same effective dielectric constant can be achieved by other combinations of h and t_g values, such as $h/\lambda = 0.24$ and $t_g / \lambda = 0.1$, as marked by the cross labelled by B in Fig.2. It is noted that the dashed curves are useful for the design of other types of structures, and will not be further elaborated here. After $\epsilon_{eff} = n_{eff}^2$ is determined for a given antenna structure, the radiation angle is determined according to (7). Thus, the set of solid curves provides the necessary information for determining the dependence of the radiation angle on the corrugation thickness.

2.2. Effect of the corrugation thickness on the radiation constant

It has been known[1-5] that the radiation constant α is proportional to t_g^2, for t_g small, and reaches a saturation value for t_g large, if the guided-wave field is evanescent in the corrugation region. For the aspect ratio $d_1/d = 0.5$, the average dielectric constant of the corrugation region is

ϵ_{ave} = 6.5, and the guided-wave field is indeed evanescent in the corrugation region. The radiation constant as a function of the corrugation thickness is shown in Fig.3. Evidently, the radiation constant α varies with the corrugation thickness t_g in the fashion expected.

On the other hand, the fabrication of a periodically corrugated dielectric antenna by machining changes not only the thickness of the corrugation region, but also that of the uniform region. Therefore, it is necessary to consider the combined effect of the changes in both the thicknesses of the corrugated and uniform regions. When a uniform dielectric slab is cut to produce the corrugation, the thickness of the remaining uniform region decreases at the same rate as the depth of the grooves increases. Based on Fig.3, it is clear that the leakage or radiation constant will increase initially as the grooves are cut deeper and deeper. However, because of the changing thickness of the remaining uniform portion that affects the basic surface wave, it is not clear at this point that if the radiation constant is still too small, any further cut can be helpful for achieving a larger radiation constant.

Fig.4 shows the variations of the radiation constant and the radiation angle θ_{rad} as the thickness of the corrugation region t_g is increased, for the case of the original thickness $h = 0.3\lambda$, the period $d = 0.25\lambda$, and the aspect ratio $d_1/d = 0.5$. When the grooves are shallow (t_g small)

the solid curve shows that the radiation constant α increases with the groove depth, as expected. However, α reaches a maximum value at $t_g \approx 0.1\lambda$ and then decreases as t_g is further increased. Such a decrease in α can be explained as follows : As t_g is increased, the remaining uniform portion of the structure becomes thinner and thinner and, as a result, the phase constant of the guided wave becomes smaller and smaller. This phenomenon is exhibited by the dashed curve for the radiation angle in Fig.4. More specifically, the radiation angle increases in the backward direction with increasing t_g. Eventually, the antenna structure will cease to radiate in the backward end-fire direction and the guided wave becomes totally bounded.

Fig.5 shows the results for a case of a thinner original uniform slab, $h = 0.25\lambda$, while all other structure parameters are kept unchanged from the proceeding case. However, it is interesting to observe that the maximum value of α occurs at the same thickness of the remaining uniform slab $t_f = 0.2\lambda$ in both cases. In fact, this result holds for any structure with $d = 0.25\lambda$ and $d_1/d = 0.5$, as long as the thickness of the original uniform slab is sufficiently large.

2.3. Effect of the aspect ratio

The numerical results presented in the preceeding section are all for the case of equal width for the teeth and grooves or the aspect ratio $d_1/d = 0.5$. In the fabrication

process, the aspect ratio can be easily controlled, if [illegible]. For comparison purpose, the radiation constant α as a function of the groove depth t_g is shown in Fig.6 for an original uniform slab of the thickness $h = 0.25\lambda$ and the period $d = 0.25\lambda$ as in Fig.5, but with wider teeth ($d_1/d = 0.8$) or narrower grooves. With such a new aspect ratio, the attainable maximum value of α is increased by a factor of about 4 from the case of $d_1/d = 0.5$, but the grooves have to be cut deeper ($t_g \approx 0.1\lambda$).

In order to fully understand the effect of the aspect ratio, the radiation constant as a function of the aspect ratio is investigated and the results are plotted in Fig.7, for the structure and parameters indicated. In the two limiting cases of the aspect ratio : $d_1/d = 0$ and 1, the periodic structure becomes uniform and it is expected that no radiation can occur. For optical structures with a relatively low dielectric constant, it is well known[7] that the maximum radiation occurs at the aspect ratio $d_1/d = 0.5$. For mm-wave antennas, however, the dielectric constant is relatively high and the field variation in the corrugation region depends strongly on the aspect ratio, and so does the radiation constant. Fig.6 shows that the value of α peaks around the aspect ratio $d_1/d = 0.7$, instead of $d_1/d = 0.5$ as usually expected. Such a shift in the aspect ratio can be explained qualitatively as follows : For the given structure, the fields in the corrugation region are evanescent for the aspect ratio $d_1/d = 0.5$; therefore, the surface wave

is only weakly perturbed by the corrugations and the radiation constant is small. When the aspect ratio is increased, more surface-wave energy is shifted to the corrugation region, resulting in a larger perturbation of the surface wave and a larger radiation constant. Thus, we may conclude that for a larger radiation constant, the aspect ratio should be relatively large ($d_1/d > 0.5$) or the grooves should be relatively narrow.

3. Discussions and conclusions

The radiation characteristics of thick corrugated dielectric antennas are relatively insensitive to the change of structure parameters. From the practical viewpoint, this property will afford a larger tolerance in a mass production of the antennas. On the basis of the numerical results presented above, we may now establish the following general guidelines for the design of the corrugated dielectric antenna structures:

(1) The thickness of the original uniform slab and the period of the corrugation are determined by the desired radiation angle according to (7).

(2) For a uniform dielectric slab, there exists a groove depth t_g that yields a maximum value of radiation constant; a desired radiation constant

smaller than the maximum value may be realized by a larger or smaller value of t_g, depending on the radiation angle desired.

(3) Within the constraint of the radiation angle, the larger the thickness of the original uniform slab, the larger the maximum value of the radiation constant α achievable.

(4) There exists a groove width or an aspect ratio that yields a maximum value of the radiation constant α and a smaller value of α may be realized by adjusting the aspect ratio.

(5) For a uniform dielectric slab of larger thickness and high dielectric constant, the maximum value of α occurs with the groove width smaller than the tooth width. In other words, cutting the groove with a larger width may not help increase the radiation constant.

In addition to those presented above, we have carried out extensive numerical results for many different

situations. In particual , for the case of relatively thin antenna structures, the radiation characteristics are generally much more sensitive to the change of structure parameters, and each structure has to be quantitatively evaluated individually. Therefore, general design guidelines for thin corrugated dielectric antennas are difficult to develop.

Acknowledgement

This work was suppoerted by U.S. Army under the Laboratory Research Coopsrative Program (LRCP), Contract No.: DAAG 29-81-d-0100 and DAAG 29-76-d-0100.

Reference

1. Klohn, K.L., Horn, R.E., Jacobs, H. and Freibergs, E., (1978) Silicon waveguide frequency scanning linear array antenna, IEEE Trans. MTT, MTT-26, 764-773.
2. Horn, R.E., Jacobs, H., Freibergs E. and Klohn, K.L., (1980) Electronic modulated beam-steerable silicon waveguide array antenna, IEEE Trans. MTT, MTT-28, 647-653.
3. Solbach, K., (1979) E-Band leaky wave antenna using dielectric image line with etched radiating elements, 1979 MTT-S Int. Microwave Symp. Dig., 214-216.

4. Peng, S.T. and Schwering, F., Dielectric (1978) grating antennas, R&d Tech. Report CORADCOM 78-3, U.S. Army CORADCOM, Ft. Monmouth, New Jersey.

5. Mittra, R. and Kastner, R., (1981) A spectral domain approach for computing the radiation characteristics of a leaky-wave antenna for millimeter waves, IEEE Trans. Antennas & Propagation, AP-29, 652-4.

6. Tamir, T., (1975) Integrated optics, Springer Verlag, New York.

7. Peng, S.T., Tamir, T. and Bertoni, H.L., (1975) Theory of periodic dielectric waveguides, IEEE Trans. MTT, MTT-23, 123.

8. Peng, S.T., (1980) Oblique guidance of surface waves on corrugated dielectric layers.

9. Peng, S.T., Oliner, A.A. and Schwering, F., (1981) Theory of dielectric grating antennas of finite width, IEEE AP-S International Symp., L.A., C.A.

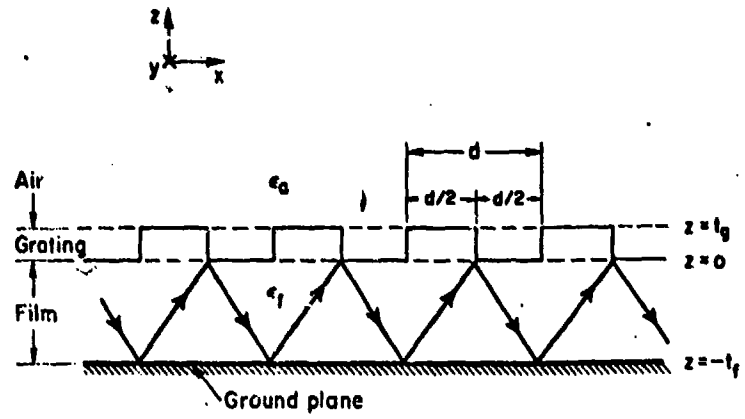

Fig. 1. Geometrical configuration of corrugated dielectric antenna.

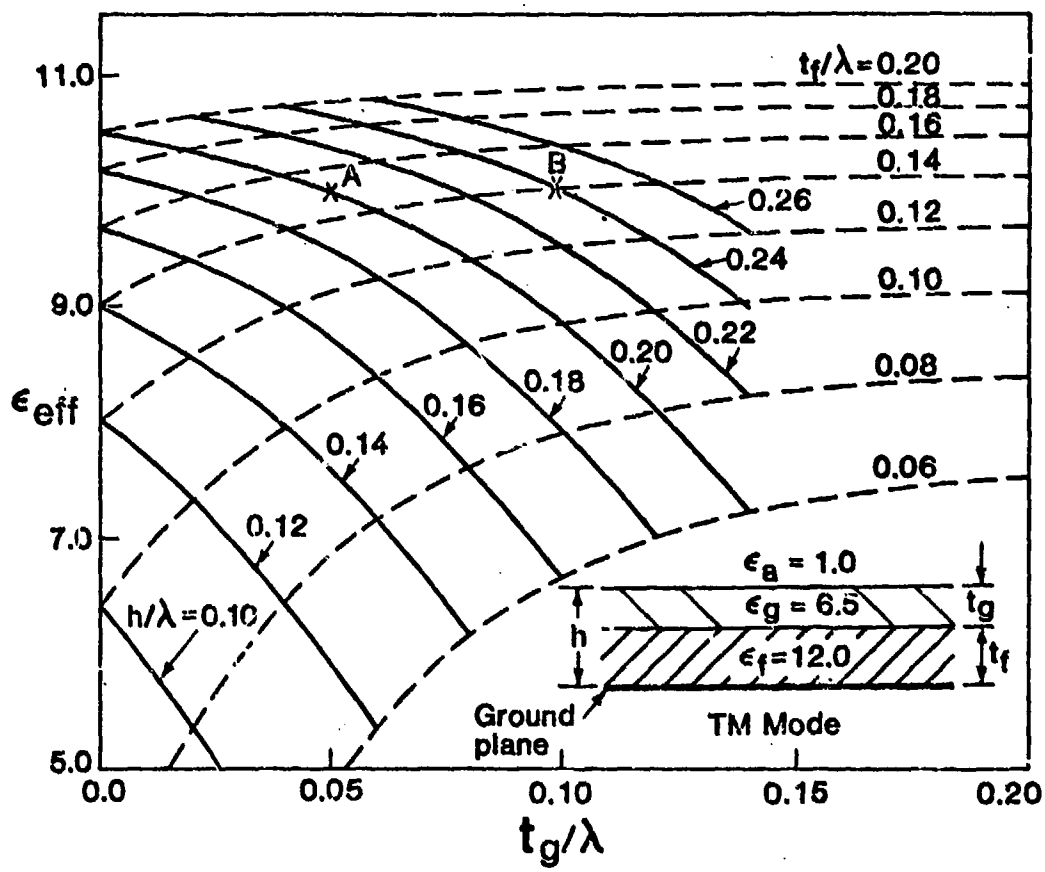

Fig. 2. Variations of effective dielectric constant vs corrugation depth t_g for uniform double-layer waveguide.

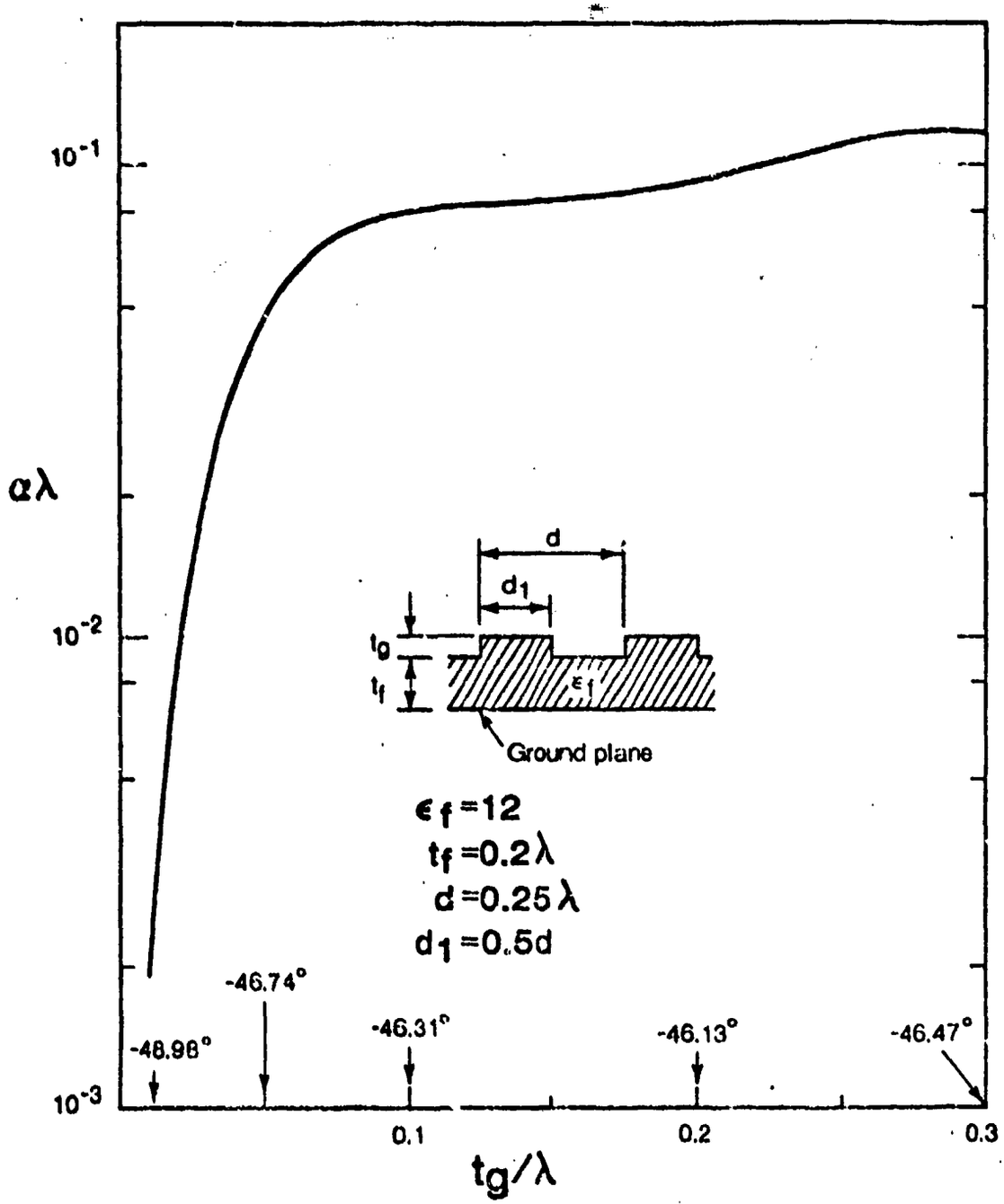

Fig. 3. Variations of radiation constant vs. corrugation depth t_g for fixed thickness of the uniform region.

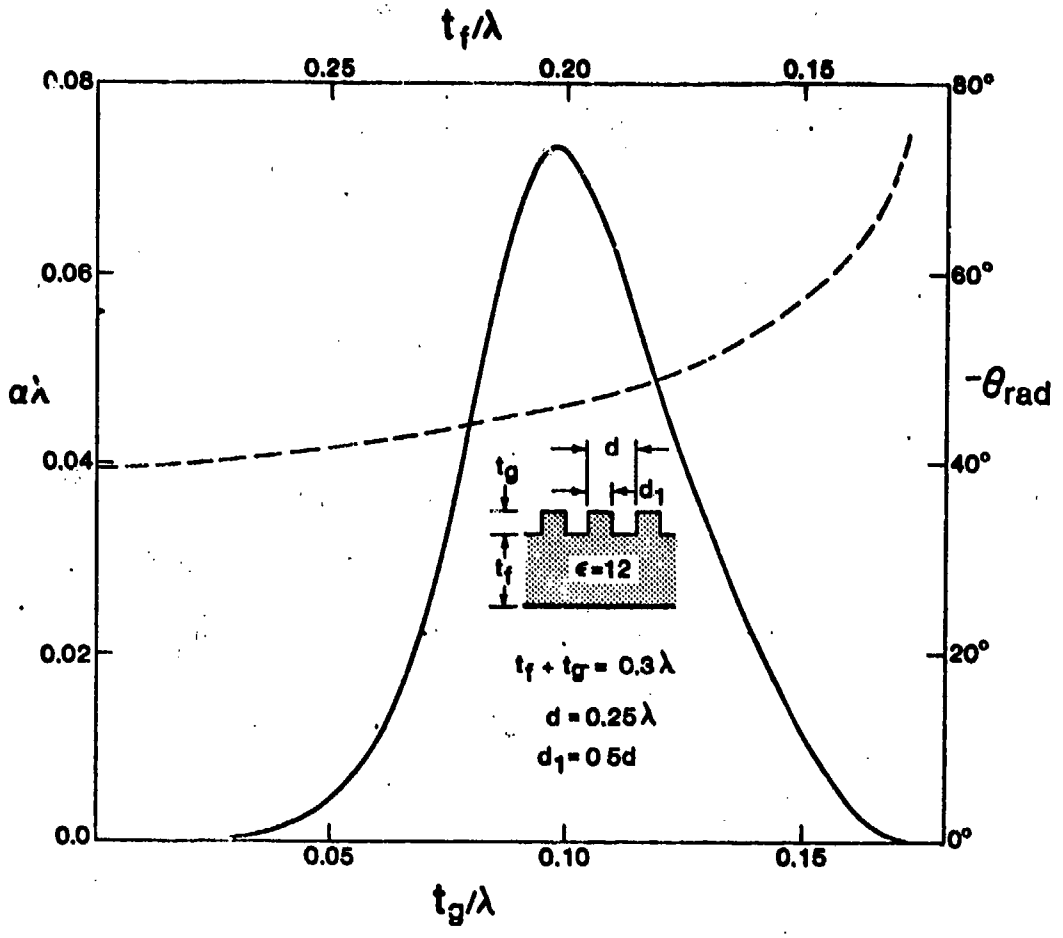

Fig. 4. Variations of radiation constant vs. corrugation depth for $t_f + t_g = 0.3\lambda$, $d = 0.25\lambda$ and $d_1 = 0.5d$.

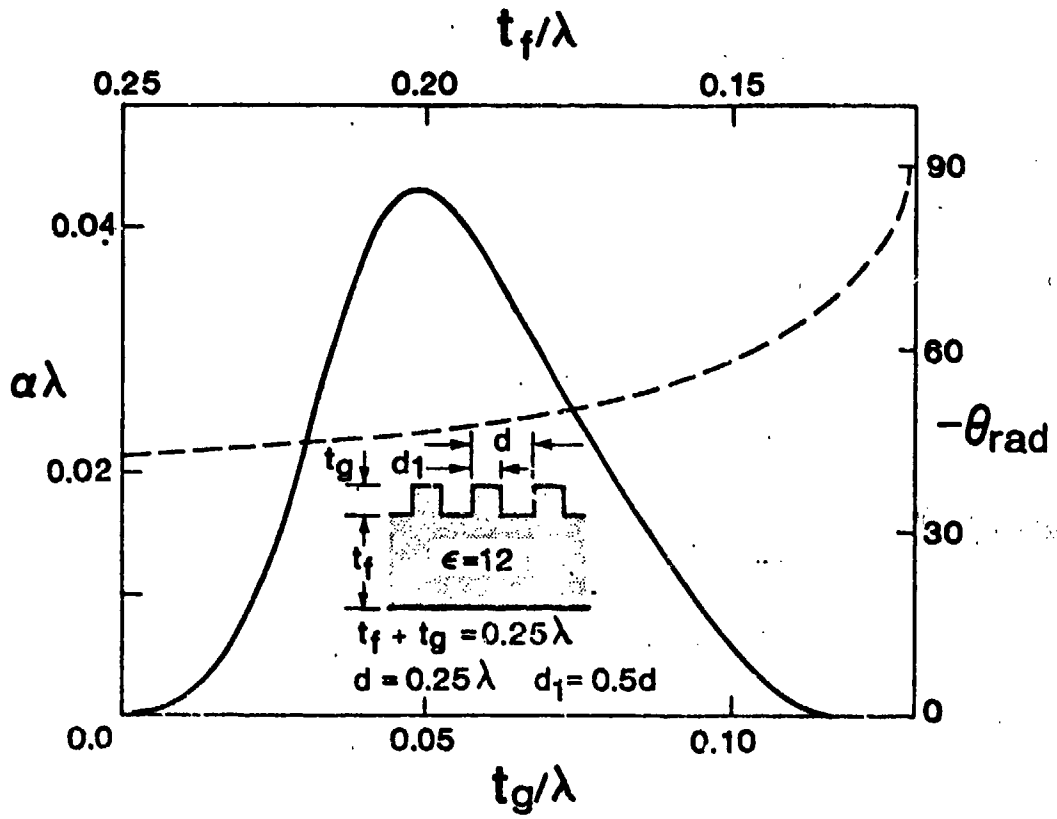

Fig. 5. Variations of radiation constant vs. corrugation depth for $t_f + t_g = 0.25\lambda$, $d = 0.25\lambda$ and $d_1 = 0.8d$.

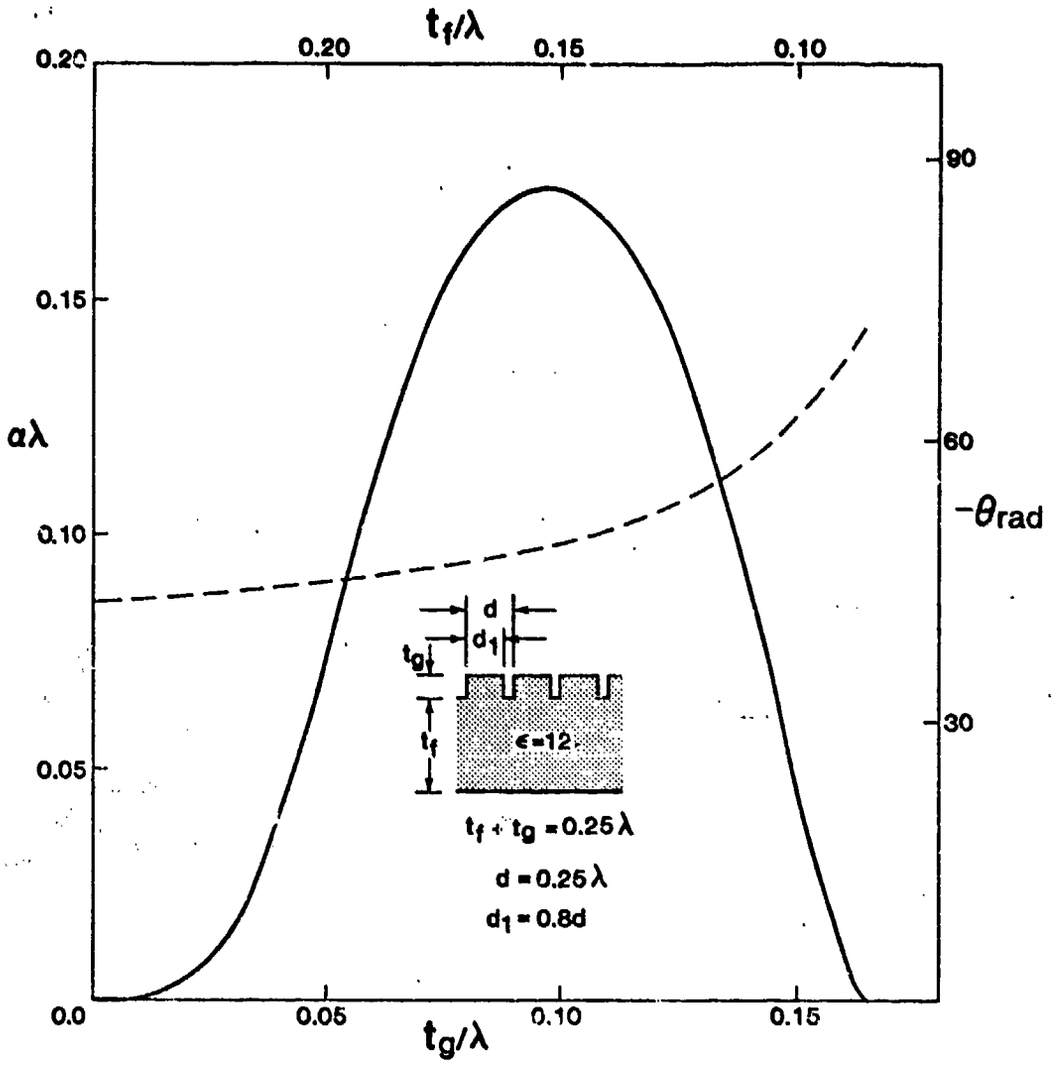

Fig. 6. Variations of radiation constant vs. corrugation depth for $t_f + t_g = 0.25\lambda$, $d = 0.25\lambda$ and $d_1 = 0.8d$.

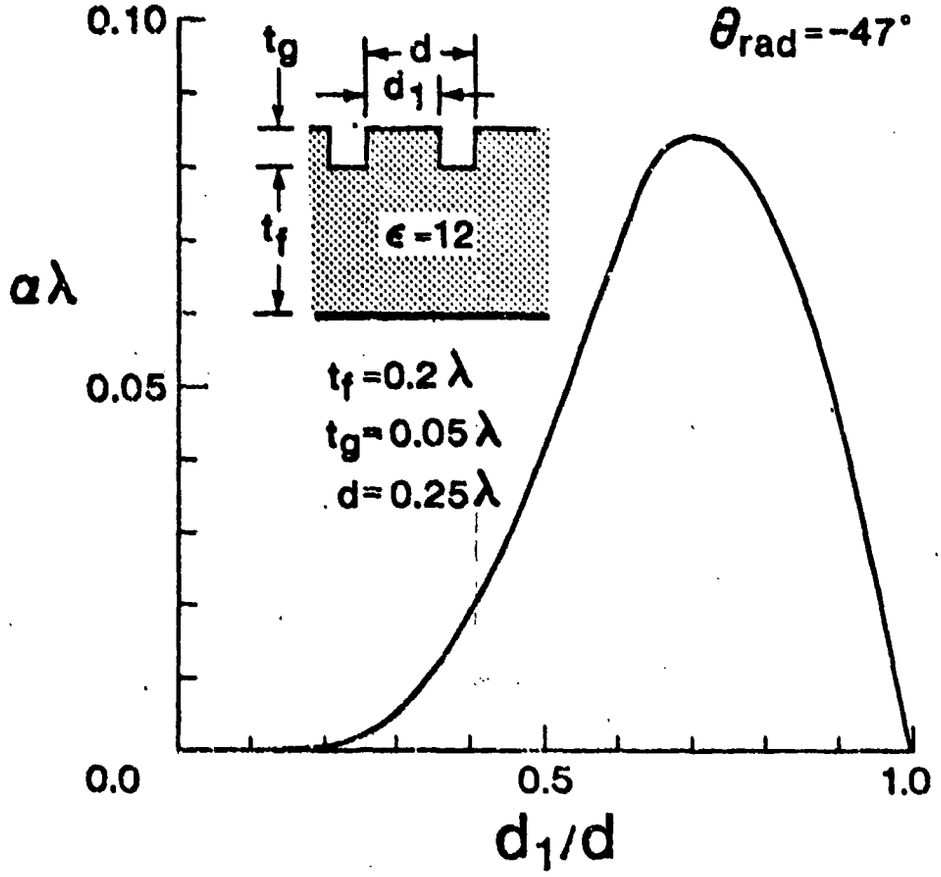

Fig. 7. Variations of radiation constant vs. aspect ratio d_1/d for $t_f + t_g = 0.25\lambda$, $t_g = 0.05\lambda$, and $d_1 = 0.5d$.

AD P001109

Electronically Steerable Spherical Array Provides Multiple Beam Coverage of a Hemisphere

Taliaferro Holmes Taylor, Jr.
Ball Aerospace Systems Division
Boulder, Colorado 80306

ABSTRACT

This paper describes the Electronically Steerable Spherical Array (ESSA) antenna and its configuration for multiple beam operation over a hemispherical coverage region. This paper discusses the ESSA's theory of operation along with its RF components.

The ESSA is unusual in that by switching between beams (which are made of sets of elements located on a spherical surface) the ESSA is able to provide constant gain and phase independent of the scan angle.

This paper concludes that the ESSA is a mature technology which has significant advantages over conventional multi-faced phased array antennas.

1.0 INTRODUCTION

In 1975 Ball Aerospace Systems Division (BASD) began to address the problems associated with providing RF coverage between TDRSS and its user satellites. The primary problem which was to be resolved was how to provide the very large solid angle coverage regions required by the user satellites. A steerable dish approach was discarded very quickly because many of the TDRSS user scientific packages required inertialess environments. After considering the

problems associated with multi-faced phased arrays, BASD began development of the switched beam hemispherical antenna which came to be known as the Electronically Steerable Spherical Array (ESSA). Since then the ESSA technology has matured through BASD's fabrication and test of both 7 and 14 dBic gain, S-band ESSA engineering models shown in Figure 1. Presently, BASD is in the final stages of fabricating a 14 dBic gain S-band ESSA as flight hardware for the Earth Radiation Budget Satellite.

2.0 THEORY OF OPERATION

An ESSA creates an aperture by the selection of a set of elements (element cluster) which all point in the desired direction. The aperture is then moved through the coverage region by switching to other elements which point in the new desired direction. The ESSA consists of a spherical surface covered with microstrip antenna elements which are selected and summed together by a switching power divider. As shown in Figure 2, the switching power divider selects the element cluster upon command from the microprocessor controller. The microprocessor selects only those elements which are located within a specified solid angle distance from the desired pointing direction. The elements are located on the spherical surface by the use of icosahedron geometry. This geometric technique insures that all elements are spaced by approximately 0.7λ. As a result of this similarity in spacing, all of the ESSA element clusters are virtually the same and are independent of scan angle. Figure 3 shows the constant gain of the ESSA compared to the rolloff of the phased array.

Another way to look at the ESSA is to consider the ESSA to be the electronic equivalent of a mechanical gimbal. With a mechanical gimbal system, the aperture is moved mechanically; with the ESSA, the aperture is moved electronically.

2 .1 Gain is a function of ESSA Diameter

Even though the ESSA gain is not a function of scan angle it is, however, a function of the ESSA's diameter. The reason for this relationship between gain and diameter is the result of the constraints which element beamwidth and aperture phase delta place on the aperture. Element beamwidth limits the aperture size so that no element used in the element cluster has higher gain away from the desired direction than it has in the desired direction. If the aperture included elements which were outside of this aperture size limit, the ESSA's beam would be broadened and its gain reduced. The second constraint, aperture phase delta, is best described by Figure 4. That figure shows that a phase delta exists between those elements located near to and far from the desired direction. That phase delta may be reduced by phase compensation and as a result improve the ESSA gain and phase; or, the ESSA aperture diameter may be restricted so that $\Delta\phi$ does not exceed 135 degrees. Both of these constraints limit the diameter of the ESSA aperture and therefore have an impact on gain. After considering cable and beam crossover losses, the ESSA gain may be plotted as shown in Figure 5.

2.2 Coverage Region

The only limit to the ESSA's coverage region is that there must be elements located so that a complete aperture may be formed in the desired direction. Hemispherical coverage therefore requires elements located over slightly more than a hemisphere. For full spherical coverage, an ESSA with hemispherical coverage is typically mounted on each side of the electronics platform.

3.0 MULTIPLE BEAM CONFIGURATION

A straightforward extension of the technology allows the ESSA to create independent multiple beams. A comparison of Figures 2 and 6 shows that the only modification required for changing from a single beam to a multiple beam ESSA is the addition of a low noise amplifier and power divider at each element and a switching power divider for each of the multiple beams.

3.1 Element Configuration

When changing from single beam to multiple beam operation, the ESSA elements must be modified. Figure 7 is a side view of a typical microstrip element used by a single beam ESSA. This element consists of the microstrip disk element which interconnects through spring loaded contacts to the microstrip polarization hybrid. The element is modified for multiple beam operation as shown in Figure 8. This figure shows that the element consists of a microstrip disk and a low noise amplifier. The microstrip branch line coupler used to provide a circular polarization in the single beam ESSA is replaced by a microstrip Lange coupler located inside the low noise amplifier assembly. Interconnection between the element and low noise amplifier is through a sliding pin contact. Incorporation of the amplifier into the element assembly serves two functions. The first is the establishment of system noise figure as close to the aperture as possible. The second is the creation of a component which may be easily tested and replaced by depot level personnel.

3.2 Power Divider/Phase Shifter Assembly

Figure 6 shows that power dividers are used to divide the output of the element assembly for input to the switching power dividers. These power dividers are arranged radially around the switching power

dividers as shown in Figure 9. By arranging the power dividers radially, a push-on RF connector may be used between the power divider assembly and the switching power divider. Push on connectors greatly simplify the testing and service of the multiple beam ESSA. Also contained within the power divider assembly are the SPD drive electronics and the phase compensation networks (if required). The phase compensation networks are switched line phase shifters which use glass packaged axial leaded PIN diodes for the switching function.

3.3 Switching Power Divider

BASD has fabricated two types of switching power dividers which may be used in the ESSA. Both radial waveguide and microstrip implementations can be used to select and combine the desired sets of elements used to create the beams. A 10 mA bias supplied to the desired input ports causes the desired SPD's PIN diodes to go to a low resistance state, thereby directing signals from the elements controlled by those PIN diodes to go to a summing junction.

3.4 Microprocessor

A 16-bit I^2L microprocessor is used to control the ESSA. This microprocessor interfaces with the SPD driver and user electronics through a serial data interface.

4.0 OPERATING MODES

The ESSA microprocessor has the capacity to cause the ESSA to operate in a variety of operating modes.

- Omnidirectional - The SPD is instructed to sum together a set of elements which provide "omni" coverage over a hemisphere.

- Program Track - The microprocessor calculates the pointing angle towards TDRSS based on ephemeris data provided periodically for both TDRSS and the user satellite.
- Directed Beam - The microprocessor causes the ESSA to point in the commanded direction.
- Automatic Acquisition - The ESSA can use a figure-of-merit such as an AGC level provided by the receiver to determine the pointing angle towards the target. No other information regarding target location is necessary.

5.0 PERFORMANCE ADVANTAGES

The ESSA's advantages over the conventional multi-faced phased array include:

- Single mounting structure
- Gain "independent" of scan angle
- Phase "independent" of scan angle
- Time delay "independent" of scan angle
- Beam shape "independent" of scan angle
- Simple phase compensation networks may be used
- Data update may be accomplished more easily
- Lower power draw

These advantages make the Electronically Steerable Spherical Array an attractive antenna for applications which require single or multiple beam coverage of large solid angle regions.

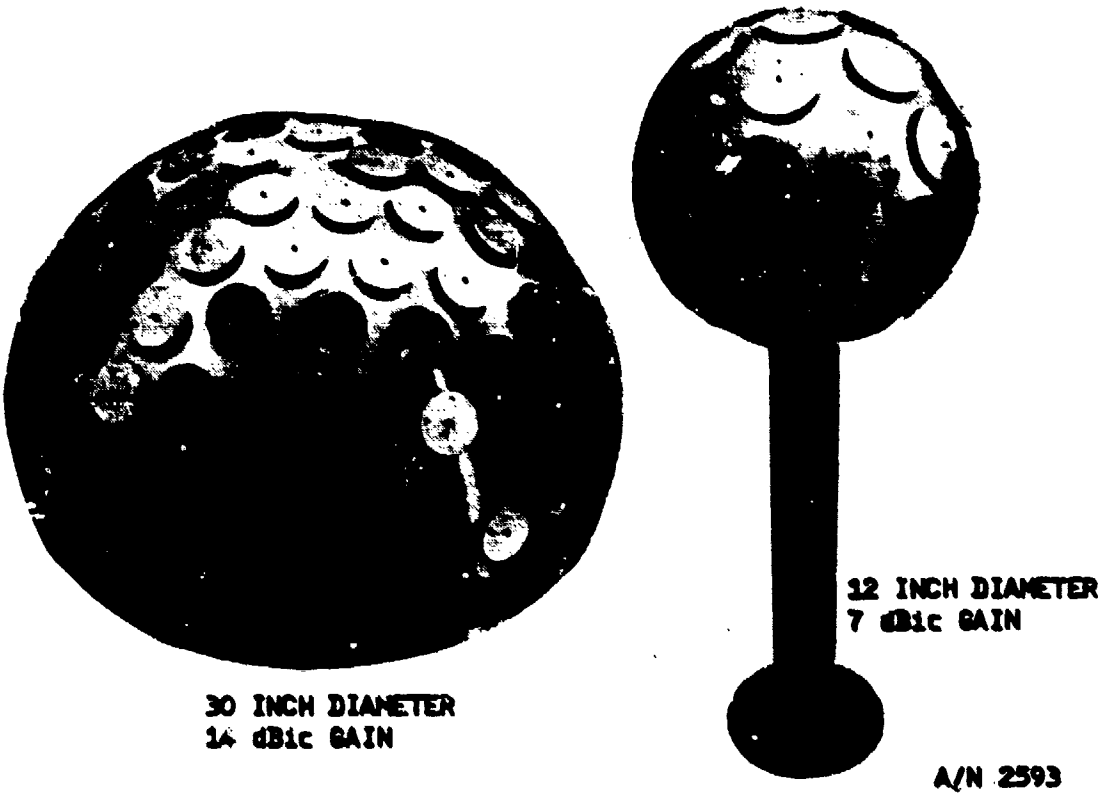

Figure 1 Engineering Models of the 7 dBic and 14 dBic Gain ESSAs Have Been Fabricated and Tested by BASD

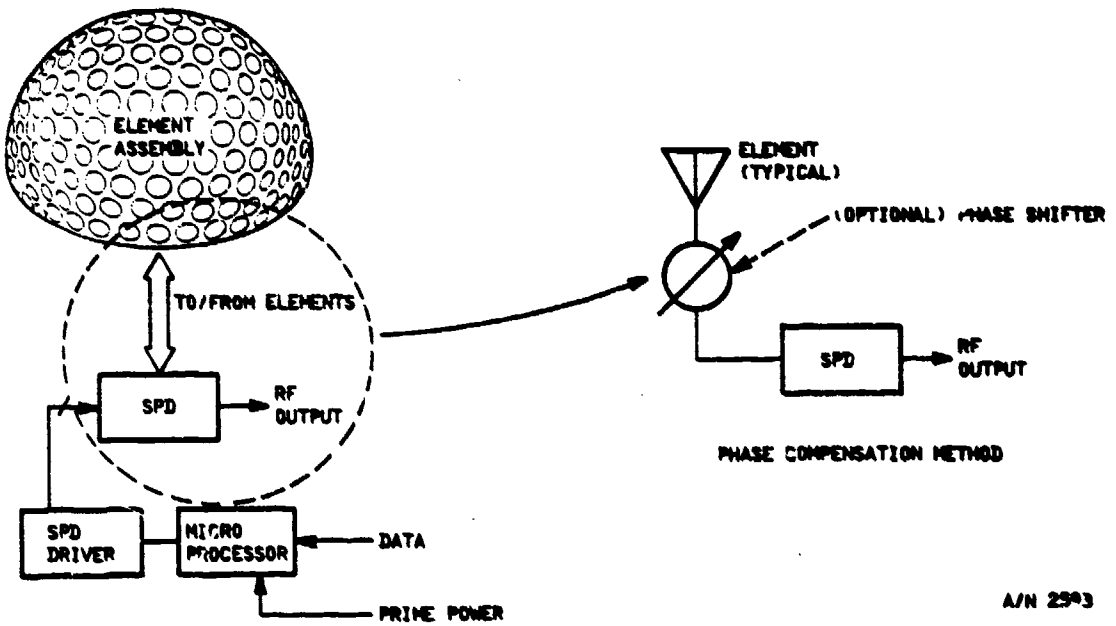

Figure 2 SPD Element Selection is Controlled by the Microprocessor

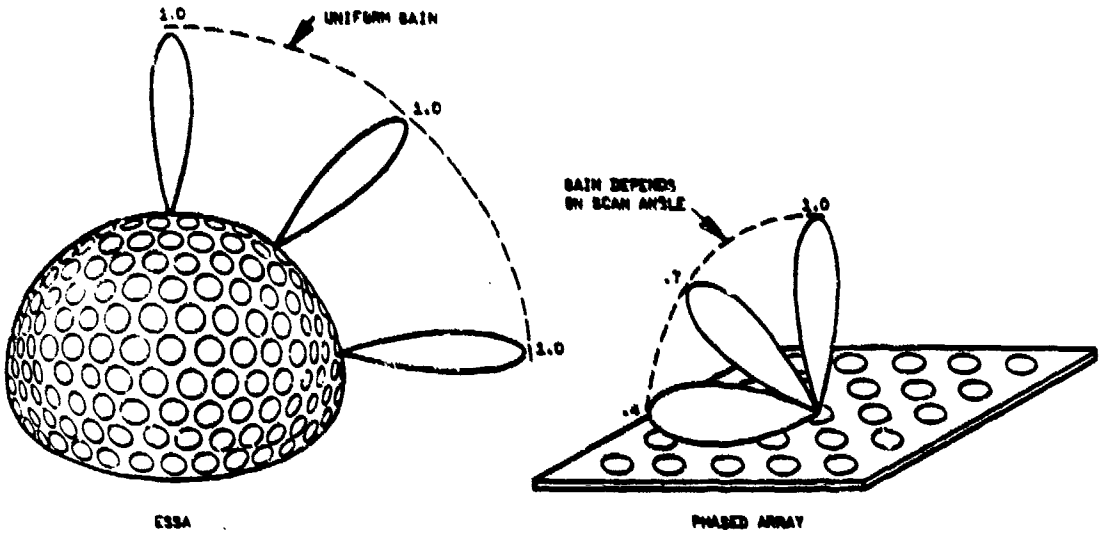

Figure 3 ESSA's Gain Remains Constant While Phased Array's Gain Rolls Off When Scanned

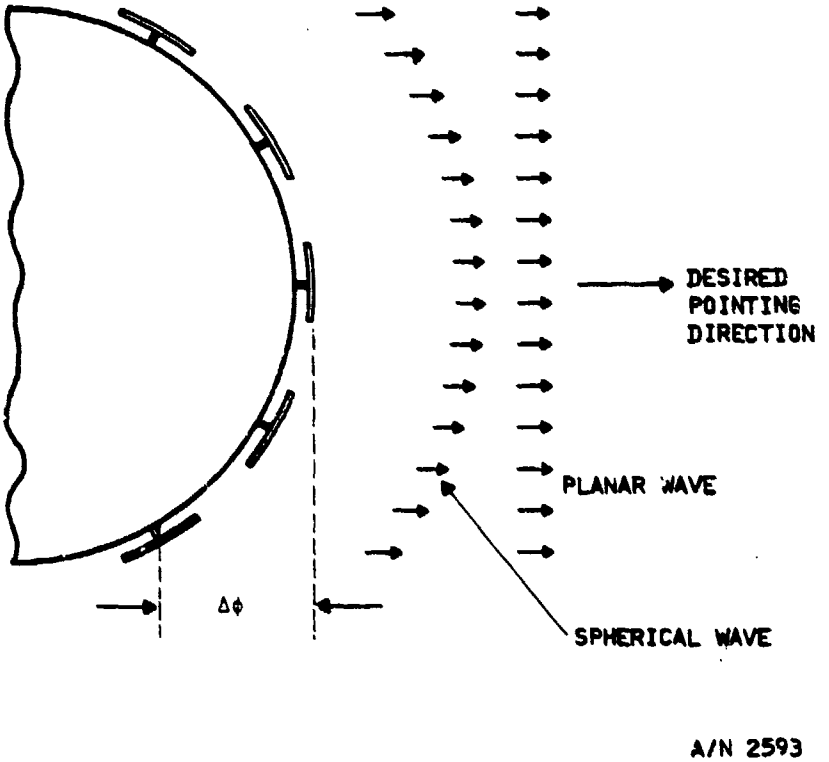

Figure 4 A Phase Difference Exists Between the Elements Used in the Aperture

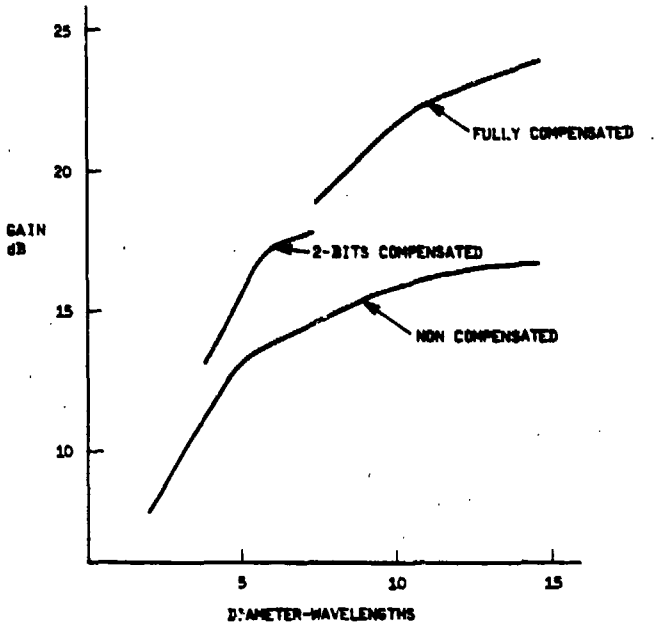

Figure 5 ESSA Gain is a Function of Size

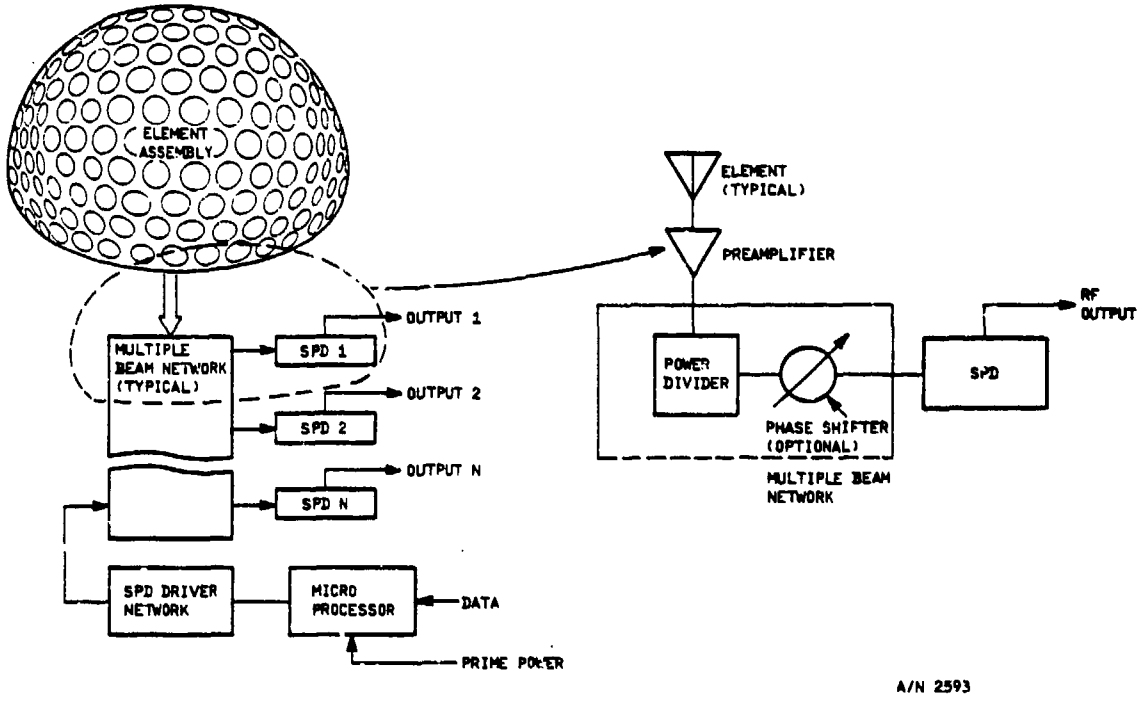

Figure 6 Multiple Beams May Be Provided With Little Change to ESSA/s Block Diagram

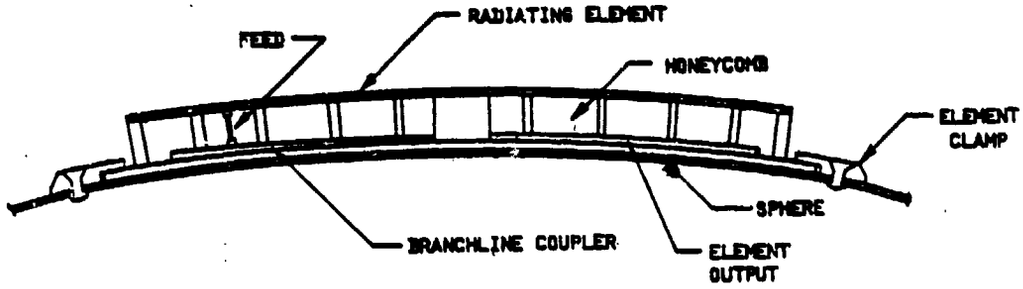

Figure 7 ESSA Element is Self Contained

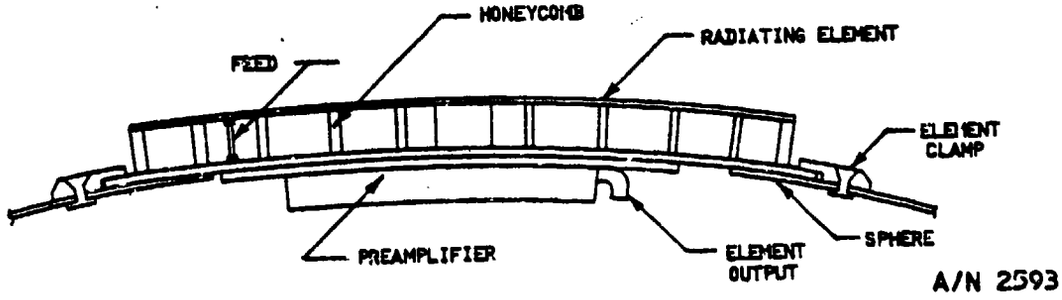

Figure 8 Multiple Beam Operation Modifies Element Only Slightly

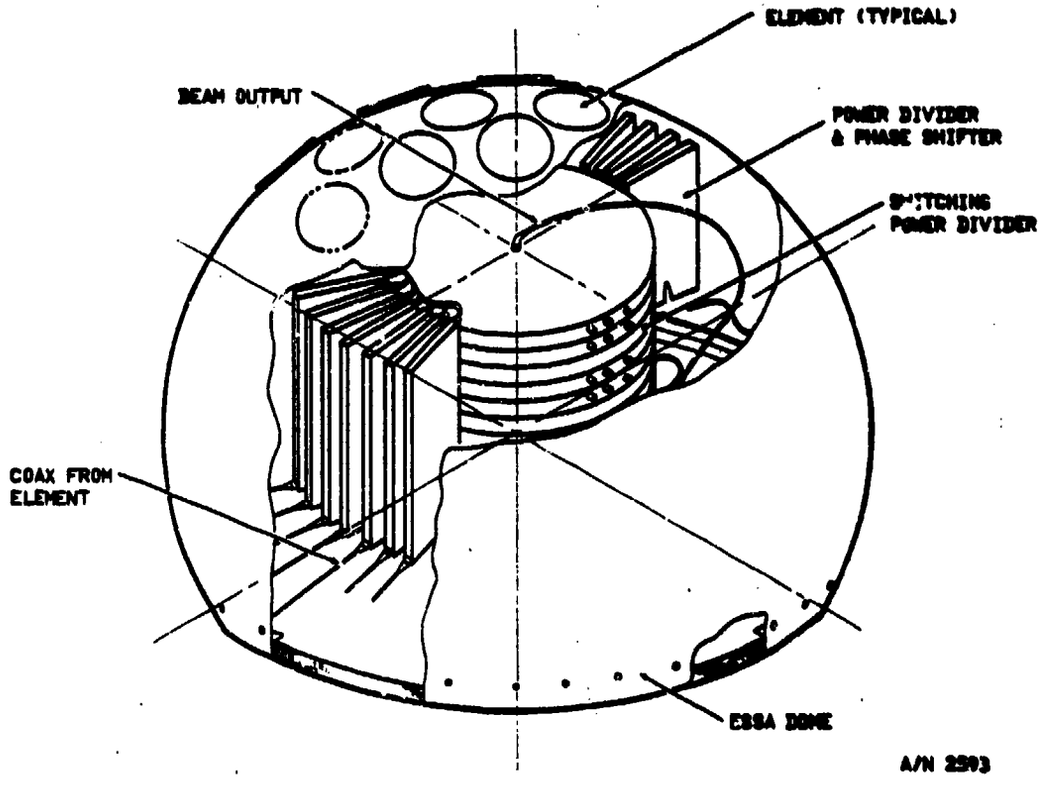

Figure 9 Multiple Beam Electronics May Be Enclosed Within the ESSA Dome

AD P001110

SPACE-FED, OFFSET, PLANE WAVE CASSEGRAIN SYSTEM FOR EHF APPLICATIONS*†

L. M. Schwab, A. R. Dion, D. L. Washington

Massachusetts Institute of Technology, Lincoln Laboratory
Lexington, Massachusetts

Abstract

This paper describes the study of a spatial combining approach to achieve a tractable design for a physically compact EHF satellite earth terminal antenna system which could address and overcome current 44 GHz solid state RF power generation limitations. Specifically, the achievement of high values (> 55 dBW) of uplink EIRP at 44.5 GHz with the use of small diameter (≤ 24 inches) reflector antennas and a single feed requires higher levels of power amplification (typically 10 watts) than currently achievable with individual solid state EHF devices. A solution to this problem is to use spatial power combining of the outputs of an array of feed horns individually driven by low power solid state amplifiers phase locked to a common source. This paper describes the numerical study of such an array used with an offset, plane-wave fed, near-field Cassegrain reflector system.

*The work reported in this paper was sponsored by the Department of the Air Force.

†"The U. S. Government assumes no responsibility for the information presented here.

PAGE BLANK-NOT FILMED

The study included modelling random phase and amplitude errors in the feed amplifiers and determining the effects of these errors on the system performance. These computed results demonstrate the feasability of using the spatial combining approach to provide high EIRP for mobile EHF communications terminals.

I. INTRODUCTION

The spatial combining approach to achieving high levels of terminal EIRP can be implemented with a variety of reflector and feed array configurations. Indeed, a previous study[1] done at Lincoln Laboratory evaluated a Cassegrain configuration consisting of a symmetric paraboloidal main reflector, ellipsoidal subreflector, and focused feed array of 32 square horns. This paper describes a different configuration, specifically an offset plane-wave fed/near-field Cassegrain (NFC) configuration consisting of a paraboloidal reflector, a confocal paraboloidal subreflector, and an unfocussed planar array of horns arranged in a hexagonal distribution. The paraboloidal reflector used in this study was constrained to be a 24-inch offset reflector (F/D = .5). The configuration was selected for both its compactness and the hardware implementation advantage of placing all feedhorns on a plane and driving all feed horns in phase (as opposed to configurations requiring non-planar positions and/or illumination phase tapers).

The near-field Cassegrain is favored over a full phased array aperture approach because providing dual frequency (receive and

transmit functions) capability with a phased array would require either providing two apertures resulting in a much larger physical envelope, or providing feed horns with dual frequency capability. Dual frequency feed horns would make a phased array undesirably complex as well as possibly leading to grating lobe difficulties due to different wavelength separation values.

The numerical analysis of this system was carried out using existing aperture antenna analysis software specifically modified to handle the near field Cassegrain geometry and to impose random error distributions on both feed phases and feed amplitudes. This software was used to parametrically study the effects of variations in array size, array location, and feed amplitude and phase errors on the directivity and aperture loss of the system. Aperture loss is defined in this study as the combination of spillover and illumination variation losses.

The baseline configuration consists of the constrained primary reflector diameter of 24 inches, a magnification ratio (of reflector to subreflector diameters) of 5, and a 19-horn feed array. When using 1/2 watt RF power amplifiers with pessimistic values of random amplitude and phase errors (-3 dB and 30° standard deviations), an EIRP of 54.3 dBW at 44.5 GHz can be achieved.

II. CONFIGURATION DETAILS

The near field Cassegrain (NFC) configuration treated in this study differs from a conventional Cassegrain configuration in several ways. The differences are summarized in Table I.

TABLE I

FEATURES OF NEAR-FIELD vs CONVENTIONAL CASSEGRAIN SYSTEMS

NEAR-FIELD CASSEGRAIN	CONVENTIONAL CASSEGRAIN
Both reflectors are paraboloidal.	One reflector is paraboloidal; one is hyperboloidal.
Both reflectors are confocal and geometries are scaled to each other.	Both reflectors have a common focus but do not scale to each other.
Subreflector is in near-field of feed array.	Subreflector is usually in far field of the feed.
Linear phase front illumination (i.e., plane-wave incident).	Curved phase front illumination (i.e., spherical-wave incident).
Requires a feed array or a horn/lens combination.	Can be fed by an array or, more typically, a single feed.
Array axial position is of secondary importance.	Axial feed position is critical.

In addition to the features described in Table I, both the near field and conventional Cassegrain systems can provide a scanned beam capability if required. The scanning mechanism implementation, however, is accomplished differently for each system. Scanning with the NFC is accomplished electronically by generating a linear phase front taper on the feed array excitation. Scanning with the conventional Cassegrain is accomplished by physically moving the feed (in the case of a single feed) or by generating a complex phase and amplitude taper (in the case of an array of feeds). A more complete description

of the general features of an NFC system and its electronic scanning capabilities can be found in Ref. [2]. The beam scanning for the NFC will not be discussed further in this paper.

The geometry of the NFC configuration considered in this study is given in Figure 1 in profile and head-on views. The unsubscripted coordinate frame has its origin placed at the parabolic vertex and the subscripted ("s") coordinate frame has its origin at the center of the reflector. The set of feed horns is pictorially shown at one of the two fixed feed positions (Z_s = -.083 inches; equivalent to Z = +4 inches). The particulars of this configuration are summarized in Table II.

TABLE II

SUMMARY OF CONFIGURATION AND GEOMETRY OF NFC

Number of Feeds:	19
Distribution of Feeds:	Hexagonal Array (3, 4, 5, 4, 3)
Individual Feed Diameters:	1 inch (nominal)
Reflector Diameter:	24 inches
Reflector f/D Ratio:	0.5
Subreflector f/D Ratio:	0.5
Distance From Reflector Center to Symmetry Axis:	14 inches
Containment Envelope:	Nominal 28 inch (Diam) X 18 inch (Height) Cylinder

The magnification ratio (reflector diameter divided by the subreflector diameter) is 5. The geometrical blockage determined by the mutual projection of the subreflector and reflector onto the x-y plane was computed as -0.12 dB. (The numerical software does not compute blockage loss so this increment must be

subtracted from the computed directivities). Feed array location along the z axis was initially a variable in determining aperture loss. Two fixed array positions, selected primarily on the basis of their suitability for incorporating a dichroic surface at a later time, were used in subsequent computations.

III. ANALYSIS

The software techniques and methods used in this analysis are based on core antenna analysis programs developed at Lincoln Laboratory. Specialized software to generate random feed array errors was appended. The methods used in the software are summarized as follows. An analytic feed model ("unit feed") is assumed for the individual elements of the hexagonal array distribution. The unit feed consists of the far field pattern of a circular aperture which has an area equal to the area of the modeled hexagonal feed apertures*. The unit feed model has 100% aperture efficiency with linear polarization which is contained in the reflector offset (i.e., Y-Z) plane. The use of the far field pattern for the circular unit feed poses some restrictions on the feed size and placement. However, a very large individual feed must be placed very close to the subreflector to cause significant error in the main lobe illumination. The 19-horn feed arrays

*The effect of mutual coupling in the feed array is neglected in this analysis. It is a secondary effect which could be included in the final array feed analysis and design but is expected to be insignificant.

discussed here are sufficiently far from the subreflector to assure insignificant error.

The far field pattern function of each unit feed is used in conjunction with geometric optics relationships (i.e., ray tracing through the subreflector to small increments of the reflector surface) to solve for the surface current on the reflector subaperture due to the unit feed. The surface currents are then vectorially summed over the number of feed sources. The total surface current density on the reflector subapertures is then analytically related to the far-field which is numerically integrated to determine the total far field of the NFC. In setting up the reflector illumination function, the individual feed amplitude weights are normalized to provide 1 watt total input power. Normalizing the total input power also makes it easier to scale the results for other input power levels. In computing the EIRP of the plane wave Cassegrain fed by the 19 horn array, the nominal (i.e., with no degradation effects) input power to each horn is $1/19 = .0526$ watt. A one-sided normal error distribution was imposed on the amplitudes of the 19-horn array along with a two-sided normal distribution on the phase errors. The one-sided amplitude distribution was selected to model the random nature of the amplifier power transfer functions and long term degradations thereof. The feeds and reflectors are assumed to have no conduction losses.

Directivity is defined as the directive gain at the pattern maximum and is given by the ratio of the radiation intensity on the peak of the beam to the radiation intensity of an isotropic source radiating the same power as the test antenna:

$$D = \frac{U_{max}}{U_o} = \frac{4\pi U_{max}}{4\pi U_o} = \frac{4\pi U_{max}}{P_{rad}} \qquad (1)$$

where Prad is the radiated power which equals the input power for the condition of no conduction losses.

Some care must be exercised in applying reflector antenna software analysis tools such as the one used here. The subreflector must be in the far field region relative to the individual feed horns as stated above. However, the subreflector must also be positioned in the near field of the overall feed array to obtain plane wave illumination of the subreflector. With extremely close feed-subreflector spacings, ($<< 2D^2/\lambda$), where D = feed horn diameter, the software modelling technique breaks down resulting in incorrect computations. However, all the feed-subreflector spacings used in this study exceed this limitation. At the other extreme of distant feed-subreflector spacings, the wavefront illumination on the subreflector approaches an undesired spherical wave resulting in low values of directivity (albeit computed using a valid algorithm). [Note: It is planned to perform calculations at a later time using measured

patterns of a circular feed horn in place of the unit feeds. The unit feed has a 100% illumination efficiency, i.e., it assumes that the equivalent hexagonal feed aperture is uniformly illuminated. It is estimated that the circular feed horns will be about 80% efficient relative to the unit feed, hence about a -1 dB difference in the directivity computations can be expected].

Edge diffraction effects associated with the near-field assumption, and the reflector edges have not been considered in this study. Their effects on directivity computations are negligible.

IV. COMPUTED RESULTS AND CONCLUSIONS

The configuration reported in this memo was shown in Figure 1 with profile (yz plane cut) and head-on (x-y plane cut) views. The baseline reflector magnification ratio (of reflector to subreflector diameters) is five. The baseline feed array consisted of 19 horns nominally 1 inch in diameter hexagonally distributed. Variations from these baseline values were also treated in the course of the study, e.g. magnification = 4 and hexagonal arrays of 7, 37, and 61 horns. The computed results for these variations is not significantly different from those for the baseline configuration. Hence, those results are not presented in this paper for the sake of brevity.

Figure 2 shows the computed value of aperture lo.) (determined by taking the difference, in dB, between the

directivity of a uniformly illuminated aperture and the computed far field on-axis directivity) vs feed array position along the z axis. The aperture loss of approximately 1.5 dB is mainly due to spillover, i.e., radiated power that misses the subreflector. In addition, there is some minor amplitude variation over the aperture which also reduces the efficiency. The portion of the curve in Figure 2 that is dashed indicates the region where the feed-subreflector distance is less than $2D^2/\lambda$, where D is the diameter of the unit feed. Based on the computed results shown in Figure 2, two fixed z-axis locations for the feed array were selected for use in subsequent computations. These positions (Z_s = -.083 inch and -3.083 inch, Y_s = -11.2 inches) approximately correspond respectively to the feed array positioned beneath the center of the reflector and slightly in front of (and above) the reflector vertex. Both feed array centers are located on a line which is parallel to the Z-axis and goes through the center of the subreflector. The selection of the optimum feed-reflector spacing depends strongly on where and how a dichroic surface (used to accomplish dual frequency operation) is placed in the configuration. The closer feed-subreflector spacing (Z_s = -.083 inch) which has slightly lower aperture loss (-1.46 dB) might be used if the dichroic surface were incorporated onto the subreflector surface. The further feed-subreflector spacing (Z_s = -3.083 inch) might be used if a planar dichroic surface were placed between the feed array and the subreflector.

In a separate study, aperture loss was computed as a function of total feed horn area with all other parameters held constant. It was found that, for the previously specified baseline parameters, the baseline feed geometry (19 feeds; total area = 13.61 sq. inches) resulted in an aperture loss which was very close to the optimum value (-1.46 dB aperture loss with Z_s = -.083 inches vs the optimum value of -1.41 dB).

Figures 3(a,b) shows the far field pattern in the yz plane for the two feed array positions. The sidelobe levels are slightly asymmetric with maximum levels of -19 and -18.5 dB.

Random error distributions were next imposed on the feed array amplitudes and phases. (Reflector surface distortion effects were not considered in this study. Any loss of gain due to such effects would add to the losses computed here and can be accounted for by standard formulas. For the size of the reflector considered here, such loss will be small.) Figures 4(a) and 4(b) give plots of maximum, minimum and mean values of directivity computed as a function of maximum deviation for uniformly distributed random phase errors. For each data point, a set of ten sequential cases were run. The maximum and minimum values computed and plotted do not necessarily represent absolute maximum and minimum values, but rather maximum and minimum values for the sets of 10 runs per data point. The feed array positions are Z_s = -0.083 inch and -3.083 inch respectively. Figures 5(a) and

5(b) are similarly computed and plotted, but for 10 random cases with normal distribution, with the abscissa giving the one sigma value of the phase error distribution. The same feed array positions (Z_s = -0.083 and -3.083 inches) are used.

In comparing Figure 4(a) and Figure 5(a) (or, alternatively 4(b) and 5(b)), one finds that, for a given abscissa value, the directivity values (max, min, and mean) are lower for the case of the normal error distribution as compared to the uniform error distribution case. For the uniform distribution case, the abscissa values represent the (+, -) maximum values of the distribution whereas, for the normal distribution, the abscissa values represent the one sigma value. Thus, the significant phase error values extending out to the three sigma points of the normal distribution account for the increased aperture loss of the normal distribution compared to the uniform distribution.

The upper limit on the phase error axes (60°) was chosen solely to show enough of the curves to understand the trend in directivity degradation. The 60° limit is likely far in excess of typical random phase errors anticipated due to phase lock loop instability, component-to-component variations, line length variations, and the like. It is interesting to note, however, that the directivity reductions at such large phase errors are, albeit undesirable, certainly not catastrophic from an operational point of view.

Computationally, the average value of EIRP is found by taking the average value over a large number of runs (10 used in this study) of the product of the computed antenna directivity (which is largely influenced by the phase error distribution) and the actual (i.e., degraded) total input power for each run. Stated as an equation, average EIRP is given as follows:

$$\text{EIRP (average)} = \frac{\sum_{m=1}^{M} \left[\left(\sum_{n=1}^{N} P_n \right)_m G_m \right]}{M} \qquad (2)$$

where: N = total number of feed horns (=19)

M = total number of runs (=10)

P_n = RF power fed to the n^{th} feed horn (watts)

G_m = computed antenna directivity for the m^{th} run

The computed average EIRP (dB) for the set of 10 successive runs is given in Figures 6(a) and 6(b) where the standard deviation of the phase distribution is used as the independent variable with parametric values of standard deviation of the one-sided amplitude distribution (0 dB, -1 dB, -3 dB, and -6 dB). Figures 6(a) and (b) also contain tabular printouts of the computed antenna directivity and the EIRP for all the error combinations used. Using these printouts, one can quickly separate the gain reduction component due to error introductions from the reduced radiated RF power component.

The graphs of EIRP vs phase error standard deviation (for constant amplitude error distributions) given in Figures 6(a) and 6(b) draw closer together with increasing phase error. This "bunching" effect is a reasonable and expected phenomenon and can be explained as follows. Comparing the 0 dB and -3 dB amplitude error curves, one finds that the gain reduction due to introducing severe phase errors (e.g., 60° phase error standard deviation) on an aperture with an approximately uniform amplitude distribution (i.e., power deviation = 0 dB) is greater than the gain reduction due to introducing the same severe phase errors (std. dev. of 60°) to the set of feeds with a one-sided normal amplitude distribution (3 dB) standard deviation) imposed on them. This difference in gain reductions for uniform vs randomly reduced amplitude distributions relates to the fact that introducing a large phase error to any of the unit amplitude feeds will have a substantial effect on gain reduction compared to introducing the same large phase error to one of the feeds with a reduced input amplitude. In the limit, a fully derated feed (-∞ dB input amplitude) can tolerate an arbitrarily large phase error with no effect other than the gain reduction due to removing the excitation from that one feed.

Finally, a combined amplitude error standard deviation of -3 dB and a phase error standard deviation of 30 degrees results in an expected EIRP reduction of -3.06 dB. Of this amount,

1.13 dB is due to the gain reduction caused by the introduction of phase and amplitude errors, and the remainder (1.93 dB) is due to the reduced RF power. If 1/2 watt RF amplifiers were used at each feed horn, the resulting EIRP for these large amplitude and phase error distributions would be 54.3 dBW. Based on these computed results, the spatial combining approach is a viable and attractive technique for achieving high EIRP for mobile EHF communications terminals.

Acknowledgements

The authors gratefully acknowledge Drs. Leon Ricardi and Alan Simmons who suggested the need for addressing this problem and provided valuable technical discussions. We also wish to thank Mr. William Cummings and Dr. Alan Fenn for reviewing and critiquing the manuscript.

References

1. Burrows, M. L. (1980), Dual-Frequency EHF Ground Terminal Antenna, Lincoln Laboratory, M.I.T. Technical Note 1980-13. (AD-A085607/0)

2. Fitzgerald, W. D. (1971), Limited Electronic Scanning with a Near-Field Cassegrainian System, Lincoln Laboratory, M.I.T. Technical Report 484. (AD-735661)

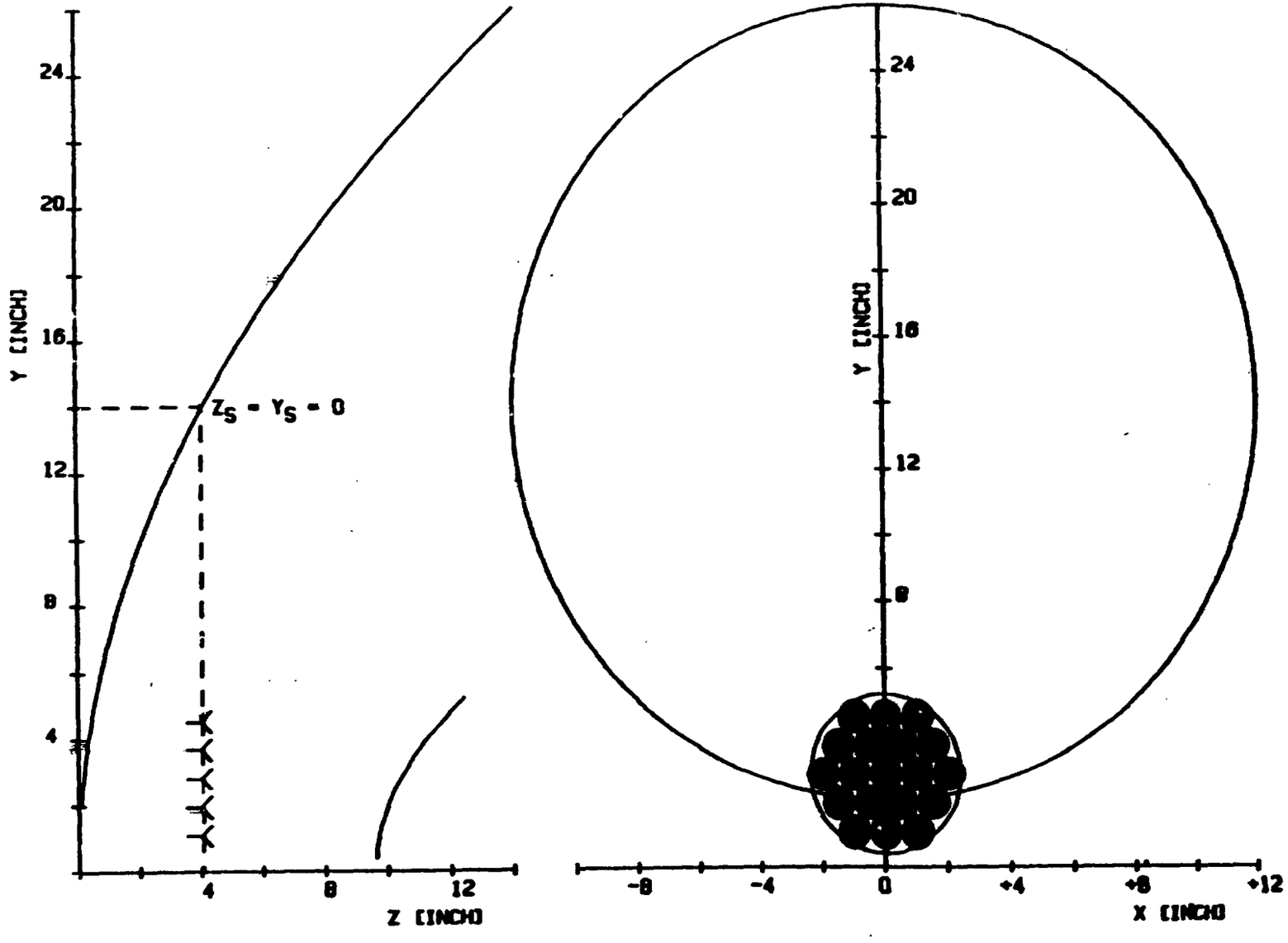

Figure 1. Baseline configuration (M = 5).

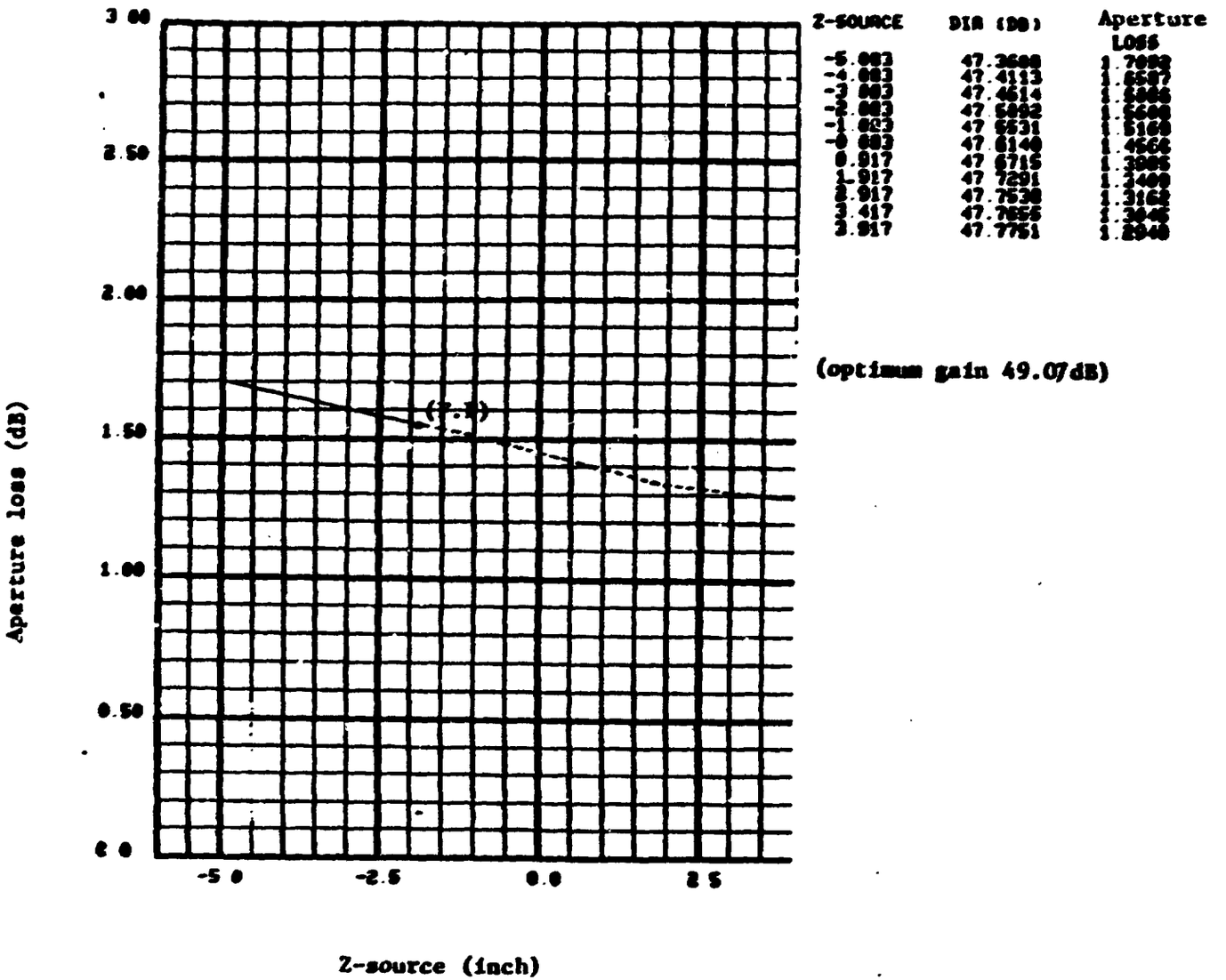

Figure 2. Aperture loss (dB) vs feed array position (inch) relative to a coordinate of reflector center.
Baseline feed array: M = 5; 19 horns; no feed errors.

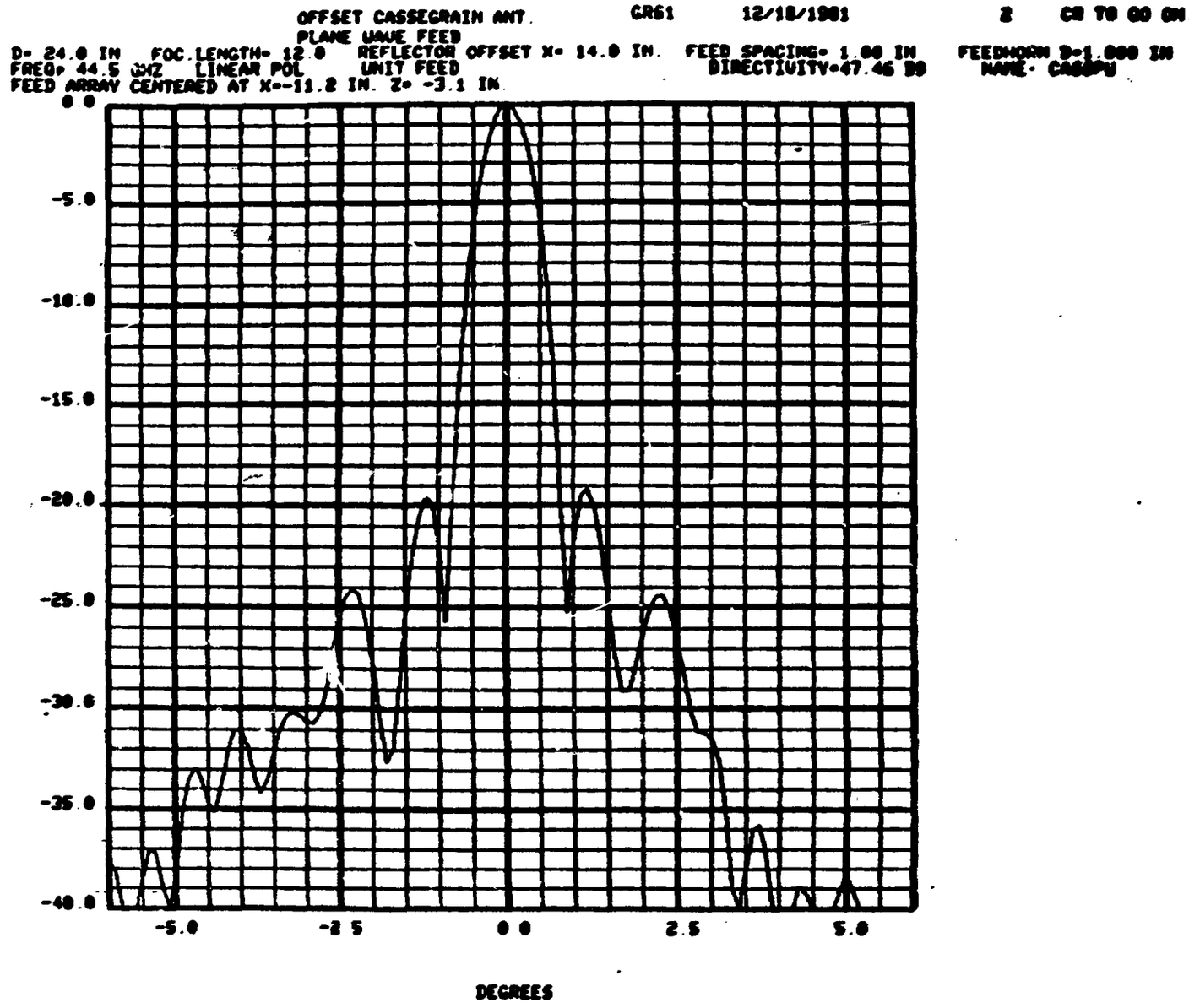

Figure 3(a). Far field pattern in the y-z plane (Z_{source} = -3.083 inches).

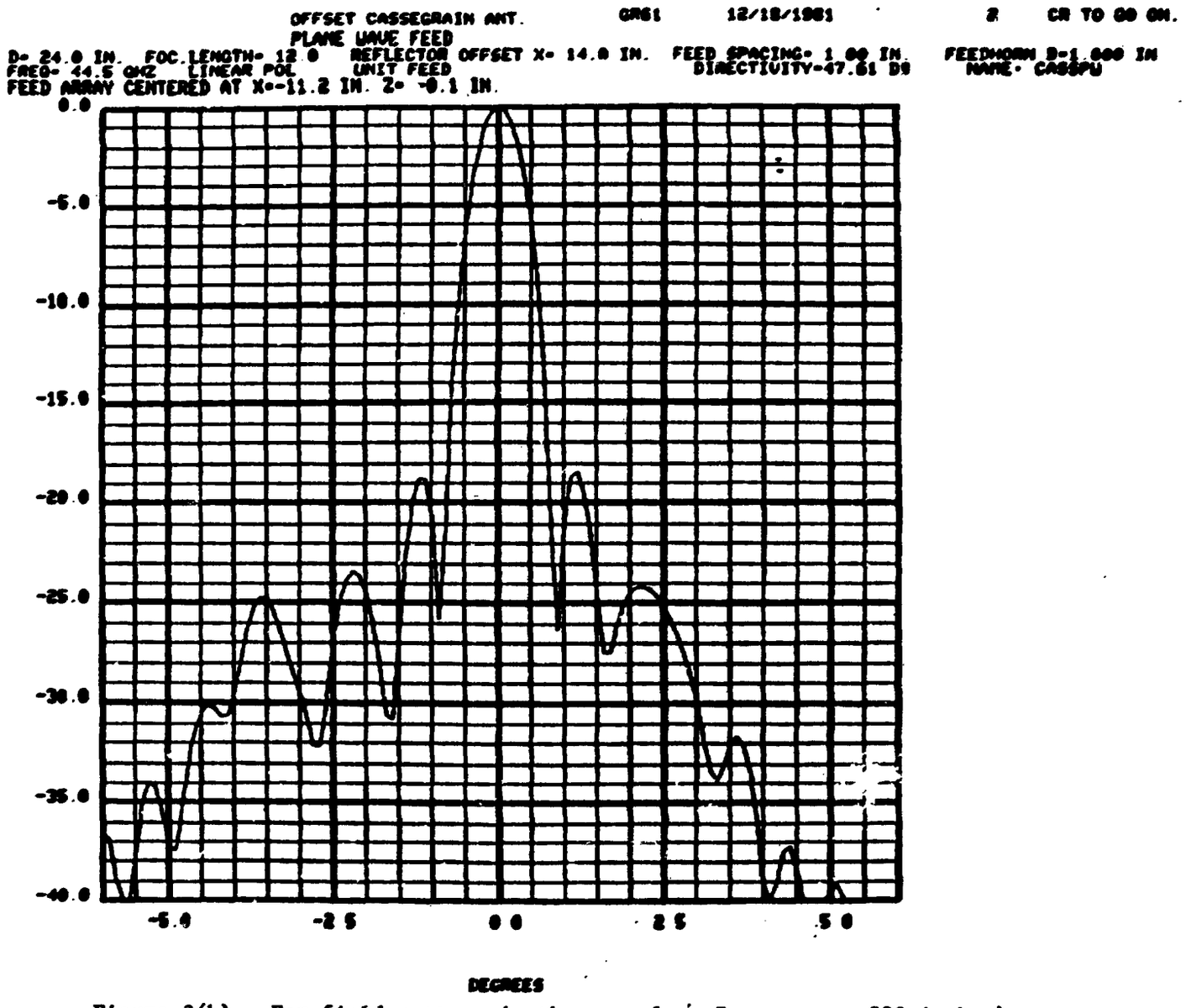

Figure 3(b). Far field pattern in the y-z plane (Z_{source} = -.083 inches).

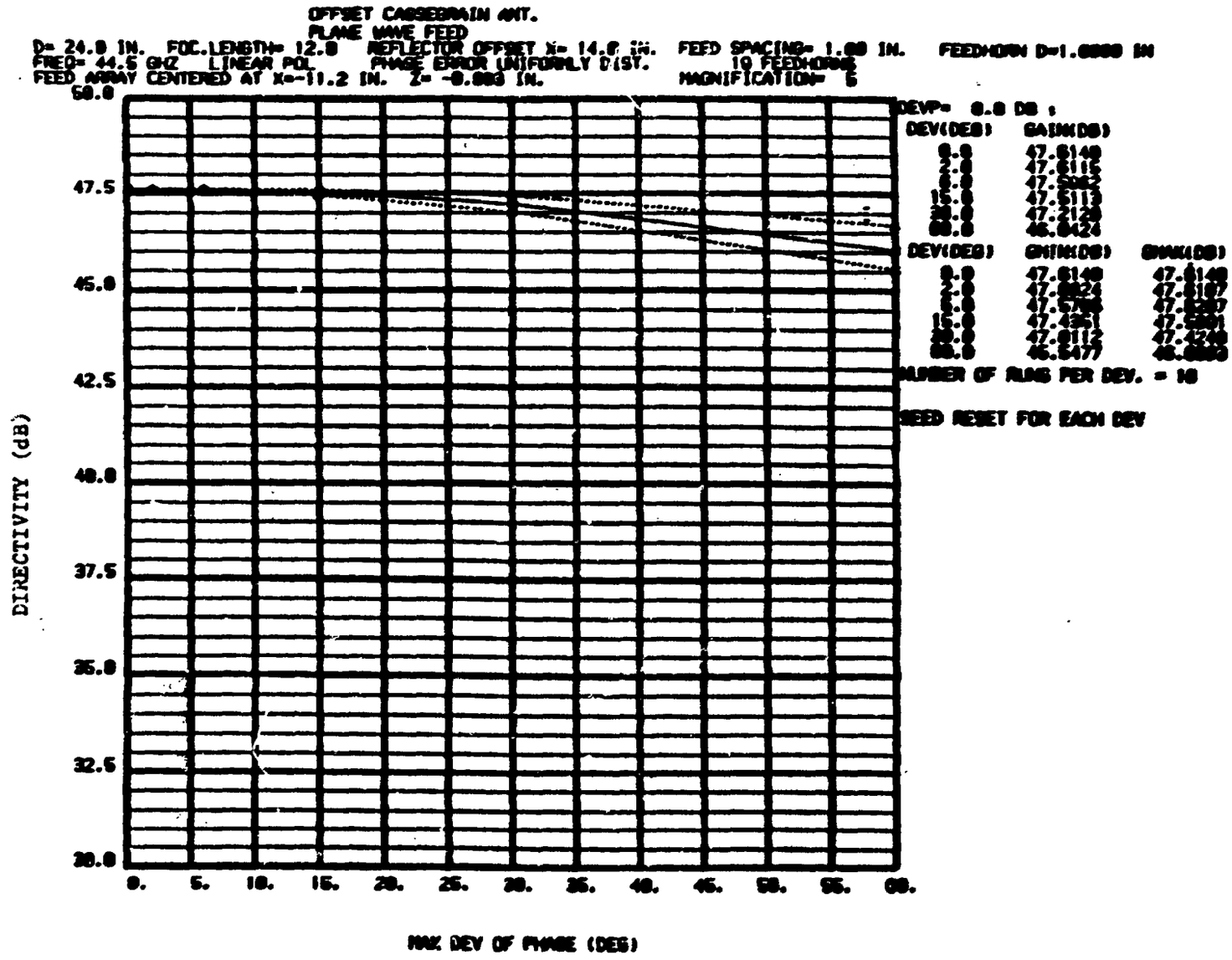

Figure 4(a). Maximum, mean, and minimum values of computed directivity vs maximum value of a uniform distribution of phase errors; Z_s = -.083 inches.

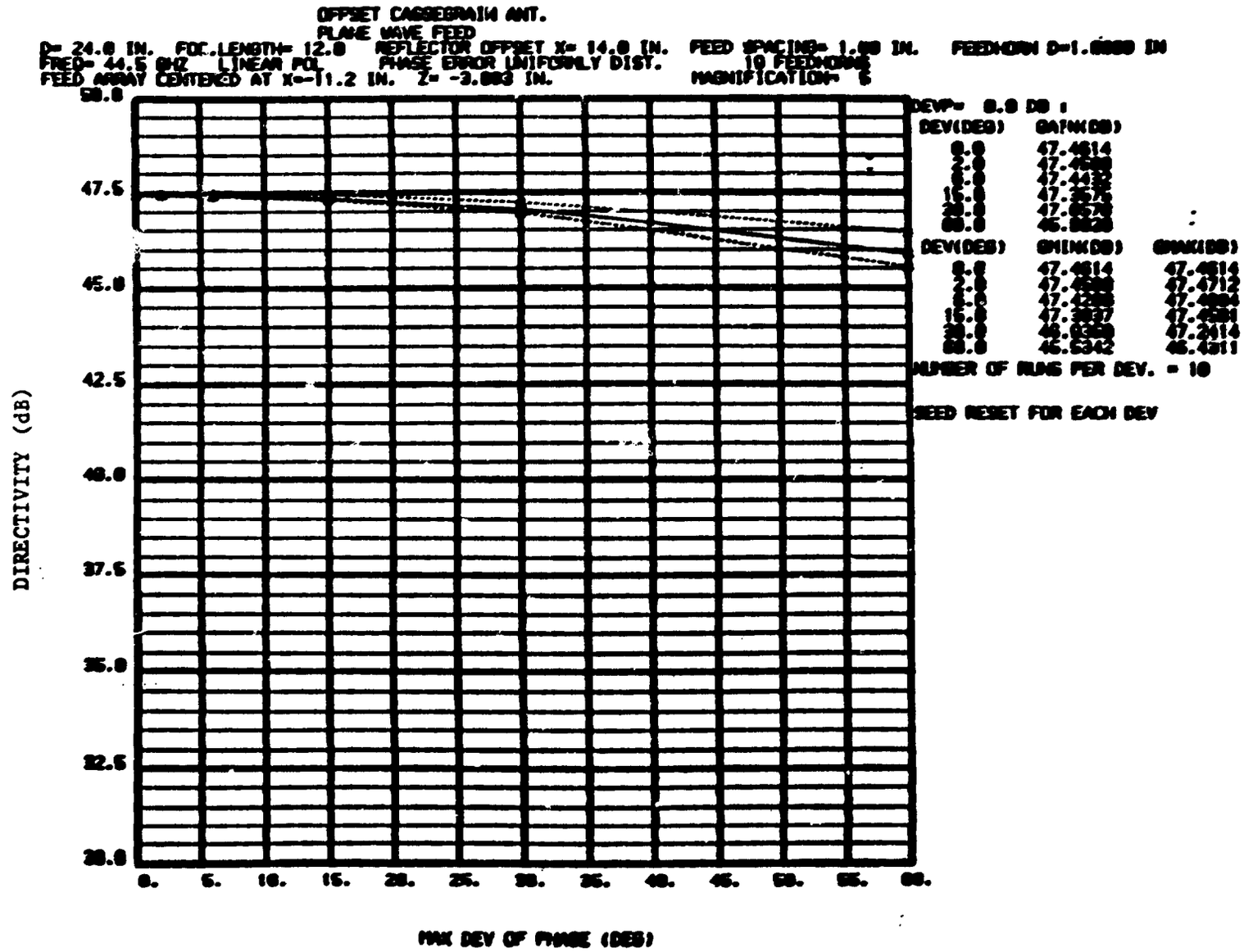

Figure 4(b). Maximum, mean, and minimum values of computed directivity vs maximum value of a uniform distribution of phase errors; Z_g = -3.083 inches.

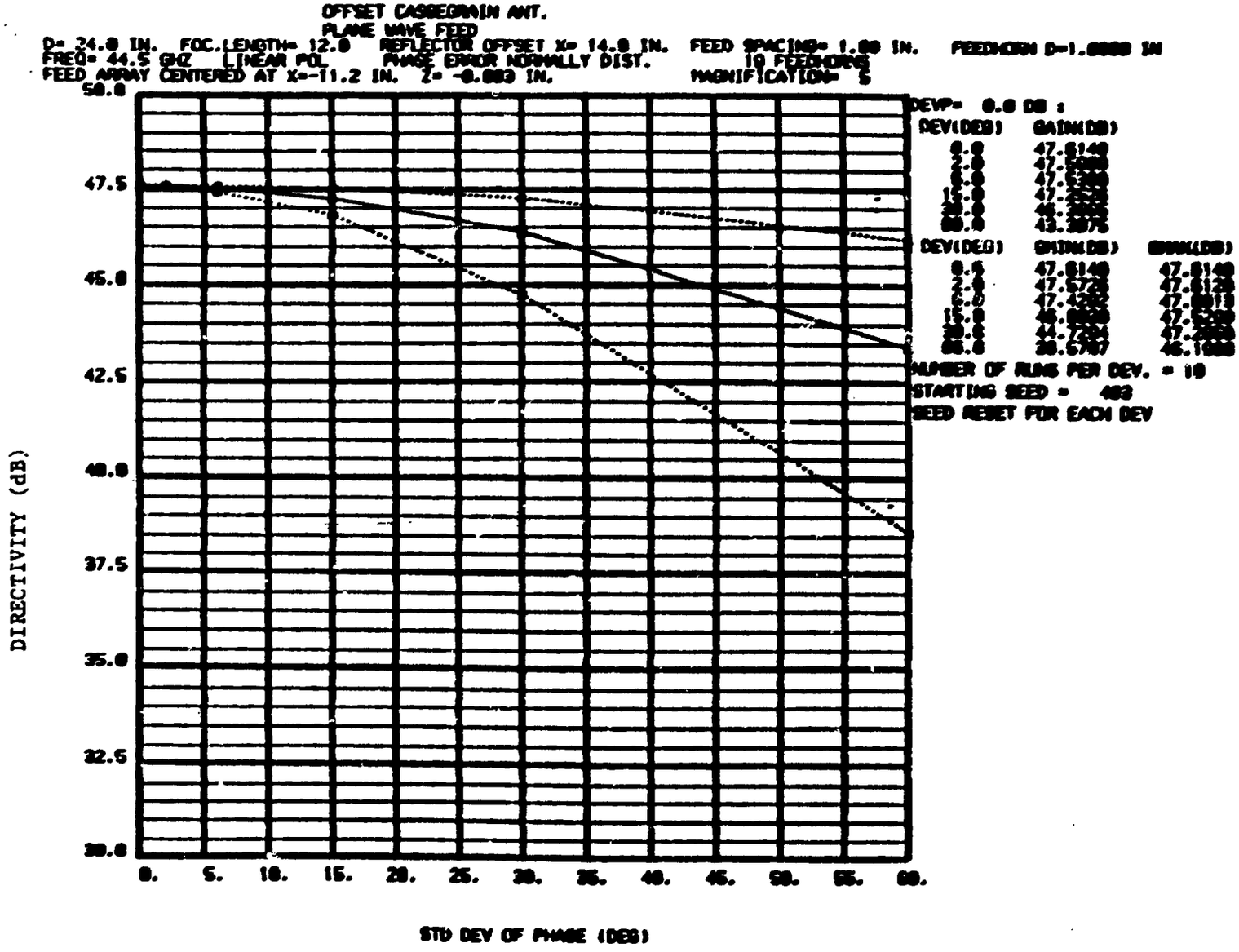

Figure 5(a). Maximum, mean, and minimum values of computed directivity vs standard deviation (1σ) for normally distributed phase errors; Z_s = -.083 inches.

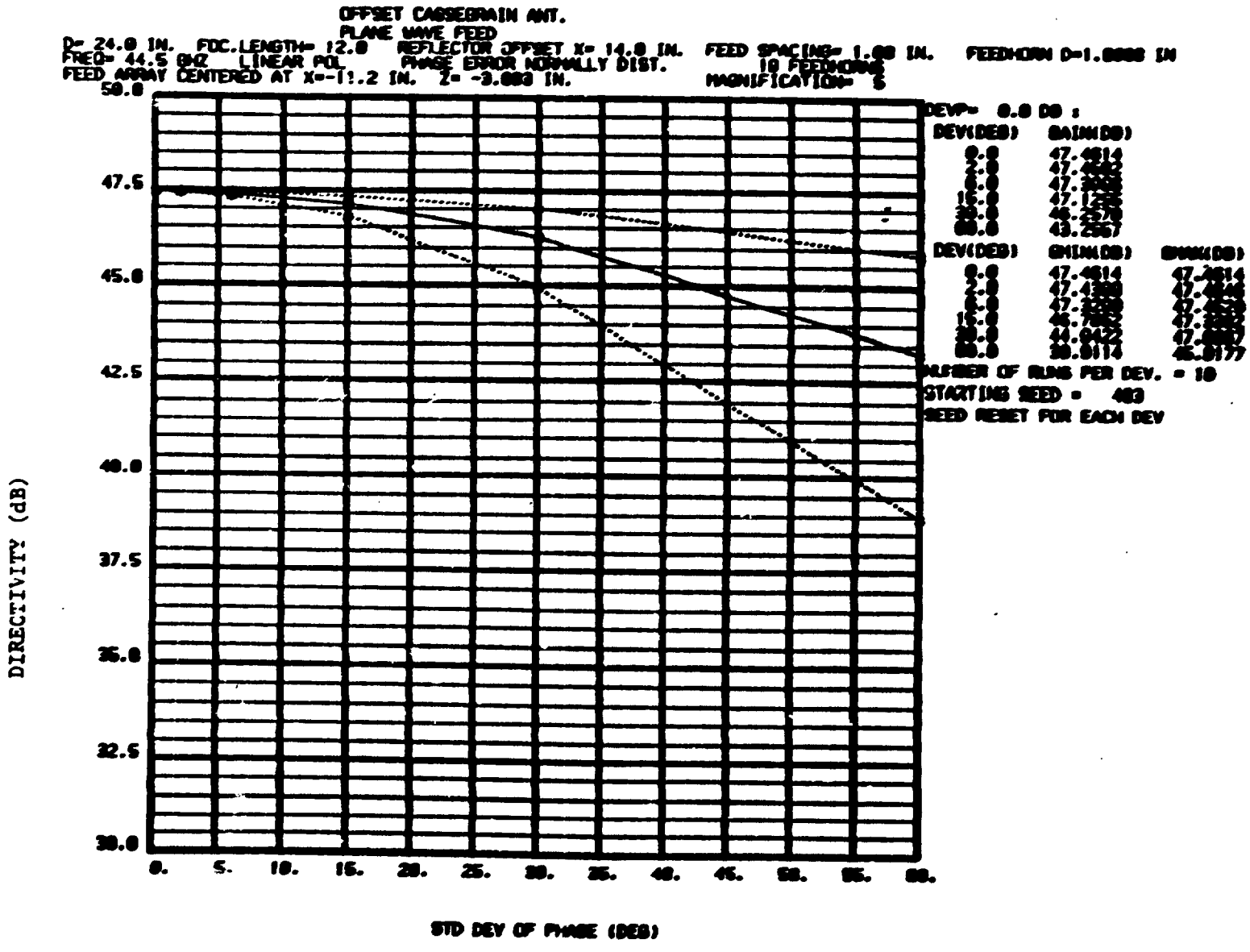

Figure 5(b). Maximum, mean, and minimum values of computed directivity vs standard deviation (1σ) for normally distributed phase errors; Z_s = -3.083 inches.

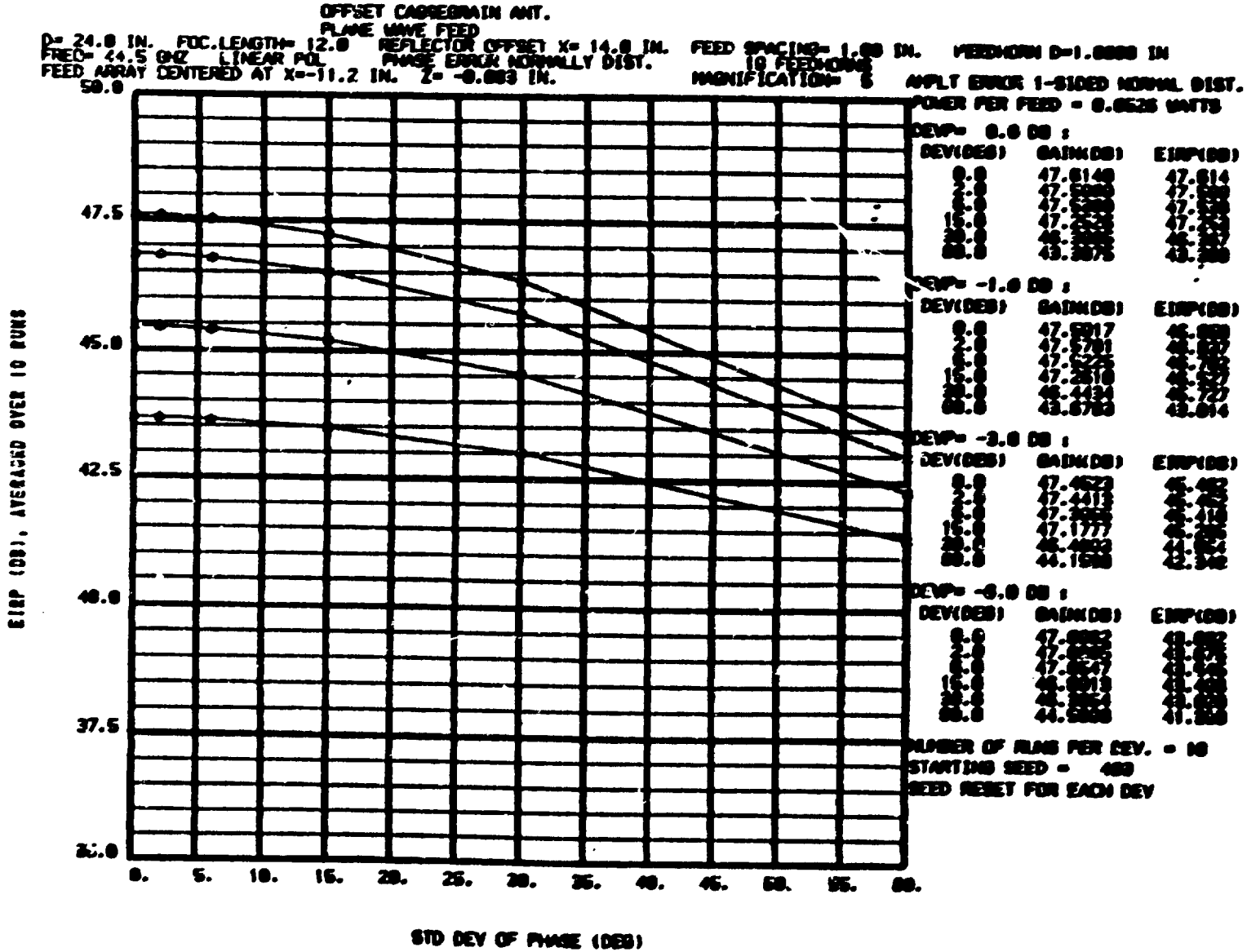

Figure 6(a). EIRP (dBW) as a function of phase and amplitude errors. (Z_s = -0.083 inches).

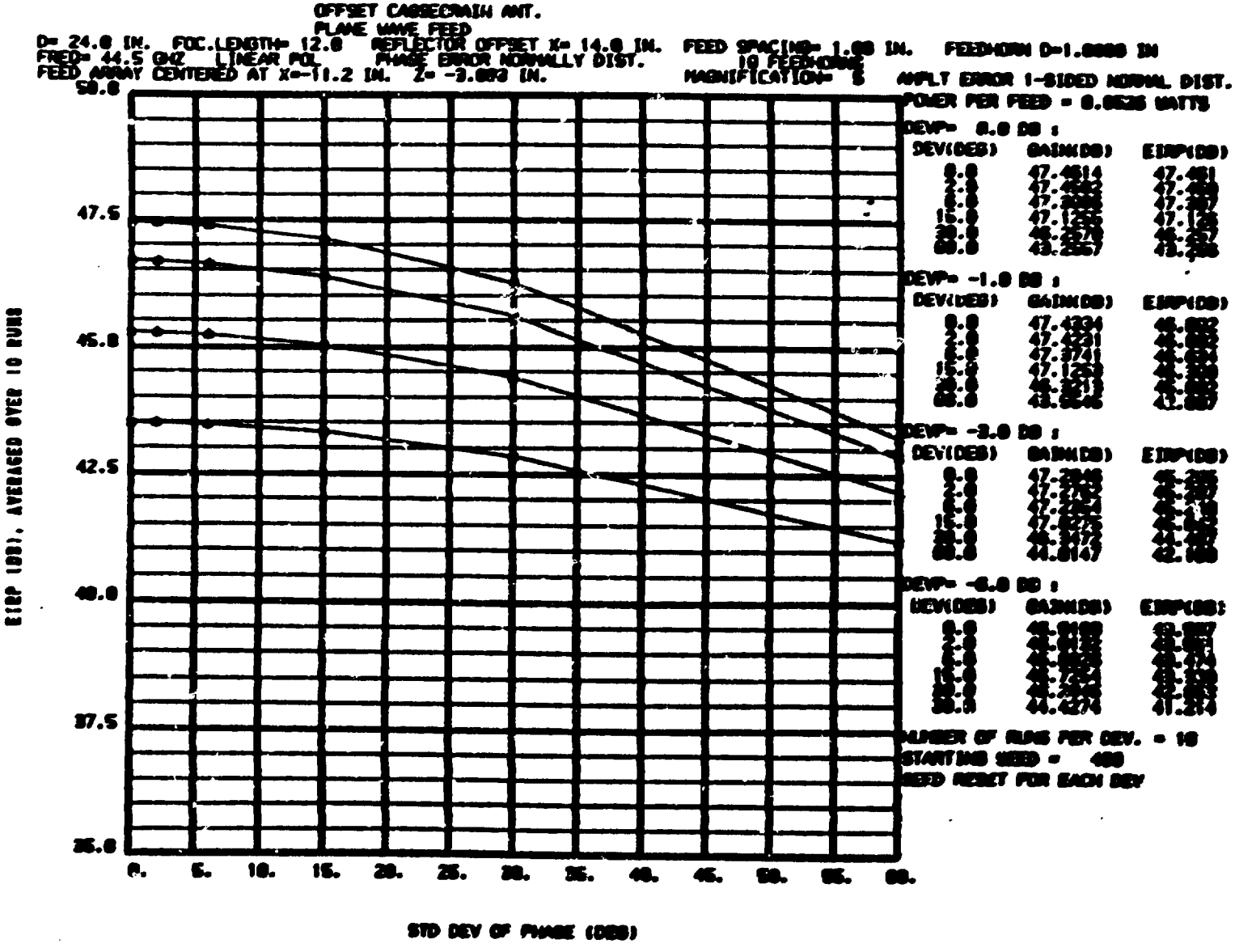

Figure 6(b). EIRP (dBW) as a function of phase and amplitude errors. (Z_s = -3.083 inches).

AD P001111

A MECHANICALLY SCANNED, SHAPED BEAM, 95GHz ANTENNA

JULIUS GREEN

HAROLD SHNITKIN

NORDEN SYSTEMS, INC.

UNITED TECHNOLOGY CORP.

NORWALK, CT 06856

PAGE BLANK-NOT FILMED

INTRODUCTION

This paper discusses the design and performance of a 95GHz mechanically scanned, shaped beam antenna which requires no electrical wiping contacts or rotary joints. The antenna was required to produce a shaped, 60° wide, beam in elevation and a 10° half-power beam width in azimuth, scanning over 180° in the azimuth plane. The peak gain required was 11dB (CP). Design approaches and theory are given, together with measured results of developmental models.

DESIGN APPROACH

Several conventional design approaches were considered. A pyramidal horn (Figure 1a) or a hog-horn (Figure 1b) with the required beam widths could be employed; however, these designs would require rotary joints, the hog-horn would be expensive to fabricate at 95GHz and would suffer from rotary joint losses and reliability as well as life problems. The approach successfully implemented utilizes a stationary pyramidal 10° by 10° HPBW horn, with its axis vertical, and a rotating shaped cylindrical reflector (Figure 1c). The reflector changes one 10° HPBW to a flat-top sixty degree wide elevation beam centered on the horizon, while the original 10° beam width is retained in azimuth. The reflector is rotated for scanning but the horn is stationary. Thus no rotary joint is required, eliminating associated r-f loss, cost, and reliability problems. The reflector mass can be made very small, alleviating mechanical bearing problems, and allowing rapid

beam scan. This approach can furthermore be extended to higher frequencies, where rotary joint problems are even more objectionable.

Both linear and circular polarizations are possible. If a linearly polarized horn is used (as in the experimental model), the polarization vector will rotate one degree for each degree of azimuth rotation as illustrated in Figure 2; this makes it ideally suitable for communication with either a LH or RH circularly polarized antenna. If a circular polarized horn is used, a CP secondary beam results.

The reflector is inexpensive to fabricate since it is contoured in one plane only. A flat-top, sharp corner, beam was generated in elevation, avoiding the usual gain reduction off the beam peak.

THEORY AND COMPUTATIONS

The beam shaping theory used is based on optics, Ref(1). It is strictly applicable to the two dimensional case, i.e., a line source and a cylindrical reflector. However, since the beam was to be shaped in one plane only and since the size of the feed horn aperture is of the same order of magnitude as the reflector size, it was assumed that the two dimensional theory would be applicable. As will be seen, this assumption was justified by the results obtained.

A brief exposition of the method follows. Referring to Figure 3a, the reflector is defined by ρ and Ψ from Ψ_1 to Ψ_2, the horn subtended angle. The radiated beam is defined over the angle θ_1 to θ_2.

From Figure 3b it can be seen that

$$\frac{\partial \rho}{\rho d\Psi} = \tan \frac{\alpha}{2}$$

where α is the included angle between the incident and reflected rays. Since from Figure 3a.

$$\alpha = \Psi - \theta$$

by integrating

$$\ln \frac{\rho(\Psi)}{\rho(\Psi_1)} = \int_{\Psi_1}^{\Psi} \tan \frac{(\Psi-\theta)}{2} \, d\Psi$$

To perform this integration, a relationship between θ and Ψ is needed. Since the energy incident on the reflector from Ψ_1 to Ψ_2 is equal to the energy reflected from θ_1 to θ_2, a normalizing factor K is found from.

$$K = \frac{\int_{\Psi_1}^{\Psi_2} I(\Psi)\, d\Psi}{\int_{\theta_1}^{\theta_2} P(\theta)\, d\theta}$$

where $I(\Psi)$ is the feed pattern and $P(\theta)$ is the desired secondary pattern, Then:

$$\int_{\theta_1}^{\theta} P(\theta)\, d\theta = \frac{1}{K} \int_{\Psi_1}^{\Psi} I(\Psi)\, d\Psi$$

yields the relation necessary for the integration of (1)

For our design, the parabolic approximation was used for the feed horn pattern, Ref (2). The desired beam pattern was defined as shown in Figure 4.

This procedure was coded for and the computations were carried out on a Hewlett Packard 9825A desk-top computer.

DESIGN AND RESULTS

The bulk of the design and testing was done at 16GHz for measurement convenience and to avoid tolerance problems. The horn was designed using the standard formulas given in Ref. 3: its aperture dimensions are 6.92λ by 4.85λ with an aperture to waveguide junction length of 21.5λ. The patterns are shown in Figures 5 and 6.

The dimensions of the first assembly built are shown in Figure 7. The shaping reflector was sized to subtend the 20dB points of the beam.

The patterns obtained are shown in Figures 8 and 9. The variations from the expected flat-top were attributed to the relatively small horn to reflector spacing: i.e., the horn did not resemble a line source. Accordingly a new model was computed and built with increased feed horn to reflector distance (Fig. 10). The reflector subtended the 10dB beam points. The measured patterns are given in Figures 11, 12, 13.

A 95GHz model was constructed and is shown in Figure 14. Measured patterns are given in Figures 15, 16, 17, 18. The measured peak gain was 17dB.

A calculation was performed to see if any improvement in system performance resulted from the flat top design. By graphical integration, the ratio of the power in the desired angular region

(±30°) to the power in the ±90° region was found. The same procedure was followed for a 60° HPBW horn pattern. The ratio of the two ratios was 1.2 or .7dB.

CONCLUSIONS

The design exceeded the system gain requirements, minimized mechanical bearing requirements, and has very high reliability and low cost compared to a design employing a rotating horn and a rotary joint.

REFERENCES

1. Silver, S, Microwave Antenna Theory and Design, McGraw Hill, 1949, pp 497-500.

2. Jasik, H, Antenna Engineering Handbook, McGraw Hill, 1961 p. 12- 5.

3. Ibid., p. 10-4,5

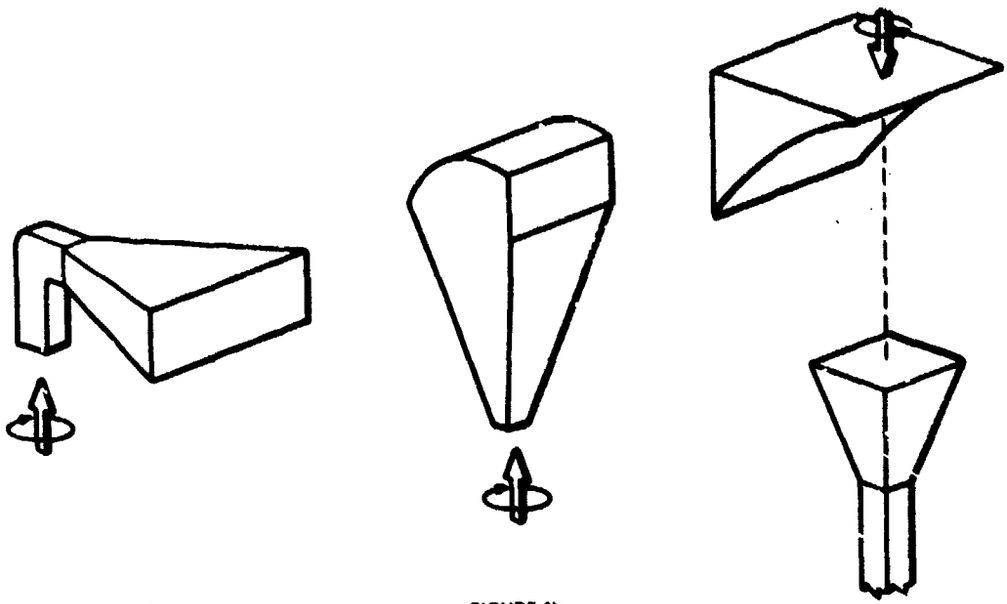

FIGURE 1a FIGURE 1b FIGURE 1c

Figure 1. Design Concepts

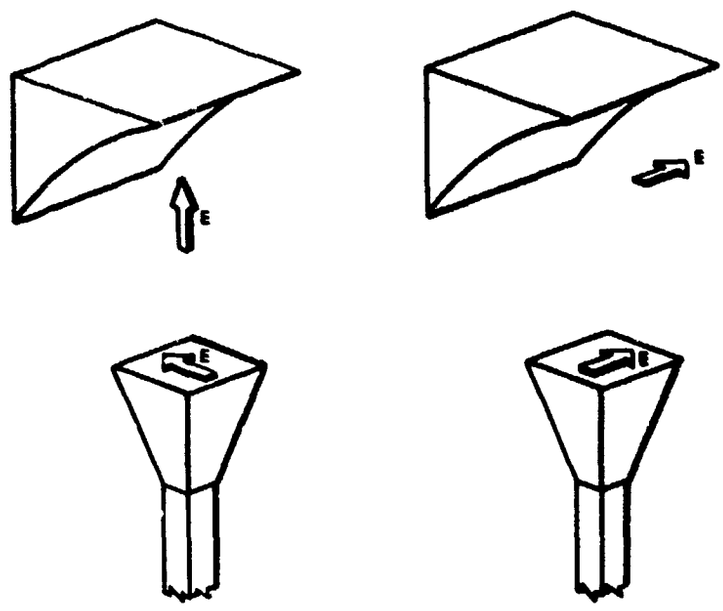

ELEVATION POLARIZATION AZIMUTH POLARIZATION

Figure 2. Polarization Change with Reflector Rotation

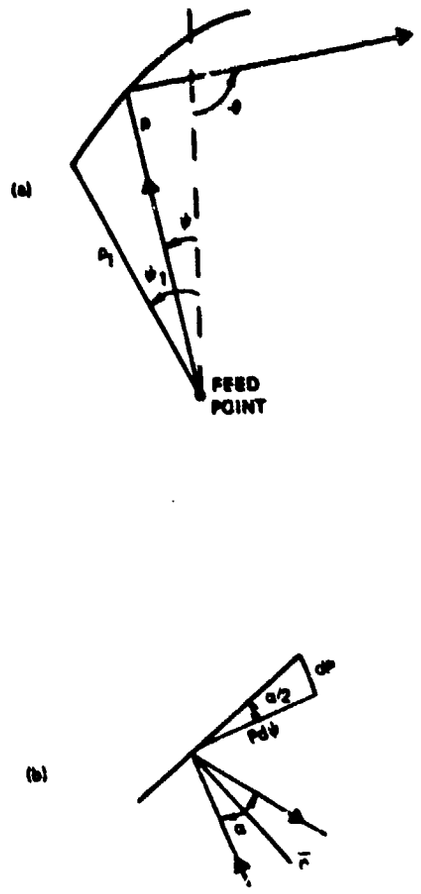

Figure 3. Geometry of Ray Reflection

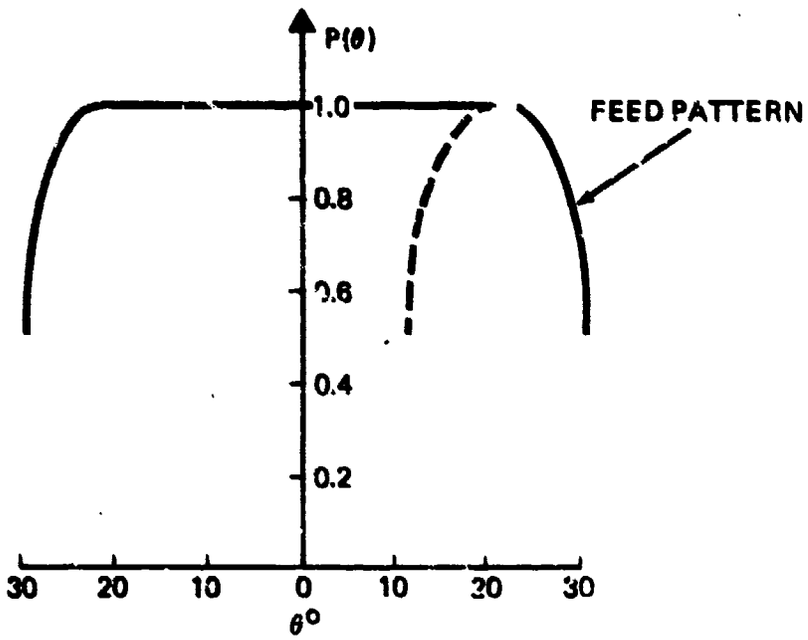

Figure 4. Desired Beam Pattern

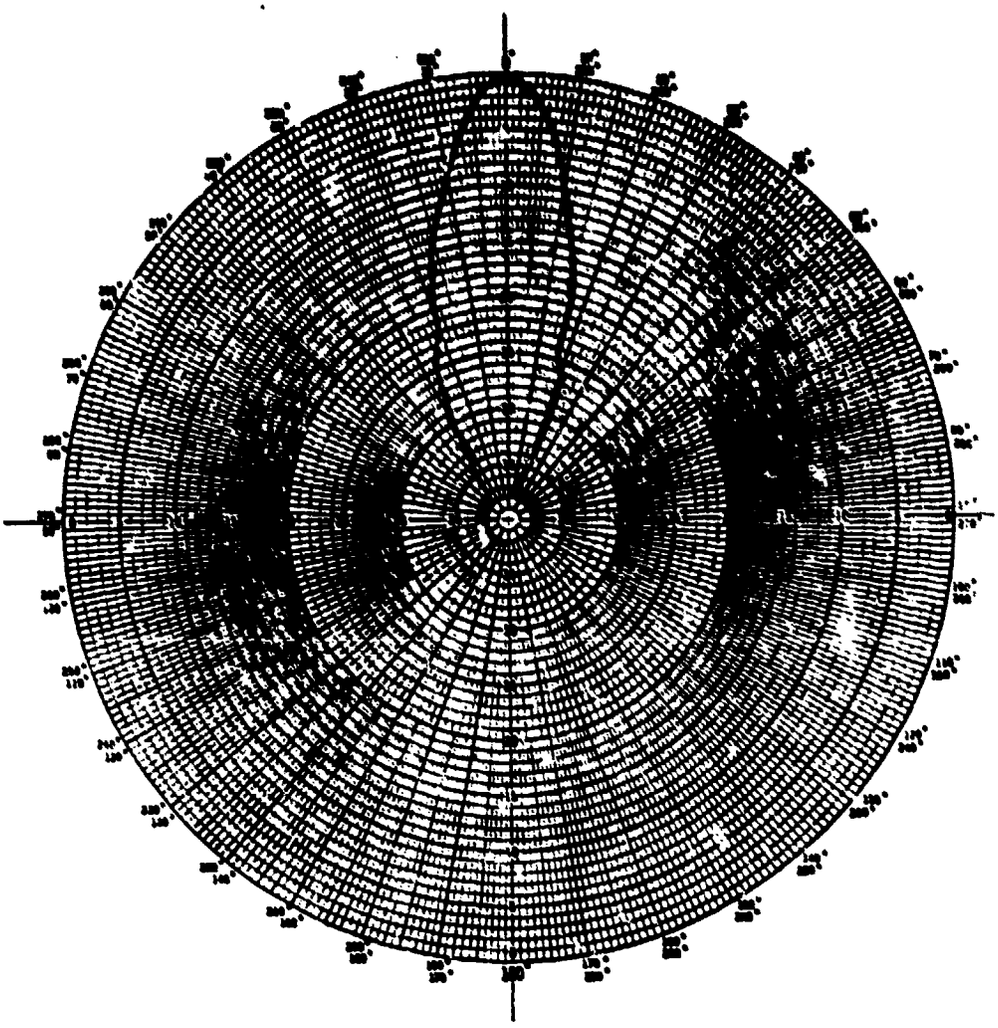

Figure 5. 16 GHz Horn Pattern -H Plane

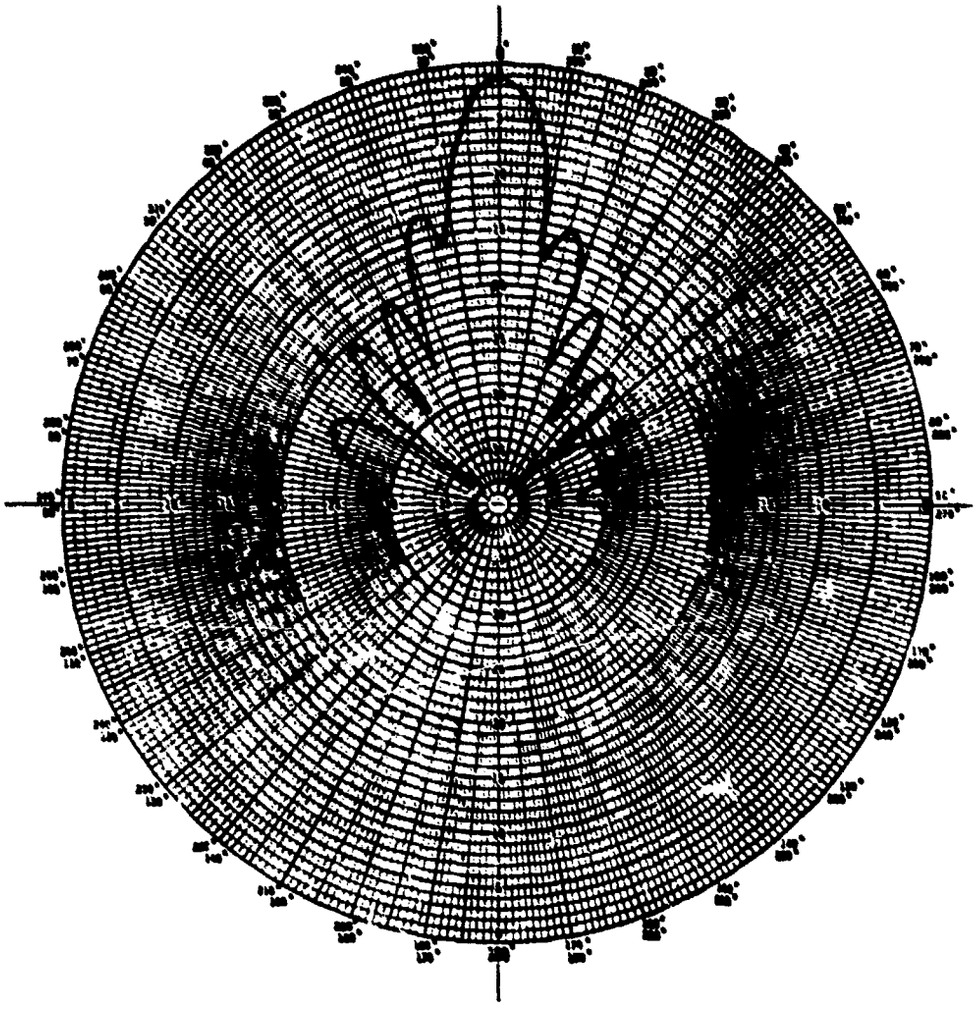

Figure 6. 16 GHz Horn Pattern -E Plane

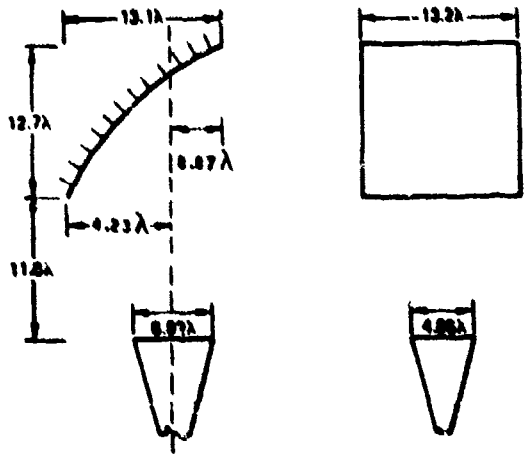

Figure 7. Dimensions -First Model

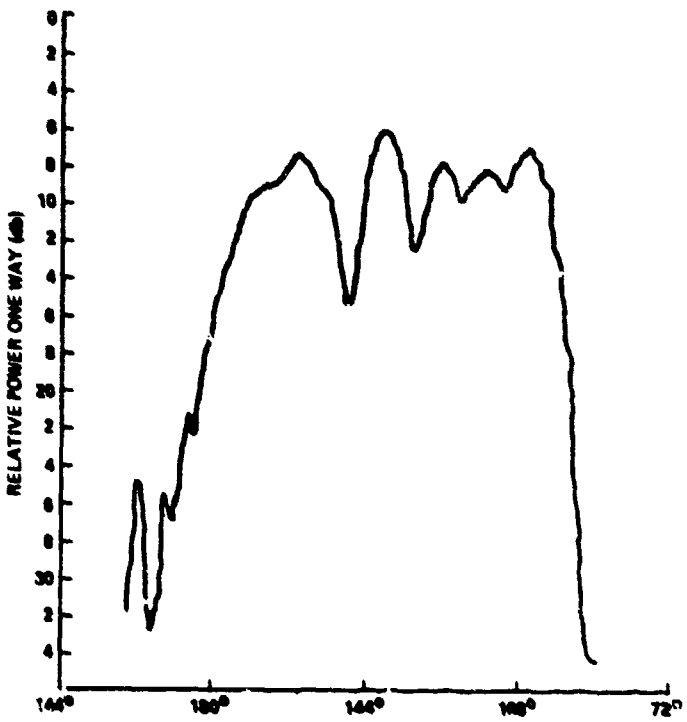

Figure 8. Elevation Pattern Azimuth Polarization 16 GHz

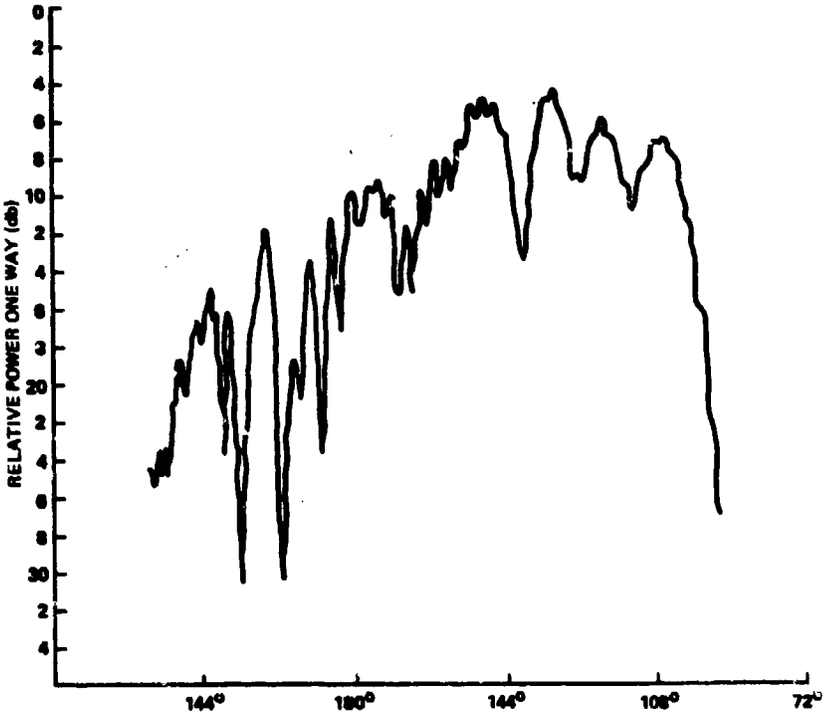

Figure 9. Elevation Pattern Elevation Polarization 16 GHz

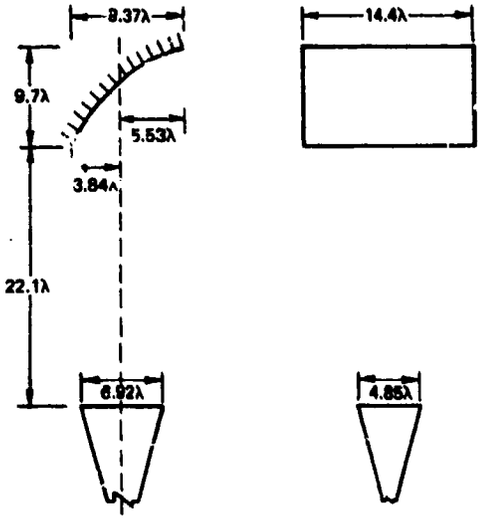

Figure 10. Dimensions Final Model

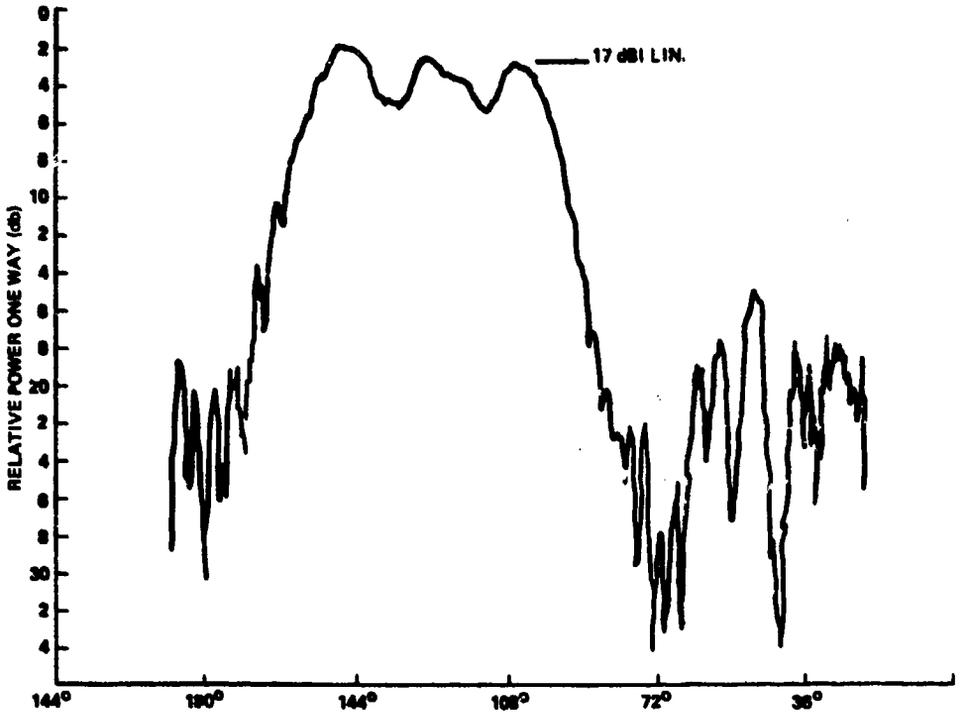

Figure 11. Elevation Pattern Azimuth Polarization 16 GHz

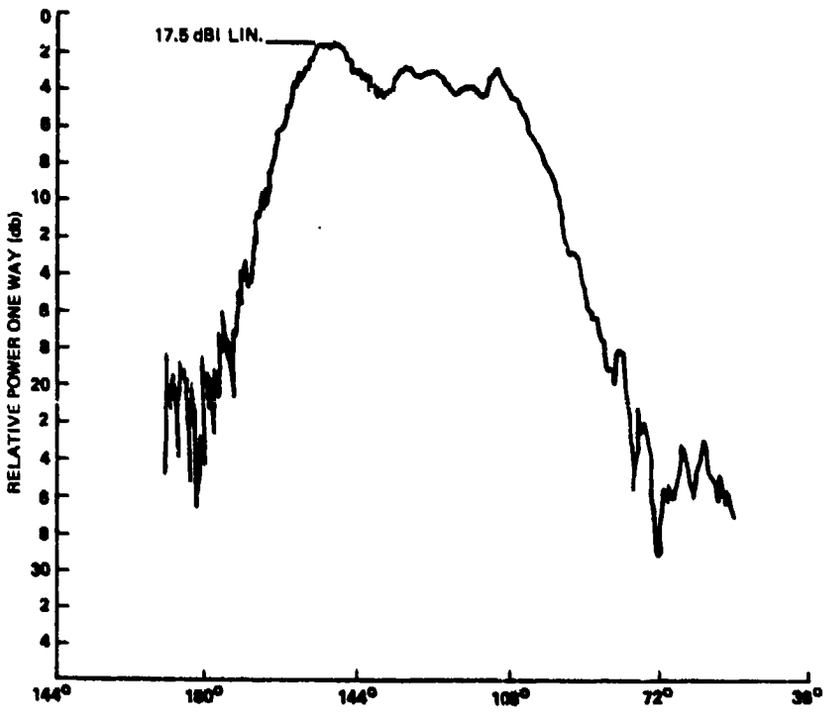

Figure 12. Elevation Pattern 45° Polarization 16 GHz

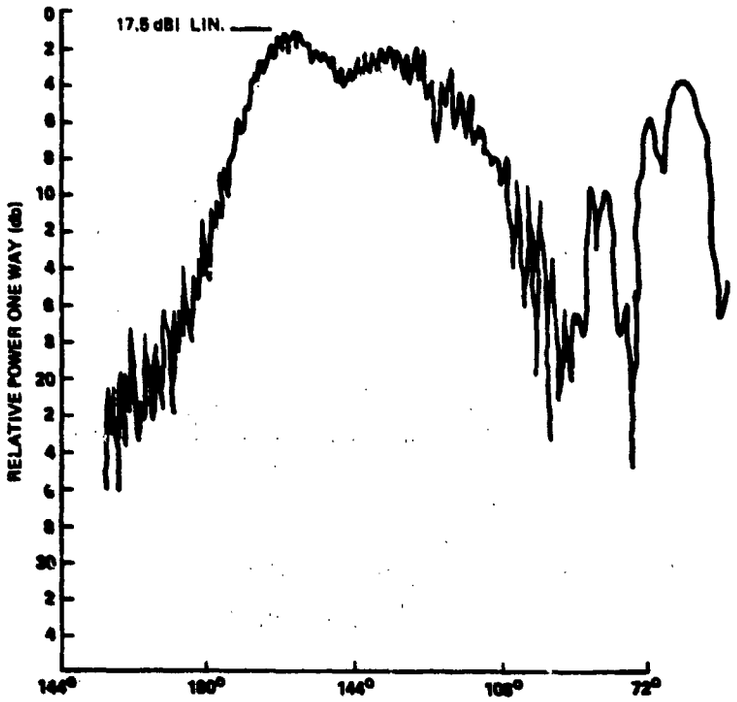

Figure 13. Elevation Pattern Elevation Polarization 16 GHz

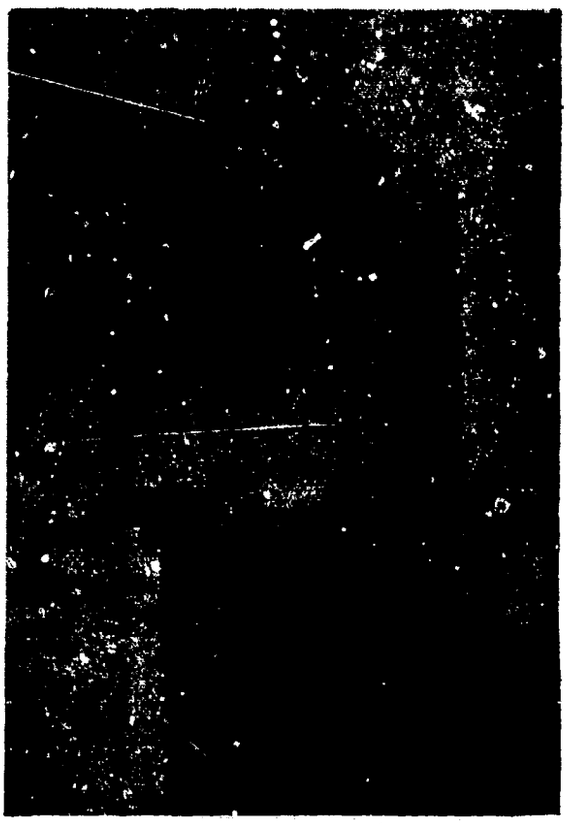

Figure 14. Final Model

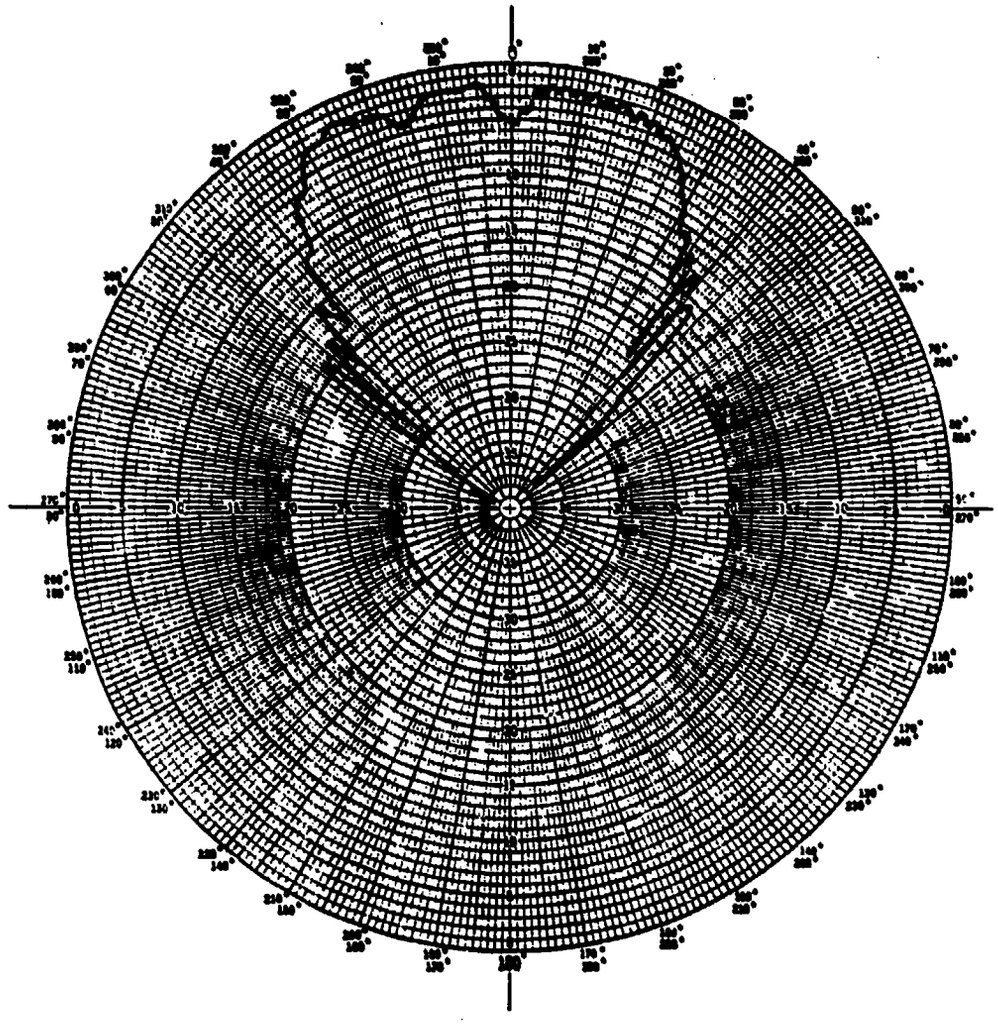

Figure 15. Elevation Pattern -95 GHz Azimuth Polarization

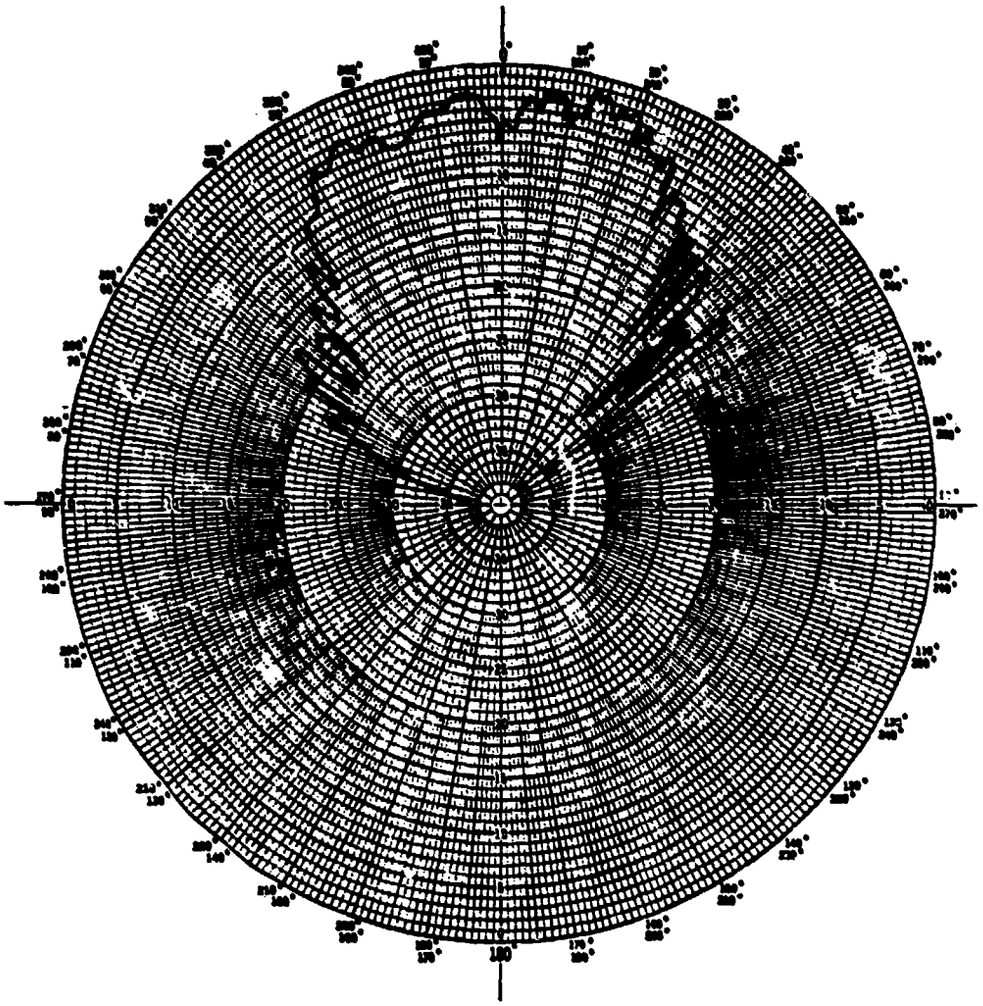

Figure 16. Elevation Pattern -95 GHz Elevation Polarization

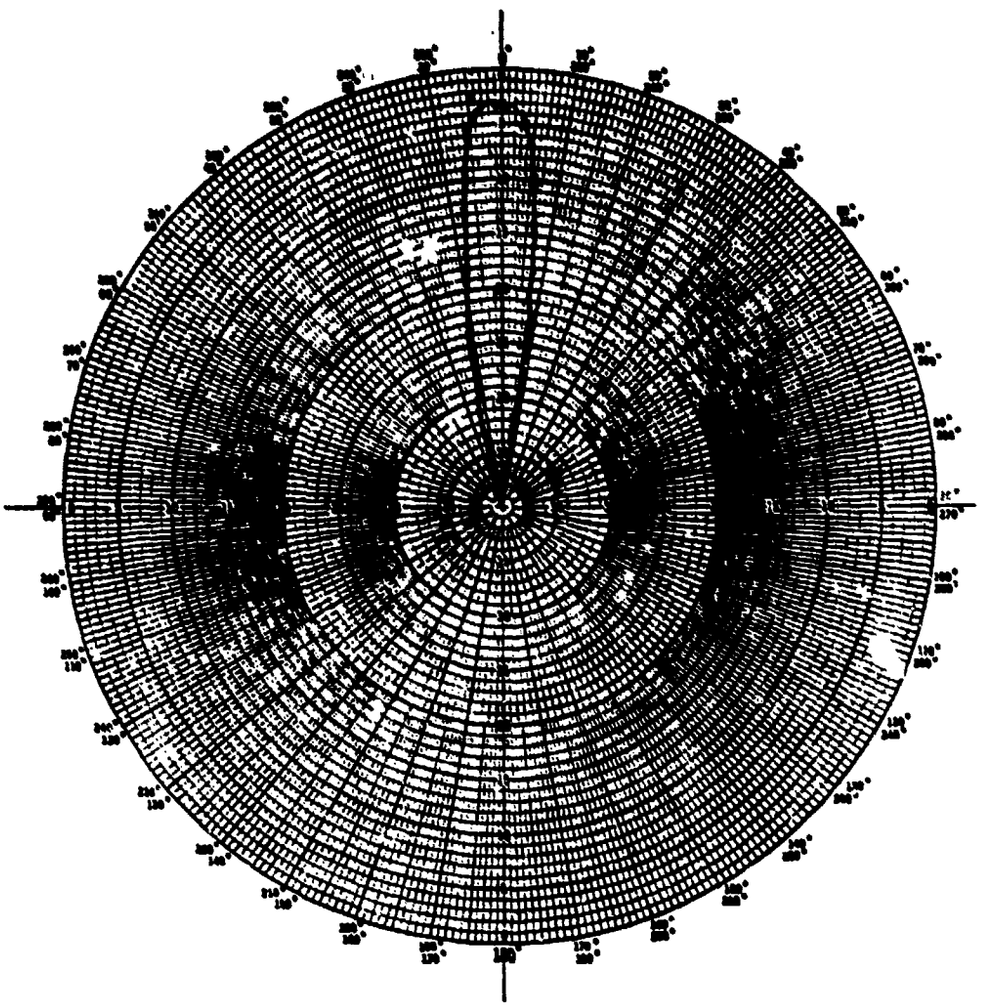

Figure 17. Azimuth Pattern 95 GHz Azimuth Polarization

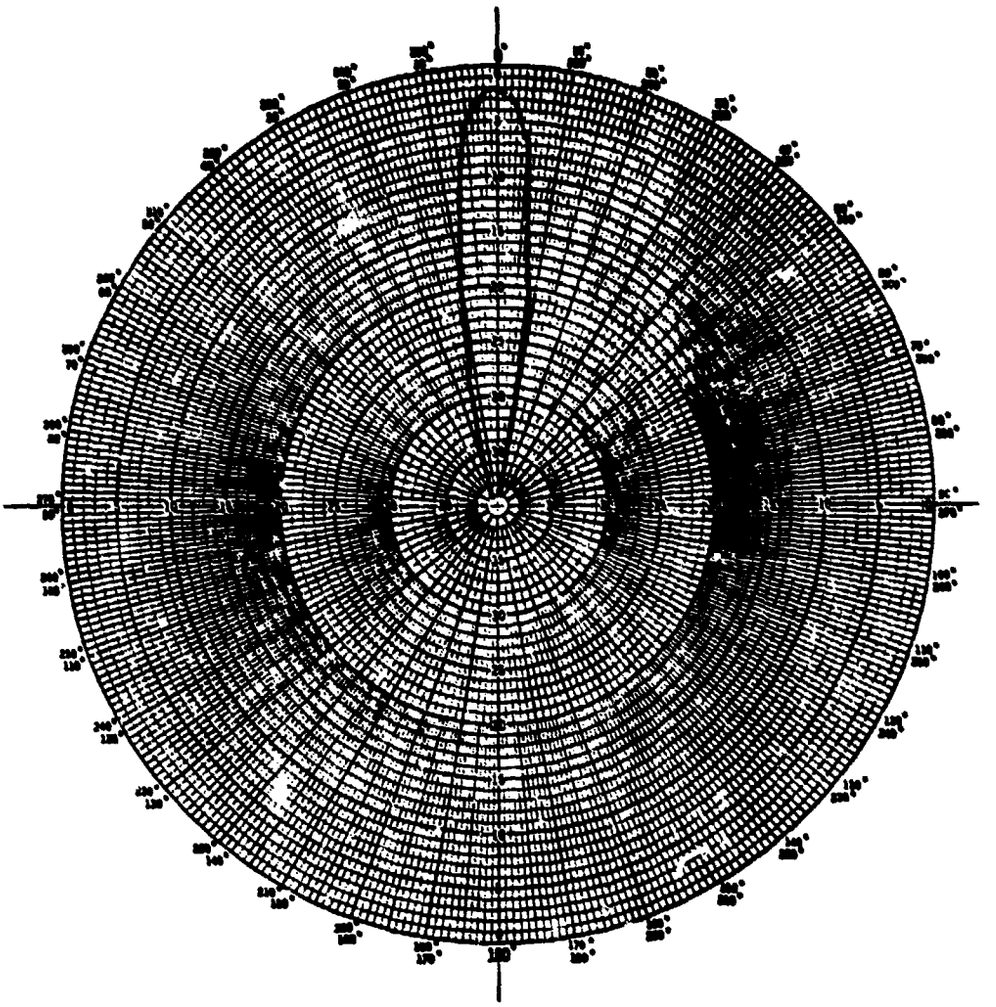

Figure 18. Azimuth Pattern -95 GHz Elevation Polarization

AD P001112

THE DESIGN OF A LOW LOSS AND LIGHTWEIGHT CONFORMAL ARRAY APERTURE

D. J. Martin, C. A. Chuang, and N. Moldovan
Harris Government Communications Systems Division
P. O. Box 92000
Melbourne, Florida 32901

1982 Symposium on Antenna Applications
September 22-24, 1982
Allerton Park
Monticello, Illinois

THE DESIGN OF A LOW LOSS AND LIGHTWEIGHT CONFORMAL ARRAY APERTURE

D. J. Martin, C. A. Chuang, and N. Moldovan

Harris Government Communications Systems Division

P. O. Box 92000

Melbourne, Florida 32901

ABSTRACT

The design and optimization of a large conformal array aperture is presented. The array lattice is designed and optimized by using a computer program to meet the gain and sidelobe requirements with a minimum number of antenna elements. The antenna is low loss, lightweight and low profile which are desirable for airborne and ground mobile applications.

The trade-offs and selection of a lightweight antenna substrate with low loss and desired RF characteristics are given. The array fabrication and integration techniques are discussed. Experimental data of a breadboard array is shown.

1. INTRODUCTION

There is a need to design a low loss and lightweight conformal array aperture for high gain airborne and ground mobile applications. The objective is to minimize the array aperture loss such that the gain of the antenna can be maximized for a given aperture, or the size and weight of the antenna can be minimized for a given gain requirement.

Techniques have been developed to minimize the antenna aperture loss by the design of a low loss, lightweight microstrip element and honeycomb substrate, and by the optimization of array grids and fabrication methods. Design and fabrication procedures were demonstrated for breadboard elements and for a 121 element passive array at S-Band. The measured active element patterns indicate a significantly wider beamwidth compared to the isolated ones, due to mutual coupling effects. The technique of designing a low loss and lightweight array aperture, illustrated in the following, is primarily for an S-Band airborne application. Nevertheless, it is applicable to frequencies other than S-Band, and is compatible for ground mobile terminal operations.

2. DESIGN CONSIDERATIONS

The design considerations for a low loss and lightweight conformal array aperture are based on the electrical and mechanical requirements of a particular application. Primary electrical requirements include gain, sidelobes, scanning volume, and polarization. The antenna gain designates the basic aperture size needed. The required scanning angles impact this aperture size significantly due to physical loss of the aperture at extreme scanning conditions. The sidelobes, in many cases, can only be met through the amplitude tapering of the aperture, resulting in the loss of aperture efficiency. The polarization requirement specifies

the maximum allowable loss in polarization efficiency. The key design consideration is to meet these requirements with minimum overall aperture loss such that the array size and weight can be reduced.

For airborne or ground mobile applications, the main mechanical requirement is to design the array to be compatible with the operational environments. The most severe considerations of reduced size, low profile, and light weight are for airborne applications due to the need of flight-qualified construction to combat the aerodynamic drag. Other mechanical considerations include vibration, temperature, pressure, host vehicle structure expansion, rain and hail impact, lightning, nuclear hardening, EMT/EMI, reliability, and maintainability. The mechanical engineering of material selection, fabrication techniques, and layout and construction methods plays an important role in the array design in meeting these operational requirements.

3. ANTENNA APERTURE DESIGN

The first step in applying the low loss and lightweight techniques is to design an effective antenna element consisting of radiation aperture, substrate, feed, and bonding skins. For an S-Band (2.2 - 2.3 GHz) receive antenna application, circular microstrip patch was selected as the lightweight radiation element due to its small size and known performance characteristics. A

variety of materials including cuflon, duroid, and honeycomb with different bonding skins has been used as substrates of the microstrip element. Fabrication techniques were investigated. Table 1 shows the performance characteristics of the elements in terms of loss tangent, efficiency, bandwidth, axial ratio at 60 degrees of the isolated pattern, and weight. As is shown, all the elements exhibit satisfactory electrical properties. The cuflon and duroid designs are not acceptable mainly due to their weight performance. The honeycomb/G10 element weighs less than 0.3 pounds per square foot.

In the process of searching for superior substrate materials, a new lightweight, low loss core material was found to be an excellent candidate for the microstrip substrate. The honeycomb consists of a uniform lattice of circular cells extruded from a polycarbonate thermoplastic resin. This lightweight honeycomb provides promising RF properties due to its uniform cell structure which is different from hexagonal honeycomb structure. It also has a lower loss tangent.

The low loss honeycomb is also an excellent radome material for high speed aircraft applications. It can provide substantial improvement in rain impact resistance without sacrificing electrical performance for multilayer construction. An electrically thin sandwich radome using this low loss honeycomb core structured for an

S-Band application is illustrated in Figure 1. At an incidence angle of 60 degrees and the incoming wave perpendicularly polarized to the plane of incidence, the radome loss was calculated to be much less than 0.1 dB.

4. ARRAY LATTICE OPTIMIZATION

The array grid of a conformal array can be optimized considering the grating lobes, sidelobes, scanning performance, and minimum number of elements required. The optimized array grid is obtained by the computation of a variety of array grids and scan conditions using a conformal array computer program. The computer program is capable of calculating the array pattern of a cylindrical array with the coordinate system as shown ir Figure 2. The process is to find the optimum spacings in the pitch and roll planes.

For an S-Band array, the array grid was optimized for the requirements of 28 dB gain, 60 degree scanning cone, and -15 dB sidelobe. The array was mounted on a 747 type of aircraft fuselage with radius equal to 128 inches. The optimum lattice was found to be a triangular grid with a 7.9 cm ($0.61\lambda_0$) pitch spacing and a 6.35 cm ($0.49\lambda_0$) roll spacing. Based on this grid, Figure 3 shows the calculated patterns for the array scanning at 60 degrees in roll, pitch, and intercardinal planes. Patterns shown indicate worst sidelobes and grating lobes, but still meet the array requirement. A 4-bit phase shifter and an element pattern with cosine on pedestal

taper were used for the computation. Calculated scan loss, conformality loss (at 60 degrees), taper loss, and quantization loss are 3.15 dB, 0.22 dB, 0.25 dB, and 0.05 dB, respectively. These calculated results represent realistic losses for an airborne conformal array.

5. ACTIVE ELEMENT PATTERNS

Active element patterns of a large array reflect the mutual coupling effects on the individual elements, and provide insights of the array scanning performance. A 121 element (11 x 11) passive microstrip array using the optimized array grid given in Section 4 was designed, fabricated, and tested. The structure of the lightweight microstrip element is illustrated in Figure 4. The dimensions of the array and ground plane are given in Figure 5. Effective fabrication process with tight tolerance control was used in the fabrication of the array.

The linearly polarized active element patterns for the center element of the array are shown in Figure 6. The gain of the active element measured using a standard gain horn is also shown in Figure 6(a). The patterns due to mutual coupling effects indicate an almost ideal pattern for a wide angle scanning array with 2 dB loss at boresight and only a 3 dB scan loss at 60 degrees. Both the E and H plane patterns are matched at wide scan angles. Circularly polarized (CP) active element patterns, shown in Figure 7, were

calculated using measured spinning linear patterns. The CP patterns are near ideal pattern of a cosine element for scanning out at 60 degrees, and indicate less than 4 dB axial ratio throughout the scanning region.

6. SUMMARY AND CONCLUSION

The design of a low loss and lightweight conformal array aperture was accomplished through the selection of antenna element, substrate and radome; the optimization of the array aperture lattice; and the use of an effective fabrication process. The fabrication process and mechanical structure used are compatible with the operational environments of airborne and ground mobile applications. The designed S-Band low loss microstrip antenna element with honeycomb substrate weighs less than 0.3 pounds per square foot. The array lattice was optimized using a conformal array computer program. The scan loss, conformality loss, taper loss, and quantization loss were calculated. The measured active element patterns of a 121 element passive element indicate a mutual coupling affected element with gain performance near the ideal pattern of a cosine element.

Table 1. Alternate Circular Microstrip Patch Element Designs

(.25" Thickness, No Adhesive Effect)

Substrate- Skin	Cuflon	Duroid	Honeycomb-TFE	Honeycomb-G/10
ϵ_r	2.1	2.21	1.14	1.19
Tan δ (Loss Tangent)	.00045	.00085	.00099	.0017
Disk Radius (cm)	2.62	2.48	3.5	3.44
Efficiency (%)	98.6	98.1	98.2	97.5
Bandwidth (%)	5.08	5.02	6.05	6.32
Axial Radio @ 60° (dB)	2.98	3.39	1.14	.64
Weight (lbs psf)	2.85	2.99	.35	.29

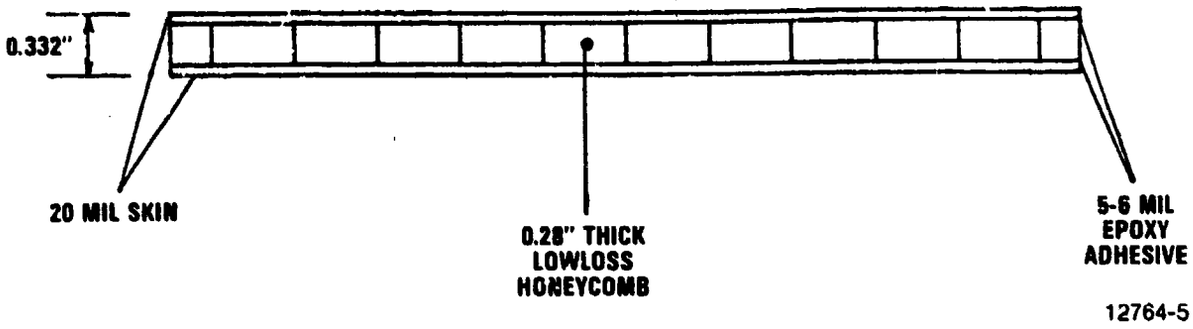

Figure 1. The Radome

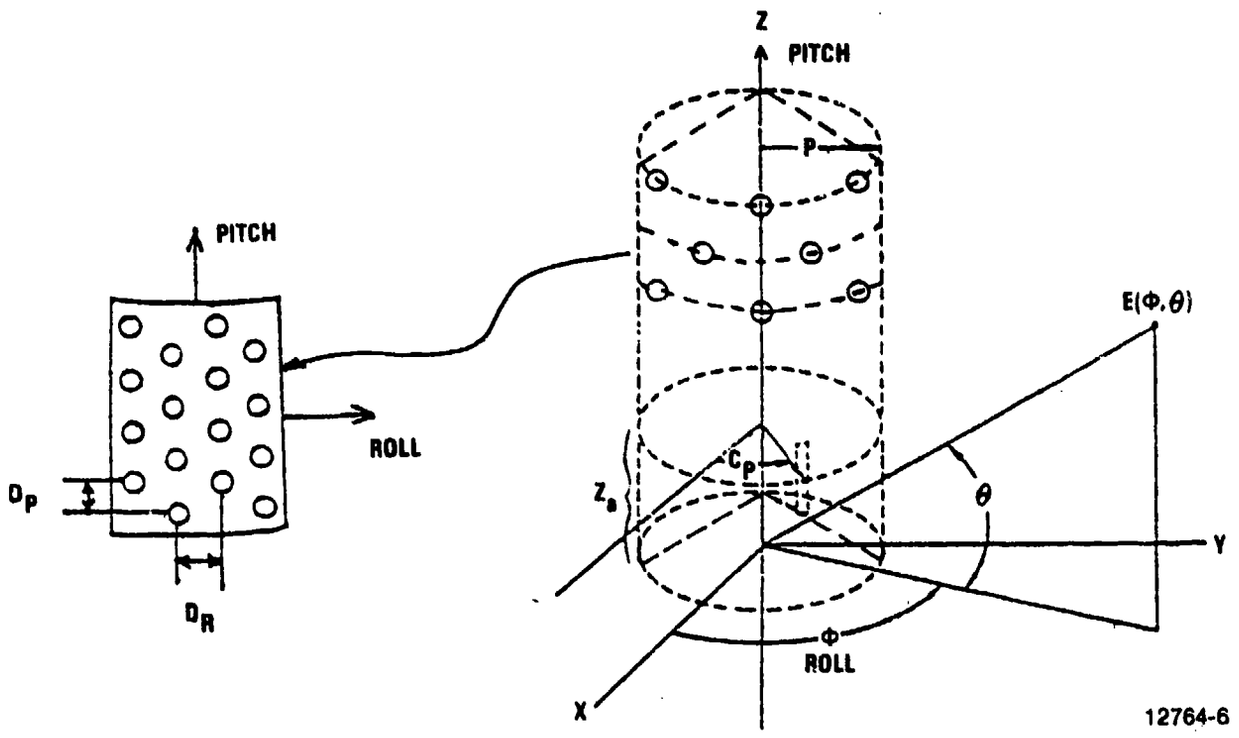

Figure 2. Array Geometry

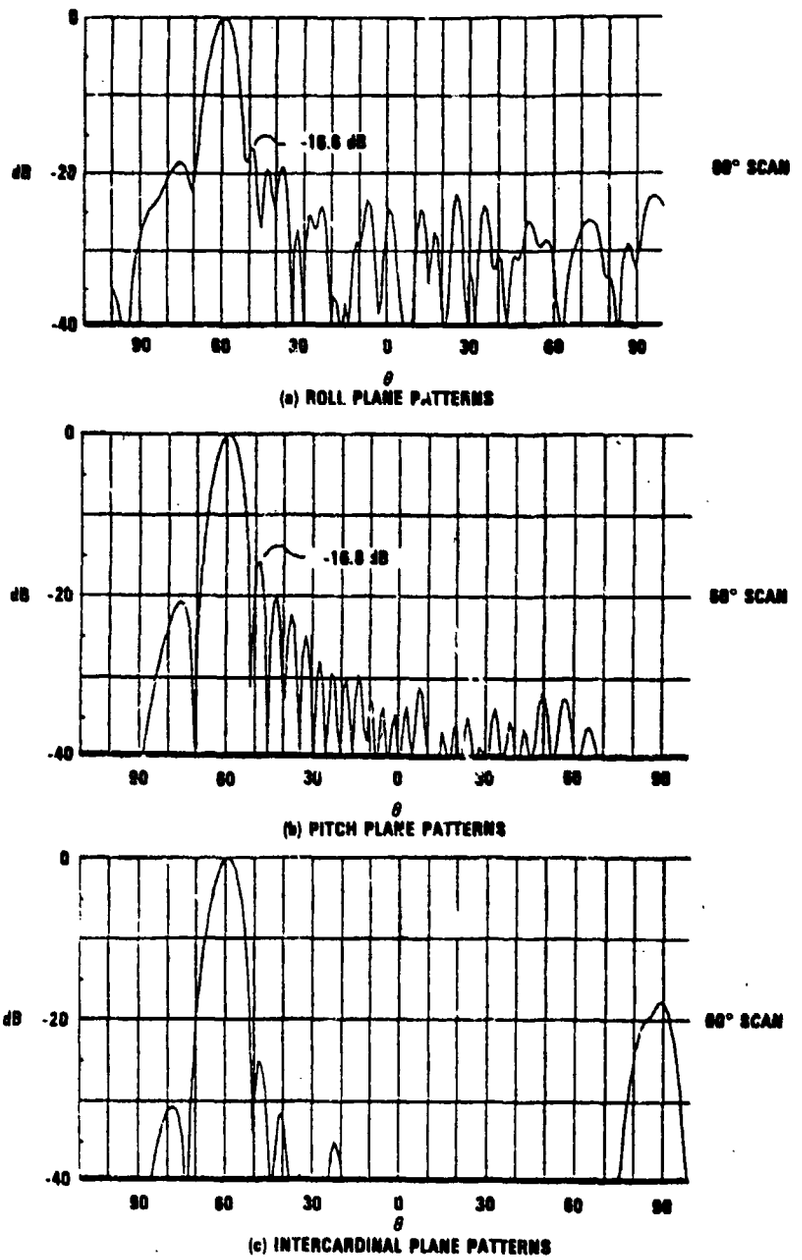

Figure 3.0. Computed Array Patterns

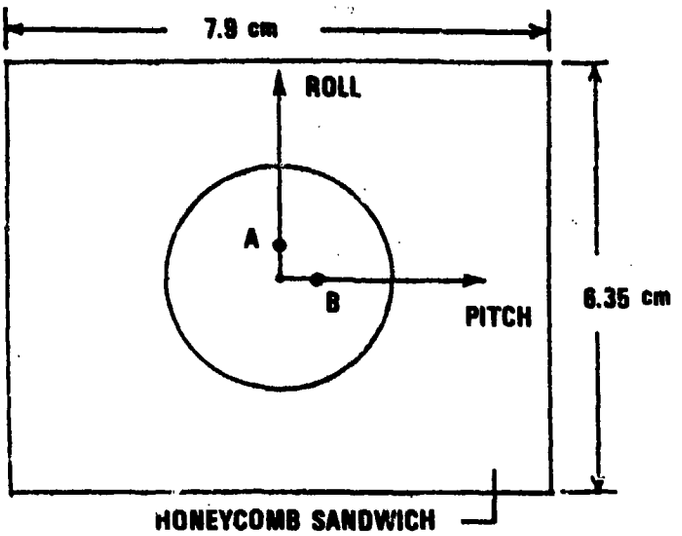

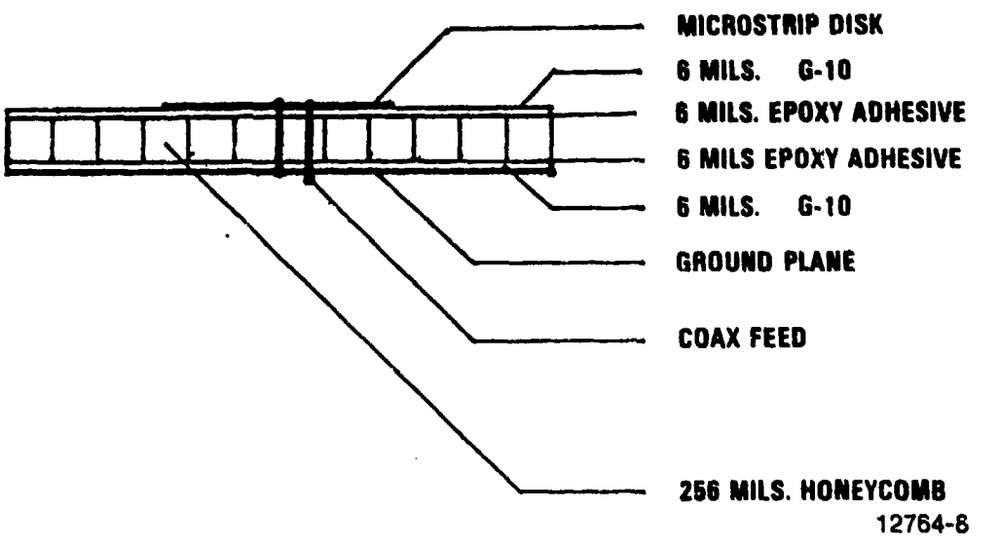

Figure 4.0 Lightweight Microstrip Element

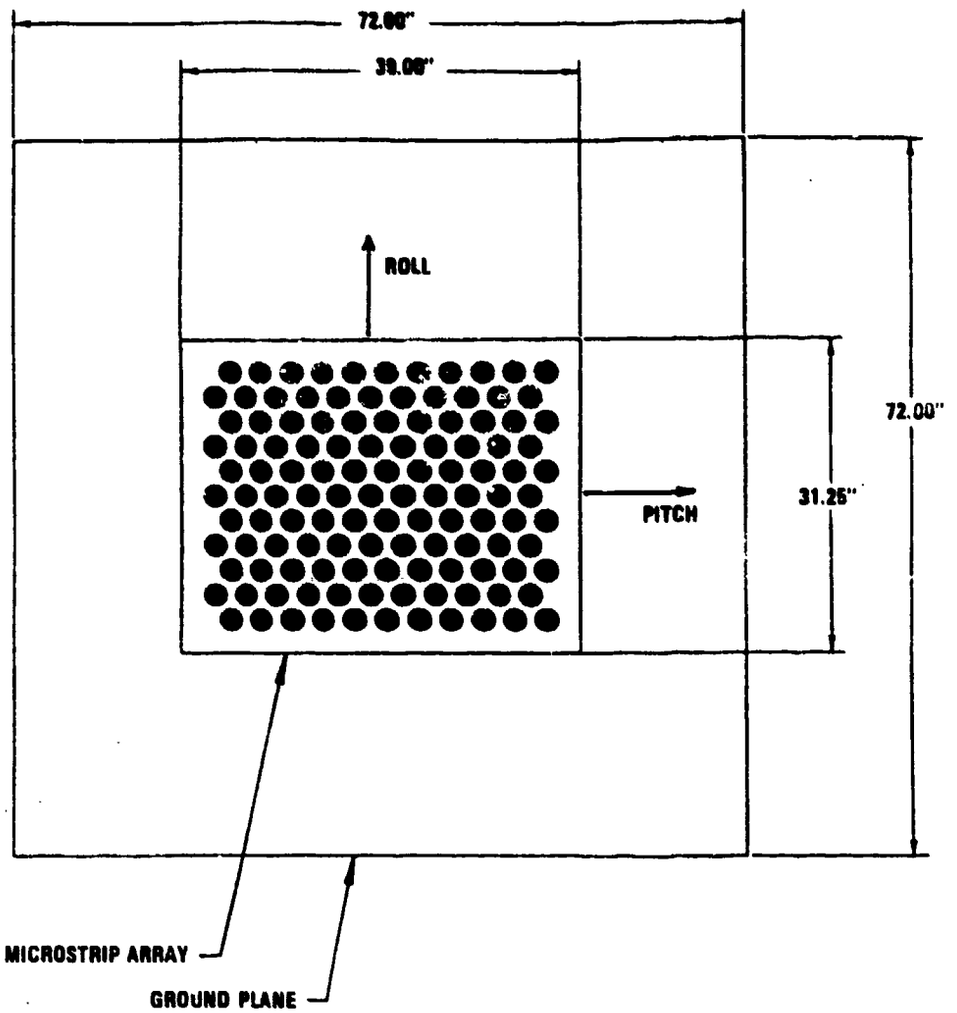

Figure 5.0 121 Element Array & Ground Plane

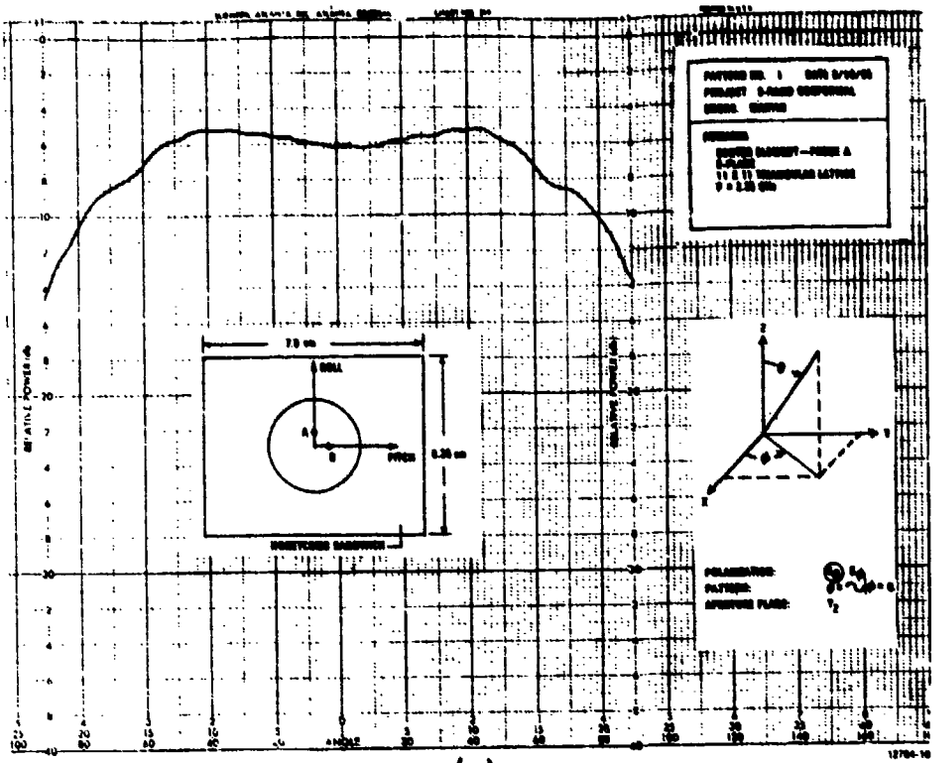

(a)

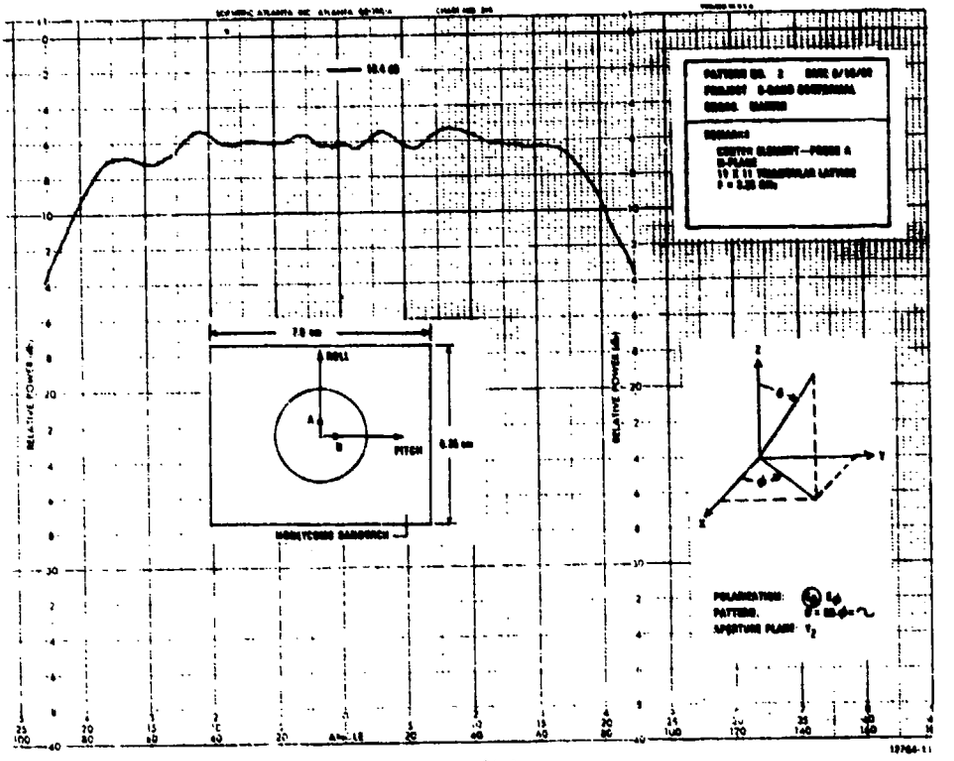

(b)

Figure 6. Measured Active Element Patterns (Linear)

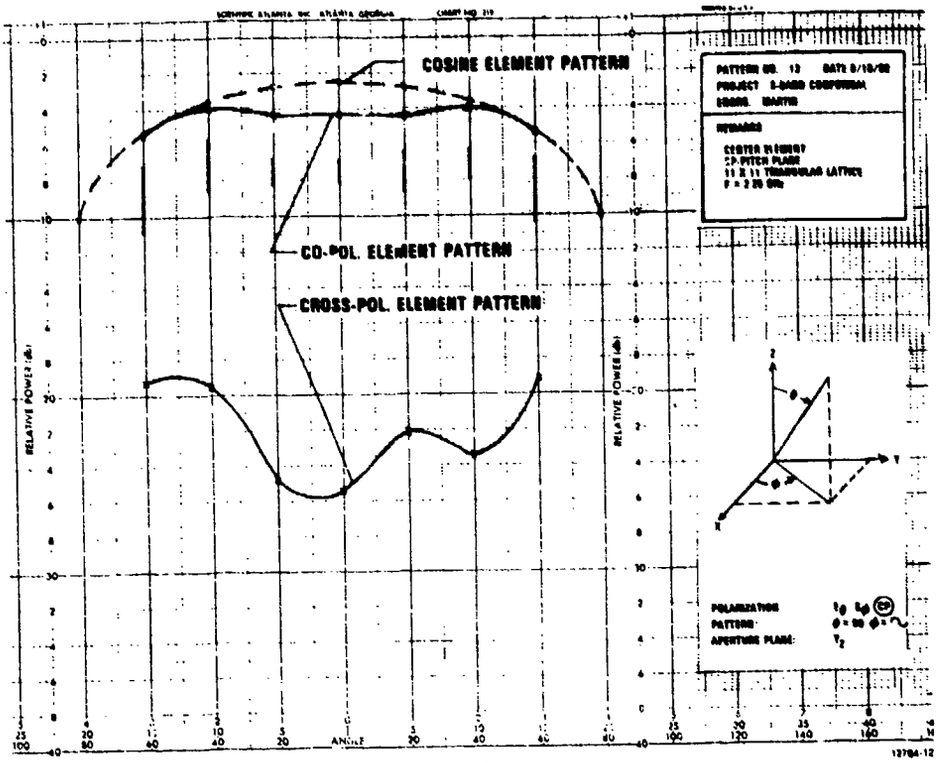

(a)

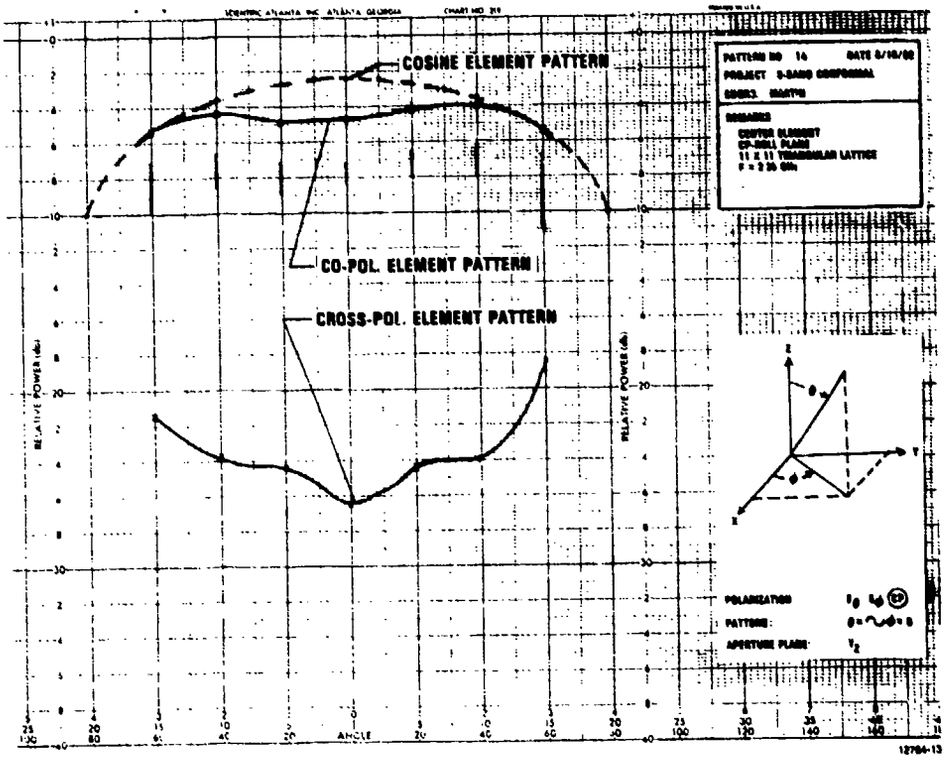

(b)

Figure 7. Measured Active Element Patterns (CP)

AD P001113

AN S-BAND CONFORMAL ARRAY ANTENNA

C. A. Chuang and D. J. Martin

Harris Government Communications Systems Division

P. O. Box 92000

Melbourne, Florida 32901

1982 Symposium on Antenna Applications

September 22-24, 1982

Allerton Park

Monticello, Illinois

PAGE BLANK-NOT FILMED

AN S-BAND CONFORMAL ARRAY ANTENNA*

C. A. Chuang and D. J. Martin

Harris Government Communications Systems Division

P. O. Box 92000

Melbourne, Florida 32901

ABSTRACT

Requirements for an S-Band Conformal Array Antenna are presented. The high gain antenna is designed to receive from a satellite at scan angles as large as 60 degrees.

Development status of low loss printed circuit techniques in the areas of array aperture, phase shifter, transmission line, combiner, and array controller is discussed. Loss budget is calculated. Planned study tasks are presented.

1. INTRODUCTION

There is a need to design high gain aircraft phased array antennas to receive low power signals from a satellite at scan angles as large as 60 degrees, which at S-Band makes the phased arrays become physically large. The problem is complicated by the conformality requirement of the array designs to be compatible with

*The work is sponsored by RADC/EEA, Hanscom AFB, Massachusetts

an aircraft in the considerations of aerodynamic performance, weight and airframe modifications. Study efforts have been conducted to reduce the size and weight of the conformal arrays through the development of low loss printed circuit techniques, and by the investigation of incorporating RF amplification at the element level. The objectives are to design low loss and lightweight S-Band conformal arrays at an affordable cost.

The study of low loss circuit techniques has been performed in the areas of antenna elements, array aperture and array electronics. A separate paper discusses the antenna aperture designs in detail; this paper defines the requirements, summarizes the development status in each area, and presents the study plan.

2. ANTENNA SPECIFICATION AND DESIGN CONSIDERATIONS

A summary of the antenna specifications is given in Table 1.

Table 1. Receive Antenna Specifications

Frequency:	2.2 to 2.3 GHz (6 MHz instantaneous)
Polarization:	Circular
Scanning:	Electronic, $\pm 60^\circ$ in azimuth and elevation
Gain:	32 dB
Sidelobe:	≤ -15 dB
VSWR:	2:1
Physical Requirements:	- Located conformally at fuselage
	- Maximum thickness of 4" and goal of 2"

The purpose of the study effort is to investigate array design techniques such that the antenna specifications can be met and the array size and weight can be optimized.

It is obvious, in the concern of antenna directivity and array loss, that a large aperture area is required in order to meet the 32 dB gain requirement at S-Band. The key of the design considerations is to minimize the array losses such that the array area can be substantially reduced. The antenna specifications which closely impact the array losses include the 60 degree scanning and -15 dB sidelobes. The array scanning generates losses which are due to the loss of array aperture and are caused by array mismatching associated with the scanning and aircraft environment operation. The scan loss contributes significantly to the total antenna loss. The -15 dB sidelobe requirement cannot easily be met due to the cylindrical ground plane of the conformal array. However, the desired sidelobe can be obtained by the use of amplitude tapering of the aperture and at the cost of an increased array loss. The conformality requirement of the array and the aircraft environment operation further complicates the size and weight considerations of the antenna design.

The antenna losses can be optimized, and its size and weight reduced by considering:

1. array aperture design optimization to increase the efficiency of the antenna;

2. low loss printed circuit techniques to reduce the losses of the components; and/or

3. RF amplification at or near element level.

The aperture design optimization can be achieved by the selection and design of element pattern and array grid, and by minimizing the scanning mismatching using array matching techniques. The use of low loss printed circuit techniques reduces the losses of antenna elements, transmission lines, phase shifters, and array combiner, and facilitates the RF amplification at subarray level. The employment of RF amplification at element level provides the definite advantages of the ultimate G/T performance of the array, and offers the potential for the reduced size and weight. The method of amplification at the subarray uses fewer amplifiers. The trade-off of the amplification approaches not only relies upon the overall array size, weight, and electrical performance, but also depends on cost and reliability for practical applications.

3. ARRAY DEVELOPMENT STATUS

Development efforts have been performed in the areas of array aperture, low loss array electronics, and array controller. The progress made is summarized in the following subsections.

3.1 Array Aperture - An array lattice study using a conformal array computer program was performed to derive an optimum array grid

in which the minimum number of elements is required to meet the grating lobe, sidelobe, and other array performance. Based on the optimized array grid, array scan loss, comformality loss, taper loss, and quantization loss were calculated.

Lightweight microstrip antenna elements using a variety of skin and substrates were designed to minimize the aperture weight and loss, and to optimize the RF performance. Element fabrication and bonding techniques were investigated to ensure the repeatability of the aperture fabrication.

3.2 Array Electronics - Studies were performed to the designs of low loss transmission lines, phase shifter, and combiner. Trade-offs were made in the selection of pin diode vs. varactor phase shifters. Computer programs such as SUPERCOMPACT and SLICE were used to calculate and analyze the theoretical and realistic losses of array electronic circuits for different stripline techniques and at a variety of package configurations. Breadboard phase shifter bits have been fabricated and tested in specially designed test fixtures for insertion loss and return loss measurements.

For a 4-bit pin diode phase shifter, the use of tne loaded line approach for 22.5° and 45° bits and the hybrid coupled approach for 90° and 180° bits, offers the optimum low loss configuration. A varactor diode phase shifter, in comparison to an equivalent 4-bit

pin diode phase shifter, offers the advantages of using a smaller number of diodes, requiring much less power, and having small size and less weight. Its main design difficulty lies in the effectiveness for reverse bias voltage control and temperature compensation.

Computer simulation was performed on various 4-bit phase shifter configurations using three types of striplines, including suspended air substrate stripline, solid dielectric stripline, and covered microstrip. The configurations of suspended substrate offer the lowest losses and weight, but have the largest volume. Breadboard phase shifters including the varactor diode phase shifter and 180° pin diode bit have been fabricated and tested using specially designed test fixtures. Figure 1 shows a typical test fixture and branch line sections.

3.3 Array Controller - In the study of the array controller, the beam pointing controller architecture was designed, the interface circuit and hardware selection criterion was defined, and performance was estimated. The basic controller approach for the S-Band conformal array is to use a digital distributed processor in which one controller serves one subarray. Each subarray controller includes the Beam Electronics Module (BEM) for phase shifter calculation, interface circuit for receiving pointing command, data memory for storing element parameters such as element location and

path length correction, and phase shifter select logic for directing output. The block diagram of the controller is shown in Figure 2. Directional cosines of the satellite are supplied to the controller by the Mission Data Processor (MDP) as the beam pointing commands.

3.4 Loss of the Array - A loss budget estimate for a 16-element subarray with RF amplification at subarray level is given in Table 2. Most of the loss details were calculated using study results in the areas of array aperture optimization and low loss components and circuits. A conformal array configuration consisting of 128 subarrays with 16 elements per subarray, is given in Figure 3.

4. PLANNED ARRAY DEVELOPMENT AND STUDY

A continued development effort is on-going in the study of low loss circuit techniques for S-Band conformal array. Planned activities include:

1. 4-bit shifter testing and analysis;
2. custom-made LNA study for element and subarray amplification;
3. trade-off of element amplification vs. subarray amplification;
4. design, fabrication, and test of a subarray; and
5. size, weight and cost estimate of 10 complete antenna systems.

Table 2. Loss Budget Estimate

(Subarray Amplification)

	Loss (dB)
Loss Due to VSWR (2:1)	0.5 *
5% Element Failure Dissipative	0.22
Phase Shifter Insertion Loss	0.9*
Combining Network Losses:	
- Dissipative	0.05*
- Reactive	0.20
Phase Quantization Loss (4-Bit)	0.05
Loss Due to Random Errors	0.05
Array Element and Hybrid Losses	0.26*
Depolarization or Axial Ratio Loss	0.22*
Loss Due to Amplitude or Phase Tapering for Sidelobe Control	0.25
Conformality Loss	0.22
Scanning Loss (60°)	3.15
Radome Loss	0.1
Beam Pointing Losses (.26 BW at 60°)	0.05**
Total Losses	6.22

*Further verification in progress
**.63 dB at Boresight

5. SUMMARY

A study has been performed to investigate low loss array techniques for the design of a high gain conformal phased array. Progress was reported in the areas of array grid optimization, designs of low loss antenna element and array electronics, and array controller. Simulation and measured results have been performed for the 4-bit lightweight phase shifter. Array controller architecture was configured. Based on the study results to date, the total array loss was estimated.

Planned activities include trade-off of element amplification and subarray amplification; subarray fabrication and test; and size, weight, and cost estimates of complete systems.

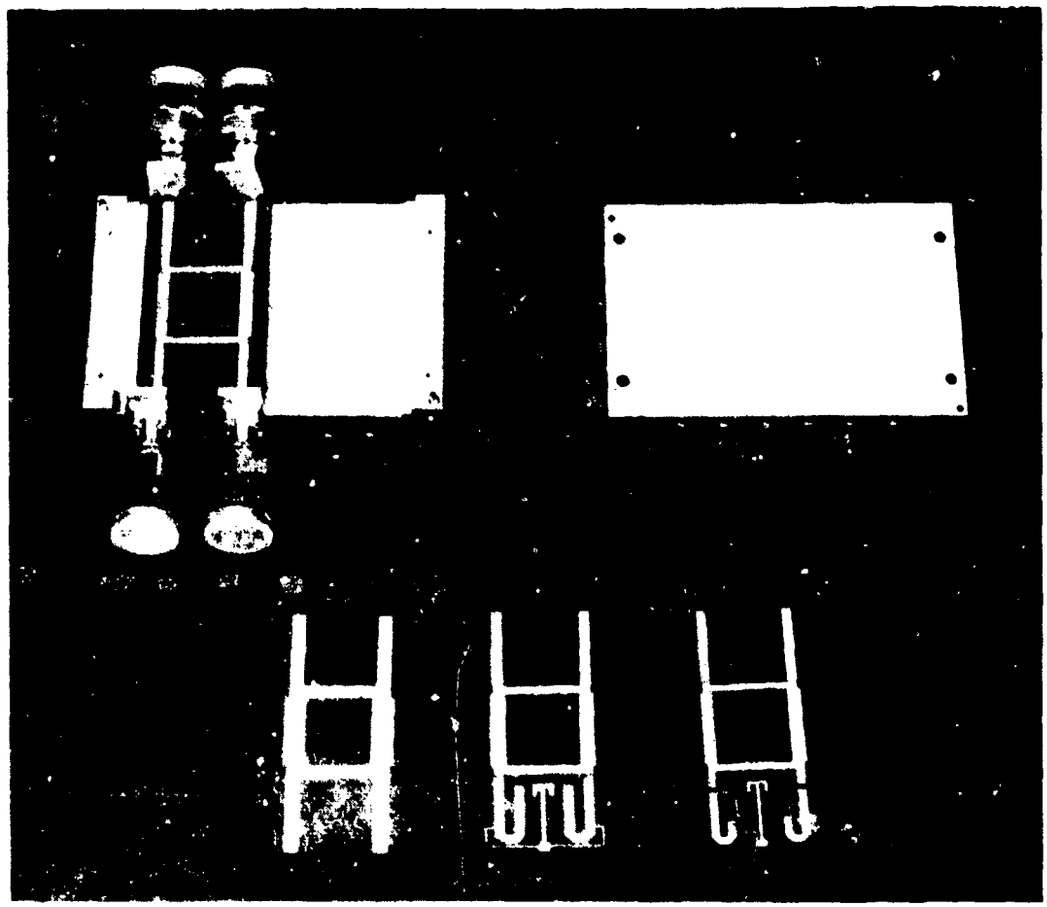

Figure 1. A Typical Test Fixture and Array Electronics

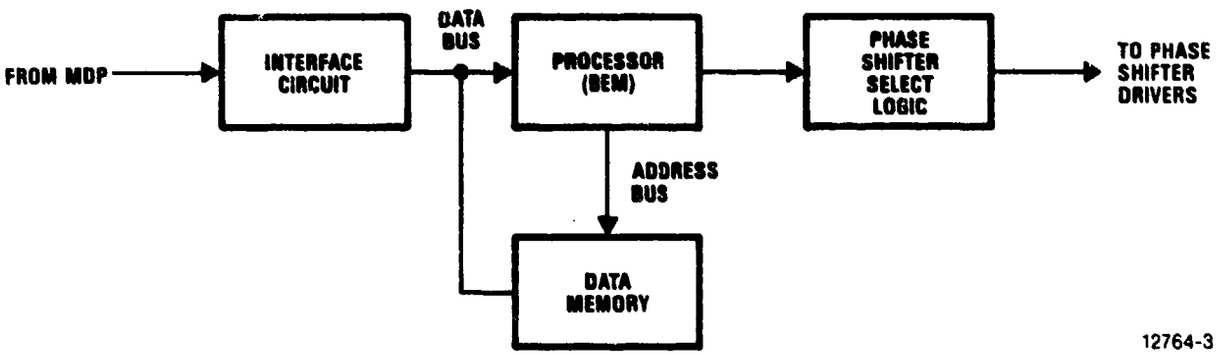

Figure 2. Controller Block Diagram

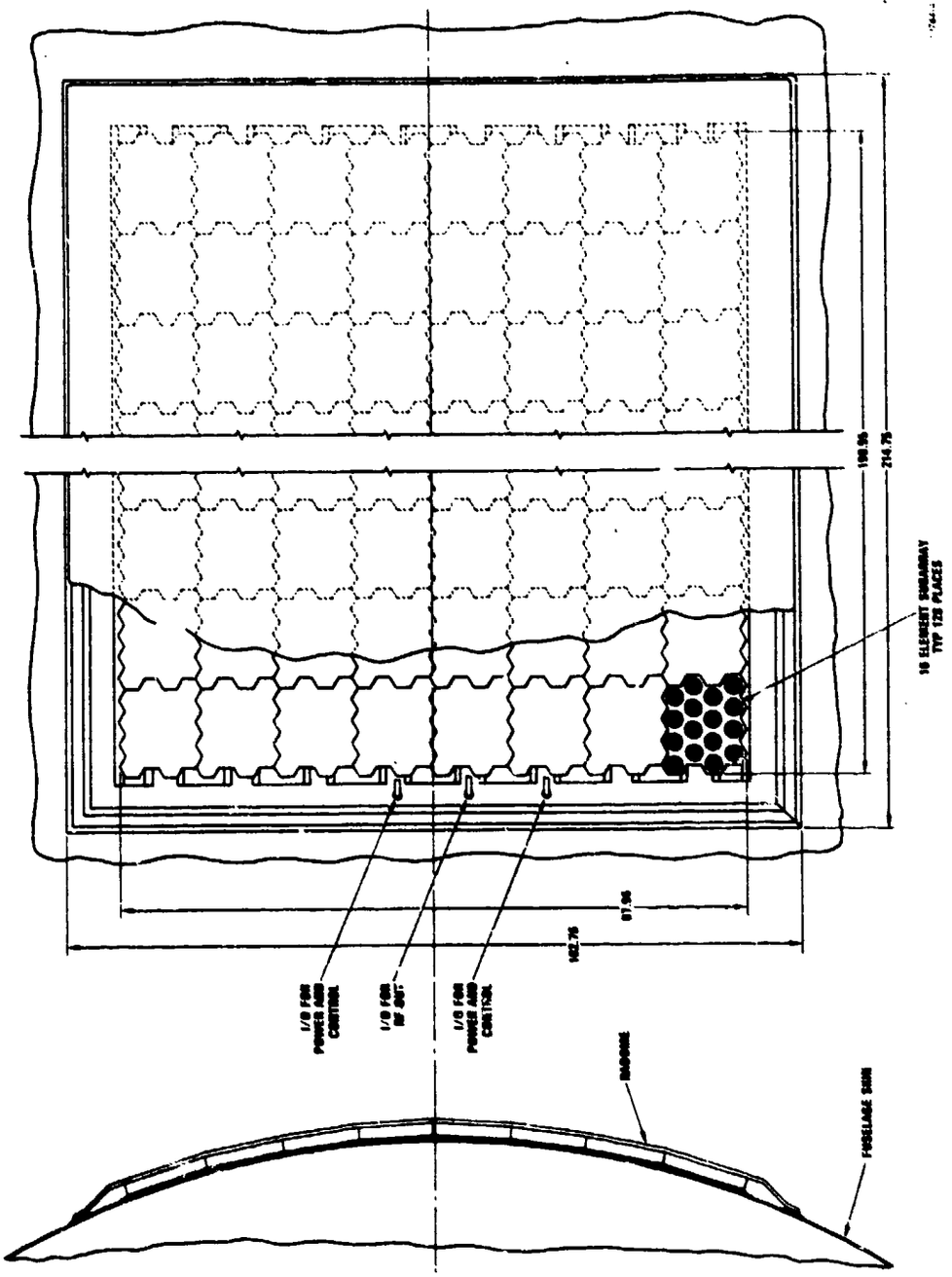

Figure 3. The S-Band Conformal Array

AD P001114

A WIRE-GRID DESIGN OF A UHF ANTENNA

BY

M. S. SOHEL
ENGINEERING SPECIALIST

T. G. PICARD
ASSOCIATE ENGINEER

GENERAL DYNAMICS
FORT WORTH, TX 76101

ABSTRACT

Cavity-backed flush mounted annular slot antennas can be employed in place of the conventionally used blade antennas for UHF communication applications. The slot antennas are large in size, fabricated from metal, and the slot installation weighs more than a blade antenna installation. Previously, Kraus proposed that a flat metal disc can be simulated with four quarter-wave long metal wires intersecting at right angles to each other at the center. However, no further data or investigations are available in the literature. In this study, an attempt is made to simulate the whole antenna (disc and cavity) with grids of metal wires etched on a fiberglass mold of the antenna. The antenna was tuned for a VSWR of from 225-400 MHz, and the antenna gain and radiation patterns were recorded at 225, 330, and 400 MHz frequencies. A comparison of the data with the baseline antenna performance data show that this concept offers hope for future light weight wire grid antenna designs for UHF communication applications.

PAGE BLANK-NOT FILMED

A WIRE GRID DESIGN OF A UHF ANTENNA

BY

DR. M. S. SOHEL
ENGINEERING SPECIALIST

T. G. PICARD
AEROSYSTEMS ENGINEER

ANTENNA SYSTEMS
GENERAL DYNAMICS
FORT WORTH, TEXAS 76101

COMPENDIUM

An all metal cavity backed flush mounted UHF (225-400 MHz) annular slot antenna (baseline) is simulated with grids of metal wires (#12) glued on a fiberglass mold of the antenna. The number of wires and grid dimensions are optimized and the antenna is tuned for a VSWR of 2:1 over the whole band. The antenna gain and radiation patterns were recorded at 225, 300, and 400 MHz frequencies; the electrical performance (VSWR, gain, radiation pattern shapes) is in excellent agreement with the electrical performances of an equivalent quarter wave stub and the baseline antenna. This antenna installation may offer significant reduction in the antenna weight for UHF

"Copyright © 1982 by General Dynamics Corporation All Rights Reserved"

The U.S. Government is authorized to reproduce and sell this report. Permission for further reproduction by others must be obtained from the copyright owner.

communication applications aboard present and future generation military aircraft.

INTRODUCTION

Cavity-backed flush mounted annular slot antennas (Fig. 1) present low aerodynamic drag and thus may be employed in place of the conventionally used blade antennas for UHF communication applications aboard military aircraft. However, the slot antennas are large in size, fabricated from metal, and the slot installation weighs significantly more than the blade installation. Metal plates may be simulated by wire grids and the overall weight of the slot antenna may therefore be reduced. Here an attempt is made to develop the whole antenna (disc and cavity) from grids of metal wires glued on a fiberglass mold of the baseline antenna. The grid dimensions and the number of wires required are optimized to achieve electrical performance similar to that of the baseline antenna.

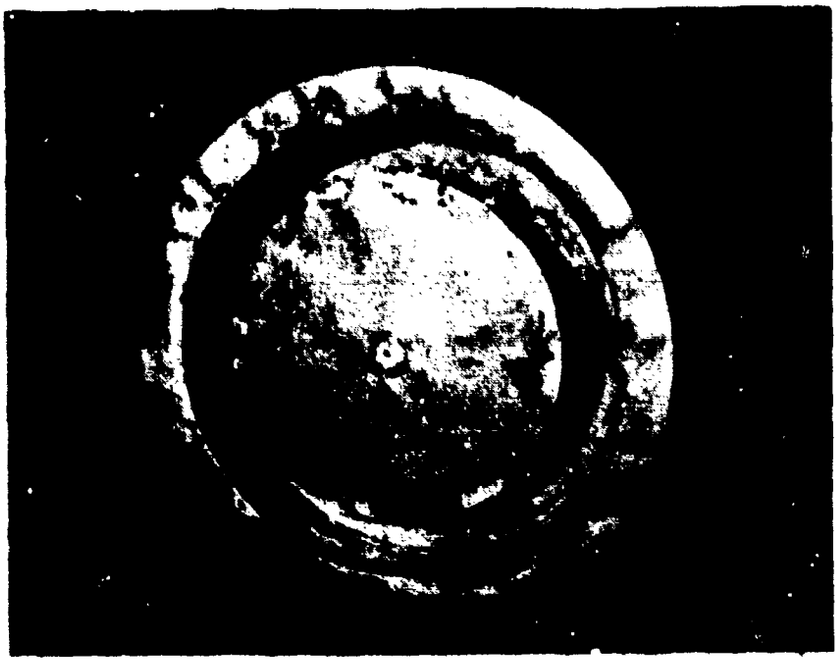

Figure 1 Cavity-Backed Annular Slot Antenna

THEORY

A flush mounted cavity-backed annular slot antenna is a modified version of a top loaded quarter-wave stub antenna installed on a perfectly conducting infinite ground plane. Radiation characteristics of both these antennas are similar. Analytically, the

radiation patterns of a slot antenna installed in an infinite ground plane (Fig. 2) have been predicted by applying the principle of duality.

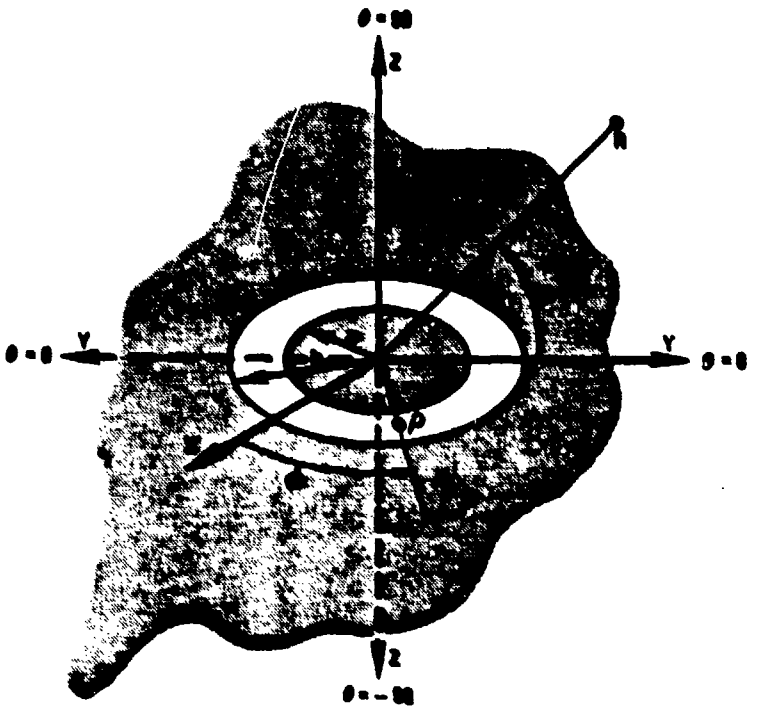

Figure 2 Installed Slot Antenna

By assuming the dominant TEM mode propagation only, one may write an expression for the far field electric field as follows:

$$E_\theta(r, \theta) = -\frac{Va \exp(-jkr)}{r \ln(b/a)} \cdot \frac{Jo(ka \cos\theta) - Jo(kb \cos\theta)}{\cos\theta} \quad (1)$$

where,

Jo = Zero order Bessel function
Va = Voltage across the slot
r = Far field distance
a = Inner slot radius
b = Outer slot radius
$k = 2\pi/\lambda$
λ = Wavelength

However for the baseline slot antenna, where a = 9", b =12" and the frequency range is from 225 to 400 MHz, one can simplify Eq. (1) due to a small argument of Bessel functions and rewrite it as follows:

$$E_\theta(r, \theta) = \frac{Va \exp(-jkr)}{4 r \ln(b/a)} (b^2 - a^2) \cos\theta \quad (2)$$

Equation (1) was programmed on a computer to predict the radiation patterns (Fig. 3) of the slot antenna. These data were used as a guideline to optimize the design of the wire grid antenna.

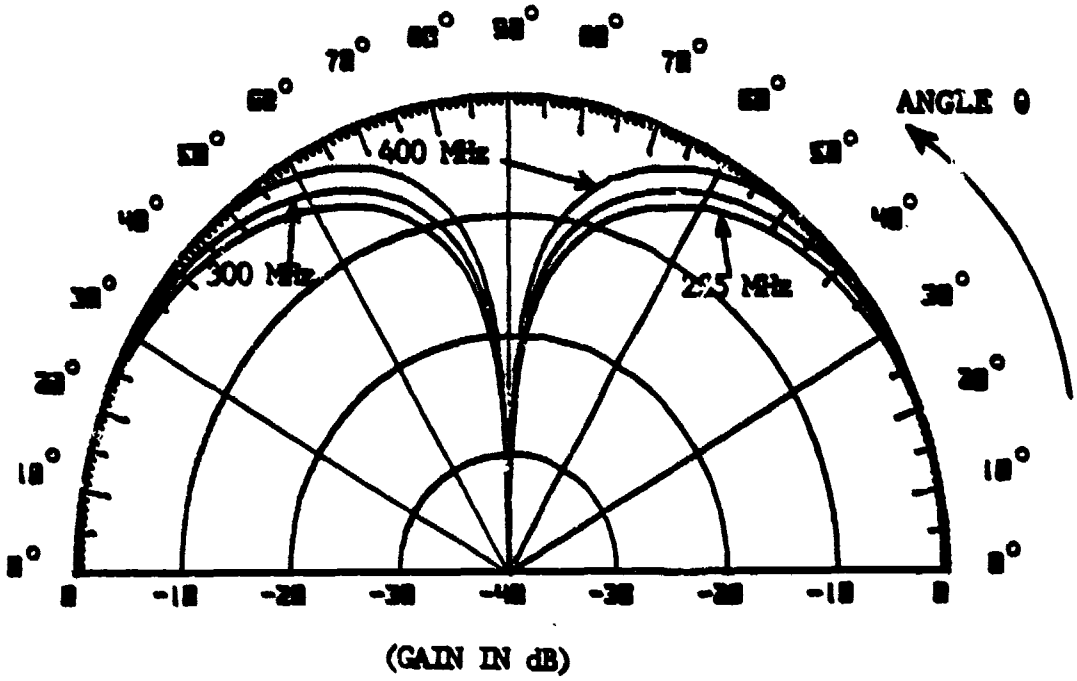

Figure 3 Predicted Radiation Patterns of a UHF Antenna

WIRE GRID DESIGN

The main objective of this task was to simulate the metal disc and cavity with a minimum number of wires required to produce a TEM dominant propagating mode and thereby generate radiation pattern and gain levels equivalent to the baseline antenna or a quarter wave stub antenna. In order to accomplish this, first a fiberglass mold of the baseline antenna was fabricated and then four metal wires intersecting at right

angles to each other at the center of the disc were glued on the fiberglass disc and terminated at a metal ring going around the periphery of the disc. This was done to simulate the metal center disc of the baseline antenna. Similarly, the metal cavity was simulated by gluing four metal wires on the inner side of the fiberglass cavity. The disc wires were fed by the center conductor of the coax and the outer conductor of the coax was terminated at the center of the cavity wires (Fig. 4). This design did not produce any constructive results.

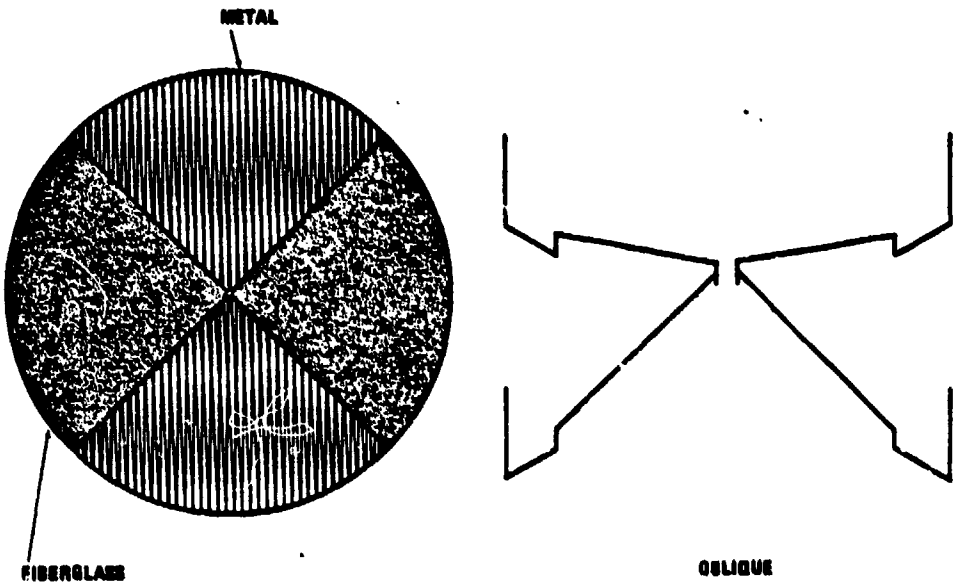

Figure 4 Initial Design of Wire Grid Antenna

Four more wires were added such that there was a wire at every 45° angle on the disc and in the cavity. The antenna seemed to be acceptably tuned at the mid and high bands; however, the VSWR did not look very favorable at the low band. It was also realized that adding more wires did not change the VSWR pattern any further. By putting a 2' x 2' piece of AN-75 RAM behind the antenna (to absorb back radiation), the antenna seemed to be tuned over 90 percent of the band. A VSWR plot of this version is shown in Fig. 5. Also, radiation patterns of this antenna were recorded at 260, 330, and 400 MHz frequencies (Fig. 6) by installing the antenna in an 8' hexagonal ground plane. The coordinate system used is shown in Figure 2.

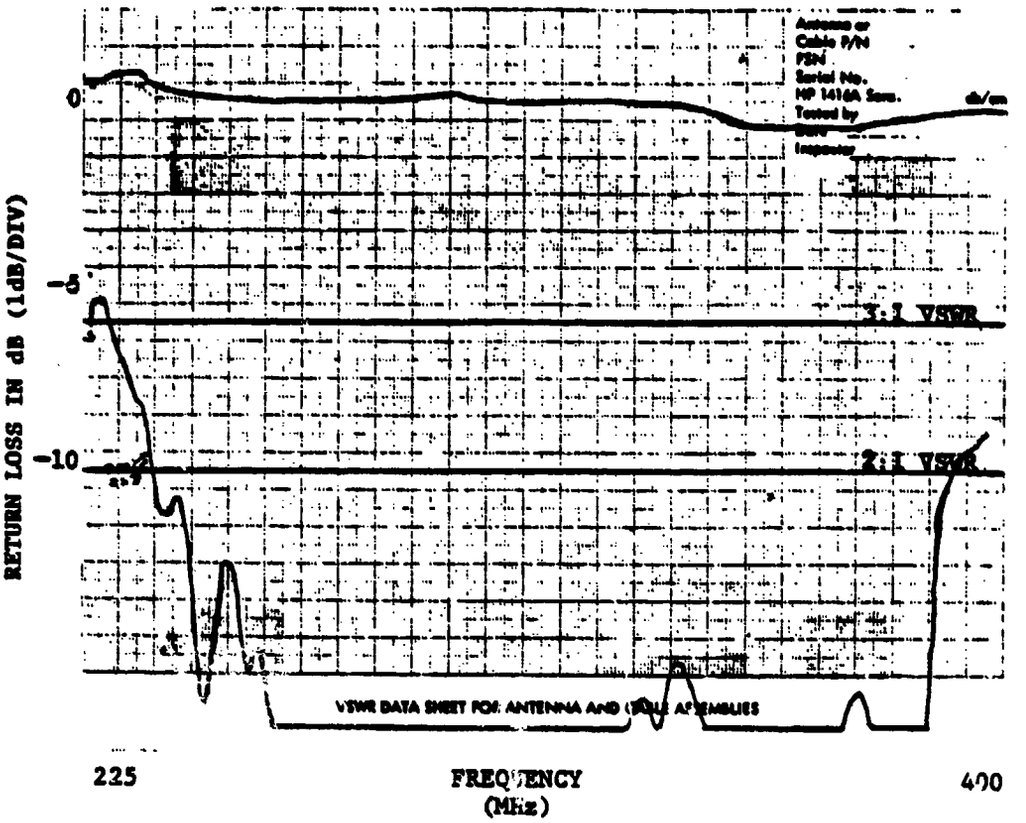

Figure 5 VSWR Plot of Modified Version Antenna

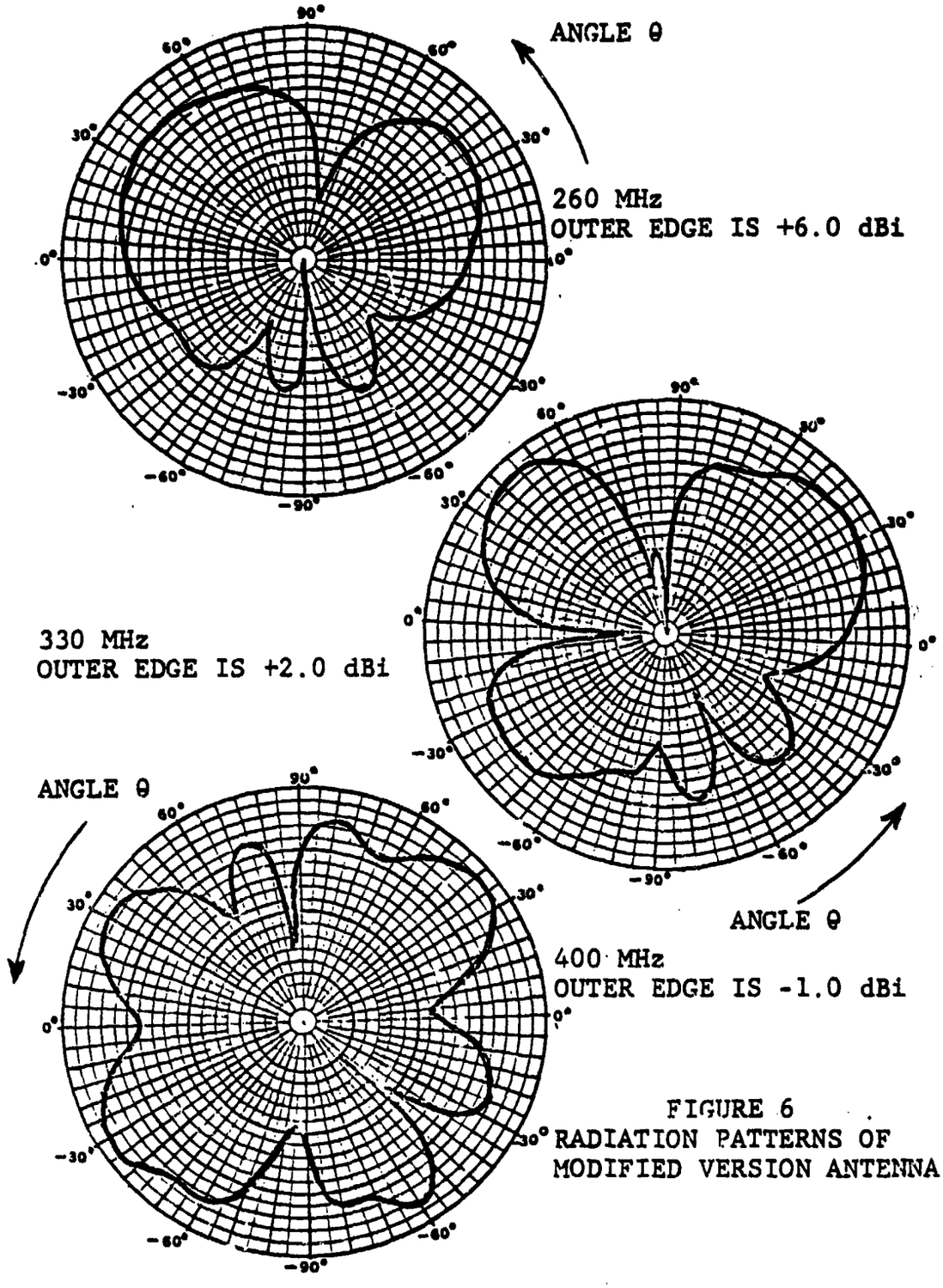

FIGURE 6
RADIATION PATTERNS OF
MODIFIED VERSION ANTENNA

As can be seen from these plots, there is still a significant amount of radiation in the aft direction and to the sides. Also, the antenna gain is very low.

The antenna was further optimized with eight more radial wires making a total of sixteen evenly spaced conductors. Also, two rings were added to the cavity at 5" and 9" from the center conductor. The VSWR was not significantly changed; however, this configuration still had significant back radiation.

After observing that the main part of the back radiation was coming out of the cone area, two more rings were added to the antenna 2½" and 7½" from the center conductor. This configuration still had a good radiation pattern at the low end of the band (225 MHz). The radiation pattern at 300 MHz was very poor with rear lobes 7 dB down from the front main lobes and nulls very close to the horizon. This implied that radiation was still coming out of the rear of the antenna. This fact was verified using the VSWR test set-up.

Two rings were added to the outer wall of the antenna. In addition sixteen more radial wires were added. These conductors ran only from the 7⅛" ring to the outer edge of the cavity. This was done because the antenna had a circular wire approximately every 2⅛" from the center. A graphical sketch of the center disc and the cavity representing this version of the antenna is shown in Figure 7, and a photograph of the antenna is shown in Figure 8.

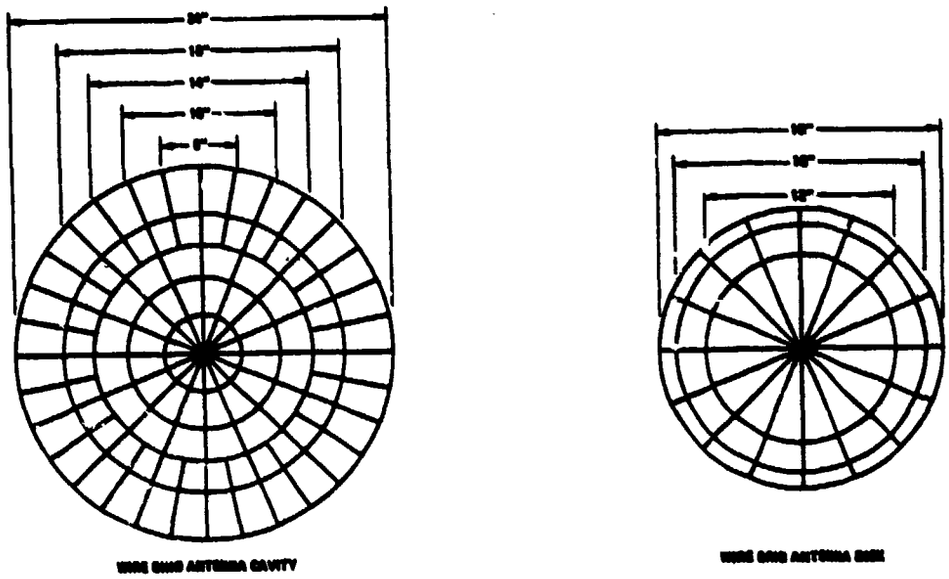

Figure 7 Graphical Sketch of Optimized Wire Grid Antenna

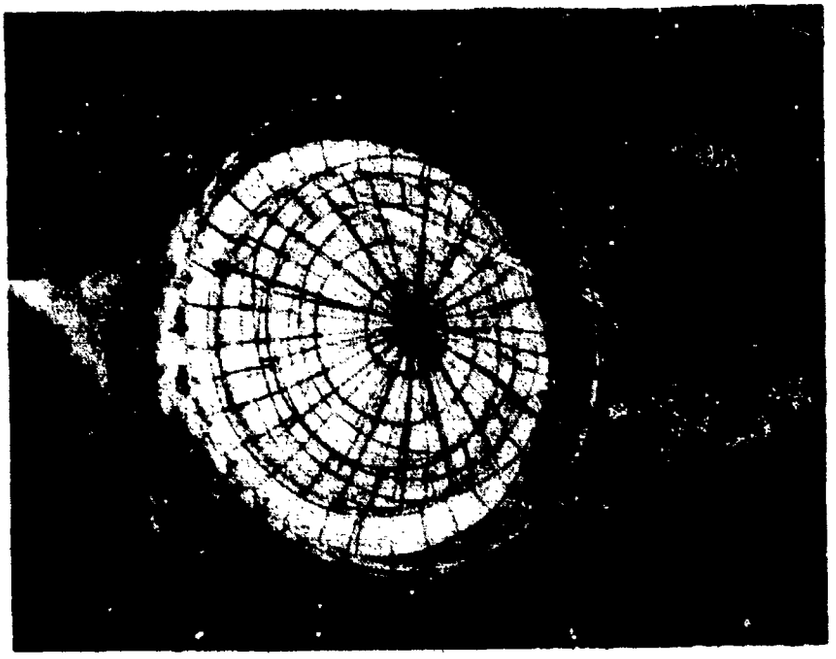

Figure 8 Optimized Wire Grid Antenna

A VSWR plot of the antenna is shown in Figure 9 and the radiation patterns recorded at 225, 260, 300, 330, and 400 MHz frequencies are shown in Figure 10. The coordinate system used is shown in Figure 2.

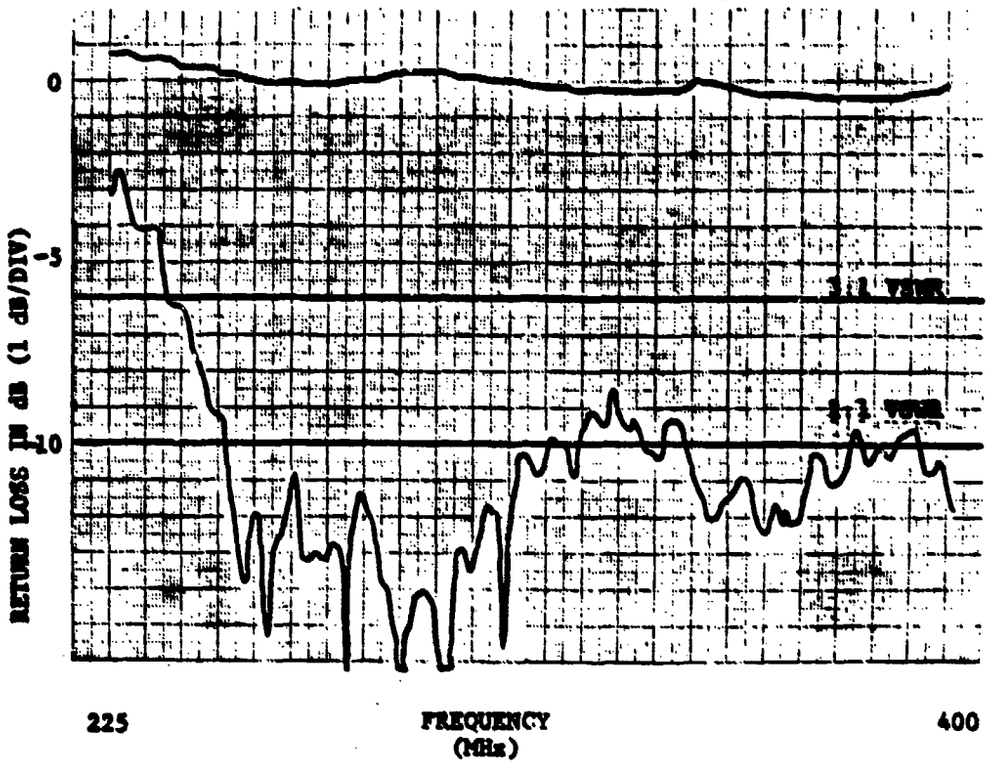

Figure 9 VSWR Plot of Optimized Wire Grid Antenna

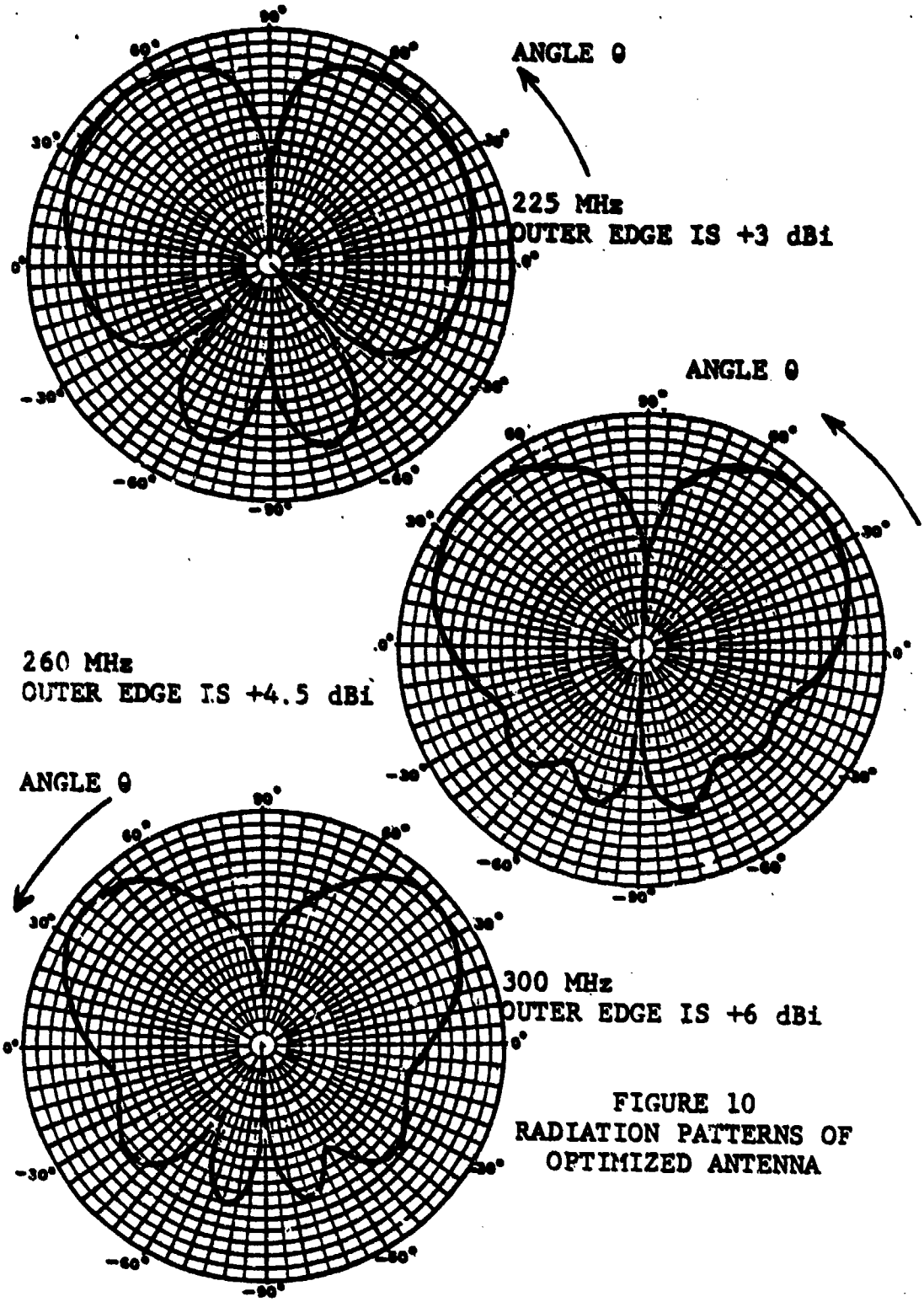

FIGURE 10
RADIATION PATTERNS OF
OPTIMIZED ANTENNA

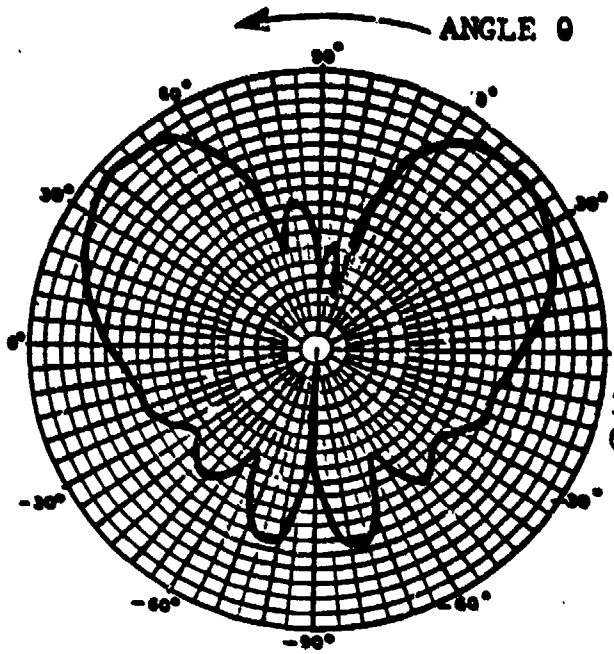

330 MHz
OUTER EDGE IS +6 dBi

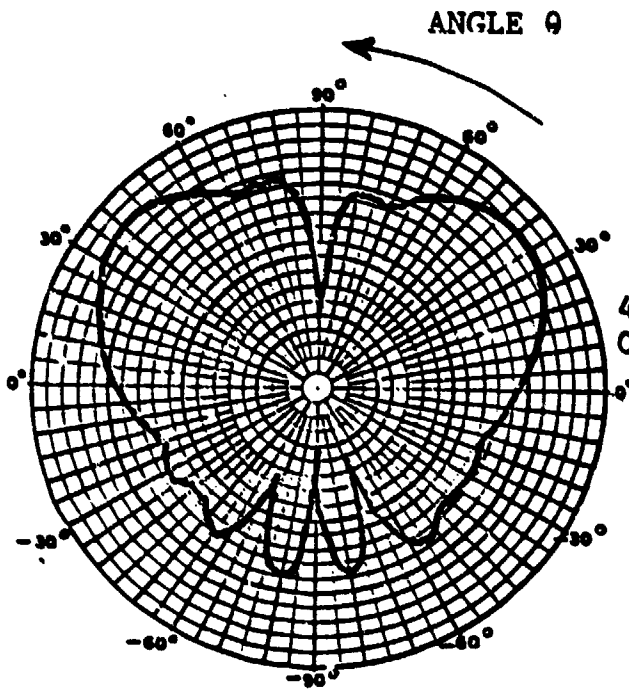

400 MHz
OUTER EDGE IS +8 dBi

FIGURE 10

DISCUSSION OF RESULTS

In order to determine the applicability of this antenna in the real world situation, radiation patterns of an equivalent quarter wave stub antenna and the baseline antenna were also recorded at 225, 300, 400 MHz frequencies. The radiation patterns of the wire grid antenna were compared with the radiation patterns of the quarter-wave stub antenna and the baseline antenna. Shown in Table 1 is a comparison of antenna peak and horizon gains for these antennas.

Table 1 Comparison of Antenna Gains

ANTENNA	FREQ IN MHz	PEAK GAIN	HORIZON GAIN
¼ Wave Stub	225	+ 1.5 dB	- 2.0 dB
Baseline		+ 0.5 dB	- 3.5 dB
Wire Grid		+ 1.0 dB	- 3.0 dB
¼ Wave Stub	300	+ 4.5 dB	- 0.5 dB
Baseline		+ 4.0 dB	- 3.0 dB
Wire Grid		+ 4.0 dB	- 6.0 dB
¼ Wave Stub	400	+ 3.0 dB	- 2.0 dB
Baseline		+ 4.5 dB	- 3.0 dB
Wire Grid		+ 4.5 dB	- 3.0 dB

ANALYSIS OF RADIATION PATTERN DATA

- At 225 MHz, the overall shape of the radiation patterns of the wire grid antenna compare well with both the baseline UHF annular slot and the ¼ wave stub antennas. Gain levels are also fairly close although they are not at the theoretical 3 to 5 dB levels. This is due to the fact that the antennas were installed in a relatively

finite 9' ground plane, causing energy to spread in the back direction.

- At 300 MHz, the peak gain of the baseline and the wire grid antennas are approximately equal and the antennas compare on pattern shape. However, the horizon gain is 2 to 5 dB lower for these antennas than the ¼ wave stub antenna. This may be due to the E vector distribution in the slots of the baseline and wire grid antennas which modifies the radiation pattern shape distribution.

- At 400 MHz, the peak and horizon gains of the wire grid, the baseline, and the ¼ wave stub antennas correlate extremely well. However, the horizon gain of the baseline and wire grid antennas is down 1 dB from the ¼ wave stub antenna gain. This difference in the measured gain is well within the margin of the test accuracy.

CONCLUSIONS

A wire grid design cavity backed UHF antenna is simulated on a fiberglass mold of an all metal cavity backed annular slot antenna. It is shown that the electrical performance (VSWR, gain, radiation patterns shapes) is in excellent agreement with the electrical performances of an equivalent quarter wave stub antenna and a baseline annular slot antenna. The peak gain of the antenna is within $\pm$ 1.5 dB of the $\frac{1}{4}$ wave stub antenna and a baseline annular slot antenna. The antenna gain at the horizon also compares well except at 300 MHz where the wire grid seems to lose 2-5 dB gain. This loss may be due to the E vector distribution in the slots of the baseline and wire grid antennas which modifies the radiation pattern shape distribution.

REFERENCES

(1) J. R. Wait; "A Low-Frequency Annular-Slot Antenna"; Journal of Research of the National Bureau of Standards; Vol. 60, Jan. 1958, pp 59-64.

(2) C. W. Harrison, Jr. and D. C. Chang; "Theory of the Annular Slot Antenna Based on Duality"; IEEE Trans. on Electromagnetic Compatibility; Vol. EMC-13, Feb. 1971; pp 8-14.

(3) C. W. Harrison, Jr. and D. C. Chang; "On The Pulse Response of a Flush-Mounted Coaxial Aperture"; IBlD; pp 14-18.

(4) C. W. Harrison, Jr. and D. C. Chang; "Compability of Annular Slot Receiving Antenna Theories"; IBlD; Vol. EMC-15 May, 1973; pp 86-87.

(5) D. E. Merewether, R. B. Cook and R. Fisher; "Receiving Properties of the Small Annular-Slot Antenna"; IBlD; Vol. EMC-22 Feb. 1980; pp 60-64.

(6) J. E. Jones and J. H. Richmond; "Application of an Integral Equation Formulation to the Prediction of Space Shuttle Annular Slot Antenna Radiation Patterns"; IEEE Trans Antennas and Propagation; Vol. AP-22 Jan 1974, pp 109-111.

(7) H. Levine and C. H. Papas; "Theory of the Circular Diffraction Antenna"; Journal of Applied Physics, Vol. 22 Jan, 1951; pp 29-43.

(8) J. Galejs and T. W. Thompson; "Admittance of a Cavity-Backed Annular Slot Antenna"; IRE Trans. Antennas and Propagation, Vol. AP-10, Nov 1962; pp 671-678.

(9) D. C. Chang; "Input Admittance and Complete Near Field Distribution of an Annular Aperture Antenna Driven by a Coaxial Line"; IEEE Trans. Antennas and Propagation; Vol. AP-18 Sept 1970; pp 610-616.

(10) E. P. Irzinski; "The Input Admittance of a TEM Excited Annular Slot Antenna"; IBlD, Vol. AP-23, Nov 1975; pp 829-834.

(11) J. D. Kraus; Antennas New York: McGraw-Hill, 1950 pp 420-422.

(12) A. A. Volkov, et al; "Electrodynamic Properties of Plane Wire Grids"; International Journal of Infared and Millimeter Waves, Vol. 3, Jan. 1982; pp 19-43.

(13) Correspondence With Rodger McNeill Sr. June 25, 1982 Dept. Manager Microwave Antennas Engineering Transco Products, Inc.

AD P001115

C-BAND
TRANSPONDER ANTENNA

Prepared by

PETER J. CONROY
PRINCIPLE STAFF ENGINEER
MOTOROLA INC., GOVERNMENT ELECTRONICS GROUP
SCOTTSDALE, ARIZONA

Prepared for THE 1982 ANTENNA APPLICATIONS SYMPOSIUM
Robert Allerton Park, Illinois

PAGE BLANK-NOT FILMED

C-BAND TRANSPONDER ANTENNA

Peter J. Conroy
Principle Staff Engineer
Motorola Inc., Government Electronics Group
Scottsdale, Arizona

ABSTRACT

This paper describes the design, fabrication, and test results of a C-Band Transponder Antenna. The antenna is a light-weight, low-profile 32 element "microstrip" wraparound-type printed circuit antenna. The unit is formed and bonded to a balanced lightweight 11.5-inch diameter magnesium ring. This paper includes a description of the interactive graphics and computer-aided design (CAD) photo generation techniques and process control for large size (42 inches long) flexible circuit boards. Also described are the design of the antenna feed system, pin-diode transmit-receive switch and receiver solid-state electronics network layout using an asymmetrical stripline printed circuit board. The use of an asymmetrical circuit system is a novel approach to reducing weight and preventing feed system ("microstrip") radiation losses while providing adequate antenna bandwidth. Finally, the paper describes the results of the prototype antenna testing.

1. INTRODUCTION

The primary purpose of this paper is to describe the Motorola GEG Antenna Engineering Work Station which is used to analyze and design printed circuit antennas and microwave networks. The C-band transponder is presented as an example of the product of the Motorola GEG Antenna Engineering Work Station.

2. C-BAND TRANSPONDER

The C-band transponder is a self-contained bolt-on unit consisting of three major elements. These are a printed circuit board, a magnesium support ring and a magnesium housed battery ring. The printed circuit board consists of a 32-element omnidirectional "microstrip patch" antenna, an asymmetrical stripline corporate feed, a pin diode transmit-receive switch and a solid-state receiver. The 11.5-inch diameter magnesium ring supports the printed circuit board and houses a solid-state transmitter and the transponder processor circuits. An unplated prototype antenna test unit is shown in Figure 1. The static balanced weight of the assembled unit is 28.6 ounces.

2.1 Transponder Printed Circuit Board Description

The C-band transponder etched printed circuit board is shown in Figure 2. This is the lower ground plane board which contains all of the RF tracks and the 32 microstrip patch antenna elements. The printed circuit board material is Rogers Corporation 5880 Duroid with 1 ounce of rolled copper. The finished board dimensions are 0.060 inch thick, 2.0 inches wide and 36.5 inches in length. The upper ground plane circuit board (not shown in Figure 2) is also 5880 Duriod and its dimensions are 0.030 inch thick, 1.2 inches wide and 37.2 inches in length. There are no RF tracks on this board. The 0.060-inch ground plane spacing on the lower ground plane was specified to provide a 5-percent microstrip patch antenna bandwidth. The upper ground plane, which covers only the feed system and the RF circuits, is half the thickness of the lower ground plane and forms an asymmetrical 0.030/0.060-inch stripline transmission system. This results in a weight reduction over a 0.060/0.060-inch symmetrical stripline with minimal loss in circuit performance.

2.2 C-Band Antenna Performance

The C-band antenna operates over a 5 percent bandwidth with a voltage standing wave ratio of less than 2:1. Coverage is required over nearly an entire hemisphere, the exceptions being a ±15 degree conical section fore and aft on the vehicle axis. A typical pitch plane pattern is shown in Figure 3, and a typical roll plane pattern is shown in Figure 4.

3. ANTENNA ENGINEERING WORK STATION

A block diagram of the Antenna Engineering Work Station used to analyze and generate the C-band transponder printed circuit board is shown in Figure 5. The work station display unit is a Tektronics 4081 interactive graphics terminal. There are two basic modes of antenna work station operation. These are the design analysis mode and the CAD-Art mode. In the design analysis mode, the 4081 unit can be operated as a terminal in a host computer environment (560 Honeywell Engineering Computer) or as a stand alone computational and graphics system. In the CAD-Art mode, the unit operates in the host computer environment only.

3.1 Design Analysis Mode

In the design analysis mode, numerous antenna analytical subroutines are available to the antenna engineer. In the design of the C-band transponder antenna, a cylinderical scattering analytical subroutine was used to optimize the antenna roll plane pattern. Both uniform and progressive phase excitations were investigated as well as the effects of a small gap in the circular array, which is a space required for the solid-state transmitter. The effects of each parameter change in the circular array design on the resulting far-field radiation pattern can be immediately viewed on the graphics terminal. An interactive error analysis can also be performed to facilitate the selection of materials and specify fabrication tolerances.

3.2 CAD-Art Mode

The CAD-Art design mode of the Antenna Engineering Design Station utilizes the Tektronics 4081 interactive graphics terminal and a complex CAD-Art software program operating on the host Honeywell 560 computer. The CAD-Art program provides the means and the link between the engineering work station and any one of three CALMA CAD-Art computers. The CAD-Art software program permits the building of an artwork file which contains a minimum of program lines or instructions that in general are proportional to the number of definable circuit elements. The artwork generation procedure is described as follows. Circuit elements are defined in the CAD-Art program subroutines and are identified as circuit elements such as: microstrip patch, line segment, power divider, Langey coupler, etc. Once the number and type of circuit elements are identified and defined in an edited file, the run program can be compiled and loaded — ready for execution.

The next step is to create a data file which corresponds one for one to the subroutine calls in the main program. Only basic coordinate points and layer information are required in the data file. Transmission line widths are automatically computed. To initially view the artwork, it is necessary only to run the program. Dimensional changes and errors can be corrected by using the data file. The major advantage of the system is that it eliminates the time consuming and costly repeated compiling and loading of the main program.

Once the engineer is satisfied with the artwork displayed on the 4081 graphics terminal, he outputs the CALMA formatted data on a seven-track tape. The CALMA CAD-Art system is then used to generate the final artwork (either film or glass) on one of three Gerber photoplotters which vary in film bed size from 16 inches by 40 inches to 20 inches by 60 inches.

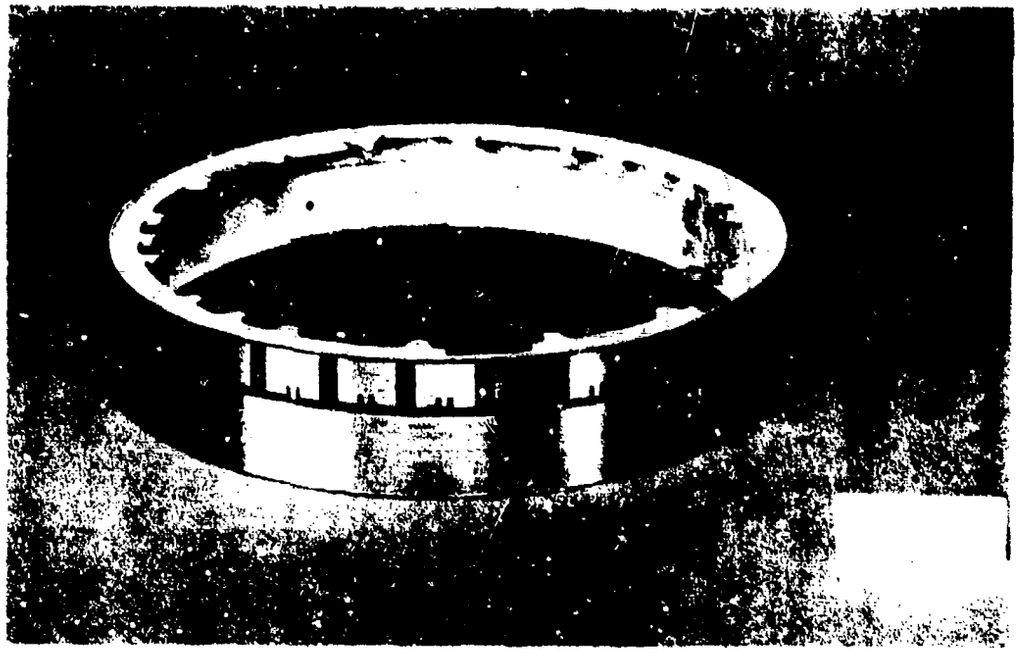

81-3788 8791-1

Figure 1. C-Band Transponder Test Antenna Bonded to Magnesium Ring

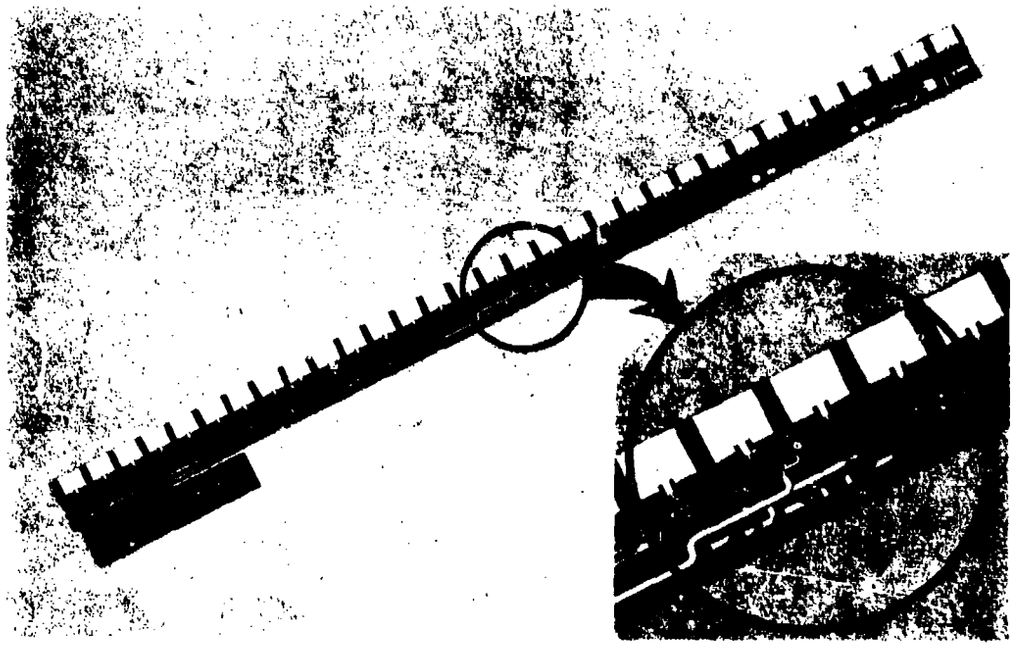

81-2984 8791-2

Figure 2. C-Band Transponder Printed Circuit Board

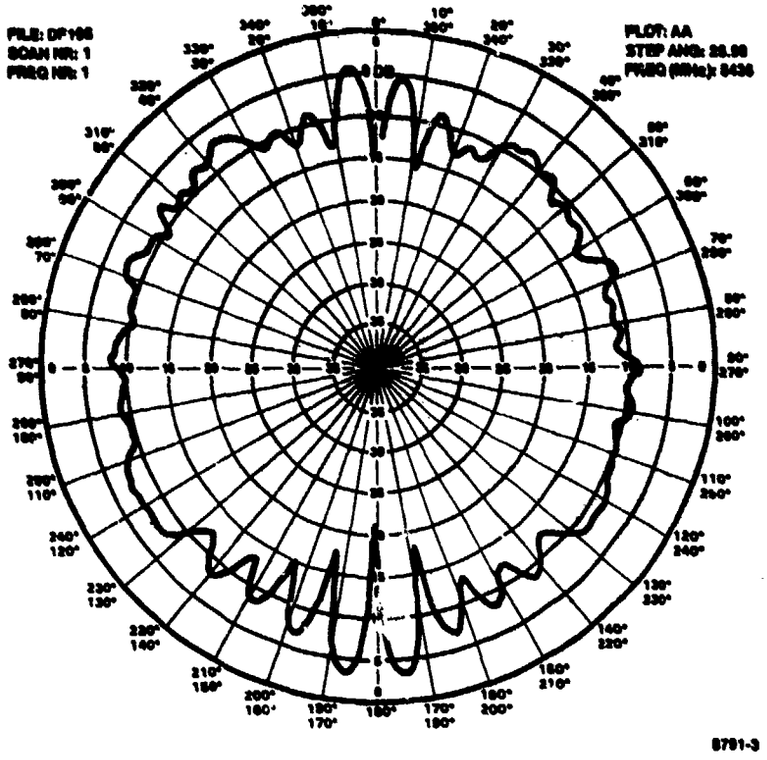

Figure 3. C-Band Transponder Pitch Plane Radiation Pattern

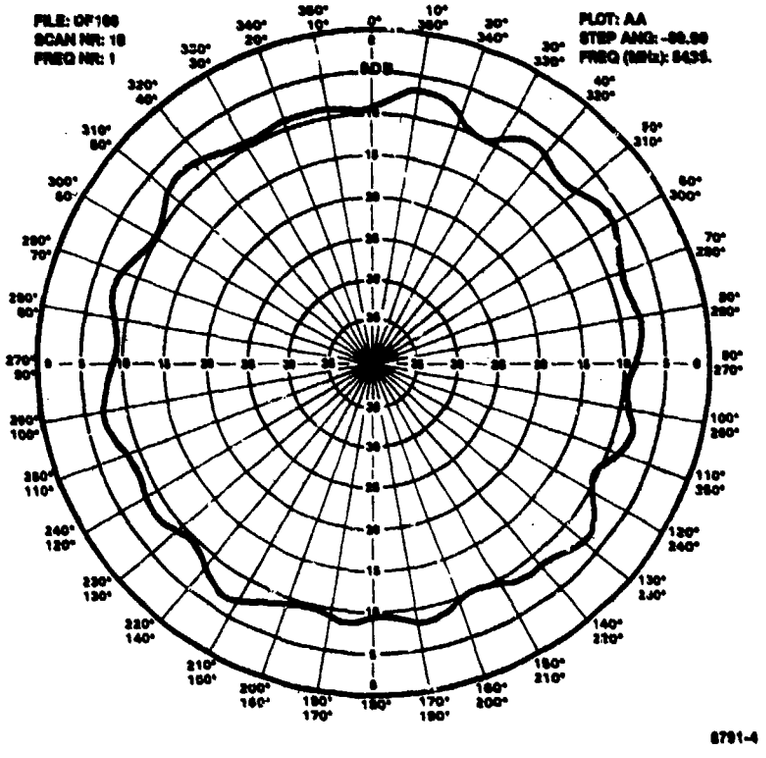

Figure 4. C-Band Transponder Roll Plane Radiation Pattern

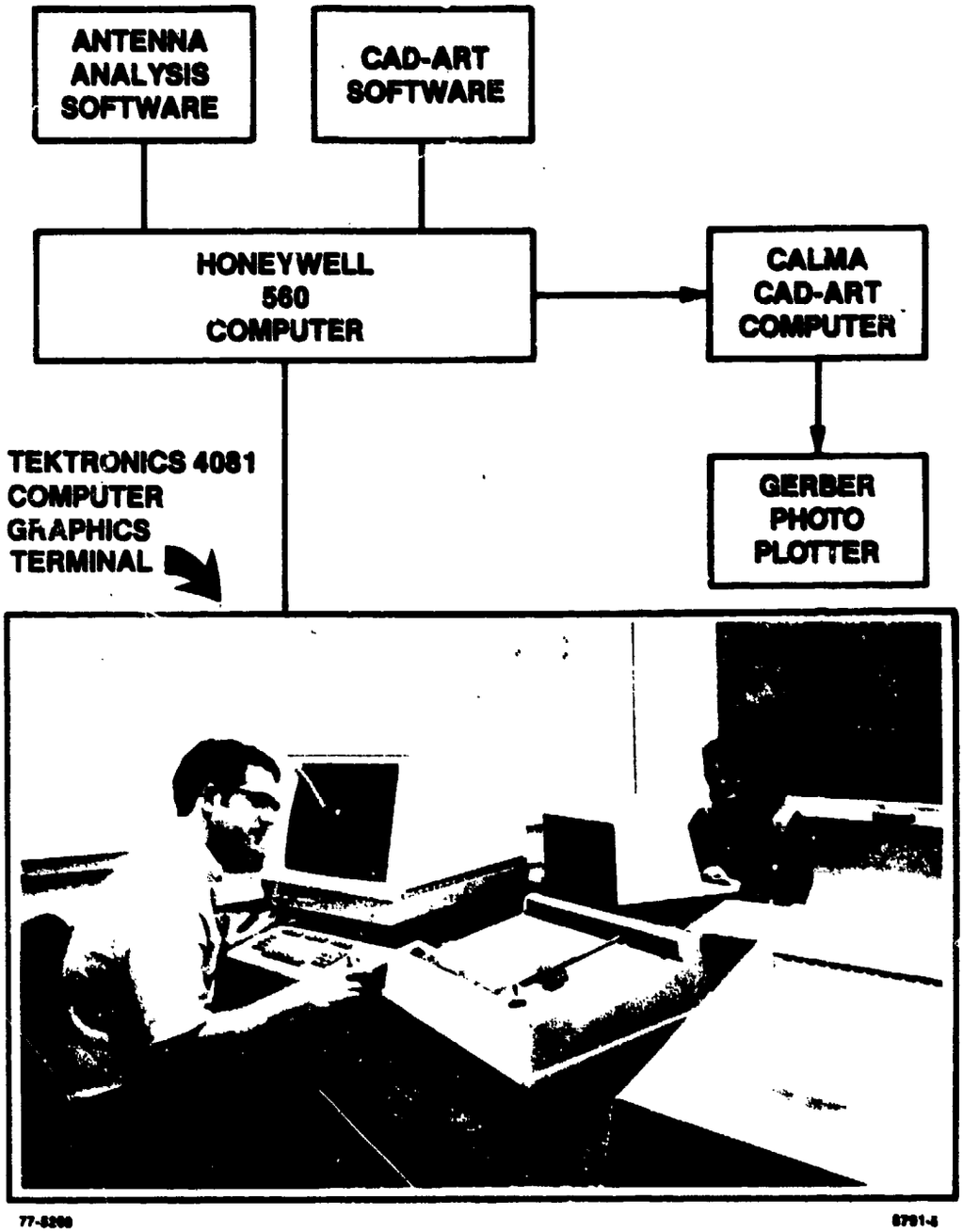

Figure 5. Antenna Engineering Work Station

AD P001116

MICROSTRIP PATCH ANTENNAS ON THICK CURVED SUBSTRATES

N.G. Alexopoulos
Electrical Engineering Department
University of California at Los Angeles
Los Angeles, California 90024

P.L.E. Uslenghi
Department of Electrical Engineering and Computer Science
University of Illinois at Chicago
Chicago, Illinois 60680

N.K. Uzunoglu
Department of Electrical Engineering
National Technical University of Athens
Athens TT-147, Greece

[illegible] BLANK-NOT FILMED

1. Abstract

Electric dipoles which are tangent to the outer surface of a dielectric layer backed by a curved metallic surface (modeled by a circular cylinder) are considered. The exact solution to this problem is utilized to obtain numerically the current distribution, input impedance and radiation pattern for a thin rectangular patch antenna, center fed or not. For very large cylinders, asymptotic solutions based on ray tracing are considered.

2. Introduction

In the previous works [1-4], the authors have considered microstrip dipoles on cylindrical and spherical surfaces. Exact solutions have been obtained via electric dyadic Green's functions for dipoles of arbitrary orientation on substrates of arbitrary thickness and material properties. The extraction of numerical results from these exact solutions is practical only if the radius of curvature of the substrate is not large compared to the wavelength. For large cylinders, an asymptotic solution has been obtained for thin substrates [2], and some progress has been made toward an asymptotic solution for thick substrates [4].

In this paper, we consider a printed dipole of finite length, and set up an integral equation for the surface current, utilizing the exact results given in [2]. This equation is solved numerically, and the input impedance is then obtained via a variational technique. The radiation pattern is also computed. All these results require a tolerable

amount of computer time for cylinders of moderate size.

For very large cylinders, we describe some initial results that we have obtained for the far field, utilizing an optical approach, i.e., ray tracing inside the curved substrate.

The time-dependent factor $\exp(-i\omega t)$ is omitted throughout the paper.

3. Surface current on rectangular printed dipole.

The geometry of the problem is illustrated in Fig. 1. A metal cylinder of infinite length and radius a is coated by a layer of dielectric material of uniform thickness $D = b - a$ and relative permittivity ε_r (i.e., refractive index $N = \sqrt{\varepsilon_r}$). The printed rectangular antenna is on the outer surface of the substrate, has length ℓ in the direction of the cylinder axis and width w in the circumferential direction, corresponding to an angular width δ as seen from the z-axis (i.e., $w = b\delta$). It is fed at a small gap which may be offset an amount z_0 from the center of the dipole.

If the width w is small compared to the wavelength, the only component I(z) of the current is in the z-direction. It can be shown that I(z) satisfies the following Hallèn-type integral equation:

$$\int_{-\ell/2}^{\ell/2} K(z,z')\, I(z')\, dz' = \int_{-\delta/2}^{\delta/2} \frac{E\, d\phi'}{\sqrt{1 - \left(\frac{2\phi'}{\delta}\right)^2}} \qquad (1)$$

where the electric field E is zero on the dipole and its integral across the feeding gap is taken as 1 volt, and the kernel

$$K(z,z') = \int_{-\delta/2}^{\delta/2} d\phi \int_{-\delta/2}^{\delta/2} d\phi' \frac{g(z,z',\phi,\phi')}{\sqrt{\left[1-\left(\frac{2\phi}{\delta}\right)^2\right]\left[1-\left(\frac{2\phi'}{\delta}\right)^2\right]}} \qquad (2)$$

where $g(z,z',\phi,\phi')$ is a known complicated function of its arguments, that can be obtained from the exact results given in [2].

To solve eq. (1), we assume that $I(z)$ may be expressed by the finite Fourier series

$$I(z) = \sum_{h=0}^{n-1} I_h \cos\left[(2h+1)\pi z/\ell\right] \qquad (3)$$

which satisfies the boundary conditions $I(\pm \ell/2) = 0$. The Fourier coefficients I_h are given in Table 1 for $n = 4$ and $n = 7$, and for $\delta = 0.03$ radians, $z_0 = 0$, $k_0 a = 1.50$, $k_0 b = 1.92$, $\varepsilon_r = 2.17$ (corresponding to $N = 1.47$); the negative integers in parentheses are exponents of power-of-ten multiplicative factors. It is seen that good convergence is obtained for n not too large. Note that the values chosen for Table 1 correspond to a substrate thickness of about one tenth of the wavelength inside the substrate.

Table 1

h	I_h for n = 4	I_h for n = 7
0	5.47(-3) + i 1.19(-2)	5.40(-3) + i 1.18(-2)
1	1.07(-4) - i 1.65(-3)	8.54(-5) - i 1.68(-3)
2	3.70(-5) - i 3.43(-4)	4.68(-5) - i 3.29(-4)
3	-3.80(-5) - i 4.96(-4)	-4.50(-5) - i 5.06(-4)
4		3.87(-5) - i 1.05(-4)
5		-3.40(-5) - i 3.02(-4)
6		3.20(-5) - i 5.10(-5)

4. Input impedance of rectangular printed dipole

The input impedance Z_{in} of the finite dipole is obtained by Galerkin's variational method, in the form:

$$\frac{1}{Z_{in}} = \frac{1}{2C_0} \int_{-\ell/2}^{\ell/2} dz\, I(z) \int_{-\ell/2}^{\ell/2} dz'\, I(z')\, K(z,z') \qquad (4)$$

where

$$C_0 = \int_0^{\delta/2} \frac{d\phi}{\sqrt{1 - \left(\frac{2\phi}{\delta}\right)^2}} \qquad (5)$$

Some numerical results for the same data used for Table 1 are given in Table 2; the first resonance occurs at $k_0\ell \approx 2.82$.

Table 2

$k_0\ell$	$Z_{in}(\Omega)$
2.0	10 + i 65.6
2.5	16.5 + i 25
3.14	23.5 - i 25
3.5	36.2 - i 51

The effect of feed gap displacement from the symmetrical position $z_0 = 0$ on the real part R_{in} and the imaginary part X_{in} of the input impedance is shown in Fig. 2, for the numerical values indicated.

5. Far field for rectangular printed dipole.

The radiation pattern is easily calculated. An example is given in Fig. 3.

6. Some considerations for large cylinders.

For an axially oriented elementary dipole, the far field in the equatorial plane $\theta = \pi/2$ may be written as

$$\underline{E}(\underline{r}) \sim -k_0^2 \frac{e^{ik_0 r}}{k_0 r} S\hat{\theta}, \quad (\rho \to \infty) \tag{6}$$

where the far-field coeffecient

$$S = \frac{-2}{\pi k_0 b} \int_C \frac{d\nu}{\sin \pi\nu} f_\nu e^{-i\frac{\pi}{2}\nu} \cos \nu\phi, \quad \phi = \phi - \phi_0 - \pi, \tag{7}$$

ϕ and ϕ_0 are the azimuthal positions of observation point and dipole, respectively, and the contour C of integration runs along the real ν-axis and just above it, from $Re\,\nu = -\infty$ to $+\infty$. The function f_ν is exactly known [2], but it is so complicated that no insight on its behavior is obtainable by direct inspection. However, for very thin substrates ($|N|k_0 D \ll 1$) and very large cylinders ($k_0 b \gg 1$), the asymptotic estimate holds:

$$f_\nu \sim \frac{-k_0 D}{H_\nu^{(1)}\left(k_0 D\right) - k_0 D H_\nu^{(1)\prime}\left(k_0 D\right)} \tag{8}$$

from which an asymptotic evaluation of S is obtainable, that leads to easy expressions for the radiated field of arrays of dipoles.

The case of thick substrates is considerably more complicated, because the simplifications ensuing from the exact solution do not lead easily to an asymptotic interpretation. However, it will be shown that simple and interesting results of easy applicability are obtained by following a ray-tracing approach within the thick curve substrate. Aside from the complication arising from the curvature of the substrate, this approach is similar to that adopted in optics, in analyzing the behavior of dielectric slab waveguides and Fabry-Perot interferometers.

7. References

[1] N.G. Alexopoulos and P.L.E. Uslenghi (1981), "Microstrip dipoles on spherical structures", National Radio Science Meeting, Los Angeles, California.

[2] N.G. Alexopoulos, P.L.E. Uslenghi and N.K. Uzunoglu (1981), "Microstrip dipoles on cylindrical structures", Proceedings of the 1981 Antenna Applications Symposium, University of Illinois at Urbana-Champaign.

[3] N.K. Uzunoglu, P.L.E. Uslenghi and N.G. Alexopoulos (1982), "Printed circuit antennas on cylindrical substrates", IEEE-AP International Symposium, Albuquerque, New Mexico.

[4] N.G. Alexopoulos, P.L.E. Uslenghi and N.K. Uzunoglu (1982), "Microstrip dipoles on thick curved substrates", National Radio Science Meeting, Albuquerque, New Mexico.

GEOMETRY OF THE PROBLEM

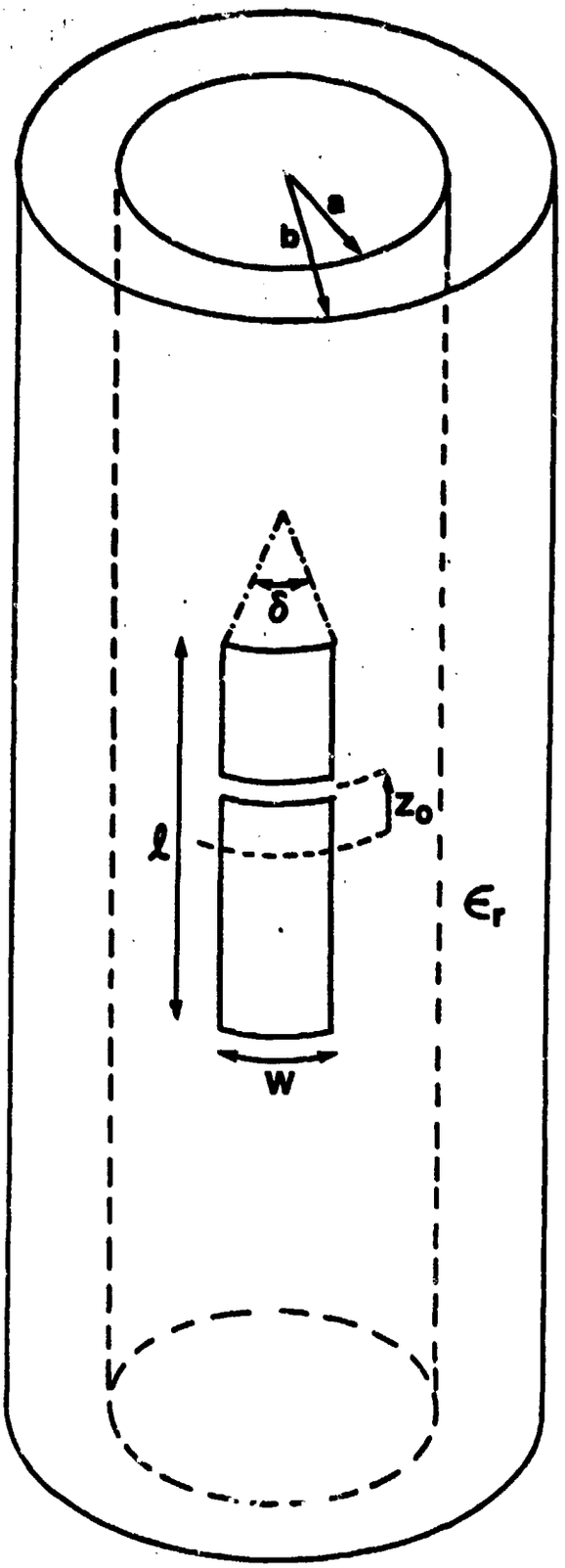

Fig. 1

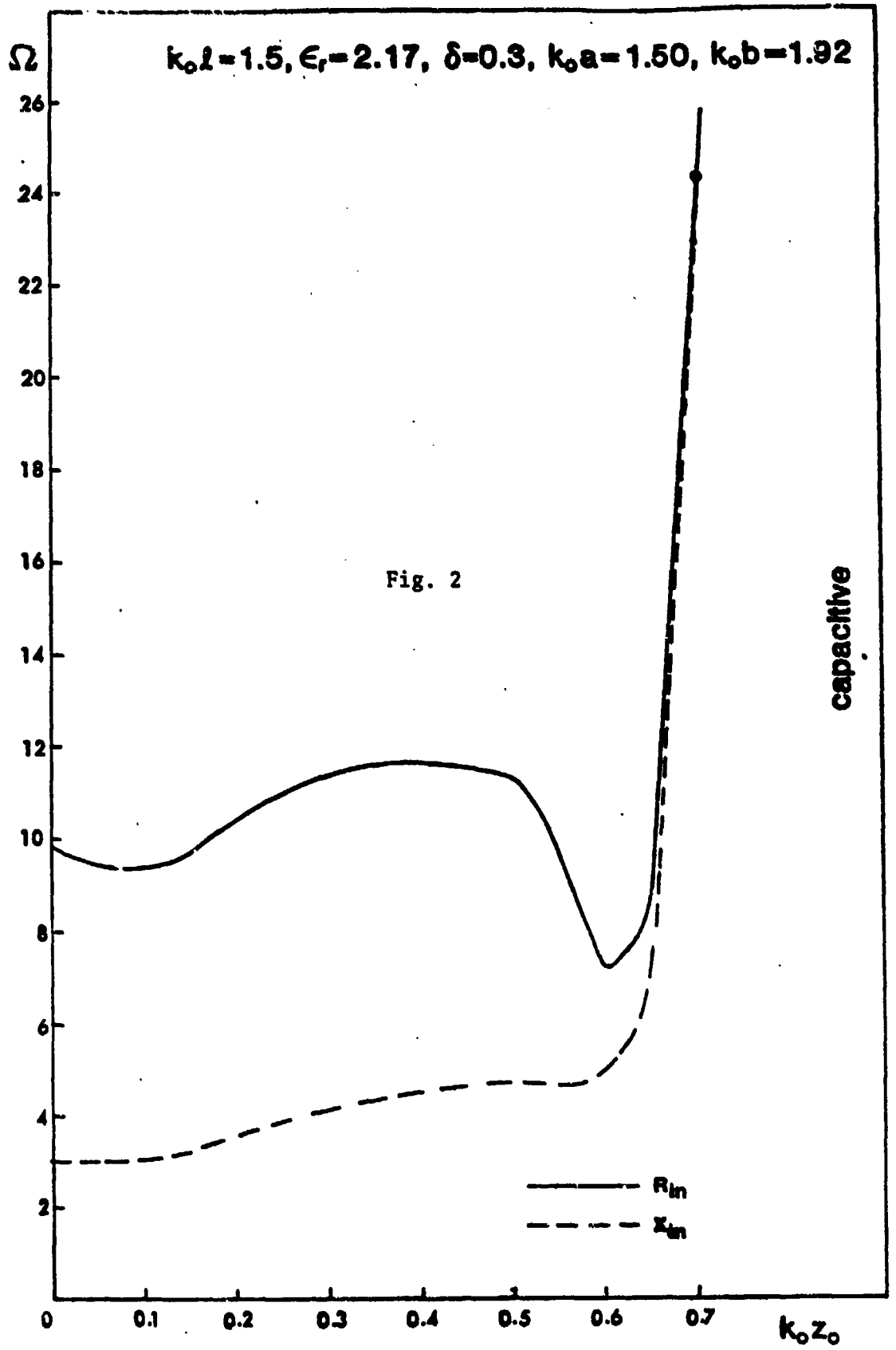
Ω
$k_o l = 1.5, \epsilon_r = 2.17, \delta = 0.3, k_o a = 1.50, k_o b = 1.92$
26
24
22
20
18
16
14
12
10
8
6
4
2
0
0.1
0.2
0.3
0.4
0.5
0.6
0.7
$k_o z_o$
capacitive
R_{in}
X_{in}

Fig. 2

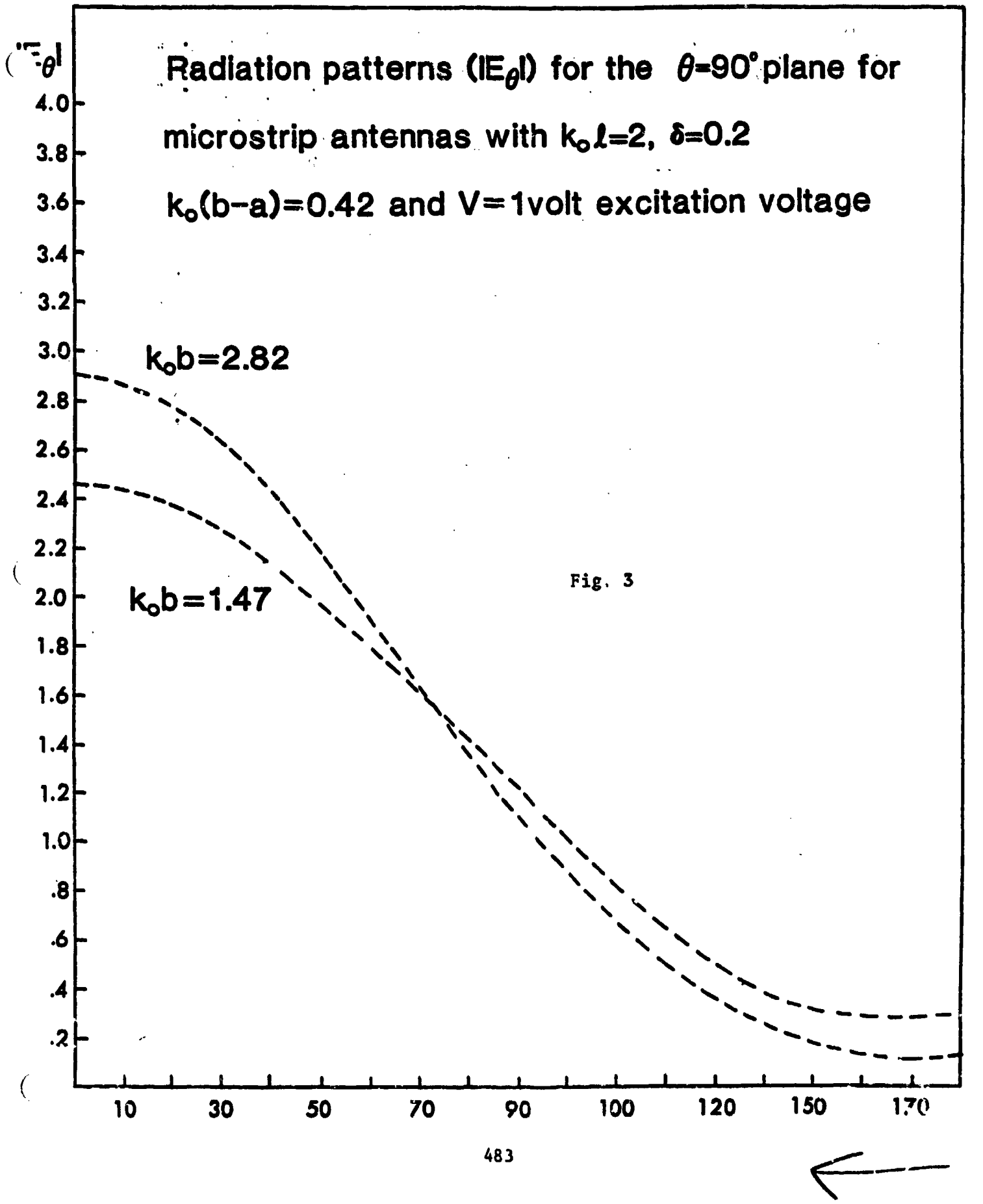
Radiation patterns ($|E_\theta|$) for the θ=90° plane for microstrip antennas with $k_o\ell$=2, δ=0.2 $k_o(b-a)$=0.42 and V=1volt excitation voltage
$|E_\theta|$
4.0
3.8
3.6
3.4
3.2
3.0
2.8
2.6
2.4
2.2
2.0
1.8
1.6
1.4
1.2
1.0
.8
.6
.4
.2
k_ob=2.82
k_ob=1.47
10
30
50
70
90
100
120
150
170

Fig. 3

AD P001117

POWER TESTING OF DUROID STRIPLINE ANTENNAS AND ASSOCIATED CIRCUITS

George J. Monser

Raytheon Company Electromagnetic Systems Division
6380 Hollister Ave.
Goleta, California 93117

Presented at

Antenna Applications Symposium

University of Illinois

September 1982

[illegible] MAY BE BLANK-NOT FILMED

POWER TESTING OF DUROID STRIPLINE ANTENNAS AND ASSOCIATED CIRCUITS

By: George J. Monser

ABSTRACT

Power testing at microwave frequencies requires elaborate test facilities with significant cost factors. Thus, each test must be designed for maximum utility and output.

This paper presents the results and analysis of tests designed to reveal the safe and upper limits of stripline antenna circuits under CW power up to 100 watts at 12 GHz, for altitudes from 1,000 to 70,000 feet with chamber ambient temperatures from 20° to 125° C.

Limitations in obtaining better than about ± 1 dB accuracy in the power measurement values during test for use in the simplified thermal model are described. Finally, a delineation of the safe power handling for various group conditions is given.

1.1 INTRODUCTION

This paper presents the results of power tests designed to reveal the safe and upper limits of stripline antenna circuits in Duroid 5880 substrates under CW power at 12 GHz. In order to conduct these tests it was first necessary to design and build several different holding fixtures. Namely, fixtures were built to evaluate line section failures, antenna failures, and maximum stress failures.

Figure 1 shows a photograph of the aluminum test fixtures used in the line failure tests. The aluminum surface opposite the side with the screw-heads was made smooth so that it could be heat-sunk for better heat transfer and thermal stability during test.

Figure 2 shows a photograph of the two antenna test fixtures. The aluminum test fixture allowed determination of the safe power handling under heat-sink conditions by clamping the smooth aluminum surface (opposite side from screw-heads) to an aluminum plate for thermal stability during test. The other test fixture shown was built in NEMA, G-10, dielectric offering a poor thermal transfer and maximum stress conditions.

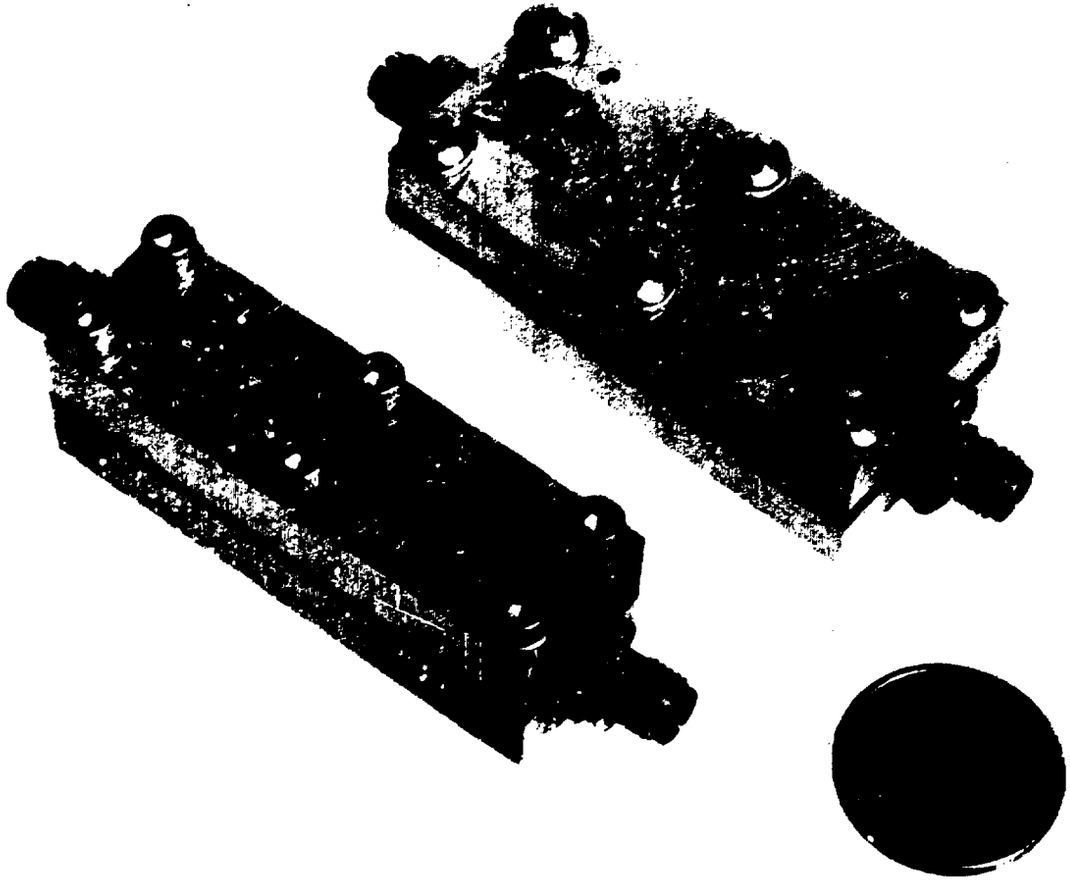

Figure 1. Stripline Test Fixtures

16109

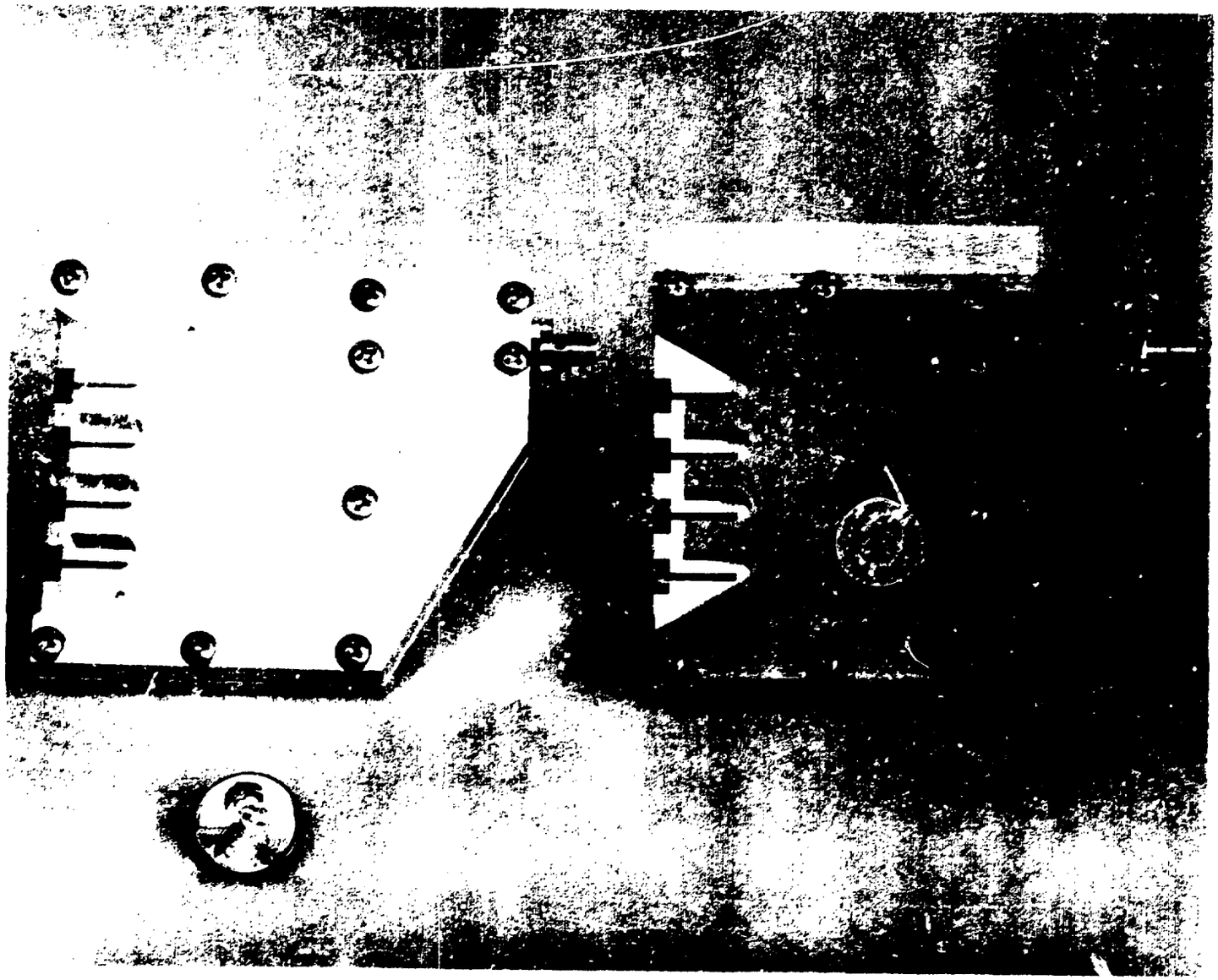

Figure 2. Antenna Test Fixtures

All tests were conducted with the samples in a chamber where various temperature and altitude conditions could be simulated. Forward and return power from the sample were monitored. Also, through-line power and radiated signal for the antenna samples were monitored. Thermo-couples were placed at various locations on the test sample, along the RF chain, on the aluminum within the chamber and another heat sink was suspended within the chamber.

2.1 CONDUCT OF TEST

Figure 3 shows the basic instrumentation for conducting the tests.

The following sequence is typical:

1. First the test sample connectors were inspected and cleaned (if necessary).

2. Next, the sample was lightly coated with thermal grease and clamped to the aluminum heat-sink block inside the chamber. Here, a dielectric block was positioned between the upper clamp and the sample so that mainly one thermal transfer path was provided.

3. RF connections were then made for the power measurements.

4. Various thermo-couples were placed in position.

5. Temperature/altitude equilibrium was established within the chamber.

6. RF input power was applied and increased, in steps, for various time intervals.

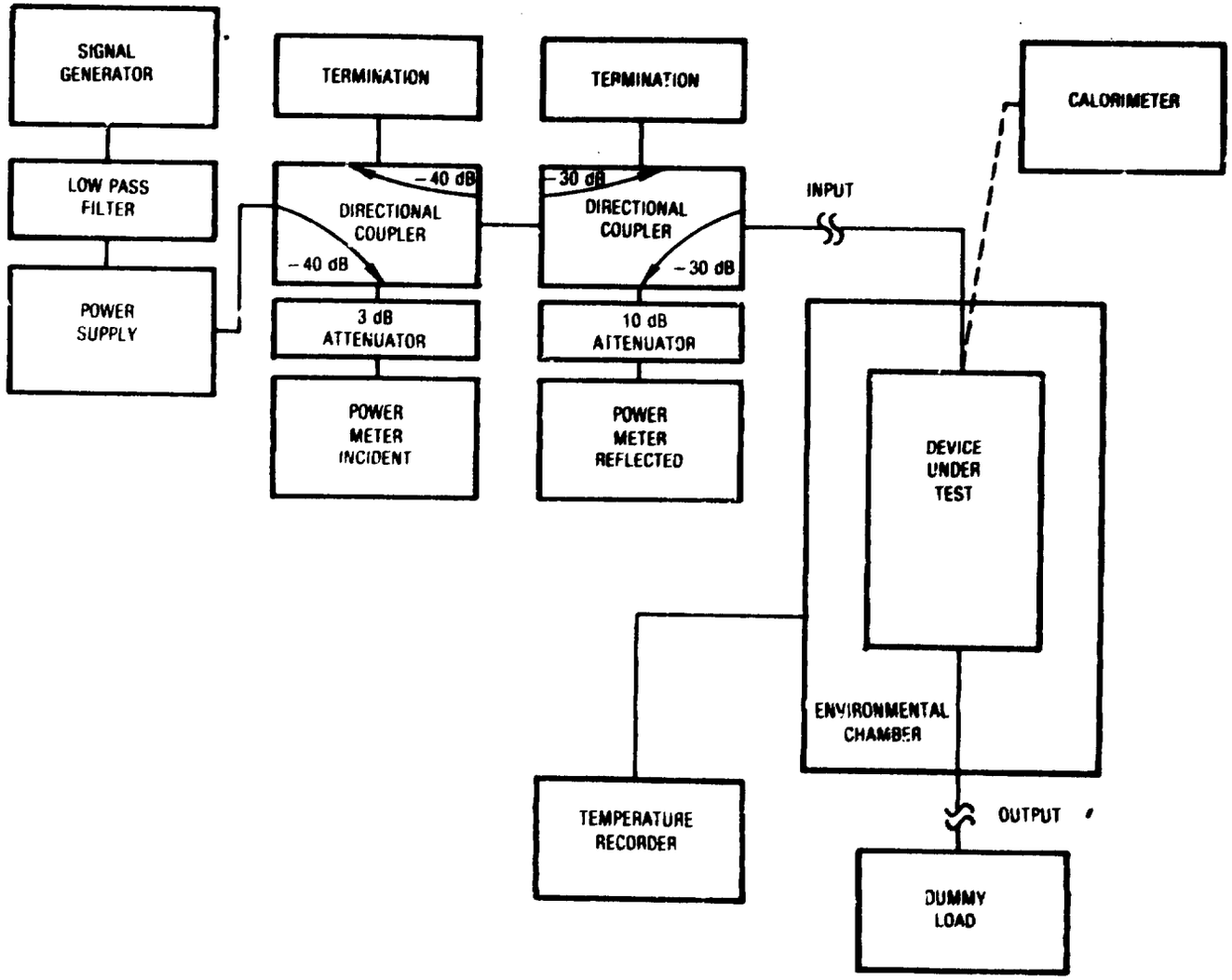

Figure 3. Test Equipment Block Diagram

7. Monitoring of all sensors, including time, were performed.

The above sequence was used and either taken to thermal equilibrium for the safe power determination or until failure for the stress-limit tests.

3.1 RESULTS

This section of the paper presents highlights of the results.

Figure 4 shows the observed temperature/time profile for the antenna in the aluminum fixture at 1,000 foot altitude, ambient 85° C, as the applied 12 GHz, CW, RF power is increased from 60 to 100 watts. (No failures.)

Figure 5 shows a repeat of the prior test at 50,000 feet. (No failures).

Figure 6 shows a repeat of the first test at 70,000 feet. (No failures.)

Figure 7 shows a repeat of the last test at 70,000 feet and ambient of 110° C. (Failure noted.)

New circuit boards and input connectors were used to replace the failed parts. Tests similar to the sequence depicted in Figures 4 to 7 were rerun. Again, failure occurred in the last test.

Figure 8 shows the disintegration of a connector experienced in a maximum stress test sequence of the antenna sample in the G-10 holding fixture (no heat sink).

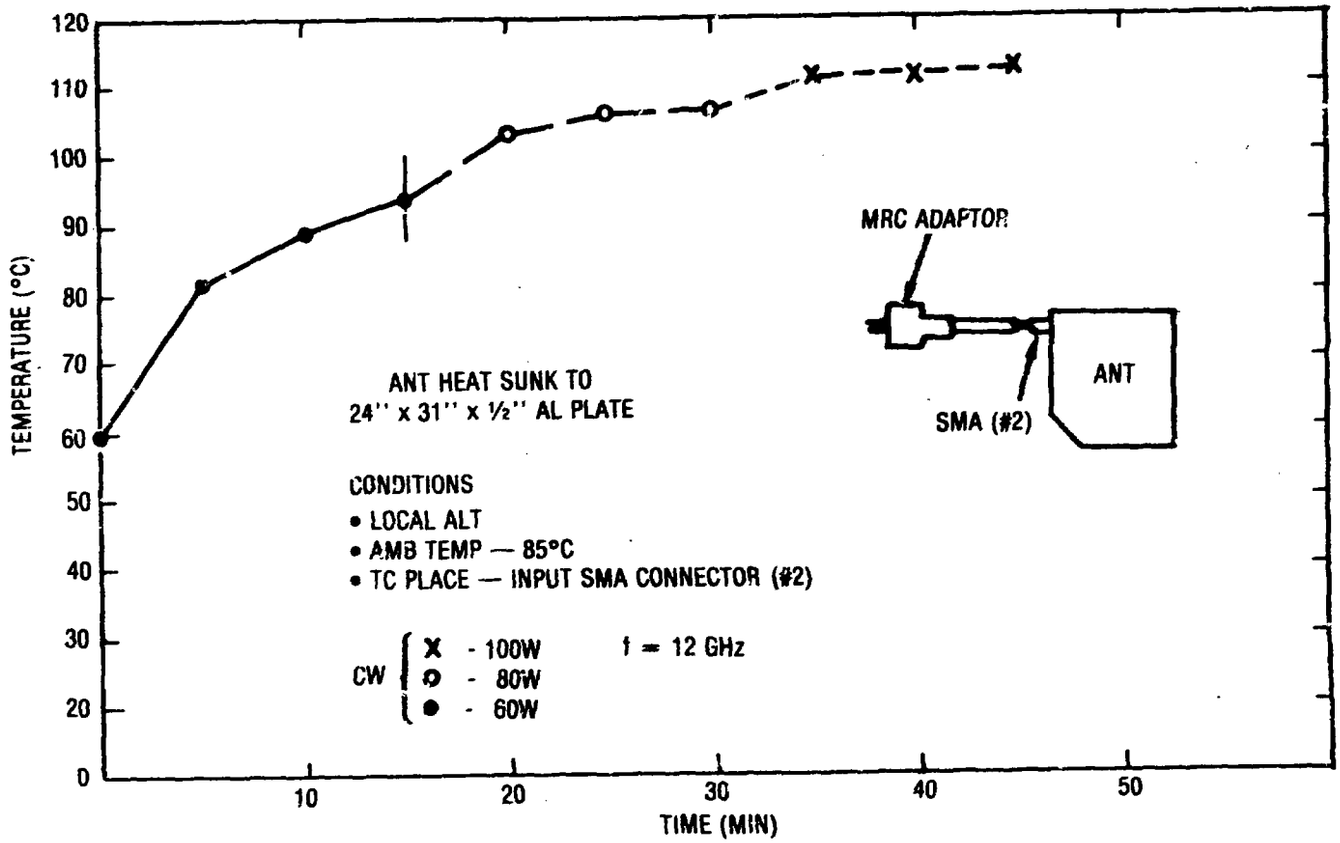

Figure 4. Temperature/Time (Profile 1)

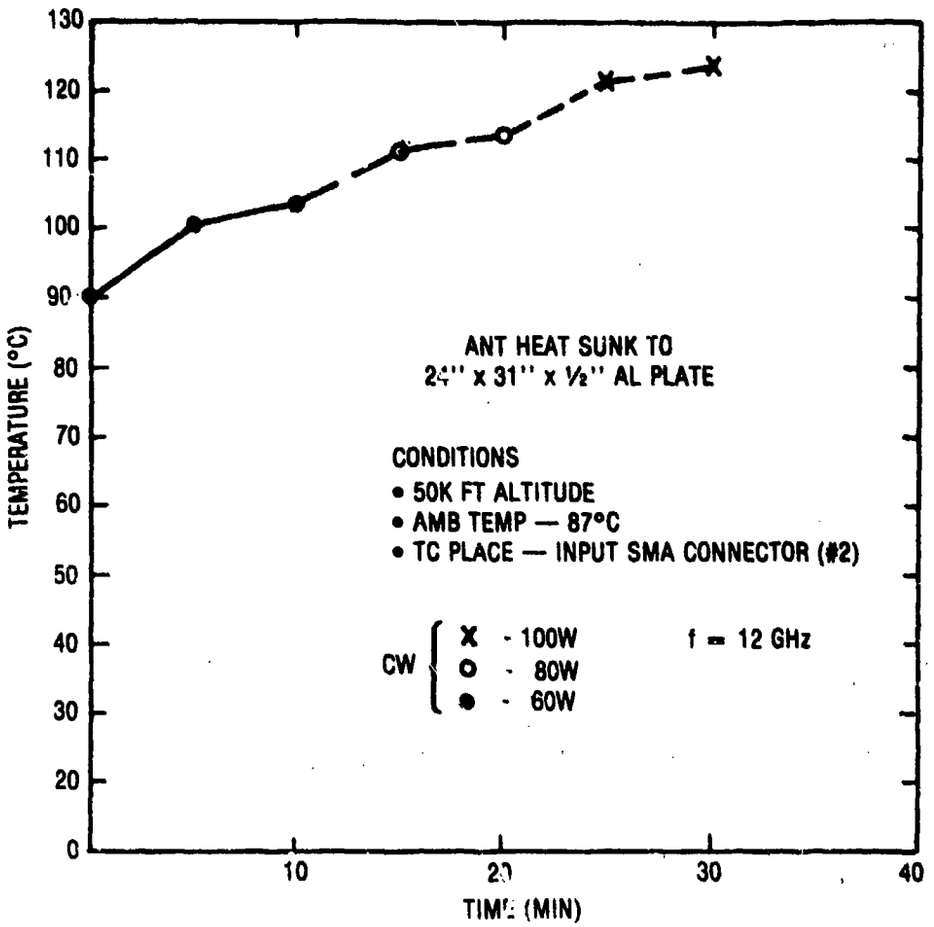

Figure 5. Temperature/Time (Profile 2)

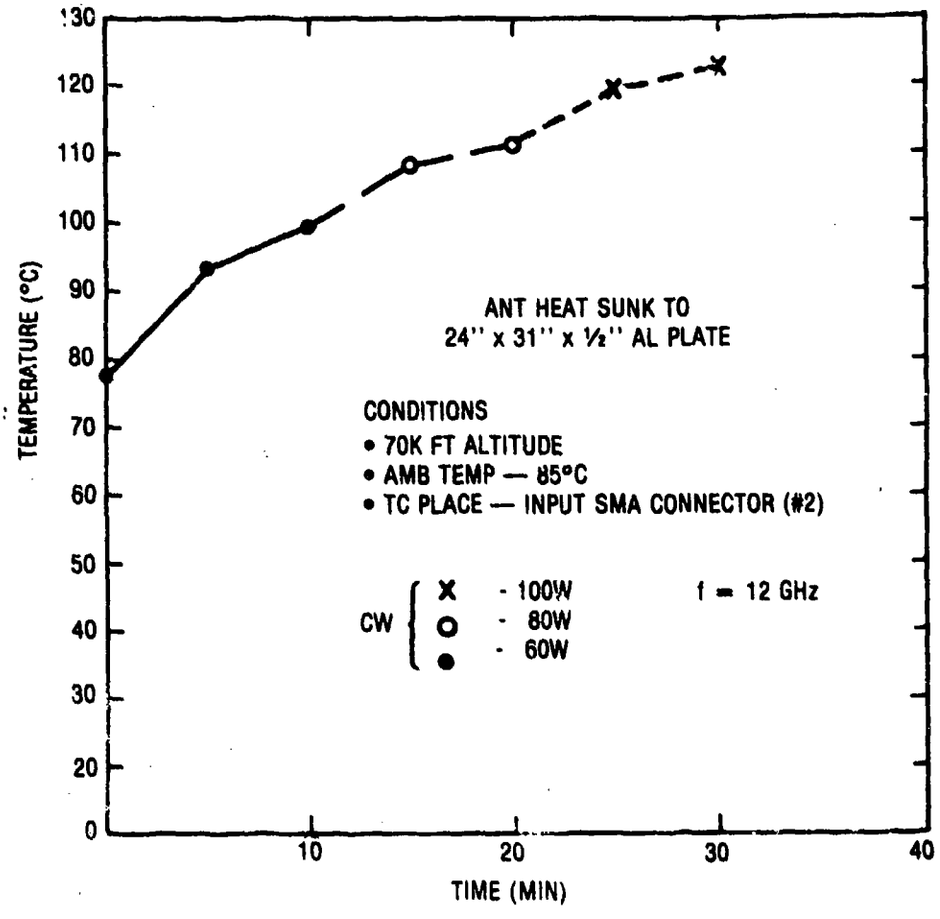

Figure 6. Temperature/Time (Profile 3)

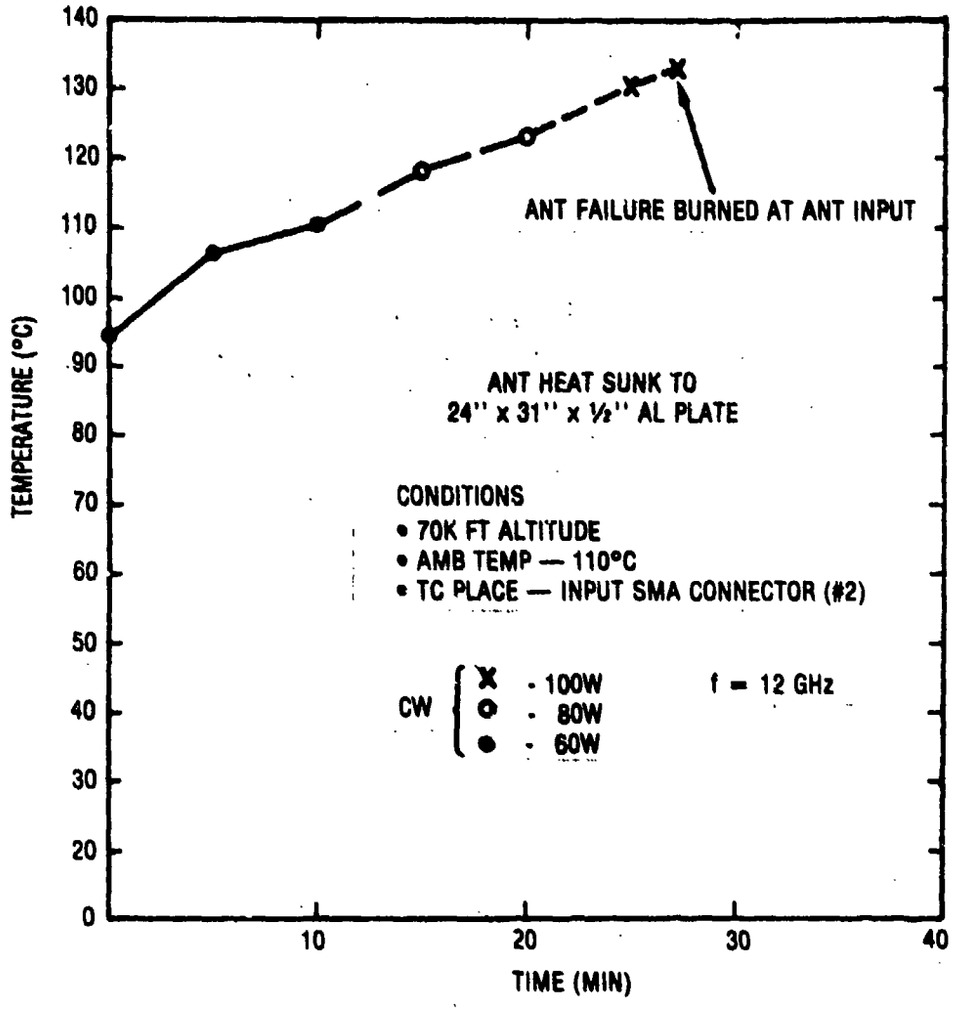

Figure 7. Temperature/Time (Profile 4)

Figure 8. 3mm Connector Failure

Figure 9 shows a failed set of circuit boards (1/32 inch thick, 50 ohm lines) and associated 3mm connectors. Also shown are two circuit boards (exterior view) and connectors which sustained damage during test in the aluminum antenna fixture. Arc-over at the connector to stripline interface was noted. Also, two small burn-through holes were evident. These holes were a result of arc-over at altitude from the stripline to a screw in the holding fixture. (Upon removal no further problem was encountered.)

Figure 10 shows one stripline set of boards opened for inspection after test. Damage at the corner was evident but no breakdown had occurred at the mitered corner (holding-fixture screw not in place.)

For the above tests to have full meaning, it is necessary to determine power flow in the antenna circuit under test. Here, power available for test was first established by measurement into a matched load with Calorimeter. Next, the antenna test sample was connected to the power cable using a precision TNC to 3mm adapter. Combined VSWRs of this adapter and the sample resulted in a reflected power of 55 watts. Analysis indicated that about 33 watts flowed in the input line of the antenna stripline during test. This further decrease in power was attributable to heat build-up in the cables and adapters ahead of the antenna terminal.

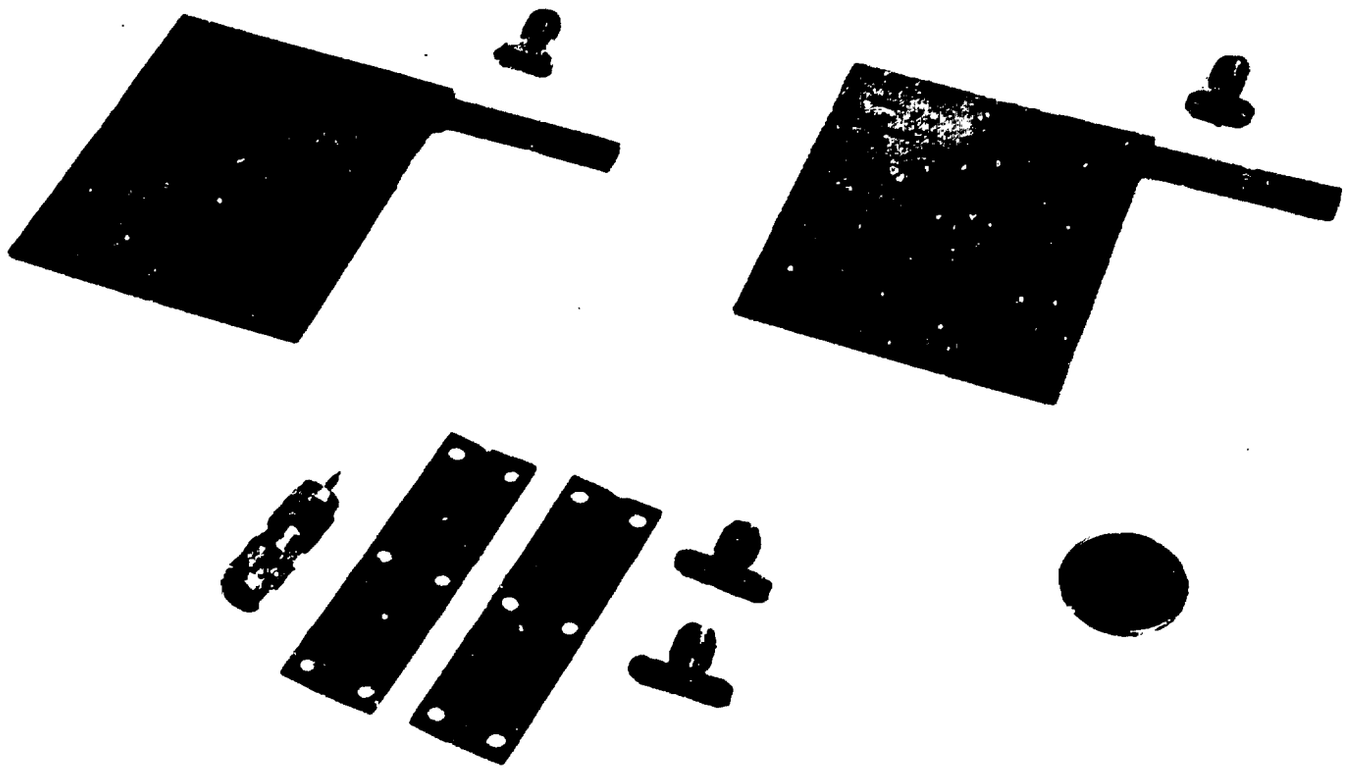

Figure 9. Failed Set of Circuit Boards and Connectors

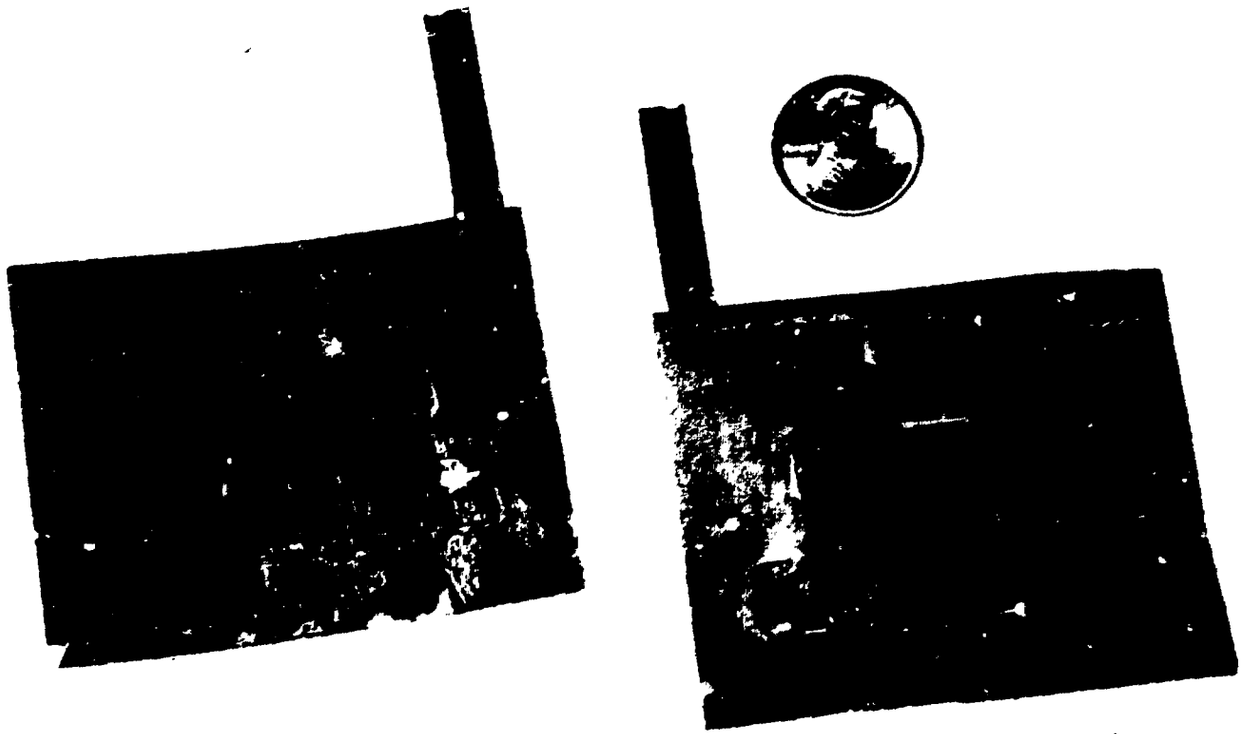

Figure 10. Circuits Opened for Inspection

4.1 ANALYSIS

Center conductor temperatures were estimated by calculations for three cases of stripline failure using temperature measured at the input 3mm connector, estimated power dissipations, and steady state analysis for simplicity.

Results indicated that two of the observed failures were probably temperature-related in that the predicted center-conductor temperatures exceeded, by 50 percent, the rated maximum of 200° C. In one failure test, at 70,000 feet, it was observed to occur with the calculated center conductor of 160° C. By inspection after test, it was confirmed that this failure was voltage-related.

5.1 CONCLUDING REMARKS

The paper has presented a "bench-mark" on the safe power handling of 50 ohm circuits in Duroid 5880.

By careful attention in assembly to avoid air-gaps, contaminants, etc. and with heat sink provisions to limit temperature rise to 85° to 100° C, 50 ohm stripline circuits in Duroid 5880 should safely handle 50 watts of CW power up to 12 GHz and altitudes up to 70,000 feet.

In general, rigorous adherence to assembly details are required. Input VSWRs under 2/1 are recommended. Both guidelines should minimize voltage-related failures at higher altitudes.

AD P001118

SHF SATCOM MICROSTRIP PHASED ARRAY ANTENNA

Brian C. Considine
Raytheon Company
Equipment Division
Wayland, MA 01778

and

David L. Wandrei
Raytheon Company
Research Division
Lexington, MA 02173

ABSTRACT

Modern airborne and ground satellite communication systems often require high gain antennas which are low profile and are capable of conforming to a variety of surfaces. A phased array utilizing distributed solid state components is capable of satisfying the wide angular scan coverage and low noise requirements. An array for receive only operation is described which utilizes monolithic microwave technology in a novel solution to the low profile constraint.

The array operates at SHF frequencies, has 128 radiating elements and associated monolithic modules, and is approximately 8 by 13 inches. Radiating elements are microstrip patches fed by a unique capacitively coupled feed network resulting in an 8% bandwidth. The power combiner network is a microstrip layer that includes active receive modules. The entire array consists of a multilayer-board less than 0.2 inches thick including row/column steering commands and bias signals for the active modules as well as all of the microstrip circuitry. The array steering is controlled by an associated Beam Steering Unit.

Prepared for presentation at the 1982 Symposium on Antenna Applications, Sept. 22 - 24, 1982, Monticello, Illinois

The receive module is a solid state hybrid package that includes monolithic microwave integrated circuits (MMIC) grown on gallium arsenide (GaAs) in addition to conventional circuit components. The circuitry is entirely in microstrip and consists of a diode limiter, single stage low noise amplifier (LNA), and three-bit phase shifter.

To date, the array has been fabricated and tested as a broadside, non-steerable array with results as predicted. Module fabrication is substantially complete and will be followed by testing of the fully filled steerable array.

INTRODUCTION

This paper describes an electronically steerable, left hand circularly polarized (LHCP), active, microstrip radiating aperture that operates over the 7250 MHz to 7750 MHz frequency band. It utilizes flush mounted construction techniques in which the various elements of the array are microwave printed circuits. The patch radiators are printed on teflon fiberglass and the circular feed/hybrid layer and the combiner layer are printed on duroid. In addition, row and column steering commands and bias signals are included in the bonded structure. The grid configuration and element spacing impact the microstrip combining network and vice-versa, hence, the design of the various layers of the antenna is interdependent.

The major features incorporated into this microstrip radiating aperture include the following:

a.) increased radiator bandwidth;

b.) minimization of radiation loss from the microstrip combiner circuit;

c.) active matching of the radiator for the array environment over a 60° scan cone;

d.) development of fabrication procedures for low-cost flush mounted array applications including modularization approaches to large array fabrication;

e.) development of active receive modules employing monolithic microwave integrated circuits (MMIC); and

f.) fabrication of an active array by incorporating the MMIC modules into the combiner layer.

Figure 1 is a block diagram of the ADM array system. Antenna steering commands are input via the TRS-80 keyboard. The Beam Steering Unit then generates the phase shifter commands that steer the array to the desired azimuth and elevation angles.

The system has two operating modes; a dual beam configuration and a single (combined) beam configuration. To change from single to dual beam operation it is necessary to remove the final 2:1 combiner that is physically mounted on the array. The array performance is summarized in Table 1.

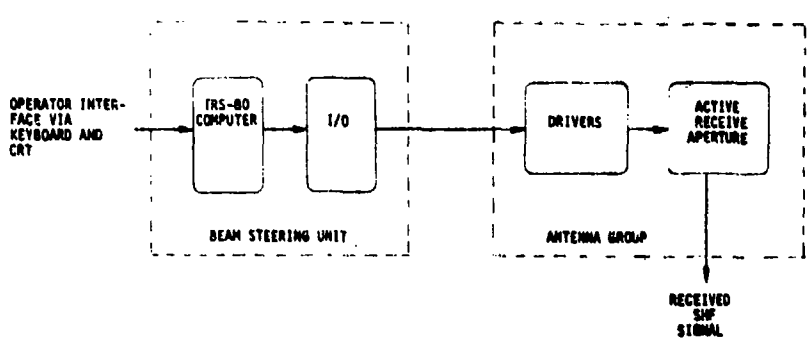

FIGURE 1. Functional Block Diagram

TABLE 1. Array Performance

Center Frequency:	7500 MHz
Bandwidth (1 dB Points):	500 MHz
Scan Method:	Electronic Phase Shifters
Scan Region:	60° scan volume
Nominal Impedance:	50 ohms resistive
Element VSWR:	Nominal 2.0:1 over scan region and frequency range
Polarization:	Left hand circular
Axial Ratio:	1.0 dB at $\phi = \theta = 0°$ with gradual degradation to 5 dB at 60° scan
RF Output:	Two RF connectors (dual beam capability)
Phase Shifter Precision:	3-bit
Efficiency:	Better than 60% compared to an ideal projected aperture of equivalent area
Sidelobe Level:	-12 dB at boresite (single beam only)
Gain:	Greater than or equal to 20 dB (single beam only)

ARRAY DESCRIPTION

A cross-sectional view of the array is shown in Figure 2. The array consists of a bonded multi-layer sandwich of five microwave and d.c. printed circuit boards. The entire assembly is bonded without the receive modules which are assembled after the layered structure is complete. Figure 3 shows the complete array.

The radiating element is comprised of two microstrip layers, a patch radiator layer and a circularly polarized (CP) feed layer. One RF feed-thru per element connects the feed point to the corporate

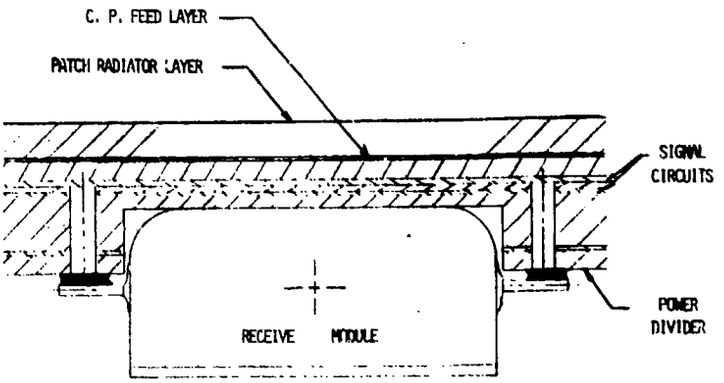

FIGURE 2. Array Cross Section

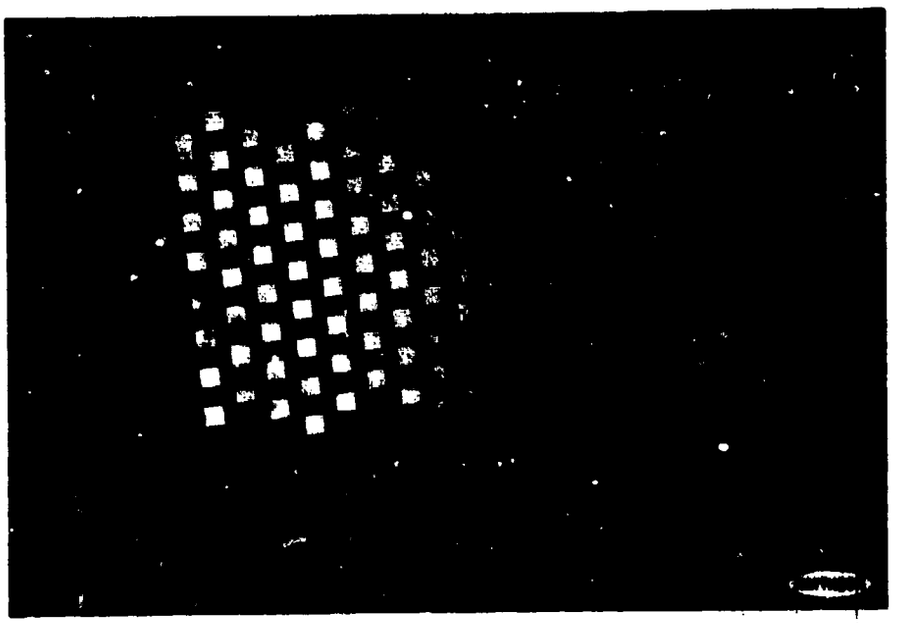

FIGURE 3. 128 Element Receive Array

combiner. Plated thru-holes are used for the RF and d.c. interconnections. In all there are over 1100 plated thru-holes in the assembly, each passing through one or two ground planes.

Receive modules are set into the 1/16" thick spacer provided below the combiner layer to accommodate the module package. Ultimately modules will be fabricated co-planar with the combiner eliminating the spacer and decreasing the array thickness.

To make the design appropriate for general use the element spacing was calculated such that the array can scan up to 60° from broadside. A triangular grid was used to minimize the number of elements for an array whose scan volume is a cone. The row spacing "d" to keep the grating lobe at the edge of real space is given by:

$$d = \lambda/(1 + \sin \theta_s) \qquad (1)$$

The element spacing calculated from the row spacing, and adjusted slightly to keep the grating lobe entirely out of real space is 0.91 inch.

ANTENNA ELEMENT

The antenna element chosen for this application is the printed circuit or patch antenna. The element differs from the usual element in that there is a layer of dielectric covering the ground plane and part of the feed (the quadrature hybrid) is printed on the radiating side of the ground plane to maximize the space available for phase shifters on other layers of the antenna. The antenna element has an operational bandwidth of 500 MHz centered at 7.5 GHz. However, be-

cause of tolerances on the dielectric constant of commercial dielectrics, the design bandwidth is about 600 MHz.

The bandwidth of a microstrip element is directly proportional to the substrate thickness. However, increasing the substrate thickness is undesirable as it enhances the coupling to the surface wave mode[1,2] and increases the radiation of the feed structure adjacent to the patch. The mutual coupling to nearby antenna elements is directly proportional to the energy in the surface wave which may cause the element pattern notch, usually associated with the grating lobe, to occur at angles for which the grating lobe is far from real space. Uncontrolled feed structure radiation will degrade performance at some angles. For these reasons, it is desirable to minimize substrate thickness.

By adding a series tuned resonant circuit to the patch it is possible to increase the bandwidth, while at the same time significantly reducing feed radiation. The feed configuration shown in Figure 4 was determined empirically. A rigorous mathematical treatment of the element was not attempted but the empirical results were modeled.

Circular polarization is obtained by feeding the two linear ports of the antenna element with a quadrature hybrid packaged with the tuned circuit on the feed layer.

ELEMENT MEASUREMENTS

Element impedance was measured for the isolated element, and in a waveguide simulator. Also, the active reflection coefficient was

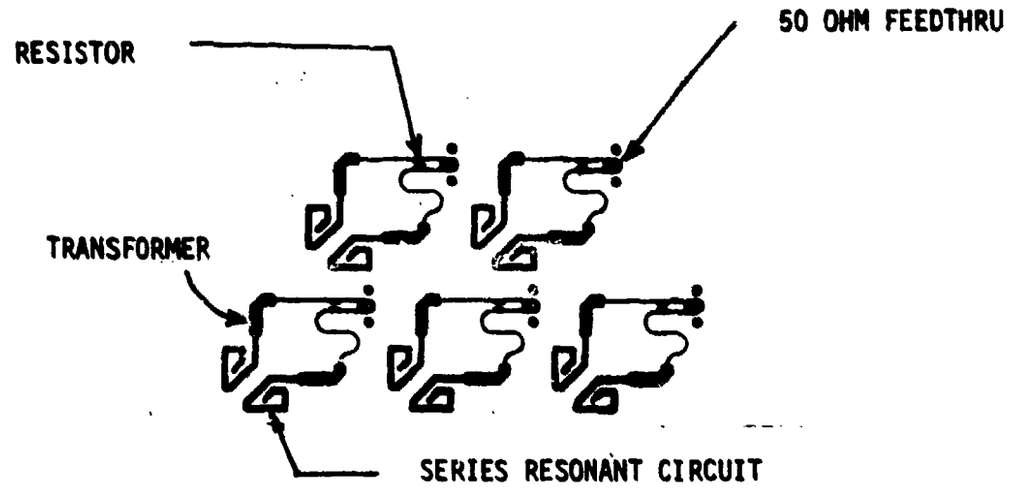

FIGURE 4. Quadrature Feeds for Five Elements

calculated from mutual coupling measurements in a 30 element array. In all cases, the impedance measurements were made at the input to the antenna feed without the quadrature feed that is normally located at that point. The element test circuit is shown in Figure 5, as is the impedance plot of the isolated element measured at the feed and referenced to point A. Although the plot is not optimally centered, it is seen that with centering the maximum VSWR is about 1.6:1 over a 600 MHz band. Patterns measured on the isolated element in a large ground plane are shown in Figure 6. It is seen that the patterns are reasonable with the "E" plane pattern broader than the "H" plane pattern. These patterns are not significantly different than the isolated patterns of a waveguide type radiator so that similar performance in an array environment is probable.

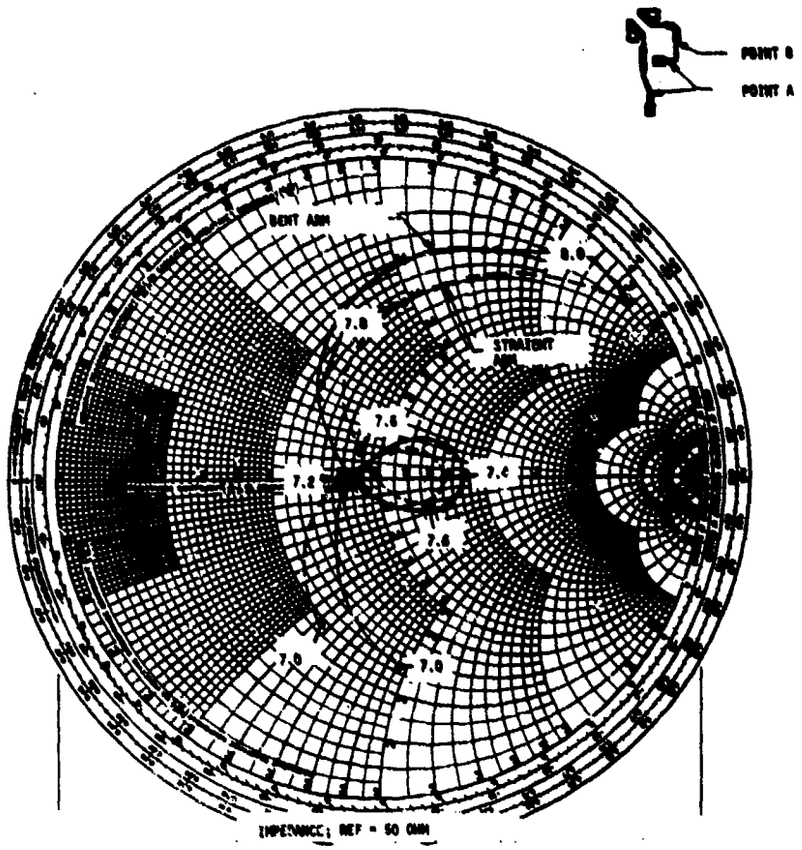

FIGURE 5. Measured Data on Isolated Element at Point "A" of Feed

Impedance data was also taken in a waveguide simulator. Data for the element in free space and in the simulator for two different scan angles are shown in Figure 7. The tested element is not the final design element. However, the results are of interest because it appears that the good isolated element match leads to acceptable results when the element is tested in a simulator indicating that the element match in an actual array will also be acceptable.

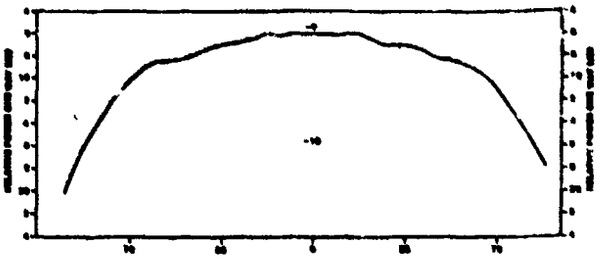

A.) ISOLATED E-PLANE ELEMENT

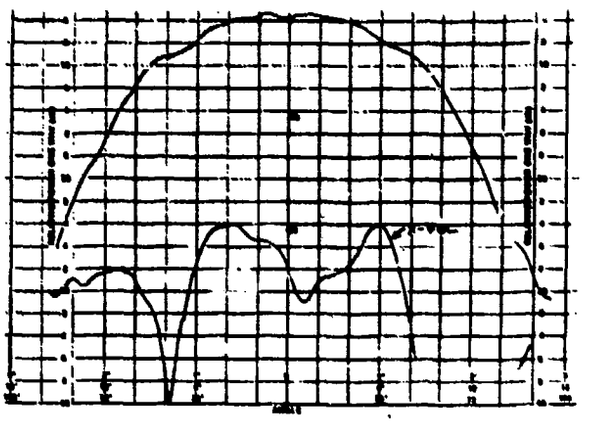

B.) ISOLATED H-PLANE ELEMENT

FIGURE 6. Patterns of 7.5 GHz Patch Radiator

MEASUREMENTS IN A SMALL ARRAY

The measurements on the isolated patch and the patch in the simulator showed no unexpected results. However, sometimes, in the array environment, unusual effects occur. It was felt that some form of verification in a small array was necessary. A 30 element array, shown in Figure 8, was built. This array was used to make pattern and mutual coupling measurements. The array was constructed in

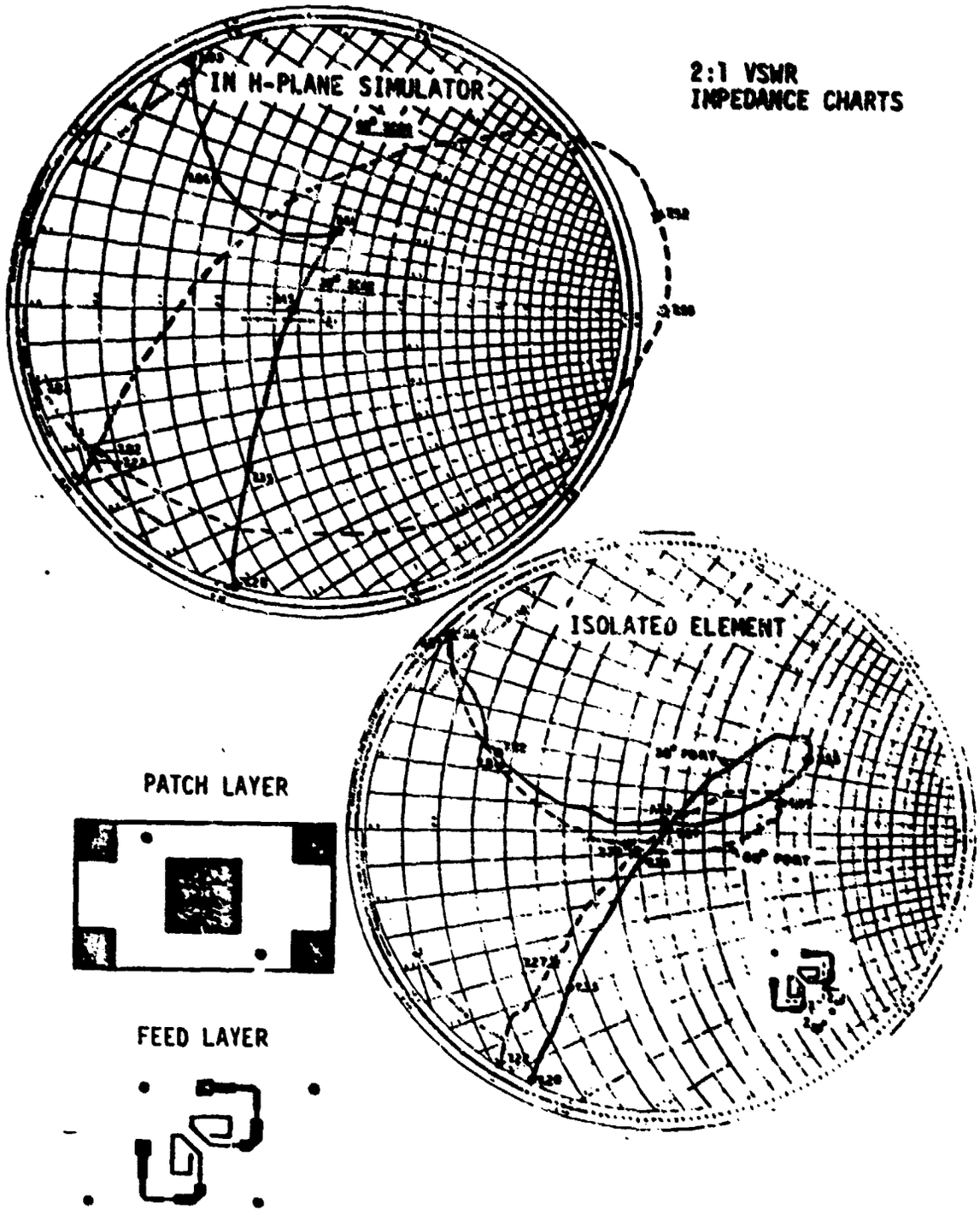

FIGURE 7. Comparison of Impedance Plots for Element in Simulator and in Free Space for 30° and 60° Scan Angles

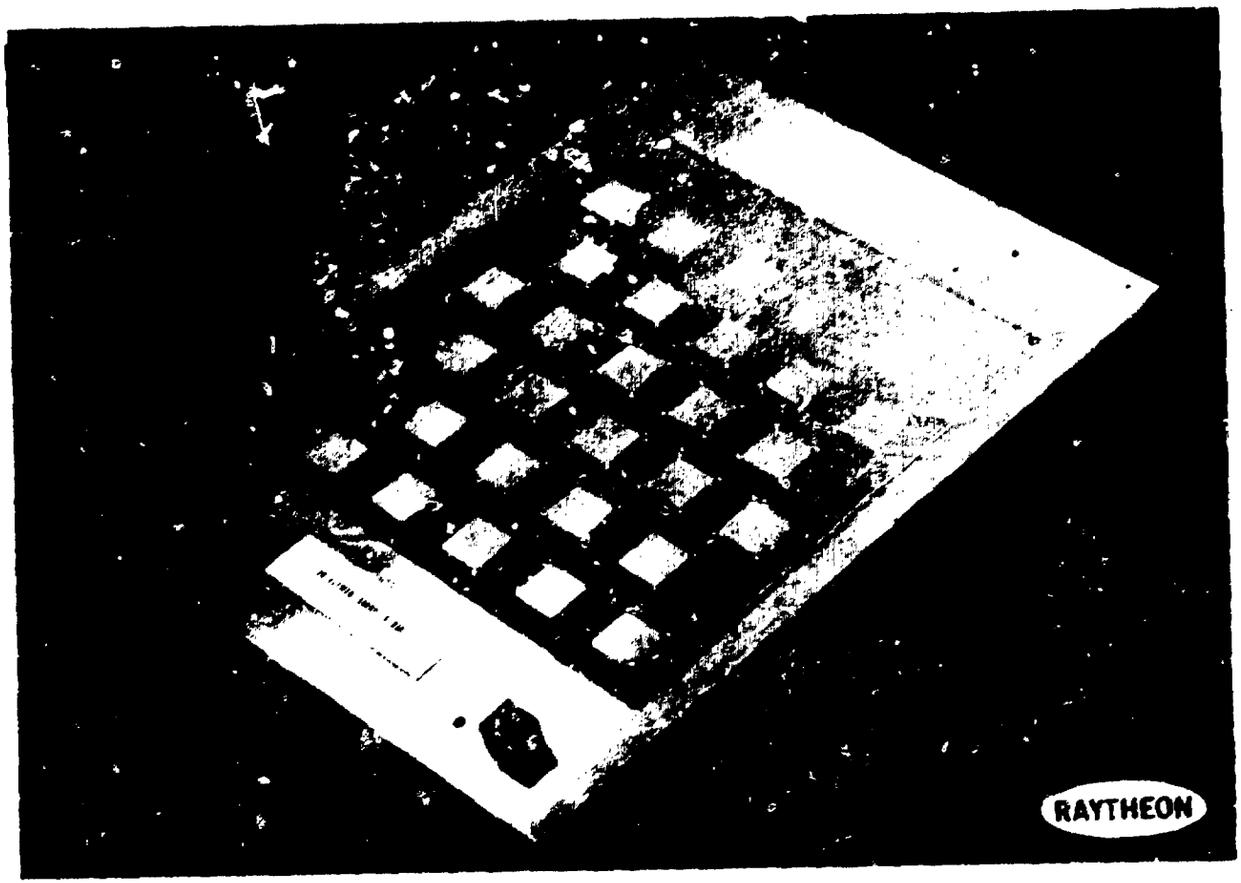

FIGURE 8. 30 Element S-band Array

'S'-band because of the availability of an element design and the non-critical nature of the assembly procedure.

PATTERN MEASUREMENTS

Patterns of a near central element were measured at 2.4, 2.5, and 2.6 GHz. The 2.5 GHz data is shown in Figure 9. The transmitting antenna radiated vertical polarization and a pattern was measured using the appropriate port on the patch. Then, the transmit antenna polarization was rotated 90° and the pattern measured using the other port on the patch. The ripples on the pattern appear to be due to the finite size of the ground plane. The gain difference is believed to be due to the ripples in the other plane. Measurements were also made for other rotations of the receive array and for other elements in the array. The following was noted:

a.) increasing the frequency narrowed the beam

b.) decreasing the frequency broadened the beam

c.) notches indicating array resonance effects were not observed

d.) the cross polarized pattern was about 16 dB down

e.) the details of the pattern, such as the exact beamwidth and ripples, should be ignored since these could be changed significantly by varying the conditions at the ground plane edges

In summary, pattern measurements in the array did not indicate that there would be problems in the use of this element.

MUTUAL COUPLING MEASUREMENTS

Mutual coupling measurements were also made on the 30 element array of Figure 8. It was found that perfect symmetry did not exist

(see Figure 9) for co-polarized coupling, hence, the active reflection coefficient is calculated using the formula:

$$\Gamma_{ACTIVE} = S_{11} + 2\sum_{N=1}^{NN} S_{1N} \cos(u \cdot x_N) + 2\sum_{\substack{M=3 \\ M \text{ odd}}}^{MM} S_{M1} \cos(v \cdot y_M) +$$

$$2\sum_{M=2}^{MM}\sum_{N=1}^{NN}\left\{ S_{MN} \cos\left[u\left(x_N + \frac{DX}{2}\right) + v \cdot y_N\right] + SP_{MN} \cos\left[u^*\left(x_N + \frac{DX}{2}\right) - v \cdot y_M\right]\right\} +$$
$$M \text{ even}$$

$$2\sum_{M=3}^{MM}\sum_{N=2}^{NN}\left\{S_{MN} \cos(u\, x_N + v\, y_M) + SP_{MN} \cos(u\, x_N - v\, y_M)\right\} \qquad (2)$$

Where SP_{MN} is the mutual coupling to the element which is located at the mirror image of the element where S_{MN} is measured.

The active driving point impedance in the "E" and "H" planes can, to a good approximation, be computed using only co-polarized coupling data. The results of this computation at an arbitrary reference plane is shown in Figure 10. Note that S_{11} has been set equal to zero. The reason for this is that previous data indicated that a good isolated element match is a reasonable choice for a good match in the array. By setting $S_{11} = 0$ and plotting the active impedance, the magnitude of the error in this assumption is easily seen. If a good match is desired at 45°, S_{11} should be about 0.2 at 2.5 GHz. Hence, the isolated element match is a good starting point in the matching procedure.

To estimate the magnitude of the coupling from the cross-polarized elements, the mutual coupling between all horizontally polarized inputs to one vertically polarized input was measured making no assumptions of symmetry (for co-polarized coupling there is symmetry between the

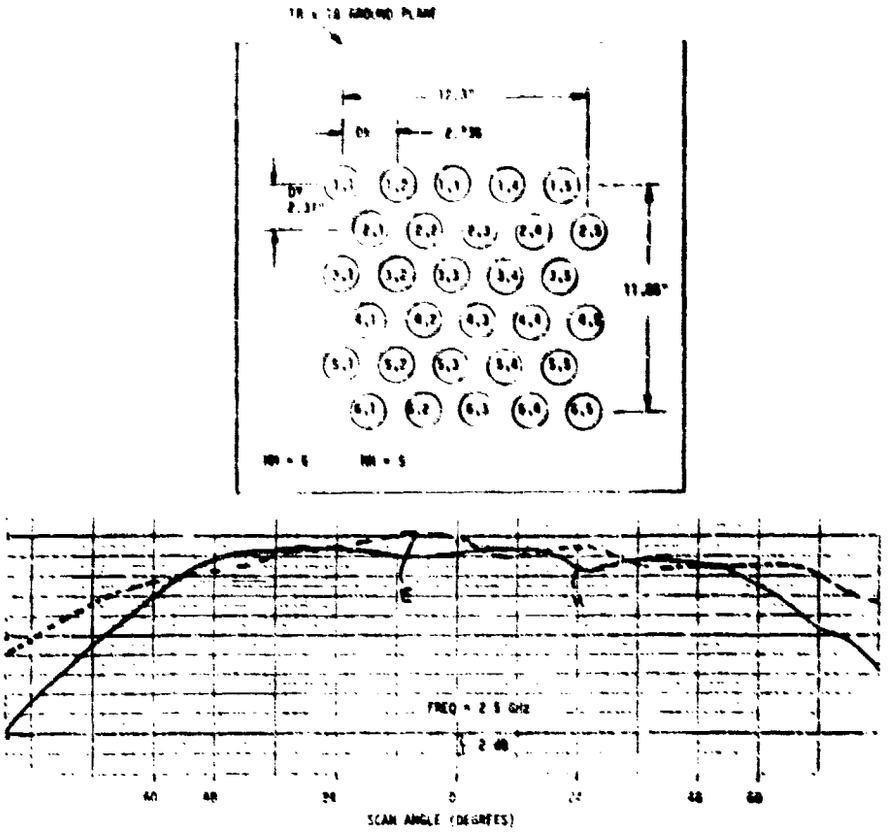

FIGURE 9 Pattern Measurement in Small Array

first and third quadrants and also between the second and fourth quadrants). The magnitude of the voltage coupled to the vertically polarized port as a function of scan angle in sine space was measured. In the principal planes, the maximum coupling is 0.11 volts and is less than 0.1 volts over most of the scan volume of interest.

Hence, a reasonable estimate of the driving point impedance can be obtained by measuring only co-polarized coupling.

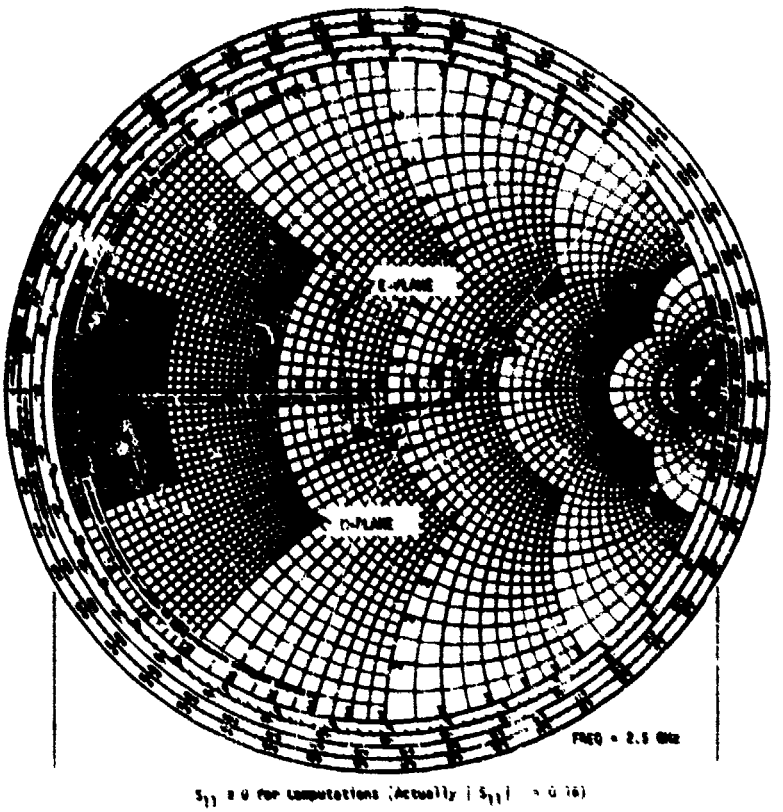

FIGURE 10. Active Principle Plane Impedance for Vertical Polarization

In estimating the performance of a phased array, it is desirable to know, among other things, the power reflected back into the terminals. Even though the cross-polarized component is not a major contributor, a complete set of measurements was taken at 2.5 GHz so that the total reflection from the straight arm (vertical polarization)

and the bent arm (horizontal polarization) could be determined assuming that the horizontally polarized arms were driven in phase quadrature with the vertically polarized arms. The results of these measurements and computations are very encouraging. For instance, at $\theta = 0°$, the reflected power is 11% of the incident power. However, data has been obtained at only one frequency for a relatively small array thus far.

RF POWER COMBINER NETWORK

The RF power distribution network combines all of the array module outputs into a single port. The combiner requirements are that equal path lengths to all elements be maintained and the circuit loss and area be minimized. Calculations of copper loss, dielectric loss,[3] and radiation losses[4] were made for various substrate materials and thicknesses. Choice of the transmission line was based on minimization of loss.

A reactive power combiner was designed because it requires less area than an isolated power combiner. It is also considerably cheaper and allows the system noise temperature to be slightly less than with an isolated combiner. However, in the event of a failure of one of the phase shifters such that it looked like an infinite mismatch, a reactive power combiner is affected much more than the isolated type. Future investigations should address resistive combiners also.

A 1:16 power combiner, that forms the basic building block in the array, is shown in Figure 11. The measured performance of the combiner is given in Table 2.

TABLE 2. 1:16 Combiner Performance

Amplitude error:	0.45 dB rms
Phase error:	3° rms
VSWR:	1.22:1 max.
Insertion loss:	0.45 dB ave.

The actual 1:64 array feed network with module locations is shown in Figure 12.

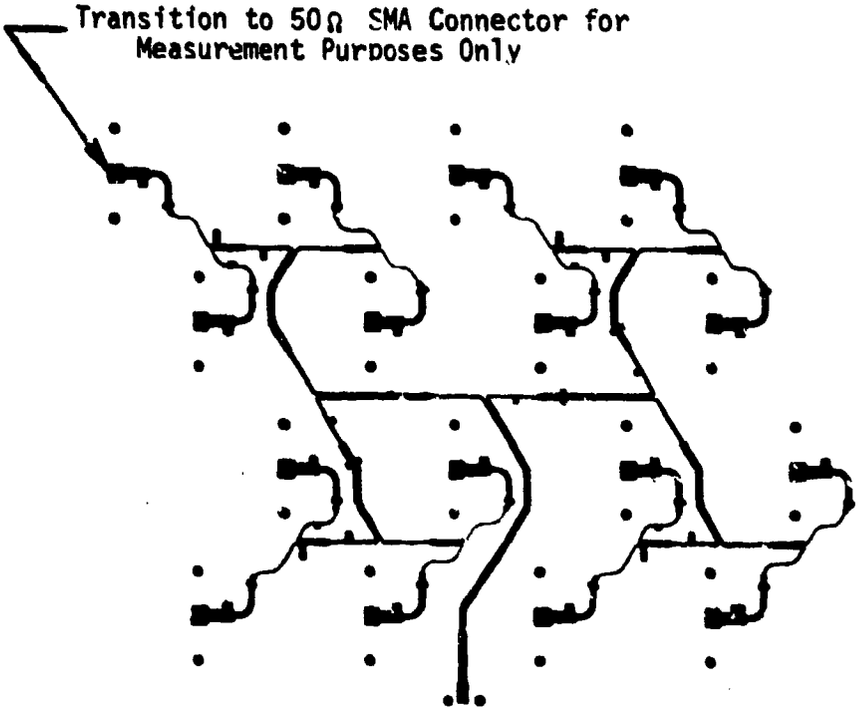

FIGURE 11. 1:16 Power Combiner

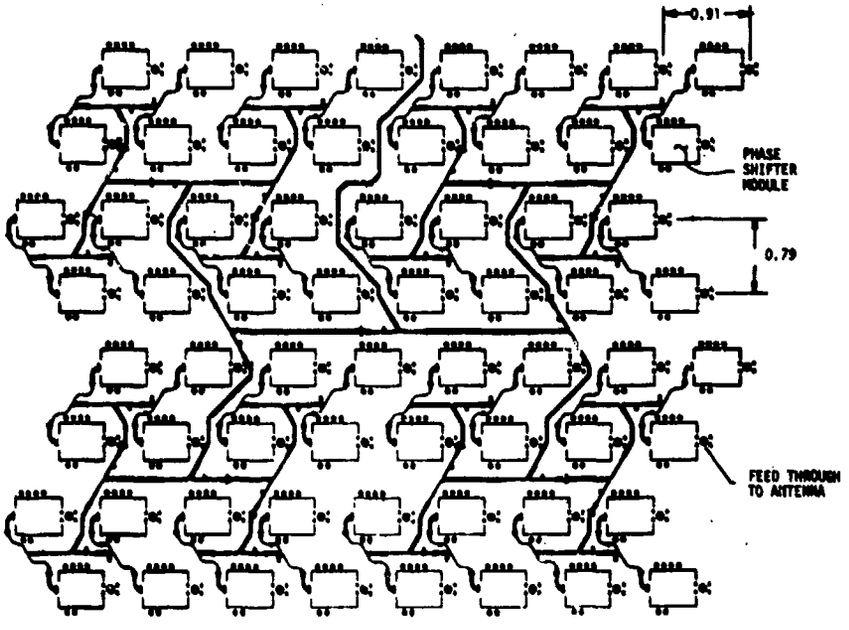

FIGURE 12. 64:1 Power Combiner With Module Space Indicated

RECEIVE MODULE

The receive module shown schematically in Figure 13, is a solid state hybrid package that includes monolithic microwave integrated circuits (MMIC) grown on gallium arsenide (GaAs) in addition to conventional circuit components. The circuitry is entirely in microstrip and consists of a diode limiter, single stage low noise amplifier (LNA), and a three-bit phase shifter. The package size of 0.400 inch by 0.500 inch by 0.170 inch thick was dictated by the combiner network layout and the array grid dimensions. Figure 14 is a photograph of the working module.

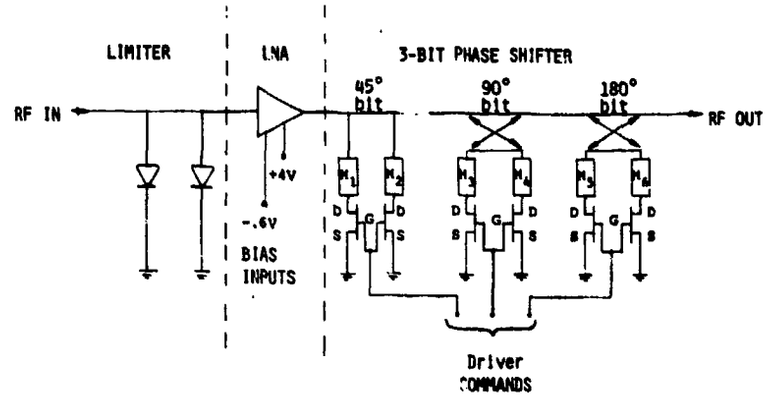

FIGURE 13. ADM Receive Module; Schematic

Module design goals are:

VSWR:	<2:1
Insertion Loss:	0 dB
Phase Precision:	3-bit
Phase Bit Accuracy:	± 10°

PHASE SHIFTER

The phase shifter for the SHF SATCOM receive module is a three bit monolithic design grown on 4 mil Gallium Arsenide. The circuit uses a loaded line design for the 45°bit and a hybrid coupled design for the 90°and 180°bits, with all R.F. lines in microstrip. Power FET's are used as switching devices in all three bits as shown schematically in Figure 13. Frequency range of operations is 7.25 to 7.75 GHz. The chip size of all bits is .080" x .185", giving the phase shifter a size of .240" x .185".

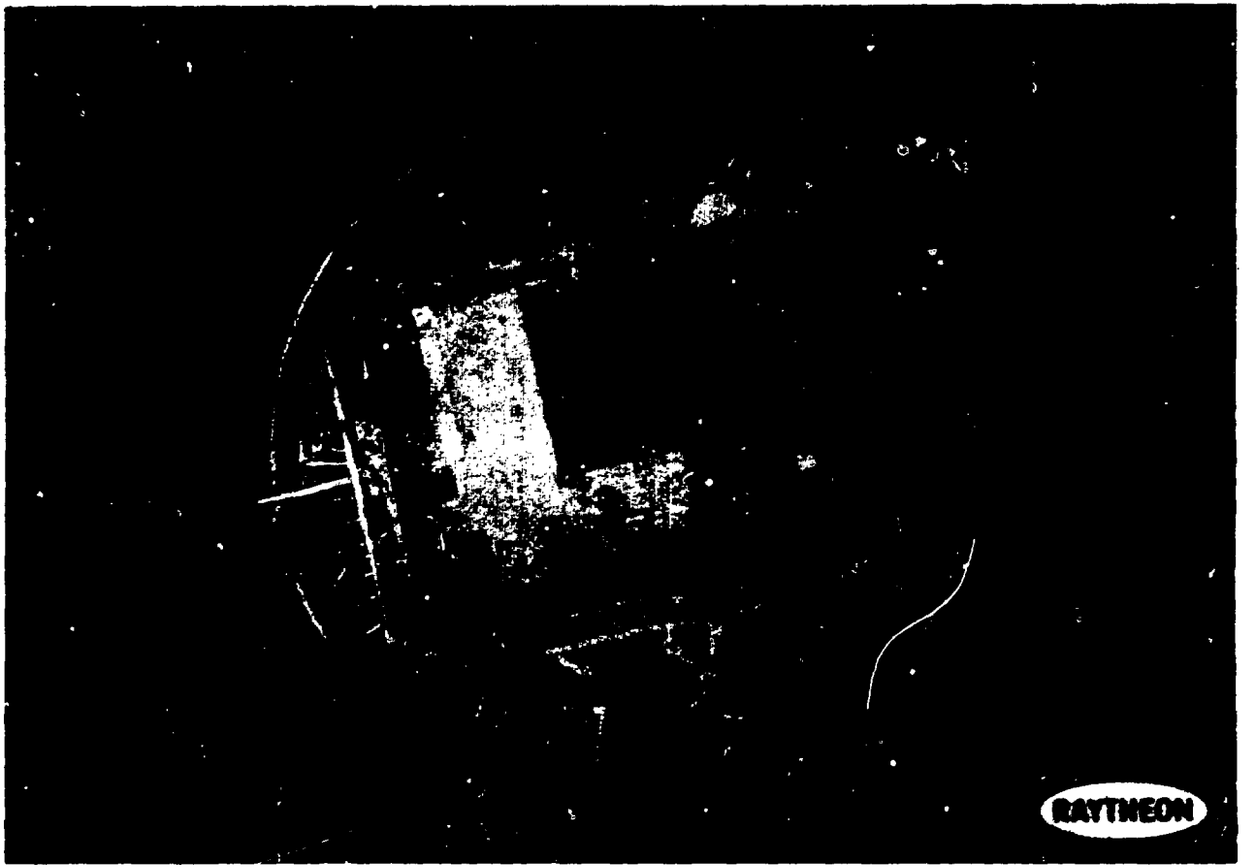

FIGURE 14. Receive Module

The FET switching device used has a gate length of one micron and a gate width of 1.6 millimeters, 16 channels of 100 microns each. The FET is used in a grounded source configuration. The source fingers are connected by gold air bridges with VIA-hole grounding at each end of the air bridge. Switching speed will be less than one nanosecond. Power handling will be more than one watt per FET.

Test of the individual bits from breadboard wafers yielded the following results. Phase shift accuracies of $\pm$ 5° per bit over an 800 MHz band were measured with VSWR $\leq$ 1.5:1 for each bit. Insertion loss of the individual bits was as follows:

45° bit	=	0.8 to 1.0 dB
90° bit	=	1.5 to 1.7 dB
180° bit	=	1.5 to 1.7 dB

LOW NOISE AMPLIFIER

A single stage monolithic GaAs FET amplifier was designed and fabricated for the SHF Microstrip array using 1 micron gate FET's monolithically grown in 4 mil GaAs. Performance is in good agreement with the design goals of 7.0 dB gain and 4.0 dB noise figure over the SHF frequency band. Test data indicate that the actual circuit is optimized about 5% lower in frequency than the model. The amplifier uses a Raytheon type 832 low noise FET having a 1 µm gate length and a 0.5 mm periphery. Distributed element RF matching circuits were grown on the GaAs chip with the FET. The design was optimized for maximum gain using CAD techniques. Blocking capacitors and biasing circuits are provided in the external module circuitry to simplify wafer processing.

LIMITER

A PIN diode limiter was designed to provide protection for the low noise amplifier in the receive module. Size constraints dictated that a substrate having a high dielectric constant (i.e., 9 to 10, similar to alumina) be used. The substrate material chosen was Epsilam-10, a ceramic power-filled TFE resin having dielectric properties similar to alumina yet being flexible and easily processed similar to the TFE laminates such as Duroid. Using .010" thick Epsilam-10 material with 1/2 ounce copper on each side,the limiter was packaged in the available [.300" x .200"] space in the module.

A conventional design utilizing two PIN diodes, spaced one-quarter wavelength, with a shorted low impedance stub for the ground return was developed. The D.C. return is provided via a shorted stub at the input. This method was chosen over an RF choke arrangement as it provides a measure of EMP protection for the SATCOM array. Performance of the prototype limiter is shown below.

Frequency:	7.25 - 7.75 GHz
Insertion Loss:	0.50 dB
VSWR:	1.24:1
P_{INPUT}:	10W CW
P_{OUTPUT}:	45MW CW

TABLE 3. Limiter Performance

BEAM STEERING UNIT

The SHF Beam Steering Unit (BSU) uses a TRS-80 model III as the basic computer. A 60 chip Augat board is used to interface the computer to the phase shifter drivers in the Array. Steering commands

for the array are computed in the TRS-80 using a program stored on tape via the cassette interface. Figure 15 is a block diagram of the BSU.

Steering the antenna is accomplished by inputing the frequency and the two beam pointing angles (azimuth and elevation) desired. The TRS-80 then computes Δx and Δy, the incremental row and column phase differences given by the equations:

$$\Delta x = 2\pi/\lambda \; dx \sin \theta_0 \cos \phi_0 \tag{3}$$

$$\Delta y = 2\pi/\lambda \; dy \sin \theta_0 \sin \phi_0 \tag{4}$$

where dx and dy are the element spacings in the rows and columns, and ϕ_0 and θ_0 are the azimuth angle and angle from the zenith. The SHF array is actually two 64 element arrays, each having 8 rows and 16 columns because of the triangular array grid. Thus, there are 48 row and column angles computed from the phase differences (Δx and Δy) which are then quantized into 22.5° increments.

These numbers are then stored in the computer. After computation, 4-bit row and column numbers are fed sequentially to the interface circuit. The interface circuit then takes this 4-bit word and sends a corresponding number of pulses to one of the 48 row and column inputs in the array. The rows and columns are fed sequentially by a 48 port multiplexer (MUX). The interface board consists of a parallel input 4-bit down counter, 1 to 48 multiplexer, and 48 TTL-to-CMOS converters to provide the proper pulse train for the drivers.

DRIVER

The phase shifter drivers utilize CMOS logic because -10 volts d.c. is required to pinch off the FET s used in the phase shifters in one bias state, the second (ungated-on) bias state being 0V d.c. The TRS-80 produces a TTL, 0 to +5V d.c., output pulse train.

The drivers consist of a counter to count the row and column pulse train and a buffer so that a new beam position can be loaded while the antenna is being used. Drivers for 8 elements are fabricated on each board using 19 IC's. The CMOS drivers can run at a clock rate of up to 4 MHz, limiting the beam switching rate to one every 500 μsec (2 KHz rate). The buffer output sets the RF downtime to 100 microseconds per beam position change. Figure 16 is a schematic diagram of the driver.

ARRAY TESTS

The breadboard receive array was used to confirm the array design in a non-steerable (broadside) configuration. The assembly was fabricated exactly as the ADM array except that the active receive modules were replaced by sections of 50 ohm transmission line in the combiner layer. 128 sections of 50 ohm line were built in .020" thick Duroid and retrofitted into the array. Thus, there are 256 splices in the combiner layer center conductor as well as in its ground plane. The VSWR of the resulting broadside array is obviously affected by this rework but, in general, the results of the breadboard array tests are excellent as shown in the following paragraphs.

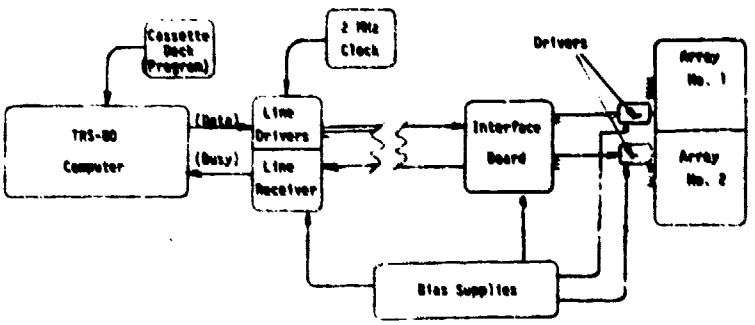

FIGURE 15. BSU Block Diagram

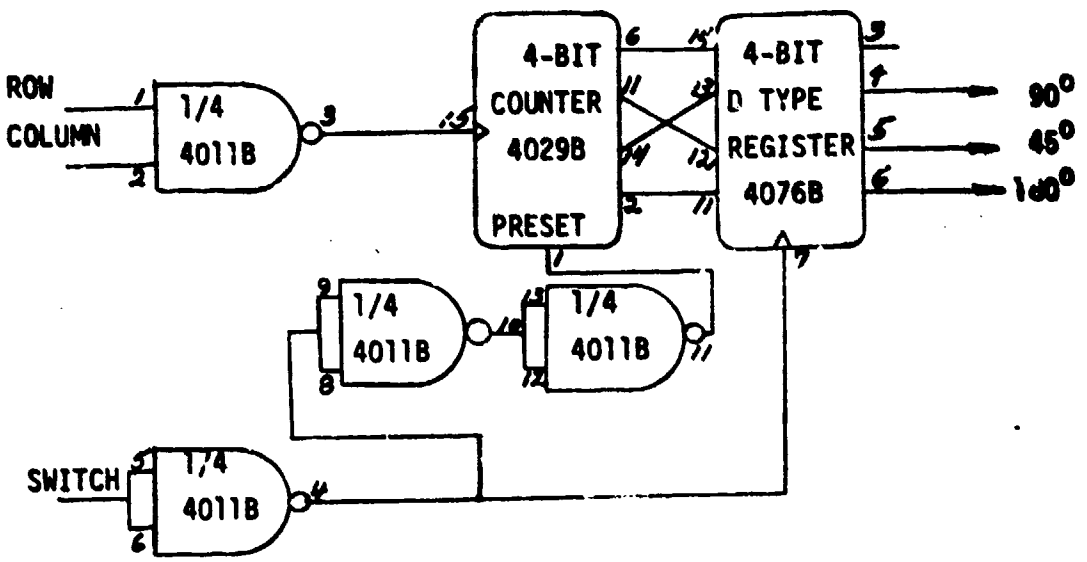

FIGURE 16. Driver Schematic

VSWR

The VSWR was measured at the two 1:64 input ports with the array radiating into an anechoic chamber. In the band of interest the VSWR is in the 1.6:1 to 2.0:1 range which is not unreasonable given the amount of rework (splicing) in the combiner microstrip layer. An array of sixteen identical elements fabricated with 50 ohm lines (in place of modules) in the combiner layer artwork had a VSWR of 1.25:1 over the same frequency band.

GAIN

Measured gain to either linear polarization of one 64 element breadboard array was 18.45 dB, compared to the calculated gain of 18.25 dB, well within the test system accuracy. Antenna efficiency of 60% was achieved measured from the input feed line including all losses.

RADIATION PATTERNS

Radiation patterns were recorded for linear vertical, linear horizontal, and circular polarization for each 64 element array as well as for the combined 128 element configuration. Patterns were recorded at 7.0, 7.25, 7.5, and 7.75 GHz. The highlights are summarized below and in Figures 17 to 19.

64 ELEMENT ARRAYS

Figure 17 shows the one way radiation patterns of the two 64 element arrays for horizontal linear polarization measured at 7.25 GHz. Peak sidelobe levels of -12 dB are as expected given the uniform illumination function and the 3 dB beamwidth of 12.5° at midband is

correct. Figure 18 is the radiation pattern at 7.25 GHz of a single beam when illuminated with a rotating linear (CP) source. Note that the axial ratio on the main beam is in the order of 0.1 dB. At 7.5 GHz and 7.75 GHz the sidelobe levels are -12 dB or lower, but the axial ratio is in the order of 1.5 dB. Measurements at 7.1 GHz are similar to 7.5 GHz, where the axial ratio is less than 1 dB and sidelobes are -12 dB or lower. These measurements indicate that the arrays exhibit the desired 500 MHz bandwidth, centered at the low end of the SHF frequency band.

128 ELEMENT ARRAY

Figure 19 is the rotating linear (CP) one way radiation patterns of the combined 128 element array. [The two 64 element array outputs are combined via equal phase cables in a 2:1 combiner.] The combined beamwidth is 6.3° and again sidelobes and axial ratios are optimum at 7.25 GHz as in the 64 element arrays.

ACKNOWLEDGMENT

The authors wish to thank Messrs. C. Dahl, L. I. Parad, and A. Valja for their contributions to the array design, and Messrs. J. McStay and W. Hall without whom the fabrication and assembly of the system would have been impossible. This work was supported by Rome Air Development Center under Contract F30602-80-C-0066.

REFERENCES

[1] Cullen, A. L. (1954) The Excitation of Plane Surface Waves, Proc. IEEE Vol. 101 Part IV: pp. 225-234.

[2] Wood, C. (1981) Analysis of Microstrip Circular Patch Antenna, Proc. IEEE Vol. 128 Pt. 4, No. 2, pp. 69-75.

[3] Pucel, R. A., Masse, D. J., and Hartwig, C. P. (1968) Losses in Microstrip, IEEE Trans. Vol. MTT-16, pp. 342-350.

[4] Lewin, L. (1960) Radiation From Discontinuities in Stripline, Proc. IEEE Part C. Vol. 107, pp. 163-170.

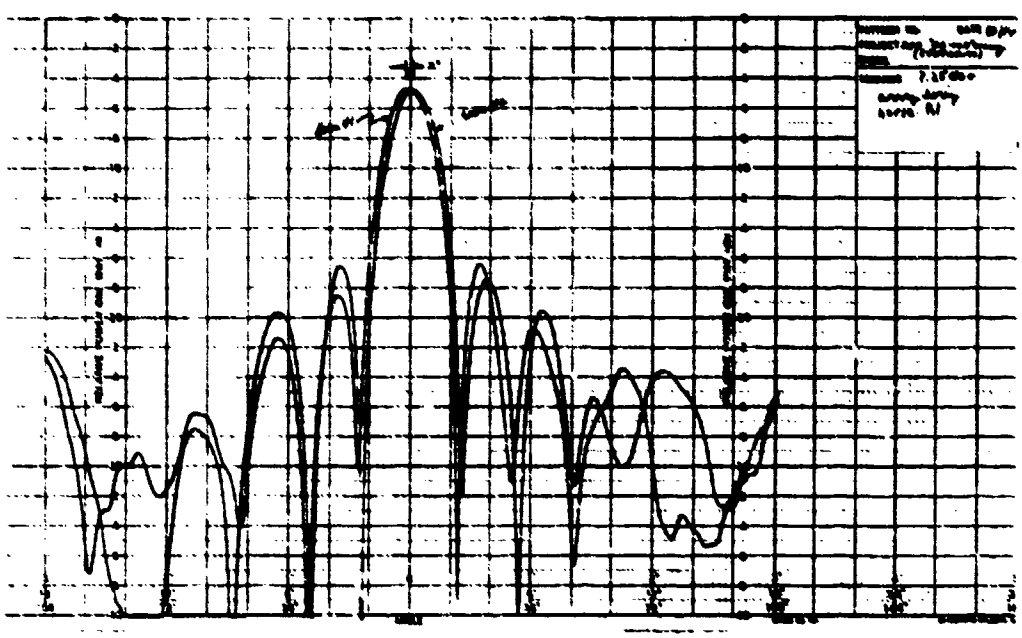

FIGURE 17. Horizontal Linear Radiation Pattern: Breadboard 64 Element Arrays

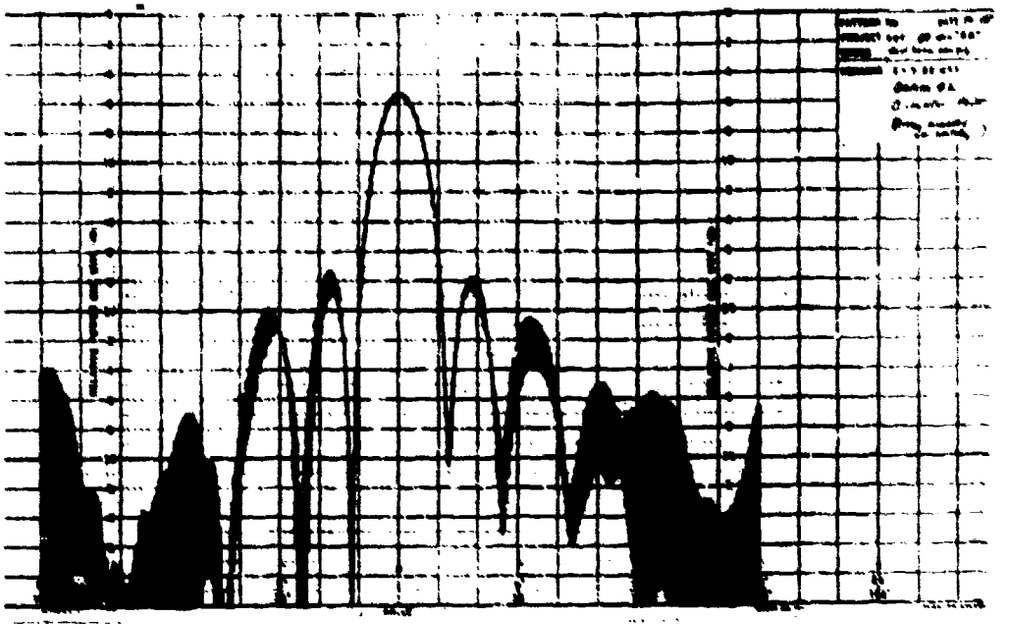

FIGURE 18. Rotating Linear (CP) Radiation Pattern: Breadboard 64 Element Array No. 2

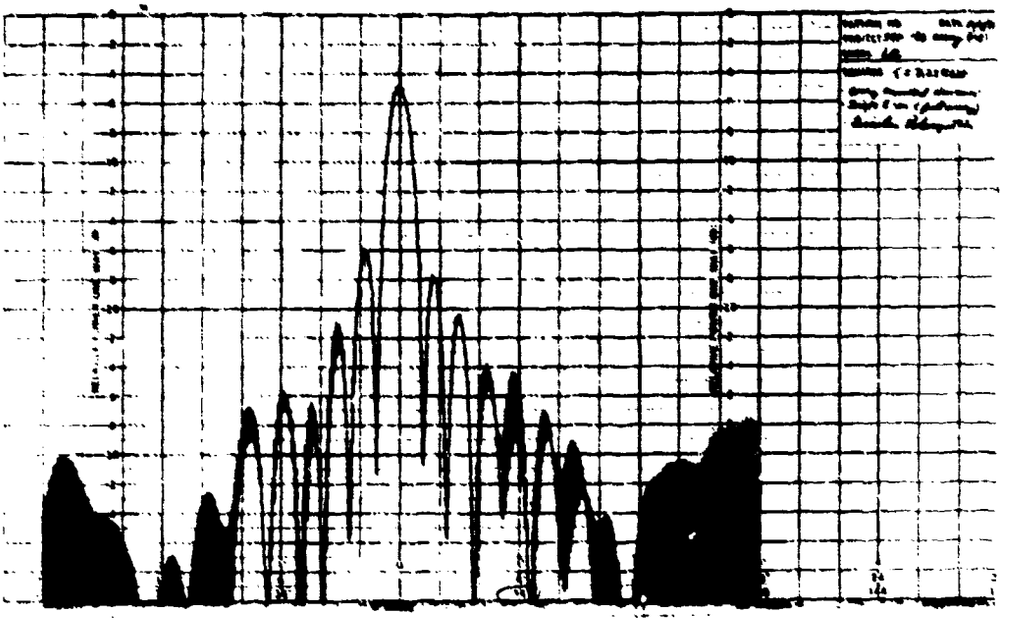

FIGURE 19. Rotating Linear (CP) Radiation Pattern: Breadboard 128 Element Array

R-82020

AD P001119

A CIRCULAR PARABOLIC REFLECTOR ANTENNA WITH OFFSET MONOPULSE FEED

M.J. Dick, D. Killion, E. Mehner, R. Justice

Cubic Corporation

ABSTRACT

Through the examination of both unorthodox and traditional techniques, a Ku band reflector antenna with offset monopulse feed was developed to meet certain requirements. In elevation, the requirement was maximum gain at 0° elevation angle, with gain falling off from the maximum no sharper than the cosecant squared of the elevation angle. In azimuth, the requirement was low sidelobes; consequently the dish was offset fed.

One technique for meeting the elevation requirements was to move the feed off focus while keeping the dish stationary; the other technique was to move the dish while keeping the feed at the focus of the dish. For the first technique, a combination ray trace/path length diagram roughly determined the desired feed location for a given elevation angle. Using these rough positions as guideposts, engineers experimentally determined more precise locations. Moving a light feed to scan elevation consumes far less power than does moving a heavy dish, as in the second technique. Moving the dish while keeping the feed at the focal point provided more gain at each elevation

angle than did moving the feed off focus. It also avoided needing a complicated scheme to move the feed to a precise position relative to the dish for each boresite elevation angle.

1.0 INTRODUCTION

1.1 PURPOSE

The purpose of this study is to develop an offset fed parabolic reflector antenna. In elevation, the requirement was maximum gain at 0^{o} elevation angle, with gain falling off from the maximum no sharper than the cosecant squared of the elevation angle. *A priori* target elevation position is assumed. In azimuth, the requirement is tracking capability and low sidelobes. The low sidelobes minimize jamming along the horizon.

1.2 TECHNIQUE

To meet the requirements, engineers used a circular parabolic dish with offset monopulse feed. The offset monopulse feed would fulfill the azimuth requirements.*

Engineers experimented with two techniques for scanning in elevation.

One technique for meeting the elevation requirements was to move the feed off focus while keeping the dish stationary. The other technique was the traditional approach of moving the dish and keeping the feed focused. For the

*Rudge and Adatia, "Offset Parabolic Reflector Antennas: A Review," Proceedings of the IEEE, December 1978.

first technique, a combination ray trace/path length diagram roughly determined the desired feed location for a given boresite angle. Using these rough positions as guideposts, engineers experimentally determined more precise locations. Moving a light feed to scan in elevation consumes far less power than does moving a heavy dish, as in the second technique. Moving the dish while keeping the feed focused provided more gain at each elevation angle than moving the feed off focus while keeping the dish stationary. This arrangement also avoided the need for a complicated scheme to move the feed to a precise position relative to the dish for each boresite elevation angle.

2.0 THEORY

2.1 SCANNING IN ELEVATION

To change a directional antenna into a scanning antenna for an unknown target location requires taking power from the main beam and spreading it out (Figure 2.1-1.) For this application, since *a priori* target position is known, the peak of the main beam can be pointed directly at the target. Thus gain loss associated with beam spreading need not occur.

Two methods of directing the peak of the main beam to specific scan angles are:

- Moving the feed off focus
- Moving the entire antenna

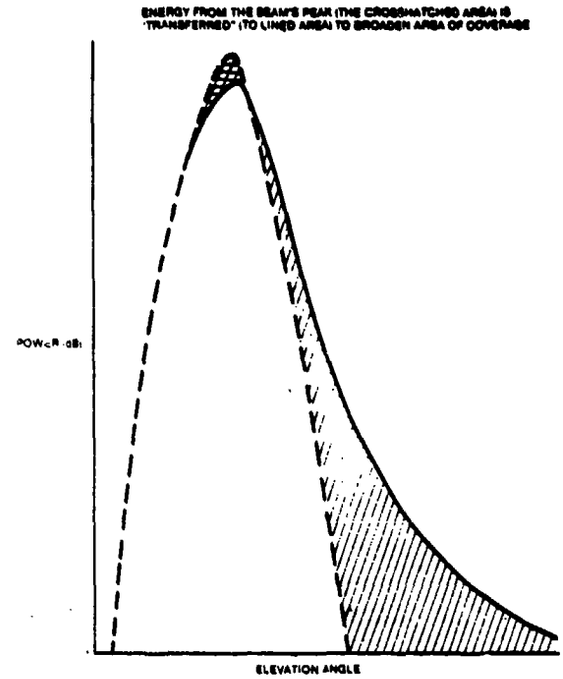

Figure 2.1-1 "Spreading Out" Directional Antenna's Main Beam for Scanning

Scanning by moving the feed off focus uses the ray-trace/path length technique (Appendix A) to determine feed location for each boresite angle. Figure 4.1-1 in Section 4.0 is a plot of this technique's results. Feed position is given relative to the dish's focal point. For scanning by moving the whole antenna—the traditional beam-pointing method--the feed is always at the focus of the dish.

2.2 AZIMUTH SIDELOBE LEVEL

Sidelobe level is a problem only on the horizon, where we anticipate the jammers will be located. Sidelobe level on the horizon is taken with respect to the peak at the boresite elevation angle. The signal arrives on boresite and the jamming arrives on the horizon. With increasing elevation boresite angle, the sidelobe level decreases.

For a second reason, the 0^{o} boresite angle is most vulnerable to jamming. As the elevation angle increases, the source gets closer to the antenna. With jammer position remaining fixed, the signal-to-jam ratio (S/J) therefore increases with boresight elevation angle.

3.0 ANTENNA DISH AND FEED

The antenna consisted of a 5'-diameter, circular parabolic dish with monopulse feed. Table 3.0-1 lists antenna parameters.

3.1 DISH

Figure 3.1-1 shows a two-dimensional view of a 2.5'-diameter cylinder intersecting a parabola to yield the circular parabolic dish. Table 3.0-1 shows detailed dish data.

Table 3.0-1. Offset Monopulse-Fed Antenna Details & Specifications

ANTENNA

Frequency band		14.40GHz - 15.35GHz
Polarization		Vertical
Beam width		(half power at 15.00GHz)
original feed	Azimuthal....	1.80°
	Elevation	.94

DISH

Circular parabolic segment*	
Diameter.....	60 inches
Focal length	50 inches
Surface tolerance.....	.006" RMS

MONOPULSE FEED

See Figures 3.2-1 and 3.2-2. (Note extension ears are oriented 45° with respect to the horn's front (open) edge.)

*Figure 3.1-1 shows how segment is determined

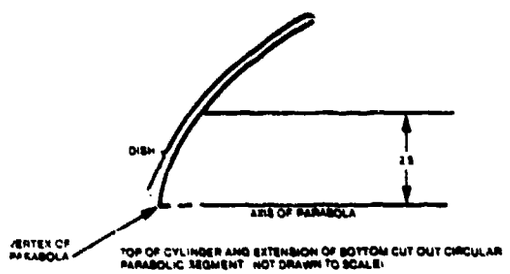

Figure 3.1-1 Circular Parabolic Dish Generation

3.2 MONOPULSE FEED

The monopulse feed (Figure 3.2-1) is a waveguide terminating in a sum and difference port hybrid on one end and a horn, with extension "ears" to reduce azimuthal sidelobes, on the other.

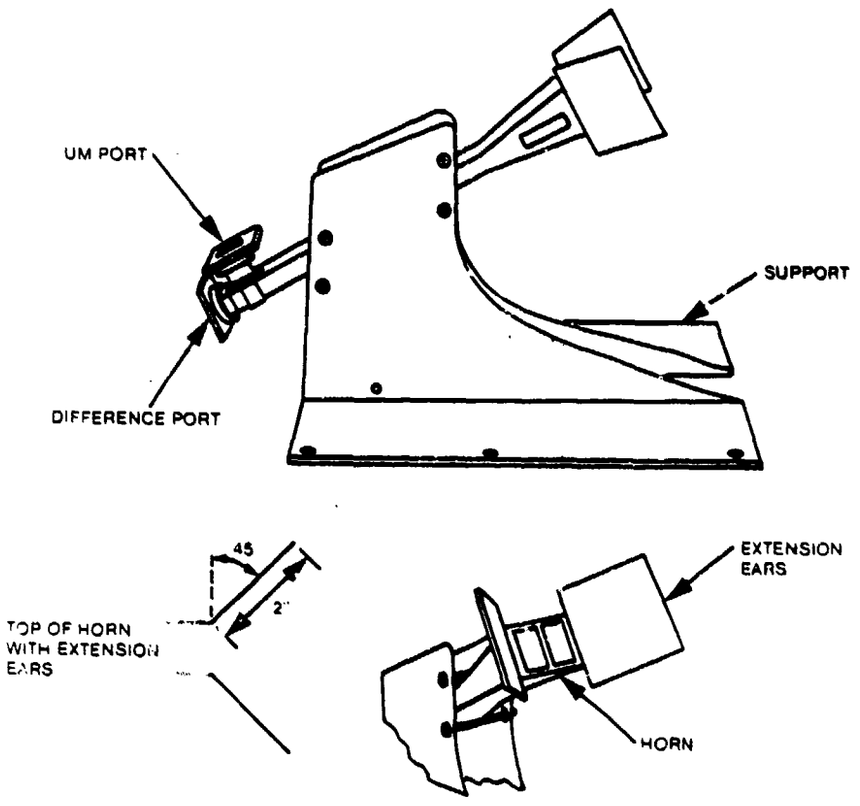

Figure 3.2-1 Antenna Feed

While the horn used for the moving-feed scan patterns was not designed specifically for this project, the one for the traditional scan patterns was.

4.0 ANTENNA TESTING: MOVING-FEED-OFF-FOCUS METHOD

4.1 FEED POSITION

Appendix A shows the ray trace/path length method of roughly determining feed location for a desired boresite angle.

Using the rough locations as guideposts, engineers experimentally determined more precise locations. Figure 4.1-1 is a plot of feed location with respect to the dish's focal point for boresite angles -15°, -10°, 0°, 10°, 20°, 30°, 40°, 45°.

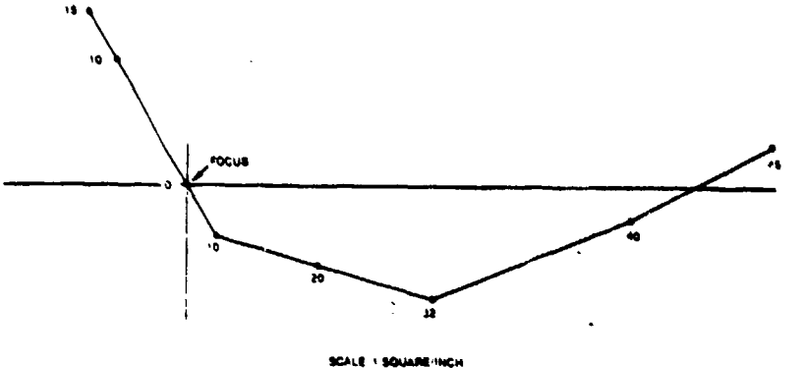

Figure 4.1-1 Feed Position for Various Boresite Elevation Angles

4.2 PATTERN RANGE

The source, a 12" diameter, front-fed dish, was circularly polarized with the horizontal component 2.5 dB greater than the vertical. Mounted on a bracket with two degrees of freedom, and positioned on the roof of Cubic's new engineering building, the dish was pointed toward the antenna on the receiving tower nearly 300' away. One worker at the source, getting gain information via walkie-talkie from a second person on the tower, pointed the source precisely to maximize gain.

On the receiving dish, a Ku-band weatherproof absorber covered the feed support structure during testing. For actual application, redesigning the support structure will make the absorber unnecessary.

4.3 AZIMUTH TEST

Figure 4.3-1 shows the antenna configuration for testing in the azimuth plane. Figure 4.3-2, along with associated Table 4.3-1, identifies patterns taken.

To determine whether low sidelobes are due to the antenna or to the test range itself, the antenna was rotated 180°. The rotation had only a random effect, indicating that some of the sidelobes were from the antenna; others, from the range itself.

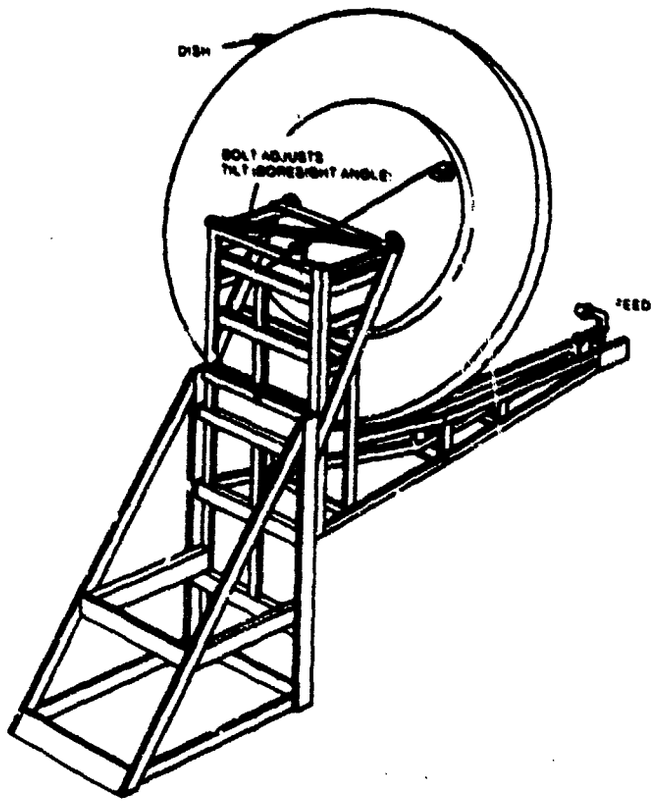

Figure 4.3-1 Azimuth Plane Test Setup for Moving Feed Off Focus Test

4.4 ELEVATION TEST

The elevation test configuration is rotated 90° from the orientation of the azimuthal test configuration so that testing can be done in the horizontal plane. This avoids the ground reflection problems of a vertical elevation plane test.

After completing these tests, engineers found experimentally a second curve for relating feed position to elevation angle. The gain for these feed positions

Table 4.3-1. Boresite Angles for Patterns Taken

Source Angle For All Patterns	Power Maximum (Boresite) Angles
$\theta = 90^{\circ}$ $\phi = 0^{\circ}$	$\theta = 90^{\circ}, 80^{\circ}, 70^{\circ}, 60^{\circ}, 50^{\circ}, 45^{\circ}, 100^{\circ}, 105^{\circ}$ Patterns taken for all 360° in azimuth θ & ϕ are defined in Figure 4.3-2

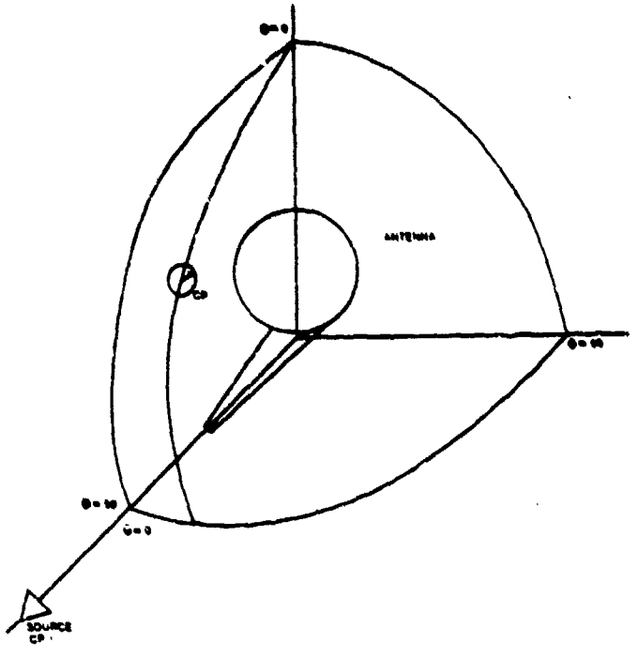

Figure 4.3-2 Coordinate System Referenced in Table 4.3-1

was even higher than for the positions that the ray trace/path length technique predicted. No patterns were taken for these feed positions.

5.0 ANTENNA TESTING: TRADITIONAL APPROACH

5.1 FEED POSITION

The feed always remained at the dish's focal point.

5.2 PATTERN RANGE

The circularly polarized signal, emitted from an 18" diameter front feed dish, traversed 825' over a canyon to the antenna mounted on the receiving tower. The source pointed at the receiving antenna to maximize gain.

5.3 AZIMUTH TEST

Figures 5.3-1a and 5.3-1b show the traditional scan azimuth test configuration. The dish support structures are simpler than those used for the moving-feed

Figure 5.3-1 Traditional Scan Test Configuration

scan (Figure 4.3-1) since an elevation/azimuth pedestal is present rather than an azimuth/elevation pedestal.

5.4 ELEVATION TEST

The elevation dish scan configuration is the same as for the azimuth test.

6.0 RESULTS

Several statistical plots communicate azimuthal sidelobe level results. To make reduction of raw sidelobe level data into a statistical format easier and more accurate, the azimuth patterns were spread out over six cycles of recording paper (10 feet). Consequently, those patterns are too big to include in this document.

Sidelobe level on the horizon is taken with respect to the peak at boresite.

6.1 MOVING-FEED-OFF-FOCUS SCAN RESULTS

6.1.1 Elevation

Figure 6.1-1 shows a composite of the elevation patterns taken with the feed positioned for each of the elevation angles 0°, 10°, 20°, 30°, 40° and 45° individually.* The feed position was not adjusted for angles other than these. Consequently, the gain drops off rapidly as elevation angle deviates from these specific angles.

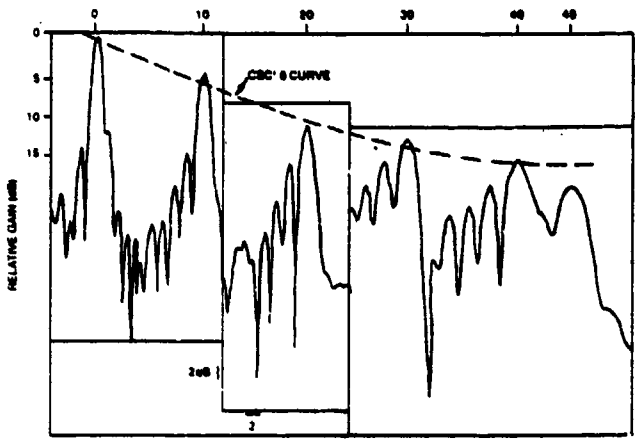

Figure 6.1-1 Composite of Elevation Patterns (Moving Feed)

A $CSC^2\theta$ curve is superimposed on the composite of the elevation patterns. Figure 6.1-1 indicates that, with the feed properly positioned, the moving-feed technique will provide enough gain to match the classical $CSC^2\theta$ pattern for angles up to 40°. At 45°, the gain is about 3 dB below that of the $CSC^2\theta$ curve.*

6.1.2 Moving-Feed Scan Azimuth

The probability a jammer can point into a sidelobe N dB below the peak of the main beam for N = 35, 40, 45, and 50 for 0° elevation is summarized for 15 GHz in 6.1-4a and b for sum and difference patterns respectively. This

*The maximum value for θ is $\tan^{-1}\frac{4.6}{45}$ where 4.6 km is source's maximum height, 45 km is its maximum range. This θ is matched up with the 0° boresite elevation angle.

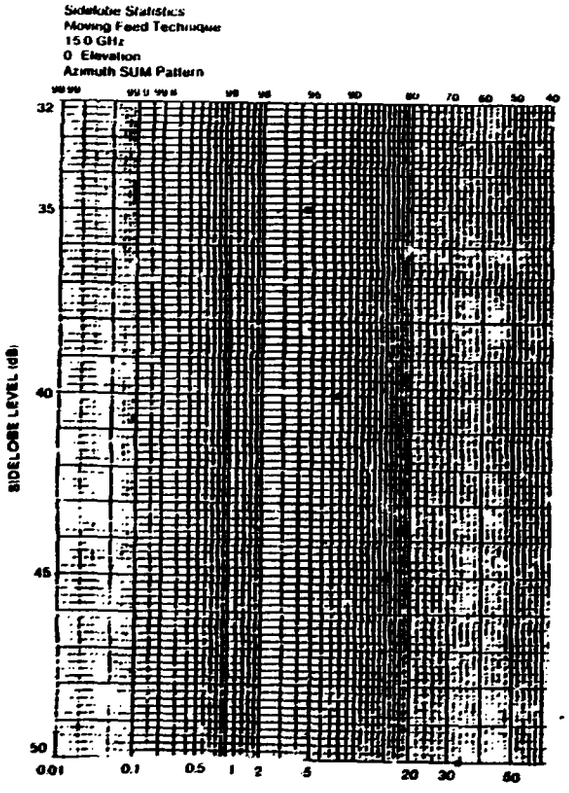

Figure 6.1-4a

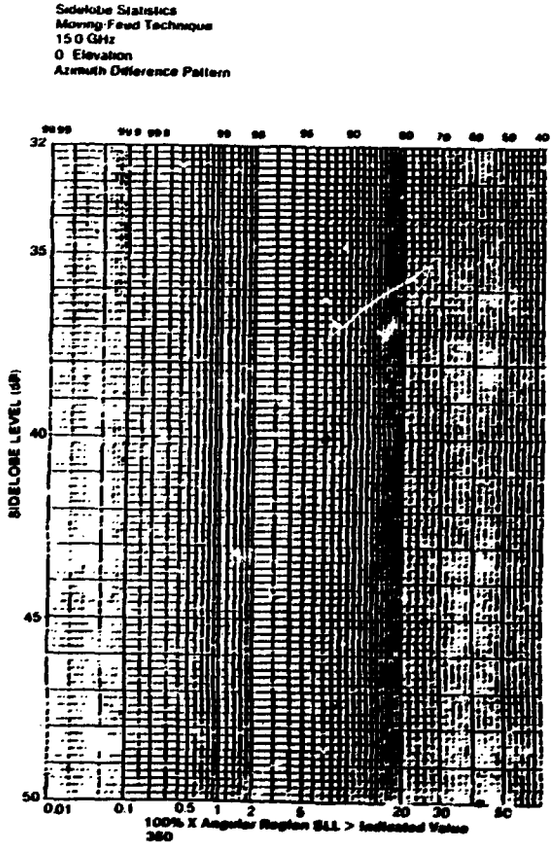

Figure 6.1-4b

probability, P_{SLL}, is the percent of the entire angular region where the sidelobe level, SLL, is greater than or equal to N dB. Figures 6.1-2a and 6.1-2b are sample plots of P_{SLL} vs elevation angle for SLL ≥ 45db.

6.2 TRADITIONAL APPROACH

The probability a jammer can point into a sidelobe N dB below the peak of the main beam for N = 35, 40, 45, and 50 vs. elevation angle is plotted for 3 frequencies in Figures 6.2-1a through d and 6.2-2a through 6.2-2d for sum and difference pattern respectively. This probability, P_{SLL}, is the percent of the entire angular region where the sidelobe level, SLL, is greater than or equal to N dB.

6.2.1 Frequency Variation

The plots of P_{SLL} vs. elevation angle were very similarly shaped for the 3 frequencies tested.

Both sum and difference plots showed the most frequency variation at 50 dB SLL at 10° and 20° boresite angles.

6.2.2 0° Boresite P_{SLL}

The P_{SLL} of greatest concern is for 0° boresite. As boresite angle increases, the source gets closer to the antenna while the jammer's distance remains the same. Table 6.2-1 shows the probability a jammer can point into a sidelobe

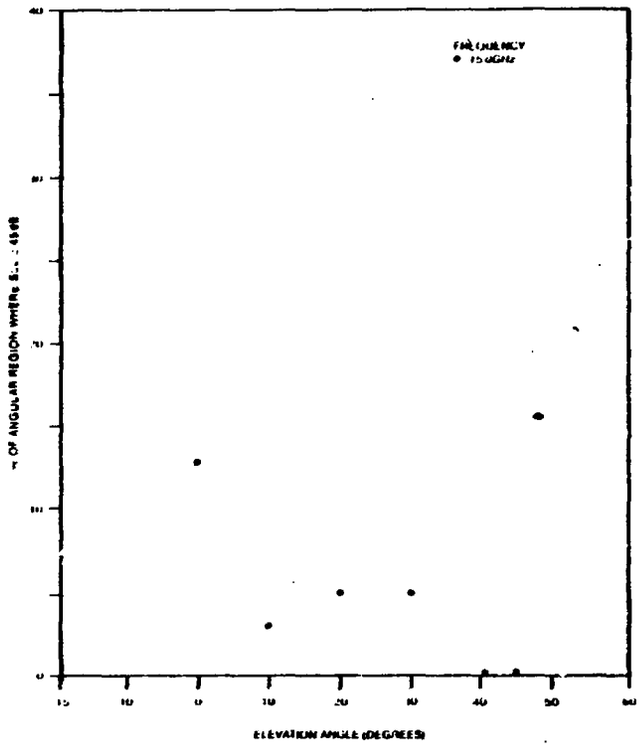

Figure 6.1-2A Statistics for 45dB, Sum Pattern (Moving Feed Off Focus)

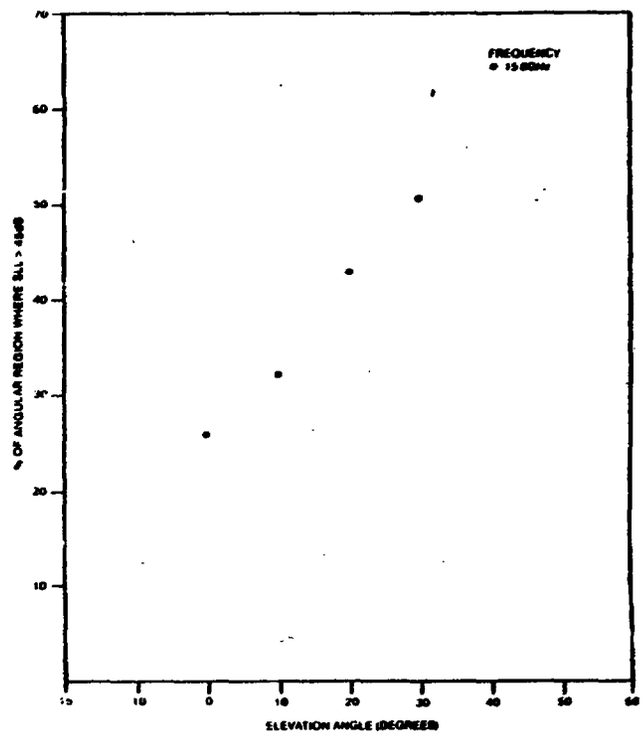

Figure 6.1-2B Statistics for 45dB Difference Pattern (Moving Feed Off Focus)

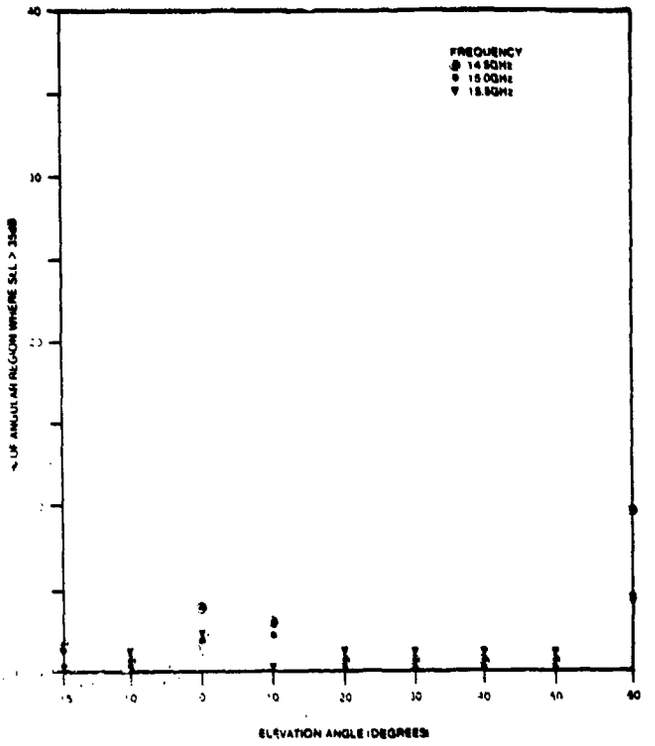

Figure 6.2-1a Statistics For 35dB Sum Pattern (Moving Entire Antenna)

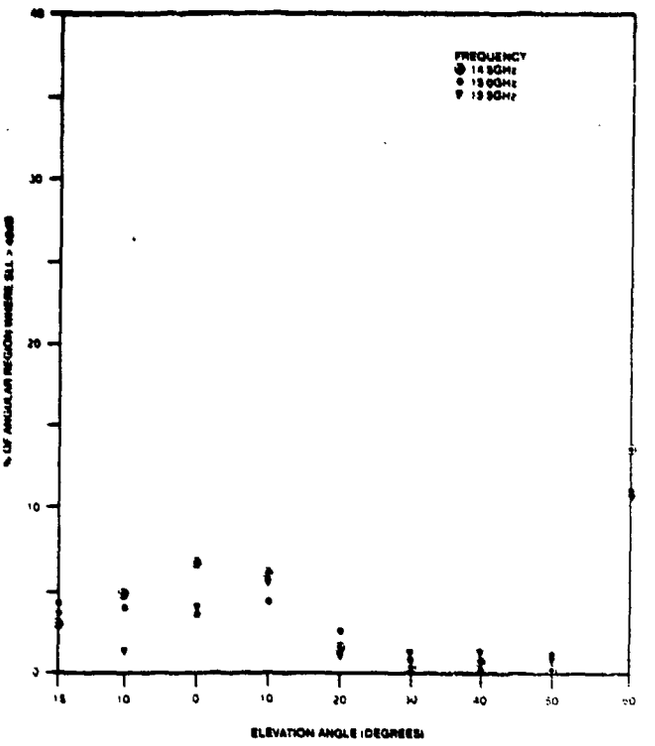

Figure 6.2-1b Statistics For 40dB Sum Pattern (Moving Entire Antenna)

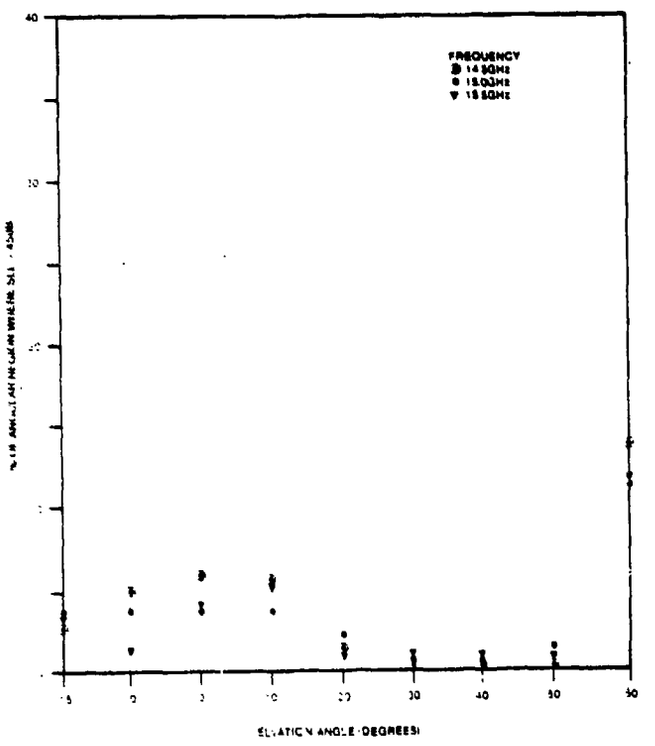

Figure 6.2-1c Statistics For 45dB Sum Pattern (Moving Entire Antenna)

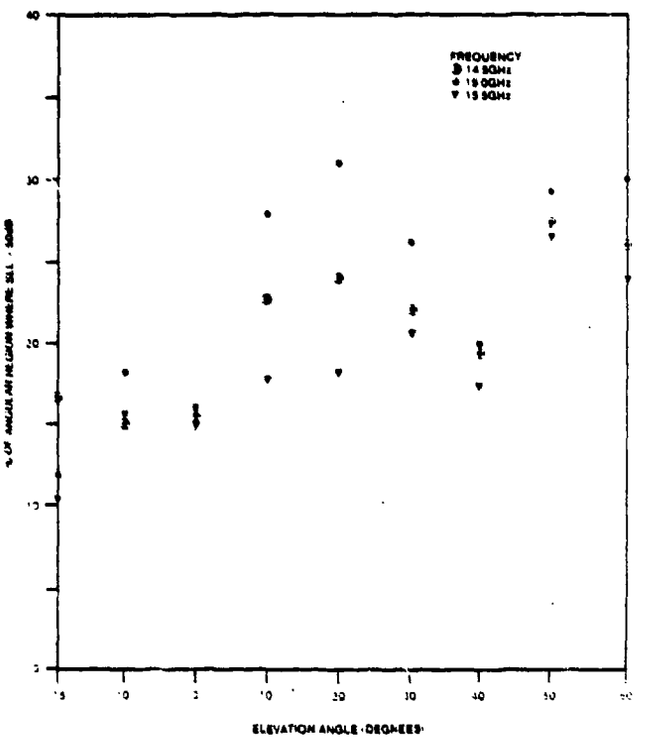

Figure 6.2-1d Statistics For 50dB Sum Pattern (Moving Entire Antenna)

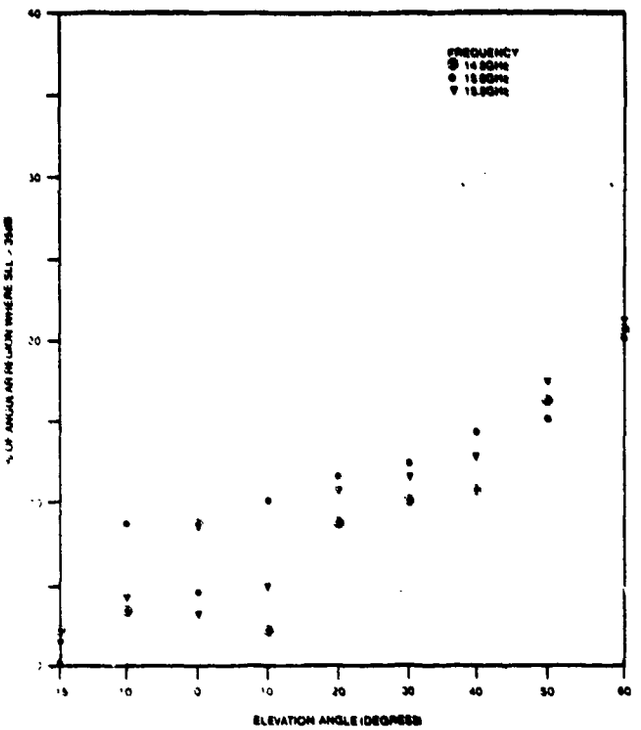

Figure 6.2-2a Statistics For 38 dB Difference Pattern (Moving Entire Antenna)

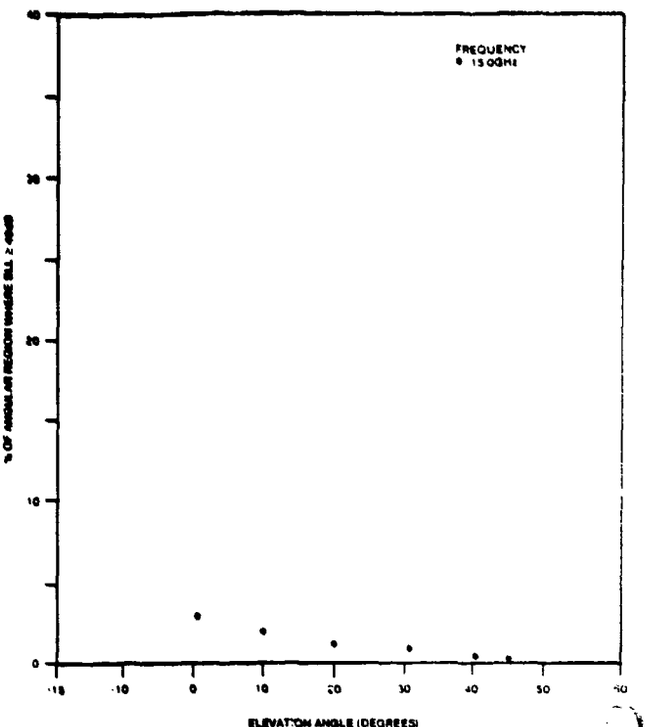

Figure 6.1-2b Statistics For 40dB, Sum Pattern (Moving Feed Off Focus)

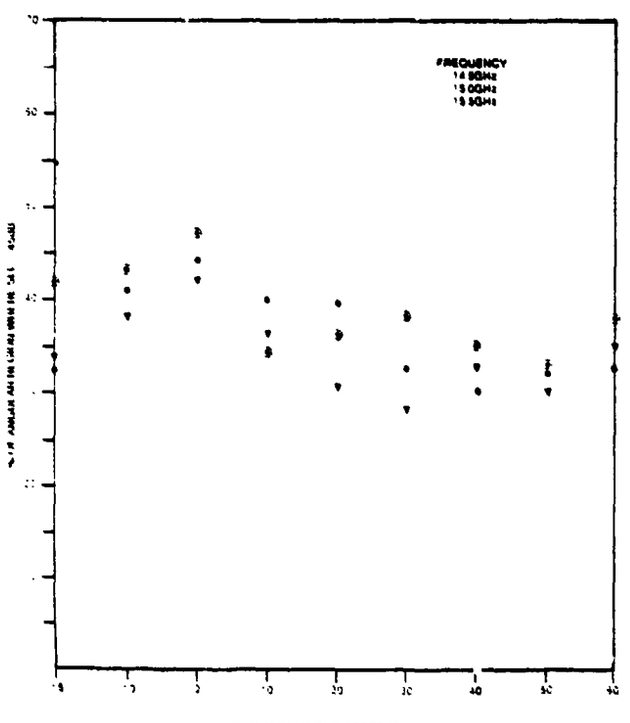

Figure 6.2.2c Statistics For 45dB Difference Pattern

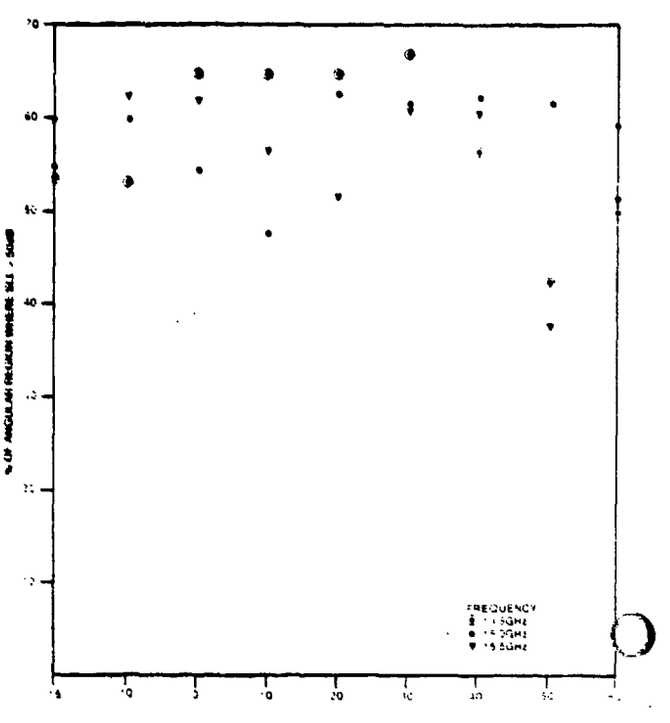

Figure 6.2-2d Statistics For 50dB. Difference Pattern

Table 6.2-1. P_{SLL} for 0° Boresite Angle

% of Angular Region Where $S_{LL} \geq$ N dB

Elevation Angle		SUM Frequency (GHz)			DIFFERENCE Frequency		
0°	N	14.5	15.0	15.5	14.5	15.0	15.5
	32	3	0	0	3	3	2
	35	4	2	1	8	4	3
	40	9	3	2	30	26	40
	45	17	8	5	48	44	42
	50	56	17	12	66	53	62

N dB down from the main beam at 0° boresite. Appendix B contains the antenna pattern near the main beam at 0° elevation.

Figures 6.2-3a aand 6.2-3b show the P_{SLL} plotted vs. N for sum and difference patterns at 0° elevation, 15.0GHz for N = 35, 40, 45, and 50dB.

6.2.3 Difference And Sum Pattern P_{SLL} Comparison

Note for the differences pattern sidelobes, the P_{SLL} for each SLL (35, 40, 45, 50 dB) are much greater than for sum patterns. The major contribution to P_{SLL} for difference pattern sidelobes is centered in the -165° and -165° regions. Since jammers would not be in back of the antenna these sidelobes do not make the antenna more vulnerable to jamming. This statistical presentation of data does not descriminate according to sidelobe positions.

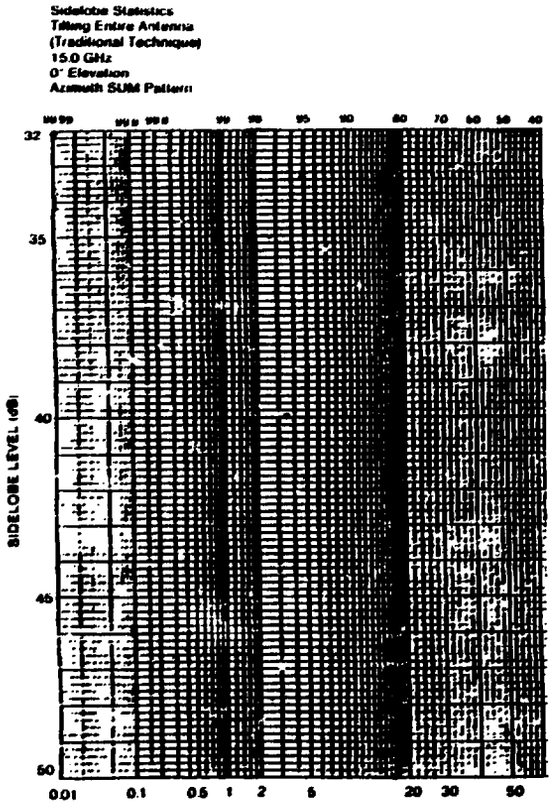

Figure 6.2-3a

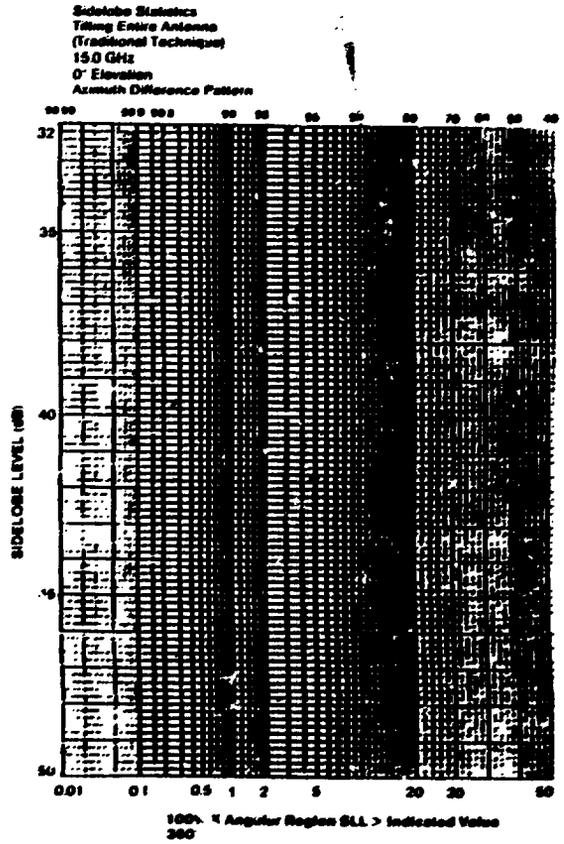

Figure 6.2-3b

6.2.4 Elevation Patterns

Appendix B shows elevation patterns of the dish with focused feed.

6.2.5 Primary Patterns

The primary patterns appear in Appendix B.

6.2.6 Gain

Antenna gain was 40dB. Gain can be improved by optimizing feed.

6.2.7 Null Depth

Appendix B shows null depth variation with frequency.

7.0 CONCLUSIONS

7.1 MOVING-FEED-OFF-FOCUS SCAN

The elevation patterns for 0°, 10°, 20°, 32°, and 40° elevation boresite angles roughly match the $CSC^2\theta$ curve. At 45°, the elevation pattern is 3 dB below that curve. Consequently, scanning by moving the feed provides adequate gain to meet a $CSC^2\theta$ scanning requirement from 0° to 40°. Improvements (see Section 8.1) may extend the elevation scan angle.

For the sum port, the greatest position where there is the probability a jammer can point into a side lobe level of either 35, 40, 45, or 50 dB down from the peak of the main beam is at the 0° elevation angle. These

probabilities are given in Section 6.1. For the difference port, the corresponding probability seems to increase with elevation angle.

7.2 TRADITIONAL SCAN

- Tilting the entire antenna to scan in elevation means gain does not change with a change in elevation angle. This readily meets elevation gain requirements.

- The elevation angle of most concern is 0°. Table 6.2-1 and Figures 6.2-3a and 6.2-3b show sidelobe imformation for this angle. For example, at 15.0 GHz, in only 8 percent of the angular region the sidelobe level is less than 45 dB below the peak of the main beam.

- Sidelobe level variation over the 14.5 GHz to 15.5 GHz band is not significant.

- The percent of the angular region where a given sidelobe level is exceeded is greater for difference pattern than for sum patterns.

- Large proportions of the difference pattern P_{SLL} are from far-out sidelobes regions unexposed to jamming.

The implications of these sidelobe data on system performance is a topic of a further study.

7.3 IMPROVING PERFORMANCE

The moving-feed technique used a different feed than the one used for the traditional technique. For the moving feed-off-focus technique, the first sidelobe level was 31 dB below (Appendix B) the peak of the main beam. For the traditional technique, it was 28 dB below the peak of the main beam. Optimizing the feed and focusing it extremely carefully should reduce this first sidelobe. Additionally, designing the feed to meet the values indicated in section 3.2 should deepen the difference in null depth.

8.0 RECOMMENDATIONS

The traditional elevation scanning method (tilting the whole antenna) has advantages over the moving-feed-off-focus method.

- The traditional method has no problems associated with moving a feed and attached cables along a complex path.

- The elevation pattern using the traditional mothod is the same for all elevation scan angles. (See Appendix B for pattern). Thus for all angles the traditional method exceeds the elevation gain requirement. The moving-feed method

presently did not meet elevation gain requirements beyond 40°.

8.1 MOVING-FEED-OFF-FOCUS TECHNIQUE

- This technique requires more experimental and theoretical work to determine the locus of points for the feed locations providing the highest gain for each elevation angle. As discussed in Section 4.4, engineers found a second curve or locus of points for feed positions for various elevation angles. Further investigation of this and other feed position curves is needed.

- Engineers should optimize the feed to improve gain.

Following both these recommendations might extend the elevation angle over which the moving-feed technique is applicable.

- Engineers should develop a mechanism for moving a feed (with attached transmission line) over a complex curved path.

8.2 TRADITIONAL TECHNIQUE: TILTING THE ENTIRE ANTENNA

- Several azimuthal cuts at small increments around 0° bore-site are needed to obtain enough data for a good estimate of sidelobe contour. A computer plot could provide these sidelobe contours.

- Engineers should redesign the feed for greater null depth and improved gain.

- For precise sidelobe v. frequency information, engineers should investigate sidelobes as frequency sweeps from 14.5 to 15.5 Ghz.

APPENDIX A - RAY TRACE/PATH LENGTH DIAGRAM

(1) Draw rays X3, H2, and J1 perpendicular to wavefront W and striking the parabola at points 1, 2, and 3. These rays reflect off the parabola to form triangle ABC.

(2) Pick a point P roughtly midway along AB; then draw arc A with radius X3 + P3 and center along the extension of line C3 (dashed line).

(3) Draw arc B with radius P3 + X3 - H2 and center along line B2

(4) Finally draw arc C with radius P3 + X3 - V1 centered along line B1

Now let Q be the single point where all 3 arcs nearly intersect. Then Q3 + X3 = Q2 + H2 = Q1 + V1.

Since these path lengths are all equal, rays traveling along them have equal phase.

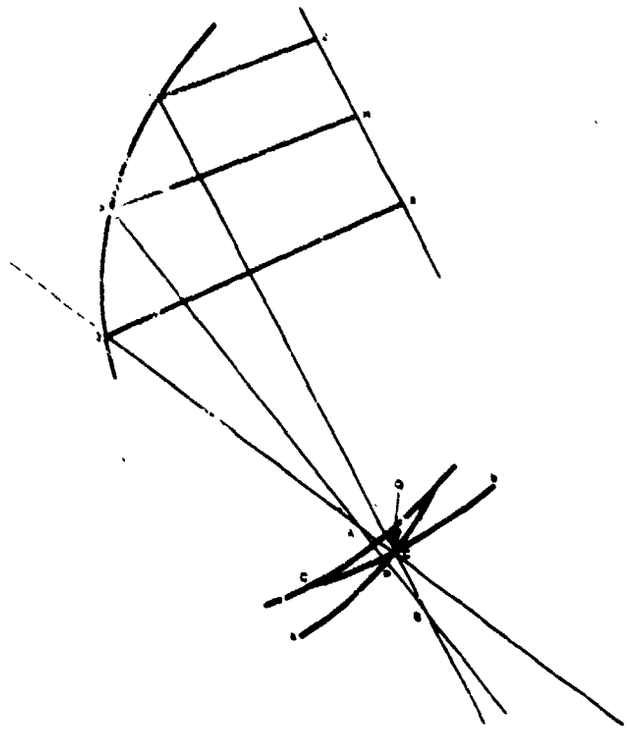

Figure A-1 Ray Trace/Path Length Diagram

APPENDIX B

Figure B-1 shows azimuth pattern of focused feed used for moving-feed-off-focus technique. The first reference mark is 26 dB below the peak of the beam; the first sidelobe level is more than 31 dB below the peak of the beam.

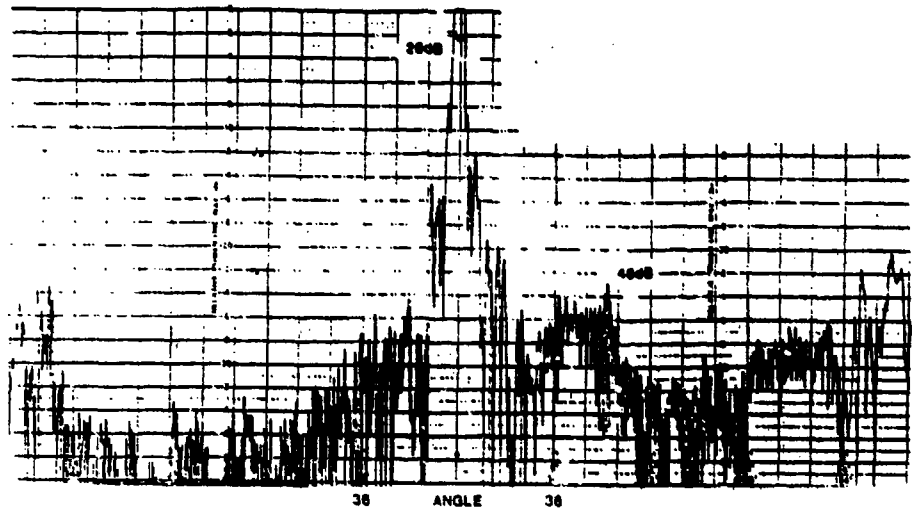

Figure 8-1 Azimuth Pattern 0° 15.0 GHz

AD P001120

LOW SIDELOBE SCANNING BEAMS FOR PARABOLIC REFLECTORS

Charles C. Hung

Lockheed Missiles and Space Company

Sunnyvale, California

ABSTRACT

Recently there has been considerable interest in extending the scan capability of reflector antennas. Shelton, Rudge and Withers, Hung and Chadwick, Hung and Mittra, among many researchers, have shown that wide angle scan capability can be achieved by using feed array consisting of many feed elements (as opposed to a single feed). Up to now, no sidelobe level requirement has been considered yet.

In this paper, it will be shown that low sidelobe scanning beams for parbolic reflectors can be achieved by using feed array with tandomly arranged orthogonal matrices. The matrix immediately behind the feed array transforms the focal field to match the aperture plane distribution including both amplitude and phase distortions induced by the feed array when located off-axis. With proper amplitude taper and phase compensation, low sidelobe scanning beams can then be realized. Feed array configurations, orthogonal matrices and secondary far field patterns will be presented in detail.

PAGE BLANK-NOT FILMED

1. Introduction

Recently there has been considerable interest in extending the scan capability of reflector antennas to many beamwidths from the boresight direction. Rudge and Withers[1] first showed experimentally that scan angles of up to fifteen beamwidths can be achieved with little pattern degradation and minimal gain loss by correcting the phase of the spatial Fourier transform of the distorted focal region field. Hung and Chadwick[2] then developed a general technique to correct the phase distortion in the off-axis beams. In this paper, it will be shown that low sidelobe scanning beams for parbolic reflectors can be achieved by using a particular family of multiple beam array as the feed of the reflectors. Feed array configurations and the determination of feed element weights are first discussed. Computed results are then presented. Some comments on the future work and conclusion are given in the end.

2. Feed array and Aperture Plane Distribution

The feed array used in the present work is a two dimensional equilateral triangular array with RN^2 elements where R and N are integers and N(R+1)/2 is also an integer. An array with R = 3 and N = 3 is schematically shown in Fig.1 . This RN^2 triangular array will produce RN^2 simultaneous, orthogonal beams in space. The analysis and synthesis of this RN^2 multiple beam array family has been carried out by J. L. McFarland[3,4,5]. The distribution of these RN^2 simultaneous beams in (u',v') space produced by the RN^2 triangular array is also an equilateral

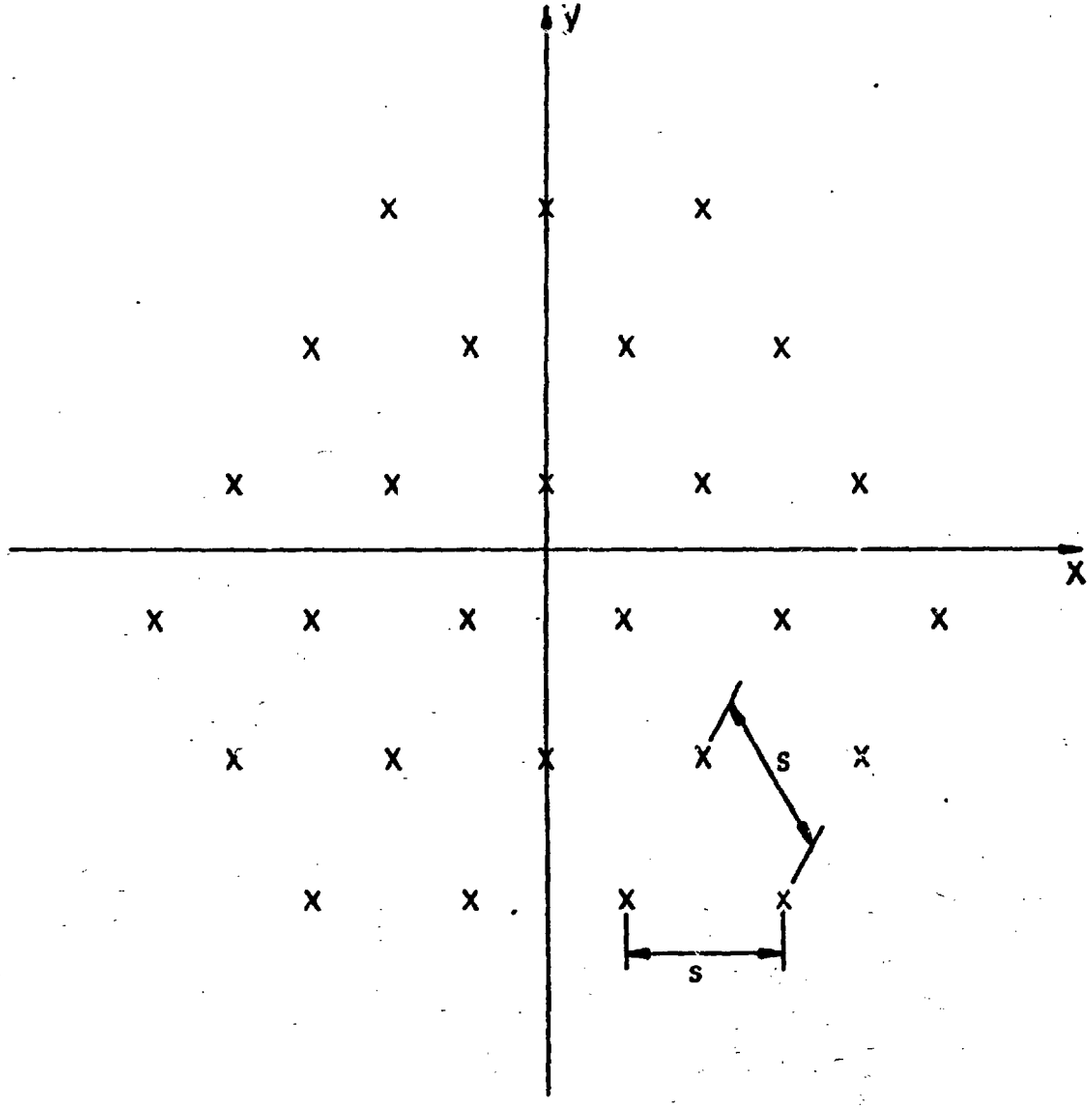

Fig.1 RN^2 triangular array R = 3 N = 3

triangular array where $u' = \sin\theta\cos\phi$ and $v' = \sin\theta\cos\phi$. Fig.2 shows the distribution of 27 beams (R =3 and N =3) in (u',v') space.

Let the location of array element be $(x,y) = (ms/2, n\sqrt{3}\, s/2)$ where s is the side of equilateral triangle. The correct phase for each element to produce a beam whose peak is at $(u',v') = (p\ell, q\sqrt{3}\,\ell)$,where $\ell = 2\pi/RNks$, is given by

$$\Phi_{mn}^{pq} = \frac{\pi}{RN}\left[(m - m_o)(p - p_o) + 3(n - n_o)(q - q_o)\right]$$

where m_o , n_o , p_o and q_o are the bias to determine the phase center in (x,y) and (u'.v') space. The pattern of beam pq is then given by

$$E_{pq} = \sum_{m,n} \mathrm{Exp}\left\{j\frac{\pi s}{\lambda}\left[(m - m_o)u + \sqrt{3}(n - n_o)v\right] - j\,\Phi_{mn}^{pq}\right\} E_{mn}$$

where E_{mn} is the element pattern of the elemcnt located at $(x,y) = (ms/2,\ n\sqrt{3}\, s/2)$.

The complete feed structure is shown in Fig.3 . At eahc port of the RN^2 multibeam array, there is also a complex weight to provide both amplitude and phase correction for each beam. All these RN^2 ports are summed up to produce one single port. The element pattern, E_{mn}, is , in general, of broad beamwidth and hence illuminates the whole parabolic reflector. The beam pattern, E_{pq} , however, is of narrow beamwidth and illuminates only a portion of the parabolic reflector. If RN^2 is sufficiently large, each beam will just illuminate a small portion of the parabolic reflector. The phase distortion in each beam and the amplitude variation between each beam can then be corrected by using the complex weight at each port. In addition to correct

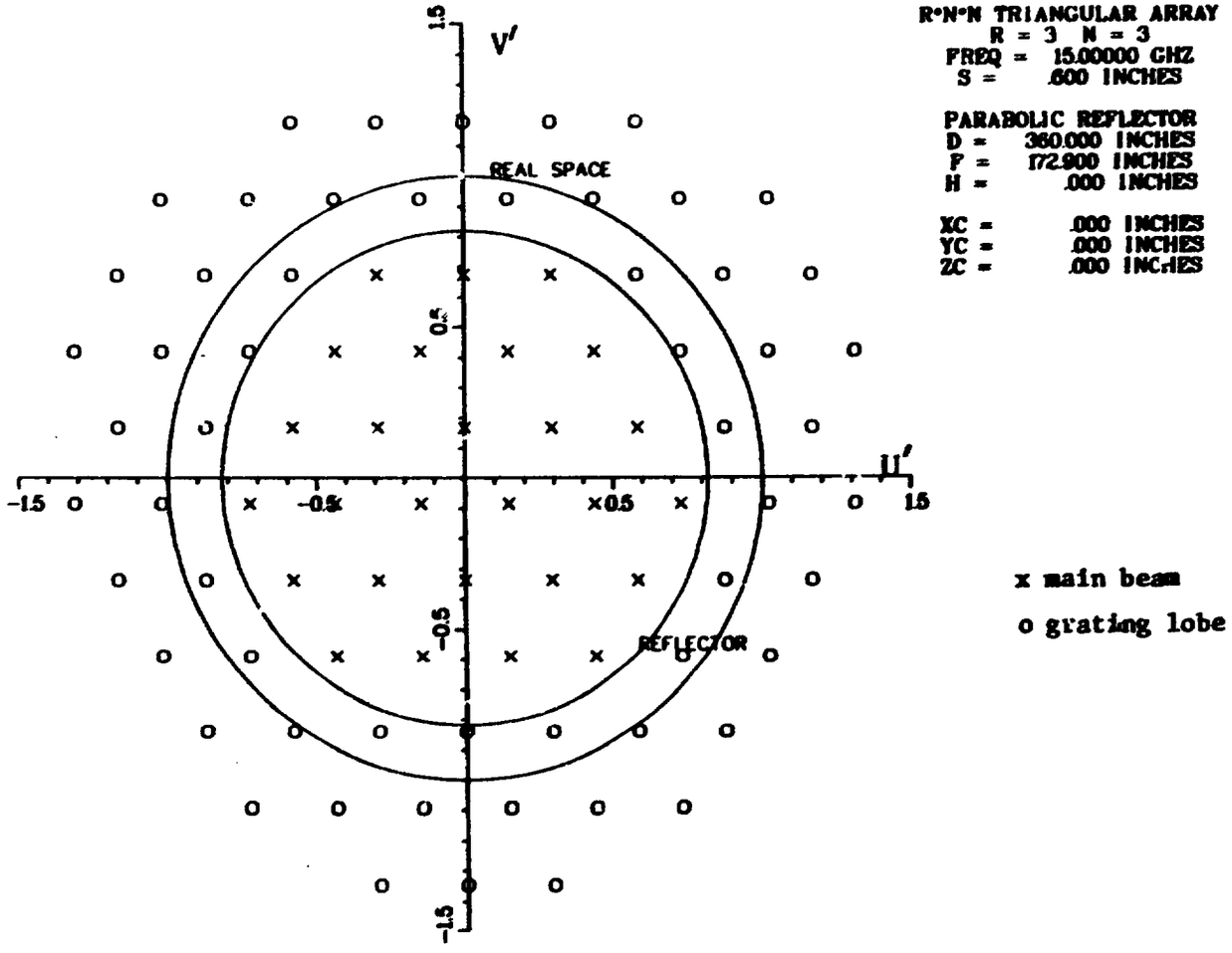

Fig.2 Beam peak distribution in (u',v') space of RN^2 triangular array

R = 3 N = 3

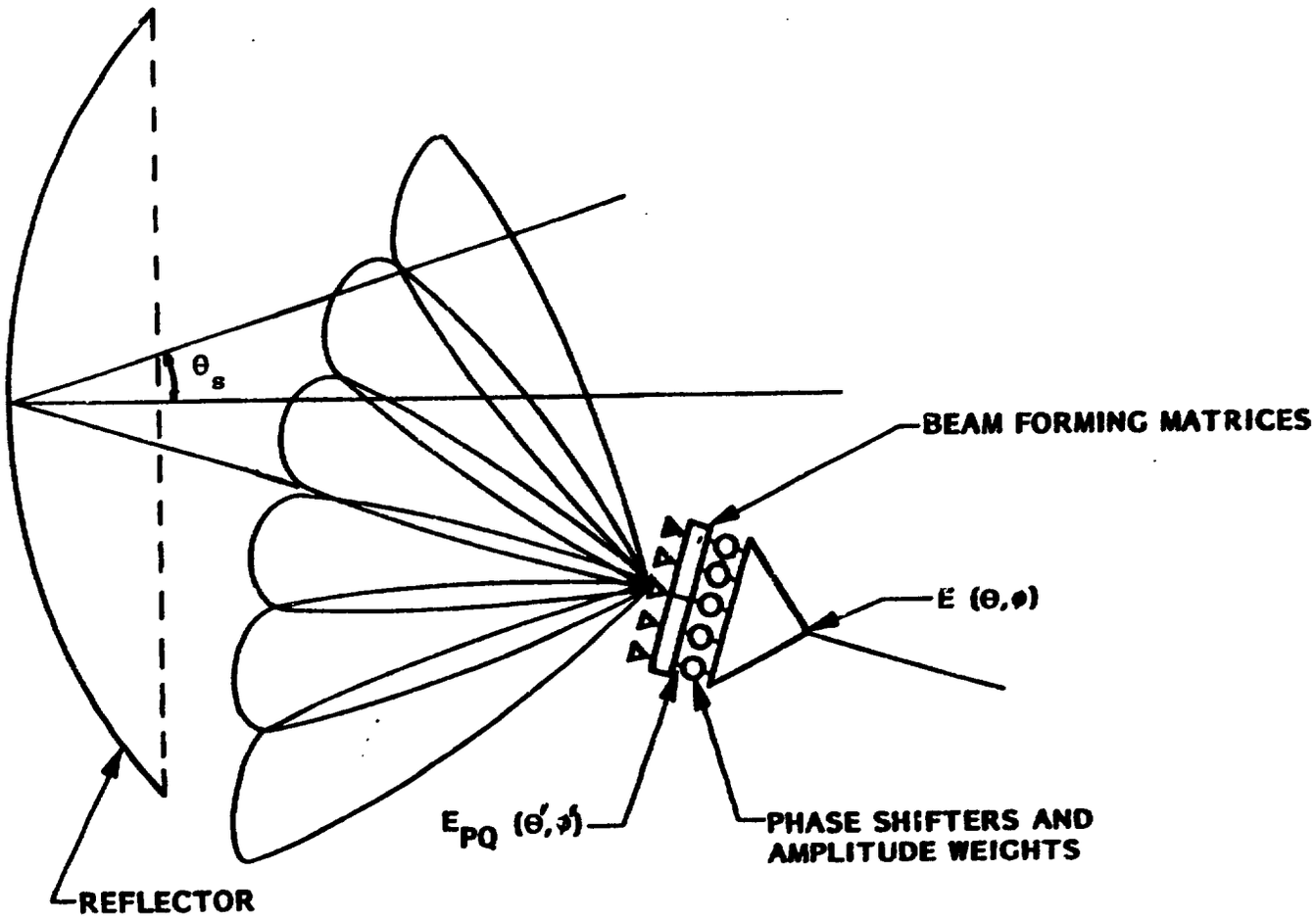

Fig.3 RN^2 triangular array as feed for parabolic reflector

the amplitude and phase distortion, the complex weights can also be used to control the aperture plane distribution. In Fig.4 only one beam from the feed array is shown to illustrate how to determine the complex weights. The complex weights, W_{pq} , to correct the amplitude and phase distortion can be considered as consisting of two parts : (1) the coma weights, W^c_{pq} , which corrects the distortion due to high order terms in the phase distribution (mainly, the coma distortion) and (2) the taper weights ,W^t_{pq} , which yields the correct tapered distribution on the projected aperture plane which is perpendicular to the direction of scan. W_{pq} is then the product of W^c_{pq} and W^t_{pq} . The coma weights, W^c_{pq} , are obtained by the method of complex conjugate matching,i.e. the weights ,W^c_{pq} , are equal to the complex conjugate of the focal region distribution at the feed location[6] . The taper weights, W^t_{pq} , in the present work, are determined by tracing the opitcal ray of the beam peak. As shown in Fig.4 , the ray going through the beam peak reaches the reflector at (x_r,y_r,z_r). This point is then projected to the aperture plane which is perpendicular to the direction of scan. Let the projected point be denoted as (x_a,y_a,z_a). The desired distribution on the aperture plane can be any distribution so long the distribution selected can produce the desired sidelobe level. In present work, zero order Sonine circular aperture distribution is selected. For different sidelobe level, only the constant in the Sonine distribution needs to be changed. The location of (x_a,y_a,z_a) determines the taper weight for beam pq.

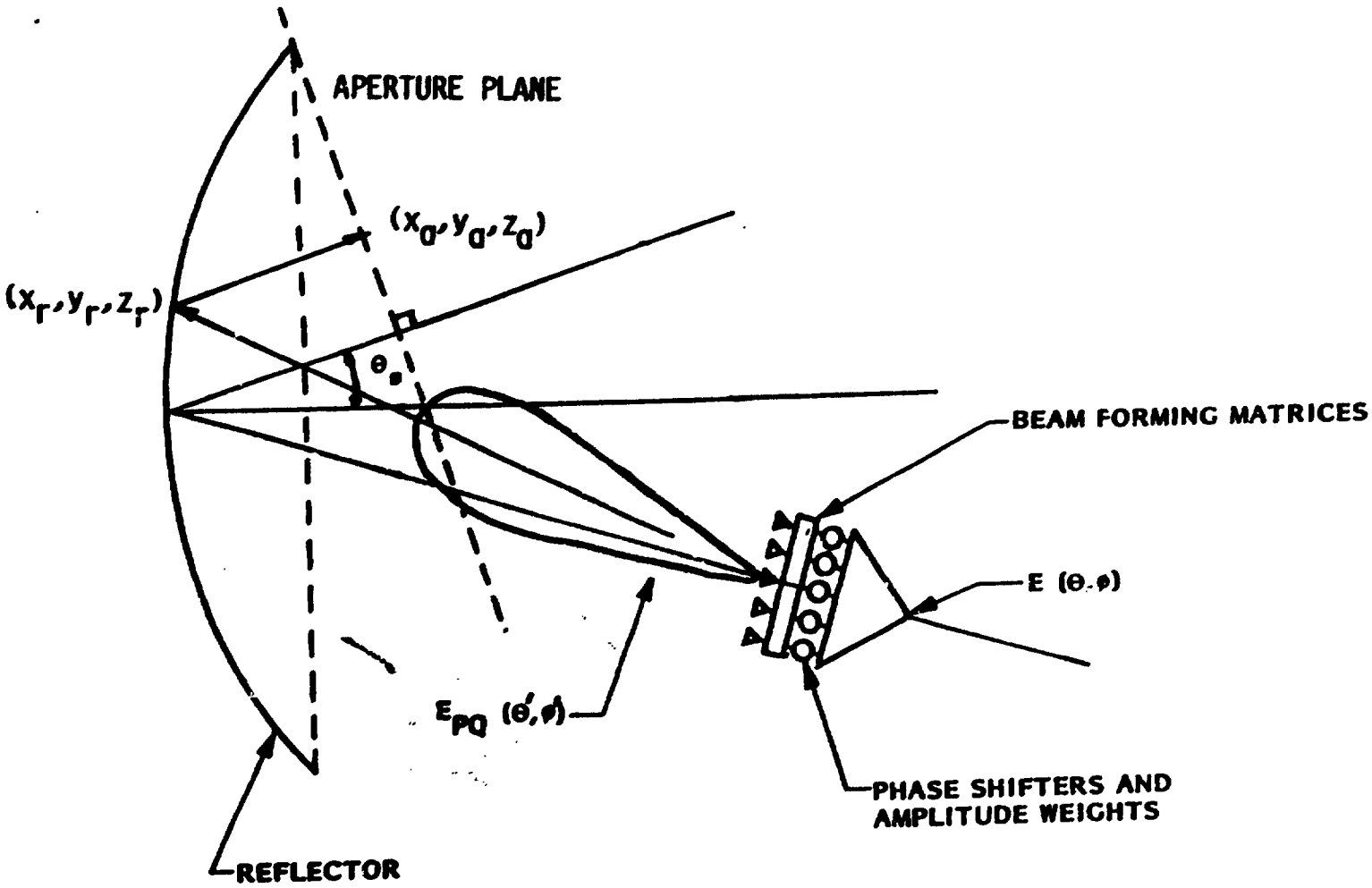

Fig.4 Beam PQ and tapered aperture distribution

The coma weghts alone should produce a uniform, constant phase aperture plane distribution, if the number of beams is sufficiently large. The taper weights then change the aplitude distribution of the aperture plane distribution from uniform to a tapered one to produce low sidelobe pattern.

3. Computed Results

Computer programs have been developed to compute the secondary far field pattern of the reflectors with RN^2 triangular array as feed. The numerical technique used in the computer program is the recently developed Fourier-Bessel series representation technique[6]. In this Fourier-Bessel technique the integrand in the physical optics integral is first expanded into a two dimensional Fourier series, of which the coefficients can be found very efficiently using the well established Fast Fourier Transform algorithm. The integration is then carried out analytically. This new numerical technique is versatile, fast and economical to use.

Fig.5 shows the on axis secondary far field pattern using different number of feed elements. The reflector diameter is 360 inches, focal length is 172.9 inches and is operating at 15 Ghz. The number of feed elements shown in Fig.5 is 12,27,48,75 and 108 (R = 3 and N = 2, 3,4,5 and 6). The spacing is all five feed arrays is 0.6 inches. With this array spacing, all the beams produced by the feed array just cover the whole reflector. In the case of 27-element feed array, the

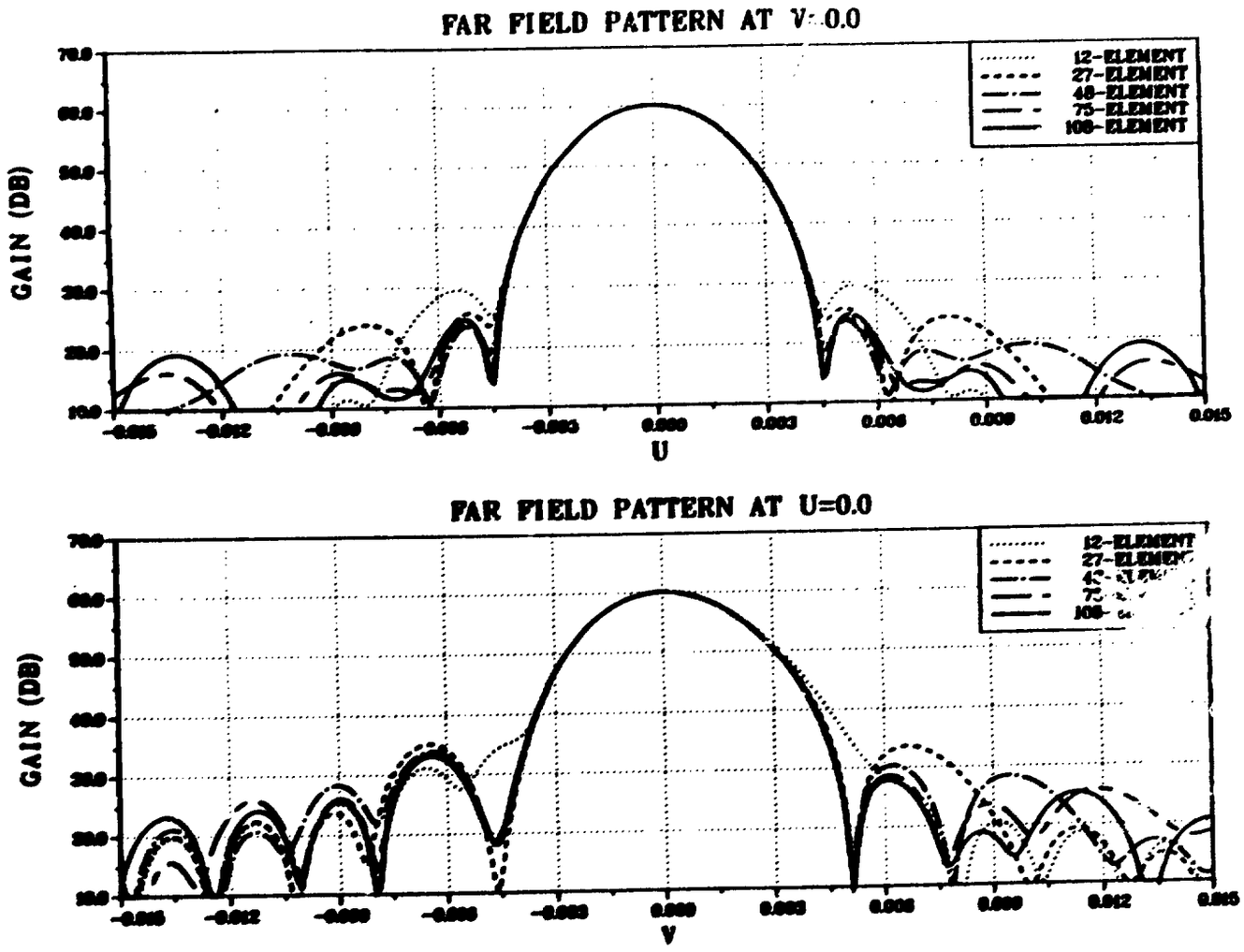

Fig.5 Secondary pattern using different number of feed elements. No scan
D= 360" F/D= 0.48 Freq= 15 Ghz Array spacing= 0.6"

beam distribution is shown in Fig.2 . There are some grating lobes in the real space, but none on the reflector. The individual feed element used is the TE_{11} mode long conical horn, of which the radiation pattern can be found in Reference 7. A -30 dB sidelobe level is desired in this case. However, from Fig.5, a sidelobe level of -25 db is achieved. It is interesting to note that once the number of feed elements reaches 27, the sidelobe level does not change substantially with increasing number of feed elements.

In Fig.6 ,the same reflector and feed arrays as those in Fig.5 are used, but with the beam scanned to two degrees. In terms of beamwidth (which is λ/D), this is a case of 16 beamwidth scan. Fig.6 (a) gives the pattern in the plane of scan and Fig.6 (b) gives the pattern in the plane which is perpendicular to the plane of scan. Here, again, a -30 dB sidelobe is desired. From Fig.6 , the scan loss is almost none and the sidelobe level of -25 dB is achieved if 108 elements are used. However, for a sidelobe level of -20 dB, only 27 elements are needed.

For a beam scanned to four degrees (32 beamwidths) with the same reflector, the pattern is shown in Fig.7. The scan loss is about 2 dB in this case. Except for 12-element feed array, a sidelobe level of -20 dB is achieved. The larger number of feed elements, the narrower beam width and hence higher peak gain. Just as in the previous two cases, the sidelobe level does not reduce substantially with increasing number of feed elements.

In the above three cases, the feed array shadow blockage is consi-

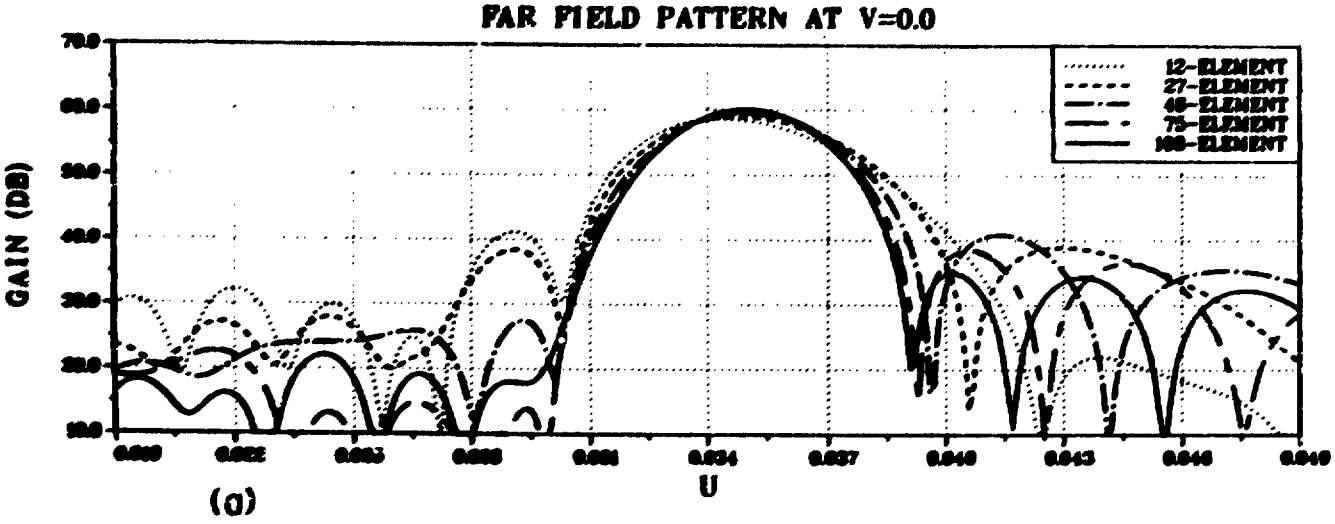

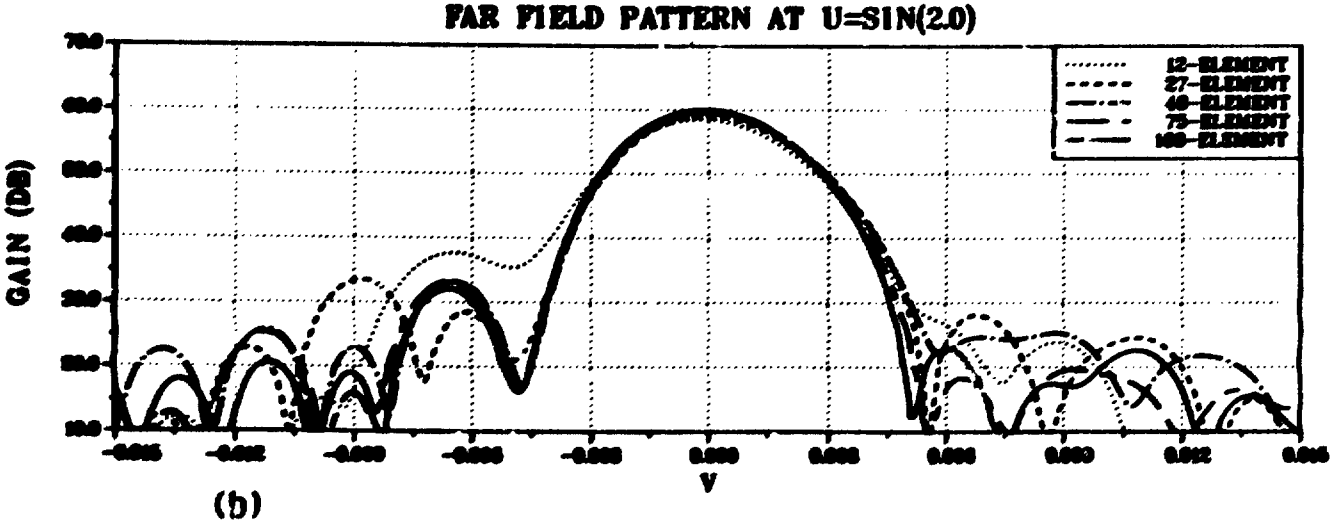

Fig.6 Secondary pattern using different number of feed elements. 2.0 degree scan
D= 360" F/D= 0.48 Freq= 15 Ghz Array spacing= 0.6"

(a) pattern in the plane of scan

(b) pattern in the plane perpendicular to the plane of scan

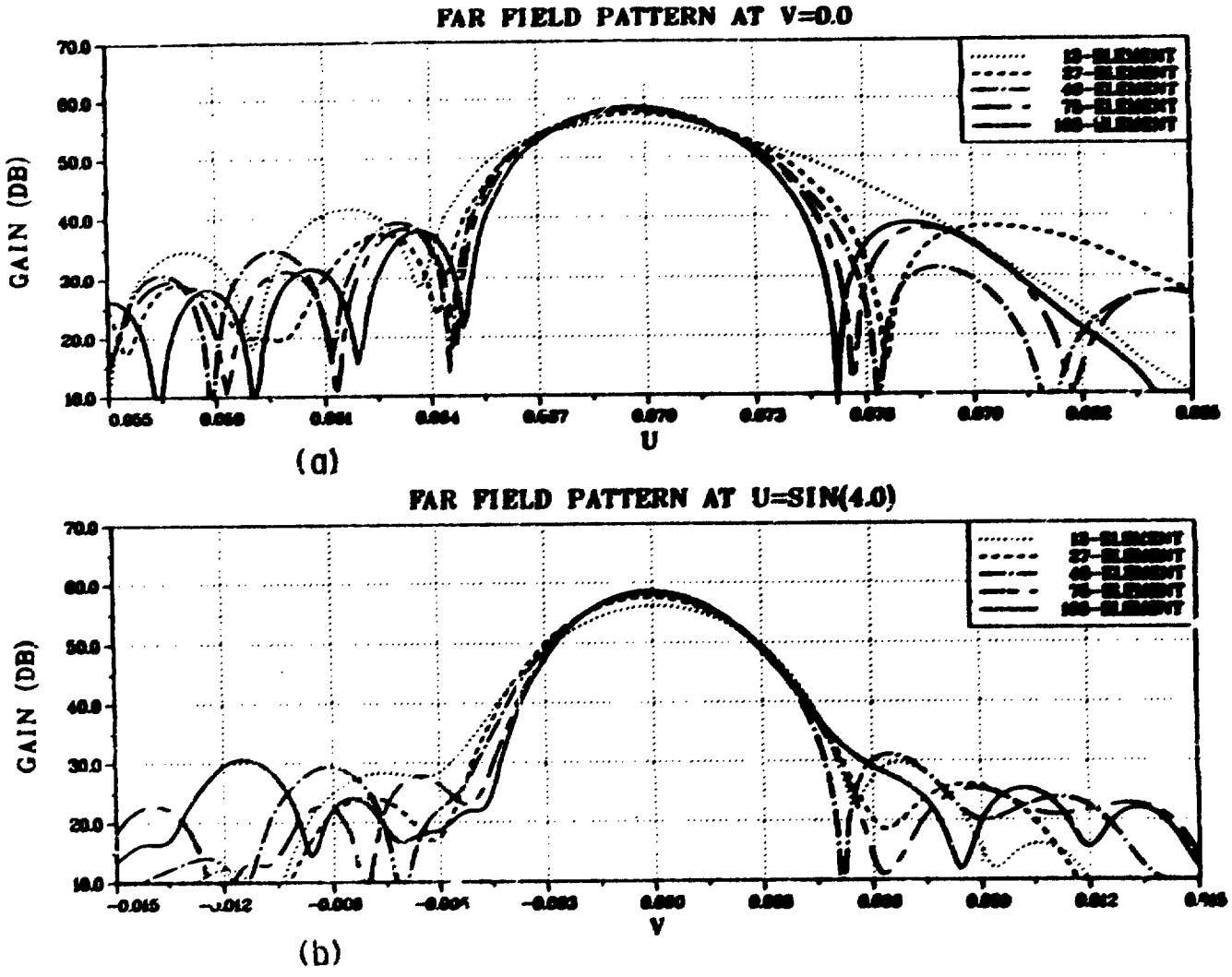

Fig.7 Secondary pattern using different number of feed elements. 4.0 degree scan
D= 360" F/D= 0.48 Freq= 15 Ghz Array spacing= 0.6"
(a) pattern in the plane of scan
(b) pattern in the plane perpendicular to the plane of scan

dered in the computation. For the case of 108-element feed array, the diameter of the circle that just covers the feed array is only 3.6 inches. Compared with the reflector diameter of 360 inches, the effect of blockage is not significant.

4. Comments and Conclusion

It has been shown that low sidelobe scanning beams for parabolic reflectors can be achieved by using the RN^2 multiple beam triangular array as feed. Much more work still needs to be done. The way to determine the taper weights should be improved. Instead of just using optical rays to determine the location of primary beam peaks to determine the taper weights, a more sophisticated algorithm should be developed to include the amplitude and phase distortion over the main beam region. Other future work includes : (1) the effect of using other desired aperture plane distribution ; (2) the effect of the array spacing on the secondary far field pattern, especially the sidelobe level; (3) the location of the feed array for scanning beams and (4) the possible effect of feed element pattern on the sidelobe level of the secondary far field pattern. The technique presented in this paper can also be applied to other type of reflectors, such as spherical reflectors.

With the fast and economical Fourier-Bessel numerical technique now available, the above-mentioned work can be carried out without incurring high computational cost.

References

1. Rudge, A.W. and Withers, M.J. (1971) New technique for beam steering with fixed parbolic reflector, Proc. IEE ,vol.118,pp857-863

2. Hung, C.C. and Chadwick, G.G. (1979) Corrected off-axis beams for parabolic reflectors. Paper presented at the IEEE/APS International Symposium, Seattle, Washington.

3. McFarland, J.L. (1978) Derivation of the feeding matrix for $3N^2$ multiple beam array family. Lockheed Missiles and Space Company Report, D522569

4. McFarland, J.L. (1979) The RN^2 multiple beam array family and beam forming matrix. Paper presented at the IEEE/APS International Symposium, Seattle, Washington.

5. Gee, W and McFarland, J.L. (1981) A generalized algebraic synthesis procedure for an RN^2 multibeam matrix network. Lockheed Missiles and Space Company Report D714648.

6. Hung, C.C. and Mittra, R. (1982) Secondary pattern and focal plane distribution of reflector antennas under wide angle scanning. Paper presented at the IEEE/APS International Symposium, Albuquerque, New Mexico.

7. Silver, S. (1949) Microwave antenna theory and design. McGraw-Hill, New York, pp. 336-341.

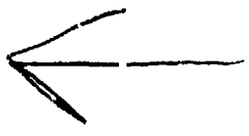

AD P001121

ADVANCED 30/20 GHz MULTIPLE BEAM ANTENNAS FOR COMMUNICATIONS SATELLITES

by

Royce W. Myhre
National Aeronautics and Space Administration
Lewis Research Center
Cleveland, Ohio 44135

E-1365

1.0 ABSTRACT

Advanced offset-fed spacecraft antenna systems are being developed for the National Aeronautics and Space Administration (NASA) that will provide multiple radiating fixed spot-beams and regional coverage scanning beams for use on communications satellites operating in the 30/20 GHz frequency bands. Design concepts under development utilize two separate spacecraft antenna systems, one uplink at 30 GHz and the other a downlink at 20 GHz, where each antenna provides multiple fixed and scanning beams.

Parallel contracts were awarded to the Ford Aerospace and Communications Corporation and TRW-Electronic Systems Group to develop the Multibeam Antenna (MBA) technology. Both contractors have completed configuration trade-off studies and breadboarding

AVAILABLE COPY

of critical technology components, and are now fabricating and testing proof-of-concept (POC) models to demonstrate the technology feasibility.

Technology developments required for the proposed systems will be presented, along with each contractor's progress to date. The new technology development areas discussed include:

1) Offset Cassegrain and shaped reflector systems for narrow beams with low sidelobes and wideangle off-axis scan.

2) Diplexed beam forming networks for dual polarization, low sidelobes, and fixed and scan-beam operation.

3) Fast switching networks for scanning beams.

4) Fabrication of precision feed components and large offset reflectors.

(Another paper, "Application of MMIC Modules in Future Multiple Beam Satellite Antenna Systems" by J. Smetana describes NASA's investigation of MBAs using MMIC feed systems)

2.0 INTRODUCTION

The continued rapid growth of communications message traffic (voice, data, and video) requires the use of additional satellite communications frequency bands before the 1990 decade. The satellite communications bands currently in use at 4 and 6 GHz are already crowded and require the implementation of operational systems at 12 and 14 GHz. With the present constraints on the 11.7 to 12.2 GHz downlink band, market study projections (contracts NAS 3-21359 and NAS 3-21366) indicate a band fill-up by the 1990 decade, requiring alternate frequency bands for expansion of satellite services. The capacity of present 6/4 and 14/12 GHz satellite communications systems are constrained by:

- Limited bandwidth available in these frequency bands.
- Large beamwidths resulting from reflector size constraints.
- Lack of flexibility to reconfigure the antenna patterns for more efficient use of RF power and frequency spectrum.
- Limited orbital positions available for satellite operating in C and Ku band frequencies.

Thus, the next higher frequency bands allocated for this purpose are the 30/20 GHz bands.

The 30/20 GHz system offers 2.5 GHz bandwidth for both uplink and downlink communications, approximately five times greater than the existing 6/4 and 14/12 GHz systems. More importantly, it permits frequency reuse by means of multiple spot beams or shaped beams for large volume trunking service, and allows multiple scanning beams to serve a large number of small volume traffic users on a time division multiple access (TDMA) basis.

Current NASA sponsored communications R&D Program efforts are aimed at developing the technology required for commercial 30/20 GHz satellite configurations which will provide both trunking and scanning-beam service applications. The trunking beams will be directed to major cities of the Continental United States (CONUS) for large volume traffic, and the scanning beams will each cover sectors of CONUS for individual communications services, all at minimum RF radiated power from the spacecraft. Spacecraft systems for both trunking and scanning-beam services are being configured to permit maximum frequency reuse for conservation of the frequency spectrum. In order to implement frequency reuse for the 30/20 GHz bands, new spacecraft antenna technologies are required wherein a number of independently fixed and/or scanning beams will be radiated from a geostationary satellite. The efforts described in this paper are to develop and demonstrate the necessary antenna technologies which will permit multiple

beams at higher frequencies and will allow maximum frequency reuse to be implemented. Other technology areas that are being pursued under separate contract efforts for the 30/20 GHz communications satellite program include: (1) baseband processor, (2) IF matrix switch, (3) low noise receivers, and (4) RF power amplifiers, both traveling-wave-tube (TWT) and solid-state IMPATT and GaAs FET transmitter devices.

The multiple-beam-antenna (MBA) parallel contract efforts described in this paper are being conducted under NASA contracts NAS 3-22498 with the Ford Aerospace and Communications Corporation (FACC), Palo Alto, California (Ref. 1) and NAS 3-22499 with TRW-Electron Systems Group (ESG) Redondo Beach, California (Ref. 2). Both contracts were started in July 1980 for a thirty-two (32) month period of performance, with the efforts funded by NASA Lewis Research Center under NASA's Advanced Communications Program Office.

3.0 OBJECTIVES AND REQUIREMENTS

The primary objectives of these contract efforts are to (1) perform technology trade-off studies of multibeam antenna systems capable of providing a number of fixed and scanning beams from a geostationary communications satellite operating at the 30/20 GHz

frequency bands, (2) evaluate and select through analytical programs the concepts that will provide optimum performance at minimum complexity, weight and cost, (3) breadboard, test and evaluate those items that are considered critical technologies in the development program, (4) fabricate and test proof-of-concept(POC) model antenna systems to demonstrate the technology, and (5) provide data inputs for designing flight hardware for a 30/20 GHz Advanced Communications Technology Satellite (ACTS) to be flown in the late 1980s.

A typical spacecraft configuration for a 30/20 GHz communications satellite system might look as shown in Fig. 1, where the smaller antenna system would provide the 30 GHz receiver uplink and the larger antenna system the 20 GHz transmit downlink. Preliminary NASA trade-off studies of multibeam antenna spacecraft configurations, link budget gain requirements, terrestrial system sizes and complexities, and proposed cities and user areas to be served, indicated that these antenna systems should have RF gains on the order of 50-53 dB (0.3 degree beam widths) for minimum cost to large numbers of terrestrial station users. These studies also indicated that spacecraft sizes and weights, based on packaging within the shuttle launch vehicle, should be limited to reflector sizes that are a maximum of 14 feet in diameter, again consistent with the concept of high-gain 0.3 degree beamwidth antenna systems.

Table 1 Operational and Demonstration Satellite Multiple Beam Antenna Specifications

ANTENNA CONFIGURATION		TRUNKING FIXED BEAM	CUSTOMER PREMISE SCANNING BEAM
OPERATION FREQUENCY RANGE (GHz)	DOWNLINK UPLINK	17.7 TO 20.2 27.5 TO 30.0	17.7 TO 20.2 27.5 TO 30.0
NUMBER OF BEAMS	OPERATIONAL	18 TX 18 REC	6 TX 6 REC
	DEMONSTRATION	10 TX 10 REC	2 TX 2 REC
MINIMUM PEAK GAIN (dBi)	20 GHz 30 GHz	53 53	50 ± 1 dB RIPPLE 50 ± 1 dB RIPPLE
BANDWIDTH (MHz)	20 GHz 30 GHz	500 500	500 500
POLARIZATION		DUAL LINEAR	DUAL LINEAR
C/I PERFORMANCE (dB)		30	>30
POINTING ACCURACY (DEGREES) RELATIVE TO SPACECRAFT BUS	PITCH & ROLL YAW	±0.02 ±0.4	<0.02 <0.4 [1]
POWER/BEAM (EIRP) dBw		58 65	63-69

3.1 PROPOSED ANTENNA COVERAGES

Fig. 2 illustrates one of the antenna coverage scenarios contemplated for an operational communications satellite system in the 1990s. There are 18 fixed beams for large volume traffic trunking service interconnecting 18 major cities of the CONUS. This 18-city coverage plans would provide approximately 20 percent of the total domestic traffic demand in the United States. The remaining 80 percent would be provided to the small terminal users by six independently scanned beams, each scanning within approximately one-sixth of CONUS on a TDMA basis. The connectivities between the small terminal scanning beams and fixed trunking beams are provided by an on-board processor. The proposed frequencies and coverage plans are:

1) The allocated 2.5 GHz bandwidth for both uplink and downlink is divided into five subfrequency bands. Each subfrequency band has 500 MHz bandwidth.

2) CONUS coverage is divided into six sectors for six scanning beams. The selection of these sector boundaries is arbitrary,, depending on the traffic demand in each of the sectors and the layout of fixed and scanning beam feeds.

3) Within the same scan sector, all fixed beams could be co-polarized. Widely spaced beams with good spatial isolation may operate at the same frequency, but closely spaced beams must operate at a different frequency or be orthogonally polarized to prevent mutual interference.

4) Fixed and scanning beams in the same sector could be of the same polarization and use only frequency for isolation, or could be orthogonally polarized and operated at different frequencies to achieve additional isolation between beams in a given area.

5) The respective scanning beams in adjacent sectors are orthogonally polarized. Unless two scanning beams are momentarily steered to the vicinities of the same boundary at the same instant, combined polarization and spatial isolation will provide over 30 dB isolation between two scanning beams.

This antenna coverage scenario (TRW's approach) requires two frequencies for fixed trunking beams with the possibility of 13 times frequency reuse, and one frequency for scanning beams with six times frequency reuse. The Ford Aerospace approach uses only one frequency for fixed beams providing 18 times frequency reuse, and one frequency for scanning beams with six times frequency reuse.

The design goals for the antenna performance are shown in Table 1. In order to obtain 53 dB gain at the peak of the beams, a four-meter diameter reflector at 20 GHz, and a three-meter diameter reflector at 30 GHz are required to produce 0.3 degree beams. Also, the requirement of a 30 dB carrier-to-interference (C/I) ratio requires large precision offset reflectors for low sidelobe radiation.

3.2 SELECTION OF ANTENNA CONFIGURATIONS

Various antenna configuration were considered for this application, including lens, reflector and array antennas. The reflector antenna approach was chosen because of its light weight, lower cost, wide bandwidth, and design simplicity. Particularly in the millimeter frequency range, it offers the advantages of low feed network losses and higher efficiencies compared with the lens and array antennas. Both contractors have completed extensive computer trade-off studies in optimizing the RF gains for their approaches. Because of the requirement to scan ±12 by ±5 beamwidth for full CONUS field of view, it was particularly important to minimize the scan abberations and thus the scan losses in order to meet the beam RF gain requirements. Each contractor's approach to solving these complex problem areas and their progress to date are described in sections 4 and 5 of this paper.

4.0 FORD AEROSPACE (FACC) MULTIBEAM ANTENNA

The MBA trade-off analysis, design, and performance calculations have been completed by FACC. The selected concept consists of an offset dual-reflector microwave optical subsystem with feed array and multiple-port beam forming network (BFN) (Fig. 3). A unique feature of the FACC concept is the computer-aided synthesis of shaped main and subreflector surfaces to minimize

abberations over the required 12 beamwidth CONUS field of view. Scan loss performance over the 12 beamwidth scan area is less than 1 dB.

The algorithm for complete synthesis of the main and subreflector surfaces is based on minimization of ray path length error surfaces for several specified feed (beam) positions in the reflector system. Thus, the resulting reflector surfaces are not portions of a figure of revolution surface, but are each generally optimized, doubly-curved surfaces. Furthermore, the feed array surface can then be specified as to size, shape (flat, doubly-curved, etc.), position, and orientation with respect to the subreflector surfaces. The dual reflector system then has no true focal point at the zero scan beam position so that worst case defocusing at the edges of the scan field of view is minimized. Other more conventional reflector designs based on classical optics were first attempted, prior to development of the doubly-curved shaped dual reflectors; however, all were found to be less desirable due to their higher scan losses over the CONUS coverage area.

During the early phases of the two parallel contract development efforts, TRW and FACC indicated that both the 20 GHz and 30

GHz antenna systems are directly scaleable between the two frequencies. As a result, FACC selected to concentrate their efforts on the design and proof-of-concept for the 20 GHz transmit antenna system, and TRW chose to develop, fabricate and test the 30 GHz receive antenna system.

4.1 FEED ARRAY

Fig. 4 shows the FACC CONUS coverage feed array for a 20 GHz operational satellite MBA system that develops 18 fixed trunking beams and 6 scanning spot beams. The BFN lattice array as shown uses 480 square radiating elements, where each horn is two (2) wavelengths on a side. A 7-element coherently-driven horn cluster for each beam then produces the 0.3 degree beam with the desired low sidelobes. Each small horn cluster is coherently excited to form each beam via a microwave power dividing circuit with nonuniform amplitude and phase coefficients applied to each element. For example, a 7-element cluster of horns is typically chosen with the central element given most of the excitation power and the six surrounding elements each given a weaker portion of the transmitted power, each with a particular phase value.

For each desired fixed beam location on a city of CONUS, a particular cluster of feed elements must be excited so as to

shape a low sidelobe envelope. A 1-to-7 port nonuniform corporate network is designed for each trunk beam. Since offset reflectors are asymmetric, each beam network coefficient would appear to be different since the abberations for a northeast corner CONUS beam are different from that of a southwest corner beam, etc. With the doubly-curved surface reflector, however, FACC has found the calculated network coefficients to be irtually identical over all of CONUS.

For the scanning beams, each scan sector contains a large number of array elements. For a given instantaneous scan secondary beam position within a given sector, the BFN function is to interconnect the sector input port to a particular 7-element cluster of the elements in the sector array such that the required beam position results. Likewise, for the next desired scan beam position in the sector, the first cluster must be disconnected, the second cluster of seven elements connected and the amplitude and phase coefficients reset to achieve the new beam position. The control system for the scanning beams will allow any one uplink or downlink beam to be independently sequenced to any one of its positions. The dwell time for a beam to be held at any position will be programmable between 10μs and 100μs, and the time to move a beam to any other position will be no greater than 500 Ns. The instructions for the beam scanning

controller will be supplied by an onboard computer. To accomplish the switching and provide the scanning beams, each scan sector contains a number of array elements for connecting a preselected 7-element cluster at any instant.

The output of each switch tree in a sector (Fig. 5) is interconnected by a single 8-1 corporate tree where a combination of VPD tree output ports can be connected to any 7-element cluster in the sector array. Behind each element is an orthomode junction with two ports - one for vertical polarization and the other for horizontal polarization. Each of the OMJ ports is connected to a diplexer. Each diplexer has two ports - one for the fixed beam band and one for the scan beam band. All sector scan network terminals connect only to the scanning diplexer terminals. For those elements contained in a fixed beam cluster, the fixed beam band diplexer port is connected to a fixed beam BFN terminal. Thus, only certain elements are operating as both fixed and scanning radiators. All of the elements, however, will become part of a scan beam cluster at one time or another.

4.2 FACC PROGRESS TO DATE

Extensive computer analysis trade-off studies have been completed for both the operational and the experimental spacecraft systems, based on a number of reflector antenna concepts. These

included the offset paraboloid and feed array, the offset Cassegrain dual reflector, offset Gregorian dual reflector and the offset Schwarzschild dual reflector, each with feed array. Each of these types of focused reflectors was optimized by minimization of calculated ray path errors for various extreme beam positions over CONUS. All were found to have performance deficiencies due to excessive scan beam aberrations over CONUS, or required complex curved feed arrays. As a result, the doubly-curved shaped dual reflector approach employing a flat focal field was developed that would provide off-axis scan with losses of less than 1 dB for CONUS coverage.

Breadboarding and testing on development of critical technology 20 GHz microwave components of the multiport feed array and BFN components have been completed. These include the 7-element cluster, OMJ, diplexer, power dividers, and engineering model ferrite scan beam components, namely, ferrite circulator switches, variable power dividers and variable phase shifters. The 20 GHz ferrite components are being developed by Electromagnetic Sciences (EMS) Corporation, Norcross, Georgia, under subcontract to FACC.

Fabrication of the 20 GHz transmit POC model MBA is now in progress. A 13.5 ft. diameter main reflector and 9.5 ft. x 4.0

ft. subreflector are under construction, with fabrication of aluminum sector plates mounted to a rigid truss structure and milled to mirror surface tolerances. Since these complex reflectors are not surfaces of revolution, their design, manufacturing and optical calibration has been subcontracted to an optical company (Tinsley Corporation, Berkeley, California) for developing the high precision surface areas. Surface tolerances are expected to be held to with .003 inches RMS over the reflecting surfaces in order to minimize off-axis beam RF losses.

A partial feed array and BFN is being fabricated for the POC model, where this subarray can be manually repositioned during the testing program to check all of the fixed beam and scan beam positions. The POC antenna support structure is now in fabrication by FACC, and EMS is under subcontract for the additional ferrite switches, variable power dividers and variable phase shifters.

The FACC anticipated POC BFN component performance is given in Table 2, and the estimated gain performance of the MBA is given in Table 3.

Table 2 Anticipated PCC BFN Component Performance, Ford Aerospace 20 GHz NBA

Characteristic	Switching Circulator	VPD	VPS	Fixed Power Divider
Center Freq, GHz	19.1	18.95	18.95	18.7
Bandwidth, MHz	500	500	500	1300
Insertion Loss, dB	0.1	0.4	0.6	0.2
Isolation, dB	23	20	--	20
Max Power, Watts	30	80	40	50
VSWR, Max	1.15	1.2	1.2	1.2
Switching Time, μs	0.4	0.4	0.4	--
Switching Energy, μJ	40	75	75	--
Range of Adjustment		0, -25 dB	0-360°, 6-Bit	0 - 6 dB
Accuracy		Possible to -30 dB	±2° to ±5°	±0.2 dB
			Over Temp & Freq.	
Size (Excl. Drivers)	.75" X .312"	4" X 1.34 X 0.5"	2.25 X 0.65" Sq.	1 X 1.5 X 0.3"
Driver	4" Sq. X .7"	2 X 4" Sq. X .7"	4" Sq. X 0.7"	--
Temp. Range	0 - 50 C	0 - 50°C	0 - 70°C	-100 to +70°C
Weight, Oz - Complement	2.0	6	1.2	2.0

Table 3 Estimated Gain Performance, Ford Aerospace 20 GHz NBA

	Fixed Beam					Scan Beam		
	Seattle	Near Beam Oklahoma City	Washington, D.C.	Boston	Miami	Seattle	Near Beam Oklahoma City	Miami
Calculated Directivity, dBi	55.1	55.0	56.3	55.2	55.9	55.1	56.1	55.8
Calculated BFN Loss, dB	-1.3	-1.1	-1.3	-1.3	-1.3	-3.2	-3.2	-3.2
Gain, dBi	53.8	54.5	54.0	54.1	54.5	51.9	52.6	52.6
	BFN Loss Breakdown, dB							
			OMJ (1)		-0.1	OMJ (1)		-0.1
			Diplexer (1)		-0.5	Diplexer (1)		-0.5
			Hybrid (2)		-0.2	Switches (6)		-0.3
			3 Way Divider (1)		-0.2	VPS (1)		-0.6
			Comm Waveguide		-0.3	VPD (3)		-1.2
					-1.3	Comm Waveguide		-0.3
								-3.2 dB

5.0 TRW MULTIBEAM ANTENNA

The trade-off analysis, design and performance calculations have been completed by TRW for the MBA concepts, where the selected approach is an offset Cassegrain reflector geometry with two hyperbolic subreflectors stacked to form a double-layer bifocal subreflector system, and two orthogonally polarized feed assemblies diplexed by the front wire-grid subreflector (Fig. 6). Each of the two feed assemblies consist of multiple fixed and scanning beam feed cluster for low sidelobe operation. The uniqueness of this arrangement is that it enables multiple fixed and scanning beams to be radiated through a large common aperture and permits the multiple beam feed assemblies to be placed close to the spacecraft body. The front gridded polarizer focuses the vertically polarized field to a point located on the right side of the parabolidal axis and is transparent to the horizontally polarized field. The back solid surface subreflector focuses the horizontally polarized field to the left. Thus, two orthogonally polarized feeds are completely separated into two focal point fed areas. In this MBA approach, the high gain characteristics of the BFN compensate for the increase in scan loss for off-axis scanned beams when using the Cassegrains paraboloid reflector approach.

During the analytical trade-off studies, two separate and complex computer programs were used to evaluate the performance

and cross-check the results of this complex antenna system - a multireflector ray tracing program and a vector diffraction computer program.

The ray tracing program does not take into account the edge diffraction and the vector nature of the scattering patterns. Nevertheless, it is a simple and useful tool for determining the subreflector boundary, best feed locus, and optimum feed orientation of each off-axis scanned beam in the preliminary design stage. For example, to improve the wide angle scanning capability of this antenna, the subreflector is substantially oversized to reduce the spillover loss from the main reflector. Although the ray tracing program provides more physical insight for optimizing the reflector/feed geometry, the analysis could not be used to determine the best feed position. As a result, the vector diffraction program using physical optic (PO) or geometric theory of diffraction (GTD) analysis was used for accurate prediction of the far-field radiation patterns. And because of the oversized hyperbolic subreflector, the PO program with the capability for computing scattered fresnel fields was used to optimize the scanning beam performance.

5.1 FEED ARRAY

Fig. 7 shows the TRW vertically polarized CONUS coverage feed layout for a 30 GHz MBA operational spacecraft providing 18

fixed trunking beams and 6 scanning spot beams. A similar type layout will provide the horizontally polarized scan beams and trunk beams in the alternate sector coverage areas. There are three types of feed clusters in this assembly: multimode conical horns for widely spaced trunking beams, diplexed circular horn clusters for closely spaced cities, and an array of square horns for scanning beams.

Since the low sidelobe beams produced by two adjacent horns are approximately two half-power beamwidths apart, any two cities separated by less than two beamwidths must use a cluster of feeds and diplexers to obtain the overlapping beams unless they are orthogonally polarized. For example, a 16-element diplexed feed cluster is being used to obtain three contiguous low sidelobe beams for Boston, New York and Washington, D.C coverages (Fig. 8). The beams for Boston and Washington will be copolarized and operate at the same frequency; the beam for New York coverage will be at a different frequency, but due to the close proximity of the three cities will share some of the same feed horns through waveguide diplexers.

The scanning beam beam-forming network (BFN) is the more complex of these three types of feeds. In the TRW approach, the feed horns and the feed network are divided into three groups,

and the feed horns are arranged in an equilateral triangular lattice. A scanning beam can be formed in the reflector by energizing any combination of three adjacent horns in the array aperture. Each horn , however, can only be energized by one of the three BFN branches, with the other two adjacent horns energized by the other two branches. Consequently, for the 19-element scan beam array being developed for the POC model, only two variable power dividers, one variable phase shifter, and 21 circulator switches are required to scan a beam to any location within the scan sector. Because of the reduction in component requirements, this feed concept will reduce the RF losses as well as the power consumption in the driver and control electronics. The estimated loss in the 19-element BFN in 2.8 dB.

5.2 TRW PROGRESS TO DATE

TRW has also completed extensive computer analysis trade-off studies for both the operational and the experimental spacecraft MBA concepts on a number of different multireflector antenna configurations. These configurations included concepts using four separate antenna systems, to concepts combining both the 20 GHz and 30 GHz frequencies into a single complex antenna system with a dichroic outer-ring main reflector to achieve the 0.3

degree beamwidths at each of the frequencies. The offset Cassegrain with the double-layer bifocal subreflectors and separate 20 GHz and 30 GHz antenna systems was selected as the optimum approach in order to reduce the complexity of each polarized feed cluster and minimize the overall losses in the BFN. The off-axis scan losses at ±12 beamwidths for this approach are expected to be approximately 1.4 dB.

Breadboarding and testing of the critical technology microwave components at 30 GHz has been completed. These include a section of a polarization wire-grid subreflector, multimode horns with sidelobes near -40 dB, diplexed feed cluster for forming three contiguous beams, two and three way power dividers, and 30 GHz engineering model ferrite circulator switches, variable power dividers and variable phase shifters. The 30 GHz ferrite components are being developed by Electromagnetic Sciences (EMS) Corporation under subcontract to TRW.

Fabrication of the 30 GHz receive POC model MBA is now in progress. A 9.5 ft. diameter graphite fibre reinforced plastic (GFRP) main reflector with surface accuracies of .003 inches RMS has been completed. The solid surface and wire-grid subreflectors are near completion, and the POC model support structure weldment assembly is near completion. The 16-element

diplexed feed cluster for the Boston/New York/Washington beams is now in testing, and a 19-element scanning beam-forming network using ferrite switches, power dividers and phase-shifters is now under subcontract to EMS. These component assemblies when completed will be assembled into a POC model that will be capable of producing 10 fixed trunk beams and 1 scan beam. These horn and cluster assemblies will be relocatable on the feed support structure in order to test alternate beam positions and adjacent beam interference conditions.

The TRW anticipated POC BFN component performance is given in Table 4, and the estimated gain performance of the MBA is given in Table 5.

Table 4 Anticipated POC BFN Component Performance - TRW 30 GHz MBA

CHARACTERISTIC	SWITCHING CIRCULATOR	VPD	VPS	3-WAY PWR DIVIDER
CENTER FREQUENCY, GHz	28.6	28.6	28.6	28.6
BANDWIDTH, MHz		1500	1500	2500
INSERTION LOSS, dB	0.15	0.6	0.85	--
ISOLATION, dB	28	25	--	--
MAX POWER, WATTS	1	1	1	--
VSWR, MAX	1.1	1.1	1.2	1.12
SWITCHING TIME, μs	0.4	0.5	0.5	--
SWITCHING ENERGY/μJ	17	45	70	--
RANGE OF ADJUSTMENT	--	-25 dB	0-360°6-bit	--
ACCURACY	--	--	3°	--
SIZE (EXCL. DRIVERS)	.85x.85x.5"	.75x1.13x3.04"	.75x.88x2.02"	2.23"lg
TEMP RANGE	0-50°c	0-50°c	0-50°c	
WEIGHT, OZ-COMPONENT	0.35	1.9	1.2	3.0

Table 5 Estimated MBA Gain Performance, TRW 30 GHz MBA

BEAM LOCATION	FIXED BEAM					SCAN BEAM	
	θ=0°	SEATTLE	S.F.	MIAMI	BOSTON	θ=0°	θ=3.5°
DIRECTIVITY, dBi	56.7	55.4	55.0	55.0	54.2	56.7 ±1.0	53.0 ±1.0
BFN LOSS, dB	2.8	2.8	2.8	2.8	1.2	2.8	2.8
GAIN, dBi	53.9	52.6	52.2	52.2	53.0	51.9 ±1.0	50.2 ±1.0

ANTENNA LOSS BUDGET	DUAL MODE HORN	CLUSTER OF HORNS	SCAN BEAM ARRAY
POLARIZATION GRID	0.25	-	0.25
REFLECTORS	0.1	0.1	0.1
WAVEGUIDES (0.25 dB/FT)	0.15	0.5	0.5
FEED HORN (IDEAL)	0.3	0.3	0.3
DIPLEXER (≤ 0.5)	-	0.3	-
SWITCHES (3)	-	-	0.45
VPD'S (2)	-	-	1.2
TOTAL LOSS, dB	0.8 dB	1.2 dB	2.8 dB

6.0 POC TESTING PROGRAM

Fabrication of the POC models by the contractors will be completed during October-November 1982. Far-field (F-F) range testing at the contractors' facilities, for various levels of testing and beam configurations (trunk beams only, scan beams, and combined testing), will be conducted during the period October 1982 through April 1983.

On delivery of the POC models to the NASA Lewis Research Center in June 1983, verification testing will be conducted in NASA's near-field antenna test range as part of the overall 30/20 GHz communications satellite feasibility program to provide data for design of flight hardware.

7.0 CONCLUSIONS

Multiple fixed and scanning beams can be radiated effectively through a large common aperature by means of offset fed multi-reflector antenna arrangements. The technologies required for successful spacecraft MBA systems have been validated by fabrication and testing of breadboard hardware in the critical technology areas. Proof-of-concept models are now being fabricated under parallel contract efforts, using two distinctly different approaches to offset-reflector technologies in demonstrating multibeam antenna capabilities. Current development

efforts will culminate in extensive range testing and evaluation, and will conclude with detailed technical reports and recommendations on multibeam spacecraft antenna systems.

Continuations of advancements in multibeam antenna technology beyond the efforts described in this report are now in process at NASA that will initiate phased array feed networks for offset-fed multireflector antenna systems where feed arrays are composed of distributed monolithic amplifier devices. These future technology approaches will reduce the spacecraft BFN losses and provide higher overall spacecraft efficiencies for improved advanced communications links.

8.0 REFERENCES

1. Scott, W.G. (1982) 30/20 GHz Communication Satellite Multibeam Antenna, Paper presented at the Ninth AIAA Communications Satellite Systems Conference, New Orleans, LA, January 1982, NAS 3-22498

2. Chen, Dr. C.C. (1982) Advanced 30/20 Multiple Beam Antenna for Future Communications Satellites, Paper presented at the IEEE International Conference on Communications, Philadelphia, PA, June 1982, NAS 3-22499

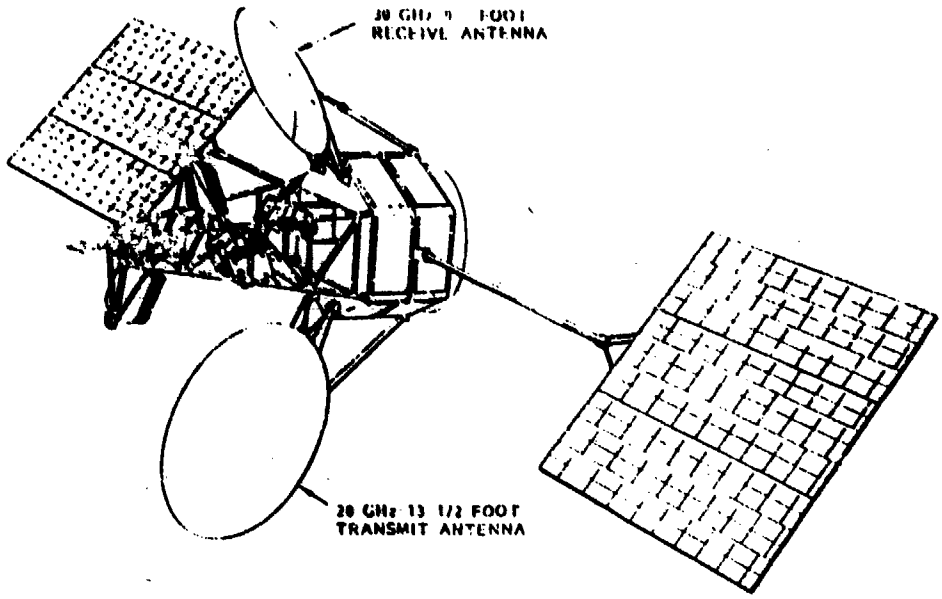

Figure 1. - Proposed 30/20 GHz experimental flight model advanced communications technology satellite.

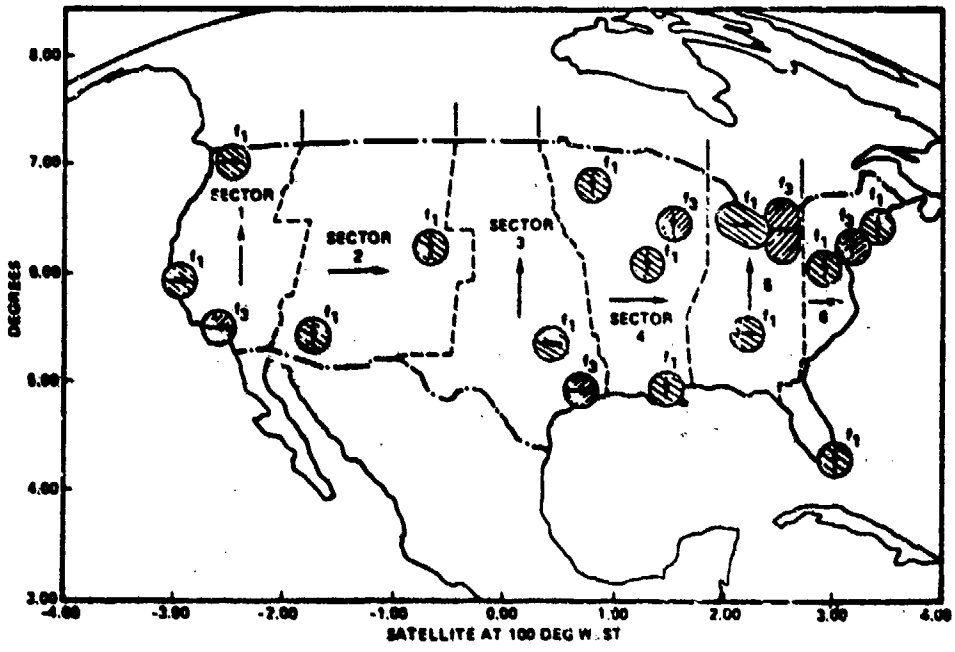

Figure 2. - 18 fixed beams and 6 scanning beams antenna coverage scenario.

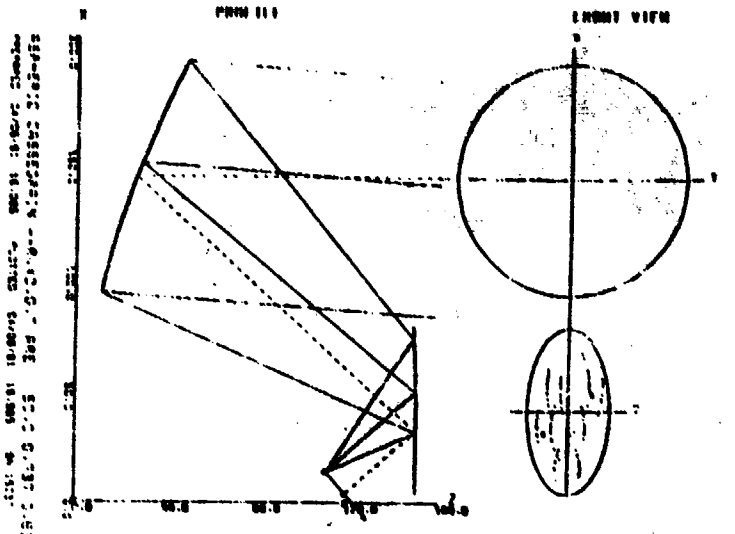

Figure 3. - FACC design of offset dual-shaped reflectors for 20 GHz MBA spacecraft antenna.

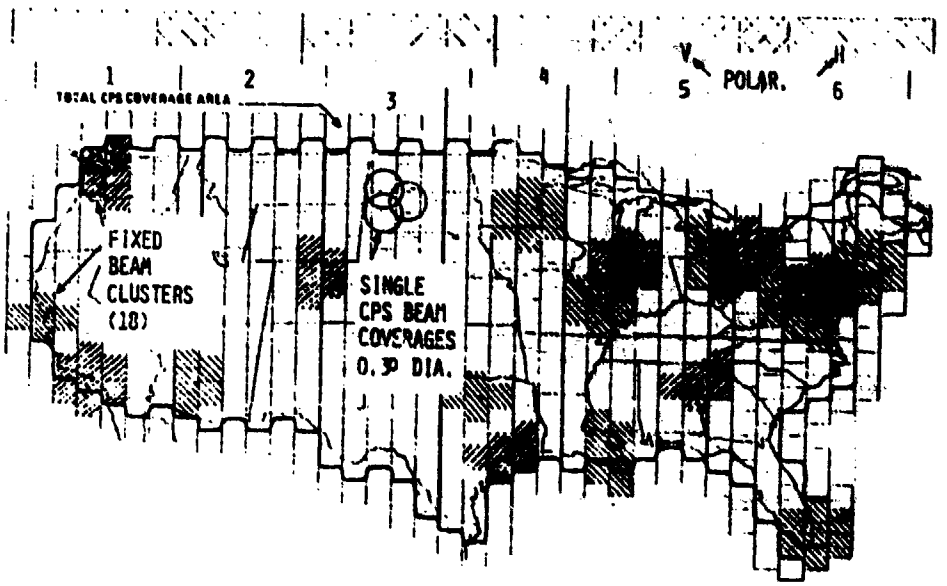

Figure 4. - FACC CONUS coverage feed array for 20 GHz MBA spacecraft antenna.

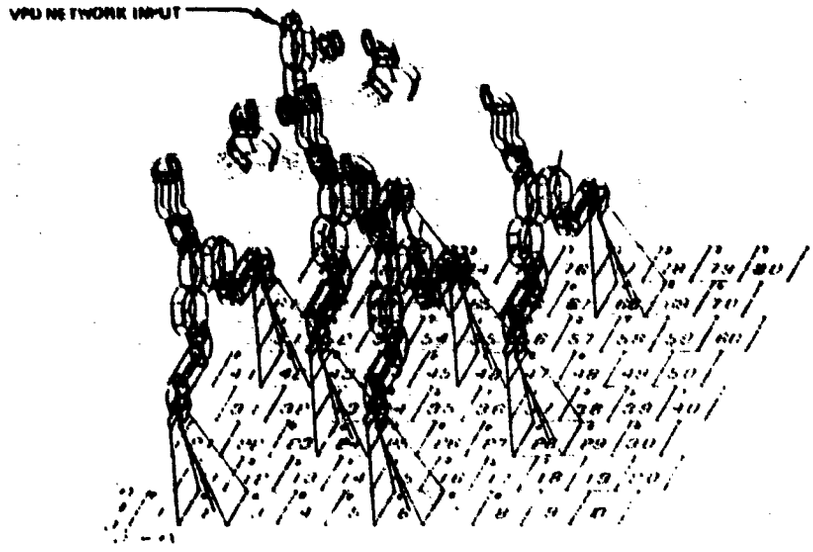

Figure 5. - FACC BFN switching tree for 20 GHz MBA spacecraft antenna.

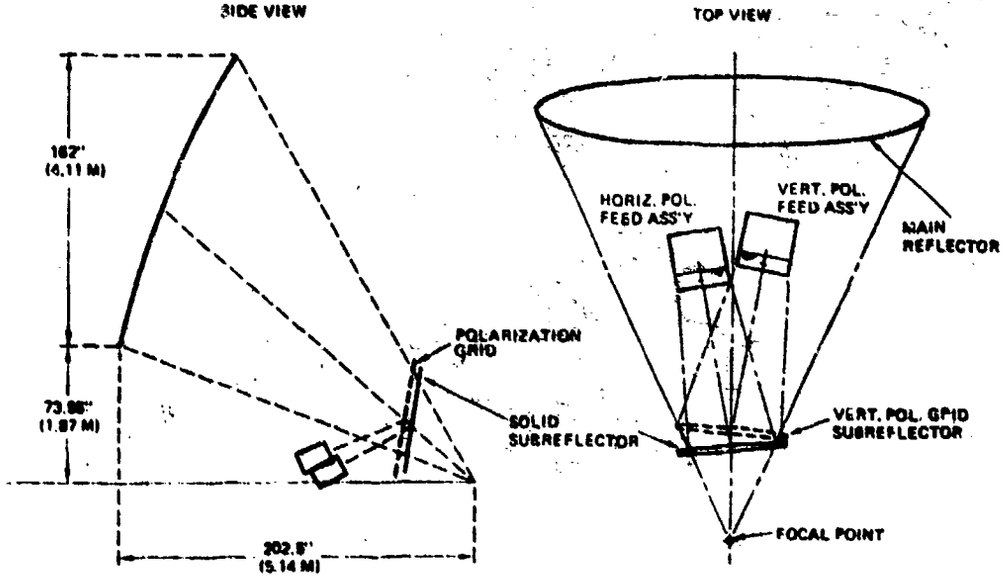

Figure 6. - TRW offset dual-subreflector for 30 GHz MBA spacecraft antenna.

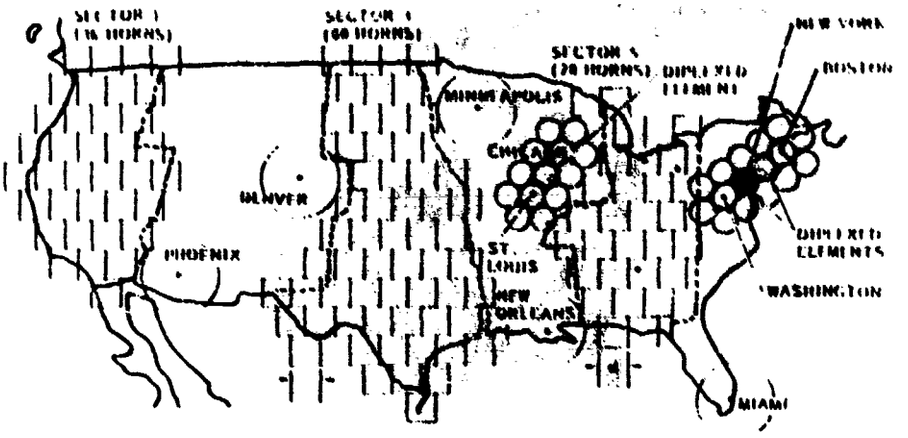

Figure 7. - TRW feed layout for 30 GHz MBA spacecraft antenna.

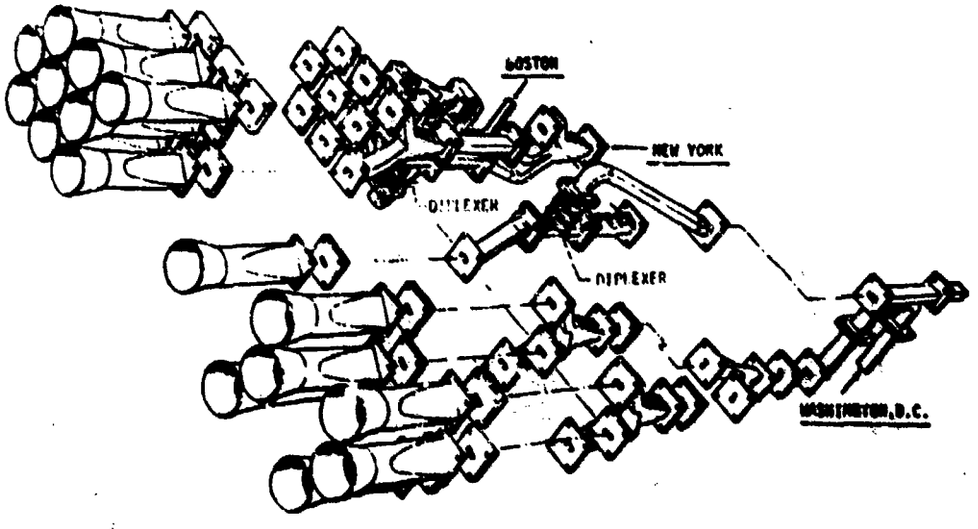

Figure 8. - TRW diplexed fixed beam feed cluster for Boston, New York, and Washington, D.C. for 30 GHz MBA spacecraft antenna.

AD P001122

R-82018

INSTANTANEOUS POLARIZATION MEASUREMENT SYSTEM

William McNaul

Cubic Corporation

ABSTRACT

This paper describes a technique for measuring the polarization of pulsed RF radiations arriving at a collection antenna which is separated from the receiver system by a single RF channel. The technique shows how new technological advances in microwave solid-state devices and microprocessors may be applied to the field of microwave propagation measurements.

1.0 INTRODUCTION

The literature [1], [2] describes several methods for measuring RF polarization in a laboratory environment where the radiation can be controlled by the experimenter. Consider, however, the situation where RF pulse width, frequency, PRI and time of arrival is random. When the measurement conditions are further complicated by the presence of a single RF path between the antenna and receiver system, all traditional polarization measurement schemes must be discarded.

A system for the measurement of RF field polarization under these conditions is presented here. By quantizing the polarization into seven basic states, this technique overcomes the difficulties imposed by random RF parameters and single-channel transmission.

1.1 THEORETICAL BACKGROUND

The E-field of an arbitrary RF wave traveling in the +Z direction may be expressed as:

$$\bar{E} = \tilde{E}_v \bar{U}_x + \tilde{E}_h \bar{U}_y$$

where $\tilde{E}_v = E_v \cos(wt + \alpha_v)$

$\tilde{E}_h = E_h \cos(wt + \alpha_h)$

$\tilde{E}_v$ and $\tilde{E}_h$ are the phasor representations of the RF field oriented vertically and horizontally, respectively. They carry the relative amplitude, M, and relative phase, $\Delta\theta$ of the two selected orthogonal components of the RF wave such that:

$$M = 20 \operatorname{Log} \frac{E_v}{E_h} \quad (2)$$

and $$\Delta\theta = \alpha_v - \alpha_h \quad (3)$$

A useful graphic representation for the polarization of an RF wave is shown in Figure 1a. Here, relative phase, relative amplitude, and other special polarization parameters such as axial ratio, polarization ellipse, slant and sense are presented.

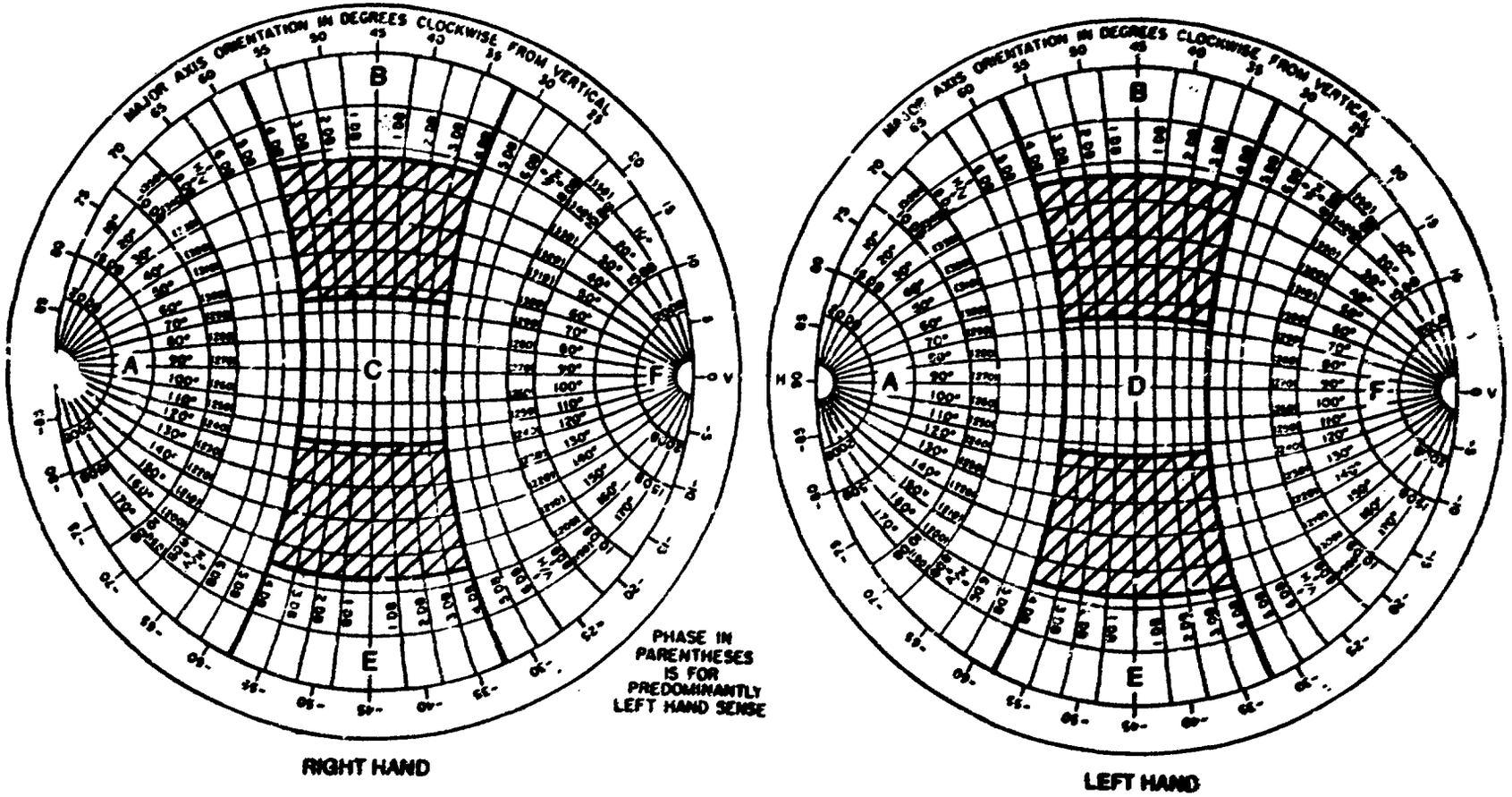

Figure 1a Polarization Chart Regions

The labeled sections in Figure 1a show regions corresponding to six of the seven quantized values of polarization used by this system. Values for relative phase, $\Delta\theta$, and relative amplitude used to specify these regions are shown in Table 1.

Table 1. Values for Relative Phase and Amplitude

Region	Polarization	$\Delta\theta$	M
A	Horizontal	X	< -4dB
B	Slant +45	$0^o \pm 22.5^o$	0dB ± 4dB
C	RHCP	$90^o \pm 22.5^o$	0dB ± 4dB
D	LHCP	$270^o \pm 22.5^o$	0db ± 4dB
E	Slant -45	$180^o \pm 22.5^o$	0dB ± 4dB
F	Vertical	X	> +4dB

The shaded regions among the six basic polarizations correspond to a seventh indeterminate state.

Figure 1b shows that regions C and D closely approximate the industry-wide accepted standard of "good" circular polarization: axial ratio equal to or less than 3dB. This "good" circular polarization region is shown as a circle concentric with the graph and centered in region C and D for right hand and left hand circular polarization, respectively.

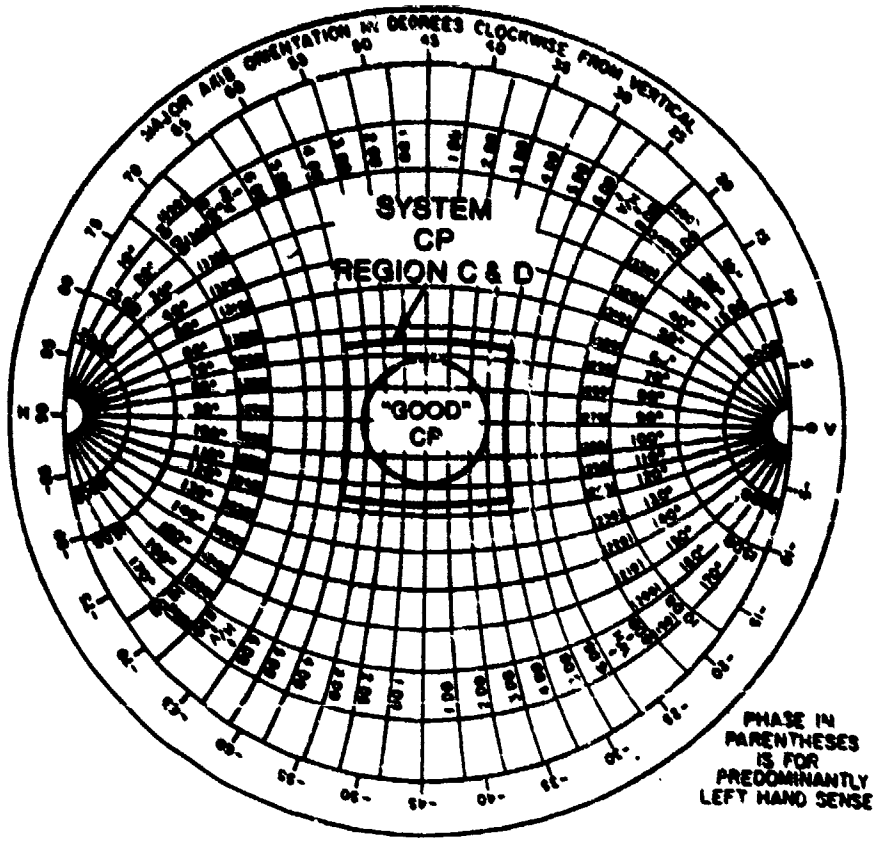

Figure 1b "Good CP"

1.2 ANTENNA

The effectiveness of a polarization measurement scheme relies on the precision of the phase and amplitude tracking of the orthogonally oriented collection antennas. The system discussed here uses a parabolic reflector fed by a crossed, log-periodic dipole for the lower microwave frequencies through C-band. However, for X- and K-band, the close phase tolerances necessary are achieved with a quad-ridged, dual-polarized horn feeding a parabolic reflector.

Figure 2 shows the phase and amplitude tracking of the high-band antenna in the region of the main beam. Note that the progressive phase shift with frequencies is due to a slight off-set in the feed probes of the horn. This phase error may be partially corrected by adjusting the differential feed line length.

1.3 RF MULTIPLEXING

Recent advances in the design of pin-diode, single-pole-double-throw, RF switches provide the basis for this instantaneous polarization measurement system. With switching speeds approaching the 10ns range, it is now possible to share a common RF channel between two orthogonal antennas and never be "blind" to either polarization for more than 100-200ns. For example, toggling rapidly between vertically and horizontally polarized feeds, two orthogonally polarized samples of a very short RF pulse may be sent, time multiplexed, through a single RF channel.

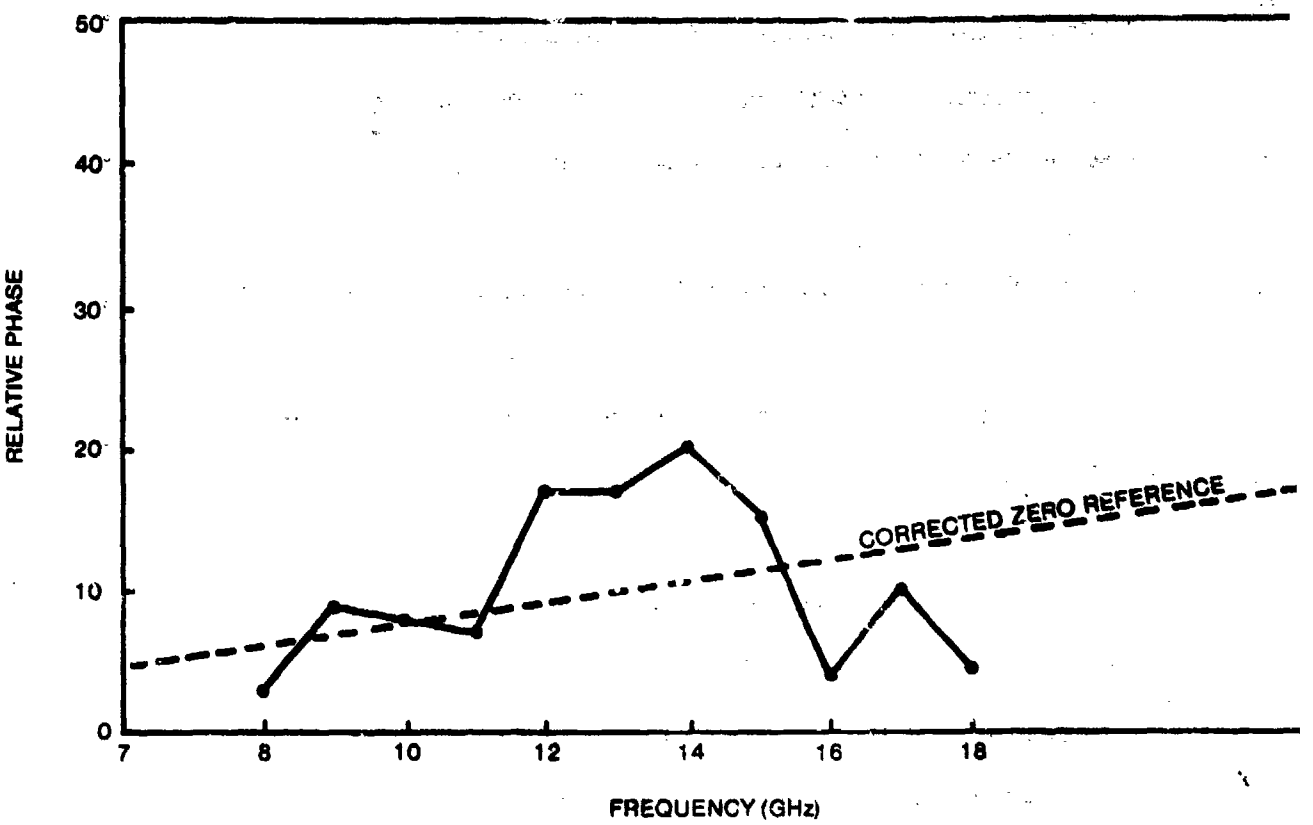

Figure 2. High Band Relative Phase Data

The recovery of relative phase and amplitude of the two orthogonal components, thereby measuring the polarization, is simplified by using a nonsymmetrical toggling duty cycle. This system uses a sequence where the horizontal transmission period is twice the vertical. If the period of vertical transmission is designated as τ , then one complete switching cycle is a sequence of three periods or states each τ long.

The RF waveform traveling down the single RF channel carries with it a complex modulation consisting of amplitude modulation, phase modulation or a combination, depending on the polarization of the intercepted RF radiation.

Pure amplitude modulation results from a vertically or horizontally polarized wave, whereas slant -45° would produce phase modulation with no amplitude modulation. Since polarization is generally elliptical, amplitude modulation and phase modulation exist together.

1.4 VIDEO DETECTION

Figure 3 illustrates a detection scheme preserving amplitude and phase modulations while providing a unique method for quantizing the polarization. The RF* with its complex modulation is split into two sections: an amplitude detection channel and a phase detection channel. The amplitude detector is a log video amplifier which has a voltage output porportional to the power input in dBm. The phase detection channel includes a polar

*Depending on the receiver, this signal also may be a broadband or narrowband IF.

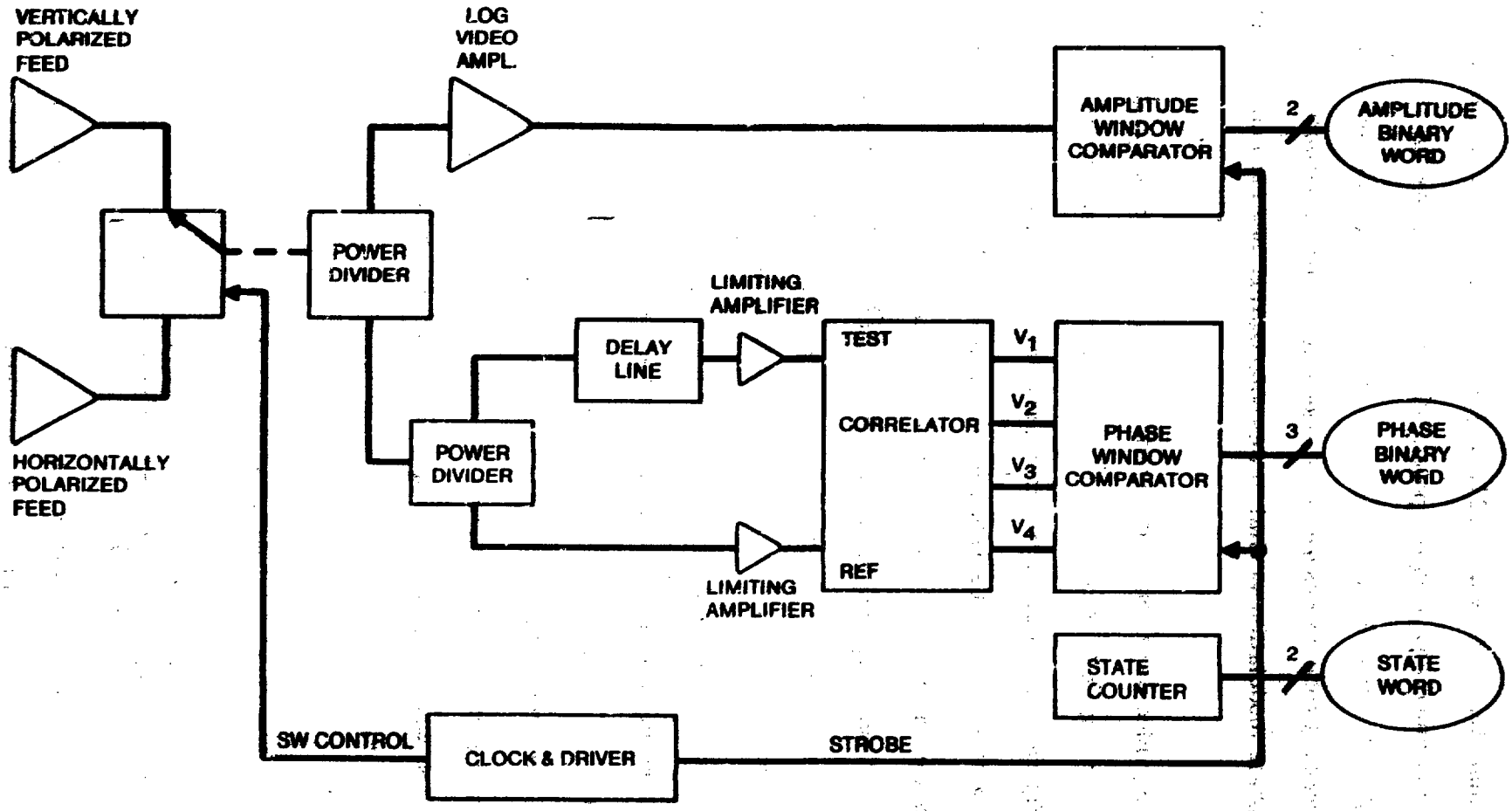

Figure 3 System Block Diagram

discriminator or correlator [3], [4] (a device present in all modern day IFM systems) and related power dividers and delay line. The block designated "clock and driver" controls the switching sequence and provides a reference strobe to ensure synchronous detection of amplitude modulation and phase modulation so vital to this polarization measurement system.

The log video wave form for a predominately vertically polarized RF field is shown in Figure 4. Also shown is a replica of the video waveform delayed by τ. Figure 4 also shows the strobe provided by the clock and driver circuit. During this strobe, the relative amplitudes of the delayed and undelayed video are compared. Note that a comparison is made every τ seconds, and, after 3τ seconds, the comparisons are repeated. The first strobe or sample (sample state 1) finds the delayed video exceeding the undelayed video by +4dB. This results in a binary word (see Figure 5) of (10). During sample state 2, the video amplitudes are equal and the binary word for amplitude is (00). During sample state 3, the complementary condition to state 1 exists resulting in a binary (01). A similar analysis may be used to generate a three-word sequence for predominantly horizontal and "other" polarizations. These sequences are tabulated in Table 2. "Other" corresponds to the condition where the ratio of the vertical to horizontal amplitudes does not exceed ± 4dB.

Table 2. Three-Word Sequence for Polarizations

STATE	VERT.	HORIZ.	OTHER
1	(10)	(01)	(00)
2	(00)	(00)	(00)
3	(01)	(10)	(00)

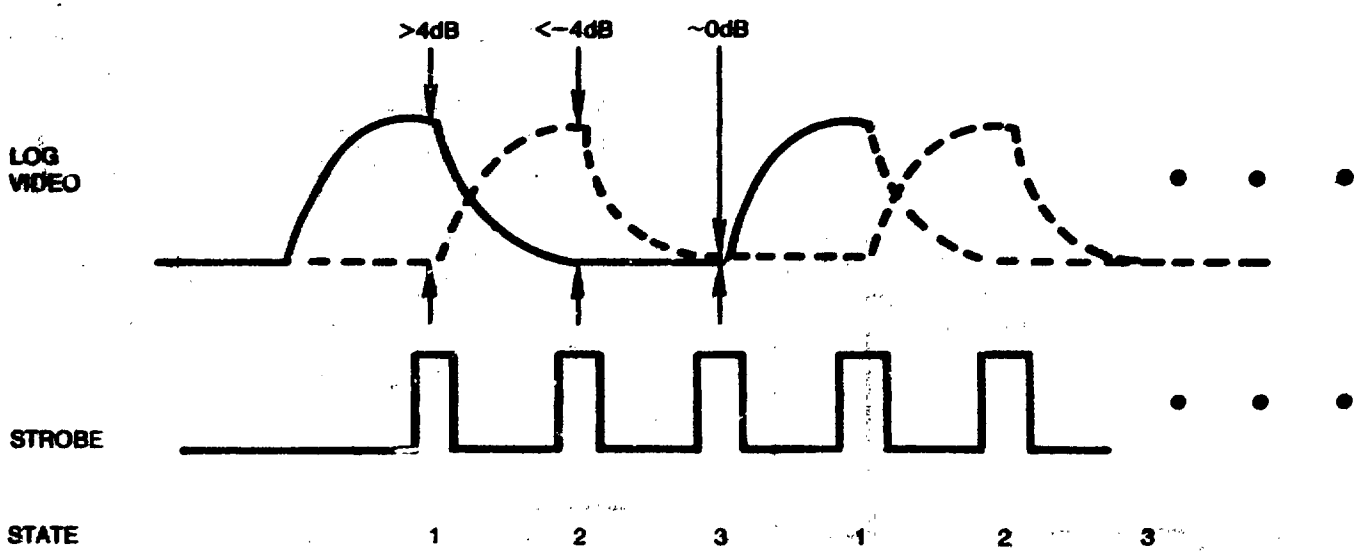

Figure 4 Amplitude Detection

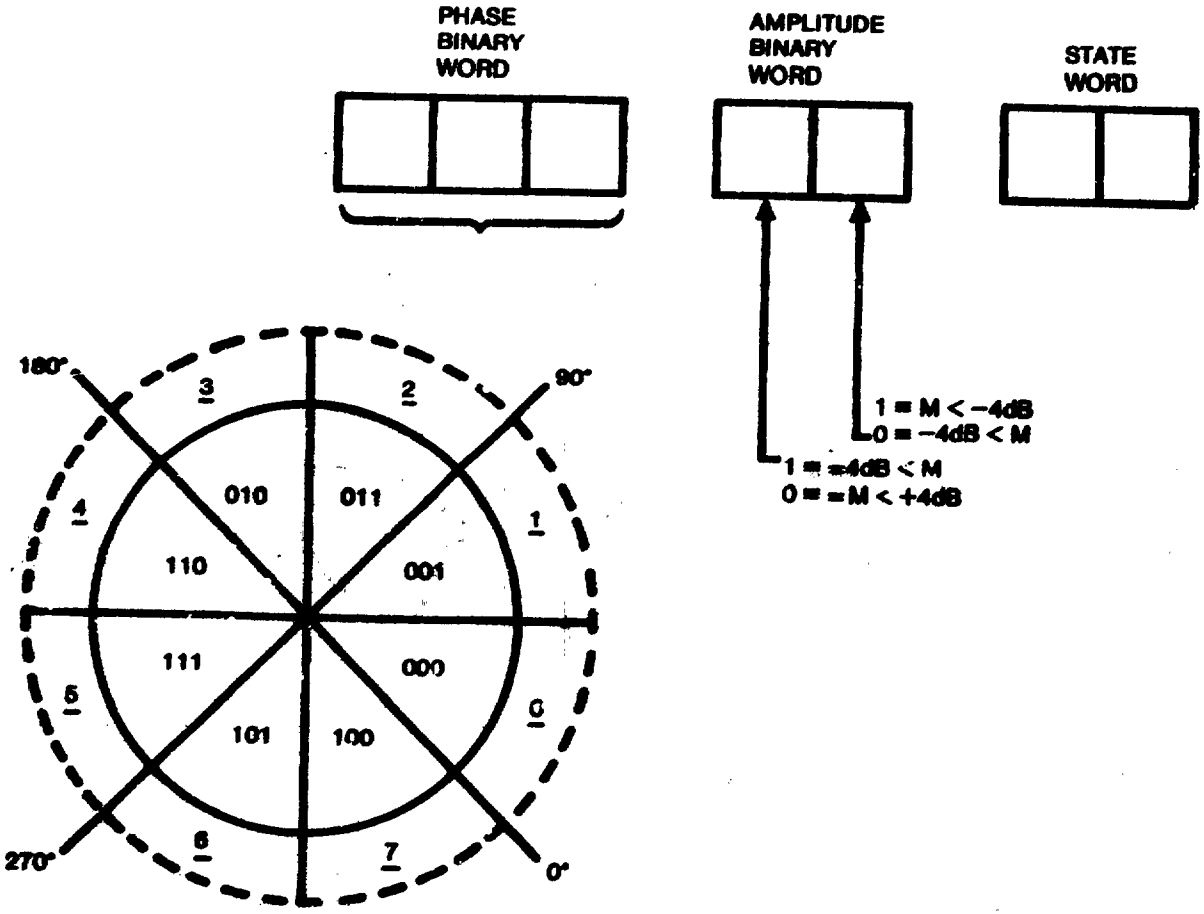

Figure 5 Raw Data Word

If the amplitude binary word sequence indicates neither vertical nor horizontal polarization exists, then phase modulations must be examined to quantize the polarization into one of the remaining senses. The "phase detection" portion of the block diagram accomplishes this task (Figure 3).

The RF (or IF) which is split off and sent to the phase detection circuitry is split once again into two paths. One path leads directly into the reference port of the correlator, while the other path delays the signal by the time τ prior to entering the correlator test port. Figure 6 shows the undelayed and delayed RF (IF) envelope at the correlator inputs. Note that the delay of τ lines up the vertical and horizontal signals so that three associations are made: vertical with horizontal, horizontal with horizontal, and horizontal with vertical. Limiters are included to remove all amplitude modulation.

The function of the correlator is to measure the relative phase between the RF signals at its two inputs. The correlator has four outputs, V_1, V_2, V_3, and V_4 which are mathematically related to the relative phase of the RF inputs as follows:

$$V_1 = K\left(\frac{1 + \cos\phi}{2}\right) \tag{4}$$

$$V_2 = K\left(\frac{1 - \cos\phi}{2}\right)$$

$$V_3 = K\left(\frac{1 + \sin\phi}{2}\right)$$

$$V_4 = K\left(\frac{1 - \sin\phi}{2}\right)$$

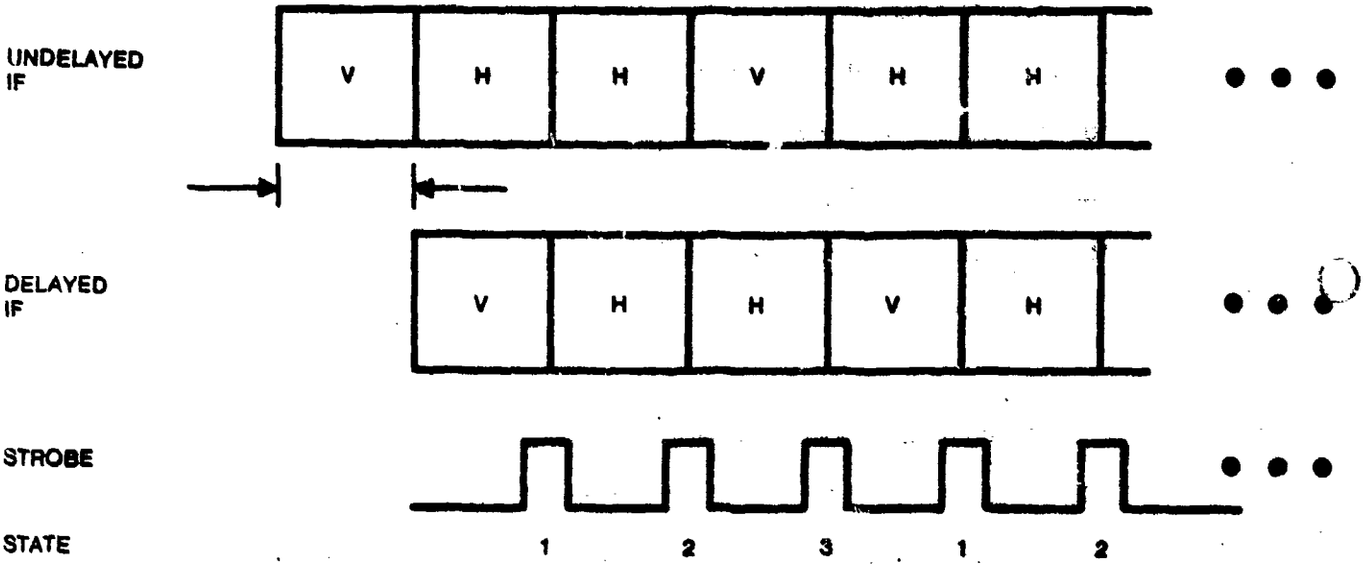

Figure 6 Phase Detection Timing

These expressions when plotted together vs ϕ show how the full 360° range of ϕ may be partitioned into 45° sectors which are defined by the indicated comparisons of the four output voltages (see Figure 7). These comparisons are performed in the block shown in Figure 3, labeled "phase window detector," which generates a three-bit gray binary word (see Figure 5). This binary word is related to the sector as shown in Figure 5.

Because the delay line may be multiple RF wavelengths, the measured angle ϕ is related to the polarization angle $\Delta\theta$ by:

$$\Delta\theta = \phi - 360\tau f \tag{5}$$

The unique 3τ switching sequence eliminates the ambiguity which would result because of the second term in equation (5) by allowing a reference period coinciding with state 2, where horizontal is compared with horizontal. For example, if a pure right hand circularly polarized field is collected, then the relative phase $\Delta\theta$ would be 90°. Assume that during state 1, the correlator output designates sector 3 as shown in Figure 6. During state 2, the reference state, sector 1, 90° away would be designated. Because state 3 is the reverse condition from state 1, the sector corresponding to the negative of state 1 will be chosen. Thus, a characteristic pattern for each of the four nonvertical or horizontal polarizations will result each 3τ cycle. This pattern will rotate as f varies, but will otherwise remain unchanged. Patterns for the four quantized states are shown in Figure 8.

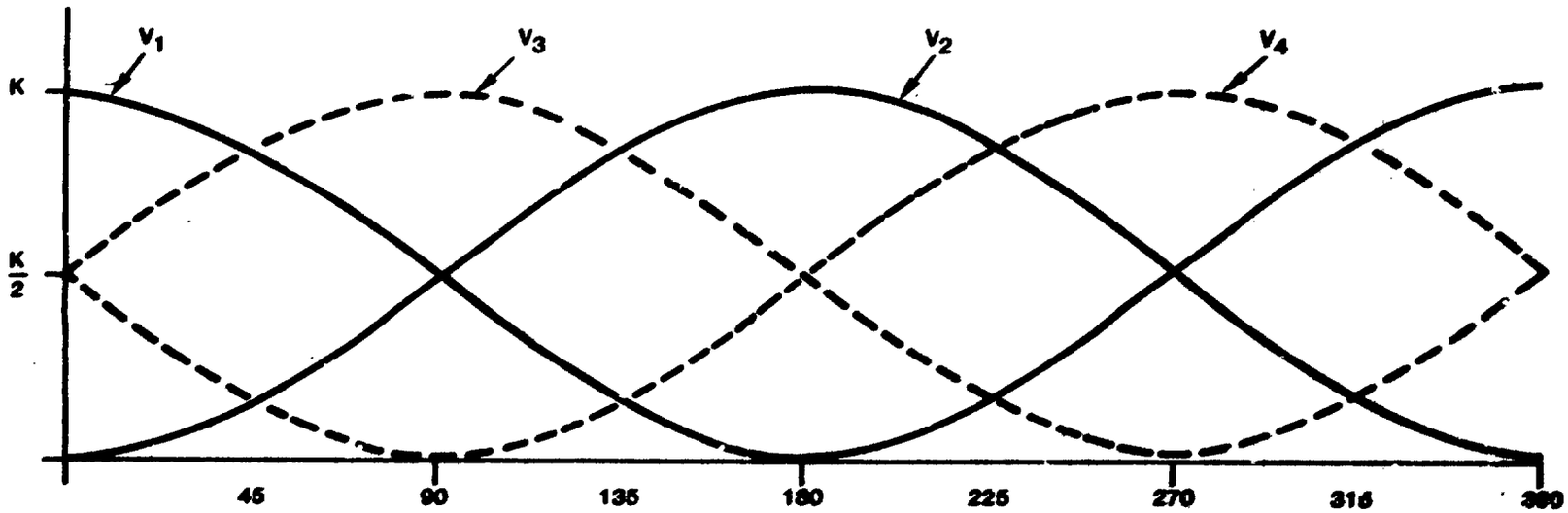

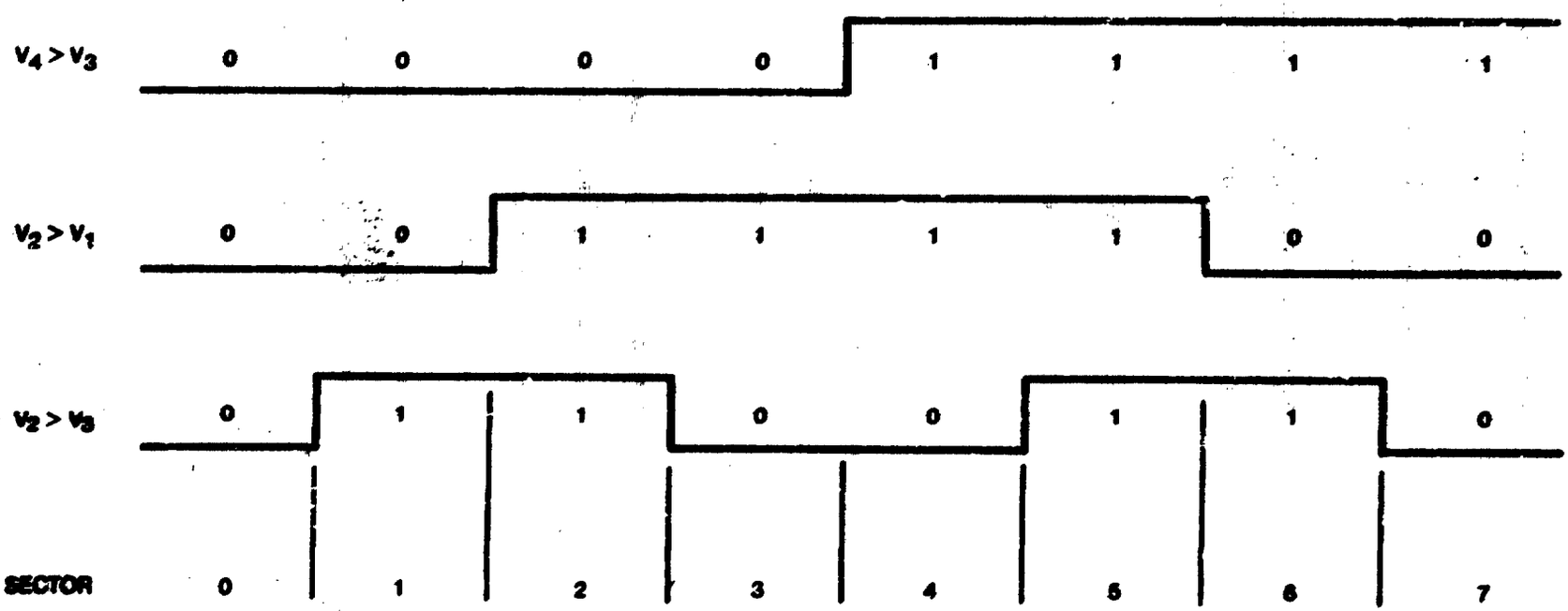

Figure 7 Correlator Output

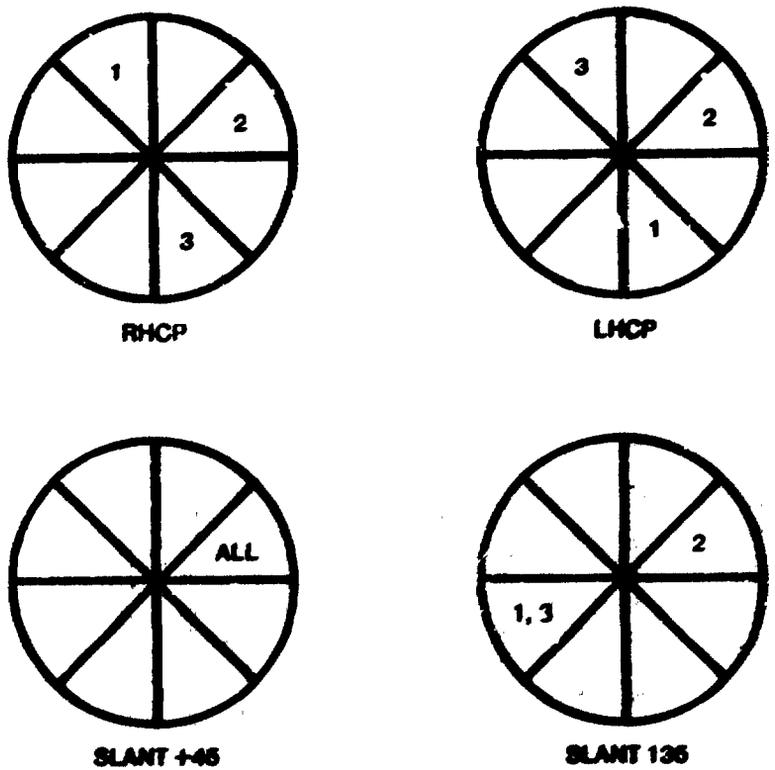

Figure 8. Polarization Sequence Patterns

Figure 5 shows a complete raw polarization data word which is updated every τ seconds. Note that the "state word" is essential to the decoding process which is performed by microprocessor circuitry.

1.5 DESIGN PARAMETERS

The following polarization measurement system parameters are important to one wishing to use this technique:

(a) Minimum pulse width for which measurement is possible

(b) Minimum PRI or system recovery time after polarization measurement is complete

(c) Polarization quantization accuracy

The minimum pulse width depends on the overall system bandwidth and the switching speed of the pin diode switch. For instance, if τ is 50ns then a complete switching cycle will be 150ns or equal to a switching rate of 6.66MHz. This would require an RF (IF) bandwidth of approximately 13MHz. Modern-day pin diodes have switching times of 10ns and may be switched at greater than 10MHz. This would suggest a lower pulse width limit of about 50ns. However, pin diode switching transients lead to video feed-through of spectral components well into the L-band region. Although video feedthrough may be reduced by filtering, the ultimate minimum pulse width presently seems to be limited to around 150ns.

Instantaneous polarization measurement is performed in two steps, the first being high-speed collection of the "raw data" words. The second stage is the

transfer of this data to a microprocessor at a slower rate dictated by the digital logic circuits. Because this transfer takes place between pulses, sufficient time between pulses (PRI) must be available. In general, 100 ns is sufficient to transfer 16 raw data words. Normally, only three of these data words are required to carry all the polarization information. However, more data allows statistical analysis to refine measurement accuracy.

Basic polarization accuracy is directly related to the phase and amplitude tracking of the antenna. This technique further adds an inaccuracy due to the quantization process in the phase measurement system. Worst-case error for phase would be ±22.5; however, depending on the RF (IF) frequency, this tolerance could be as low as ±0°. The result is that at some frequencies, marginal CP or slant polarizations may be quantized as indeterminant, while at other frequencies the same polarizations would be quantized correctly.

1.6 CONCLUSION

The success of this instantaneous polarization measurement system shows how new developments in other fields can advance state-of-the-art in microwave field measurements. The new high-speed, pin-diode switch and compact versatile microprocessor circuits have been used here to overcome obstacles which would otherwise have rendered polarization measurement impossible.

ACKNOWLEDGEMENT

The author wishes to thank Herbert Parker for his expert assistance in the development of the system prototype and Christopher Powell for guidance in the area of microprocessor-based measurement systems.

REFERENCES

[1] Jasik, H. Antenna Engineering Handbook. New York: McGraw-Hill, 1961, p. 17-5.

[2] . Kraus, J., "Antennas," McGraw-Hill, 1950, pp. 466-485.

[3] . Myers, Glen and Cummings, R.C., "Theoretical response of a polar-display instantaneous-frequency meter," IEEE Trans. on Instrumentation and Measurement, vol. 20, no. 1., February 1971.

[4] . Grossbach, R., "Degradation of polar-discrimination performance by non-ideal components," Microwave Journal. December 1974, p.68.

[5] . _____"Polar Frequency Discriminators," Microwave Journal. September 1974, p.36.

AD P001123

PRACTICAL ASPECTS OF SPHERICAL NEAR-FIELD TESTING

Joseph J. Tavormina
Scientific-Atlanta

I. ABSTRACT

Near-field antenna testing has become a reality over the past decade. Antenna engineers in several testing facilities now rely on near-field testing to verify antenna performance. Some of the sophisticated antenna systems which are now under development will have to be tested using near-field techniques, as conventional techniques cannot offer the accuracy required for an affordable cost.

In this paper, attention is focused on the practical aspects of near-field antenna testing in spherical coordinates. The requirements for the antenna range and the antenna testing procedure are reviewed. The sources of measurement error are identified and several estimates of the error levels are made. Examples of near-field test results are compared with measurements taken on a compact range.

II. INTRODUCTION

Near-field antenna testing is an alternative to conventional far-field antenna test techniques. In both conventional and near-field antenna testing, a range or probe antenna (usually the transmitting antenna) is used to illuminate the antenna under test (usually the receiving antenna). In conventional far-field testing the distance between the range and the test antenna determines the extent to which the illuminating field approximates the desired plane-wave illumination. In near-field testing, the finite distance between the range and test antenna becomes an explicit test parameter. The antenna under test is measured using the non-planar near-field illumination; calculations performed on the measured data yield the performance characteristics of the test antenna under the condition of plane-wave illumination.

Several major drawbacks exist with conventional far-field antenna testing. Since the range antenna and the test antenna must be separated by a considerable distance, an outdoor antenna range is often required. Consequently, control of the test environment is poor. The antenna test is subject to adverse weather conditions and test measurements are corrupted by range reflections. Also a sufficiently large tract of land may require a large financial outlay.

If the distance requirement permits, conventional testing may be performed in an indoor anechoic chamber. Indoor testing is more convenient than outdoor testing. Stray electromagnetic reflections are controlled through the use of microwave absorber. Since the testing is moved indoors, weather conditions no longer represent a problem. Control of the environmental temperature and humidity provide for more stable and more accurate test results. The cost of a suitable anechoic chamber can be quite high, however. Since the quality of the field illumination is a function of the separation distance, a large chamber may be required to produce acceptable test results. The larger the chamber, the greater the cost of the microwave absorber which must be used to line the walls, ceiling, and floor of the chamber. Often a compromise must be made between the size of an anechoic chamber and performance that the chamber can deliver.

The compact range test method was invented in the late 1960's to overcome the high cost of indoor antenna measurements. In the compact range a large geometric reflector (usually parabolic) is used to simulate a plane wave in a portion of the anechoic chamber. That is to say, the large reflector acts as an antenna whose near-field radiation pattern is a plane wave. The test measurement is made by immersing the antenna under test in the planar near-field of the large reflector. All of the advantages of indoor testing apply to testing with the compact range. In addition, the anechoic chamber which is required is smaller than that required for conventional far-field testing, and cost savings become apparent. The compact range test technique does have limitations, however. The size of the test zone in which the field approximates a plane wave is limited by the size of the reflecting surface. Diffraction from the edges of the reflecting surface becomes a problem at low frequencies of operation, whereas the tolerance of the reflecting surface

becomes a problem at high frequencies of operation. Another limitation results from asymmetries in the illumination of the reflecting surface. This can cause depolarization of the test field which results in degradation of the measurement unless a special compensating reflector feed antenna is used.

Near-field testing constitutes a second alternative to conventional far-field indoor testing. Instead of physically simulating plane wave illumination via a large reflector as in the compact range, near-field measurements are made using non-planar illumination of the test antenna in conjunction with a numerical computation to determine the calculated result for planar illumination. In a sense, near-field testing numerically simulates plane wave illumination of the test antenna.

A primary advantage of near-field testing is the ability to perform the measurement with the range antenna very close to the antenna under test. This makes the size requirements for the anechoic chamber minimal. Another primary advantage of near-field scanning is the high degree of accuracy which can be achieved.[1] A disadvantage of near-field testing is the requirement for a computer and the time required to execute the computation algorithm. Due to the finite speed and finite memory of computers, near-field computation algorithms are limited to test antennas which do not exceed a maximum electrical size. Maximum capacities tend to be between 100 and 1000 wavelengths, but practical considerations relating to the amount of data which must be collected and the time required to acquire the data often impose a more severe limitation than the capacity of the computation algorithm. Table 1 is a comparison of the range configurations which have been discussed.[2]

Table 1

Comparison of Antenna Test Ranges

	Conventional Outdoor	Conventional Indoor	Compact Range	Near-Field Indoor
Land Investment	High	Low	Low	Low
Building Investment	Low	High	Moderate	Moderate
Special Equipment	None	None	Reflector	Computer
Convenience	Poor	Good	Good	Good
Control of Test Environment	Poor	Good	Good	Good
Control of Stray Signals	Poor	Good	Good	Good
Overall Accuracy	Moderate	Good	Good	Excellent
Data Processing Required	No	No	No	Yes
Limitations	Range Length Stray Signals	Range Length	Test Aperture Test Frequency	Electrical Size of Antenna

III. SPHERICAL NEAR-FIELD TEST PROCEDURE

In conventional antenna testing, the measured results are normally expressed in terms of spherical coordinates. Spherical coordinates represent a logical choice when the primary purpose of the measurement is to determine antenna characteristics as a function of pointing direction. In spherical near-field testing both the near-field measurement and the far-field calculation are performed in spherical coordinates. This is a unique characteristic as compared with near-field testing in other coordinate systems, such as planar or cylindrical scanning. In planar scanning, the near-field measurement is performed in either cartesian[3] or polar coordinates,[4] whereas the result is expressed in spherical coordinates. In

cylindrical scanning the measurement is performed in cylindrical coordinates; again the result is expressed in spherical coordinates. It is only in spherical scanning that both the measured data and the calculated result are expressed in spherical coordinates.

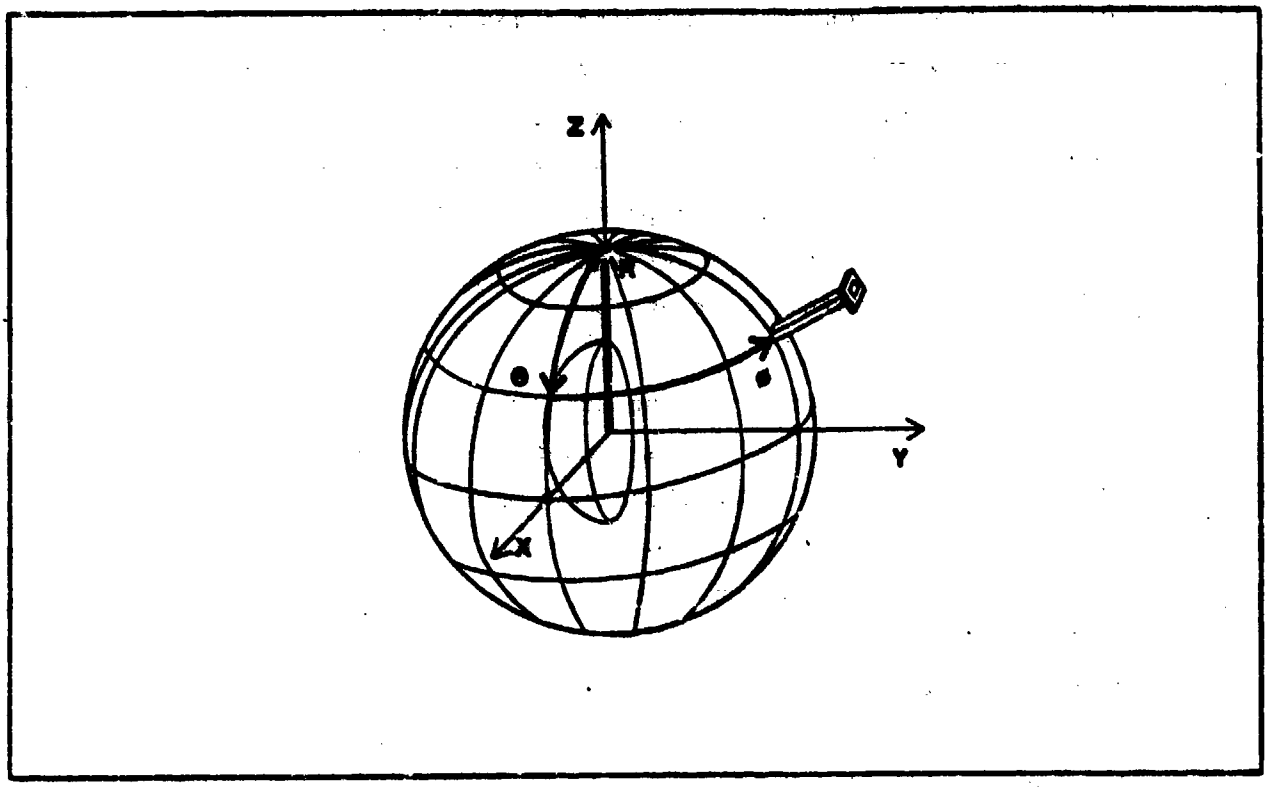

Figure 1. Spherical Near-Field Scanning

Figure 1 illustrates spherical scanning in a schematic fashion. The direction coordinates θ and ϕ represent the two primary independent variables and are used to characterize the radiation pattern of the test antenna. The polarization coordinate χ is used to characterize the polarization characteristics of the test antenna. The range separation corodinate R explicitely characterizes the curvature of the illuminating electromagnetic field. R is held constant during the course of a measurement, so that the measurement is made on a spherical surface. Once the measurement data has been acquired, the near-field computation algorithm is used to calculate a new

data set for an alternate range separation. Most often, the measurement separation R_1 is chosen to be a small number, and the computed separation coordinate R_2 is chosen to approximate an infinite separation. Thus, the computation algorithm transforms the data which was actually measured on a spherical surface of radius R_1 into data which would have been measured had the spherical surface been of radius R_2.

Figure 1 shows a spherical near-field measurement in which the major portion of the radiation energy exits at the equator of the test sphere. This is the orientation normally used in most conventional far-field measurements. It is relatively easy to find the boresight of an antenna in this orientation. Also, if linear polarization is used, this orientation maintains the polarization match between the range antenna and the test antenna for small excursions in θ and ϕ.

An alternate orientation for the test antenna is one in which the major portion of the radiated energy exits the pole of the test sphere. This orientation is sometimes used to characterize feed antennas for parabolic reflectors. It is more difficult to boresight an antenna in this orientation, and unless circular polarization is used, the polarization match between the range antenna and the test antenna can become a bothersome detail. This orientation may offer some advantages in the theoretical calculation of certain antenna patterns, and may result in greater efficiency in near-field measurements, as will be shown later. Another consideration which may enter into the selection of a test orientation is the final presentation of the antenna test data. Unless a computer algorithm is available to numerically rotate the test results from one orientation to the other, the orientation in which the antenna is tested will be the same orientation in which the results are available. This may be an overriding consideration if the results must be presented in a two-dimensional cartesian format, as in the case of a cartesian contour graph. In such a case, the antenna test engineer must use the equatorial orientation to produce usable test results. Figure 2 illustrates the equatorial and polar orientations.

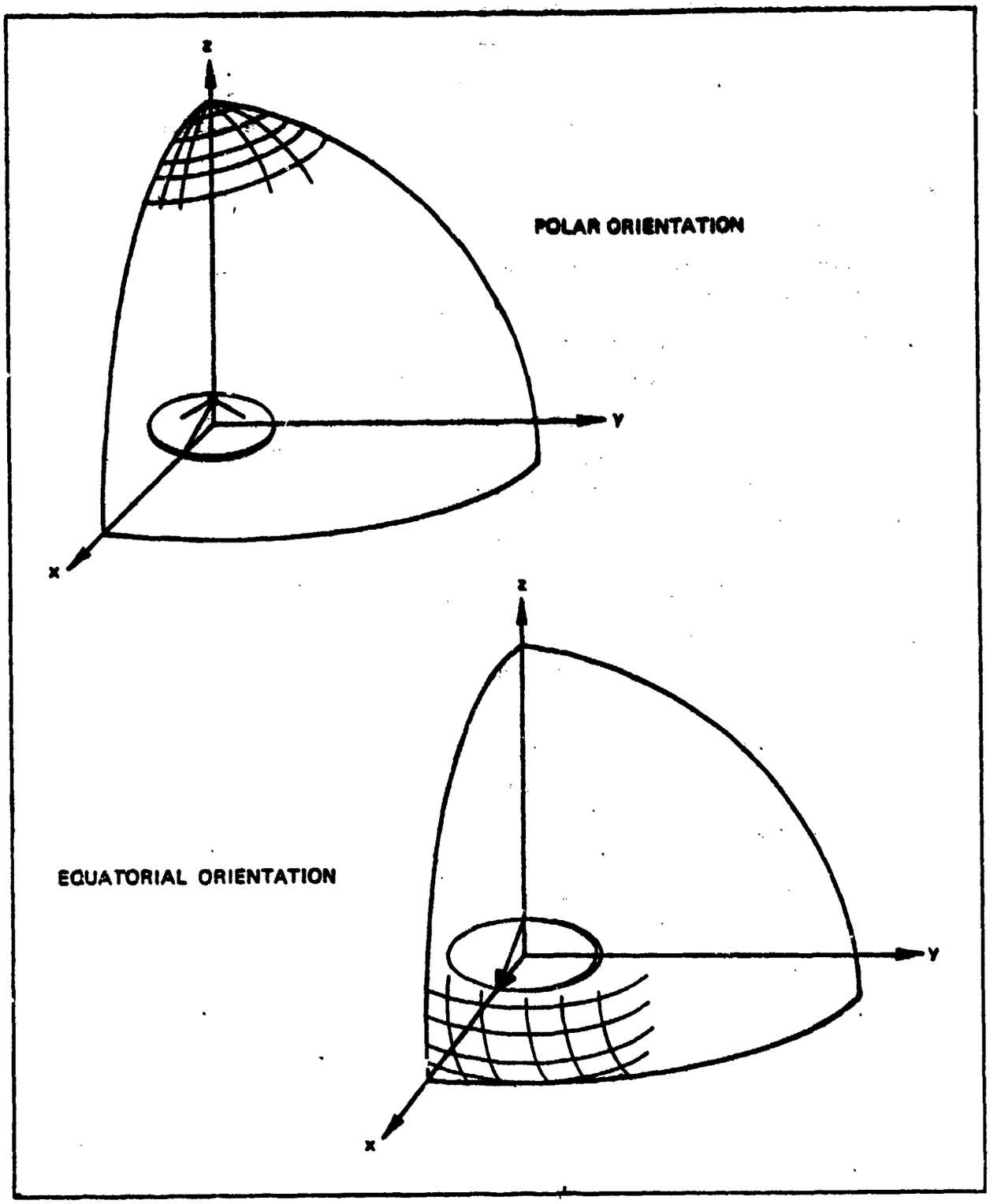

Figure 2. Equatorial vs Polar Orientation

A notable characteristic of near-field antenna testing is the requirement for data collection over a finite portion of the measurement surface, even when the computation results are required for only a single far-field direction. In principle, every measurement point on the surface of the near-field sphere will contribute to a given far-field calculation point. In practice it is possible to perform a calculation using a truncated sphere of measured data which is carefully chosen such that the truncation error is ngeligible. It is not feasible, however, to calculate a result for a single value of θ and ϕ from a single measurement in the near-field. This means that in order to determine the maximum far-field gain of the test antenna, which is a single result corresponding to the peak of the radiation pattern, a substantial set of near-field measurements must be made. The same measurement requirement would apply to the determination of an antenna boresight. In conventional far-field antenna testing and in compact range antenna testing these measurements could be made directly.

The data acquisition process consists of digitally sampling the radiation pattern of the test antenna on the surface of the scanning sphere. As indicated in Figure 1, the sampled data points are regularly spaced in θ and ϕ. The sampling interval which is used must not exceed the Nyquist interval, which is the inverse of the electrical size of the test aperture. The test aperture diameter D is determined not only by the test antenna size, but also by the manner in which the antenna is mounted on the test positioner. Figure 3 illustrates the determination of the test aperture diameter for the same antenna mounted on several different test positioners. The electrical size of the test aperture is determined by dividing the test aperture diameter by the wavelength λ. The Nyquist interval in radians is given by

$$\Delta\theta_{Nyq}, \Delta\phi_{Nyq} = \lambda/D \qquad (1)$$

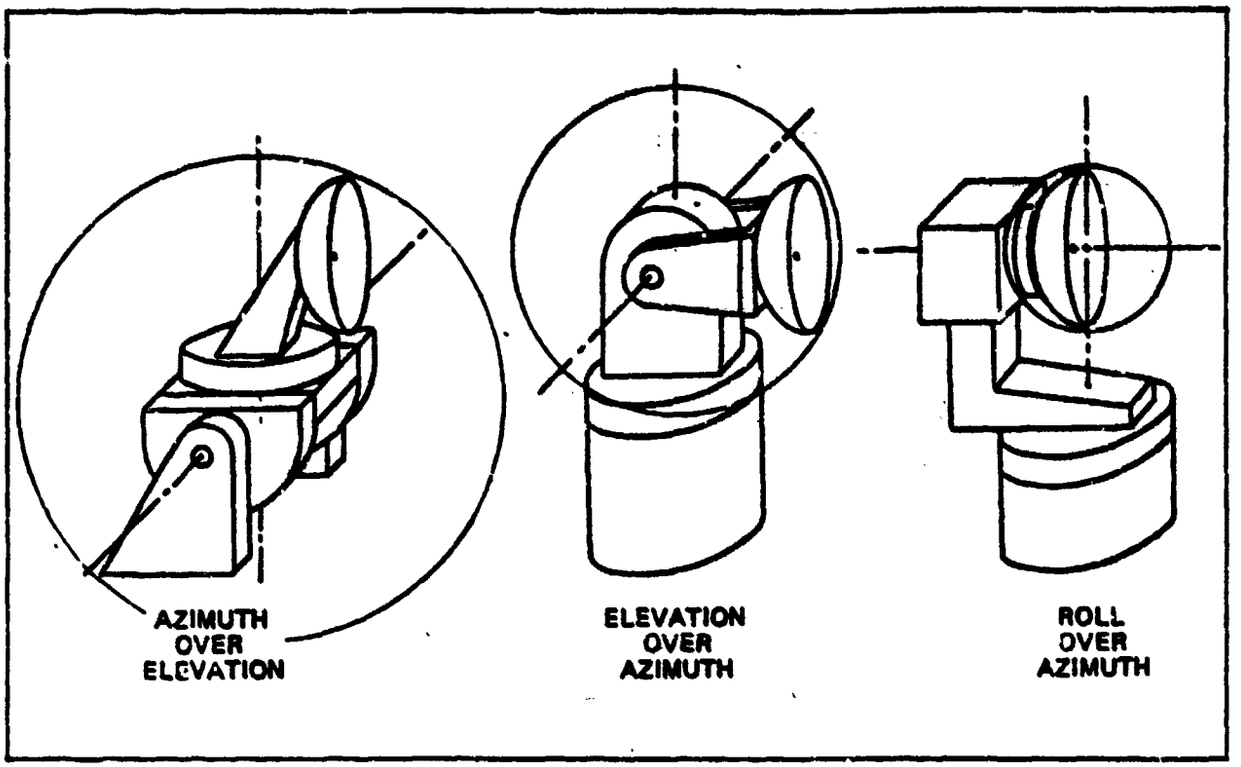

Figure 3. Determination of Test Aperture Diameter

It is evident that the larger the electrical size of the test aperture, the greater the amount of data. Given the Nyquist sampling rule, the number of samples required to fully characterize the radiation pattern may be determined. Full spherical coverage implies a 180° range in θ and a 360° range in ϕ. The number of data points is calculated by dividing these ranges by the respective angular increments. Table 2 illustrates the exponential growth of the data storage requirements with increasing electrical size of the test aperture. The figures given assume that data is collected over the entire test sphere for a single test frequency and that two orthogonal polarizations are required for each position on the test sphere. Each data point consists of an amplitude value and a phase value for the measured signal at a given position on the test sphere for a given polarization. It is

assumed that the amplitude and the phase values require two bytes each of computer memory for storage. As can be seen, the computer storage requirements become formidable as the electrical size increases.

Table 2

Data Storage Requirements vs Electrical Size

Electrical Size (D/λ)	Sampling Interval (Δθ,Δφ)	Number of Sample Points (Full Sphere)	Bytes of Storage Required*
28	2.0°	16 x 10^3	0.3 x 10^6
57	1.0°	64 x 10^3	1.0 x 10^6
114	0.5°	259 x 10^3	4.1 x 10^6
286	0.2°	1,620 x 10^3	25.9 x 10^6
572	0.1°	6,480 x 10^3	103.7 x 10^6

*Assuming 16 bytes are required for each data point, which consists of the amplitude and phase for each of two polarizations, with no angular information stored.

As previously mentioned, it is often practical to perform calculations on a partial sphere of measured data. Figure 4 suggests different types of partial spheres which may be employed for various orientations of the antenna under test. The truncation errors which result are a complex function of the shape of the test antenna radiation pattern, the percentage of the radiated energy sampled in the data acquisition process, and the range length at which the measurement is performed. Practical experience has indicated that the use of truncated spheres is feasible as long as "most" of the energy radiated from the test antenna is subtended by the partial sphere which is used. The use of partial spheres is most applicable for the testing of directive antennas. Omni-directional antennas often require that a full sphere be used, as any truncation will result in the loss of accountability for a significant portion of the radiated energy.

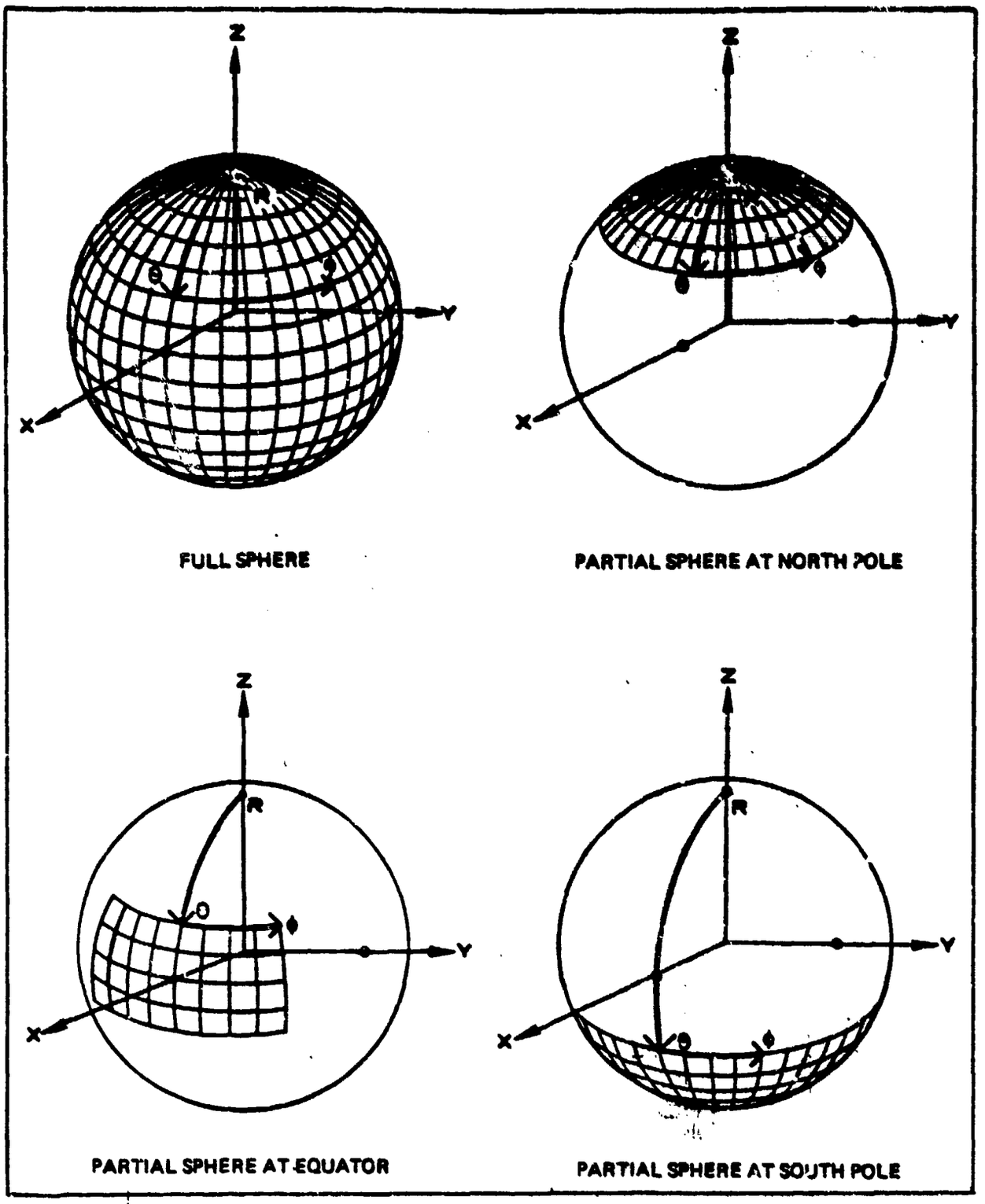

Figure 4. Usage of Partial Test Spheres

The use of partial spheres is desirable from the consideration of data storage requirements and the consideration of total test time.[5] Both the data storage required and the time required to perform data acquisition are related to the solid angle of the spherical surface over which data must be acquired. Full spherical coverage corresponds to a 180° range in θ and a 360° range in ϕ. A partial sphere which covers a 60° range in θ and a 60° range in ϕ represents only 1/18 the surface area required for a full sphere. Thus the data storage requirement for this partial sphere is only 6% of the requirement for the full sphere. If we assume that the data acquisition time is porportional to the solid angle covered, then the acquisition time for this partial sphere is similarly 6% of the time required for the full sphere. A time savings is also apparent in the computation phase of the antenna test. Through the use of numerical symmetries, the computation algorithm can avoid a substantial amount of data processing with an associated reduction in the execution time of the algorithm. Table 3 illustrates the test times required for several spherical coverages, as measured using the Scientific-Atlanta Model 2022 Spherical Near-Field Antenna Analyzer.

Table 3

Antenna Test Time vs Partial Sphere Coverage

Angular Span θ x ϕ (Degrees)	Solid Angle Covered (Steradians)	Typical Data* Acquisition Time	Typical Data Transformation Time	Typical Total Test Time
180 x 360	4π (full sphere)	4 hrs	3-1/2 hrs	7-1/2 hrs
180 x 180	2π (hemisphere)	2 hrs	2 hrs	4 hrs
60 x 60	0.22π	1/2 hr	3/4 hr	1-1/2 hrs
36 x 35	0.08π	1/4 hr	1/2 hr	3/4 hr

*Assuming partial sphere is at the equator of the test sphere and that 1° sampling intervals are used.

IV. RANGE ALIGNMENT

The mathematics which forms the basis of the near-field to far-field spherical transformation algorithm requires that the measurement of the test antenna be performed on the surface of a sphere. The schematic illustration in Figure 1 implies that the test antenna is held fixed while the range antenna covers the spherical surface during the scanning process. In common practice the reverse is true. The range antenna is normally stationary and the test antenna is rotated by a two-axis angular positioner. Several common positioner configurations have been shown in Figure 3.

If the acquired data is to truly represent data collected on a spherical surface, it is important that the axes of the test positioner be aligned. Care must also be taken to insure that misalignment of the range antenna's polarization axis does not introduce measurement errors. The requirements for proper range alignment are that the two axes of the test positioner θ and ϕ be orthogonal and intersect at a point. In addition, the polarization axis χ of the range antenna must be orthogonal to and intersect the lower axis θ of the test positioner.

The relationship between the θ and ϕ axes is of a fairly critical nature. An intersection error will result in a periodic distortion of the range separation parameter R, such that a sphere is no longer an accurate description of the measurement surface. The two maximum range separation errors will occur at opposite sides of the test sphere along the equator. At a minimum, this will result in an electrical phase error of the measured test signal at the extremal points which is equal to the ratio of the intersection error and the wavelength. An orthogonality error between the θ and ϕ axes will cause a distortion of the measurement grid on the surface of the test sphere. In the vicinity of the equator this will amount to a simple translation of the cartesian-like grid. Near the poles of the sphere, the result is more dramatic since the coordinate origin translation is applied to a polar-like grid.

The relationship between the θ and χ axes is not as critical as the relationship between the θ and φ axes, particularly when a broad-beamed range antenna is used. In such a case, the wavefront which illuminates the test antenna will be invariant for a relatively large error in the orientation of the χ axis, and the data which is acquired will be identical to data resulting from a proper alignment of the χ axis. An intersection error in the χ axis will cause an angular offset in the measured antenna pattern, the angular offset being determined by the ratio of the displacement of the χ axis and the range length. When directive range antennas are used, such that significant amplitude taper is apparent in the test aperture, the alignment of the χ axis becomes more critical. In such a case, an error in the orientation of the χ axis will cause an asymmetrical illumination of the test antenna, and the data which is acquired will differ from an error-free data set.

Range alignment is readily accomplished using optical and mechanical techniques. The reader is referred to reference [6] for a complete discussion of range alignment procedures. It is convenient to refer intersection errors to the wavelength of the test signal, and orthogonality errors to the Nyquist angular sampling interval. It is advisable to limit the intersection and orthogonality errors to several percent of the wavelength and the Nyquist respectively. Figure 5 shows an optical alignment fixture which employs a double sided mirror with crosshairs. By sighting the mirror from both sides, mechanical adjustments which align the two test axes are easily accomplished.

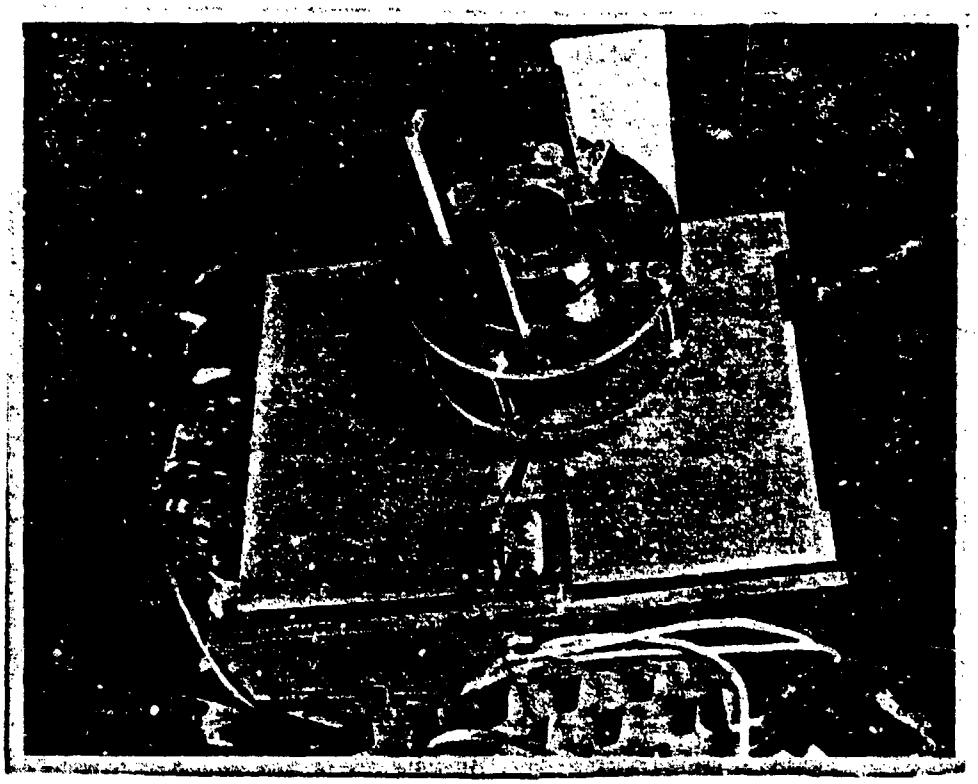

Figure 5. Photograph of Axis Alignment Fixture

V. PATTERN MEASUREMENTS

Pattern measurements are required to determine antenna characteristics such as directivity, beamwidth, null depth, and sidelobe level. In pattern measurements, the absolute power contained in the test signal is not of interest, since only the relative power of the test signal as compared to an arbitrary reference is required to determine the desired antenna characteristics. Most often, the reference level which is used is the maximum power level at the peak of the antenna pattern. The signal level at this point is usually set to 0 dB.

Pattern measurements are easy to perform since only relative data is required. The measurement equipment must be stable during the course of data acquisition and must provide a linear response, but no absolute calibrations are required.

To perform a near-field measurement in the least time, the angular sampling intervals are normally chosen to be close to the Nyquist intervals. The coarse sampling of the radiation field minimizes the time required for both data acquisition and for data processing. Upon completion of the data transformation, the test engineer is ready to calculate the antenna parameter desired from the transformed data. Although the Nyquist sampling criterion guarantees that the sampled data set contains all the information required to perform parameter calculations, the coarse spacing of the transformed data often represents an inconvenience.

To produce a finely sampled antenna pattern, interpolation algorithms may be used to calculate several data points between each pair of coarsely sampled data points. Interpolation is especially useful if the transformed data is to be presented graphically. A multi-dimensional interpolation may be performed if a two dimensional representation of the data is required. If an appropriate interpolation algorithm is used, the interpolation error will be well below the pattern noise due to other error sources. In principle, using an interpolation algorithm based on Fourier analysis, it is possible to reconstruct a pattern with no interpolation error.

Antenna characteristics such as boresight cannot be determined directly in near-field testing, as they can be in far-field testing. To measure boresight via a near-field measurement, it is necessary to acquire the near-field data, perform a data transformation, and determine the boresight position from the calculated far-field data. Antenna characteristics such as boresight may be determined by inspection of interpolated data, but a more direct approach might be beneficial. By performing a curve-fitting operation on the resulting antenna data, more accurate results could be obtained in less time. Curve-fitting algorithms would not require as much interpolation (or perhaps no interpolation) of the antenna data as compared with a graphical determination of the boresight by inspection.

VI. GAIN MEASUREMENTS

The measurement of gain requires an absolute calibration of the measurement equipment. The most readily implemented method of making an absolute calibration is to measure an antenna with a known gain, and to compare the measurement of the test antenna against the known standard. In far-field antenna measurements, the gain comparison is made directly; both the gain standard and the test antenna are measured in the far-field and the range separation parameter R is assumed to remain constant. In near-field testing, the pattern of the antenna under test cannot be directly compared with the pattern of the gain standard, since a data transformation must be performed. In fact, the gain standard might also be measured in its near-field, so that both the test antenna data and the gain standard data must be transformed prior to a comparison.

To insure that a meaningful gain comparison can be made, the transformation algorithm must properly account for the change in the pattern levels as they undergo the near-field to far-field transformation. The transformation algorithm is designed to produce the signal that would have been measured at a range separation of R_2 from the measured data at a range length of R_1. This means that the far-field pattern level will fall off to an infinitesimal level as R_2 approaches infinity, since the radiated power decreases as 1/R in the far-field. To overcome this problem, the transformation algorithm normalizes the transformed data by a factor $e^{(ikR)}/R$ (where k is the wave number; $k = 2\pi/\lambda$). Thus, with proper bookkeeping, a comparison of the level of the transformed gain standard pattern can be made with the level of the transformed test antenna pattern.

VII. POLARIZATION MEASUREMENTS

Measurements of the polarization characteristics of a test antenna can be readily made via near-field testing. As in far-field testing, the range antenna is often assumed to be an ideal dipole radiator with precisely linear polarization. Given this assumption, the result which is obtained will be as

good as that allowed by the polarization characteristics of the range antenna, whether the measurement be performed in the near-field or the far-field of the test antenna.

In far-field testing, the three antenna method is sometimes used to obtain a more precise characterization of polarization characteristics.[7] In this method, the reduction of measured data produces a precise valuation of the polarization characteristics of three antennas through the solution of a series of simultaneous equations. Using this measurement technique, the range antenna may be polarization calibrated.

Given the polarization calibration parameters of the range antenna, a more precise near-field measurement may be performed. Instead of assuming that the range antenna polarization is that of an ideal dipole, the actual polarization of the range antenna is used. When the acquired data is transformed, the far-field result may be computed for the same range antenna or for a different range antenna (including an ideal dipole). In this way, the polarization accuracy of the near-field measurement is no longer limited by the polarization purity of the range antenna, but by the accuracy to which the range antenna can be calibrated and by the stability of the range antenna.

VIII. MEASUREMENTS WITH PROBE CORRECTION

An assumption which is commonly made in far-field antenna measurements is that the range antenna uniformly illuminates the test aperture. Expressed in another way, it is assumed that there is no amplitude taper due to the directivity of the range antenna in the region that the antenna under test occupies. It is easy to insure that this assumption is a valid one in a far-field test, since the far-field constraint on the range separation R requires that the range and the source antenna be distant. At a far-field distance, the angle subtended by the test antenna as seen from the range antenna is usually much smaller than the beamwidth of the range antenna.

In near-field testing, the range separation is relatively small. It is sometimes inconvenient or impossible to satisfy the condition of no amplitude taper in the test aperture. If this condition is met, than the testing is

somewhat simplified. On the other hand, if significant amplitude taper is present, than the radiation pattern of the range antenna must be taken into account to produce accurate measurement results. When the radiation pattern of the range antenna is explicitly accounted for in the near-field measurement, we say that the measurement is performed with probe correction.

In order to avoid probe correction, it is necessary to choose the beamwidth of the range antenna and the near-field range separation distance R such that no significant amplitude taper is present in the test aperture. The beamwidth of the range antenna θ_{Beam} is approximately given by

$$\theta_{Beam} \sim \lambda/d \qquad (2)$$

where d is the aperture size of the range antenna. At a range separation distance R, the test aperture will subtend an angle θ_{Aper} given by

$$\theta_{Aper} = D/R \qquad (3)$$

where D is the test aperture diameter. In order to assure that amplitude taper does not result, we would like θ_{Beam} to be several times θ_{Aper}

$$\theta_{Beam} = K\,\theta_{Aper} \qquad (4)$$

where K is equal to 2 or 3. If we combine these equations, we get an expression for the required range separation R as a function of the other parameters

$$R > K\,D\,d/\lambda \qquad (5)$$

If this condition is not satisfied, it will be necessary to perform the near-field measurement with probe correction. Also, for extremely accurate measurements, probe correction may be required even when this condition is met.

The precursor to probe corrected near-field measurements is probe calibration. Polarization calibration of the range antenna was discussed in the previous section. Full probe correction requires that the pattern of the range antenna be calibrated as well. Probe calibration consists of measuring the radiation pattern of the range antenna and calculating the coefficients of the spherical model functions which give rise to the measured pattern. The pattern measurement of the range antenna can be performed in the far-field or in the near-field. Since the range antenna normally has an aperture which is much smaller than a typical test antenna, satisfying the rule for prevention of amplitude taper is usually not a problem when the range antenna is measured.

When probe corrected near-field measurements are made, alignment of the range antenna becomes more critical. Since the amplitude taper has been explicitly accounted for, it is necessary to assure that orientation of the range antenna is such that the actual illumination present in the test aperture matches the assumed illumination which results from the probe calibration. Thus it is important not only to assure the probe θ/χ axis alignment, but to assure that the range antenna is properly attached to the χ axis. A mechanical or optical reference is often used to aid in the proper alignment of a calibrated range antenna.

IX. MEASUREMENT ERRORS DUE TO RANGE EFFECTS

The near-field transformation algorithm assumes that the radiation pattern of the test antenna remains constant during the course of the measurement, and that for the case in which the antenna is tested in the transmit mode, all the energy received by the near-field probe emanates from the test aperture. (Reciprocity applies for the case in which the antenna is tested in the receive mode.) Thus, no account is taken for antenna interactions with a ground plane or for other multipath effects, for stray signal radiation, or for mutual coupling between the test antenna and the range antenna. These effects result in a violation of one or both of the algorithm assumptions, and constitute a source of measurement error. These sources of error are to be avoided through sutiable design of the antenna test range.

The amount of noise power which is introduced into the measurement can be quantified in terms of the equivalent stray signal level. Figure 6 illustrates a situation in which the test signal is contaminated by stray radiation from a reflection from an absorber-covered wall. As can be seen in the illustration, a noise source of given relative noise power will cause a greater uncertainty at low pattern levels than at high pattern levels. The concept illustrated applies to both near-field and far-field measurements. In general, it is difficult to predict how measurement noise in the near-field pattern transforms into the far-field.

Ground interactions and mutual coupling interactions are usually negligible if the test antenna is separated from conducting surfaces and from the range antenna by at least 10 wavelengths. This does not represent a problem at frequencies greater than several Gigahertz, but can become a major difficulty at UHF and low microwave frequencies. If sensitive measurements are to be made, a more rigorous analysis might be performed to insure that mutual coupling is not present in a given test situation. Needless to say, ground reflection ranges cannot be used for near-field testing.

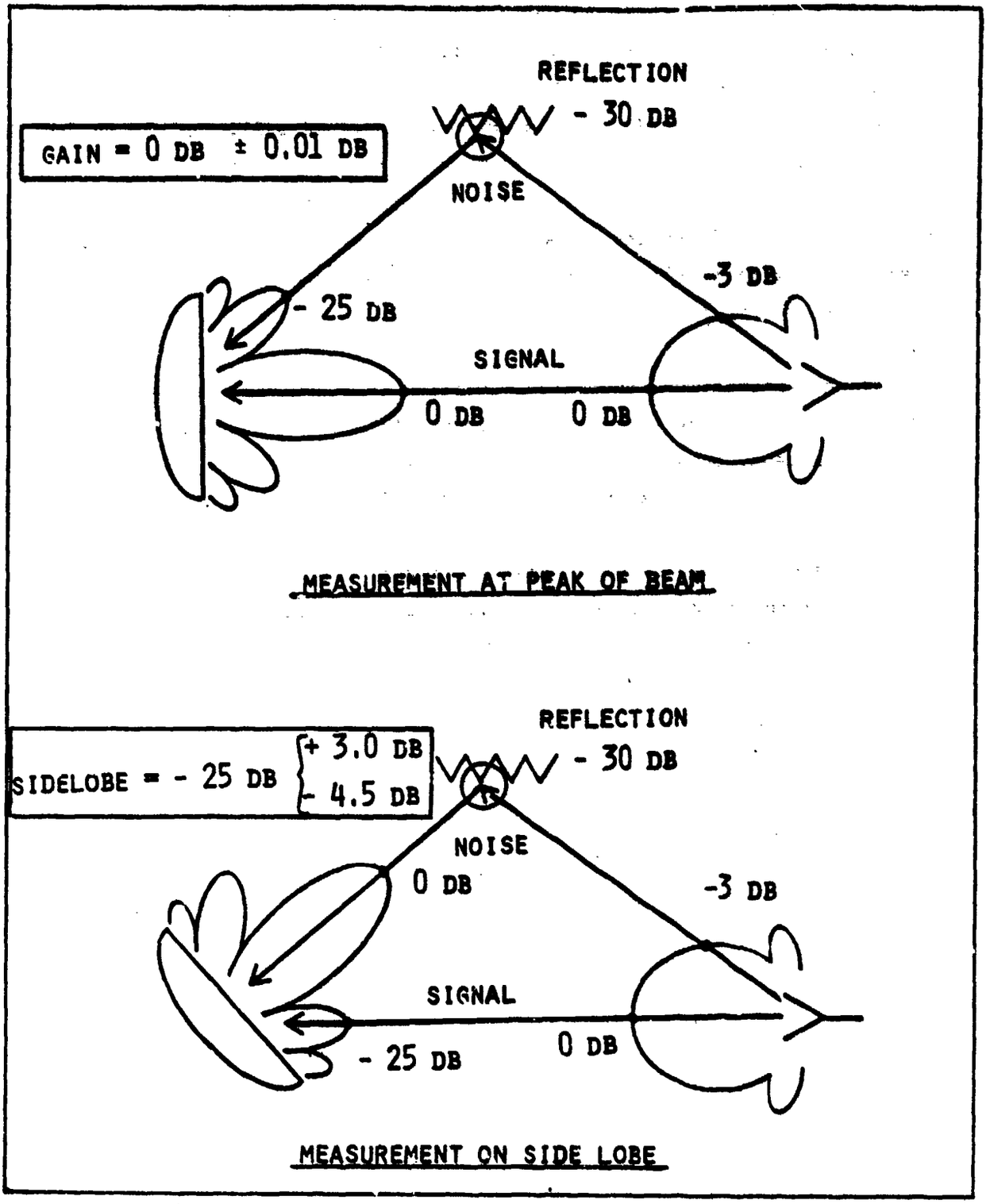

Figure 6. Effect of Stray Signal

X. OUTDOOR MEASUREMENTS

Outdoor near-field measurements require special consideration in several key areas. The first consideration is the manner in which the phase reference for the coherent microwave receiver is provided. Near-field testing requires that the phase as well as the amplitude of the antenna pattern be measured. The phase must be measured against a phase reference which is invariant with respect to the orientation of the test antenna, since the phase characteristics are required as a function of position on the test sphere in order to perform the far-field calculation. Furthermore, the phase reference must be invariant with respect to the polarization of range antenna, such that the phase for each probe polarization is measured against the same reference.

In an indoor test range, where the range antenna is separated from the test antenna by only a short distance, the phase reference is usually obtained from an RF coupler which transmits the reference signal to the receiver via a coaxial cable. The range antenna in this situation is normally the transmitting antenna, and the coupler is placed in the line which feeds the range antenna.

In an outdoor test range, the range separation is such that it is not normally practical to transmit the phase reference via coaxial cable. In outdoor testing, the phase reference may be obtained through the use of an auxiliary antenna in the proximity of the antenna under test. The reference antenna is held stationary during the course of the test, as the test antenna is rotated through the test angles, and thus provides a stable phase reference. A problem occurs when the polarization of the range antenna is switched, as this might cause a variation in the phase of the signal received by the reference antenna. Compensation for such a phase variation must be provided. Figure 7 illustrates the differences between the routing of the phase reference for indoor and outdoor testing.

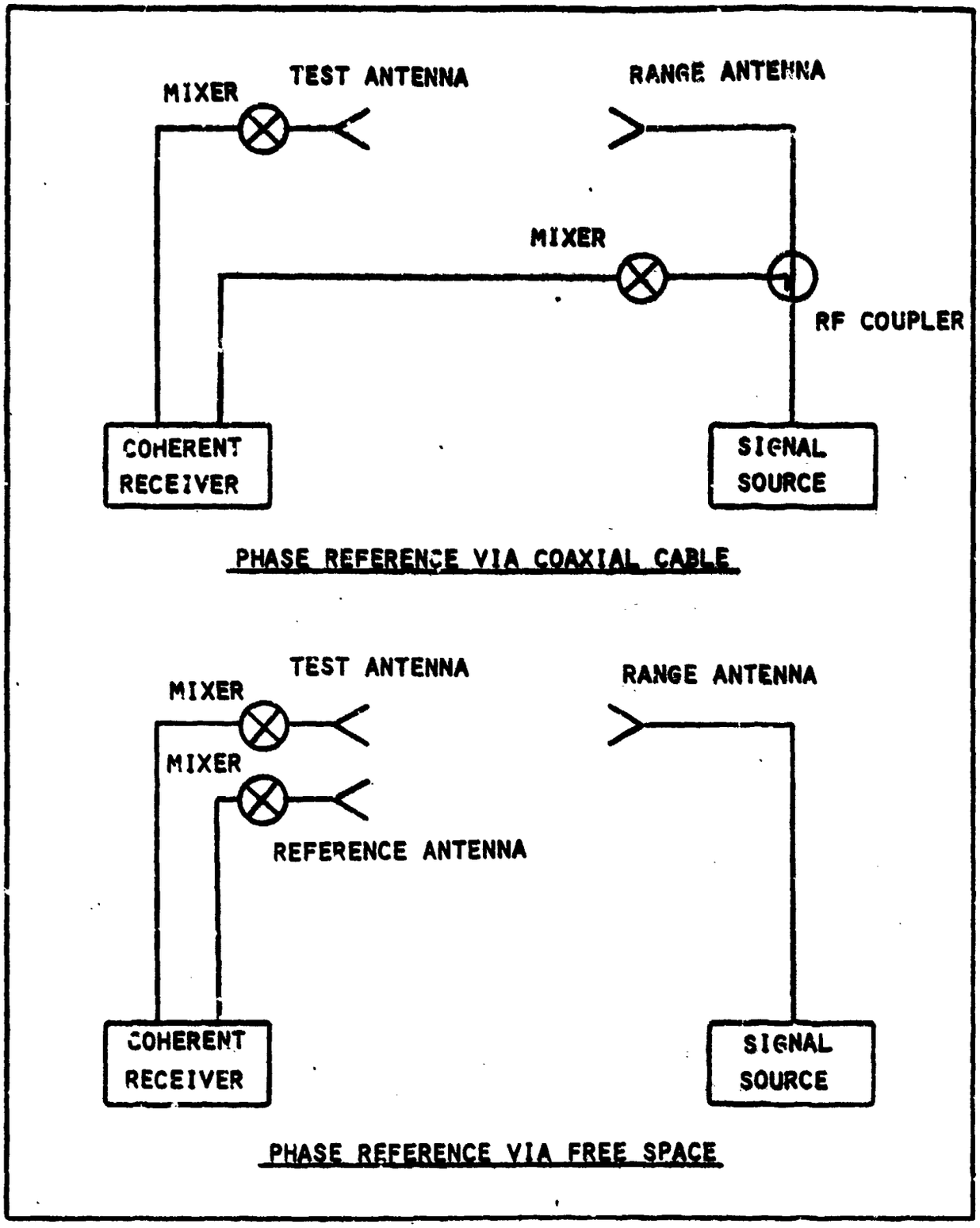

Figure 7. Routing of Phase Reference

A second consideration which must be given to outdoor testing is the phase stability of the measurement. In indoor testing, the temperature of the test environment can be well controlled, usually to within one or two degrees Celsius. In outdoor testing, it is much more difficult to control the environmental temperature. Control of the temperature is important because of the temperature effects on the electrical length of the various cables required for the test. Temperature fluctuations can cause differential changes in signal path lengths, resulting in phase errors in the measured data. To minimize this source of error, the temperature of the test cables should be stabilized as much as possible, cables with low temperature coefficients should be chosen, and the physical lengths of the test cables should be matched to curtail differential changes in the electrical lengths.

XI. POWER CONSIDERATIONS

A cursory analysis of the signal source power required to perform a near-field measurement might lead to the erroneous conclusion that the received signal power would always be greater in a near-field test than in a far-field test, the line of reasoning being that the near-field test avoids the $1/R^2$ fall-off in power. In fact, there are situations in which the near-field received power is less than in a far-field test. This is due to the fact that a low-gain range antenna is normally used for near-field testing, whereas a high-gain range antenna is used for far-field testing. Also, the $1/R^2$ fall-off does not necessarily apply in the near-field region of the radiation pattern, where the radiated energy is apt to be collimated.

A detailed discussion of the power required from the signal source is given in reference [6]. A summary is given below.

Throughout the following discussion we will assume that the test antenna and the range antenna are polarization matched. Also, we will assume that the efficiencies of the test antenna and the range antenna are unity. We wish to determine the maximum power that will be received in the measurement, in order that the dynamic range of the measurement may be optimized.

In the near-field, the radiation pattern of a directive antenna normally represents a collimated wave. Thus, we do not expect a power variation due to changes in the range distance in the near-field. The power P_o supplied to the test antenna by the signal source is distributed in a more or less uniform manner to create the near-field aperture distribution. The maximum power P_{NF} received by the range antenna is given roughly by the gain of the near-field probe G_{R-NF} times the power density in the test aperture. Thus

$$\frac{P_{NF}}{P_o} = G_{R-NF} \left(\frac{1}{A_{Aper}}\right)$$

$$= G_{R-NF} \left(\frac{4}{\pi D^2}\right) \qquad (6)$$

where A_{Aper} is the area of the test aperture and D is the diameter of the test aperture.

As we move from the near-field to the far-field of the test antenna, the radiated energy is progressively focused and the apparent gain of the test antenna will increase. When we reach the far-field, the radiation pattern is fully formed, and no further gain variations result. In the far-field, radiation from the test antenna is no longer collimated. The power received by the range antenna falls off as the square of the range length. The power P_o supplied to the test antenna by the signal source is focused into a radiation beam. The maximum power P_{FF} received by the range antenna is given roughly by the gain of the far-field probe G_{R-FF} times the maximum power density in the far-field. Thus

$$\frac{P_{FF}}{P_o} = G_{R-FF}\ G_T \left(\frac{1}{S_{Sphere}}\right)$$

$$= G_{R-FF}\ G_T \left(\frac{1}{4\pi R^2}\right) \qquad (7)$$

where S_{Sphere} is the surface area of the test sphere and G_T is the gain of the test antenna and R is the far-field range length.

The gain of the test antenna may be estimated by

$$G_T = \left(\frac{\pi D}{\lambda}\right)^2 \qquad (8)$$

where D is the diameter of the test aperture and λ is the wavelength. Also we may substitute for the far-field range length R the expression

$$R = \frac{2D^2}{\lambda} \qquad (9)$$

By substituting equations (8) and (9) into equation (7), we obtain

$$\frac{P_{FF}}{P_o} = G_{R-FF}\left(\frac{\pi^2 D^2}{\lambda^2}\right)\left(\frac{1}{4\pi}\right)\left(\frac{\lambda^2}{4D^4}\right)$$

$$= G_{R-FF}\left(\frac{\pi}{16\ D^2}\right) \qquad (10)$$

We can now compute the ratio of the near-field to the far-field received power by dividing equation (6) by equation (10)

$$\frac{P_{NF}}{P_{FF}} = \left(\frac{64}{\pi^2}\right)\frac{G_{R-NF}}{G_{R-FF}}$$

$$= 8\ \text{dB} + \frac{G_{R-NF}}{G_{R-FF}} \qquad (11)$$

Thus, the ratio of the near-field to the far-field power is a function of the ratio of the gains for the two range antennas used. If the same range antenna were used for both the near-field and the far-field measurement, then

the near-field measurement would result in 8 dB greater power. In practice, the gain of the near-field probe is usually substantially less than the gain of the far-field probe, resulting in a lower signal in the near-field measurement.

In both the near-field and the far-field measurements, the gain of the range antenna should be chosen so as to maximize the received signal level without introducing amplitude taper in the test aperture. Thus, the beamwidth Ω_R of the range antenna is given by

$$\Omega_R = \frac{D}{R} \qquad (12)$$

The gain G_R of the range antenna is related to the beamwidth by

$$G_R \propto \left(\frac{1}{\Omega_R}\right)^2 \qquad (13)$$

Thus, the gain selected for the range antenna will vary as

$$G_R \propto \left(\frac{R}{D}\right)^2 \qquad (14)$$

Since the test aperture diameter D is assumed to remain constant, the gain of the range antenna may increase as the square of the range length R without introducing amplitude taper in the test aperture. In practice, the far-field range antenna is normally chosen to have a beamwidth which is twice the beamwidth of the test antenna, or a gain which is 6 dB less than the test antenna. The near-field range antenna is normally chosen to have a gain which is low, on the order of 3-5 dB, in order that the beamwidth be wide enough to allow close-in testing.

XII. SUMMARY

Spherical near-field antenna testing offers a unique set of advantages and disadvantages over other antenna measurement techniques. It is important to understand the special characteristics of near-field testing if an

intelligent choice is to be made regarding a test method. This paper has been an attempt to cover several of the key issues in spherical near-field methodology.

Spherical near-field testing requires the collection of more data than is normally required in conventional far-field antenna testing, due to the nature of the data transformation and the influence that each near-field data point has on a given far-field data point. Near-field testing also requires the additional step of data transformation as compared to conventional far-field testing. Near-field testing does allow considerable savings on the size of the test range, however, and does produce test results which are potentially of a very high quality.

In order to maximize the accuracy of near-field test results, the test range must be properly designed to minimize range noise, as is the case in conventional far-field testing. In addition, special attention must be paid to the proper alignment of an antenna range which is used for near-field testing.

Antenna pattern measurements, gain measurements, and polarization measurements all may be performed using near-field testing, with some modification to conventional test procedures. As in far-field testing, the three antenna polarization calibration method may be employed to increase the accuracy of polarization measurements beyond the polarization purity of the range antenna. In addition, near-field measurements may be performed with probe pattern correction to take into consideration the amplitude taper in the test aperture.

XIII. REFERENCES

1. Hess, D. W. and Tavormina, J. J. (1981) Verification Testing of a Spherical Near-Field Algorithm and Comparison to Compact Range Measurements. Paper presented at the 1981 International IEEE/APS Symposium, Los Angeles, CA.

2. Tavormina, J. J. and Hess, D. W. (1980) Spherical Near-Field Antenna Measurements with the Scientific-Atlanta Model 2022. Application Note AN-22, Scientific-Atlanta.

3. Harmening, W. A. (1979) Implementing a Near-Field Antenna Test Facility, Microwave Journal, September.

4. Far-Field Antenna Pattern from a Near-Field Test, NASA Tech Briefs, Spring 1981.

5. Hess, D. W. and Tavormina, J. J. (1982) An Algorithm with Enhanced Efficiency for Computing the Far-Field from Near-Field Data on a Partial Spherical Surface. Program of the U. S. National Radio Science Meeting, p. 185, January.

6. Series 2020 Antenna Analyzer Spherical Near-Field Range Configuration Manual, (1982) Scientific-Atlanta.

7. Antenna Measurement Handbook (1961) Scientific-Atlanta

dupe

Dupe of AD-A117 744

ULTRALOW SIDELOBE PLANAR NEAR FIELD MEASUREMENT STUDY

Kenneth R. Grimm

Technology Service Corporation
Washington Division

Prepared for:

1982 Antenna Applications Symposium
Allerton Park, Illinois

September 22-24, 1982

ABSTRACT

An analytic study has extended existing methods of estimating antenna pattern errors when testing by the method of planar near field probing. Improved error bounds are given for very low sidelobe levels based only on the measured near field data and known tolerances due to probe positioning and multipath. These bounds are useful for certifying array performance independent of standard far field antenna range tests. They also can serve as improved design criteria for the construction of quality near field testing systems. An optimum probe for low sidelobe testing is shown to be one which minimizes its back scatter while simultaneously contributing minimum mean square error to the sidelobe region. That this is impossible for the commonly used dominant-mode waveguide probes is acknowledged, and a recommendation is made to design an alternate probe based on a single (or small array cluster) of radial mode dipoles. The principle study recommendation is to confirm the improved error estimates developed herein by conducting a test of a qualified very low sidelobe array at the National Bureau of Standards, in order to demonstrate the fundamental limits of measurement accuracy of planar near field probing.

Work reported herein was performed during the period 1 January - 30 June 1982 as exploratory development for the Office of Naval Technology (Contract N00014-82-C-0115) under the Defense Small Business Advanced Technology (DESAT) Program.

1.0 INTRODUCTION

Planar Near Field (PNF) antenna scanning has come into increasing use for the testing of microwave array antennas which have been designed for use in advanced DOD electronic systems. This measurement technique is attractive because it is based on short-range distances, is easily accommodated indoors, and because it is inherently accurate, since so few measurement approximations are involved [1, 2, 3]. It does however, require the acquisition of large sets of PNF data, and the execution of a computer data transform in order to recover the desired test antenna's Far Field (FF) properties. The purpose of this study is to estimate the accuracy by which this may be accomplished for an arbitrary low sidelobe array. "Low Sidelobe" refers to relative field levels which may be radiated in any of the antennas modes, pattern planes, or polarizations which are at least 30 dB below the antenna's peak directivity. The approach of this study is to extend, and modify as necessary, existing error bounds when applied to an arbitrary low sidelobe array. Only the planar scanning geometry is considered, although cylindrical and spherical geometries have also been in use [4].

2.0 PROBLEM FORMULATION

A general test array is assumed to be operating in free space, in a single mode and frequency such that the desired radiation is directed normally outward through its mechanical or electronically steered pointing direction. A planar NF probing scanner is situated close to (and nearly parallel to) the array aperture. (see sketch in Figure 1). For this type of test, possible FF sidelobe errors will be introduced by NF measurement errors, including:

- sampling area truncation
- probe positioning errors
- RF instrument conversion errors
- multiple probe/array reflections
- probe pattern and numerical transform uncertainties.

A Far Field (FF) fractional error ratio, valid throughout the entire pattern, E(r), may be written as:

$$\eta(r) \leq \left| \frac{|E(r) \pm \Delta E(r)| - |E(r)|}{|E(r)|} \right| \leq \frac{|\Delta E(r)|}{|E(r)|} \qquad (1)$$

and $\Delta E(r)$ is the fractional FF error due to each NF measurement uncertainty. A discussion of useful error bounds is found in [2, 3, 5]. In this paper, however, only NF multipath is addressed.

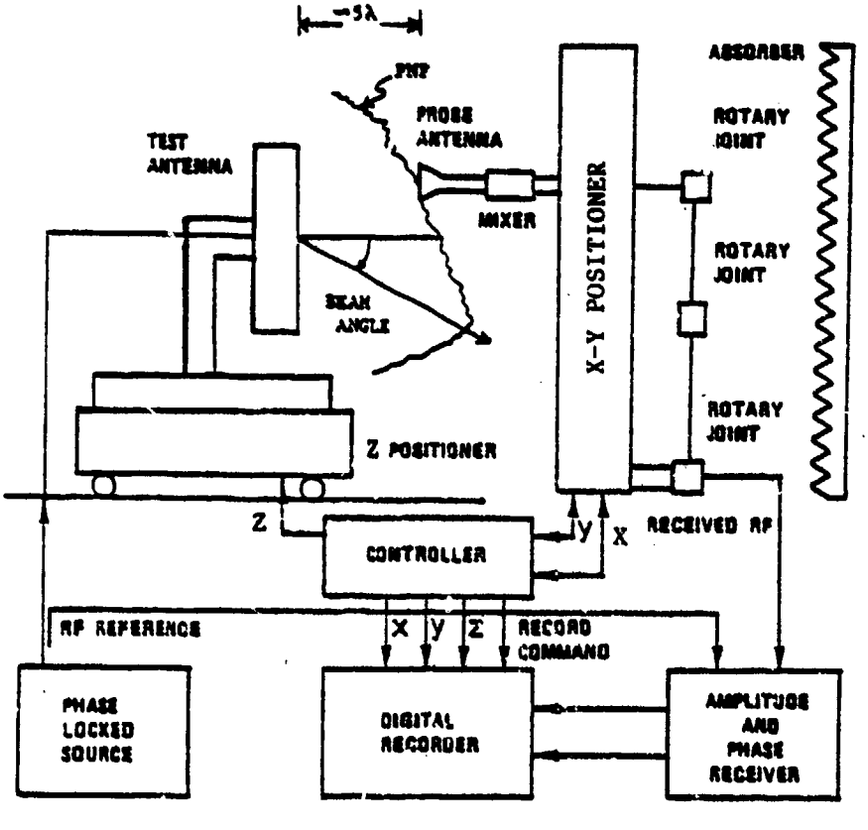

Figure 1. Basic Planar Near Field Measurement

3.0 IMPROVED ERROR BOUND DUE TO MULTIPATH

3.1 Multipath Mechanism

The primary NF interference mechanism is due to the multiple round trip paths between the moving probe and the nearly parallel array aperture. Specular reflection geometries are also possible, due to scanner and room reflections, but these can be easily minimized in a well-designed facility. However, the perpendicular probe/array reflections are always present, and represent a fundamental limit to the achievable accuracy of planar NF testing for low sidelobe antennas. The effect of these reflections is to cause interference patterns in the NF as shown in Figure 2. These curves show measured relative probe output as a function of increasing probe/array Z-separation, for three probe reference locations in the scan plane. The ripples which have a period of about $\omega = \lambda/2$ are due to unavoidable probe/array reflection paths. The peak-to-peak magnitude of one ripple period (indicated as Δ^{mr}) is the parameter used to estimate the resulting sidelobe error in the far field in accordance with the following expression,

$$\eta(r) \leq (\epsilon^{mr}/2)\ g(r) \qquad (2)$$

where

$$\epsilon^{mr} = \begin{cases} \text{average amplitude ratio of multiple reflection to total NF} \\ 20 \log \left(\frac{\rho-1}{\rho+1}\right)\ ,\ \rho = \log^{-1}(\Delta/20)\ ,\ \Delta^{mr} \text{ shown in Figure 2} \end{cases}$$

$g(r)$ is the specified sidelobe level of interest.

The utility of equation (2) at very low sidelobe levels is the present concern.

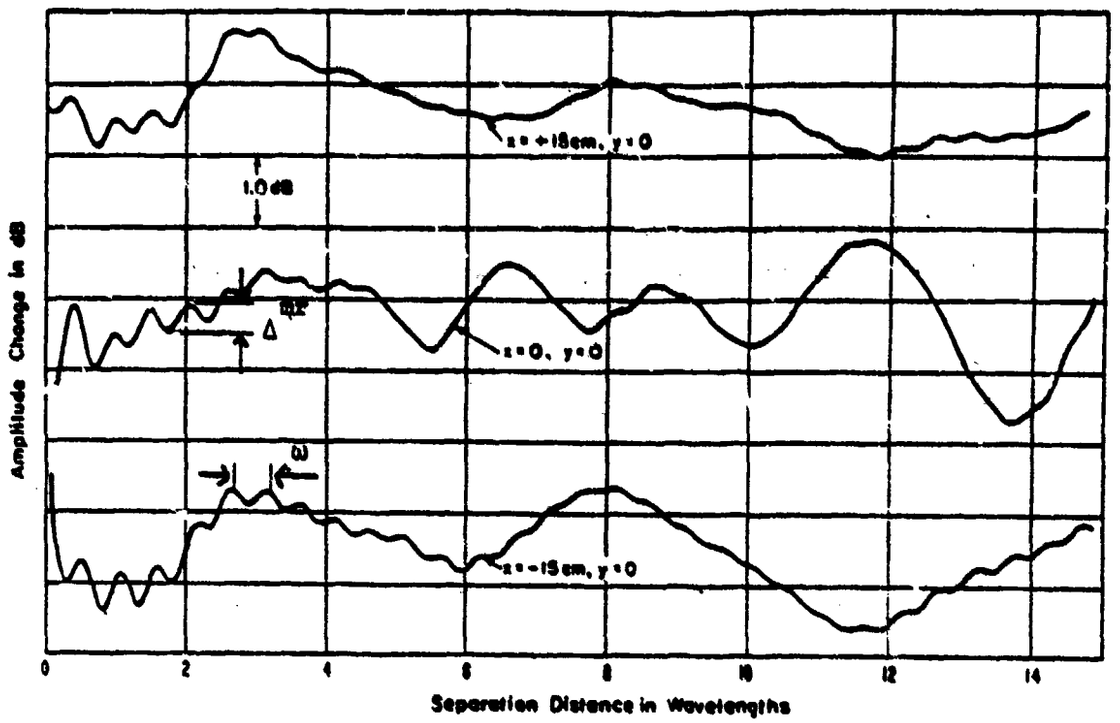

Figure 2. Measured z-dependent NF Amplitude for Three Reference Locations in the Scan Plan Showing the Peak Interference Magnitude Δ^{mr} Occuring with Period $\omega = \lambda/2$ due to Probe/Array Multipath [Ref. 2]

3.2 Present Bound - Example

Equation (2) predicts worst-case FF sidelobe error due to NF multipath. For example, from Figure 2, a peak interference ripple magnitude of $\Delta^{mr} \approx .5$ dB was measured during a NF test program of an X-band array at NBS [6]. Such interference magnitudes corresponds to reflection fields which are about 31 dB below the direct ray path ($\epsilon^{mr} = .0288$), but if one uses this interference value in equation (2) to estimate the error at the -40 dB FF sidelobe, a worst-case but unreasonably large error is predicted, i.e.,

$$\eta^{dB}(-40\ dB) \leq 20 \log [1 + (.0288/2)100]$$

$$\leq 7.74\ dB \qquad (3)$$

This estimate is valid only if the multiply reflected NF phase is nearly uniform in the scan area, which of course it isn't, since the probe views a changing (and periodic!) reflection environment as it scans over the array elements in the aperture plane. To test the sensitivity of the existing bound to realistic phase properties of reflection fields and to various NF amplitude tapers, the following numerical simulation has been performed. The goal of the exercise is to find scale factors for the critical parameter ϵ^{mr} in equation (2), such that more realistic error bounds may be found for very low level sidelobes.

3.3 Multipath Phase Error Simulation

Assume the reflected fields between probe and array remain same sense polarized and interact with the direct fields at the probe to generate error fields which have the simple NF functional form:

$$\Delta E_{NF}^{mr} = \epsilon^{mr} E_o \cos^n(\pi x/a) e^{j2\pi(x/\lambda_1 + y/\lambda_2)} \qquad (4)$$

where

- E_o is maximum error-free NF amplitude
- ϵ^{mr} is the proportionality constant between direct and reflected field
- x,y is the probe scan direction
- a is the maximum dimension of the projected aperture on the scan plane
- $\lambda_{1,2}$ are arbitrary reflection phase constants describing the rate of change of NF phase error with x, y probe scan

Uniform NF Case When $n = 0$ (uniform illumination) and the projected aperture on the scan plane is circular with diameter a, then the far error field is found from a Fourier Transform of (4), i.e.,

$$\Delta E_{FF}^{mr} = [\bullet] \int_A \varepsilon^{mr} E_o e^{i2\pi(x/\lambda_1 + y/\lambda_2)} e^{\frac{-ik\hat{R}\cdot P}{r}} dP \qquad (5)$$

where

R, r are source and field radial directions.

$[\bullet]$ is a FF radiation kernel $\sim \frac{e^{jkR}}{r}$.

P is probe transverse (x, y) location.

A is the projected aperture area having a NF amplitude of form $\cos^n(\frac{\pi x}{a})$ and zero outside, and k is the propagation direction.

Expressing the integration variables in (5) with polar form and carrying out the indicated transform analytically for n = 0, find

$$\Delta E_{FF}^{mr} = [\bullet] \; a \varepsilon^{mr} E_o \frac{J_1(2\pi aB/\lambda)}{B} \qquad (6)$$

where

$$B = \sqrt{(\lambda/\lambda_1 - \sin\theta\cos\phi)^2 + (\lambda/\lambda_2 - \sin\theta\sin\phi)^2}$$

Now allow $\lambda_{1,2} \to \infty$ in equation (4) so that the multipath phase variation with probe scan is made to approach zero, representing the error-free NF. Again by a Fourier Transform (in polar coordinates), get,

$$E_{error\text{-}free} = E_o \, a(\cos^2\theta + \sin^2\theta \cos^2\phi)^{1/2} \frac{J_1(\frac{2\pi a \sin\theta}{\lambda})}{\sin\theta} \qquad (7)$$

Consider only a single FF pattern plane, i.e., choose $\phi = 0$, and assume that the multipath reflection plane constants are the same in both scan directions, i.e., $\lambda_1 = \lambda_2 = \lambda_0$. Then the sought FF fractional error ratio η becomes a simple function of pattern angle, and preserves the dependence on possible NF multipath phase error ratios a/λ_0 . Thus, from (6) and (7), find

$$\eta(\theta) = \Delta E^{mr}_{FF} / E_{error\text{-}free}$$

$$= \frac{\varepsilon^{mr} \sin\theta \left| J_1\left(\frac{2\pi a B}{\lambda}\right) \right|}{B \left| J_1\left(\frac{2\pi a}{\lambda} \sin\theta\right) \right|} \qquad (8)$$

where

$$B \text{ becomes } \sqrt{2\,\lambda/\lambda_0(\lambda/\lambda_0 - \sin\theta) + \sin^2\theta}\,.$$

Equation (8) has been plotted in Figure 3 for a 12λ aperture and six possible values of multipath phase error given by a/λ_0 = 0.1, 0.3, 1.0, 2.5, 5.0, 8.0. From the figure, when the multipath-induced phase change across the scan plane is nearly constant ($a/\lambda_0 < 1$), the envelope of the FF error ratio approaches ε^{mr} throughout the sidelobe region, but peaks at about $1.7\varepsilon^{mr}$ in the near-in sidelobes. When the NF multipath phase error is moderate ($a/\lambda_0 \approx 1$), the FF error envelope approaches ε^{mr} more slowly, and when the NF multipath phase change is large ($a/\lambda_0 > 1$), the envelope of FF sidelobe errors is small and never exceeds $.6\varepsilon^{mr}$ throughout the whole plotted sidelobe region. These results show the sensitivity of the existing error bound to measurable NF phase change, and are useful for selecting a scaled value of ε^{mr} to use in equation (2).

Tapered NF Case A procedure analogous to the example just shown is followed for the low sidelobe case, by including a NF taper factor to account for an arbitrary symmetric aperture illumination. Thus, the assumed multipath FF error fields have functional form,

$$\Delta F^{mr}_{FF} = [\bullet] \int_A \varepsilon^{mr} E_0 \cos^n(\pi x/a)\, e^{i2\pi(x/\lambda_1 + y/\lambda_2)}\, e^{\frac{-ikR\cdot P}{r}}\, dP \qquad (9)$$

The taper factor, $\cos^n(\pi x/a)$, disallows (9) from being integrated analytically, however, a standard numerical integration can be performed

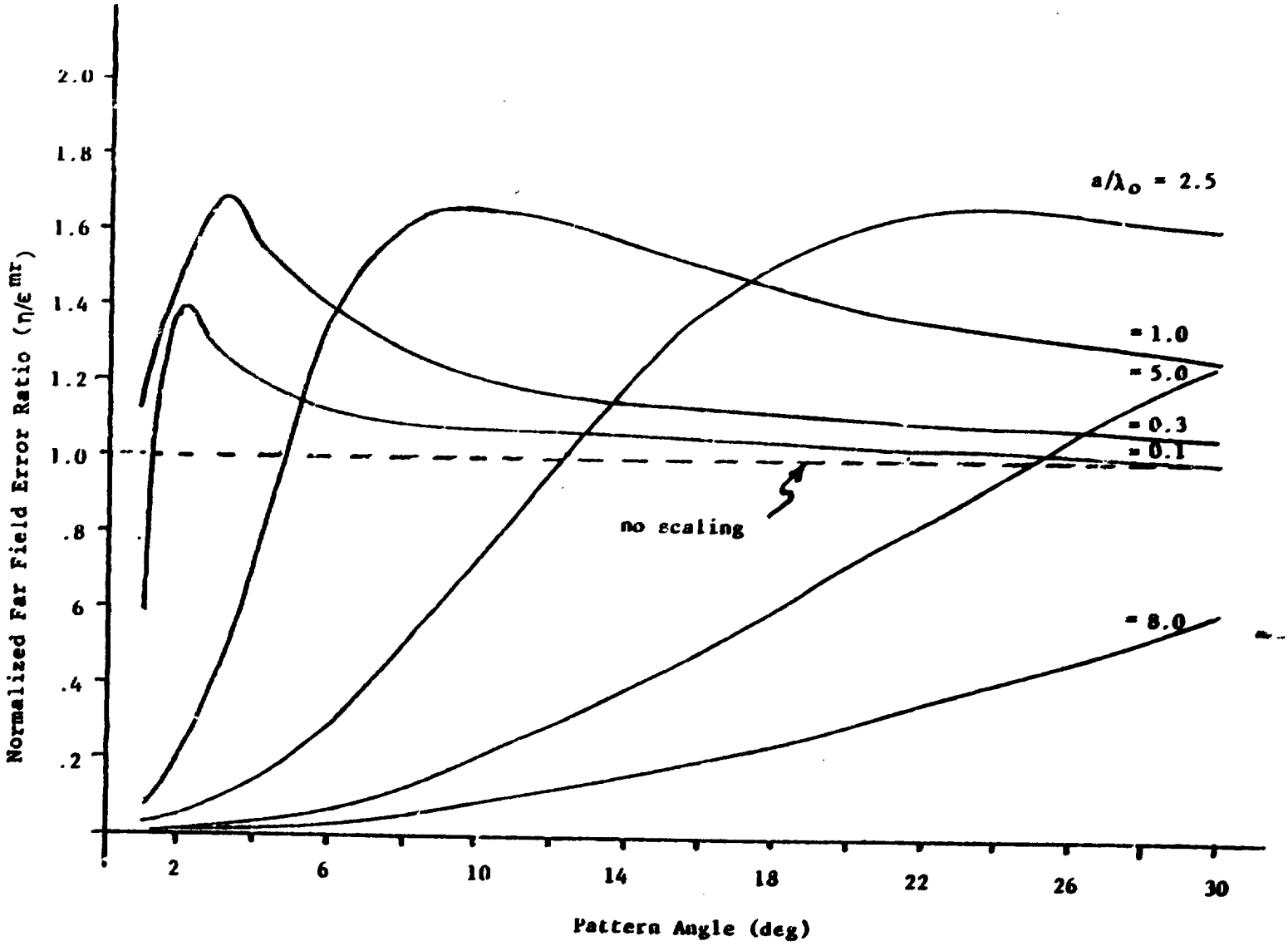

Figure 3. Computed Interference Ratio Scalings for Modifying the Upperbound Error Ratio of a Uniform Aperture Having Various Assumed MF Phase Changes Due to Probe/Array Multiple Reflection

for both ΔE_{FF}^{mr} and $E_{error\text{-}free}$, and their magnitude ratio formed as before. Choosing just one possible phase error state, $a/\lambda_0 = 1$ (moderate multipath), and investigating the effect of various increasing NF taper factors (n = 1, 2, 3), the results in Figure 4 have been generated. In general, the more tapered is the NF, the larger the sidelobe error bound becomes, but interestingly only for the near-in sidelobe region. This data again assumes a 12λ aperture as in the previous example. Figure 4 also shows that the sidelobe error bound approaches the same limiting value ($.35\epsilon^{mr}$) for all three tapers evaluated, since only a single NF multipath phase error value was assumed. This demonstrates that predicted sidelobe error for a low sidelobe illumination will have a smaller maximum bound than presently specified by equation (2), but only in the far out sidelobe region. Conversely, the nearer-in sidelobes are predicted to be in larger error than previously estimated. Of course actual values will depend upon the NF taper and measured NF multipath phase error in a specific measurement problem. It is thus quite important to measure not only the peak NF interference ripple magnitude as in Figure 2, but also to measure or estimate the NF multipath-induced phase error across the scan plane. From the latter, a scale factor can be found to modify the critical parameter ϵ^{mr}, and consequently to improve FF error estimation on very low sidelobes. For this exercise, the scaling factor for ϵ^{mr} was in the range $.35<k<2.7$.

4.0 OPTIMUM PROBES

Huddleston has demonstrated that there exists an "optimum" waveguide probe for use in most PNF testing problems [7] The thrust of his work was to prove that the probe FF pattern should be "matched" in some sense to the available NF scan length. For such a probe, the sampled NF could be transformed to the desired array spectrum which would have a minimum Mean Square Error (wrt true spectrum), i.e.,

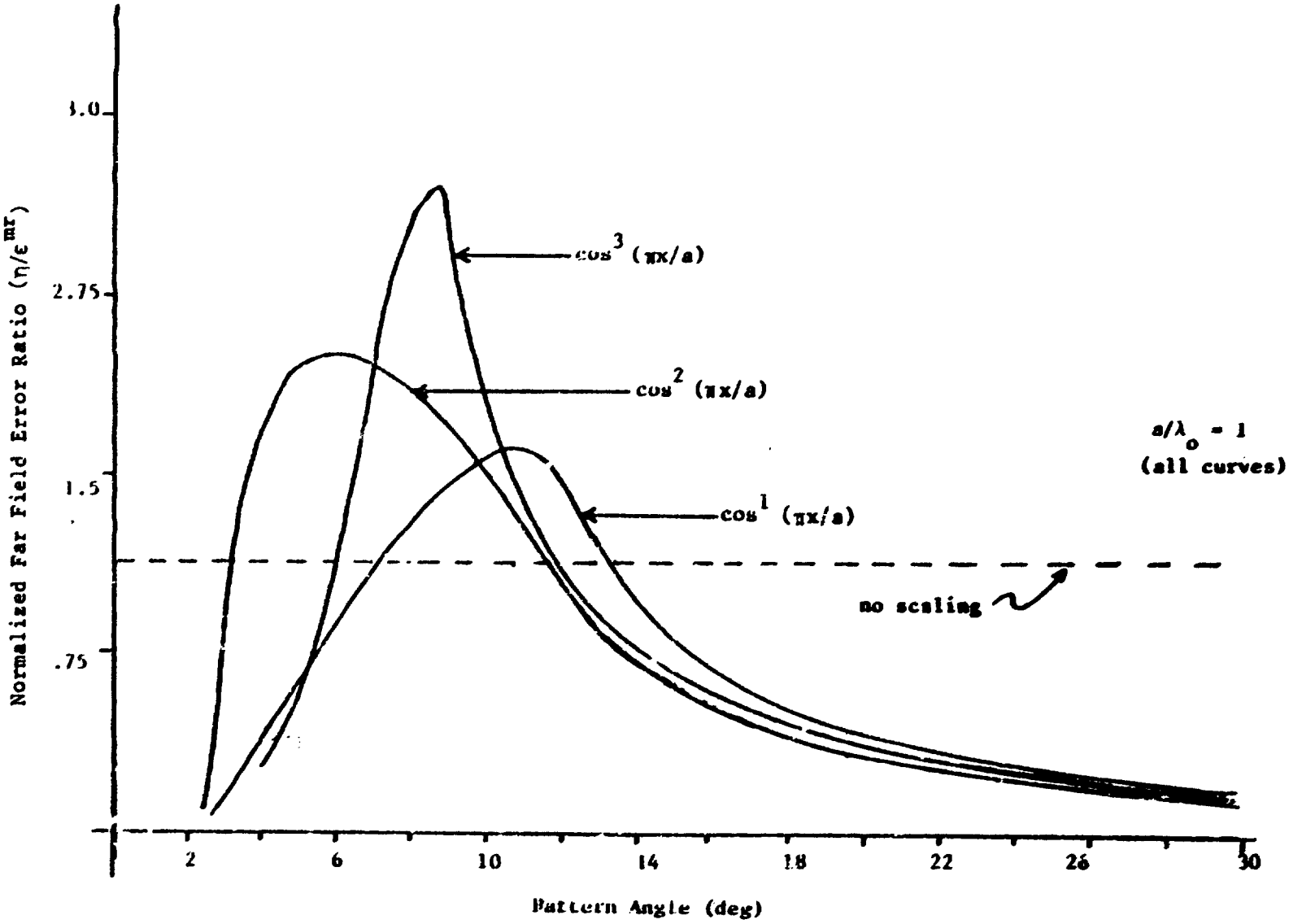

Figure 4. Computed Interference Ratio Scalings for Modifying the Upperbound Error Ratio of a Tapered Near Field Having a Single NF Phase Change ($a/\lambda_o = 1$) Due to Probe/Array Multiple Reflection

$$\min \text{MSE} = \min \int_{-k_{max}}^{k_{max}} \left| A(k_x) - \hat{A}(k_x) \right|^2 dk_x \qquad (10)$$

where

$A(k_x)$ is the true visible array spectrum

$$\hat{A}(k_x) = \begin{cases} \text{the measure of that spectrum} \\ A(k_x)\ B(k_x) * P(k_x) \end{cases}$$

with $B(k_x)$ = probe spectrum

$P(k_x)$ = transform of sampling window function (scan length)

$*$ = indicates convolution.

He shows that the minimum Mean Square Spectral Error will result if a waveguide probe concentrates its power response over the available scan length, i.e., if $v(x) = a(x)e^{i\phi(x)}$ is the X-dependent NF, then

$$\frac{\int_{L_x} |v(x)|^2 dx}{P_\infty} \triangleq 1 - \delta_x^2 \qquad (11)$$

where

P_∞ is the total radiated power in the forward hemisphere

δ_x^2 is the fraction of power <u>not</u> intercepted by the probe as it travels over scan length, L_x

For the class of waveguide probes considered by Huddleston, the optimality condition in (11) which satisfies the error criterion in (10) has been shown to occur when the probe aperture has a critical E-plane dimension of 1λ. The H-plane dimension is less critical, but 1λ is also recommended. A summary of Huddleston's design analysis which certifies the optimum waveguide probe dimensions is reprinted in Figure 5 below. The plot shows that the critical E-plane probe dimension of bp = 1λ produces the smallest <u>unconcentrated</u> response,

δ_x^2 , i.e., has the optimum directivity. Such a probe best intercepts the planar near field for all possible scan lengths, L_x. The relation between L_x and the plotted coordinate $\sin\theta_{max}$ is shown in the inset. Values of b_p , either less than or greater than 1λ, produce larger values of δ_x^2 , and hence are suboptimum (MSE sense). Note that this is true only for the class of dominant-mode waveguide probes considered by Huddleston. These results were calculated from a simulation for the PNF of a 45 element phased array operating at C-band.

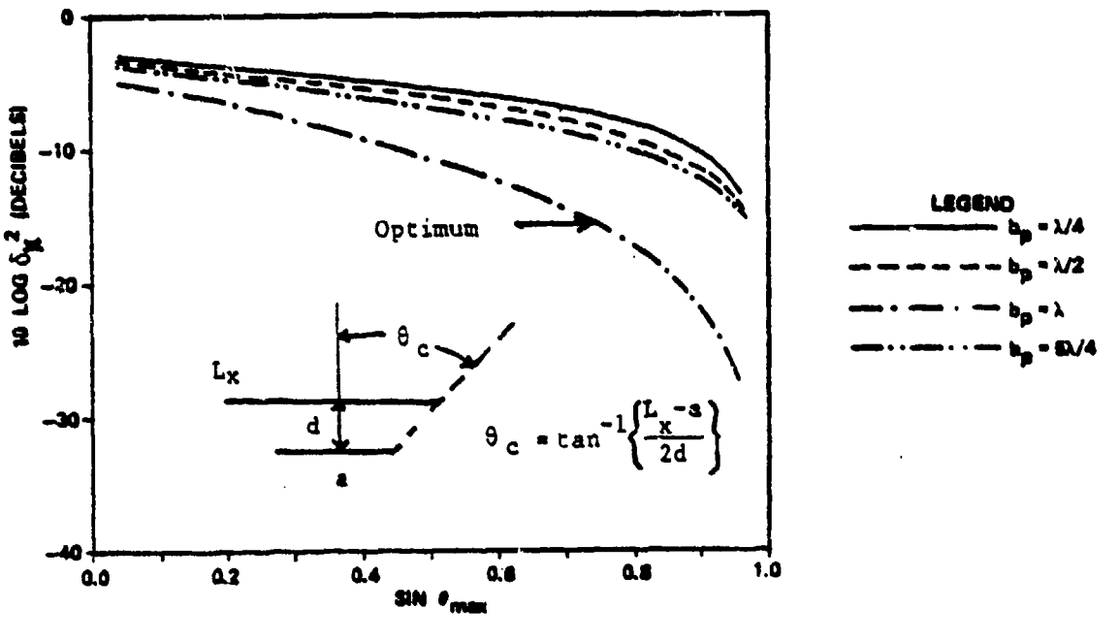

Figure 5. Computed Probe Concentration Factor, δ_x^2 versus $\sin\theta_{max}$ for Waveguide Probes Whose Apertures Have Height b_p when Testing a Simulated Phased Array Scanned to 45° in Elevation [Huddleston, p. 89]. The $b_p = 1.0\lambda$ Probe is Optimum in a Mean Square Sense.

4.1 Alternate Design Criteria for Low Sidelobe PNF Probe

The MSE criterion in equation (10) is obviously dominated by mainbeam contributors, i.e., large errors in the transformed sidelobe spectrum will not appreciably affect the Mean Square Error, but even small errors in the mainbeam spectrum will make large contributions. An alternate probe criterion might lead to alternate probe design for improved accuracy in low sidelobe testing. Such an alternate probe, if it exists, should minimize the weighted MSE, where the weight will be selected to emphasize the sidelobe spectrum. This idea implies that sidelobe and mainbeam spectral errors cannot simultaneously be minimized during a single measurement. For improved sidelobe accuracy, we seek a probe (probes) whose PNF response can be processed to minimize a Weighted Mean Square Error (WMSE) criterion, suggested as

$$\min\ (\text{WMSE}) = \min \int_{-k_{max}}^{k_{max}} \left| W(k_x)[A(k_x) - \hat{A}(k_x)] \right|^2 dk_x \qquad (12)$$

where

$$w(k_x) = \begin{cases} 1 & k_c < |k_x| < k_{max} \quad \text{(sidelobes)} \\ 0 & 0 \leq |k_x| \leq k_c \quad \text{(mainlobe)} \end{cases}$$

and k_c is the first zero wavenumber (first null). Thus, $W(k_x)$ is a wavefilter which effectively notches out the mainbeam of the test array as sketched in Figure 6. The realizability of this wavefilter from the usual dominant-mode waveguide class of probes is obviously impossible. Thus, a new class of probes is required.

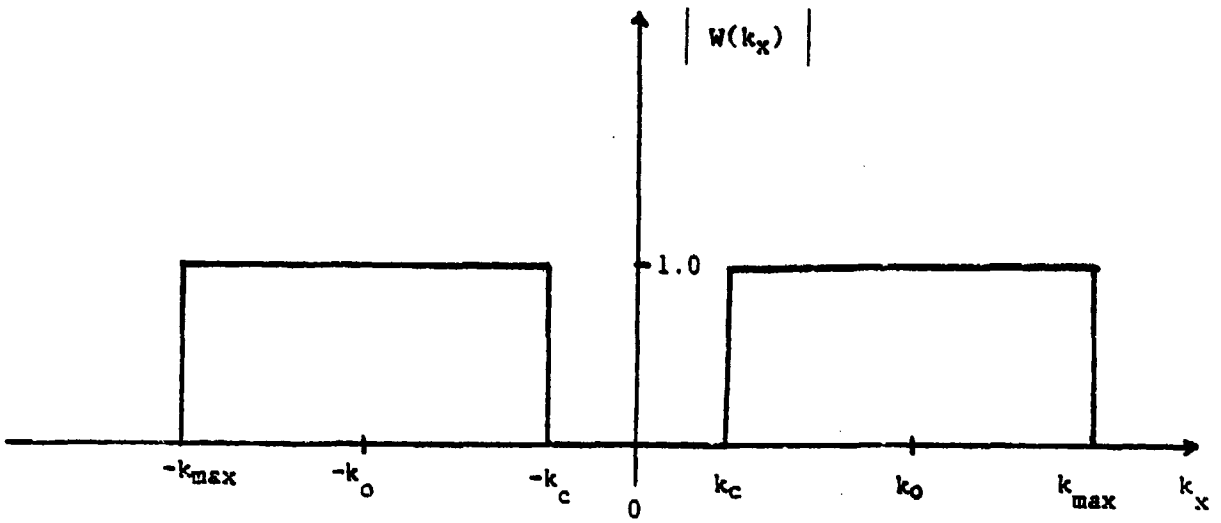

Figure 6. Proposed Alternate WMSE Probe Spectrum where $|k_{max}|$ is the Maximum Visible Wave Number, and $|k_c|$ is the First Zero Wave Number

4.2 Design Approach for Optimum Low Sidelobe PNF Probe

A design approach for synthesizing an acceptable approximation to the wavefilter shown in Figure 6 is as follows. Consider a small probe array of clustered radial dipoles as shown in Figure 7. Here the number of elements N, their relative spacing Δs, and their complex weight b_n, are design parameters to be selected by conducting a MSE numerical optimization design study. The resulting transverse FF probe array pattern is to be a best-fit to the optimum WMSE wavefilter, when the probe array is constrained to have the fewest number of dipole elements, the smallest possible spacing, and realizable complex element weights, b_n.

Such a design optimization is presently being conducted by TSC. A summary of the optimization problem, however, serves to establish the feasibility of the design approach.

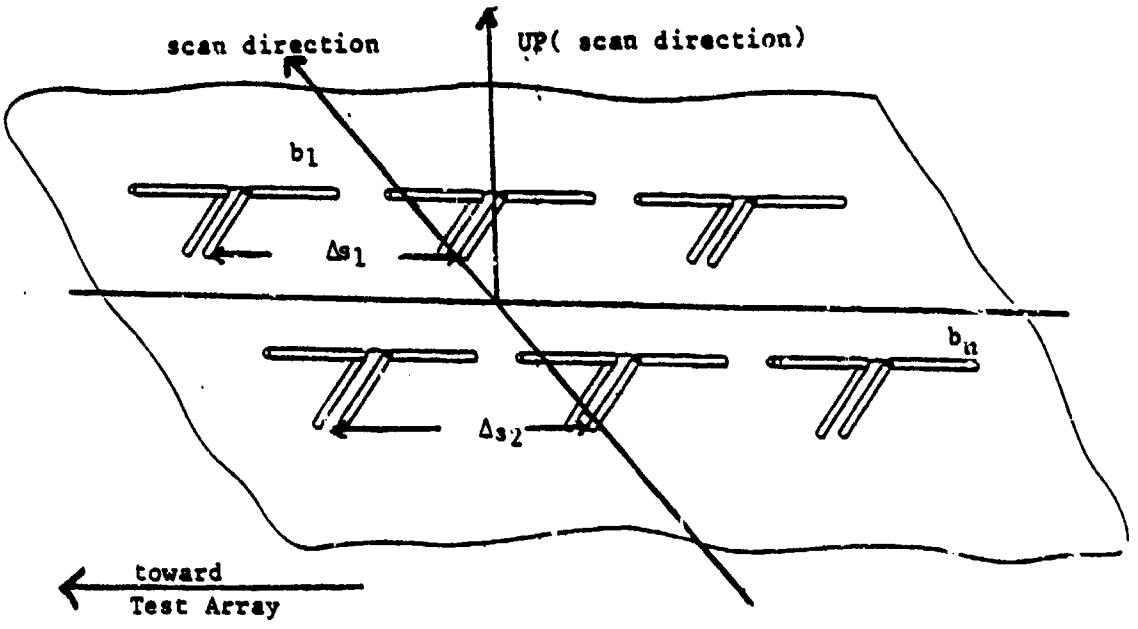

Figure 7. Geometry for Optimization Analysis for Defining the Realizable WMSE Probe

WMSE Probe Design Optimization Summary

1) Specify the general planar array probe illumination,

$$v(x) = \sum_{n}^{N-1} b_n \, \delta(x - n\Delta x)$$

2) Find the family of probe array patterns from (1) via Fourier Transform,

$$B(k_x) = \mathcal{F}\{v(x)\}$$

$$= E(k_x) \sum_{n=0}^{N-1} b_n e^{-in\Delta x k_x}$$

where $E(k_x)$ is the elemental pattern.

3) Select the specific $B(k_x)$ which minimizes equation (12) i.e., find $B(k_x)$ such that

$$\min(\epsilon) = \min \int_{-k_{max}}^{k_{max}} \left| W(k_x)[A(k_x) - \hat{A}(k_x)] \right|^2 dk_x$$

where $\hat{A}(k_x) = A(k_x)B(k_x)*P(k_x)$

with * indicating convolution over the measurement region, p(x), subject to the following probe design constraints:

$$\left.\begin{array}{l} N \le N_{max} \\ \Delta x \le \Delta_{max} \\ b_n \text{ realizable} \end{array}\right\} \text{ constraints on size of probe array}$$

When found, the set of dipoles N whose planar lattice has element spacing Δs, and whose complex weights are b_n, will radiate a best approximation to the desired WMSE wavefilter, while simultaneously presenting the smallest scattering cross-section. Selectable overhead null widths, to match an arbitrary test array mainbeam width, may be achieved for selectable weight sets, b_n. During DESAT phase 2, both a single element radial dipole probe and an optimally-designed probe array cluster, will be used in tests of sidelobe measurement accuracy with a very low sidelobe array.

5.0 CONCLUSIONS

This study has extended the existing methods of estimating far field array pattern error when testing low sidelobe arrays by the method of planar near field probing. Existing bounds have been reviewed in [5] to show that probe/array multipath and probe positioning errors are the dominant contributors to overall sidelobe error.

In this paper an improved bound on FF sidelobe error due only to NF multipath is shown to depend upon a scaled value of the measured multipath peak interference magnitude. Scale factors depend upon the multipath NF phase change. Simulation results showed that scale factors vary between .35 and 2.7 (scale factor = 1 is no scaling) for a class of tapered NF varying as $\cos^n(\pi x/\ell_{max})$, n = 1, 2, 3, ℓ_{max} is aperture length. The larger scale factors increase the bound on the near-in sidelobes, while the smaller scale factor applies in the far-out sidelobe region. Scale factors are unique to each probe and array.

An optimum probe for testing low sidelobe arrays is required to have the following properties:

- minimum response in direction of test array's mainbeam
- maximum response in direction of test array's sidelobes
- minimum backscatter.

A class of probes with these properties is a small probe array cluster of radial mode dipoles. Such a probe array can be designed by performing a numerical optimization study as suggested in section 3.2. The essential property of the alternate probe is to be most responsive to PNF energy propagating to the array FF sidelobes.

6.0 ACKNOWLEDGEMENT

This study was prepared for the Defense Small Business Advanced Technology (DESAT) program - Phase 1. The original work of A. D. Yaghjian and A. C. Newell at the National Bureau of Standards and E. B. Joy and G. K. Huddleston at Georgia Institute of Technology is the basis of the present study. The demonstration of the several results

developed during phase 1 provide the basis of a phase 2 DESAT testing exercise planned during 1983, and using the AWACS engineering array and the NBS PNF scanner.

7.0 REFERENCES

1. G. P. Rodrigue, et al., "An Investigation of the Accuracy of Far-Field Radiation Patterns Determined From Near-Field Measurements," (DDC ascension # AD 766776), August 1973.

2. A. C. Newell, "Upperbound Errors in Far Field Antenna Parameters Determined from Planar Near Field Measurements - Part II - Analysis and Computer Simulation," Lecture Notes for NBS Short Course, July 7-11, 1975.

3. A. D. Yaghjian, "Planar Near Field Measurement Techniques on High Performance Arrays - Part I: Error Analysis for Nonscanning Beam Patterns," NBS, Technical Note 667, October 1975 (DDC ascension # AD A014397).

4. P. E. Wacker, "A Qualitative Survey of Near Field Analysis and Measurement," NBSIR 79-1602, National Bureau of Standards, June 1979.

5. K. Grimm, "Ultralow Sidelobe Planar Near Field Measurement Study," TSC-W41-142, 30 June 1982.

6. A. C. Newell, M. L. Crawford, "Planar Near Field Measurements on High Performance Array Antennas," NBSIR 74-380, July 1974.

7. G. K. Huddleston, "Optimum Probes for Near Field Antenna Measurements on a Plane," Ph.D. Dissertation, Georgia Institute of Technology, August 1978, available from University Microfilms International, Ann Arbor, Michigan (#7823710).

AD P001124

R-82018

SIDELOBE IDENTIFICATION AND DISCRIMINATION

PAUL R. EBERHARDT

CUBIC CORPORATION, SAN DIEGO, CALIFORNIA

ABSTRACT

Instantaneously measuring Direction of Arrival of an arbitrary signal yet escapes most ESM systems. This paper presents a successful method for reducing this problem.

Athough principles of Sidelobe Identification and Discrimination (SLID) will be briefly discussed here this article primarily addresses SLID technology since the initial report appearing in the 1979 Antenna Applications Symposium Proceedings.

Research and development efforts resulted in prototype hardware; antenna modifications are relatively simple and applicable to a variety of antennas. General limitations and performance parameters are presented herein.

1.0 INTRODUCTION

Directional antennas respond to signals from all directions to some degree. These multiple responses make instantaneous Direction of Arrival (DOA) determination difficult. A variety of systems have been developed to deal

with this problem. The technique described in this paper, Sidelobe Identification and Discrimination (SLID), is particularly suited for multi-octave, highly directive antenna systems especially when used with extremely sensitive intercept receivers.

SLID depends upon a modulation or label impressed upon any pulse not received on an antenna mainbeam. The modulation is inserted in signals associated with sidelobe DOA by an appropriately modified antenna system. The modulation is detectable only in otherwise undesired signals. Signals of interest in the antenna mainbeam are therefore undisturbed by this technique.

2.0 BACKGROUND

The SLID process is based upon a fundamental characteristic common to any directive antenna radiation pattern. Radiation patterns can be divided into these two regions: the mainlobe and the sidelobes. Mainlobe characteristics are basically determined by the overall antenna dimensions and are modified only by major changes in the antenna. Sidelobes, rather, are controlled by subtle features of the antenna aperture distribution. This difference in sensitivity provides the key to the SLID process.

Delicate disturbances of an aperture produce inconsequential and often undetectable modifications to the antenna main beam. When viewed from a more volatile sidelobe, that disturbance produces significant changes.

This effect is often observed when a minor adjustment is made to an antenna. A seemingly insignificant change causes profound alterations to the antenna sidelobe structure.

SLID introduces a delicate disturbance into the antenna aperture distribution. This modulation will then appear only in signals received through sidelobes and hence a determination of DOA (mainbeam vs. sidelobe) can be made immediately upon reception of a single pulse.

Figure 1 shows a typical antenna radiation pattern exhibiting SLID modulation.

Another view of the SLID modulation is presented by Figure 2. Two pulses are shown. The larger pulse is typical of a signal arriving on a mainbeam. The smaller pulse on the right has been received on a sidelobe where the impressed modulation is clearly evident.

The presence or absence of modulation is used to determine DOA. Relative amplitudes of the two pulses are meaningful parameters only when the transmitted level and range are known. This is not always the case, particularly when multiple scanning sources are being analyzed.

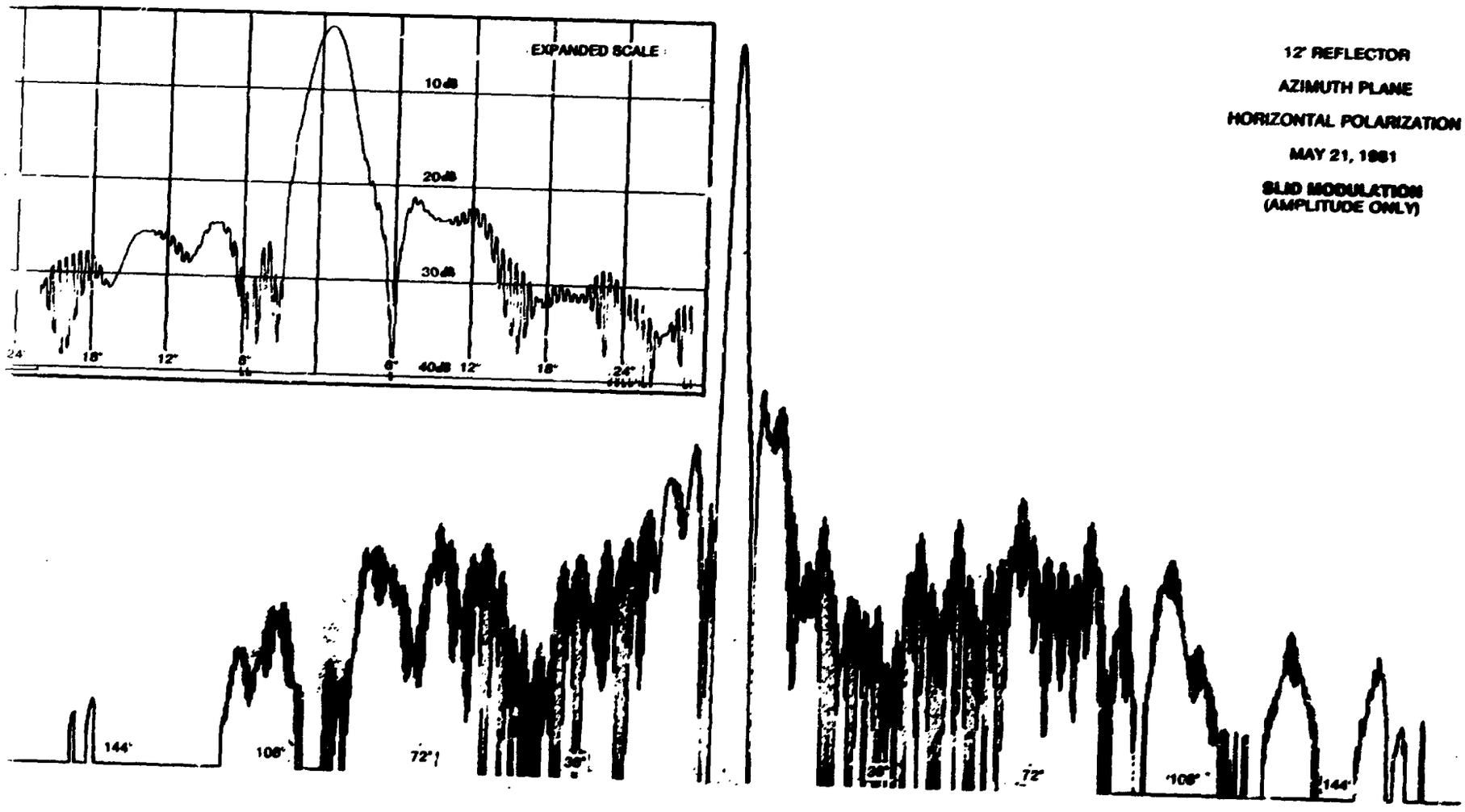

TYPICAL SLID MODULATION

Figure 1

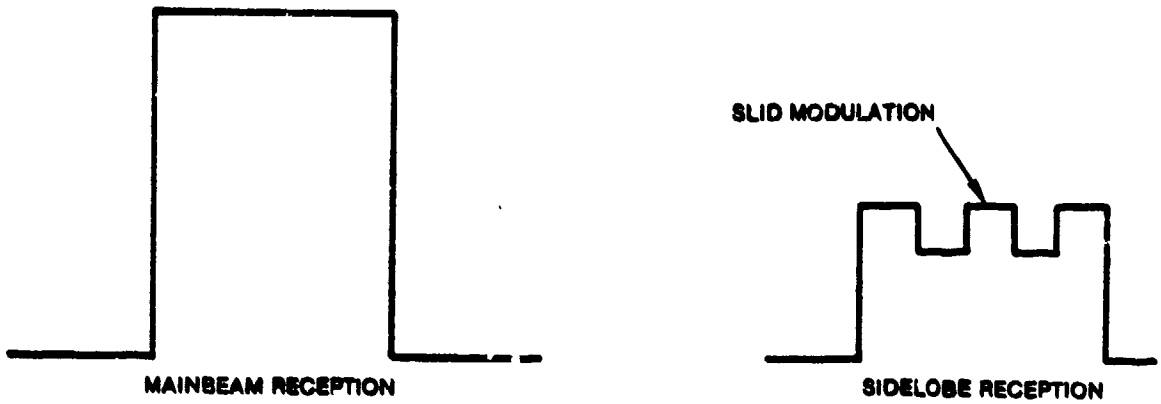

Sample Video Pulses

Figure 2

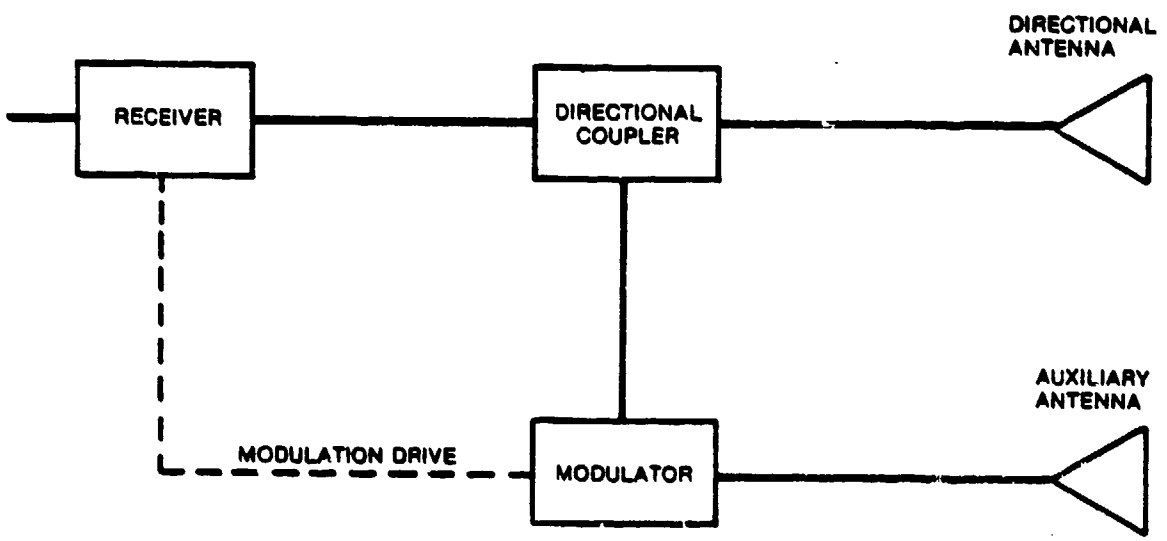

Figure 3

3.0 BASIC SYSTEM MODEL

Various techniques have been used to introduce SLID modulation, the most successful of which includes elements shown in Figure 3.

The receiver and directional antenna represent any ESM system. The auxiliary antenna, modulator and directional coupler are added to introduce low level modulated RF into the system.

An incoming signal generates responses in both the main and auxiliary antennas. The signal in the auxiliary line is modulated at a known rate. The now separate signals are recombined at an arbitrary phase angle and specific coupling level in the directional coupler (see Figure 3). The resultant vector sum generally exhibits both phase and amplitude shifts in response to the auxiliary channel modulation. In Figure 4, the phasor diagram, shows the basic model for SLID.

This vector model provides another viewpoint of the basic SLID mechanism. Comparing the ratio of the main to auxiliary signals on the antenna mainbeam ratios of 30 dB or more are observed. In contrast, sidelobe to auxiliary ratios are about 0 dB which accounts for the significant modulation seen in the sidelobes and the absence of detectable modulation in the mainbeam. (See Figures 1 and 5).

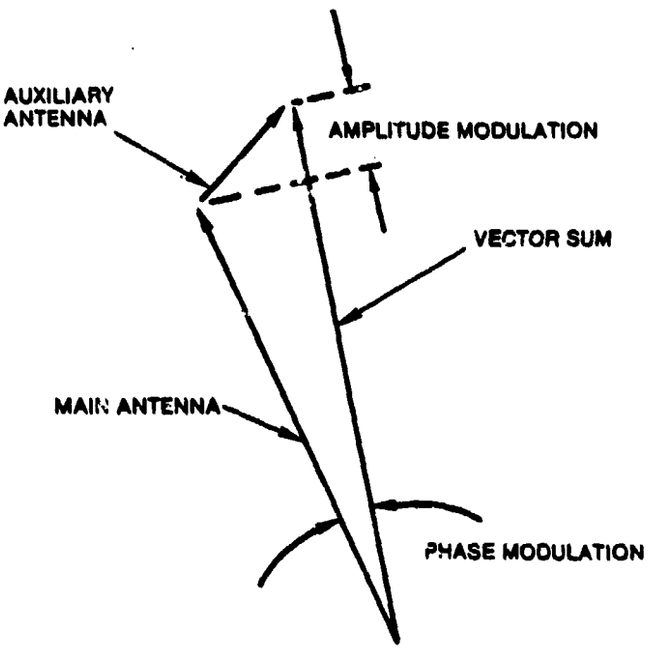

Basic Phasor Diagram

Figure 4

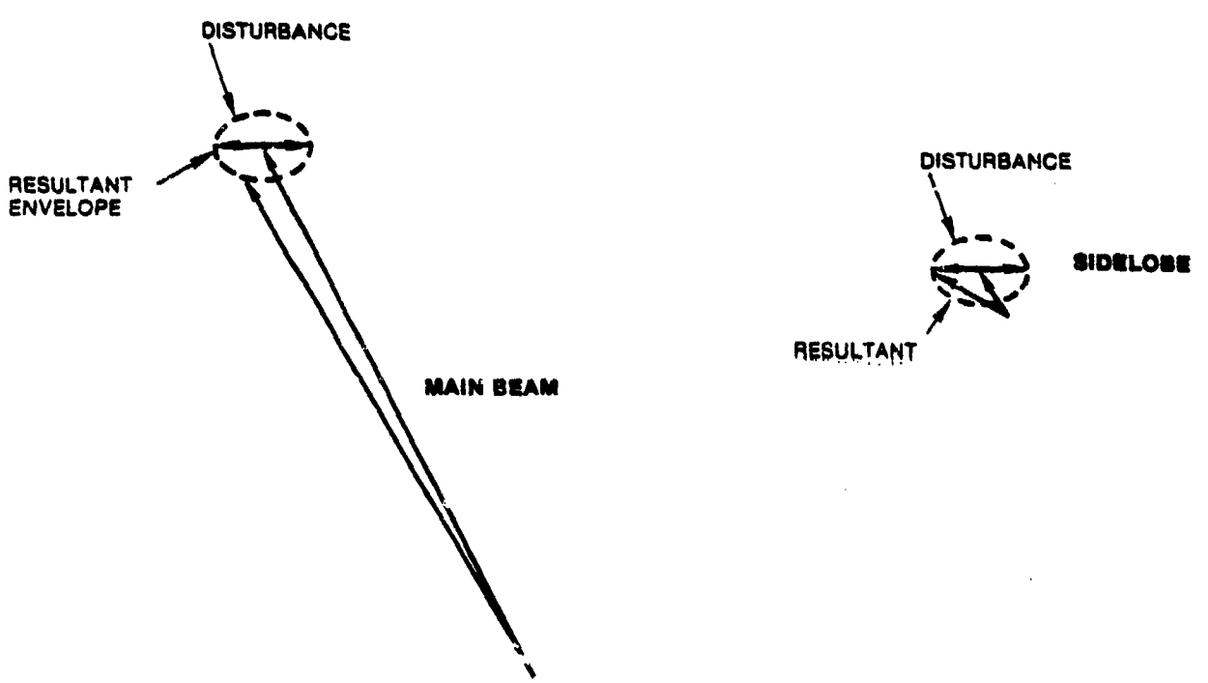

SLID Phasor Model

Figure 5

4.0 SYSTEM DEVELOPMENT

Improvements to this technique since its initial discovery fall into three categories: modulator, detector and auxiliary antenna.

The earliest modulator was a mechanical device, quickly rejected because of its limited speed. Mechanical modulators have produced the most uniformly modulated radiation patterns but the severe speed limitation makes them impractical. Higher rates are necessary to label narrow pulses. PIN diode and double-balanced mixer modulators were next. A disturbance exhibiting either phase modulation, amplitude modulation or both (depending upon signal DOA) was produced. The PIN switch technique is limited to about 10 MHz modulation rates and by lower modulation levels when compared to a double-balanced mixer.

Present applications use a single side-band mixer (SSB) because it guarantees the presence of both phase and amplitude modulation on any sidelobe independent of antenna position. This simplifies the detection circuit which presently limits the maximum modulation rates. When compared to a double-balanced mixer the SSB modulator exhibits comparable modulation speeds, slightly higher conversion loss and slightly reduced RF bandwidth. The disadvantages are presently overbalanced by improvements in the detector circuitry which are not compatible with the double balanced mixer technique (Figure 6 compares the various modulators).

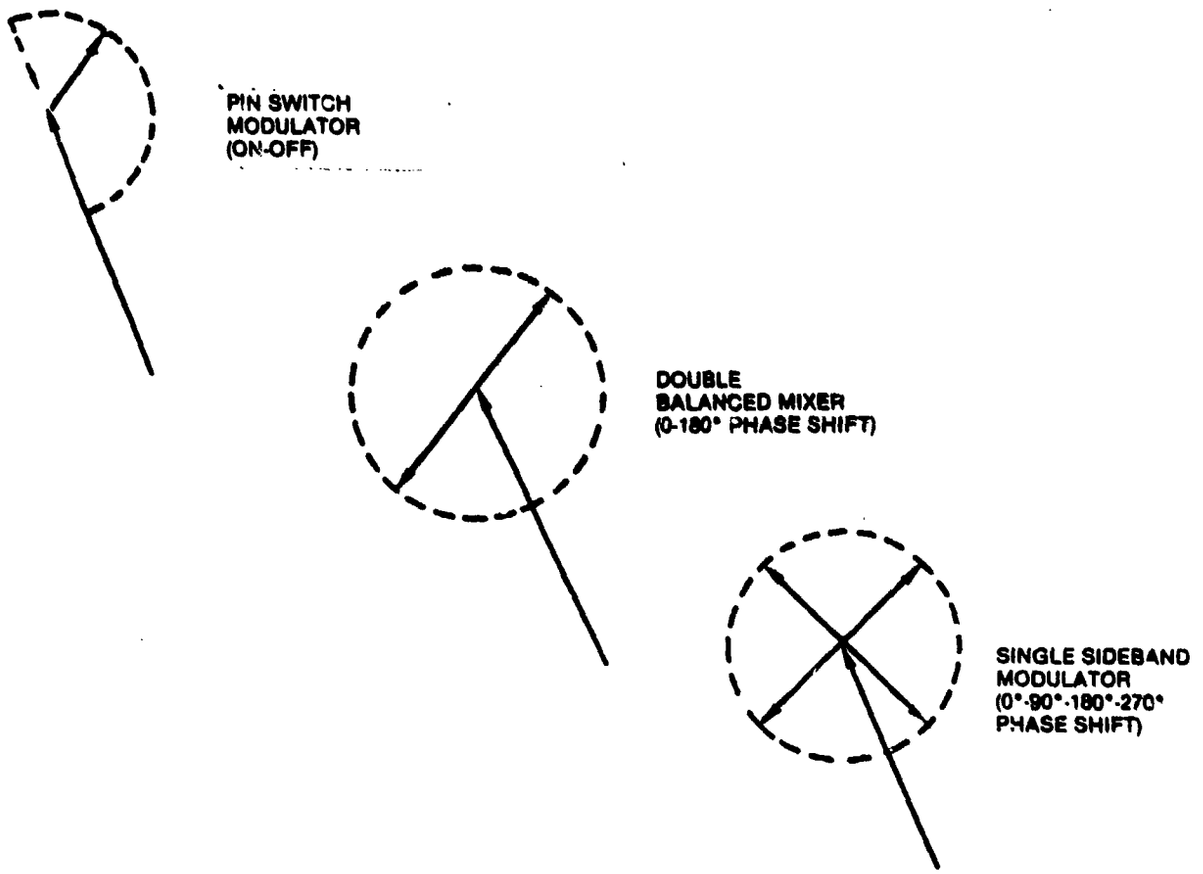

Comparison of Various Modulators

Figure 6

Detector design involved developing of two subsystems. Phase modulation detection centers around various polar discriminator circuits similar to a single cell of an IFM (Instantaneous Frequency Measurement) receiver. Amplitude modulation detection depends upon logarithmic amplifiers to extract percent modulation. Log amplifiers with sufficiently short relaxation times and bandwidth have limited modulation to 10-20 MHz. Current efforts center about a SSB.

The present prototype uses a SSB modulator and polar discriminator at 30 Mhz. This will allow mainbeam/sidelobe decisions on a pulse by pulse basis for pulses as short as 100 nsec.

The final element in the SLID system is the auxiliary antenna. This element introduces the disturbance which is used to label sidelobe DOA. Surprisingly SLID is not critically dependent upon the auxiliary antenna performance. Unless severe sensitivity requirements exist. The auxiliary antenna gain and main antenna sidelobe levels need to be close (within ±10 db) for sufficient modulation. Increased main beam to auxiliary isolation is possible when the auxiliary radiation pattern includes a null coincident with the main antenna boresight or main beam. This feature allows significant improvements in DOA accuracy but has not yet been exploited. The ideal auxiliary pattern is therefoe a cardoid which generally covers the main antenna sidelobes and has a null in the main beam direction. Other auxiliary patterns however, have been used and were quite satisfactory. A designer has significant latitude in this area.

5.0 PROTOTYPE DEVELOPMENT

SLID hardware has been developed for two distinct applications, contrasted in Table 1.

There are two differences between the development programs presented here. The U.S. Navy system includes a highly directive antenna with high sidelobes and a computerized analysis system. Computerized ESM has generally been unsuccessful because the tremendous processing requirements generated in today's dense electronic environments. The Development of SLID significantly reduce this problem by facilitating the rejection of pulses received through antenna sidelobes prior to computer processing. This combination of sidelobes and computer (for the Navy system) processing places severe design constraints on the SLID hardware. In comparison the USAF system is manually operated and only moderately directive. Consequently a less complicated design was possible.

Table 1 SLID Prototype Hardware

U.S. NAVY	U.S. AIR FORCE
ANTENNA: 12' PARABOLA	3' PARABOLA
GAIN: 45 dBi TYPICALLY	25 dBi
SIDELOBE LEVEL: 10-20 dB	20 dB
FREQUENCY COVERAGE: 5 OCTAVES	5 OCTAVES
APPLICATION: COMPUTERIZED ELINT	MANUAL ELINT

6.0 USAF PROTOTYPE

Cubic produces a portion of the QRC system used by the U.S. Air Force. Figure 7 shows an overview of the QRC system and a prototype antenna with SLID modifications. This system was used to test SLID in a controlled environment. Two emitters and a collection antenna (Figure 8) were placed in an anechoic chamber. Without sidelobe identification polar displays similar to Figure 9 are observed when all elements are in rotation.

With SLID the display format changed dramatically. Figure 10 shows a single fixed source (30° relative) without SLID. Figure 11 shows the same source with SLID. (These experiements occured under identical conditions.)

Figure 12 shows a more complicated experiement. Two fixed sources (30° and 330° relative) are active with SLID modulation off. Figure 13 shows the improvement with SLID, activiated. The improvement in DOA measurement accuracy is clearly shown, particularly when multiple emitters must be processed simulataneously.

7.0 U.S. NAVY SYSTEM

A SLID system is presently being developed for a U.S. Navy data collection platform. The antenna, Figure 14, is a 12 foot reflector with a five octave frequency coverage band.

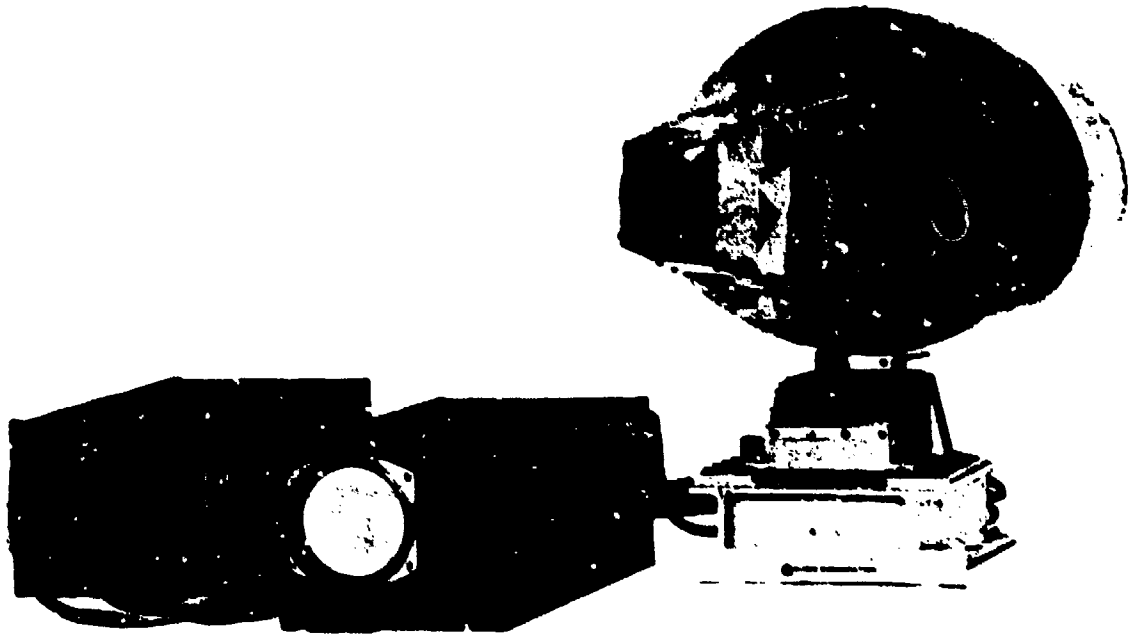

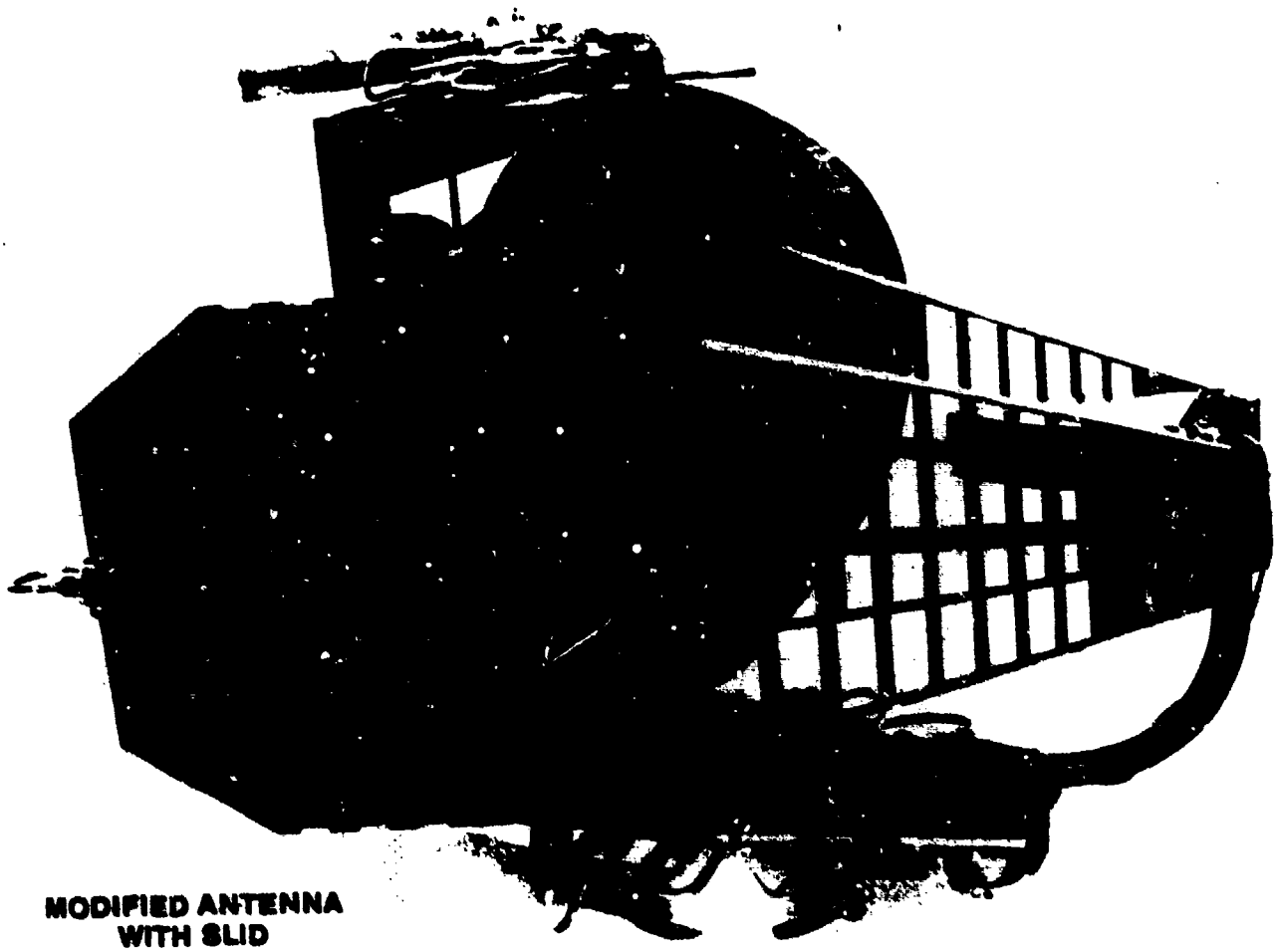

MODIFIED ANTENNA
WITH SLID

QRC SYSTEM OVERVIEW

Figure 7

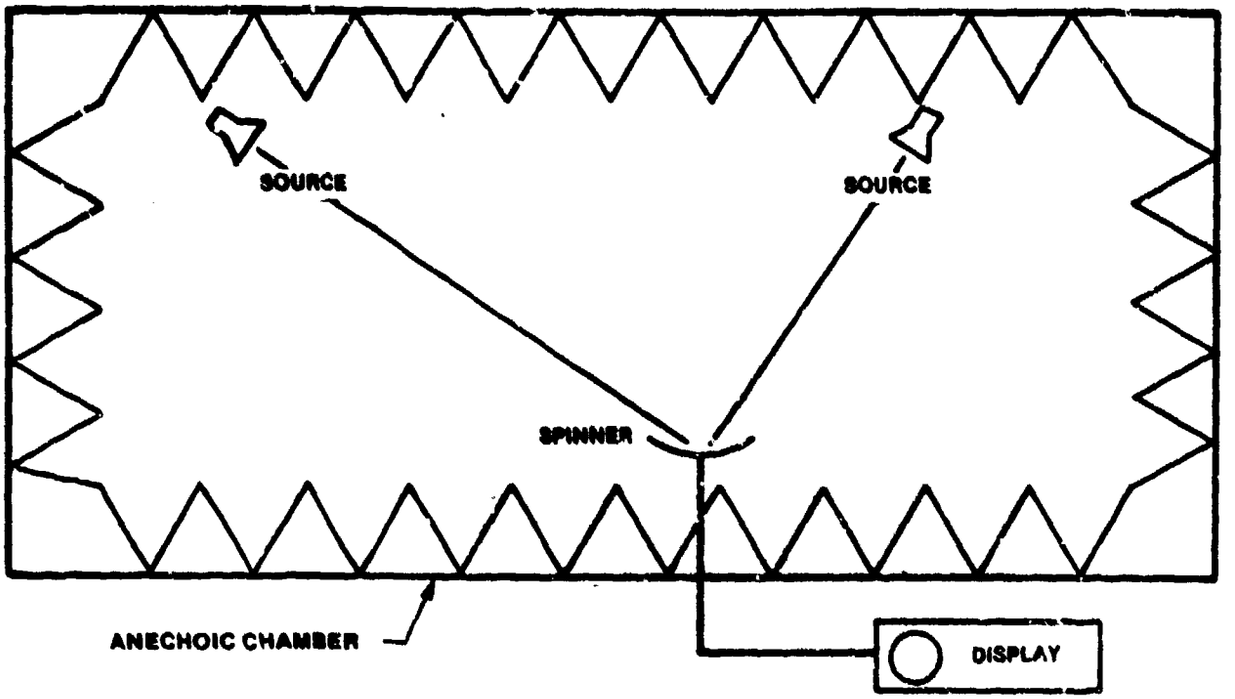

Laboratory Test Model

Figure 8

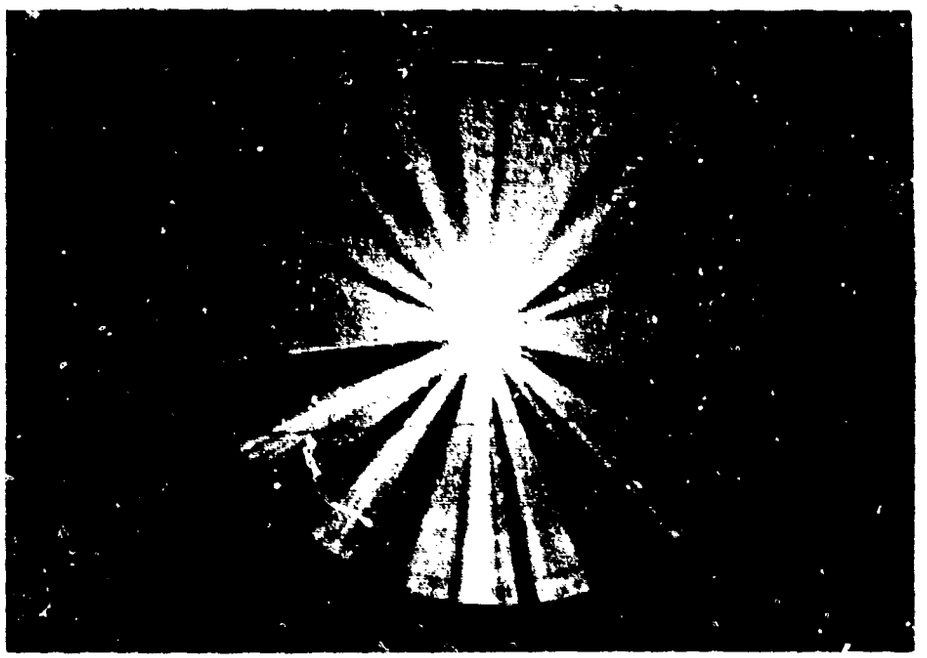

NORMAL DISPLAY
MULTIPLE SOURCES (30° AND 330° RELATIVE)

Figure 9

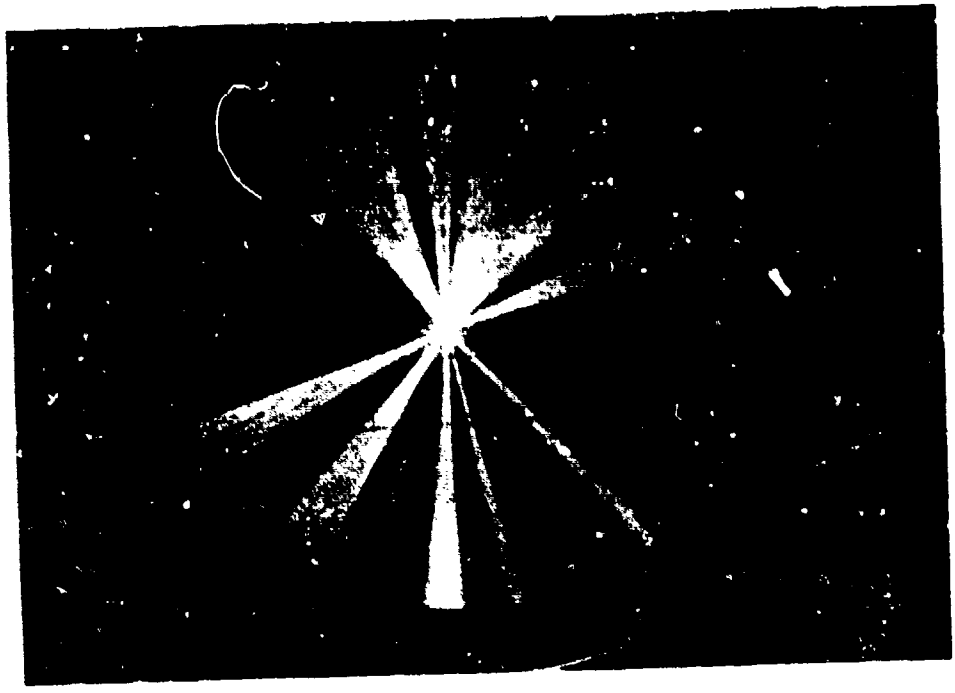

SINGLE SOURCE (30°)
WITHOUT SLID

Figure 10

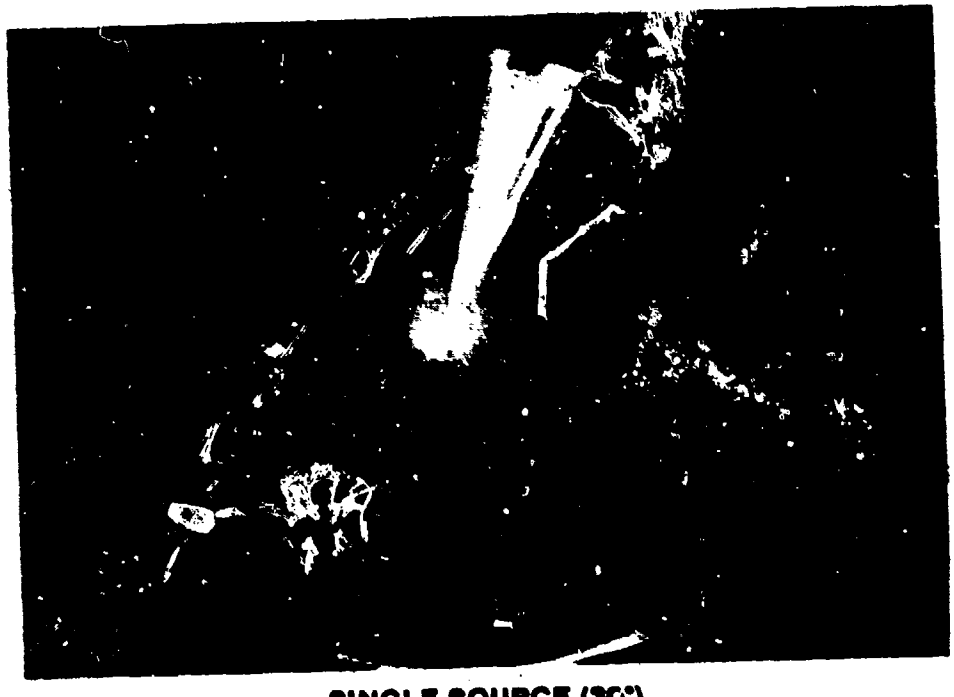

SINGLE SOURCE (30°)
WITH SLID ACTIVE

Figure 11

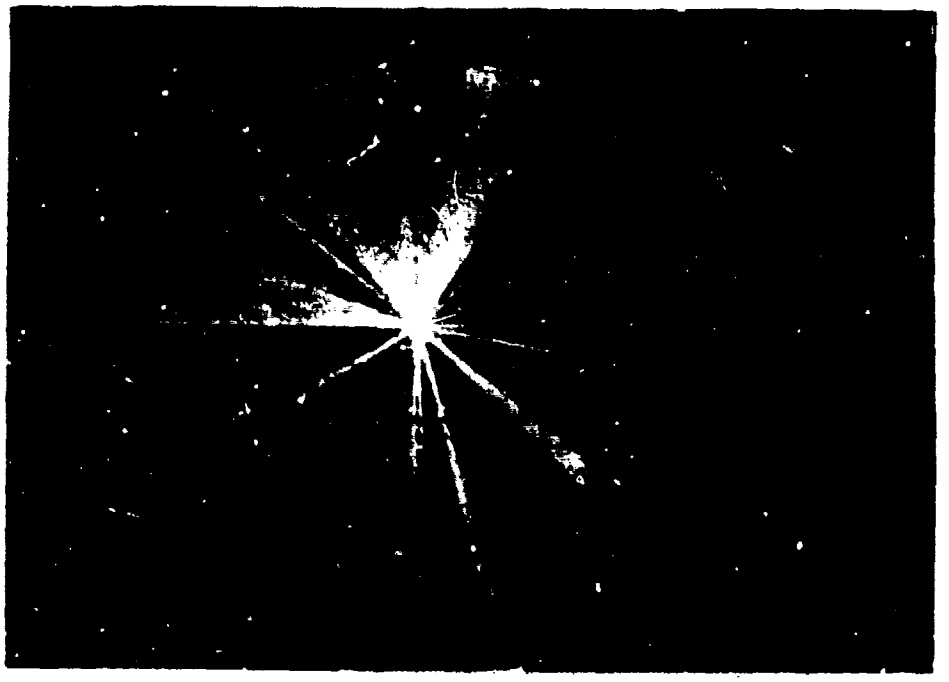

TWO SOURCES (30° AND 330°)
WITHOUT SLID

Figure 12

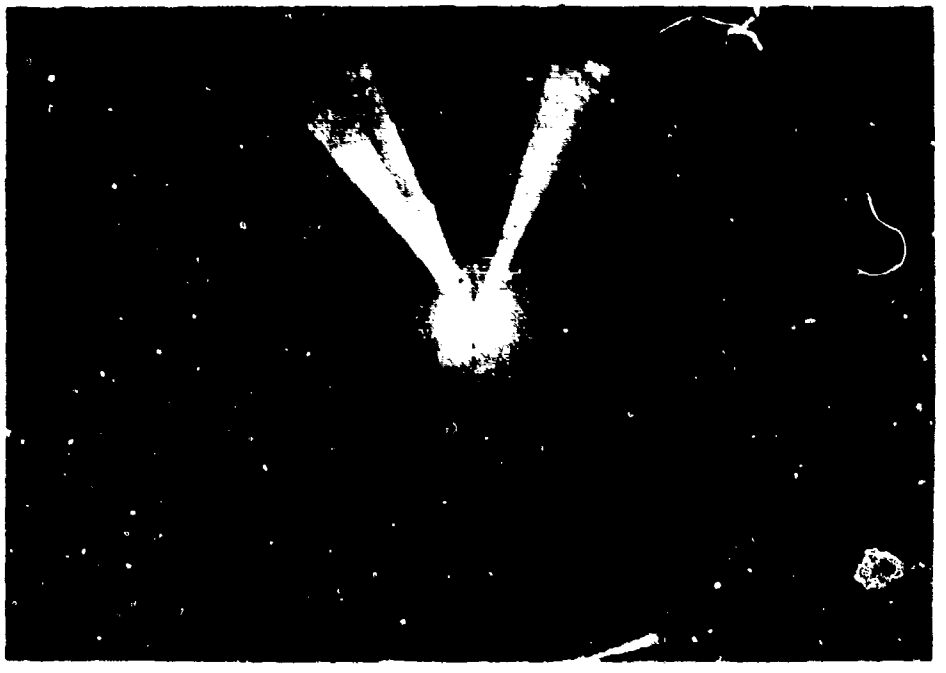

WITH SLID ENABLED

Figure 13

Figure 14

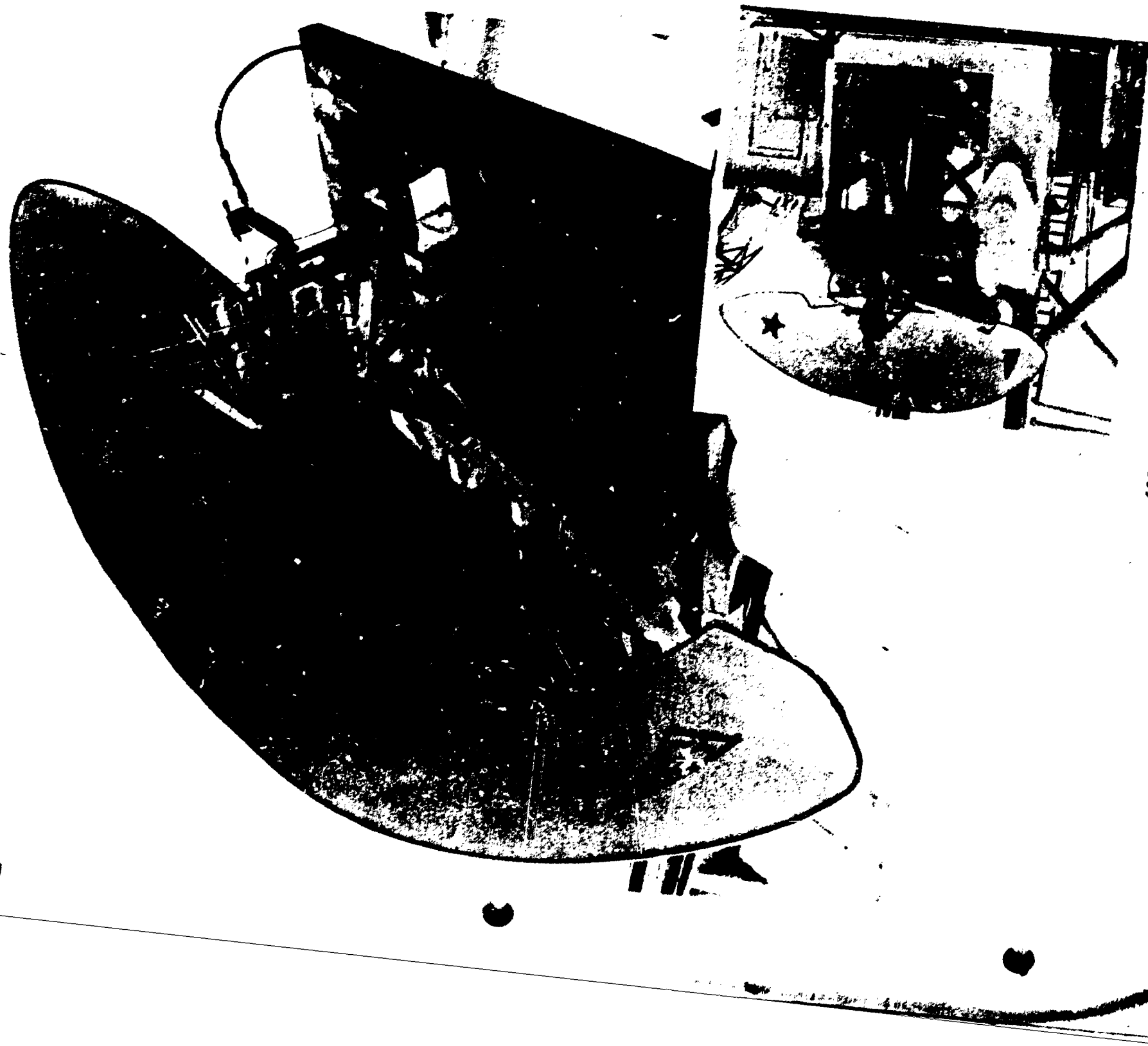

An initial prototype with partial band coverage has been flight tested and compared to a conventional omni-guard sidelobe rejection system. The result of this test in a multi emitter environment is summarized in Table 2.

Table 2 SLID/OMNI-GUARD Comparison

ENVIRONMENT: 40 KNOWN; 25 UNKNOWN EMITTERS

	SLID	OMNI-GUARD
MAINBEAM ACCEPTANCE	80%	80%
SIDELOBE REJECTION	90%	34%

Further development is contracted and presently underway to provide full SLID function over the entire five octave frequency band for this system; delivery is projected for March 1983.

8.0 SUMMARY

Prototype hardware demonstrates SLID's success. The 12 foot reflector system presented significant technical challenges to the auxiliary antenna and SLID processor. The smaller QRC unit is representative of a more typical system. Sidelobe rejection performance is very good for both systems. SLID presents a low cost, effective alternative to the development of ultra low sidelobe antennas. Moreover it works well with multi-octave,

highly directive intercept systems. SLID is applicable to systems which develop DOA as a parameter particularly when the system has the potential to be mislead by signals arriving on other than the antenna mainbeam.

ACKNOWLEDGEMENTS

The author would like to recognize the major contributions made by William McNaul, Raymond Justice and J. Thomas Baylor, as well as other members of the Cubic Corporation antenna group. Without their participation this technology would not exist today.

BIBLIOGRAPHY

(1) Eberhardt, P. R. and McNaul, W. F., "Sidelobe discrimination technique," Antenna Application Symposium, Sept. 22, 1971.

(2) Eberhardt, P. R. and McNaul, W. F., "Sidelobe discrimination," U.S. Patent No. 4266226, issued May 5, 1981.

(3) Hurley, R., et. al., "Interrogator/transponder sidelobe inhibition," Naval Research Laboratory IFF Symposium, March 15, 1980.